TRANSITION PHYSICS AND BOUNDARY-LAYER STABILITY: COMPUTATIONAL MODELING IN COMPRESSIBLE FLOW

A Dissertation

by

ETHAN SAMUEL BEYAK

Submitted to the Graduate and Professional School of
Texas A&M University
in partial fulfillment of the requirements for the degree of

DOCTOR OF PHILOSOPHY

Chair of Committee,	Helen L. Reed
Committee Members,	Rodney D. W. Bowersox
	Edward B. White
	Prabir Daripa
Head of Department,	Ivett A. Leyva

August 2022

Major Subject: Aerospace Engineering

ABSTRACT

Laminar-to-turbulent transition of boundary layers remains a critical subject of study in aerodynamics. The differences in surface friction and heating between laminar and turbulent flows can be nearly an order of magnitude. Accurate prediction of the transition region between these two regimes is essential for design applications.

The objective of this work is to advance simplified approaches to representing the laminar boundary layer and perturbation dynamics that usher flows to turbulence. A versatile boundary-layer solver called DEKAF including thermochemical effects has been created, and the in-house nonlinear parabolized stability equation technique called EPIC has been advanced, including an approach to reduce divergent growth associated with the inclusion of the mean-flow distortion. The simplified approaches are then applied to advance studies in improving aircraft energy efficiency.

Under the auspices of a NASA University Leadership Initiative, the transformative technology of a swept, slotted, natural-laminar-flow wing is leveraged to maintain laminar flow over large extents of the wing surface, thereby increasing energy efficiency. From an aircraft performance perspective, sweep is beneficial as it reduces the experienced wave drag. From a boundary-layer transition perspective, though, sweep introduces several physical complications, spawned by the crossflow instability mechanism. As sweep is increased, the crossflow mechanism becomes increasingly unstable, and can lead to an early transition to turbulence. The overarching goal of the present analysis then is to address the question, *how much sweep can be applied to this wing while maintaining the benefits of the slotted, natural-laminar-flow design?* Linear and nonlinear stability analyses will be presented to assess various pathways to turbulence.

In addition, companion computations are presented to accompany the risk-reduction experiment run in the Klebanoff-Saric Wind Tunnel at Texas A&M University. Linear analyses assess a wide range of various configurations to inform experimentalists where relevant unstable content resides. A comparison between simulation and experimental measurements is presented, for which there is a good agreement.

DEDICATION

a single verse

may well be

all we get

ACKNOWLEDGMENTS

> "Gratitude is the foundational understanding that many millions of things must come together and live together and mash together and breathe together in order for us to take even one more breath of air." -David Whyte

Throughout my time here in College Station, I have been incredibly blessed by such a warm, friendly, and welcoming group of people who have helped guide my studies at Texas A&M. The work presented here would be a shell of what it is if it weren't for the collaboration and engagement together on all fronts.

I would like to first thank my advisor Dr. Helen Reed, for she has been phenomenal to me. By first granting me the opportunity to pursue this graduate degree in 2017, she has relentlessly believed in me, given me the chance to grow and flourish as an engineer and as a human. She seamlessly causes me to assess my own technical analysis and presentation more critically in ways I hadn't before, which is a habit I'll hold onto for the rest of my career. I am indefinitely grateful for the education provided by Dr. Reed and the opportunity to advance science together.

I've been graced with such an intelligent and varied group of colleagues while in the Computational Stability and Transition lab. I would like to acknowledge that from day one, my colleagues Alex Moyes, Travis Kocian, Andrew Riha, and Daniel Mullen helped usher me into graduate school and get me started as a young computationalist. We've shared quite a few laughs together along the way, and for that, I am thankful. I must give special mention to the visiting scholars we've had join us during my time at A&M: Fernando Miró Miró, Koen Groot, and Ludovico Zanus. Fernando and Koen sparked a sudden rush in all of us to code up a new the boundary-layer solver, DEKAF. I do not want to understate its importance: DEKAF forms the heart of all of the presented stability analysis in this dissertation. Developing it together wasn't just an excellent opportunity to learn important skills as I was entering graduate school, but it was *fun* too. For that, I am thankful. And to Ludo: he is an incredibly kind soul and smart individual. His fresh per-

spective on stability methods brought us as a lab closer together, challenging us to become better scientists and engineers. He also was perennially ready for a quick chess game or two. I'm also hugely grateful to have collaborated so closely with my labmates Danny Heston, Madeline Peck, and Jay Patel. Danny brought the well-needed light-heartedness as well as the heart-to-heart conversations. Madeline and Jay have cemented joy in all of our lab conversations, bringing a wealth of indispensable, technical knowledge as well as the memes. For that, I am thankful.

I want to acknowledge all the help Dr. Ed White provided concerning our analysis with experiments on the X207.LS. His guidance was well-needed and grounding, without which there would be no appreciable comparison between the simulations and experiments. I would like to make a special point to acknowledge the experimentalist, Jeppesen Feliciano. It was at first the work that brought us close, considering the same physical phenomena from two different perspectives. But what brought us even closer was our friendship on newly born ground. From strangers to roommates to now someone I could call a brother, Jeppesen and I have shared countless moments of joy, of sadness, of depth and laughter. Thank you for making these years what they have been, for simply being you, effortlessly you.

I would like to thank the other members of my committee, Dr. Rodney Bowersox and Dr. Prabir Daripa for their helpful advice, suggestions, and unique perspectives during our conversations. I'm grateful to have taken the courses Aerothermodynamics from Dr. Bowersox and Hydrodynamic Stability from Dr. Daripa: both have laid the well-needed foundation for aerospace and mathematics education that I hold dear.

The Texas A&M staff who have made this possible, I would like to thank them especially: Rebecca Marianno, Leona Bay, Kendall Lackey, Gail Rowe, and countless others. Navigating the graduate student experience was never without support, organization, and experience. Our whole lab would be lost without the work they've done.

Of course, all of this would not be possible without my family and friends across the country. They've supported me when I needed it the most, and believed in me every step of the way. I love them all deeply.

CONTRIBUTORS AND FUNDING SOURCES

Contributors

This work is supported by a dissertation committee consisting of my advisor, Helen L. Reed and professors Rodney D. W. Bowersox, Edward B. White, and Prabir Daripa. Experimental measurements of flow over the X207.LS have been provided by Jeppesen G. Feliciano. The pressure coefficients over multiple configurations of the S207 have been computed with NASA's OVERFLOW by Dr. James G. Coder.

Funding Sources

This material is based upon work supported by the National Aeronautics and Space Administration (NASA) under cooperative agreement award number NNX17AJ95A. Swept-wing analysis presented in this dissertation is part of a NASA University Leadership Initiative (ULI) aimed to design an ultra-efficient airframe for next-generation aircraft. Led by The University of Tennessee, Knoxville (UTK), several universities across the U.S. paired with industry seek to accomplish this goal together with A&M. This work has been supported by the U.S. Air Force through the National Defense Science and Engineering Graduate (NDSEG) Fellowship Program and a graduate research assistantship through Texas A&M University's Aerospace Engineering department.

NOMENCLATURE

English variables, lowercase

a	Speed of sound
a, b	Coefficients to Orr-Sommerfeld ODE: Eq. (5.3)
a_L, a_R	$O(1)$ constants used in the mean-flow distortion's α limiters: Eq. (5.22)
c	Representative chord length along the x coordinate of the wing
c_1, c_2, c_3, c_4	Complex-valued coefficients for the analytical solution $\hat{v}$: Eq. (5.4)
c_p	Specific heat at constant pressure
c_{ph}	Three-dimensional phase speed of a disturbance: Eq. (6.8a)
$\vec{c}_{ph}$	Three-dimensional phase velocity: Eq. (7.2)
c_v	Specific heat at constant volume
cst	Arbitrary constant
d_{DRE}	Discrete roughness element (DRE) diameter
$\mathrm{d}\theta$	Representative small angle: Fig. 2.1
e	Internal energy
$\hat{e}_s, \hat{e}_y, \hat{e}_z$	Unit vectors for the computational-relevant frame: §6.3.1
$\hat{e}_{X_t}, \hat{e}_{Y_t}, \hat{e}_{Z_t}$	Unit vectors for the wind-tunnel frame: §6.3.1
f	Frequency
$f_{(n,k)}$	Nonlinear forcing vector in NPSE: Eq. (4.37)
$f_{(n,k)}^{\mathrm{quad}}$	Quadratic (second-order) interaction terms: appendix B
$f_{(n,k)}^{\mathrm{cubic}}$	Cubic (third-order) interaction terms: appendix B

f	Self-similar velocity whose $\partial f/\partial\eta = \overline{u}/\overline{u}_e$: §7.2.2
g	Gravitational acceleration near Earth's surface: $9.81\,\mathrm{m/s^2}$
g_{ij}	Metric tensor
h	Static enthalpy
h	Arbitrary function of a single variable (Chapter 5)
h_i	Square root of g_{ii} entry, also known as a scaling factor for orthogonal, curvilinear coordinates along coordinate x^i: Eq. (2.7)
h_{tot}	Total enthalpy
i	Index of discretized, streamwise coordinate s
i	Imaginary unit whose square is -1
k	Integer multiple on spanwise wavenumbers $k \equiv \beta/\beta_0$
k_1, k_2, k_3	Values of k for three disturbances: see §4.3.1.3
k_1, k_2	Wavenumbers for the analytical solution $\hat{v}$: Eq. (5.4)
k_{B}	Boltzmann constant
k_{DRE}	Discrete roughness element (DRE) height
$\vec{k}$	Complex-valued wave vector: Eq. (6.8h)
$\mathrm{mean}(V_{\mathrm{hw}},\, z)$	Spanwise average of V_{hw}
n	Integer multiple on frequencies $n \equiv \omega/\omega_0$
n_1, n_2, n_3	Values of n for three disturbances: see §4.3.1.3
n_{sam}	Number of samples of a data set: §6.4
n_{sw}	Number of spanwise waves along curvilinear z
p	Pressure
q	Vector of flow variables $[u, v, w, T, \rho]$
$\hat{q}^{\mathrm{aug}}$	Augmented eigenfunction for LST: Eq. (4.5)
r_1, r_2, r_3, r_4	Real-valued coefficients for the analytical solution $\hat{v}$ with $\alpha = 0$: Eq. (5.12)

s_1	First streamwise coordinate of s
s_{equi}	Equispaced s-domain
s_g	Preliminary surface coordinate of airfoil geometry (Chapter 3)
s_i, s_f	Initial and final values of the s coordinate
s_{stag}	Attachment-line value of s_g (Chapter 3)
$\breve{s}$	Slowly varying s coordinate: Eq. (4.9)
s, y, z	Streamwise, wall-normal, and spanwise coordinates of an orthogonal, curvilinear coordinate system, right-handed
t	Time
$\hat{u}_{\text{extr}\,\hat{v}}$	$\hat{u}$ evaluated at an extremum of $\hat{v}$ inside the boundary layer
$\overline{u}_s, \overline{w}_s$	Velocity components parallel and orthogonal to the local inviscid streamline: Eq. (6.5)
u	Measured hot-wire velocity within the boundary layer: only §6.3.2
u_{avg}	Spanwise-averaged hot-wire velocity u: only §6.3.2
u, v, w	Physical velocity components along the s, y, and z directions, respectively
u_t, v_t, w_t	Velocity components along X_t, Y_t, Z_t: §6.3.1
u^j	Velocity along generalized coordinate x^j
w_0	Freestream velocity component parallel to the leading edge
x	Abscissa of airfoil cross-section coordinates
x^1, x^2, x^3	Generalized coordinates, right-handed
y	Wall-normal coordinate (see s and z)
z	Spanwise coordinate (see s and y)

English variables, uppercase

A	Representative amplitude of a disturbance

A_0	Initial amplitude
A_ξ, B_ξ, a_ξ	Coefficients associated with $\tanh$-mapping: §3.3
C_1	Continuity integration constant: Eq. (5.20)
$C_p^{\text{in}}, C_p^{\text{out}}$	Pressure coefficient values at the inboard and outboard of the X207.LS model
$C_p^{Q_\infty}$	Pressure coefficient based on the resultant velocity: Eq. (3.1)
$C_p^{\overline{u}_\infty \overline{v}_\infty}$	Pressure coefficient based on the leading-edge-orthogonal velocity component: Eq. (3.1)
$C_{p,\max}^{\overline{u}_\infty \overline{v}_\infty}$	Maximally attainable isentropic pressure coefficient: Eq. (3.2)
C_μ	Sutherland's combined constant: Eq. (2.6a)
$\mathrm{D}/\mathrm{D}t$	Substantial derivative operator: Eq. (2.3)
Ec	Reference Eckert number
$F_{(m_1,m_2)}^{\text{quad}}$	Summand of $f_{(n,k)}^{\text{quad}}$, accounting for harmonic balancing: appendix B
$F_{(m_1,m_2,m_3)}^{\text{cubic}}$	Summand of $f_{(n,k)}^{\text{cubic}}$, accounting for harmonic balancing: appendix B
Gr_ℓ	Reference Grashof number
H	Boundary-layer shape-factor: Eq. (6.6)
K	Summation bound of k in NPSE ansatz: Eq. (4.22)
K	Coefficient matrix to the Orr-Sommerfeld boundary-value problem: Eq. (5.7)
K_{por}	Acoustic impedance of a cylindrical pore
L	Representative length
LU	LU-decomposition of $\mathcal{L}$
M	Reference Mach number
N	N-factor, or integrated growth of a disturbance: Eq. (6.7)
N	Summation bound of n in NPSE ansatz: Eq. (4.22)

N	Number of gas particles: Eq. (2.20)
N_m	Number of Fourier modes necessary to solve PDEs for in NPSE: §7.4.1.3
$N_{m,\,\mathrm{full}}$	Full number of Fourier modes in NPSE simulation (including conjugates)
$N_{s,\mathrm{equi}}$	"Equivalent equispaced" streamwise resolution: Eq. (4.20)
Pr	Reference Prandtl number
Q	Arbitrary quantity
Q_∞	Freestream resultant velocity
Re	Reference Reynolds number
Re'	Unit Reynolds number
R_1, R_3	Radii of curvature in the s and z directions, respectively
$\mathrm{R}_1, \mathrm{R}_2, \mathrm{R}_3$	Rotation matrices: Eq. (6.11)
R_g	Specific gas constant
$\mathrm{Real}, \mathrm{Imag}$	Operators to select the real and imaginary parts of a complex variable
S_μ	Sutherland's constant: Eq. (2.6a)
T	Temperature
T_{ref}	Sutherland's reference temperature: Eq. (2.6a)
T_v	Vibrational temperature
U, V, W	Velocity components along the (X, Y, Z) coordinates
U	Measured hot-wire velocity in the inviscid flow: only §6.3.2
V_{hw}	Velocity projected onto plane orthogonal to the hot-wire's axis: Eq. (6.14)
$\vec{V}^c$	Velocity vector in the computational-relevant frame: Eq. (6.9)
$\vec{V}^t$	Velocity vector in the wind-tunnel frame: Eq. (6.9)

$\mathcal{X}$	Logical coordinate, equispaced on $[0, 1]$: §3.3
X, Y, Z	Cartesian coordinates, right-handed
X^1, X^2, X^3	Cartesian coordinates, right-handed
X_t, Y_t, Z_t	Coordinates for the wind-tunnel frame: §6.3.1
Y_c	Ordinate of airfoil cross-section coordinates

Miscellaneous symbols

ℓ	Representative length scale for nondimensionalization, sometimes referred to as the Blasius length: Eq. (2.13)
$\nabla\cdot$	Divergence operator over Cartesian coordinates (X, Y, Z)
$\propto$	"Proportional to"

Greek letters, lowercase

α	Angle of attack
α	Streamwise wavenumber along the s-coordinate
$\alpha_{\text{map}}, \beta_{\text{map}}, \gamma_{\text{map}}$	Constants associated with power-law mapping: Eqs. (4.14) and (4.18)
α_i	Imaginary part of α
$\alpha^*_{i_1}$	First positive root of $\det(K)$ as a function of α_i
$\alpha^{\overline{v}_\infty}_{\overline{u}_\infty}$	Angle of attack defined as $\arctan \frac{\overline{v}_\infty}{\overline{u}_\infty}$
β	Spanwise wavenumber along the z-coordinate
β_0	Smallest spanwise wavenumber in an NPSE simulation
β_{VT}	Volumetric coefficient of thermal expansion
β_{H}	Beta-Hartree parameter: Eq. (3.5)
γ	Ratio of specific heats
δ	Representative boundary-layer height
δ_{50}	Height where $\overline{u}/\overline{u}_e = 0.50$

δ_{99}	Boundary-layer height based on $\overline{u}/\overline{u}_e = 0.99$
δ_1^*	Boundary-layer displacement thickness
$\delta_{100.1}^{h_{\text{tot}}}$	Boundary-layer height where $h_{\text{tot}}/h_{\text{tot},e} = 1.001$
ϵ	Representative measure of error or uncertainty
ϵ_s	Shift within power-law mapping: Eq. (4.18)
$\epsilon_{\text{tol, LST}}$	Convergence tolerance of the governing LST equations
$\epsilon_{\text{tol, nl}}$	Convergence tolerance of the nonlinear iterations in NPSE: Eq. (4.53)
$\epsilon_{\text{tol, }\alpha}$	Convergence tolerance of the auxiliary equation in PSE: Eq. (4.40)
$\epsilon_{\alpha,\,(n,k)}$	$\lvert\Delta\alpha_{(n,k)}\rvert$: Eq. (4.40)
ϵ_ξ	Shift within power-law mapping: Eq. (4.19)
ε_p	Mathematical epsilon for perturbation variables: Eq. (2.21)
ε_s	Mathematical epsilon for slowly varying variables: Eq. (4.9)
η	Wall-normal self-similar coordinate for DEKAF
η	Wall-normal logical coordinate over a domain $[0, 1]$ for EPIC: Eq. (4.7)
η^*	Wall-normal logical coordinate clustered via cosine mapping: Eq. (4.8)
θ	Local angle along airfoil's surface: Eq. (6.10)
ϑ	Argument of the PSE wave: Eq. (4.56)
κ	Coefficient of thermal conductivity
λ	Resultant wavelength in the direction of the wave angle: Eq. (6.8g)
λ_s	Streamwise wavelength along the s-coordinate
λ_v	Second viscosity coefficient
λ_z	Spanwise wavelength along the z-coordinate

$\lambda_{z,\mathrm{DRE}}$	Discrete roughness element (DRE) wavelength
λ_{H}	Hermite constant
μ	Dynamic viscosity coefficient
μ_B	Bulk viscosity
μ_{ref}	Sutherland's reference viscosity: Eq. (2.6a)
ν	Kinematic viscosity μ/ρ
ξ	Self-similar streamwise coordinate used in DEKAF: Eq. (3.6)
ξ	Streamwise logical coordinate as implemented in EPIC
ξ_i, ξ_f	Initial and final values of the ξ coordinate
ρ	Density
σ	Relaxation parameter
$\sigma_{q'}$	Complex-valued streamwise wavenumber with non-parallel effects from q': Eq. (6.7)
σ_x	Standard deviation of a data set x: §6.4
$\sigma_{\overline{x}}$	Standard deviation (error) of the mean of a data set x: §6.4
ϕ	Arbitrary quantity
φ	Representative phase of a wave
ψ_w	Local inviscid streamline angle: Eq. (6.5)
ω	Angular frequency $2\pi f$
ω_0	Smallest angular frequency in an NPSE simulation

Greek letters, uppercase

Δ	Representative change of a quantity
Θ	Boundary-layer momentum thickness
Λ	Sweep angle
$\Lambda_{\sqrt{\overline{u}_\infty^2+\overline{v}_\infty^2}}^{\overline{w}_\infty}$	Sweep angle defined as $\arctan \frac{\overline{w}_\infty}{\sqrt{\overline{u}_\infty^2+\overline{v}_\infty^2}}$

Φ	Representative norm for the N-factor: Eq. (6.7)
$\Phi_{\mathrm{num}}, \Phi_{\mathrm{den}}$	Representative norm values in the numerator and denominator of Eq. (4.39)
$\hat{\Phi}_{(n,k)}$	Intermediate forcing vector in LU substitution: Eq. (4.52)
Ω_p	Switch to include/exclude the streamwise pressure gradient of the shape-function: Eq. (7.2)
Ω_{Re}	Switch to include/exclude slowly varying viscous terms: appendix A
$\Omega_{s,\ell}^{(i,j)}$	Collision integral of order (i,j) of species pair (s,ℓ)

Calligraphic fonts

$\mathcal{A}, \mathcal{B}, \mathcal{C}$	Coefficient matrices for Linear Stability Theory (LST): Eq. (4.3)
$\tilde{\mathscr{D}}_{\mathrm{os}}$	Orr-Sommerfeld parallel operator
$\tilde{\mathscr{D}}_{\mathrm{os,\,np}}$	Orr-Sommerfeld non-parallel operator
$\mathbf{I}$	Identity matrix
$\mathcal{I}$	Representative integral
$\mathcal{L}$	Discretized linear operator for PSE
$\mathcal{L}_2, \mathcal{L}_1, \mathcal{L}_0$	Coefficient matrices for LST as a quadratic, eigenvalue problem: Eq. (4.4)
$\mathcal{L}_1^{\mathrm{aug}}, \mathcal{L}_0^{\mathrm{aug}}$	Coefficient matrices for LST as an augmented, linear, generalized eigenvalue problem: Eq. (4.5)
$\mathcal{LNS}$	Linearized Navier-Stokes operator
$\mathcal{M}_{sy}$, $\mathcal{M}_{yy}$, $\mathcal{M}_s$, $\mathcal{M}_y$, $\mathcal{M}_0$	Coefficient matrices for PSE on s and y
$\mathcal{M}_{\xi\eta}$, $\mathcal{M}_{\eta}$, $\mathcal{M}_{\xi}$, $\mathcal{M}_{\eta}$, $\mathcal{M}_0$	Coefficient matrices for PSE on ξ and η
$\tilde{\mathcal{M}}_{ss}$, $\tilde{\mathcal{M}}_{sy}$, $\tilde{\mathcal{M}}_{yy}$, $\tilde{\mathcal{M}}_s$, $\tilde{\mathcal{M}}_y$, $\tilde{\mathcal{M}}_0$	Coefficient matrices for AH(L)NSE on s and y
$\mathcal{N}$	Nonlinear component of the Navier-Stokes operator
$\mathcal{NS}$	Navier-Stokes operator, assembling Eqs. (2.14)

$\mathcal{NS}_{\partial/\partial t=0}$	Steady Navier-Stokes operator
$\mathbf{O}$	Zero matrix
$\mathbb{T}$	Viscous stress tensor: Eqs. (2.2) and (2.5)
$\mathcal{T}$	Temporal period $1/f = 2\pi/\omega$: Eq. (4.48)
$\mathbf{V}$	Velocity vector $[U, V, W]$ over Cartesian coordinates
$\mathcal{V}$	Volume
$\mathcal{W}_{(n,k)}$	Weighted growth of complex $\alpha_{(n,k)}$: Eq. (4.25)

Subscripts

q_{adiab}	Adiabatic surface quantity
q_{base}	Quantity of a baseline resolution: Eq. (7.1)
q_{crit}	Critical quantity
q_{DRE}	Quantity related to a discrete roughness element (DRE)
q_e	Edge quantity
q_{enth}	Quantity referring to a solution using the enthalpy form of the energy equation
q_{field}	Field of coordinates (both surface and off-wall)
q_i	Clustering value of some quantity
q_i	Quantity at streamwise station i (uncommon)
q_{i+1}	Quantity at streamwise station $i + 1$ (uncommon)
q_{int}	Quantity referring to a solution using the internal energy form of the energy equation
$q_{\text{I,LPSE}}$	Quantity at the branch-I neutral point predicted by LPSE
q_{lam}	Quantity of a laminar boundary layer
q_{max}	Maximum value of some quantity
q_{MFD}	Quantity of the mean-flow distortion (MFD)
q_{min}	Minimum value of some quantity

$q_{(n,k)}$	Quantity of (n,k)-Fourier mode
$q_{\mathrm{ph,ref}}$	Quantity at a reference phase location
q_{Q_∞}	Quantity whose reference velocity is the resultant
q_{ref}	Reference quantity used for nondimensionalization: Eq. (2.13)
q_{RMS}	Root-mean-square quantity
q_{SCF}	Quantity related to stationary crossflow
q_{surf}	Surface coordinate
q_{tr}	Quantity of a transitional boundary layer
q_{traverse}	Quantity corresponding to the traverse
q_{TCF}	Quantity related to traveling crossflow
q_{TE}	Quantity related to the airfoil trailing edge
q_{TS}	Quantity related to Tollmien-Schlichting
$q_{\overline{u}_s}$	Quantity parallel to $\overline{u}_s$
$q_{\overline{u}_\infty \overline{v}_\infty}$	Quantity whose reference velocity is leading-edge-orthogonal
q_w	Wall value of a quantity
q_{wall}	Surface or 'wall' value of a quantity
$q_{\overline{w}_s}$	Quantity parallel to $\overline{w}_s$
$q_{z,\,\mathrm{ref}}$	Reference spanwise freestream quantity
q_ξ	Quantity related to the ξ coordinate
$q_{\delta_{99}}$	Quantity at the δ_{99} height
q_∞	Freestream quantity

Superscripts

q^{i+1}	Quantity at streamwise station $i+1$
q^{linear}	Linear component of a quantity

q^{new}	New quantity: Eq. (4.52)
$q^{p_{\mathrm{nl}}}$	Quantity at previous nonlinear iteration: §4.3.3.1
$q^{p_{\mathrm{nl}}+1}$	Quantity at current nonlinear iteration: §4.3.3.1
q^{p_α}	Quantity at previous α iteration: §4.3.1.5
$q^{p_\alpha+1}$	Quantity at current α iteration: §4.3.1.5
q^{RMS}	Root-mean-square quantity
q^{quad}	Quantity related to quadratic (secord-order) interactions: appendix B
q^{cubic}	Quantity related to cubic (third-order) interactions: appendix B
q^{T}	Transpose of matrix q
$q^{\overline{u}_\infty \overline{v}_\infty}$	Quantity whose reference velocity is leading-edge orthogonal
q^*	Dimensional quantity (Chapter 2)
$q^\dagger$	Complex conjugate of some quantity
$q^{(i)}$	Quantity related to disturbance index i: appendix B
q'	Perturbation quantity
q'	Derivative of a function of a single variable (Chapter 5)

Accents

$\overline{q}$	Laminar base-flow quantity
$\overline{q}$	Dummy variable of integration (uncommon)
$\vec{q}$	Vector quantity
$\tilde{q}$	Dummy variable of integration
$\hat{q}$	Eigenfunction/shape-function quantity
$\breve{q}$	Slowly varying quantity

TABLE OF CONTENTS

Page

LIST OF FIGURES

FIGURE Page

LIST OF TABLES

TABLE Page

1. MOTIVATION AND BACKGROUND

1.1 Motivation

Navigating the space that is being human in modern civilization requires confronting the global catastrophic risks our collective existence faces. With the advancement of technology across the generations, so too has the number of existential threats drastically increased: artificial intelligence, biotechnology, cyberattacks, nanotechnology, and nuclear destruction, to name a few. All of these demand the close attention and research of scientists and thinkers across the globe. But one imminent threat whose effects are already widespread in today's setting is the climate crisis. To address this, the Intergovernmental Panel on Climate Change (IPCC) issued a report in 2018 delineating different approaches to limit global warming to 1.5°C from pre-industrial levels [2]. IPCC researchers estimated only an additional 420 Gt of carbon can be released into the atmosphere such that there is still a $2/3$ chance of restricting global warming to the level of 1.5°C [3]. Beyond these levels of warming, threats to human health, food, water, security, and economic growth all increase, not to mention the irreversible damage and destruction to many ocean ecosystems: with warmer ocean temperatures, less dissolved oxygen is available for marine life [2]. With an estimated 42 Gt of carbon globally released into the atmosphere per year, 2028 is the projected year of reaching the 1.5°C warming limit [3]. However, this projected year may now be inaccurate, as the most recent IPCC report of August 2021 has stated that the earth has already achieved warming of 1.1°C from pre-industrial levels [4]. It is paramount that every sector of technology and industry does its part to reach net zero carbon emissions immediately, else the global impacts of the climate crisis will be devastating.

Within the aerospace industry, commercial aviation is responsible for 2-3% of the global carbon emissions and is one of the top 10 carbon emitters [5]. In 2009, the International Air Transport Association (IATA) established three targets to mitigate CO_2 emissions from air transport: a) on average, improve fuel efficiency by 1.5% per year until 2020; b) cap net emissions from 2020

onward; and c) reduce net emissions by 50% by 2050, relative to 2005 levels. Realizing these targets requires designing new ultra-efficient airframes, propulsion, and advancing the integration of them both [6].

To this end, it is the goal of this research to use and advance computational models in aerodynamics with a focus on improving energy-efficiency of subsonic and transonic commercial aircraft.

1.2 Objectives

The objective of this dissertation is to advance the capabilities of reduced-order methods for boundary-layer stability and transition prediction. In the context of important engineering problems, the versatility of these codes such as DEKAF and EPIC will be demonstrated. For this research, the application of boundary-layer stability analysis will focus on swept wings in compressible flow.

1.3 Background on laminar-to-turbulent transition

Laminar boundary layers, when exposed to freestream disturbances and/or surface roughness, can develop perturbations that grow exponentially, spawned by *primary* instability mechanisms. When these perturbations become large enough, the boundary-layer mean flow deviates from the laminar behavior, and this is often marked by an increase in wall shear or heat flux. This point may be argued to be the onset of transition for the boundary layer after which *secondary* instability mechanisms develop perturbations of their own. Upon significant growth of these, the transitional boundary layer undergoes breakdown and turbulence soon follows.

This story in particular is but one pathway to turbulence from forcing environmental disturbances on a laminar boundary layer. Other pathways involve the mechanics of transient growth and bypass [1, 7, 8]. However these are out of the scope of the current work. Figure 1.1 shows the possible transition pathways. The first part of process, known as receptivity, is where freestream disturbances (e.g., sound, vorticity, entropy variations) enter the boundary layer and form the initial conditions of the disturbance leading the laminar flow to breakdown. How the boundary layer transitions to turbulence is ultimately determined by the amplitude of these environmental distur-

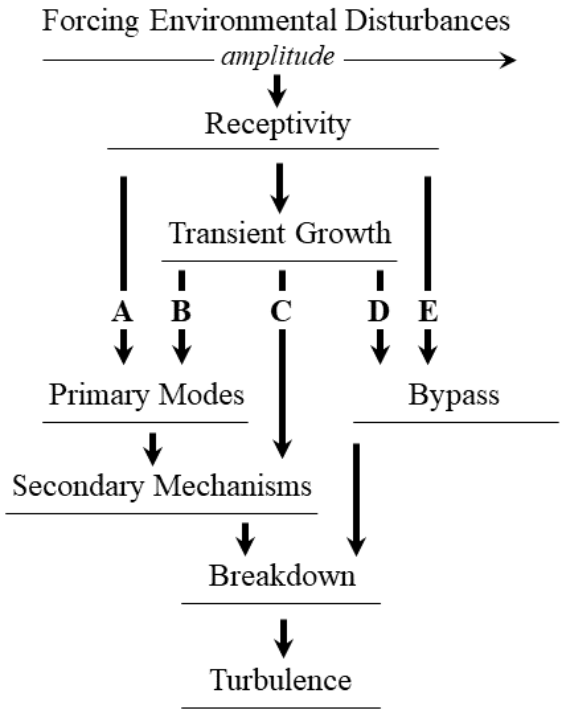

Figure 1.1: The pathways from receptivity to transition [1].

bances: larger disturbance amplification leads to different pathways. The present work focuses on path *A* with the lowest environmental disturbance levels, motivated by the fact that external flows (e.g., flight) are often accompanied by weak freestream disturbances [7]. There is another observation that much of the streamwise extent of the transition process is governed by the linear growth of primary modes compared to that of the nonlinear region for streamwise instabilities, so transition prediction methods of path *A* are often modeled by linear analysis including an amplification factor [7]. In the present work, both linear and nonlinear analyses are applied to study comparative growth for configuration studies and to assess the transition processes at play, respectively.

For completeness, the other pathways will be described briefly. Path *B* specifies that transient growth occurs and provides a slightly higher initial amplitude to the primary modes before their exponential growth. Path *C* experiences amplification through the nonorthogonality of eigenfunctions in the spectrum of linear modes, often the continuous spectrum containing highly stable and oblique modes. Path *D* is largely for internal flows (e.g., wind tunnels) with higher freestream

disturbance levels. Path *E* has such large amplitude forcing that no linear growth occurs before breakdown is reached [9].

For the foundational texts of boundary-layer stability theory, works by Mack and Arnal provide extensive descriptions of the both incompressible and compressible stability problems, including analysis of three-dimensional boundary layers [10, 11]. These include discussions on computational methods surrounding Linear Stability Theory (LST). For a more physically inclusive theory, the Parabolized Stability Equations (PSE) incorporate non-parallel effects: see Herbert [12] for a thorough discussion. These reduced-order models of boundary-layer disturbances will be leveraged heavily in the work presented in this dissertation.

Briefly, the work of theory, computations, and experiments have shown that the following mechanisms can lead to transition for laminar boundary layers:

- Tollmien-Schlichting
- Görtler Instability
- Stationary Crossflow
- Traveling Crossflow
- First-Mode Instability (High-Speed Flow)
- Mack Second-Mode Instability
- Supersonic Mode
- Leading-Edge Contamination
- Attachment-Line Instability
- Transient Growth

All of these demand extensive theoretical discussion and experimental evidence. However, for the scope of this dissertation, only a few relevant to the analysis presented will be highlighted.

The Tollmien-Schlichting (TS) instability is an unsteady wave of vorticity and is formed as a result of a viscous mechanism (i.e., destabilized in the presence of dynamic viscosity) [10]. These waves propagate in the boundary layer and are traveling approximately in the direction of the local inviscid streamline angle. TS can be responsible for transition in 2-D flow over subsonic wings. To stabilize the growth of these waves, favorable pressure gradients, wall suction, and wall cooling may be used [10, 13].

The crossflow instability gives rise to a streamwise-oriented, co-rotating vortex in a bound-

ary layer. The instability is present in flowfields where nonzero pressure gradients act on swept surfaces or on rotating disks [14] and was first experimentally and theoretically analyzed by Gregory et al. [15]. At the boundary-layer edge, the sweep and pressure gradient combine to create curved inviscid streamlines. Within the boundary layer, streamwise velocity is reduced, but the pressure gradient is identical. This leads to an imbalance between the centripetal acceleration and the pressure gradient, twisting the velocity profile through the boundary layer. Since the crossflow velocity component is zero at the wall and at the boundary-layer edge, this leads to an inflection point which provides the source of the inviscid crossflow instability. The growth of this instability may be stabilized by using minimal pressure gradients, wall suction, and low sweep while discrete roughness elements may be used to control it [14].

1.4 Computational approach to laminar-to-turbulent transition

Given the involved physics and the additional effort required for stability analysis, there exist in the literature several correlations that have been used for transition prediction. One example is the ratio of Reynolds number based on momentum thickness divided by the edge Mach number $\mathrm{Re}_\Theta/\mathrm{M}_e$ exceeding a certain criterion which provides an estimate of transition location. Reshotko, however, has demonstated that this ratio is more accurately connected to an altitude from reentry flights rather than a transition location [16, 17]. These methods can lose the physical basis of the problem—that for many pathways to transition, the process is driven by small initial disturbances that grow exponentially within the boundary layer [1].

Staying rooted in the physics, one of the first approaches to model instabilities within was Linear Stability Theory (LST), which first originated in the 1930s [18, 19] and later significantly advanced by Mack [10, 20]. Based on a modal form, LST can predict compute growth rates and shapes of boundary-layer disturbances presuming parallel-flow, i.e., wall-normal velocity and streamwise change are neglected. Based on order of magnitude arguments from the method of multiple scales, linearization provides a powerful way to identify the linear dynamics of boundary-layer disturbances. Through experience, experiment, and computation, it became evident that the streamwise development of these disturbances needed to be included in order to more accurately

describe the boundary-layer instability mechanisms. For that reason, Herbert & Bertolotti in the early 1990s formulated the mathematics of the disturbance assumption known as the Parabolized Stability Equations, or PSE [21, 22, 12]. The equations were written in both a linear (LPSE) and a nonlinear (NPSE) variant, the latter of which would be able to optionally account for nonlinear processes within boundary-layer stability (e.g., mean-flow distortion; subcritical and [simultaneous] multiple instability mechanisms). Non-parallel effects and streamwise history could now be accurately and seamlessly captured in the computational process. The method captured the attention and application from researchers across the globe [23, 24]. Borrowing an idea from the method of multiple scales, PSE leverages the assumption that the laminar base-flow and the disturbance slowly evolve in the streamwise direction. This ultimately approximates the elliptic nature of the wave-like disturbance as parabolic. Using NPSE, Haynes & Reed simulated a stationary cross-flow vortex over a swept wing achieving excellent validation with the measurements by Reibert et al. in the mid-1990s [25, 26]. Joslin et al. demonstrated strong agreement between Direct Numerical Simulations (DNS) and NPSE for several different instability mechanisms at low-speeds [27]. Parades et al. have shown that NPSE and DNS also match very well in highly compressible, hypersonic flow [28].

The practicality of the method hinges on the assumption of slow streamwise variation. When simulating flows with strong variation in multiple dimensions, more physically inclusive disturbance models may be required to accurately simulate the boundary-layer disturbances. With the explosive growth in available computing power, the last two decades have seen a number of methods developed to address boundary-layer instabilities over complex configurations. A two-dimensional extension of LST is known as spatial BiGlobal (SBG), which may be oriented in either a spanwise or streamwise direction [29, 30, 31]. Similarly, the extension of PSE is referred to as plane-marching PSE [32]. Additional linear methods include linearized Direct Numerical Simulations (LDNS) [33], One-Way Navier Stokes [34, 35], Adaptive Harmonic (Linear) Navier-Stokes Equations [36, 37], forced DNS with sparsity-promoting Dynamic Mode Decomposition [38], wavepacket tracking [39], and Input/Output analysis [40]. As they are linear methods, nonlin-

ear physics are not captured (e.g., mean-flow distortion; secondary, subcritical, and [simultaneous] multiple instability mechanisms). However, for crossflow and other vortical instabilities, if the mean-flow distortion is captured in the basic state and these methods are then applied, secondary instability mechanisms can be successfully modeled. All of these methods have promising futures in the computational approach to laminar-to-turbulent transition analysis.

For the work presented in this dissertation, the applications will focus on flow over swept wings. Given the assumption that the laminar base-flows are spanwise-invariant and slowly varying in the streamwise direction, the PSE method is well suited for the analysis.

1.5 Background on present-day computational codes

To model the physics of various instability mechanisms, several boundary-layer stability codes have been developed and are in used in the present-day transition community. These include STABL2D/3D, LASTRAC, VESTA, and EPIC. STABL2D & STABL3D are two codes developed by the engineers at University of Minnesota with capabilities of modeling the Linear Parabolized Stability Equations (LPSE) including thermochemical nonequilibrium (TCNE) effects in the gas modeling and a functional GUI for Linux workstations [41, 42]. LASTRAC is a code developed by engineers at NASA Langley with capabilities for various instabilities, both LPSE and NPSE options, and extensive verification and validation published openly across all speed regimes and canonical geometries [43]. NPSE is available for assumptions such as calorically perfect gases (CPG), but has currently not been developed for high-enthalpy relevant assumptions such as TCNE, whereas LPSE has been implemented for TCNE gases [44]. VESTA is a suite of codes from boundary-layer stability solvers to computer algebra manipulation developed by students and professors at the von Karman Institute of Fluid Dynamics (VKI) and is managed by Dr. Fabio Pinna [45, 46]. Its modeling capabilities include the recently added NPSE with a gas in TCNE. However, the methodology of the computer algebra manipulation makes it unfeasible to print out the governing equations for code-to-code verification, as each species s of the mixture is directly specified—all sums are made explicit. EPIC is the boundary-layer stability code developed by students and professors at Texas A&M University and serves as the primary code relevant to this

research's work [47, 48, 49, 50]. At present, its capabilities include calorically perfect gases up to NPSE and has been validated in hypersonics. It is paired with another in-house computer algebra code written by the author called DERIVE which generates the disturbance equations used in EPIC.

The main advantage to developing an in-house code rather than using another's is direct access and manipulation of source code. This permits the possibility to perform certain computational modeling features that have not been implemented before: the leading edge of science is not just obtainable, but can be directed. Additionally, it is powerful to have in-house computational capability in conjunction with such advanced experimental facilities here at Texas A&M for boundary-layer transition: the Mach 6 Quiet Tunnel (M6QT; [51]) and the Klebanoff-Saric Wind Tunnel (KSWT; [52]), to name a few.

1.6 Outlook

The work presented in this dissertation is a selection of analysis performed on swept wings as well as theory and modeling to demonstrate code development. Chapter 2 lists the governing equations of a compressible fluid and sets the stage for the laminar-to-turbulent computations. Chapter 3 outlines the methodology used to compute the laminar base-flows in this work, converting a wing's surface pressure into boundary conditions relevant for the boundary-layer code, DEKAF. Chapter 4 discusses the detail of various stability methodologies used in this dissertation and their implementation into the in-house code, EPIC. Chapter 5 mathematically analyzes some numerical phenomena observed with the mean-flow distortion as simulated in the Parabolized Stability Equations and proposes a new treatment to quell the numerical divergence. Chapters 6 and 7 demonstrate both linear and nonlinear boundary-layer stability analysis over swept, slotted, natural-laminar-flow wings in the subsonic and transonic speed regimes. Finally, chapter 8 provides cumulative conclusions, summarizes the analysis, and outlines future work.

2.1 Conservation of mass, momentum, and energy

Compressible flows are governed by the conservation of mass, momentum, and energy [53]. Below are the dimensional equations expressed in a Cartesian coordinate frame for an unsteady, three-dimensional, viscous flow [54].[1] The order of the equations is given as a) conservation of mass, b-d) conservation of X-,Y-, and Z-momentum, and e) conservation of energy.

$$\frac{\partial \rho^*}{\partial t^*} + \nabla^* \cdot (\rho^* \mathbf{V}^*) = 0, \tag{2.1a}$$

$$\rho^* \frac{\mathrm{D}U^*}{\mathrm{D}t^*} = -\frac{\partial p^*}{\partial X^*} + \frac{\partial \mathbb{T}^*{}_{XX}}{\partial X^*} + \frac{\partial \mathbb{T}^*{}_{YX}}{\partial Y^*} + \frac{\partial \mathbb{T}^*{}_{ZX}}{\partial Z^*}, \tag{2.1b}$$

$$\rho^* \frac{\mathrm{D}V^*}{\mathrm{D}t^*} = -\frac{\partial p^*}{\partial Y^*} + \frac{\partial \mathbb{T}^*{}_{XY}}{\partial X^*} + \frac{\partial \mathbb{T}^*{}_{YY}}{\partial Y^*} + \frac{\partial \mathbb{T}^*{}_{ZY}}{\partial Z^*}, \tag{2.1c}$$

$$\rho^* \frac{\mathrm{D}W^*}{\mathrm{D}t^*} = -\frac{\partial p^*}{\partial Z^*} + \frac{\partial \mathbb{T}^*{}_{XZ}}{\partial X^*} + \frac{\partial \mathbb{T}^*{}_{YZ}}{\partial Y} + \frac{\partial \mathbb{T}^*{}_{ZZ}}{\partial Z^*}, \tag{2.1d}$$

$$\begin{aligned} \rho^* \frac{\mathrm{D}\left(e^* + |\mathbf{V}^*|^2/2\right)}{\mathrm{D}t^*} &= -\nabla^* \cdot p^* \mathbf{V}^* + ... \\ &+ \frac{\partial}{\partial X^*}\left(\kappa^* \frac{\partial T^*}{\partial X^*}\right) + \frac{\partial}{\partial Y^*}\left(\kappa^* \frac{\partial T^*}{\partial Y^*}\right) + \frac{\partial}{\partial Z^*}\left(\kappa^* \frac{\partial T^*}{\partial Z^*}\right) + ... \\ &+ \frac{\partial\left(U^* \mathbb{T}^*{}_{XX}\right)}{\partial X^*} + \frac{\partial\left(U^* \mathbb{T}^*{}_{YX}\right)}{\partial Y^*} + \frac{\partial\left(U^* \mathbb{T}^*{}_{ZX}\right)}{\partial Z^*} + ... \\ &+ \frac{\partial\left(V^* \mathbb{T}^*{}_{XY}\right)}{\partial X^*} + \frac{\partial\left(V^* \mathbb{T}^*{}_{YY}\right)}{\partial Y^*} + \frac{\partial\left(V^* \mathbb{T}^*{}_{ZY}\right)}{\partial Z^*} + ... \\ &+ \frac{\partial\left(W^* \mathbb{T}^*{}_{XZ}\right)}{\partial X^*} + \frac{\partial\left(W^* \mathbb{T}^*{}_{YZ}\right)}{\partial Y^*} + \frac{\partial\left(W^* \mathbb{T}^*{}_{ZZ}\right)}{\partial Z^*} \end{aligned} \tag{2.1e}$$

Here, asterisks are used to indicate all dimensional quantities. The velocity components U^*, V^*, and W^* are associated with the X^*-, Y^*-, and Z^* coordinates; t^* is time, p^* is static pressure, ρ^* is mass density, and T^* is temperature. Note that the energy equation here is expressed in terms of internal energy e^*. The pressure is linked to density and temperature through an assumption of

[1] These equations assume there is no body force (e.g., gravity), no chemical reactions, no radiative heat transfer throughout the volume, no electric or magnetic fields, the internal energy distribution is accurately described by a single temperature T, and that heat conduction follows Fourier's law. The quantitative reasoning for neglecting gravity will be demonstrated later in §2.3.

an ideal gas: $p^* = \rho^* R_g^* T^*$, where R_g^* is the specific gas constant. This assumption is appropriate given the low static pressures experienced in most aerodynamic applications and temperatures considered. The boldface $\mathbf{V}^*$ represents the vector $[U^*, V^*, W^*]$, and κ^* is thermal conductivity. Suppose the fluid is Newtonian. Then $\mathbb{T}^*$ is the symmetric, viscous stress tensor with its components enumerated below:

$$\begin{aligned}
\mathbb{T}^*{}_{XY} &= \mathbb{T}^*{}_{YX} = \mu^* \left(\frac{\partial V^*}{\partial X^*} + \frac{\partial U^*}{\partial Y^*} \right) \\
\mathbb{T}^*{}_{YZ} &= \mathbb{T}^*{}_{ZY} = \mu^* \left(\frac{\partial W^*}{\partial Y^*} + \frac{\partial V^*}{\partial Z^*} \right) \\
\mathbb{T}^*{}_{ZX} &= \mathbb{T}^*{}_{XZ} = \mu^* \left(\frac{\partial U^*}{\partial Z^*} + \frac{\partial W^*}{\partial X^*} \right) \\
\mathbb{T}^*{}_{XX} &= \lambda_v^* (\nabla^* \cdot \mathbf{V}^*) + 2\mu^* \frac{\partial U^*}{\partial X^*} \\
\mathbb{T}^*{}_{YY} &= \lambda_v^* (\nabla^* \cdot \mathbf{V}^*) + 2\mu^* \frac{\partial V^*}{\partial Y^*} \\
\mathbb{T}^*{}_{ZZ} &= \lambda_v^* (\nabla^* \cdot \mathbf{V}^*) + 2\mu^* \frac{\partial W^*}{\partial Z^*}
\end{aligned} \tag{2.2}$$

where μ^* is dynamic viscosity and λ_v^* is the second coefficient of viscosity. The substantial derivative $\mathrm{D}/\mathrm{D}t^*$ is defined as

$$\frac{\mathrm{D}Q}{\mathrm{D}t^*} = \frac{\partial Q}{\partial t^*} + U^* \frac{\partial Q}{\partial X^*} + V^* \frac{\partial Q}{\partial Y^*} + W^* \frac{\partial Q}{\partial Z^*} \tag{2.3}$$

for some quantity Q. These equations, both Eqs. (2.1) and (2.2), are foundational to simulating the dynamics observed for a compressible fluid. For analyzing general geometries however, a Cartesian frame is insufficient. Instead, we consider the above dimensional equations formulated with general tensor calculus using the metric tensor g_{ij}.

$$\begin{aligned}
\frac{\partial \rho^*}{\partial t^*} + \left(u^{*j} \rho^* \right)_{,j} &= 0 \\
\rho^* \frac{\partial u^{*i}}{\partial t^*} + \rho^* u^{*j} u^{*i}{}_{,j} &= -g^{ij} p^*_{,j} + \mathbb{T}^{*ij}_{\ \ ,j}, \quad \forall i \in [1,2,3] \\
\rho^* \frac{\partial h^*}{\partial t^*} + \rho^* u^{*j} h^*_{,j} &= \frac{\partial p^*}{\partial t^*} + u^{*j} p^*_{,j} + g_{ik} \mathbb{T}^{*kj} u^{*i}_{\ \ ,j} + \left(\kappa^* g^{ij} T^*_{,i} \right)_{,j}
\end{aligned} \tag{2.4}$$

Subscript and superscript indices refer to covariant and contravariant indices, respectively and indices following a comma specify differentiation with respect to that dimension: see Aris' text for an excellent review [55].[2] Repeated indices in a single term are free and summed over using Einstein's summation notation. The independent variables are general position coordinates x^{*i} and time t^*.

For the work presented in this dissertation, the energy equation is expressed in terms of static enthalpy h^* as opposed to internal energy e^*.[3] The viscous stress tensor is now more concisely written given as:

$$\mathbb{T}^{*ij} = \lambda_v^* g^{ij} u_{,k}^{*\,k} + \mu^* \left(g^{jk} u_{,k}^{*\,i} + g^{ik} u_{,k}^{*\,j} \right) \tag{2.5}$$

Stokes' hypothesis is assumed for the entirety of this work. That is, the bulk viscosity $\mu_B^* \equiv 0$, implying $\lambda_v^* = -2/3\mu^*$. This is a common assumption in calorically perfect, compressible flows. Sutherland's law is used for μ^*. A constant Prandtl number is assumed, linking thermal conductivity κ^* directly to μ^*. Mathematically, the expressions are given as

$$\mu^* = C_\mu \frac{T^{*\,3/2}}{T^* + S_\mu}, \qquad C_\mu = \frac{\mu_{\text{ref}}^*}{T_{\text{ref}}^{*3/2}} \left(T_{\text{ref}}^* + S_\mu \right), \tag{2.6a}$$

$$\kappa^* = \frac{\mu^* c_p^*}{\text{Pr}} \tag{2.6b}$$

where c_p^* is the specific heat at constant pressure. All used constants will be specified with the corresponding analysis.

[2] Hildebrand is also a helpful text: [56].

[3] This statement does not include the section §4.4.

2.2 Metric tensor

In this work, the coordinate system used will be orthogonal curvilinear. Then metric tensor then may be expressed as a 3×3 diagonal matrix whose elements are h_i^2.

$$g_{ij} = \begin{bmatrix} g_{11} & 0 & 0 \\ 0 & g_{22} & 0 \\ 0 & 0 & g_{33} \end{bmatrix} = \begin{bmatrix} h_1^2 & 0 & 0 \\ 0 & h_2^2 & 0 \\ 0 & 0 & h_3^2 \end{bmatrix} \tag{2.7}$$

To discuss the general form, let us define an indexed set of Cartesian coordinates (X^1, X^2, X^3) and general position coordinates (x^1, x^2, x^3). The entries of g_{ij} are then written as [55, Eq. (7.23.4)]

$$g_{ij} = \sum_{k=1}^{3} \frac{\partial X^k}{\partial x^i} \frac{\partial X^k}{\partial x^j} \tag{2.8}$$

such that the diagonal entries g_{ii} simplify to the sum of the squares of the partial derivatives:

$$g_{ii} = \sum_{k=1}^{3} \left(\frac{\partial X^k}{\partial x^i} \right)^2 \tag{2.9}$$

There is a common approximation made to this definition based on the fact that the metric tensor relates distance to the infinitesimal coordinate increments by a scaling factor. Let the orthogonal curvilinear surface coordinate $x^1 \equiv s$. Suppose this is locally perpendicular to the wall-normal, orthogonal curvilinear second coordinate $x^2 \equiv y$. Then the h_1 metric may be written relating the surface distance to the off-wall streamwise distance for a small angle $\mathrm{d}\theta$. The sketch below in Fig. 2.1 demonstrates this local circular assumption where the streamwise radius of curvature at a given point is R_1.

The expression for h_1 simplifies to

$$h_1 = 1 + \frac{y}{R_1} \tag{2.10}$$

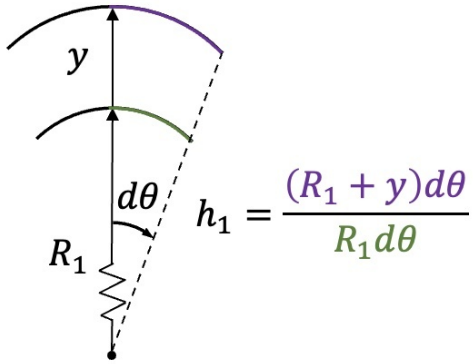

Figure 2.1: A sketch of the scaling factor h_1. The streamwise radius of curvature is R_1 and a small angle subtended is $\mathrm{d}\theta$. The wall-normal distance off of the surface is given by y. The surface arc distance Δs is shown by the green line: $R_1\mathrm{d}\theta$. The off-wall streamwise arc distance on the grid is similar: $(R_1 + y)\mathrm{d}\theta$

Of course, this equation fails at the limit of $R_1 = 0$, but the surface would represent a singularity and is not physical. This usage of h_1 approaches the definitions in Eqs. (2.7) and (2.9) as the product $R_1\mathrm{d}\theta = \Delta s \to 0$. However, for finite Δs, there is a slight error with respect to the original definition. For the grids considered in this dissertation, the y coordinate does vary in s—grid clustering is a function of s. The change of y, though, with respect to s is presumed to be small for an appropriately small Δs. This assumption on the wall-normal coordinate not changing over Δs is equivalently expressed as

$$h_2 = 1 \tag{2.11}$$

For very small R_1, the present circular approximation is dubious and demands an extremely small $\mathrm{d}\theta$. For the present application of swept wings, the only locations with small R_1 are near the leading edge. In that region, Δs by construction is assigned to be very small as well to avoid additional error.

For more general geometries that have a finite spanwise radius of curvature R_3, say a cone, then the sketch can be drawn analogously for the spanwise dimension. Then

$$h_3 = 1 + \frac{y}{R_3} \tag{2.12}$$

These approximations of h_1, h_2, and h_3 in Eqs. (2.10), (2.11), and (2.12), respectively, are used in this dissertation rather than the formal definition in Eq. (2.9).

2.3 Nondimensional equations

A deep and beautiful power in physics lies in the result of the Buckingham π theorem: that its laws do not rely on any specific unit system. It is common, especially in fluid dynamics, to express the equations without units, or nondimensionally. Let us nondimensionalize the above governing equations then. All of the relevant definitions for nondimensionalization are shown in Eq. (2.13). Most variables have been directly nondimensionalized by their reference quantities, denoted with a subscript ref. The few exceptions are a) pressure is nondimensionalized by dynamic pressure, not static; b) second viscosity coefficient by dynamic viscosity; and c) time by a length over velocity.

$$\begin{aligned}
&\rho = \frac{\rho^*}{\rho^*_{\mathrm{ref}}}, \quad u^i = \frac{u^{*^i}}{u^{*^1}_{\mathrm{ref}}}, \quad x^i = \frac{x^{*^i}}{\ell}, \quad \ell = \sqrt{\frac{\mu^*_{\mathrm{ref}} X^{*^1}_{\mathrm{ref}}}{\rho^*_{\mathrm{ref}} u^{*^1}_{\mathrm{ref}}}}, \quad t = \frac{t^* \ell}{u^{*^1}_{\mathrm{ref}}}, \\
&p = \frac{p^*}{\rho^*_{\mathrm{ref}} \left(u^{*^1}_{\mathrm{ref}}\right)^2}, \quad R_g = \frac{R^*_g}{R^*_{g,\mathrm{ref}}}, \quad \mu = \frac{\mu^*}{\mu^*_{\mathrm{ref}}}, \quad \lambda_v = \frac{\lambda^*_v}{\mu^*_{\mathrm{ref}}}, \\
&h = \frac{h^*}{h^*_{\mathrm{ref}}}, \quad c_p = \frac{c^*_p}{c^*_{p\,\mathrm{ref}}}, \quad c_v = \frac{c^*_v}{c^*_{v\,\mathrm{ref}}}, \quad T = \frac{T^*}{T^*_{\mathrm{ref}}}, \quad \kappa = \frac{\kappa^*}{\kappa^*_{\mathrm{ref}}}
\end{aligned} \tag{2.13}$$

These reference quantities may be taken as freestream values or anywhere in the computational solution with nonzero velocities. The length scale ℓ is sometimes referred to as the Blasius length and the present choice of $X^{*^1}_{\mathrm{ref}}$ inside of the square root is arbitrary. Substituting these into Navier-Stokes, the tensorial form of the nondimensional equations is written as

$$\frac{\partial \rho}{\partial t} + \left(u^j \rho\right)_{,j} = 0 \tag{2.14a}$$

$$\rho \frac{\partial u^i}{\partial t} + \rho u^j u^i_{,j} = -g^{ij} p_{,j} + \frac{1}{\mathrm{Re}} \mathbb{T}^{ij}_{,j}, \quad \forall i \in [1,2,3] \tag{2.14b}$$

$$\rho \frac{\partial h}{\partial t} + \rho u^j h_{,j} = \mathrm{Ec} \left(\frac{\partial p}{\partial t} + u^j p_{,j} \right) + \frac{\mathrm{Ec}}{\mathrm{Re}} g_{ik} \mathbb{T}^{kj} u^i_{,j} + \frac{1}{\mathrm{RePr}} \left(\kappa g^{ij} T_{,i} \right)_{,j} \tag{2.14c}$$

where upon algebraic manipulation, the natural definitions of the reference, nondimensional pa-

rameters are found as

$$\gamma = \frac{c^*_{p\,\mathrm{ref}}}{c^*_{v\,\mathrm{ref}}}, \quad \mathrm{M}^2 = \frac{\left(u^{*^1}_{\mathrm{ref}}\right)^2}{\gamma R^*_{g,\mathrm{ref}} T^*_{\mathrm{ref}}}, \quad \mathrm{Re} = \frac{\rho^*_{\mathrm{ref}} u^{*^1}_{\mathrm{ref}}\, \ell}{\mu^*_{\mathrm{ref}}}, \\ \mathrm{Ec} = \frac{\left(u^{*^1}_{\mathrm{ref}}\right)^2}{h^*_{\mathrm{ref}}}, \quad \mathrm{Pr} = \frac{\mu^*_{\mathrm{ref}}\, c^*_{p\,\mathrm{ref}}}{\kappa^*_{\mathrm{ref}}}, \tag{2.15}$$

Here, γ is the ratio of specific heats, M is the Mach number, Re is the Reynolds number, Ec is the Eckert number, and Pr is the Prandtl number. Note that the nondimensional pressure is written as

$$p = \frac{\rho T}{\gamma \mathrm{M}^2} \tag{2.16}$$

Note for all thermally perfect gases, $R_g = 1$ (as that is a function of the molecular mass of the gas), $c_p \neq 1$, and $c_v \neq 1$. For calorically perfect gases, however, $c_p = c_v = 1$ as well as $h = T$, since $h^* = c^*_p T^*$. The Eckert number may be simplified for calorically perfect gases:

$$\mathrm{Ec} = \frac{\left(u^{*^1}_{\mathrm{ref}}\right)^2}{h^*_{\mathrm{ref}}} = \frac{\gamma R^*_{g,\mathrm{ref}} T^*_{\mathrm{ref}}}{c^*_{p\,\mathrm{ref}} T^*_{\mathrm{ref}}} \underbrace{\frac{\left(u^{*^1}_{\mathrm{ref}}\right)^2}{\gamma R^*_{g,\mathrm{ref}} T^*_{\mathrm{ref}}}}_{\mathrm{M}^2} = \underbrace{\frac{\gamma R^*_{g,\mathrm{ref}}}{c^*_{p\,\mathrm{ref}}}}_{\gamma - 1} \frac{\cancel{T^*_{\mathrm{ref}}}}{\cancel{T^*_{\mathrm{ref}}}} \mathrm{M}^2 = (\gamma - 1)\mathrm{M}^2 \tag{2.17}$$

since from the definitions of the specific heats

$$c^*_{p\,\mathrm{ref}} - c^*_{v\,\mathrm{ref}} = R^*_{g,\mathrm{ref}}, \\ 1 - \frac{1}{\gamma} = \frac{R^*_{g,\mathrm{ref}}}{c^*_{p\,\mathrm{ref}}}, \\ \gamma - 1 = \frac{\gamma R^*_{g,\mathrm{ref}}}{c^*_{p\,\mathrm{ref}}}. \tag{2.18}$$

For all analysis presented, the gas is assumed to be calorically perfect.

As an addendum, one may wonder why gravity has been neglected in the present governing equations. Recall from White that buoyant forces scale with the ratio $\mathrm{Gr}_\ell/\mathrm{Re}^2$, where Gr_ℓ is the

Grashof number [54, §4.14]. The definition is given as

$$\mathrm{Gr}_\ell = \frac{g^* \beta^*_{\mathrm{VT\,ref}} \, \Delta T^*_{\mathrm{ref}} \, \ell^3}{\left(\nu^*_{\mathrm{ref}}\right)^2} \tag{2.19}$$

where $g^* = 9.81\,\mathrm{m\text{-}s^{-2}}$, $\beta^*_{\mathrm{VT\,ref}}$ is a reference volumetric coefficient of thermal expansion of the fluid, $\Delta T^*_{\mathrm{ref}}$ is a reference change in temperature, ℓ is a length scale relevant for buoyant effects, and ν^*_{ref} is a reference kinematic viscosity. For the present cruise applications of interest, suppose an altitude of 44,000 ft, which implies $T^*_{\mathrm{ref}} = 216.65\,\mathrm{K}$. From ideal gas relations,

$$\begin{aligned}
\beta^*_{\mathrm{VT}} &\equiv \frac{1}{\mathcal{V}} \left(\frac{\partial \mathcal{V}}{\partial T} \right)_p, \\
&= \frac{1}{\mathcal{V}} \left(\frac{\partial}{\partial T} \frac{N k_{\mathrm{B}} T}{p} \right)_p, \\
&= \frac{1}{\mathcal{V}} \left(\frac{N k_{\mathrm{B}}}{p} \right), \\
&= \frac{N k_{\mathrm{B}}}{N k_{\mathrm{B}} T}, \\
&= \frac{1}{T}
\end{aligned} \tag{2.20}$$

where $\mathcal{V}$ is the volume of the fluid, p is absolute pressure, T is absolute temperature, N is the number of gas particles, and k_{B} is the Boltzmann constant. Recall the subscript p implies differentiation while holding p constant. Then the coefficient $\beta^*_{\mathrm{VT\,ref}} = 1/T^*_{\mathrm{ref}}$. The adiabatic temperature T^*_{adiab} of the surface on the wing in flight is nominally $234\,\mathrm{K}$ for a large portion of the chord, so $\Delta T^*_{\mathrm{ref}} = T^*_{\mathrm{adiab}} - T^*_{\mathrm{ref}} = 17.35\,\mathrm{K}$. The laminar boundary-layer thickness is on the order of $\delta_{99} = 3\,\mathrm{mm}$. With standard parameters of Sutherland's law, $\nu^*_{\mathrm{ref}} \approx 5.7 \times 10^{-5}\,\mathrm{m^2\text{-}s^{-1}}$. All together, the Grashof number based off of the boundary-layer thickness is $\mathrm{Gr}_{\delta_{99}} \approx 6.5 = O(1)$. Since the Reynolds numbers based on the chord of the wing are $O(10^6$–$10^7)$, the ratio $\mathrm{Gr}_{\delta_{99}}/\mathrm{Re}^2$ is extremely small, which implies that buoyant effects may be safely neglected in the present analysis.

This completes the discussion on the governing equations. For the remainder of the dissertation, all dimensional quantities reported will have their asterisks omitted for brevity.

2.4 Decomposition into a laminar and perturbation component

To model the transition process of the boundary layer, the governing equations are derived based on the principle that the vector of flow variables $q = [u, v, w, T, \rho]$ can be decomposed into a steady, laminar component $\overline{q}$ and a perturbation (or disturbance) q'.

$$q(s, y, z, t) = \overline{q}(s, y, z) + \varepsilon_p q'(s, y, z, t) \tag{2.21}$$

The instantaneous flow q is presumed to satisfy the full Navier-Stokes equations, represented by the operator $\mathcal{NS}$ and shown in the previous section as Eq. (2.14).

$$\mathcal{NS}(q) = 0 \tag{2.22}$$

The laminar base-flow is presumed to satisfy the steady Navier-Stokes equations, written as $\mathcal{NS}_{\partial/\partial t=0}(\overline{q}) = 0$. By substituting this into (2.22), the dynamics of the perturbation can be expressed as

$$\mathcal{LNS}(\varepsilon_p q') = \mathcal{N}(\varepsilon_p^2 q' q', \varepsilon_p^3 q' q' q') \tag{2.23}$$

where $\mathcal{LNS}$ represents the linear operator on q' from the Navier-Stokes equations, while $\mathcal{N}$ accounts for the nonlinear terms. Note for compressible, calorically perfect gases, there are both second- and third-order nonlinearities when the state vector q is expressed primitively as $\{u, v, w, T, \rho\}$.[4]

The subject of the next chapter will detail some relevant methodology to compute the laminar base-flow $\overline{q}$ over a swept wing. Following, the subsequent chapter will discuss the perturbation q' in the context of both linear and nonlinear stability theories of LST, LPSE, and NPSE. Detail will be provided as to how they are applied in the in-house stability code, EPIC.

[4] An example of a quadratic nonlinearity is $\overline{\rho}\, v'\, \partial u'/\partial y$ from momentum conservation expressed in a Cartesian frame. A cubic nonlinearity is similarly written as $\rho'\, v'\, \partial u'/\partial y$.

3. SWEPT WINGS AND BOUNDARY-LAYER SOLUTIONS WITH DEKAF[1]

Swept wings are a canonical, complex configuration that are and will always be relevant across all speed regimes. From subsonic aircraft to jets and shuttles with delta wings—even fins on cones may be modeled as swept wings. Given their ubiquity in aerospace design, it is worth analyzing in-depth such that the fundamental understanding of the complex configuration can then be transferred across the application space.

The present chapter will discuss the methodology used to convert a pressure coefficient into appropriate conditions to compute a viscous boundary-layer solution over a swept wing. These methods are implemented in the open-source code DEKAF, co-developed by the author.

3.1 Overview

A pressure coefficient of the swept wing must be provided to the boundary-layer solver to generate a viscous solution. There are several options to construct the pressure coefficient. First, one could use a Navier-Stokes CFD solver (e.g., OVERFLOW) and extract the pressure at the wall. Second, if the data are present, an experimentally measured pressure coefficient can prescribe boundary conditions in a boundary-layer solver instead. Third, the pressure coefficient from an inviscid code (e.g., MSES) can be input directly into in a boundary-layer solver [57]. Each has their benefits and nuances. CFD of course provides higher-fidelity simulations over inviscid codes. However, there is a greater computational cost and set-up time (i.e., grid generation). Experimental measurements provide a chance for direct comparison with what is observed rather than simulated. However, pressure taps installed on a model may induce uncertainty and other experimental complications may need to considered. Various applications benefit by analyzing the resulting flowfield over two or even all three of the stated methodologies. The work presented in this dissertation uses a combination of a) OVERFLOW solutions and b) MSES solutions.

[1]Portions of this chapter are reprinted with permission from "Boundary-Layer Stability of a Natural-Laminar-Flow Airfoil" by Koen J. Groot, Ethan S. Beyak, Daniel T. Heston and Helen L. Reed in AIAA 2020-1024. Copyright 2020 by Koen J. Groot, Ethan S. Beyak, Daniel T. Heston, and Helen L. Reed.

Pivoting to the boundary-layer solver, let us first hash out some details on nomenclature and conventions used. The coordinate system used in DEKAF is the leading-edge-orthogonal frame. That is to say, the quantity s traces from the attachment line along the airfoil's surface perpendicular to the leading edge. The coordinate y is wall-normal and z is parallel to the leading edge. The velocity components in these directions will be referred to as $(\overline{u}, \overline{v}, \overline{w})$, respectively. Base-flow quantities will be distinguished with an overbar.

The laminar basic state (i.e., base flow) is assumed to be steady: $\partial/\partial t = 0$. Additionally, the basic state is assumed to be spanwise-invariant: $\partial/\partial z = 0$. Even though s represents a curved path, the curvature of the path along the surface is neglected in the boundary-layer calculation as a consequence of the boundary-layer assumptions. A critical assumption in boundary-layer theory is that the flow is slowly developing in s [54]. For the swept wings of interest (e.g., Natural-Laminar-Flow wings), there are no sudden geometric excrescences that would violate this assumption. However, in transonic flow, the presence of shocks quickly violates this assumption and the simulation at and beyond those stations should be neglected.

The working fluid is air, and the compressible conditions considered in this dissertation permit the calorically-perfect-gas assumption. That is, the specific heat at constant pressure c_p is constant. Pressure $\overline{p}$ is assumed to satisfy the ideal gas relation, $\overline{p} = \overline{\rho} R_g \overline{T}$, where $\overline{\rho}$ is the mass density of the fluid, R_g is the specific gas constant, and $\overline{T}$ is the temperature. Sutherland's law and Stokes's hypothesis are used for dynamic viscosity μ and the second viscosity coefficient λ_v, respectively. A constant Prandtl number is imposed to calculate thermal conductivity κ. More sophisticated models may be used for transport properties of course, but they are unnecessary and inappropriate for the subsonic/transonic analysis present in this dissertation.

3.2 Conversion of pressure coefficient data into boundary-layer edge quantities

The pressure coefficient is defined in Eq. (3.1) and is used to construct edge conditions that satisfy isentropic relations, which serve as boundary conditions for DEKAF. The following section will delineate how it is implemented into DEKAF. This section will not go into detail on the boundary-layer solver as a whole. The curious reader is referred to Groot et al. [58].

Near the surface of the wing, the freestream velocity undergoes acceleration and evolves into the inviscid-edge velocity components $\overline{u}_e$ and $\overline{w}_e$. Because of the spanwise-invariant assumption, $\overline{w}_e$ is globally constant over the wing. For this, it is sometimes given a special subscript: $\overline{w}_0 \equiv \overline{w}_e = \overline{w}_\infty$ for all s, y, and z. The attachment line is a defining characteristic of swept-wing flows. Along it, the streamwise component of the inviscid-edge velocity $\overline{u}_e = 0$ while the spanwise component still $\overline{w}_e \neq 0$. When using the dynamic pressure scaled with the leading-edge-orthogonal velocity component $\sqrt{\overline{u}_\infty^2 + \overline{v}_\infty^2}$ to construct the pressure coefficient, this coefficient will reach its isentropic value. That is, with the pressure coefficient written as

$$C_p^{\overline{u}_\infty \overline{v}_\infty} \equiv \frac{\overline{p}_e - \overline{p}_\infty}{\frac{1}{2}\overline{\rho}_\infty \left(\overline{u}_\infty^2 + \overline{v}_\infty^2\right)} = \frac{\overline{p} - \overline{p}_\infty}{\frac{1}{2}\overline{\rho}_\infty \overline{Q}_\infty^2 \cos^2 \Lambda} = \frac{C_p^{Q_\infty}}{\cos^2 \Lambda} \geq C_p^{Q_\infty}. \tag{3.1}$$

the maximally attainable isentropic pressure coefficient is given as

$$C_{p,\max}^{\overline{u}_\infty \overline{v}_\infty} = \frac{\overline{p}_\infty}{\frac{1}{2}\overline{\rho}_\infty \left(\overline{u}_\infty^2 + \overline{v}_\infty^2\right)} \left(\frac{\overline{p}_0}{\overline{p}_\infty} - 1\right) = \frac{2}{\gamma \mathrm{M}_{\overline{u}_\infty \overline{v}_\infty}^2} \left(\left(1 + \frac{\gamma - 1}{2} \mathrm{M}_{\overline{u}_\infty \overline{v}_\infty}^2\right)^{\frac{\gamma}{\gamma - 1}} - 1\right) \tag{3.2}$$

Here, care is taken with subscripts and superscripts to indicate the reference velocity wherever relevant. The Mach number $\mathrm{M}_{\overline{u}_\infty \overline{v}_\infty} = \sqrt{\overline{u}_\infty^2 + \overline{v}_\infty^2}/\overline{a}_\infty$ is the leading-edge-orthogonal freestream Mach number; and $\overline{a}_\infty = \sqrt{\gamma R_g \overline{T}_\infty}$ is the freestream speed of sound.

DEKAF's inputs require the pressure coefficient values $C_p^{\overline{u}_\infty \overline{v}_\infty}$ versus leading-edge-orthogonal x/c, where c is a reference length along the x axis (commonly the chord). Converting the pressure coefficient to edge values in DEKAF requires additional inputs, delineated below:

airfoil thickness coordinate (versus x/c):	Y_c/c	$[-]$
leading-edge-orthogonal chord:	c	$[\mathrm{m}]$
resultant freestream Mach number:	$\mathrm{M}_{\overline{Q}_\infty} = Q_\infty/\overline{a}_\infty$	$[-]$
sweep angle:	$\Lambda = \arctan \dfrac{\overline{w}_\infty}{\sqrt{\overline{u}_\infty^2 + \overline{v}_\infty^2}}$	$[\mathrm{deg}]$
angle of attack:	$\alpha = \arctan \dfrac{\overline{v}_\infty}{\overline{u}_\infty}$	$[\mathrm{deg}]$
specific gas constant:	R_g	$[\mathrm{J}/(\mathrm{kg\,K})]$
ratio of specific heats:	γ	$[-]$
freestream temperature:	$\overline{T}_\infty$	$[\mathrm{K}]$
freestream static pressure:	$\overline{p}_\infty$	$[\mathrm{kg}/(\mathrm{m\,s}^2)]$

Alternatively, there are some physical scenarios where $\mathrm{M}_{\overline{u}_\infty \overline{v}_\infty}$ is a more useful input than M_{Q_∞} (e.g., sweep variation while maintaining leading-edge-constant velocity). Either is acceptable as an input.[2] Next, the following steps are performed in DEKAF:

1. Build the airfoil geometry's surface coordinate s_g. Its origin is placed at the trailing edge, wrapping clockwise around the airfoil in the xY_c-plane.

2. Interpolate the geometry coordinates and the pressure-data coordinates onto a dense, equispaced s_g grid.

3. Identify the attachment-line location on this dense grid s_{stag} by querying for the maximum value of $C_p^{\overline{u}_\infty \overline{v}_\infty}$. Spline interpolation is selected over alternatives for continuity of derivatives. However, it has the unphysical side-effect from the overshooting to slightly *move* the location of the attachment line on the wing with respect to the original data. Additionally, the

[2] As an aside, the pressure coefficient does intrinsically encode the freestream Mach number. It could be directly extracted by inverting the maximally attainable pressure coefficient equation at the attachment line: see Eq. (3.2). However, since DEKAF optionally performs Prandtl-Glauert transformations, always supplying the Mach number is simpler programmatically.

result of spline interpolation can cause the new maximum value of $C_p^{\overline{u}_\infty \overline{v}_\infty}$ to either under- or overshoot the maximally attainable isentropic pressure $C_{p,\max}^{\overline{u}_\infty \overline{v}_\infty}$. In these situations, surrounding data points serve as fixed anchors while the fit of the pressure coefficient in between the anchors is gradually and iteratively adjusted until the $C_{p,\max}^{\overline{u}_\infty \overline{v}_\infty}$ is achieved and undershot with a tolerance of 2.2×10^{-16}.

4. The edge temperature $\overline{T}_e$ is computed through isentropic relations, whereas $\overline{\rho}_e$ is then given through the equation of state. The dynamic viscosity $\overline{\mu}_e$ is given by the desired transport equation—typically Sutherland's law.

5. Differentiate the pressure coefficient $C_p^{\overline{u}_\infty \overline{v}_\infty}$ on the dense s_g-grid with a fourth-order regular finite difference scheme. A central-oriented stencil is used throughout the interior, while mixed and one-sided stencils are used at the boundaries of s_g, i.e., near the trailing edge. This derivative is used to quantify $\mathrm{d}\overline{p}_e/\mathrm{d}s_g$.

6. Integrate the compressible s-momentum conservation equation.

$$\overline{u}_e^2(s_g) = \overline{u}_{e,\mathrm{TE}}^2 - 2\int_{s_{g,\mathrm{TE}}}^{s_g} \frac{1}{\overline{\rho}_e(\bar{s}_g)} \frac{\mathrm{d}\overline{p}_e}{\mathrm{d}\bar{s}_g}(\bar{s}_g)\,\mathrm{d}\bar{s}_g, \tag{3.3}$$

   Here, $\overline{u}_{e,\mathrm{TE}}$ is assigned such that the velocity component at the attachment line is identically zero, i.e., $\overline{u}_e(s_{\mathrm{stag}}) = 0$. Integration is performed from the trailing edge (TE) toward the attachment line using integration matrices.

7. When taking the square root of $\overline{u}_e^2$, the sign of $\overline{u}_e$ is set to be positive on the side of the wing of interest. Here, the 'sides' of the wing are divided consequently by the location of the attachment line, not necessarily by the geometric coordinates of the airfoil.

8. The quantity $\mathrm{d}\overline{u}_e/\mathrm{d}s$ for all points except at the attachment line is found through rearranging s-momentum.

$$\frac{\mathrm{d}\overline{u}_e}{\mathrm{d}s_g} = -\frac{1}{\overline{\rho}_e\,\overline{u}_e}\frac{\mathrm{d}\overline{p}_e}{\mathrm{d}s_g}. \tag{3.4}$$

At the attachment line itself, we differentiate $\overline{u}_e(s_g)$ numerically, as the above formula would achieve a singularity.

9. Calculate the Hartree parameter β_{H} now that all of the required quantities have been computed:

$$\beta_{\mathrm{H}} = \frac{2\xi}{\overline{u}_e}\frac{\mathrm{d}\overline{u}_e}{\mathrm{d}\xi} \tag{3.5}$$

At the attachment line, $\beta_{\mathrm{H}} \equiv 1$.

10. Calculate the self-similar streamwise coordinate ξ as

$$\xi(s_g) = \xi(s_{g,\mathrm{TE}}) + \int_{s_{g,\mathrm{TE}}}^{s_g} \overline{\rho}_e(\bar{s}_g)\,\overline{u}_e(\bar{s}_g)\,\overline{\mu}_e(\bar{s}_g)\,\mathrm{d}\bar{s}_g, \tag{3.6}$$

Here, the integration constant can be set as we so choose. It is convenient to enforce $\xi(s_{\mathrm{stag}}) = 0$, so $\xi(s_{g,\mathrm{TE}})$ is assigned appropriately.

11. Similarly, define the surface coordinate $s = \pm(s_g - s_{\mathrm{stag}})$ such that $s = 0$ at the attachment line and $s > 0$ in the downstream direction of interest. Remove the nodes where s is negative and interpolate onto the required ξ-grid with the appropriate resolution for a converged boundary-layer solution.

This routine has generated the necessary inputs now for the standard operation of DEKAF. In other words, this concludes the airfoil pre-processing routine. For a discussion on the remaining methodology of DEKAF, see the paper by Groot et al. [58].

3.3 Streamwise mapping

As an appendix onto the last point in the above outline, typical analyses over swept wings thus far have found $N_\xi = 2000$ to be appropriate to demonstrate convergence when clustering with the $\tanh$-distribution. Briefly, the $\tanh$-distribution is based on assigning a streamwise step of $\Delta\xi \propto \tanh(\mathcal{X})$, where $\mathcal{X}$ is an equispaced domain from $[0, 1]$ with N_ξ points. Additionally, it is

desirable to control the value of $\Delta\xi$ at $\mathcal{X} = 0$, so we may add a shift of A_ξ:

$$\Delta\xi(\mathcal{X}) = \big(A_\xi + a_\xi B_\xi \tanh(a_\xi \mathcal{X})\big)\Delta\mathcal{X} \tag{3.7}$$

Recall the integral of hyperbolic tangent is the logarithm of hyperbolic cosine. Then take the limit as $\Delta\mathcal{X} \to 0$ and from integration we have:

$$\xi(\mathcal{X}) = \xi_{\min} + A_\xi \mathcal{X} + B_\xi \ln(\cosh(a_\xi \mathcal{X})) \tag{3.8}$$

where the coefficients depend on domain size and the streamwise clustering specified. The function $\Delta\xi$ is specified in the $\mathcal{X}\Delta\xi$-plane by indicating a point on the curve as $(\mathcal{X}_i, \Delta\xi_i)$. Another important parameter, as mentioned above in the context of A_ξ, is $\Delta\xi_{\min}$: the $\Delta\xi$ value at $\mathcal{X} = 0$. The asymptote of the $\tanh$ reaches $\Delta\xi_{\max}$. Through some algebra, the appropriate coefficients are found:

$$\begin{aligned} A_\xi &= \Delta\xi_{\min}(N_\xi - 1), \quad a_\xi = \frac{1}{\mathcal{X}_i} \tanh^{-1}\left(\frac{\Delta\xi_i}{\Delta\xi_{\max}}\right), \\ B_\xi &= \frac{\xi_{\max} - \xi_{\min} - \Delta\xi_{\min}(N_\xi - 1)}{\ln(\cosh(a_\xi))} \end{aligned} \tag{3.9}$$

where $\xi_{\min} = 0$, as ξ begins at the attachment line. Out of this wide array of constants, the analyst can control two: $\mathcal{X}_i$ and the ratio $\Delta\xi_i/\Delta\xi_{\max}$. The third and final constant is asserted in DEKAF to equal

$$\Delta\xi_{\min} = \frac{1}{100}\frac{\xi(s_{g,\mathrm{TE}})}{N_\xi - 1} \tag{3.10}$$

Usual values are $\mathcal{X}_i = 0.5$ and $\Delta\xi_i/\Delta\xi_{\max} = 0.85$, which will be employed for all DEKAF solutions present in this dissertation. When paired with $N_\xi = 2000$ and a fourth-order accurate marching scheme, the boundary-layer properties are often converged below $O(10^{-6})$ for swept-wing solutions. An example of this will be shown in Chapter 7. This function was created by Dr. Fernando Miró Miró and the author, first presented in the conference paper [59] and later refined in the journal article [60]. The curious reader is referred to the dissertation of Miró Miró for a relevant sketch and more detail [46, §7.3.1].

3.4 Preparation for stability calculations

After the laminar boundary layer has been calculated with DEKAF, the solution is interpolated onto a different domain and a different set of points. This is required to prepare the input for the stability problem that operates with a different discretization. To elaborate, the wall-normal extent of the domain must be larger for the stability problem than that defined by $\eta_{\max}$ for the boundary-layer problem. The perturbation can extend much farther out beyond the boundary-layer height, especially near the attachment line. As a result, extrapolation of the base-flow profiles must be performed following the asymptotic relations of boundary-layer theory stated in (3.11).

$$\frac{\partial \overline{v}}{\partial y}(\eta > \eta_{\max}) = \frac{\partial \overline{v}}{\partial y}(\eta = \eta_{\max}), \qquad \overline{q}(\eta > \eta_{\max}) = \overline{q}(\eta = \eta_{\max}), \quad \overline{q} \in \{\overline{u}, \overline{w}, \overline{T}, \overline{\rho}\} \tag{3.11}$$

The profiles are extrapolated to a selected height. GICM interpolation is used on the DEKAF profiles for the nodes whose $\eta < \eta_{\max}$, see [58] for an in-depth discussion on GICM. Clustering is applied to the grid going into the stability problem by way of Malik's mapping: y_i is assigned to be identical to that resulting from the Illingworth transformation on the DEKAF solution. The grid's resolution is assigned to be $N_y = 250$ with this GICM/extrapolation procedure. Following this, the basic state is ready to be input into the in-house stability code, EPIC—the subject of the next chapter. First though, contributions of the author specific to DEKAF are outlined below.

3.5 Contributions

It would be remiss to not mention many of the capabilities of DEKAF related to high-enthalpy flows, as much research has been done using the high-enthalpy modeling capabilities of the boundary-layer solver. The contributions of the author relevant to the high-enthalpy effects in DEKAF include but are not limited to:

1. Multi-species chemical assumptions, including chemical nonequilibrium (CNE) and local thermodynamic equilibrium (LTE) with constant elemental composition.

2. Two-temperature thermal assumptions, i.e., thermal nonequilibrium (TNE) or grouping the

translational and rotational energy modes into T and the vibrational, electronic, and electron energy modes into T_v. This may occur simultaneously with chemical nonequilibrium, creating thermochemical nonequilibrium (TCNE).

3. Different diffusion indexing, i.e., modeling diffusion as each species into another species or approximating diffusion by indexing only each species into the mixture as a whole.

4. Different working fluids based on air:

   (a) containing chemical species like He, Ar, or $\mathrm{CO_2}$ from surface gas injection;

   (b) under dissociation into the five core species of (N, O, $\mathrm{N_2}$, NO, $\mathrm{O_2}$);

   (c) under ionization into the eleven core species including the additional six of ($\mathrm{N^+}$, $\mathrm{O^+}$, $\mathrm{N_2^+}$, $\mathrm{NO^+}$, $\mathrm{O_2^+}$, $\mathrm{e^-}$), where $\mathrm{e^-}$ represents a free electron;

   (d) and carbon products from thermal protection systems: (C, $\mathrm{C_2}$, $\mathrm{C_3}$, CN, CO, $\mathrm{CO_2}$).

5. Different data sets of collision integrals $\Omega_{s,\ell}^{(i,j)}$ are tabulated to match the simulations of previous researchers, such as Stuckert, Park, and Mortensen [61, 62, 63].

6. Various transport models for dynamic viscosity and thermal conductivity including:

   (a) Power law

   (b) Sutherland's law for the mixture

   (c) Blottner's curve fits [64] with Eucken's relation [65] and Wilke's mixing rule [66], abbreviated as Blottner-Eucken-Wilke or BEW

   (d) Sutherland's law for each species and Wilke's mixing rule

   (e) Gupta's curve fits [67] with Wilke's mixing rule

   (f) Chapman-Enskog (CE) [68, §7-8]

   (g) Yos' approximations to CE [69]

   (h) Brokaw's approximation [70]

7. Diffusion models:

    (a) Constant Schmidt number or Lewis number

    (b) For binary diffusion coefficients, 1^{st}-order Chapman-Enskog relations can be used.

    (c) Multicomponent diffusion coefficients may be calculated with:

        i. Ramshaw's relations [71, 72]

        ii. Stefan-Maxwell equations [68]

    (d) Ambipolar diffusion, or diffusion caused by charge differences interacting with an electric field, may be accounted for in flows with ionization [71].

8. Thermal models assume Rigid Rotor and Harmonic Oscillator (RRHO) [73, 74, 75].

These various computational models have led to two co-authored journal articles ([76, 60]) as well as two co-authored conference articles: [77, 59]. Other developments in DEKAF performed by the author include

1. Converting the pressure coefficient into edge conditions that satisfy isentropic relations, which serve as freestream boundary conditions for the boundary layer.

2. Verified DEKAF directly against DPLR calculations (one of NASA's CFD codes)

3. Extended capability to complex configurations in hypersonics provided a surface pressure distribution.

    (a) For instance, work in Texas A&M M6QT has analyzed flow over a part-straight/part-flared cone. Given the surface pressure from a DPLR solution, DEKAF was provided the edge conditions again generated through isentropic relations and a boundary-layer was computed. This computed boundary-layer solution matched the DPLR solution excellently throughout the flare region, despite neglecting curvature and wall-normal pressure variation. Some of the research performed by the author can be found in the to-be-published conference article [78].

4. Led the process to make DEKAF an official, open-source code endorsed by three international universities: Texas A&M University, TU Delft, and The von Karman Institute for Fluid Dynamics

5. Established the git repository for DEKAF on gitlab.com and added extensive documentation to increase user-friendliness.

This concludes the main contributions by the author with regards to DEKAF. The next chapter will discuss stability analysis and the various methodologies as implemented in the in-house code, EPIC.

4. STABILITY ANALYSIS WITH EPIC

EPIC is an in-house stability code at the Computational Stability and Transition (CST) lab at Texas A&M University. First primarily developed by Nick Oliviero in 2015, the core algorithms for solving Linear Stability Theory (LST), the Linear Parabolized Stability Equations (LPSE), and the Nonlinear Parabolized Stability Equations were established with verification on hypersonic cones and subsonic swept wings [47, 48]. Travis Kocian significantly improved the capability of EPIC by introducing wall-normal interpolation of arbitrary three-dimensional base flows for stability analysis, analyzing crossflow and the fundamental breakdown in hypersonics [49]. The author entered the lab in 2017 and led the development of a new in-house code known as DERIVE that automatically derives the governing disturbance equations through a computer algebra system known as Maxima [79]. Using DERIVE, the author and Alex Moyes determined that the equations implemented in EPIC for LPSE and NPSE were missing a handful of terms as a result of the error-prone hand derivation done prior. This combined with the fact that that version of EPIC was not easily workable prompted the author and Alex Moyes to rewrite EPIC using modern features of Fortran. Extensibility and flexibility is the core of the code's architecture, using language aspects such as derived types and modules to easily share data across the program while also creating space for new features. Through reading and understanding modern Fortran tools and capability, EPIC was (re-)created. While Moyes focused on translating the core numerical algorithms of LST, LPSE, and NPSE, the author created the surrounding backbone, including but not limited to compilation, regular finite differences for discretization, interpolation, interfacing with DERIVE, unit testing, regression testing, input handling, and general Fortran utilities. With these tools established, Moyes validated EPIC in the hypersonics regime—especially its NPSE capability—with HIFiRE-5b flight tests and BOLT wind-tunnel tests, as well as direct numerical simulations [50]. Mullen used EPIC to analyze the sensitivity of various instability mechanisms to change in geometry/computational mesh, as well as changes in vehicle conditions at hypersonic speeds [80]. EPIC continues to be developed and used for analysis across the speed regimes. Work by Dr. Koen Groot

& Jay Patel have analyzed energy budgets of stationary crossflow mechanisms on pitched cones in hypersonic flow as well as the saturation and nonlinear development of Görtler vortices [81, 82]. Peck has demonstrated an excellent match between EPIC's LPSE and the higher-fidelity, elliptic equations of AHLNSE in supersonic flow for the oblique first mode [37].

With the background presented, let us now discuss the stability theory surrounding and implemented in the code, starting with the fundamentals—Linear Stability Theory.

4.1 Linear Stability Theory

Given that the highest gradients in viscous boundary layers tend to be in the wall-normal y direction, Linear Stability Theory (LST) first supposes that the laminar base flow is *only* a function of y. This is known as the parallel-flow assumption, as it demands the wall-normal velocity $\overline{v}$ to vanish. On the other hand, the strong y-dependence lends form to the disturbance's 'amplitude-function' to again only depend on y. The other dimensions of the problem—surface coordinate s, spanwise coordinate z, and time t—are accounted for by assuming the disturbance is a wave. The first LST analysis was demonstrated by Tollmien in 1930 followed by computations of Schlichting in 1933 [18, 19]. Thorough reviews are given by Reed et al. and Mack [13, 10]. A brief mathematical description is given below. The laminar base-flow $\overline{q}$ and disturbance ansatz q' are written as

$$\begin{aligned} \overline{q} &= \overline{q}(y), \\ q'(s,y,z,t) &= \underbrace{\hat{q}(y)}_{\text{shape}} \underbrace{\mathrm{e}^{(\mathrm{i}(\alpha s+\beta z-\omega t))}}_{\text{wave}} + \text{c.c.} \end{aligned} \tag{4.1}$$

Here, a complex-valued $\hat{q}(y)$ determines the shape and phase of the LST disturbance in y. It is a vector that has five components with one entry for each state variable $\hat{q} = [\hat{u}, \hat{v}, \hat{w}, \hat{T}, \hat{\rho}]$. Spatial wavenumbers α and β are related to the spatial wavelengths λ_s and λ_z in the s and z directions, respectively, as $\alpha = 2\pi/\lambda_s$ and $\beta = 2\pi/\lambda_z$. The angular frequency of the wave ω is related to its frequency f by $\omega = 2\pi f$. A negative sign is placed in front of ω in Eq. (4.1) by convention. The 'c.c.' is short-hand for the complex conjugate of the previous term and is necessary because the disturbance is real-valued in nature. To be explicit, the expression for the complex conjugate is

written as

$$\hat{q}^{\dagger}(y)\,\mathrm{e}^{\left(-\mathrm{i}(\alpha^{\dagger}s+\beta^{\dagger}z-\omega^{\dagger}t)\right)} \tag{4.2}$$

where the dagger superscript † indicates complex conjugation. Depending on the framework chosen, various wavenumbers may be strictly real, causing its complex conjugate to equal itself. For example, the 'spatial' framework for solving LST assumes that ω is provided as a real input and α and β are complex. In contrast, the 'temporal' framework assumes the contrapositive: α and β are provided as real inputs while ω is complex. The focus of this dissertation will cast LST in the spatial framework. Additionally, it is assumed that disturbances will not grow in the z direction, but only the s direction. This has the consequence that β is real while α remains complex. Now in this context, the real part of β is additionally input with ω and α is computed, following the discussion below. From the form of Eq. (4.1), note that a negative imaginary part of α represents exponential growth of the disturbance, whereas a positive imaginary part represents exponential decay.

When one substitutes in the LST disturbance into the governing Navier-Stokes equations and presumes a steady, laminar flow, the governing disturbance equations take the form

$$\mathcal{A}\frac{\mathrm{d}^2\hat{q}}{\mathrm{d}y^2}+\mathcal{B}\frac{\mathrm{d}\hat{q}}{\mathrm{d}y}+\mathcal{C}\hat{q}=0 \tag{4.3}$$

where $\mathcal{A}$, $\mathcal{B}$, and $\mathcal{C}$ are coefficient matrices of size 5×5. Each entry corresponds to the terms acting on a given variable in the vector $\hat{q}$ within a given conservation equation. These coefficient matrices are functions of α and the equation may be rewritten as

$$\left(\mathcal{L}_2\alpha^2+\mathcal{L}_1\alpha+\mathcal{L}_0\right)\hat{q}=0 \tag{4.4}$$

This form of the equations is mathematically a quadratic eigenvalue problem where α is the eigenvalue and $\hat{q}$ is the eigenfunction.[1] There is a clever algebraic manipulation of these equations that

[1] Once the problem is discretized in y, the nomenclature switches from 'eigenfunction' to 'eigenvector' for $\hat{q}$.

allows them to be written as a *linear, generalized* eigenvalue problem: see Bridges & Morris [83].

$$(\mathcal{L}_0^{\text{aug}} - \alpha \mathcal{L}_1^{\text{aug}})\, \hat{q}^{\text{aug}} = 0 \tag{4.5}$$

with the following substitutions

$$\mathcal{L}_0^{\text{aug}} = \begin{bmatrix} -\mathcal{L}_1 & -\mathcal{L}_2 \\ \mathbf{I} & \mathbf{O} \end{bmatrix} \quad \mathcal{L}_1^{\text{aug}} = \begin{bmatrix} -\mathcal{L}_0 & \mathbf{O} \\ \mathbf{O} & \mathbf{I} \end{bmatrix} \quad \hat{q}^{\text{aug}} = \begin{bmatrix} \alpha\hat{q} \\ \hat{q} \end{bmatrix} \tag{4.6}$$

where $\mathbf{I}$ and $\mathbf{O}$ are the identity matrix and zero matrix, respectively. The adjective *generalized* in this context refers to the fact that $\mathcal{L}_1^{\text{aug}}$ is not the identity matrix. As written, the augmented matrices $\mathcal{L}_1^{\text{aug}}$ and $\mathcal{L}_0^{\text{aug}}$ are size 10×10. However, there are no physical terms in the governing conservation equations that include second derivatives of $\hat{\rho}$, so one row and column may be omitted. In sum, the augmented matrix equation is 9×9 when the state vector $\hat{q} = [\hat{u}, \hat{v}, \hat{w}, \hat{T}, \hat{\rho}]$.

For a computational approach, the flowfield is discretized along the wall-normal y direction and each point in the grid must satisfy the governing Eqs. of (4.6), barring the prescribed boundary conditions at the surface and in the freestream.

For surface or 'wall' boundary conditions, the instantaneous flow velocity is assumed to reach zero according to the no-slip assumption and no-penetration. This propagates into conditions on $\hat{u} = 0$, $\hat{v} = 0$, and $\hat{w} = 0$ at the wall $y = 0$. For the temperature wall condition, if both the laminar base-flow $\overline{T}$ and the instantaneous T are isothermal, then the disturbance $\hat{T} = 0$ at the surface. On the other hand, if the laminar base-flow $\overline{T}$ is adiabatic, then the boundary condition is more nuanced. It is argued that for stationary disturbances ($\omega = 0$), the appropriate boundary condition is indeed also adiabatic: $\mathrm{d}\hat{T}/\mathrm{d}y = 0$. For traveling disturbances ($\omega \neq 0$), it is argued that the time scale of the disturbance is much faster than the scale of heat transfer for the surface material. In this instance, the disturbance achieves an *isothermal* boundary condition $\hat{T} = 0$ in spite of an adiabatic, laminar base flow [10]. For density $\hat{\rho}$, the equation corresponding to y-momentum is used as the boundary condition. The nomenclature for this is y-momentum is a *compatibility condition* for $\hat{\rho}$.

For freestream boundary conditions at the top boundary, the disturbance is presumed to decay to zero, as its energy is primarily located within the boundary layer. In this instance, $\hat{u} = 0$, $\hat{v} = 0$, $\hat{w} = 0$, and $\hat{T} = 0$ in the freestream at $y = y_{\max}$. Alternatively, one may presume the disturbance asymptotes to a zero slope in the freestream. This is helpful in scenarios when the wall-normal domain must be small (e.g., a bounding shock from above or other reasons discussed in chapter 5.) That is, $\mathrm{d}\hat{\phi}/\mathrm{d}y = 0$ for $\hat{\phi} \in \{\hat{u}, \hat{v}, \hat{w}, \hat{T}\}$ at $y = y_{\max}$. Some disturbances however do propagate a significant amount of energy into the freestream and the above boundary conditions are consequently inappropriate. An example of such a disturbance is the supersonic Mack mode [84, 85, 86]. In those situations, reflecting boundary conditions are appropriate, but it is beyond the scope of the dissertation. The density component $\hat{\rho}$ may be presumed to be either a) zero valued, b) zero slope, c) or satisfy some compatibility condition, such as continuity or y-momentum.

The boundary conditions in conjunction with the augmented system at each interior node of the wall-normal grid form now a large matrix system of size $9N_y \times 9N_y$, where N_y is the number of points in the y domain. With the mathematical form of a linear, generalized eigenvalue problem, this may be numerically solved with standard LAPACK Fortran subroutines. A local approach uses a Krylov-subspace method, and with an initial guess for an eigenvalue of interest, solves for a finite number of eigenvalues nearby through approximation [87]. In this procedure, ultimately the equation form is transformed back to a regular eigenvalue problem through a Hessenberg form, permitting use of `ZGEEV` [88]. For reasonably resolved problems, a sample Krylov subspace dimension will be no more than 100 to obtain an appreciably accurate answer. A global approach makes no approximations and solves for all of the eigenvalues of the matrix, i.e., the *spectrum*. This procedure makes use of LAPACK's `ZGGEV` using the classical QZ algorithm and is not often performed due to the additional computational cost [89].

In the spectrum of eigenmodes, there are solutions that are near one another and form continuous branches throughout the complex plane while there also exist some solutions that are disconnected from these branches—deemed *discrete* eigenmodes. The curious reader is referred to Grosch & Salwen for more detail [90]. The system's dynamics are determined by the summation

of all of the eigenmodes by way of eigenfunction expansion methods [91]. However, it is often assumed with these modal stability theories that the system's dynamics can be approximated by considering just *one* of the discrete eigenmodes in the spectrum. This may not always be appropriate in boundary-layer stability analysis as some mechanisms are reliant not primarily on one eigenmode, but two: see the analysis of the supersonic Mack mode by Tumin [91, 84]. For other primary instability mechanisms such as Tollmien-Schlichting or stationary crossflow, a discrete eigenmode is a reasonable approximation when compared to high-fidelity computations or experimental measurements. After selecting a discrete eigenmode from the spectrum, the eigensolution may be confirmed or 'purified' by substituting it into the governing ordinary differential equations of Eq. (4.3) and iterating with Newton-Raphson until the residual is below some desired tolerance.

4.1.1 Wall-normal coordinate y

To cluster nodes in the wall-normal coordinate for the stability solution, the shape of laminar boundary layer is leveraged. In the results section, specific values for clustering height y_i and the max of the domain $y_{\max}$ will be specified. With an equispaced, logical domain $\eta = [0, 1]$, the wall-normal clustering function used is

$$y = \frac{y_{\max} y_i \, \eta}{y_{\max} - y_i - \eta \left(y_{\max} - 2 y_i \right)} \tag{4.7}$$

inspired by Malik & Orszag [92]. With this formulation, the computational nodes are split such that half of them are placed below the clustering height y_i to the surface, while the other half is above y_i up to $y_{\max}$.

Note that this function may be used with a *non-equispaced* logical coordinate as well. For example, a cosine-mapped η^* may be input to (4.7) to maintain reasonable resolution at the boundaries. In this case, η^* is a function of the equispaced, logical domain $\eta = [0, 1]$ as

$$\eta^* = \frac{1}{2} \left(1 - \cos(\pi \eta) \right) \tag{4.8}$$

such that $\eta^* \in [0, 1]$ as well.

4.2 Linear Parabolized Stability Equations

The disturbance formulation of LST may be expanded slightly to be more physically inclusive. Streamwise development and non-parallel effects now are partially included in the formulation, taking inspiration originally from the multiple-scales methodology [93]. The form of these equations, known as the Linear Parabolized Stability Equations (LPSE), were written first for incompressible flows by Herbert & Bertolotti [94], and then extended to compressible flows in Bertolotti's dissertation [22] and simultaneously by Chang et al. [23]. The seminal review for PSE is written by Herbert [12]. A brief mathematical description is written below.

One may introduce a factor $\varepsilon_s \ll 1$ that follows the streamwise change of all flow variables

$$\frac{\partial}{\partial s} = \varepsilon_s \frac{\partial}{\partial \breve{s}} \tag{4.9}$$

which yields a definition of a new streamwise coordinate $\breve{s} = \varepsilon_s s$. With this substitution in mind, consider now the compressible continuity equation for the laminar base-flow, assuming a Cartesian coordinate system.

$$\begin{aligned} \frac{\partial(\overline{\rho}\,\overline{u})}{\partial s} + \frac{\partial(\overline{\rho}\,\overline{v})}{\partial y} &= 0, \\ \varepsilon_s \frac{\partial(\overline{\rho}\,\overline{u})}{\partial \breve{s}} + \frac{\partial(\overline{\rho}\,\overline{v})}{\partial y} &= 0, \\ \implies \overline{v} = \varepsilon_s \bigg(-\frac{1}{\overline{\rho}} \int_0^{y_{\max}} \frac{\partial(\overline{\rho}\,\overline{u})}{\partial \breve{s}}\, \mathrm{d}y \bigg) & \end{aligned} \tag{4.10}$$

which indicates that the wall-normal velocity component $\overline{v}$ is on the order of ε_s as well. In the derivation process for LPSE—similar to that of LST—first-order terms of ε_s are kept while higher-order terms ε_s^n, $n \geq 2$ are assumed negligible.

The wave in the ansatz is also modified in PSE with respect to LST's, borrowing a methodology sometimes used in quantum mechanics known as the WKBJ technique [95]. Now the streamwise wavenumber α obtains some of the streamwise variation in the coordinate $\breve{s}$ as well as the shape-

function $\hat{q}$. The base-flow assumption then with the LPSE disturbance ansatz is written as

$$\begin{aligned} \overline{q} &= \overline{q}(\breve{s}, y), \\ q'(s, y, z, t) &= \hat{q}(\breve{s}, y)\, \mathrm{e}^{\mathrm{i}\left(\int_{\breve{s}_1}^{\breve{s}} \alpha(\overline{s})\, \mathrm{d}\overline{s} + \beta z - \omega t\right)} + \text{c.c.} \end{aligned} \tag{4.11}$$

where $\overline{s}$ is a dummy variable of integration over $\breve{s}$. This form is used in the derivation of the governing equations and subsequent analysis. Once implemented into the program for computations, however, there is no distinction necessary between s and $\breve{s}$. The governing equations from continuity, momentum, and energy conservation are expressed now in terms of s with $\partial/\partial s$ terms acting on $\hat{q}$:

$$\mathcal{M}_{sy} \frac{\partial^2 \hat{q}}{\partial s\, \partial y} + \mathcal{M}_{yy} \frac{\partial^2 \hat{q}}{\partial y^2} + \mathcal{M}_s \frac{\partial \hat{q}}{\partial s} + \mathcal{M}_y \frac{\partial \hat{q}}{\partial y} + \mathcal{M}_0\, \hat{q} = 0 \tag{4.12}$$

These disturbance equations for LPSE can be found in appendix A. Similar to LST, the wavenumber β and angular frequency ω are provided and the equations must be solved for $\hat{q}$ and α. However, the problem formulation differs here, as it is no longer an eigenvalue problem with the presence of the streamwise derivative $\partial/\partial s$. A supplementary equation is provided, known as a normalization condition or auxiliary equation, in order to close the system. The concept is to minimize the streamwise change in $\hat{q}$, since its second-order derivatives are neglected in the problem formulation. From Herbert, one way to accomplish this is to minimize growth at a representative height in the domain or in an integral sense over the entire boundary layer [12]. This is accomplished iteratively by moving much of the shape-function's streamwise growth and decay into the complex wavenumber α. Details on this procedure will be left for nonlinear discussion in §4.3.

The mathematical form of the governing differential equation in Eq. (4.12) is now different than that of LST. Instead of an ordinary differential equation, it is a *partial* differential equation. With the appearance of only first-order derivatives in s, it is presumed to be parabolic in nature, much like the heat equation. In this sense, an initial condition is provided at the first s-station, say s_1, and subsequently 'marched' downstream in the s coordinate as far as desired. Note, however, the parabolic presumption is an approximation on the physical reality of the problem. With the

inclusion of s-derivatives, there are second-order terms that do prompt the proper treatment as a boundary-value problem. That problem formulation is elliptic in nature and must be computationally solved everywhere in the domain simultaneously, which is discussed further in §4.3.

The initial condition can be prescribed in multiple ways, but by far the most common is to select a single discrete eigenmode from LST. It is reasonably close to satisfying the PSE equations, but of course there are discrepancies from non-parallel effects. This error then is visualized as a spatial transient upon initialization. Often within 4-5 streamwise steps, this 'LST-transient' will decay out and the proper PSE solution will be present. If the flow is appreciably non-parallel early on and the parallel LST eigenmode is too far off in the complex plane from the corresponding PSE solution, then solving the governing equations can fail catastrophically, as the solution begins to hover near complex zero. Sometimes this is colloquially referred to as 'losing the mode' and often indicates that the LST initial condition is inappropriate. In this regard, initializing LPSE with an LST solution has a chance of failure, but for a wide range of scenarios, the methodology is successful.

Another methodology to initialize LPSE is by providing another PSE solution or even a component from a DNS simulation. These are helpful when available for verification between codes, but is not commonly performed for most analyses.

The wall-normal boundary conditions for LPSE are formulated identically as LST's, and for brevity, are omitted. This completes the brief discussion on the LPSE formulation. The section on discretization relevant to LPSE is given below.

4.2.1 Computational discretization

The wall-normal coordinate is clustered as used in the LST problem, that is, using the mapping inspired by Malik & Orszag. However, for this formulation, note the distributions for y_i and $y_{\max}$ vary in s, causing the physical y grid to modulate. Additionally, the computed distributions of y_i or $y_{\max}$ can optionally be fit with a polynomial if desired. Briefly, polynomials of order 1 through 20 are queried for the fit. The order whose polynomial minimizes the square error with respect to the original data is selected.

4.2.2 Streamwise coordinate s

The streamwise surface coordinate s is generated by a cumulative sum of

$$s_{i+1} = s_i + \sqrt{(x_{i+1} - x_i)^2 + (Y_{c,\,i+1} - Y_{c,\,i})^2} \tag{4.13}$$

with $s_1 \equiv 0$. Here, x is the leading-edge-orthogonal, chord-axis coordinate of the airfoil and Y_c is the vertical airfoil coordinate. The coordinate s in the grid used for stability analysis is, most of the time, equispaced and is made so via spline-interpolated (not-a-knot). In these scenarios, the logical coordinate $\xi = s$ such that $\mathrm{d}\xi/\mathrm{d}s = 1$. However, there are several cases relevant for PSE application that warrant streamwise clustering. The first of which is characterizing the crossflow instability in swept-wing flows. The extremely favorable pressure gradients that follow in the region of the attachment line trigger very high growth rates of the crossflow instability. A high resolution in the stability grid is needed to successfully converge near-attachment line properties, like the branch-I location of the disturbance. Additionally near the attachment line, there may be appreciable surface curvature, thus demanding smaller Δs to reduce the error incurred by the approximation of the h_i metrics (see §2.2). However, beyond the attachment-line region, the governing pressure gradients of a swept wing become much less severe farther downstream and surface curvature decreases. In this region of the domain, streamwise clustering is no longer needed. Now, the devil's advocate may say, with modern computing power and near-endless storage, why not just run a high streamwise resolution that is equispaced? That is a reasonable solution—in fact, the author himself has done this for the much of the earlier linear analysis presented [96, 97]. In the spirit of computational efficiency and speed however, deresolving the streamwise domain away from regions of strong gradients is desired.

Another application that warrants streamwise clustering in PSE is characterizing the fundamental breakdown (also known as primary resonance) in a hypersonic boundary layer. In the complex nonlinear transition process, there is the initial stage of linear growth of the $(1, 0)$ Mack second mode. Here, only a moderately low number of streamwise nodes are required for an accurate so-

lution. It is not until the mean-flow distortion grows to a significant amplitude and the streamwise vortex mode $(0,1)$ exceeds the amplitude of the $(1,0)$ second mode. At this stage, nonlinear effects are dominant and there can be abrupt changes in the shape-functions. See DNS results by Hader & Fasel as a demonstration of the above transition process [98]. In the nonlinear regime, a higher streamwise resolution may be desired—high enough to resolve the nonlinear dynamics while avoiding the step-size criterion causing sudden divergence of the solution.

There are many different ways to cluster computational nodes. For instance, Malik mapping is excellent for wall-normal distributions in unbounded shear flows (e.g., boundary layers). Here, the author follows with a simple yet robust power law: $s \propto \xi^{\text{cst}}$. The actual formula used has additional properties to improve its practicality, shown below:

$$\frac{s - s_i + \epsilon_s}{s_f - s_i} = \alpha_{\text{map}} \left(\frac{\xi - \xi_i + \epsilon_\xi}{\xi_f - \xi_i + \epsilon_\xi} \right)^{\beta_{\text{map}}} + \gamma_{\text{map}} \left(\frac{\xi - \xi_i + \epsilon_\xi}{\xi_f - \xi_i + \epsilon_\xi} \right) \tag{4.14}$$

The only variables are s and ξ; the rest are constants. Constants s_i and s_f indicate the initial and final s values of the s coordinate, while ξ_i and ξ_f are analogous for the ξ coordinate. Constants ϵ_s and ϵ_ξ are numerical shifts to reduce numerical underflow. The primary mapping parameters are α_{map}, β_{map}, and γ_{map}. Here, α_{map} may be computed based where a third may be computed from specifying β_{map}, and γ_{map}, as shown below.

Each feature in Eq. (4.14) has its reasoning. The explanation and thought-process is outlined below:

- Without the final linear term $\propto \gamma_{\text{map}}\xi$, the derivative $\mathrm{d}s/\mathrm{d}\xi$ at $\xi = \xi_i$ would be zero, implying that $\mathrm{d}\xi/\mathrm{d}s \to \infty$. This value, however unused directly by a PSE code,[2] could be problematic, as integration could propagate infinity throughout the domain, diluting a calculation. A nonzero γ_{map} then specifies the slope of $s(\xi)$ near ξ_i.

- When performing any transformation between computational and physical variables, it is ideal to have the numbers on the same order of magnitude to minimize any loss of preci-

[2] Values of $\mathrm{d}\xi/\mathrm{d}s$ are only used from a streamwise index of 2 and onward, i.e., directly after of ξ_i.

sion in subsequent calculation, i.e., numerical underflow. For this reason, the choice was made to assign $\xi_i \equiv s_i$ and $\xi_f \equiv s_f$, provided $s_i < s_f$. Even though they have the same numerical value, the s coordinate has dimensional units of length (e.g., meters) whereas the ξ coordinate is unitless by construction. This choice leads to the function

$$\frac{s - s_i}{s_f - s_i} = \alpha_{\text{map}} \left(\frac{\xi - \xi_i}{\xi_f - \xi_i} \right)^{\beta_{\text{map}}} + \gamma_{\text{map}} \left(\frac{\xi - \xi_i}{\xi_f - \xi_i} \right) \tag{4.15}$$

- The above formula is nearly there, but it has one flaw. For values of $\beta_{\text{map}} < 1$, the derivative $\mathrm{d}s/\mathrm{d}\xi$ at $\xi = \xi_i \to \infty$. We choose to then shift each numerator on the right-hand side by some positive quantity, call it ϵ_ξ. With a positive numerator now within the power law at $\xi = \xi_i$, the derivative $\mathrm{d}s/\mathrm{d}\xi$ will stay finite for all β_{map}. We also include ϵ_ξ in the denominator such that evaluation of the argument at ξ_f goes to unity. With a shift on the right-hand side, it is appropriate that the left-hand side also includes a shift, call it ϵ_s, bringing us to the final form, repeated below for convenience:[3]

$$\frac{s - s_i + \epsilon_s}{s_f - s_i} = \alpha_{\text{map}} \left(\frac{\xi - \xi_i + \epsilon_\xi}{\xi_f - \xi_i + \epsilon_\xi} \right)^{\beta_{\text{map}}} + \gamma_{\text{map}} \left(\frac{\xi - \xi_i + \epsilon_\xi}{\xi_f - \xi_i + \epsilon_\xi} \right) \tag{4.16}$$

- Let us evaluate $s(\xi)$ at the end points to give us two relations between these various constants.

$$\begin{aligned} \xi = \xi_i \,, s = s_i : \quad & \frac{\epsilon_s}{s_f - s_i} = \alpha_{\text{map}} \left(\frac{\epsilon_\xi}{\xi_f - \xi_i + \epsilon_\xi} \right)^{\beta_{\text{map}}} + \gamma_{\text{map}} \left(\frac{\epsilon_\xi}{\xi_f - \xi_i + \epsilon_\xi} \right) \\ \xi = \xi_f \,, s = s_f : \quad & 1 + \frac{\epsilon_s}{s_f - s_i} = \alpha_{\text{map}} + \gamma_{\text{map}} \end{aligned} \tag{4.17}$$

[3] In programming this equation, the values of $s(1) = s_i$ and $s(N_s) = s_f$ are assigned after the function evaluation to ensure the domain exactly contains those input values. This accommodates for the natural and slight error through underflow.

- Solve for α_{map} in the second equation, substitute into the first, and solve for ϵ_s.

$$\alpha_{\text{map}} = 1 + \frac{\epsilon_s}{s_f - s_i} - \gamma_{\text{map}}$$
$$\epsilon_s = \frac{s_f - s_i}{1 - \left(\frac{\epsilon_\xi}{\xi_f - \xi_i + \epsilon_\xi}\right)^{\beta_{\text{map}}}} \left((1 - \gamma_{\text{map}}) \left(\frac{\epsilon_\xi}{\xi_f - \xi_i + \epsilon_\xi} \right)^{\beta_{\text{map}}} + \gamma_{\text{map}} \left(\frac{\epsilon_\xi}{\xi_f - \xi_i + \epsilon_\xi} \right) \right) \tag{4.18}$$

- Finally, choose ϵ_ξ such that the positive constant is on the order of ξ, reducing numerical underflow.

$$\epsilon_\xi = \max(|\xi_i|, |\xi_f|) \tag{4.19}$$

With these above equations, the equation leaves β_{map} and γ_{map} as free parameters, allowing the user to specify them as they please. Note that an equispaced domain is recovered if $\beta_{\text{map}} = 1$ and $\gamma_{\text{map}} = 0$. For physical intuition, suppose $\gamma_{\text{map}} > 0$. Then $\beta_{\text{map}} > 1$ implies clustering occurs near the front of the domain, whereas $\beta_{\text{map}} < 1$ implies clustering downstream at the rear of the domain. The former case may be useful for linear crossflow calculations on swept wings while the latter may be helpful for nonlinear PSE calculations. Further, there are some combinations of β_{map} and γ_{map} that cause $\max(s) > s_f$ or $\min(s) < s_i$. These combinations are rejected for all practical purposes, as monotonicity is required. A sample streamwise mapping to cluster near the front of the domain uses $\gamma_{\text{map}} = 0.5$ and $\beta_{\text{map}} = 15$. This clustering with $N_s = 250$ and $s \in [0, 1]$ is shown in Fig. 4.1. The top panel indicates s mapped against logical coordinate ξ, where s_{equi} is the equivalent equispaced domain. The orange circle indicates the last streamwise station where clustering occurs, i.e., where $\mathrm{d}s/\mathrm{d}\xi < 1$. The second panel indicates the change in s, calculated by the chain rule $\Delta s \approx \Delta\xi \, \mathrm{d}s/\mathrm{d}\xi$. The third panel indicates what is referred to as the "equivalent equispaced" streamwise resolution. That is, if the domain were equispaced for the current Δs, the

quantity represents the number of total nodes. This quantity is derived briefly as

$$\begin{aligned} \Delta s &= \frac{L_s}{N_{s,\text{equi}} - 1}, \\ \Delta\xi \frac{\mathrm{d}s}{\mathrm{d}\xi} &= \frac{L_s}{N_{s,\text{equi}} - 1}, \\ \implies N_{s,\text{equi}} &= 1 + \frac{L_s}{\Delta\xi \frac{\mathrm{d}s}{\mathrm{d}\xi}} \end{aligned} \tag{4.20}$$

where L_s is the length of the domain in the s coordinate, i.e., $s_f - s_i$. The third panel indicates the power of the mapping: the domain may achieve a streamwise resolution of nearly $N_{s,\text{equi}} = 1000$ near the front while smoothly deresolving at the back of the domain where the changes in the solution are less so. As mentioned earlier in the section, this is excellent for performing efficient yet still accurate stability analysis of crossflow over a swept, natural-laminar-flow airfoil. Given the steep slope in the pressure coefficient for these wings upstream for $x/c < 0.05$, high streamwise resolution is required (e.g., $N_{s,\text{equi}} \approx O(1000)$) to achieve appreciably small streamwise errors: see Fig. 10a in [97]. At the same time, given the mild pressure gradient over the remainder of the chord, extremely high streamwise resolution is no longer required and can be safely deresolved. An alternative to this approach that may accomplish the same means follows the hyperbolic tangent distribution for Δs. Upon integration, a natural logarithm of a hyperbolic cosine is used for $s = s(\xi)$, akin to the one described in previous chapter: see §3.3. This particular mapping has the added benefit of not successively deresolving at the back of the domain, however it is not yet implemented into EPIC.

With the streamwise s domain defined, derivatives necessary for coordinate transformations are readily computed from Eq. (4.7): $\partial\eta/\partial y$ and $\partial^2\eta/\partial y^2$. After the derivatives $\partial y_i/\partial s$ and $\partial y_{\max}/\partial s$ are computed via finite differences, the streamwise derivatives $\partial\eta/\partial s$ and $\partial^2\eta/\partial s\partial y$ are then computed. Derivatives in the η direction are computed by polynomial differentiation described by Weideman & Reddy [99, §2], using fourth-order accuracy. Note that differentiation of the base-flow uses second-order accurate, central, regular finite differences in the streamwise s direction, while it drops to first-order accurate, one-sided at the boundaries. To avoid the ill-posedness of

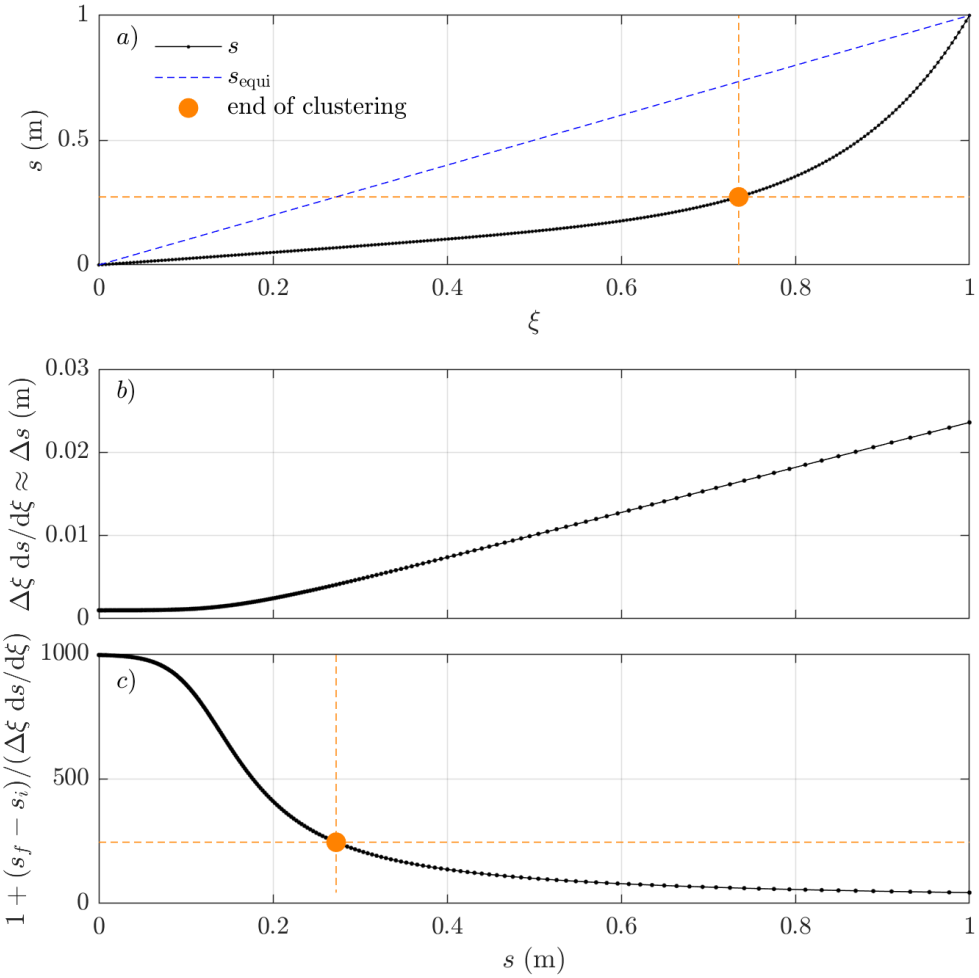

Figure 4.1: Streamwise mapping on s for a selected $N_s = 250$, $\gamma_{\text{map}} = 0.5$, and $\beta_{\text{map}} = 15$, as given by Eq. (4.14). a) Streamwise coordinate s versus logical coordinate ξ, shown in black. The dashed blue line indicates an equispaced $s \equiv s_{\text{equi}}$, while the orange circle indicates the last streamwise station where clustering occurs, found by examining the slope exceeding unity. b) Difference in streamwise coordinate s, as calculated by $\Delta\xi\,\mathrm{d}s/\mathrm{d}\xi$. c) "Equivalent equispaced" streamwise resolution $N_{s,\text{equi}}$ as a function of s, as defined in Eq. (4.20).

PSE at these near-incompressible speeds (discussed in §4.3.3.2), a first-order backward regular finite difference scheme is used for this problem.

Differentiation operators in terms of physical coordinates s and y are then expressed through

the multivariate chain rule as

$$\begin{aligned}
\frac{\partial}{\partial s} &= \frac{\partial \xi}{\partial s}\frac{\partial}{\partial \xi} + \frac{\partial \eta}{\partial s}\frac{\partial}{\partial \eta}, \\
\frac{\partial}{\partial y} &= \frac{\partial \eta}{\partial y}\frac{\partial}{\partial \eta}, \\
\frac{\partial^2}{\partial s\,\partial y} &= \frac{\partial \eta}{\partial y}\frac{\partial \xi}{\partial s}\frac{\partial^2}{\partial \xi\,\partial \eta} + \frac{\partial \eta}{\partial s}\frac{\partial \eta}{\partial y}\frac{\partial^2}{\partial \eta^2} + \frac{\partial^2 \eta}{\partial s\,\partial y}\frac{\partial}{\partial \eta}, \\
\frac{\partial^2}{\partial y^2} &= \left(\frac{\partial \eta}{\partial y}\right)^2 \frac{\partial^2}{\partial \eta^2} + \frac{\partial^2 \eta}{\partial y^2}\frac{\partial}{\partial \eta}
\end{aligned} \tag{4.21}$$

Note that $\partial^2/\partial s^2$ is not needed since it is not present in the governing equations of the disturbance, Eqs. (4.12). With these operators defined, derivatives of any quantity of interest (e.g., base-flow, disturbance) are readily computed with respect to the physical coordinates.

This completes the description of the streamwise discretization. Let us move now to a longer discussion on the nonlinear variant of PSE.

4.3 Nonlinear Parabolized Stability Equations

This section will thoroughly discuss the Nonlinear Parabolized Stability Equations, or NPSE, methodology which serves as an extension of the LPSE methodology to finite amplitudes. A derivation of the governing equations will be presented in conjunction with boundary conditions, initial conditions, and a final outline of the solution procedure.

4.3.1 Derivation of the governing equations

It is common in physics and engineering to model a wave-like disturbance or a force as a sum of finite harmonics—temporally and/or spatially [93]. The Parabolized Stability Equations (PSE) approach does so as well, accounting for a selected number of disturbances that are multiples of the fundamental frequency and spanwise wavenumber. The disturbance may be written as a Fourier transform of the physical perturbation with respect to time t and spanwise coordinate z. For practical computations, the infinite double sum is truncated in both time and space, given in

Eq. (4.22), where there are $2N+1$ Fourier modes in time and $2K+1$ in span.

$$q'(s,y,z,t) = \sum_{n=-N}^{N} \sum_{k=-K}^{K} \underbrace{\frac{A_{0\,(n,k)}}{2}\, \hat{q}_{(n,k)}(\breve{s},y)\, \mathrm{e}^{\mathrm{i}\left(\int_{\breve{s}_1}^{\breve{s}} \alpha_{(n,k)}(\overline{s})\,\mathrm{d}\overline{s} + k\beta_0 z - n\omega_0 t\right)}}_{q'_{(n,k)}} \tag{4.22}$$

Since the disturbance is real-valued, the summations consider the negative wavenumbers and frequencies to effectively take the real part of the argument. This is because the $(-n,-k)$-harmonic represents the complex conjugate of the (n,k)-harmonic. As an aside, in this dissertation, the phrases '(n,k)-harmonic' and 'Fourier mode' will be used interchangeably in the context of PSE. This avoids the use of 'mode', as that is reserved for solutions to eigenvalue problems [9].

Here, $A_{0\,(n,k)}$ is the amplitude at a certain reference location in s and can be complex-valued to express phase relations of the different harmonics at that reference location. The division by 2 eases the assignment programmatically such that a value of $A_{0\,(n,k)}$ is distributed equally across the (n,k)-harmonic and its complex conjugate.[4] The wavenumbers $(\omega_0,\beta_0) \in \mathbb{R}$ are the smallest nonzero spanwise wavenumbers and angular frequency of interest in the problem (smallest in terms of absolute magnitude). The numerical problem now is centered around solving for the complex-valued shape-function $\hat{q}_{(n,k)}$ and the streamwise wavenumbers $\alpha_{(n,k)}$ of each Fourier mode. Note that the shape-function is a vector with 5 components here:

$$\hat{q}_{(n,k)} = \{\hat{u}_{(n,k)},\, \hat{v}_{(n,k)},\, \hat{w}_{(n,k)},\, \hat{T}_{(n,k)},\, \hat{\rho}_{(n,k)}\} \tag{4.23}$$

4.3.1.1 Negative wavenumbers and frequencies

Let us discuss further the presence of negative effective wavenumbers and frequencies present in the PSE ansatz of Eq. (4.22). Since the total disturbance represents a physical value, q' must be real. Consider then a single (n,k) Fourier mode and assert that its complex conjugate must be

[4] Admittedly, the division by 2 is unnecessary in the problem formulation. Note that the mean-flow distortion $(0,0)$ is its own complex conjugate, so the division by 2 is omitted *only* for this particular disturbance.

equal to itself. Since $(\omega_0, \beta_0) \in \mathbb{R}$,

$$\hat{q}_{(n,k)} \mathcal{W}_{(n,k)} \mathrm{e}^{(\mathrm{i}(k\beta_0 z - n\omega_0 t))} = \hat{q}^{\dagger}_{(n,k)} \mathcal{W}^{\dagger}_{(n,k)} \mathrm{e}^{(-\mathrm{i}(k\beta_0 z - n\omega_0 t))} \tag{4.24}$$

where the dagger superscript † indicates complex conjugation and $\mathcal{W}_{(n,k)}$ is defined as $A_{0\,(n,k)}$ multiplied by the streamwise component of the wave:

$$\mathcal{W}_{(n,k)} \equiv A_{0\,(n,k)}\, \mathrm{e}^{\,\mathrm{i} \int_{s_1}^{s} \alpha_{(n,k)}\, \mathrm{d}\tilde{s}} \neq 0 \tag{4.25}$$

The variable $\mathcal{W}$ is chosen as an ode to WKBJ methods, as alluded to in the previous LPSE section [95]. In the expression on the right of Eq. (4.24), switch the signs of (n, k) to $(-n, -k)$:

$$\begin{aligned} \hat{q}^{\dagger}_{(n,k)} \mathcal{W}^{\dagger}_{(n,k)} \mathrm{e}^{(-\mathrm{i}(k\beta_0 z - n\omega_0 t))} &= \hat{q}^{\dagger}_{(-n,-k)} \mathcal{W}^{\dagger}_{(-n,-k)} \mathrm{e}^{(-\mathrm{i}(-k\beta_0 z - (-n)\omega_0 t))} \\ &= \hat{q}^{\dagger}_{(-n,-k)} \mathcal{W}^{\dagger}_{(-n,-k)} \mathrm{e}^{(\mathrm{i}(k\beta_0 z - n\omega_0 t))} \end{aligned} \tag{4.26}$$

Equate Eq. (4.24) and Eq. (4.26) to find

$$\begin{aligned} \hat{q}_{(n,k)} &= \hat{q}^{\dagger}_{(-n,-k)}, \\ \mathcal{W}_{(n,k)} &= \mathcal{W}^{\dagger}_{(-n,-k)} \end{aligned} \tag{4.27}$$

which implies the useful relations

$$\begin{aligned} \hat{q}^{\dagger}_{(n,k)} &= \hat{q}_{(-n,-k)}, \\ \mathcal{W}^{\dagger}_{(n,k)} &= \mathcal{W}_{(-n,-k)} \end{aligned} \tag{4.28}$$

Evaluating the expression for $\mathcal{W}_{(n,k)}$ at the first streamwise node $s = s_1$, the integral vanishes:

$$A^{\dagger}_{0\,(n,k)} = A_{0\,(-n,-k)} \tag{4.29}$$

Consider the expression for $\mathcal{W}_{(n,k)}$ now for $s > s_1$:

$$\begin{aligned} A^{\dagger}_{0\,(n,k)} \mathrm{e}^{-\mathrm{i}\int_{s_1}^{s} \alpha^{\dagger}_{(n,k)}\,\mathrm{d}\tilde{s}} &= A_{0\,(-n,-k)} \mathrm{e}^{\mathrm{i}\int_{s_1}^{s} \alpha_{(-n,-k)}\,\mathrm{d}\tilde{s}}, \\ \mathrm{e}^{-\mathrm{i}\int_{s_1}^{s} \alpha^{\dagger}_{(n,k)}\,\mathrm{d}\tilde{s}} &= \mathrm{e}^{\mathrm{i}\int_{s_1}^{s} \alpha_{(-n,-k)}\,\mathrm{d}\tilde{s}}, \\ -\alpha^{\dagger}_{(n,k)} &= \alpha_{(-n,-k)} \end{aligned} \tag{4.30}$$

The complex-conjugate relations for $\hat{q}_{(-n,-k)}$ and $\alpha_{(-n,-k)}$ in Eq. (4.28) and Eq. (4.30) imply that not all considered $(2N+1)(2K+1)$ Fourier modes need to be calculated directly by solving their governing equation. Instead, only $n \geq 0$ need to be considered across the entire nk-plane. And along the k-axis, only $k \geq 0$ need to be considered as well. The total number of Fourier modes then that are solved via the governing PDEs reduces to $(N+1)(2K+1) - K$ while the remaining Fourier modes are computed with Eq. (4.28) and Eq. (4.30). A graphical example is shown in Fig. 4.2 to visualize this pattern.

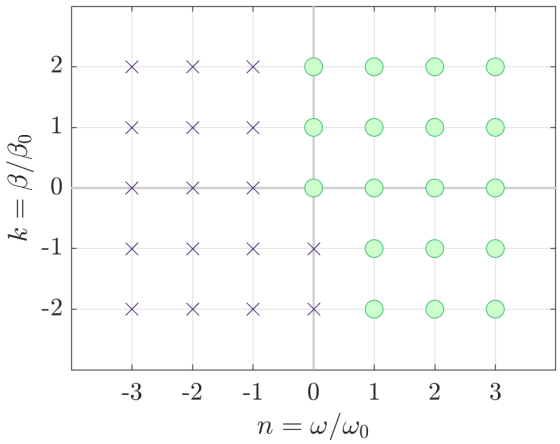

Figure 4.2: Fourier modes (n, k) in the wavenumber-multiple nk-plane for $N = 3$ and $K = 2$. Green circles indicate Fourier modes for which the governing PDEs must be solved, while purple crosses indicates those for which complex-conjugate relations may be used.

4.3.1.2 *Symmetry relations in z*

There exist relations in addition to the above conjugate relationships that arise when when $\overline{w} = 0$. These are:

$$\begin{aligned} \hat{q}_{(n,k)} &= \hat{q}_{(n,-k)} \quad \hat{q} \neq \hat{w}, \\ \hat{w}_{(n,k)} &= -\hat{w}_{(n,-k)}, \\ \alpha_{(n,k)} &= \alpha_{(n,-k)} \end{aligned} \tag{4.31}$$

which has the special implication for stationary Fourier modes with $n = 0$:

$$\begin{aligned} \hat{q}_{(0,k)} &= \hat{q}_{(0,-k)} = \hat{q}^{\dagger}_{(0,k)} \quad \hat{q} \neq \hat{w}, \\ \hat{w}_{(0,k)} &= -\hat{w}_{(0,-k)} = -\hat{w}^{\dagger}_{(0,k)}, \\ \alpha_{(0,k)} &= \alpha_{(0,-k)} = \alpha^{\dagger}_{(0,k)} \end{aligned} \tag{4.32}$$

These equations imply that $\hat{q}_{(0,k)}$, $\hat{q} \neq \hat{w}$ and $\alpha_{(0,k)}$ are real-valued, since they are equal to their complex conjugates. On the other hand, $\hat{w}_{(0,k)}$ is purely imaginary since its equal to its negative conjugate. The present symmetry conditions in z further reduce the Fourier modes needed to be calculated via PDEs to only (n, k) where both $n \geq 0$ and $k \geq 0$. That is, in terms of the nk-space, only the first quadrant needs to be considered in the simulation, solving $(N + 1)(K + 1)$ PDEs in total. These relations are crucial to enforce symmetry. Relevant examples include a Görtler vortex at zero sweep or a fundamental breakdown on a cone, zero degrees angle of attack. See work by Patel leveraging these symmetry conditions in EPIC [82].

4.3.1.3 *Harmonic balancing*

If the amplitudes are presumed to be infinitesimal, then the linear PSE (or LPSE) are recovered for each considered Fourier mode. These equations are found by supposing $\varepsilon_p \ll 1$, i.e., ε_p^2 is negligible in Eq. (2.23). However, if amplitudes are finite, nonlinear PSE (or NPSE) are required. Consider substituting the PSE model, or ansatz, into the governing equations with only quadratic

terms. Then

$$\begin{aligned}\mathcal{LNS}\left(\sum_{n=-N}^{N}\sum_{k=-K}^{K} A_{0\,(n,k)}\hat{q}_{(n,k)}\,\mathrm{e}^{\mathrm{i}\left(\int_{s_0}^{s}\alpha_{(n,k)}\,\mathrm{d}\tilde{s}+k\beta_0 z-n\omega_0 t\right)}\right) = \\ \mathcal{N}\Bigg(\sum_{n_1=-N}^{N}\sum_{k_1=-K}^{K} A_{0\,(n_1,k_1)}\hat{q}_{(n_1,k_1)}\,\mathrm{e}^{\mathrm{i}\left(\int_{s_0}^{s}\alpha_{(n_1,k_1)}\,\mathrm{d}\tilde{s}+k_1\beta_0 z-n_1\omega_0 t\right)} \\ \sum_{n_2=-N}^{N}\sum_{k_2=-K}^{K} A_{0\,(n_2,k_2)}\hat{q}_{(n_2,k_2)}\,\mathrm{e}^{\mathrm{i}\left(\int_{s_0}^{s}\alpha_{(n_2,k_2)}\,\mathrm{d}\tilde{s}+k_2\beta_0 z-n_2\omega_0 t\right)}\Bigg)\end{aligned} \tag{4.33}$$

Equations 4.33 represent a system of $(2N+1)(2K+1)$ equations where each harmonic (n,k) is forced by particular interactions with the other harmonics in the system, represented by the Fourier modes (n_1,k_1) and (n_2,k_2). These interactions are governed by *harmonic balancing*, which is derived by equating the phases of the above equations that are independent in s and y. This uses the fact that oscillating functions at unequal wavenumbers and frequencies are orthogonal to each other on an appropriate domain. For each (n,k),

$$\begin{aligned}\exp\left[\mathrm{i}(k\beta_0 z-n\omega_0 t)\right] &= \exp\left[\mathrm{i}(k_1\beta_0 z-n_1\omega_0 t)\right]\,\exp\left[\mathrm{i}(k_2\beta_0 z-n_2\omega_0 t)\right], \\ k\beta_0 z-n\omega_0 t &= (k_1+k_2)\beta_0 z-(n_1+n_2)\omega_0 t, \\ \Rightarrow k &= k_1+k_2 \quad \text{and} \quad n=n_1+n_2\end{aligned} \tag{4.34}$$

In other words, for second-order (or quadratic) nonlinearities, the wavenumbers and frequencies of the harmonics that force the (n,k)-mode are related by the conditions $n=n_1+n_2$ and $k=k_1+k_2$. A straightforward extension of this holds for third-order (or cubic) nonlinearities, showing that the tuple $((n_1,k_1),(n_2,k_2),(n_3,k_3))$ forces the (n,k) Fourier mode if and only if $n=n_1+n_2+n_3$ and $k=k_1+k_2+k_3$. As an example, consider the case for when the double sum is truncated with $N=1$ and $K=1$ for 9 total Fourier modes. All quadratic interactions that force the $(1,1)$ are

listed as

$$\begin{aligned}(1,1) &= (0,1) + (1,0),\\ &= (1,0) + (0,1),\\ &= (0,0) + (1,1),\\ &= (1,1) + (0,0)\end{aligned} \tag{4.35}$$

where the $+$ operator is equivalent to vector addition in the (n,k)-plane. An important example is given by $(0,0) = (n,k) + (-n,-k)$ for all considered n, k. Hence, the number of forcing, second-order interactions on the $(0,0)$ Fourier mode is simply *equal* to the number of Fourier modes considered—9 in this example. Similarly for larger N and K, the $(0,0)$-harmonic, also referred to as the mean-flow distortion, is forced by all modes and their complex conjugates. Harmonics that sit at a corner of the Fourier space are forced by the least number of Fourier modes. It is important to note that an infinitely accurate solution would be represented with N and K tending to infinity and there would be an infinite number of interactions for any harmonic. By truncating N and K, dropping many of those interactions represents one of the introduced inaccuracies. For large n and k, we expect that the amplitude of those harmonics tend toward zero, which reduces the magnitude of the introduced inaccuracy.

4.3.1.4 Governing equations

Let us proceed with the derivation of the governing equation for the (n,k) Fourier mode. If the base-flow is assumed to be a function of the streamwise coordinate s and wall-normal coordinate y, as is appropriate for infinite swept wings, then Eq. (2.23) may be expressed as a system of non-linear, partial differential equations: three equations for momentum conservation, one for energy conservation, and one for mass continuity.

$$\begin{aligned}\mathcal{W}_{(n,k)}\Bigg(\tilde{\mathcal{M}}_{ss}\frac{\partial^2\hat{q}_{(n,k)}}{\partial s^2} + \tilde{\mathcal{M}}_{sy}\frac{\partial^2\hat{q}_{(n,k)}}{\partial s\,\partial y} + \tilde{\mathcal{M}}_{yy}\frac{\partial^2\hat{q}_{(n,k)}}{\partial y^2} + \tilde{\mathcal{M}}_{s}\frac{\partial\hat{q}_{(n,k)}}{\partial s} + \ldots\\ \tilde{\mathcal{M}}_{y}\frac{\partial\hat{q}_{(n,k)}}{\partial y} + \tilde{\mathcal{M}}_{0}\,\hat{q}_{(n,k)}\Bigg) = f_{(n,k)}\end{aligned} \tag{4.36}$$

where the complex-valued coefficient matrices $\tilde{\mathcal{M}}_{ss}$, $\tilde{\mathcal{M}}_{sy}$, $\tilde{\mathcal{M}}_{yy}$, $\tilde{\mathcal{M}}_{s}$, $\tilde{\mathcal{M}}_{y}$, and $\tilde{\mathcal{M}}_{0}$ are functions

of the base-flow, the metric tensor, the effective spanwise wavenumber $\beta \equiv k\beta_0$ and angular frequency $\omega \equiv n\omega_0$, and the streamwise complex wavenumber $\alpha_{(n,k)}$. The right-hand-side nonlinear forcing $f_{(n,k)}$ term collapses the $\mathcal{N}$ operator from Eq. (2.23). Some authors evaluate the term in physical space [100, 86, 101]. In the presently used implementation of the code, $f_{(n,k)}$ is evaluated in the spectral domain directly. The evaluation of $f_{(n,k)}$ is detailed in appendix B.

With the appearance of the second streamwise derivative $\partial^2\hat{q}_{(n,k)}/\partial s^2$, the equation set would have to be solved simultaneously for all s-stations, because this term renders an elliptic equation. The approach used to solve the fully elliptic problem is called the Adaptive Harmonic (Linear) Navier-Stokes Equations (AH(L)NSE), whose linear form is given in recent papers [36, 37]. This is a computationally expensive procedure and beyond the scope of the dissertation. Instead of solving the above equations of Eq. (4.36), NPSE asserts that the streamwise variation of the shape-function is small, which allows $\partial^2\hat{q}_{(n,k)}/\partial s^2$ to be neglected while retaining first-order s derivatives. Additionally, $\overline{v}$ as well as streamwise derivatives of $\alpha_{(n,k)}$, base-flow quantities, and curvilinear metrics are assumed to be slowly varying with a scale $\varepsilon_s \ll 1$, such that ε_s^2 is negligible. Together, NPSE solves the following equation set in Eq. (4.37):

$$\mathcal{M}_{sy}\frac{\partial^2\hat{q}_{(n,k)}}{\partial s\,\partial y} + \mathcal{M}_{yy}\frac{\partial^2\hat{q}_{(n,k)}}{\partial y^2} + \mathcal{M}_{s}\frac{\partial\hat{q}_{(n,k)}}{\partial s} + \mathcal{M}_{y}\frac{\partial\hat{q}_{(n,k)}}{\partial y} + \mathcal{M}_{0}\,\hat{q}_{(n,k)} = \frac{f_{(n,k)}}{\mathcal{W}_{(n,k)}} \tag{4.37}$$

where the tilde accents have been dropped from the coefficient matrices to indicate that their elements have also changed by assuming $\partial/\partial s \ll 1$. Some authors choose to additionally neglect the mixed derivative $\partial^2\hat{q}_{(n,k)}/\partial s\,\partial y$, as it does originate from the viscous terms multiplied by $1/\mathrm{Re} \ll 1$. However, that is an additional assumption placed unnecessarily on the streamwise variation and for the computations presented in this dissertation, the mixed derivative is included. Note that if $f_{(n,k)} = 0$, the linear equations (LPSE) are recovered. Setting $\varepsilon_s = 0$ recovers the equations of linear stability theory (LST). The governing LPSE disturbance equations are detailed in appendix A.

4.3.1.5 Auxiliary equation

Observe that the system of 5 equations of Eqs. (4.37) has 6 unknowns: the 5 components of $\hat{q}_{(n,k)}$ and $\alpha_{(n,k)}$, as the wavenumber appears in the coefficient matrices and the nonlinear forcing vector. Therefore, an additional equation must be provided to close the system. In the literature, this is often referred to as the auxiliary equation, or a normalization or supplementary condition. Its formulation is not unique and there have been several analyses comparing the effect of different auxiliary equations in the PSE system. The philosophy behind the auxiliary equation is to mitigate the effect of neglecting the shape-function's $\partial^2\hat{q}_{(n,k)}/\partial s^2$ terms. In Herbert's words, "ideally we would like [the shape-function] to be independent of s [...]" [12]. To accomplish this, one meaningful example is an integral norm that is based on the streamwise derivative of $|\hat{q}_{(n,k)}|^2$:

$$\begin{aligned}\int_0^{y_{\max}} \frac{1}{2}\frac{\partial|\hat{q}_{(n,k)}|^2}{\partial s}\,\mathrm{d}y &= \int_0^{y_{\max}} \hat{q}^{\dagger}_{(n,k)} \cdot \frac{\partial\hat{q}_{(n,k)}}{\partial s}\,\mathrm{d}y, \\ &= \int_0^{y_{\max}} \left(\hat{u}^{\dagger}_{(n,k)}\frac{\partial\hat{u}_{(n,k)}}{\partial s} + \hat{v}^{\dagger}_{(n,k)}\frac{\partial\hat{v}_{(n,k)}}{\partial s} + \hat{w}^{\dagger}_{(n,k)}\frac{\partial\hat{w}_{(n,k)}}{\partial s} + \hat{T}^{\dagger}_{(n,k)}\frac{\partial\hat{T}_{(n,k)}}{\partial s} + \hat{\rho}^{\dagger}_{(n,k)}\frac{\partial\hat{\rho}_{(n,k)}}{\partial s} \right) \mathrm{d}y\end{aligned} \tag{4.38}$$

where the dagger superscript † indicates complex conjugation. Directly using this auxiliary condition set to zero creates a system of nonlinear, integro-partial differential equations, which can be arduous to solve. One could discretize the differentiation and integration operators (e.g., with finite differences and a trapezoidal rule) and attempt to solve the resulting banded, algebraic system. However, that is not the commonly taken approach in literature. Instead, an iterative loop is performed. Let the superscript on $\alpha_{(n,k)}$ indicate the iteration counter p_α. Starting with an assumed initial value for $\alpha^0_{(n,k)}$ for the $p_\alpha = 0$ iteration, Eqs. (4.37) are solved for $\hat{q}_{(n,k)}$. This allows computing the nonzero value of the auxiliary equation Eq. (4.38), and placing that value directly back into the imaginary part of $\alpha^1_{(n,k)}$ for the for the $p_\alpha = 1$ iteration. This redirects the computed growth from the shape-functions into the streamwise wavenumber, mitigating the effect of neglecting the shape-function's $\partial^2\hat{q}_{(n,k)}/\partial s^2$ terms. Instead of using the quantity in Eq. (4.38), we may normalize that expression by the y-integral of the sum of squares of the shape-function

components, following [100]. For the current α-iteration of $p_\alpha + 1$, $\alpha_{(n,k)}^{p_\alpha+1}$ is then computed as

$$\begin{aligned}
\Phi_{\text{num}} &= \hat{u}_{(n,k)}^{\dagger} \frac{\partial \hat{u}_{(n,k)}}{\partial s} + \hat{v}_{(n,k)}^{\dagger} \frac{\partial \hat{v}_{(n,k)}}{\partial s} + \hat{w}_{(n,k)}^{\dagger} \frac{\partial \hat{w}_{(n,k)}}{\partial s} + \hat{T}_{(n,k)}^{\dagger} \frac{\partial \hat{T}_{(n,k)}}{\partial s} + \hat{\rho}_{(n,k)}^{\dagger} \frac{\partial \hat{\rho}_{(n,k)}}{\partial s} \,, \\
\Phi_{\text{den}} &= |\hat{u}_{(n,k)}|^2 + |\hat{v}_{(n,k)}|^2 + |\hat{w}_{(n,k)}|^2 + |\hat{T}_{(n,k)}|^2 + |\hat{\rho}_{(n,k)}|^2 \,, \\
\alpha_{(n,k)}^{p_\alpha+1} &= \alpha_{(n,k)}^{p_\alpha} - \mathrm{i} \frac{\int_0^{y_{\max}} \Phi_{\text{num}} \, \mathrm{d}y}{\int_0^{y_{\max}} \Phi_{\text{den}} \, \mathrm{d}y}
\end{aligned} \tag{4.39}$$

where the shape-function is evaluated at the previous iteration p_α. Equation (4.39) then defines one step of an α-iteration. When the iterative change in the nondimensional $\alpha_{(n,k)}$ reaches below a threshold for all considered Fourier modes, the α-iterations are deemed converged. That is, suppose $\epsilon_{\alpha,\,(n,k)}$ is defined as

$$\epsilon_{\alpha,\,(n,k)} = \left| \alpha_{(n,k)}^{p_\alpha+1} - \alpha_{(n,k)}^{p_\alpha} \right| \equiv |\Delta \alpha_{(n,k)}| \tag{4.40}$$

Then the computations are deemed converged when $\max_{(n,k)} |\epsilon_{\alpha,\,(n,k)}|$ is less than some chosen tolerance $\epsilon_{\text{tol},\,\alpha}$. An alternative approach, whose form resembles an original proposal by Airiau, leverages a relative difference on both the real and imaginary parts of $\alpha_{(n,k)}$ [24, §1.3.3]. That is, computations are deemed converged when

$$\frac{\left| \mathrm{Real}\left(\Delta \alpha_{(n,k)}\right) \right|}{|\alpha_{(n,k)}^{p_\alpha}|} < \epsilon_{\text{tol},\,\alpha} \quad \text{and} \quad \frac{\left| \mathrm{Imag}\left(\Delta \alpha_{(n,k)}\right) \right|}{|\alpha_{(n,k)}^{p_\alpha}|} < \epsilon_{\text{tol},\,\alpha} \tag{4.41}$$

for all (n, k). Here, the operators Real and Imag select the real and imaginary parts of the complex argument, respectively. This nomenclature is used to avoid confusion with the Reynolds number, Re.

4.3.1.6 *Taylor-series expansion of transport variables*

The transport variables of dynamic viscosity μ and thermal conductivity κ are expanded out to linear Taylor series. In other words,

$$\mu = \overline{\mu} + \mu' \approx \overline{\mu} + \frac{\mathrm{d}\overline{\mu}}{\mathrm{d}\overline{T}} T' \tag{4.42}$$

where the analogous expression holds for κ. Previous work by Moyes et al. has demonstrated that for stationary disturbances in some hypersonic flowfields, a more accurate nonlinear solution can be obtained by using Taylor series of order greater than one (e.g., quadratic, cubic, etc.), which affects the higher superharmonics noticeably differently than those of the linear expansion [102]. This nuance is neglected for the current subsonic and transonic analysis, as temperature perturbations are small relative to the velocity perturbations.

4.3.2 Boundary conditions and initial conditions

4.3.2.1 *Wall-normal boundary conditions*

For each Fourier mode, the disturbance is assumed to satisfy no-slip and no-penetration at the surface: $u'_{(n,k)}(s,0) = 0$, $v'_{(n,k)}(s,0) = 0$, and $w'_{(n,k)}(s,0) = 0$. This translates into the shape-function components obtaining a zero value at the wall, also referred to as a homogeneous Dirichlet condition: $\hat{u}_{(n,k)}(s,0) = 0$, $\hat{v}_{(n,k)}(s,0) = 0$, and $\hat{w}_{(n,k)}(s,0) = 0$.

The temperature boundary condition of each Fourier mode is dependent on the temperature boundary condition of the base flow. That is, if the base flow is isothermal, then the total temperature disturbance $T'(s,0) = 0$, which is accomplished by assigning $T'_{(n,k)}(s,0) = 0$ or $\hat{T}_{(n,k)}(s,0) = 0$. This is not relevant for the cases considered in this dissertation, because all provided base flows are assumed to be adiabatic. When the base flow is adiabatic, the set-up is not as clear. One could suppose all *unsteady* Fourier modes cannot thermally equilibrate with the adiabatic wall temperature [103] while the *steady* Fourier modes can thermally equilibrate. This would lead to isothermal conditions for the individual, unsteady Fourier modes while an adiabatic condition would be ap-

plied to the individual, steady Fourier modes. In other words,

$$\begin{aligned} \hat{T}_{(n,k)}(s,0) &= 0, \quad \forall n \neq 0, \\ \frac{\partial \hat{T}_{(n,k)}(s,0)}{\partial y} &= 0, \quad \forall n = 0 \end{aligned} \tag{4.43}$$

One could also presume though that all Fourier modes in the system can reach the adiabatic temperature regardless of their frequency, i.e., $\partial \hat{T}_{(n,k)}(s,0)/\partial y = 0$. There is an inherent uncertainty in the computational modeling regarding this boundary condition. Discrepancies in this modeling process are not relevant for the data presented in the dissertation, as all results are based off of stationary disturbances. As such, all wall disturbance boundary conditions are simply asserted to be adiabatic, as the base flow is adiabatic.

The density boundary condition of each Fourier mode at the surface is given through a compatibility condition satisfying y-momentum. A choice could be made for continuity providing the compatibility condition for $\hat{\rho}_{(n,k)}(s,0)$; however, some have noted the condition number of $\mathcal{L}$ of various linear stability problems tends to worsen using compatibility conditions based on continuity [104].

For the freestream boundary conditions, all disturbances are presumed to decay to zero for velocity and temperature components, i.e.,

$$\hat{u}_{(n,k)}(s,y_{\max}) = 0, \quad \underbrace{\hat{v}_{(n,k)}(s,y_{\max}) = 0}_{(n,k)\neq(0,0)}, \quad \hat{w}_{(n,k)}(s,y_{\max}) = 0, \quad \hat{T}_{(n,k)}(s,y_{\max}) = 0 \tag{4.44}$$

The density perturbation is presumed to satisfy continuity in the freestream as a compatibility condition. As an exception to the above boundary conditions, the mean-flow distortion Fourier mode $(0,0)$ is handled specially in the freestream. The MFD can be viewed as the difference between the time- and spanwise-averaged transitional boundary layer and the undisturbed, laminar boundary layer. It is directly responsible for changes in displacement and momentum thickness of the transitional boundary layer. Through a control volume analysis assuming incompressible flow,

it can be shown that

$$\begin{aligned} \delta^*_{1,\mathrm{MFD}} &\equiv \delta^*_{1,\mathrm{tr}} - \delta^*_{1,\mathrm{lam}}\,, \\ \frac{\mathrm{d}\delta^*_{1,\mathrm{MFD}}}{\mathrm{d}x} &= \hat{v}_{(0,0)}\big|_{y\to\infty} \end{aligned} \tag{4.45}$$

provided a homogeneous Neumann boundary condition is applied to $\hat{v}_{(0,0)}$ in the freestream [101]. Here, δ^*_1 is the displacement thickness with the subscript 'tr' for a transitional boundary layer and 'lam' for a laminar boundary layer [101]. This consequence of mass continuity demands that $\hat{v}_{(0,0)}(s, y_{\max})$ is nonzero, provided $y_{\max}$ is close enough to ∞ for the scale of the perturbation. Many authors indeed prescribe a homogeneous Neumann condition for $\hat{v}_{(0,0)}(s, y_{\max})$ [86, 101, 49, 50]. However some leave the value unprescribed, that is, the nonlinear governing disturbance equations are simply evaluated at $y = y_{\max}$ for $\hat{v}_{(0,0)}$ [100, 28].

Numerical experiments have shown that there can exist strong oscillations associated with the MFD $\hat{v}_{(0,0)}$, especially in subsonic flows and in freestream regions. In previous work analyzing highly compressible, hypersonic flows, the mean-flow distortion exhibited strong oscillatory behavior in the freestream that tends to decay and settle after 20 streamwise stations or so. Hein asserts that this behavior is due to a numerical inconsistency: a nonzero $\alpha_{(0,0)}$ is inconsistent with a homogeneous Neumann freestream boundary condition [101]. However, the proof was not detailed. Assigning the wavenumber $\alpha_{(0,0)} = 0$ does remove these strong wall-normal oscillations and allows the solution to converge beyond a few streamwise stations for subsonic/transonic flows. This does come at a cost though, as now all of the streamwise growth of this Fourier mode is expressed directly in its streamwise derivative of the shape-function $\partial\hat{q}_{(0,0)}/\partial s$, which ideally should be small (algebraic) by the PSE approximation. Hence this assignment of $\alpha_{(0,0)} = 0$ should only be made as a last resort. Other researchers have observed these oscillations as well creating difficulty with NPSE initialization in incompressible flow. Airiau identified the source of the supposed numerical instability in the freestream behavior of the mean-flow distortion [24]. As a remedy, Airiau proposed a "cut-off" procedure, truncating the wall-normal domain to about 2 boundary-layer thicknesses [24]. Chapter 5 discusses the numerical difficulties surrounding the mean-flow distortion and the above claims in an incompressible context.

4.3.2.2 *Initial conditions*

The initial condition at the first s-node $s = s_1$ of the simulation depends on the Fourier mode. If $A_{0\,(n,k)}$ is prescribed, then $\hat{q}_{(n,k)}(s_1, y)$ and $\alpha_{(n,k)}(s_1)$ are provided by solving a compressible, parallel, spatial LST formulation for the effective wavenumbers $\omega = n\omega_0$ and $\beta = k\beta_0$. For the Fourier modes whose $A_{0\,(n,k)}$ are left unspecified, then the shape-function is assigned to the trivial vector: $\hat{q}_{(n,k)}(s_1, y) = 0$. This is a reasonable guess, as it agrees with the prescribed boundary conditions. The complex-valued wavenumbers $\alpha_{(n,k)}(s_1)$ are supplied based on simple wave addition with respect to the already-initialized Fourier modes. For example, if Fourier modes $(0, 1)$ and $(1, 0)$ have been found through parallel LST, a relation used at $s = s_1$ could be written as:

$$\alpha_{(n,k)} = n\alpha_{(1,0)} + k\alpha_{(0,1)} \tag{4.46}$$

however, this is not exactly as it is implemented in EPIC. For Fourier modes with both nonzero n, k, there is a preference to the *diagonal* of the discretized Fourier space instead of the axes, as Eq. (4.46) implies. For example, the real part of $\alpha_{(2,3)}$ is given by the real part of $\alpha_{(2,2)} + \alpha_{(0,1)}$, which is unequal to the real part of $2\alpha_{(1,0)} + 3\alpha_{(0,1)}$. This subtlety in implementation is quite useful for mixed-mode simulations, and the author is in debt to those who created it [49, 50].

Note if spanwise subharmonics are considered, then the fundamental Fourier mode, say $(0, k)$ with $k > 1$, is found via LST. Then $\alpha_{(0,1)} = (1/k)\,\alpha_{(0,k)}$ is defined, which permits use of Eq. (4.46) for the remaining Fourier modes considered. The analogous routine would occur for temporal subharmonics as well, relating the fundamental $(n, 0)$ with $n > 1$ to the subharmonic $(1, 0)$, i.e., $\alpha_{(1,0)} = (1/n)\,\alpha_{(n,0)}$

One methodology for initialization may use the above relations for the full, complex-valued $\alpha_{(n,k)}$ while another methodology may only use the real part of the resulting $\alpha_{(n,k)}$ value and assigning the imaginary part to zero. The difference in these two methodologies is very small; in a few streamwise stations, numerical experiments show the two solutions are essentially indistinguishable. The results in this dissertation will initialize with the real part only, keeping the initial

imaginary parts zero for the harmonics for a few streamwise stations.

Initializing PSE with a solution from LST causes a spatial transient as the solution adjusts to satisfy the governing PDE. Not only does this transient occur for the fundamental Fourier modes, but there is an additional spatial transient as the solution recovers from the initial guesses of $\hat{q}_{(n,k)}$ and $\alpha_{(n,k)}$ for the other harmonics. Attempting to converge all Fourier modes to prescribed tolerances in these first few streamwise stations can prove to be intractable because of these spatial transients. As a workaround, the harmonics are excluded from the convergence criteria of the nonlinear terms and α, i.e., excluded from Eq. (4.53) and Eq. (4.40), for the first few streamwise stations. Commonly, Fourier modes $(n, k) \neq (0, 0)$ are excluded from convergence until the streamwise s-index $i = 5$ and the mean-flow distortion $(0, 0)$ is excluded from convergence until $i = 7$. If not specified in the description of the analysis, these default values are used.

An additional effect that can worsen these initial spatial transients is incorporating the cubic nonlinear terms in $f_{(n,k)}$ early on. This is not an issue for these near-incompressible flows discussed in this dissertation, as the cubic-order terms result from density perturbations and the energy equation. However, for highly compressible flows (e.g., hypersonics), the initialization region may need to exclude the cubic terms for the first several steps for solution convergence. For analysis in this dissertation, cubic terms are included for all streamwise stations without concern.

Let us return to the shape functions for the (n, k) Fourier modes that are initialized with LST eigenfunctions. The phase of these complex profiles $\hat{q}_{(n,k)}$ can be left uncontrolled. That is to say, when solving the LST eigenvalue problem, since the eigenfunction can be multiplied by any complex constant and remain a solution to the equation, the complex phase of the collective profile is arbitrary. Of course, the phase $\texttt{atan2}(\mathrm{Imag}(\hat{q}_{(n,k)}), \mathrm{Real}(\hat{q}_{(n,k)}))$ is a function of y in general, but the whole profile rotated in the complex plane by an equal amount is an equivalently appropriate initial condition for PSE. This is essential when considering problems of initial phase differences and their effect on say, a subharmonic-breakdown transition process [105].

The magnitudes of these disturbances initialized by LST eigenfunctions can be prescribed by various definitions of $A_{0\,(n,k)} = |\hat{\phi}_{(n,k)}|_{\mathrm{ref}}$. They can correspond to prescribing $|\hat{\phi}_{(n,k)}|_{\mathrm{ref}}$ to the

wall-normal maximum value of $|\hat{\phi}_{(n,k)}|$ for a choice of the eigenfunction component, $\hat{\phi}$. Alternatively, the wall value $|\hat{\phi}_{(n,k)\,\mathrm{wall}}|$ could be selected as the prescribed $|\hat{\phi}_{(n,k)}|_{\mathrm{ref}}$. Note $\hat{\phi}$ is commonly chosen as $\hat{u}$, $\hat{T}$, or $\hat{p}$.[5] For unsteady Fourier modes, when comparing results against that of experiments, discussing physical perturbation amplitudes may be easier when expressed in terms of root-mean-square values:

$$A^{\mathrm{RMS}}_{0\,(n,k)} = |\hat{\phi}_{(n,k)}|_{\mathrm{RMS}} = \sqrt{\frac{1}{\mathcal{T}}\int_0^{\mathcal{T}} \left|q'_{(n,k)}\left(s,y,z,t\right)\right|^2_{\mathrm{ref}}\,\mathrm{d}t} \tag{4.48}$$

where $\mathcal{T} = 2\pi/(n\omega_0)$ is the temporal period. Performing the integration after substituting the real part of the definition from Eq. (4.22) at $z = 0$ gives

$$A^{\mathrm{RMS}}_{0\,(n,k)} = \begin{cases} |\hat{\phi}_{(n,k)}|_{\mathrm{ref}} & n = 0 \\ \frac{1}{\sqrt{2}}|\hat{\phi}_{(n,k)}|_{\mathrm{ref}} & n \neq 0 \end{cases}$$

using the half-angle identity $2\cos^2 u = 1 + \cos(2u)$.

As a brief note, the generalized eigenvalue problem for LST is solved using the Krylov subspace method [87]. One of the discrete eigenmodes is selected (as opposed to an eigenmode from the continuous spectrum) for each Fourier mode of interest in NPSE. Then the solution is purified/confirmed by performing Newton-Raphson on the LST equations to a prescribed tolerance of $\epsilon_{\mathrm{tol,\,LST}} = 10^{-11}$.

[5] Since $\hat{p}$ is not a component of the state vector, it must be reconstructed through use of the nondimensional, ideal equation of state. At the initial $s = s_1$, assume amplitudes are infinitesimal. Suppose this may be applied to any (n,k)-harmonic that has been initialized with an eigensolution.

$$\begin{aligned} p &= \frac{\rho T}{\gamma \mathrm{M}^2} = \frac{1}{\gamma \mathrm{M}^2_{\mathrm{ref}}}\left(\overline{\rho}\overline{T} + \overline{\rho}T' + \overline{T}\rho' + \rho' T'\right), \\ p' &= \frac{1}{\gamma \mathrm{M}^2_{\mathrm{ref}}}\left(\overline{\rho}T' + \overline{T}\rho' + \rho' T'\right) \approx \frac{1}{\gamma \mathrm{M}^2}\left(\overline{\rho}T' + \overline{T}\rho'\right), \\ \hat{p} &= \frac{1}{\gamma \mathrm{M}^2}\left(\overline{\rho}\hat{T} + \overline{T}\hat{\rho}\right) \end{aligned} \tag{4.47}$$

4.3.2.3 *Computational discretization*

For base-flow quantities and curvilinear metrics, central, second-order accurate, regular finite difference stencils are used for $\partial/\partial\xi$. At the streamwise boundaries, the accuracy drops to first order. For the perturbation quantities $\hat{q}_{(n,k)}$ and $\alpha_{(n,k)}$, backward, first-order accurate, regular finite difference stencils are used. The number of streamwise points N_s for each case will be specified with the results.

The equations as presented in Eqs. (4.37) previously are not directly solved within EPIC, as s and y do not form an orthogonal grid. Instead, the differentiation operators are sent to the orthogonal, logical coordinates ξ and η by inverting Eqs. (4.21). Performing the substitution and collecting, we have

$$\mathcal{M}_{\xi\eta}\frac{\partial^2\hat{q}_{(n,k)}}{\partial\xi\,\partial\eta}+\mathcal{M}_{\eta\eta}\frac{\partial^2\hat{q}_{(n,k)}}{\partial\eta^2}+\mathcal{M}_{\xi}\frac{\partial\hat{q}_{(n,k)}}{\partial\xi}+\mathcal{M}_{\eta}\frac{\partial\hat{q}_{(n,k)}}{\partial\eta}+\mathcal{M}_0\,\hat{q}_{(n,k)}=\frac{f_{(n,k)}}{\mathcal{W}_{(n,k)}} \tag{4.49}$$

where the coefficient matrices are defined as

$$\begin{aligned}
\mathcal{M}_{\xi\eta}&=\mathcal{M}_{sy}\frac{\partial\eta}{\partial y}\frac{\partial\xi}{\partial s},\\
\mathcal{M}_{\eta\eta}&=\mathcal{M}_{yy}\left(\frac{\partial\eta}{\partial y}\right)^2+\mathcal{M}_{sy}\frac{\partial\eta}{\partial s}\frac{\partial\eta}{\partial y},\\
\mathcal{M}_{\xi}&=\mathcal{M}_{s}\frac{\partial\xi}{\partial s},\\
\mathcal{M}_{\eta}&=\mathcal{M}_{yy}\frac{\partial^2\eta}{\partial y^2}+\mathcal{M}_{sy}\frac{\partial^2\eta}{\partial s\,\partial y}+\mathcal{M}_{y}\frac{\partial\eta}{\partial y}+\mathcal{M}_{s}\frac{\partial\eta}{\partial s}
\end{aligned} \tag{4.50}$$

4.3.3 Solution procedure

4.3.3.1 *Nonlinear iterations*

An additional complication to solving Eqs. (4.49) is that the right-hand-side forcing vector $f_{(n,k)}$ is a function of $\hat{q}_{(n,k)}$ itself. This nonlinearity adds an additional iterative step to solving the system. If we discretize the ξ-differentiation operators with backward stencils on $\partial/\partial\xi$ and the η-differentiation operators with any stencil of our choice, we can express the partial differential

equations of Eqs. (4.49) as the algebraic system

$$\mathcal{L}\hat{q}^{i+1}_{(n,k)} = \underbrace{f^{\text{linear}}_{(n,k)} + \frac{f_{(n,k)}}{\mathcal{W}_{(n,k)}}}_{b_{(n,k)}} \tag{4.51}$$

where the superscript $i+1$ indicates the current s-station being solved for. The term $f^{\text{linear}}_{(n,k)}$ arises from the backward s-differentiation stencil, containing the previous shape functions from s-indices i, $i-1$, etc. —however long the stencil extends backward in s. It is typical to use first-order differences for $\partial/\partial s$, however higher-order stencils may be used provided the step-size criterion isn't reached [106]. As a side note, since the mean-flow distortion Fourier mode is entirely real, $b_{(0,0)}$ must also be entirely real. Dealing with complex-valued data types programmatically unfortunately allows slight underflow to the imaginary part of $b_{(0,0)}$—often several orders of magnitude smaller than 10^{-16}. This imaginary part on the forcing is truncated out in the program, which ensures that $\hat{q}_{(0,0)}$ is entirely real after the solve phase.

The LHS matrix $\mathcal{L}$ can be decomposed into a product of lower- and upper-triangular matrices, i.e., $\mathcal{L} = LU$. Then, if we define $\hat{\Phi}_{(n,k)} \equiv U\hat{q}^{\text{new}}_{(n,k)}$, through the two-step process of forward and backward substitution, $\hat{q}^{i+1}_{(n,k)}$ is obtained as

$$\begin{aligned} L\hat{\Phi}_{(n,k)} = b_{(n,k)} \implies \hat{\Phi}_{(n,k)}, \\ U\hat{q}^{\text{new}}_{(n,k)} = \hat{\Phi}_{(n,k)} \implies \hat{q}^{\text{new}}_{(n,k)} = \hat{q}^{i+1}_{(n,k)} \end{aligned} \tag{4.52}$$

The LU decomposition and substitution is performed with the state-of-the-art algebraic solver MUMPS [107]. Since $b_{(n,k)}$ is a function of the shape-function itself though, this becomes an iterative process. Let the second superscript on $\hat{q}^{i}_{(n,k)}$ indicate the iteration counter p_{nl}. One could guess the value of $\hat{q}^{i+1,0}_{(n,k)}$ at iteration $p_{\text{nl}} = 0$ as identically equal to the converged shape-function at the previous s-index, i.e., $\hat{q}^{i+1,0}_{(n,k)} = \hat{q}^{i}_{(n,k)}$. Linear extrapolation could alternatively be performed for the initial guess based on the streamwise derivative of the previous s-index: $\hat{q}^{i+1,0}_{(n,k)} = \hat{q}^{i}_{(n,k)} + \Delta s\, \partial\hat{q}^{i}_{(n,k)}/\partial s$. This can speed up the iterative convergence of $\hat{q}^{i+1}_{(n,k)}$, but in regions of sudden

change, it can lead the solution astray, causing solution divergence. Once $\hat{q}_{(n,k)}^{i+1,\,0}$ is assigned, its spatial derivatives are computed, and then $b_{(n,k)}$ is computed. Through substitution, Eqs. (4.52) is solved, resulting in a value $\hat{q}_{(n,k)}^{i+1,\,1}$ for the $p_{\mathrm{nl}} = 1$ iteration. This process repeats to compute $\hat{q}_{(n,k)}^{i+1,\,p_{\mathrm{nl}}+1}$ from the previous value of $\hat{q}_{(n,k)}^{i+1,\,p_{\mathrm{nl}}}$. An iterative error $\epsilon_{\mathrm{nl},\,(n,k)}$ is then computed for each of the shape-function components between the previous nonlinear iteration p_{nl} and the current nonlinear iteration $p_{\mathrm{nl}} + 1$ as

$$\epsilon_{\mathrm{nl},\,(n,k)} = \frac{\max_y \left| \hat{\phi}_{(n,k)}^{i+1,\,p_{\mathrm{nl}}+1} - \hat{\phi}_{(n,k)}^{i+1,\,p_{\mathrm{nl}}} \right|}{\max_y \left| \hat{\phi}_{(n,k)}^{i+1,\,p_{\mathrm{nl}}} \right|} \quad \forall \hat{\phi}_{(n,k)} \in \{u_{(n,k)}, v_{(n,k)}, w_{(n,k)}, T_{(n,k)}, \rho_{(n,k)}\} \tag{4.53}$$

Once Eq. (4.53) reaches below a given threshold for all shape-function components and all Fourier modes considered in the simulation, then the nonlinear iterations are deemed converged. It is common to choose this threshold for nonlinear convergence as $\epsilon_{\mathrm{tol,\,nl}} = 10^{-8}$ or lower at 10^{-11}. With the nonlinear iteration procedure described, now one can see an advantage to performing an LU decomposition on the LHS matrix $\mathcal{L}$: factors L and U do not change between nonlinear iterations, so the forward/backward substitution is a computationally efficient process. This also provides reasoning as to why $\hat{q}_{(n,k)}^{i+1}$ is chosen to be converged first through the nonlinear iterations instead of converging $\alpha_{(n,k)}$ first through the α-iterations.

When the nonlinear terms constructing $b_{(n,k)}$ become appreciable with respect to the linear system, a numerical approach may require underrelaxation to prevent divergence of this simple procedure. That is, instead of asserting $\hat{q}_{(n,k)}^{i+1,\,p_{\mathrm{nl}}+1} = \hat{q}_{(n,k)}^{\mathrm{new}}$, one can use a relaxation factor of $0 < \sigma \leq 1$ as

$$\hat{q}_{(n,k)}^{i+1,\,p_{\mathrm{nl}}+1} = \sigma \hat{q}_{(n,k)}^{\mathrm{new}} + (1 - \sigma) \hat{q}_{(n,k)}^{i+1,\,p_{\mathrm{nl}}} \tag{4.54}$$

There are various ideas for introducing a non-unity value for σ. If the nonlinear iterative error $|\epsilon_{\mathrm{nl},\,(n,k)}|$ becomes large (e.g., $O(1)$), then one may want to decrease σ from its current value by a small amount, say 0.1. Additionally, if the number of nonlinear iterations required are high, that may be due to the shape-function hitting a limit cycle in the complex plane. In those cases, decreasing σ further by a small amount may be just enough of a change to the system to cause

$\hat{q}_{(n,k)}^{i+1,\,p_{\mathrm{nl}}+1}$ to iteratively converge.

In another approach, one may provide σ based on some physical amplitudes of the problem. That is, one could define σ based on the u' amplitude of the mean-flow distortion $(0,0)$. For example, one could say σ ought to reach a value of 0.5 once $\max_y |u'_{(0,0)}|$ becomes 5% of $\overline{u}_\infty$ and a value of 0.25 once $\max_y |u'_{(0,0)}|$ becomes 30%. These values could then be fit with an exponential curve, defining a floor as $\sigma = 0.1$, such that the problem becomes successively more underrelaxed as the MFD grows larger. These sorts of schedules for the relaxation parameter σ help converge the perturbation much farther downstream with NPSE into the nonlinear stages of transition than without relaxation: see Fig. 9 in Moyes et al. [102].

4.3.3.2 Regularization techniques for the ill-posedness of PSE

It has been shown that the formulation of PSE is inherently ill-posed [106]. This is a result of treating the underlying boundary-value problem as an initial-value problem [34]. There is rich spectral analysis that can be performed on the PSE operator revealing this ill-posedness, and the curious reader is referred to the following papers: [108, 34]. Several approaches have been put forward in the literature to regularize and stabilize the linear PSE marching procedure. The first of which is using a streamwise step $\Delta s > \Delta s_{\mathrm{crit}}$ such that for compressible, three-dimensional disturbances,

$$\Delta s_{\mathrm{crit}} = \frac{1}{\left|\mathrm{Real}(\alpha) + \frac{\omega \mathrm{M}_{\mathrm{ref}}^2 - \beta \mathrm{M}_{\mathrm{ref}} \mathrm{M}_{z,\,\mathrm{ref}}}{1 - \mathrm{M}_{\mathrm{ref}}^2}\right|} \tag{4.55}$$

where $\mathrm{M}_{\mathrm{ref}}$ and $\mathrm{M}_{z,\,\mathrm{ref}}$ are the freestream Mach numbers in the streamwise and spanwise directions, respectively [108]. Note the subscript of (n,k) has been omitted on α. The existence of this limit Δs_{crit} makes it impossible to rigorously show numerical convergence of the solution in s as $\Delta s \to 0$. In practice, however, the linear PSE discretized is well-behaved if the step size exceeds this limit while remaining small to capture the slow, algebraic variation of the shape function $\hat{q}$ [108].

Consider the mean-flow distortion with $\mathrm{Real}(\alpha) = 0$ and $(\omega, \beta) = (0,0)$. Then $\Delta s_{\mathrm{crit}} \to \infty$. In this case, additional stabilization must then be applied to make PSE more useful. One technique

is to affect the streamwise derivative of the pressure component of the shape function, $\partial\hat{p}/\partial s$, borrowing the methodology from the Parabolized Navier-Stokes (PNS) approach [23, 109, 106].

$$\frac{\partial p'}{\partial s} = \left(\mathrm{i}\alpha\hat{p} + \Omega_p \frac{\partial \hat{p}}{\partial s} \right) \exp(\mathrm{i}\vartheta) \tag{4.56}$$

where some authors use the Vigneron parameter from PNS applied to Ω_p based on the local Mach number along the wall-normal profile. For the cases of interest, $\Omega_p = 0$ is assigned for all stationary Fourier modes. Note, though, that this does not solve the issue outright—the targeted branch cut is only modified, not removed [108, §2.2]. For stationary disturbances, it has been demonstrated that dropping this term from the governing equations yields a very small model error [110, 111].

With the s-momentum equation (and the energy equation if using the enthalpy formulation) as the only considered governing equations where $\partial p/\partial s$ appears, there are only a few terms in its $f_{(n,k)}$ quadratic components that contain $\partial\hat{p}_{(n,k)}/\partial s$. A rigorous suppression of the pressure shape-function streamwise gradient would also eliminate this contribution. However, for simplicity, the nonlinear contribution of $\partial\hat{p}_{(n,k)}/\partial s$ is not suppressed in the current analysis. Keeping this nonlinear contribution may cause NPSE to diverge when marching through a strongly nonlinear regime of a transitional boundary layer. Including it though does not incur any physical inaccuracy, provided that the equations converge.

An additional method for PSE regularization has been proposed to damp the eigenvalues responsible for the ill-posedness by introducing a term proportional to the truncation error [112]. This method, however, is not used in this dissertation.

4.3.3.3 Outline of NPSE solution procedure

An outline of the programming procedure based on the above discussion is given below:

1. Solve LST for the effective wavenumbers of Fourier modes whose $A_{0\,(n,k)}$ values have been specified for initial conditions on $\alpha_{(n,k)}$ and $\hat{q}_{(n,k)}$.

2. Assign initial values of $\alpha_{(n,k)}$ and $\hat{q}_{(n,k)}$ to the remaining Fourier modes as discussed in 4.3.2.2 and Eq. (4.46). Begin marching in the streamwise coordinate s.

3. Given the solution at the previous s-index of $\hat{q}^{i}_{(n,k)}$ and $\alpha^{i}_{(n,k)}$, guess the values at the current s-index $\hat{q}^{i+1}_{(n,k)}$ and $\alpha^{i+1}_{(n,k)}$ through a zeroth- or first-order extrapolation for all Fourier modes.

4. Compute $\mathcal{W}_{(n,k)}$ and the s-derivative of $\alpha^{i,\,p_\alpha}_{(n,k)}$.

5. Compute the matrix $\mathcal{L}$ and decompose it into its LU factors. Begin the nonlinear iterative loop.

6. Compute the s-, sy-, y-, and yy-derivatives of $\hat{q}^{i+1,\,p_{\rm nl}}_{(n,k)}$ for the first iteration, $p_{\rm nl} = 0$, for all Fourier modes.

7. Compute $f_{(n,k)}$ (see appendix B) and adjust boundary values to be consistent with the prescribed boundary conditions. Then compute $b_{(n,k)}$.

8. Enforce that the MFD is purely real by setting $b_{(0,0)}$ to be purely real, truncating off any very small imaginary parts that arise through slight numerical underflow.

9. Perform forward/backward substitution to compute $\hat{q}^{\rm new}_{(n,k)}$.

10. Compute the iterative error $\epsilon_{{\rm nl},\,(n,k)}$ for each Fourier mode, and if desired, adjust the underrelaxation value σ.

11. Compute $\hat{q}^{i+1,\,p_{\rm nl}+1}_{(n,k)}$ via Eq. (4.54).

12. Update the complex conjugate Fourier modes' shape-functions by the relation Eq. (4.28).

13. Repeat steps 6 through 12 until $\max_{(n,k)} |\epsilon_{{\rm nl},\,(n,k)}| < \epsilon_{{\rm tol},\,{\rm nl}}$.

14. Compute $\alpha^{i,\,p_\alpha+1}_{(n,k)}$ through the auxiliary condition of Eq. (4.39).

15. Update complex conjugate Fourier modes' $\alpha_{(n,k)}$ wavenumbers by the relation Eq. (4.30).

16. Repeat steps 3 through 15 until $\max_{(n,k)} |\epsilon_{\alpha,\,(n,k)}| < \epsilon_{{\rm tol},\,\alpha}$. The solution at s-index $i+1$ is now deemed converged and the next streamwise station may be solved by repeating this procedure. That is, march the disturbance in this fashion for the remaining s-coordinates of the computational grid.

4.4 Selection of the formulation for the energy equation

As an appendix onto the above discussions, it is worth discussing a small nuance in the computational formulation for stability analysis regarding the choice of the energy equation form. Mentioned in the governing equations of §2.3, the selected energy equation uses the *enthalpy* formulation. That is,

$$\rho\frac{\partial h}{\partial t}+\rho u^j h_{,j}=\mathrm{Ec}\left(\frac{\partial p}{\partial t}+u^j p_{,j}\right)+\frac{\mathrm{Ec}}{\mathrm{Re}}g_{ik}\mathbb{T}^{kj}u^i_{,j}+\frac{1}{\mathrm{RePr}}\left(\kappa g^{ij}T_{,i}\right)_{,j} \tag{4.57}$$

However, just as easily, one may select the *internal energy* formulation of the energy equation, written as

$$\frac{1}{\gamma}\left(\rho\frac{\partial e}{\partial t}+\rho u^j e_{,j}\right)=-\mathrm{Ec}\,p\,u^j_{,j}+\frac{\mathrm{Ec}}{\mathrm{Re}}g_{ik}\mathbb{T}^{kj}u^i_{,j}+\frac{1}{\mathrm{RePr}}\left(\kappa g^{ij}T_{,i}\right)_{,j} \tag{4.58}$$

The solutions to these equations are of course mathematically identical. However, in numerical stability analysis, various steps in the methodology are performed such that the results are no longer identical. The first of which is *linearization*. In the enthalpy formulation, the term $u^j p_{,j}$ leads to a triple product of perturbation quantities when pressure $p=\rho T/\left(\gamma \mathrm{M}^2\right)$. This term is simply not present in the internal energy formulation, as there are no derivatives of pressure present: see the term $p\,u^j_{,j}$. As a result, the linearization of each equation gives a different result. The disturbance growth is distributed slightly differently across the shape-function components and the streamwise wavenumber. In other words, since the pressure terms are nonlinear for this choice of the state vector q, the linearizations of the two formulations are not equivalent. For nonlinear simulations, there is still a discrepancy in the initial condition as supplied by the corresponding LST solution for the distinct formulations.

The second approximation performed in stability analysis that causes these formulations to differ numerically is the presence of the pressure gradient term $p_{,j}$. Recall from the PSE approximation that steady Fourier modes require the shape-function pressure streamwise gradient $\partial\hat{p}_{(0,k)}/\partial s$ to vanish in order to regularize the equations (see the previous §4.3.3.2). Since the enthalpy form of energy includes a pressure gradient term $p_{,j}$ whereas the internal energy form does not, the

two equations then deviate slightly in their results when simulating steady Fourier modes in PSE. In this regard, the internal energy formulation might be considered to be slightly more accurate; however, numerical experiments with simultaneous verification against DNS would either support or reject this claim. On another note, the internal energy form carries fewer terms in the governing equation, so the numerical procedure becomes more computationally efficient for PSE when compared to that of the enthalpy form.

The third approximation performed in stability analysis is the discretization of the governing equation. Since the differentiation stencils are applied to the streamwise coordinate s, each equation will commit slightly different discretization error. To demonstrate this in the enthalpy formulation, $u^j p_{,j}$ for a Cartesian coordinate system would produce the triple product $u'\rho'\partial T'/\partial s$, among others. Similarly, in the internal energy form, $p\,u^j_{,j}$ would produce $\rho' T' \partial u'/\partial s$. The discretization of $\partial/\partial s$ applied to different shape-function components $\hat{T}$ and $\hat{u}$ commits slightly different error across the two forms.

The next section will compare NPSE solutions using either the enthalpy and internal energy formulation, assessing the effect of these various approximations in highly compressible flow.

4.4.1 Nonlinear experiments comparing the enthalpy and internal energy formulations

Let us consider an example case then to demonstrate a case with minimal difference between these two formulations as implemented in EPIC. One such case is flow over an axisymmetric, flared cone as tested in the Boeing/AFOSR Mach 6 Quiet Tunnel (BAM6QT) at Purdue University. The solution of the flowfield is computed with NASA's CFD code DPLR, as shown in Fig. 4 of Moyes et al. [102]. Briefly, the conditions selected are given in Table 4.1, where Re' is the unit Reynolds number of the freestream (before/upstream the shock). The angle of attack is $0°$, the constant Prandtl number is assumed as 0.72, and the cone is $x = 0.49$ meters long in axial extent. Gas parameters used are $R_g = 287.058\,\mathrm{J/kg\text{-}K}$ as well as Sutherland's constants of $\mu_{\mathrm{ref}} = 1.716 \times 10^{-5}\,\mathrm{kg/(m\,s)}$, $T_{\mathrm{ref}} = 273.111$ K, and $S_\mu = 110.556$ K.

Linear analysis (not shown) reveals that for this flowfield, the most amplified frequency of the Mack second mode is nominally $f = 286\,\mathrm{kHz}$. For the present NPSE simulation, the Mack second

mode and the mean-flow distortion will be simulated.

M_∞	$\mathrm{Re}'\,(1/\mathrm{m})$	$T_w\,(\mathrm{K})$	$T_\infty\,(\mathrm{K})$	$p_\infty\,(\mathrm{Pa\ abs.})$
6	10.3×10^6	300	52.8	611.1

Table 4.1: Selected conditions for flow over a flared, axisymmetric cone as tested in the BAM6QT.

The simulation inputs are briefly outlined. The s-domain is equispaced with $N_s = 150$ from $x = 0.1\,\mathrm{m}$ to the end of the cone: $x = 0.49\,\mathrm{m}$. The wall-normal y-domain has $N_y = 200$ and has the boundary-layer clustering parameter defined as $y_i = \delta_{100.1}^{h_{\mathrm{tot}}}$, where $\delta_{100.1}^{h_{\mathrm{tot}}}$ is the height where total enthalpy $h_{\mathrm{tot}}/h_{\mathrm{tot},e} = 1.001$. Here in supersonic flow, the edge value $h_{\mathrm{tot},e}$ is defined as the value just underneath/downstream of the enveloping shock wave at each streamwise location. Before employing Malik's clustering, a polynomial fit of 12^{th}-order is applied to y_i. The shock height is estimated from heuristic rules off of local pressure gradients and the maximum height of the domain $y_{\max}$ is selected as just underneath this wall-normal height, again fit with a polynomial: 9^{th}-order here. Freestream Dirichlet conditions are supplied at this subsequent $y_{\max}$ height for all shape-function components. Continuity is used as a compatibility condition on $\hat{\rho}_{(n,0)}$ at the wall. NPSE's convergence criteria are selected as $\max_{(n,0)} |\epsilon_{\alpha,\,(n,0)}| < 10^{-11}$ and $\epsilon_{\mathrm{nl},\,(n,0)} = 10^{-11}$. The initial amplitude of the $(1,0)$ Fourier mode is selected as $\max_y |u'_{(1,0)}|/\overline{u}_{\mathrm{ref}} = 10^{-7}$ at $x = 0.1\,\mathrm{m}$, where $\overline{u}_{\mathrm{ref}} = 871.6873\,\mathrm{m/s}$. The initial phase of the $(1,0)$ is left uncontrolled from the selected LST eigenmode. The mean-flow distortion's streamwise wavenumber $\alpha_{(0,0)}$ is nonzero and purely imaginary. First-order Taylor series are used for the transport variables' expansions.

Figure 4.3 shows the temperature amplitude distributions against the cone's x for the two different energy equation formulations. In black, the results of the enthalpy formulation are shown whereas in a dashed, red line, those of the internal energy formulation are shown. The left panel indicates the distributions over the range relevant for the $(1,0)$ amplitudes, whereas the right panel

zooms onto the intervals relevant post-saturation, highlighting the discrepancies between the two solutions. From our earlier discussion, these discrepancies arise from several factors: a) the presence of the shape-function streamwise pressure gradient in the enthalpy equation, and b) different discretization error.

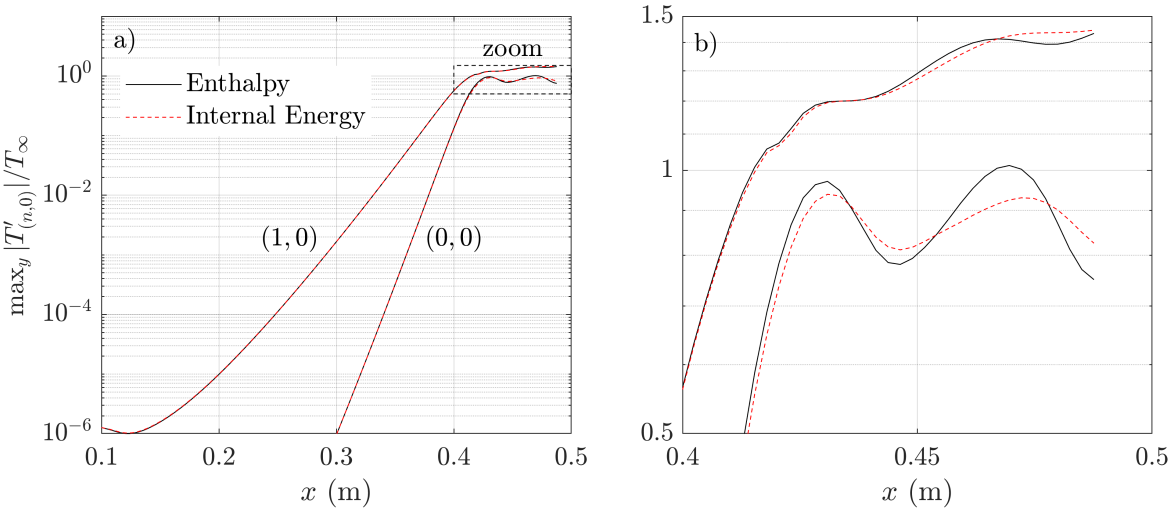

Figure 4.3: a) Temperature amplitude distribution of a Mack second mode $(1, 0)$ of $f = 286\,\mathrm{kHz}$ and the mean-flow distortion $(0, 0)$ in hypersonic flow over a flared cone. The axial coordinate x of the cone is shown in meters. The solution computed using the enthalpy form of the energy equation is shown in black, whereas the result of the internal energy formulation is shown in a dashed, red line. A dashed box shows the interval following saturation, which defines the bounds for the right, zoomed figure. b) Temperature amplitudes are highlighted within the zoomed region, as indicated in panel a).

The relative error between the solutions is computed and is shown in Fig. 4.4. Here, the relative error is defined as

$$\epsilon\left(T'_{(n,0)}\right) \equiv \frac{\left|\max_y |T'_{(n,0)}|_{\mathrm{enth}} - \max_y |T'_{(n,0)}|_{\mathrm{int}}\right|}{\max_y |T'_{(n,0)}|_{\mathrm{enth}}} \tag{4.59}$$

where the subscript enth corresponds to the solution from the enthalpy formulation whereas int corresponds to that of the internal energy formulation. From Fig. 4.4, the relative errors are less than 10% for the $(0, 0)$, barring the initialization of the $(0, 0)$ soon after $x = 0.1\,\mathrm{m}$. For the $(1, 0)$, the largest discrepancy is 3% in the laminar breakdown region. These levels are not negligible,

and perhaps are influenced by the large initial error in the mean-flow distortion that persists in the flowfield as the disturbances advect downstream.

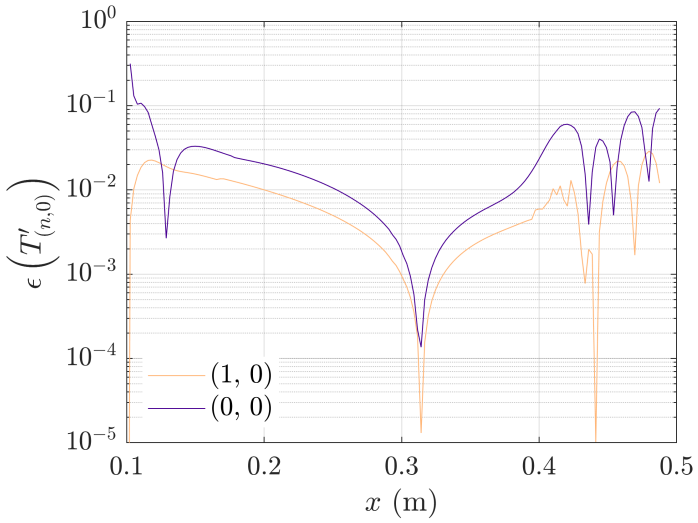

Figure 4.4: Relative error between the enthalpy and internal energy NPSE solutions versus x over a flared cone in hypersonic flow. Error is defined in Eq. (4.59). The Mack second mode's error is shown in bright orange, whereas the mean-flow-distortion's error is shown in purple.

In the spirit of computational efficiency, it is worth quantifying the change in the computation time between the two cases. For the simulation using the enthalpy formulation, the computation took 5 minutes and 30.5 seconds, whereas it took 4 minutes and 51.8 seconds for that of the internal energy equation. In other words, the simulation was done in 88% of the time using the internal energy equation. This is not insignificant, and is expected to scale for problems with additional evaluations of the nonlinear RHS forcing vector (as we will see in the next example).

Continuing forward, it is worth quantifying the same discrepancy for another case in hypersonic flow. This time, let us consider stationary crossflow saturation over the HIFiRE-5b flight case. Similarly, the solution is computed with NASA's DPLR code with the same gas parameters as before. The test conditions are taken at a representative flight time of $514.8\,\mathrm{s}$ on the leeward side of the elliptical geometry, indicated below in Table 4.2 and originally printed in Table 4 of Moyes

et al. [102]. As a PSE simulation of stationary crossflow must eliminate the streamwise pressure gradient of the shape-function, it is expected that SCF will exhibit higher levels of relative error when comparing the results of the enthalpy form against that of the internal energy equation.

Linear analysis (not shown) reveals that for this flowfield, the most amplified SCF whose number of locally spanwise waves at the rear of the vehicle is $n_{\mathrm{sw}} = 470$. For the present NPSE simulation, the SCF $(0, 1)$ and the mean-flow distortion will be simulated.

M_∞	$\mathrm{Re}'\,(1/\mathrm{m})$	$T_w\,(\mathrm{K})$	$T_\infty\,(\mathrm{K})$	$p_\infty\,(\mathrm{Pa\ abs.})$
7.793	8.83×10^6	373	216	3380

Table 4.2: Selected conditions for flow over the elliptical cone HIFiRE-5b in flight at $514.8\,\mathrm{s}$.

The simulation inputs are briefly outlined. The domain is initialized near the LST neutral point of the $n_{\mathrm{sw}} = 470$ disturbance at $x = 0.1026\,\mathrm{m}$. The marching path is chosen as a 'vortex path', i.e., following the compressible, generalized inflection point of $\overline{\rho}\,\overline{w}$ in the flowfield. The spanwise wavenumber β is locally varied in the streamwise direction s as the neighboring inviscid streamlines converge and diverge: see chapter 4 of Kocian [49]. In spite of this, the term $\mathrm{d}\beta/\mathrm{d}s$ is presently neglected in the governing equations. The s-domain has $N_s = 159$ points and is equispaced. The y-domain contains $N_y = 200$ points. The shock height is found and underneath it serves as the y-domain height $y_{\max}$ after being fit with an 11^{th}-order polynomial. The clustering height for the boundary layer is the same as before: $y_i = \delta^{h_{\mathrm{tot}}}_{100.1}$ and is subsequently fit with a 4^{th}-order polynomial. Freestream Dirichlet conditions are supplied at the $y_{\max}$ height for all shape-function components. Continuity is used as a compatibility condition on $\hat{\rho}_{(0,k)}$ at the wall. NPSE's convergence criteria are selected as $\max_{(n,k)} |\epsilon_{\alpha,\,(n,k)}| < 10^{-11}$ and $\epsilon_{\mathrm{nl},\,(n,k)} = 10^{-11}$. The initial amplitude of the $(1, 0)$ Fourier mode is selected as $\max_y |u'_{(0,1)}|/\overline{u}_{\mathrm{ref}} = 1.7 \times 10^{-5}$, where $\overline{u}_{\mathrm{ref}} = 2237.338\,\mathrm{m/s}$. The initial phase of the $(0, 1)$ is left uncontrolled from the selected

LST eigenmode. The mean-flow distortion's streamwise wavenumber $\alpha_{(0,0)}$ is nonzero and purely imaginary. First-order Taylor series are used for the transport variables' expansions.

Figure 4.5 shows the SCF temperature amplitude distributions against the cone's x for the two different energy equation formulations. The description matches the figure of the previous example of the Mack second mode (Fig. 4.3). It is important to note that even though the fundamental has its pressure gradient $\partial\hat{p}_{(0,1)}/\partial s = 0$, the discrepancy between the two solutions is not appreciably different than that of the Mack second mode case. Specifically, Fig. 4.6 shows the relative error between the two cases, as defined before in Eq. (4.59). The error in the mean-flow distortion $(0,0)$ is slightly above 10% just as SCF is saturating near $x = 0.6\,\mathrm{m}$, whereas the SCF $(0,1)$ approaches 8% near $x = 0.6\,\mathrm{m}$ as well. Recall from before that the Mack second mode only reached maximum error levels of nominally 3% for the sample case—this suggests that error is slightly higher for stationary instabilities. This is likely due to the assignment $\partial\hat{p}_{(0,k)}/\partial s = 0$.

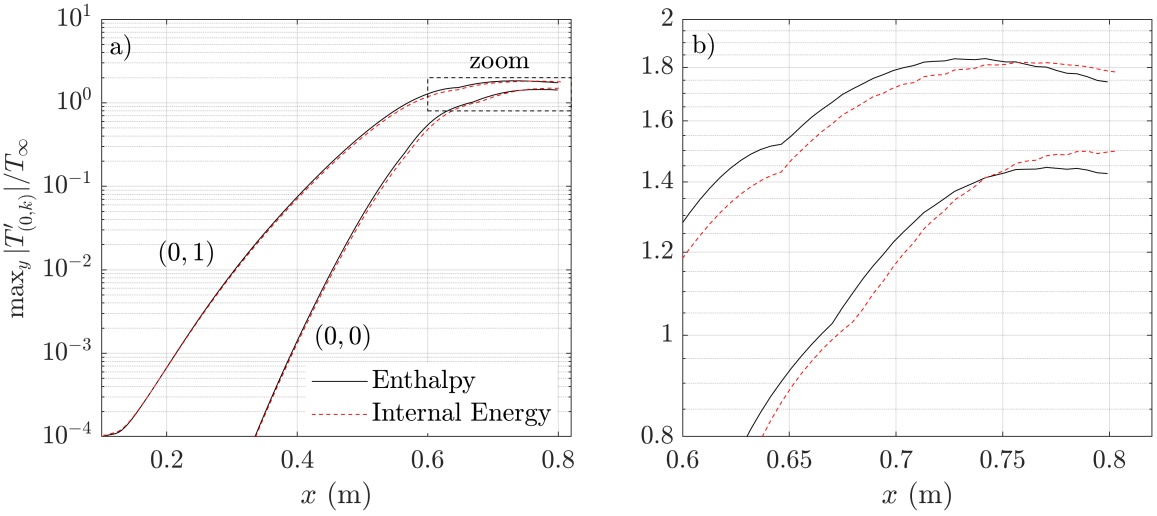

Figure 4.5: a) Temperature amplitude distribution of a stationary crossflow disturbance $(0,1)$ and the mean-flow distortion $(0,0)$ in hypersonic flow over HIFiRE-5b in flight. The axial coordinate x of the cone is shown in meters. The solution computed using the enthalpy form of the energy equation is shown in black, whereas the result of the internal energy formulation is shown in a dashed, red line. A dashed box shows the interval following saturation, which defines the bounds for the right, zoomed figure. b) Temperature amplitudes are highlighted within the zoomed region, as indicated in panel a).

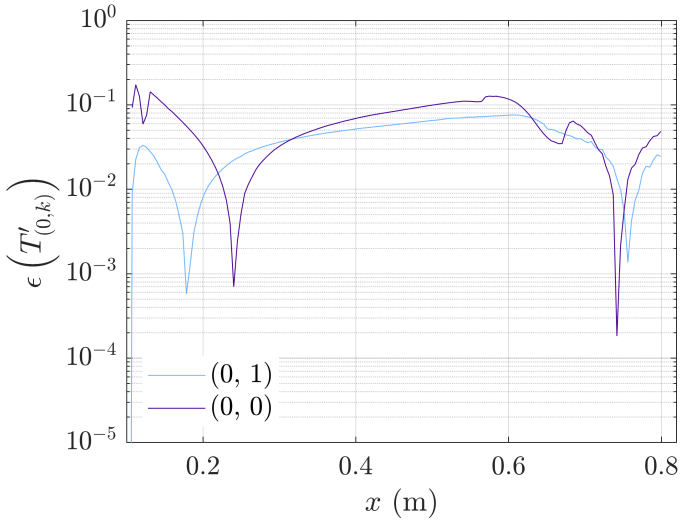

Figure 4.6: Relative error between the enthalpy and internal energy NPSE solutions versus x over HIFiRE-5b in flight. Error is defined in Eq. (4.59) analogously for $T'_{(0,k)}$. The stationary crossflow's error is shown in light blue, whereas the mean-flow-distortion's error is shown in purple.

As before, it is worth quantifying the computation time between the two cases. For the simulation using the enthalpy formulation, the computation took 5 minutes and 10.2 seconds, diverging at step $i = 148$; whereas it took 3 minutes and 41.2 seconds for that of the internal energy equation, diverging at step $i = 149$. In other words, the simulation completed in 71% of the time using the internal energy equation—even marching slightly farther down the cone. This is more significant of a speed up than the previous example of the Mack second mode, and is expected to scale even greater for problems with additional harmonics and long extents of nonlinear regions.

From these brief numerical experiments in hypersonic flow, it is clear that the choice of the energy equation in NPSE has a noticeable effect on temperature disturbances for relevant, primary instability mechanisms. To assess the physical accuracy, a close comparison and verification with DNS must be made. As a representative verification, Paredes et al. demonstrate an excellent comparison between DNS and NPSE for an oblique breakdown in hypersonic flow [28], while in the dissertation of Paredes, it is mentioned that the enthalpy formulation of the energy equation is used [113]. For the remainder of the simulations in this dissertation, the enthalpy formulation of the energy equation will be selected. This is done to remain commensurate with previous analysis

performed with EPIC and other PSE computationalists.

This concludes the discussion on stability methodology in EPIC. The next section will detail some of the author's contributions to EPIC.

4.5 Contributions

Throughout the author's time at Texas A&M, there have been several direct contributions in support of EPIC and stability analysis. These include but are not limited to:

1. Creation of the computer algebra code, DERIVE, as written in Maxima. This code uses the rules of algebra and calculus to derive the governing stability equations as used in EPIC for all of its analysis: LST, LPSE, and NPSE. Even further, DERIVE has laid the necessary groundwork for the other stability codes in the CST lab, such as Andrew Riha's Spatial BiGlobal code, BLAST, and Madeline Peck's AHLNSE code, HAL. Those codes are now running and performing stability analysis using the equations reliably created with DERIVE. The general framework is established such that a relatively easy extension has been performed for non-orthogonal grids and more physically inclusive disturbance models. DERIVE has been written in a simple way such that extensions can easily be included without breaking previous behavior. For instance, Madeline has already extended DERIVE's capability to compute the non-reflecting boundary conditions in AHLNSE.

2. Implemented a more accurate LU solver into PSE. Previously, for much of the PSE analysis performed with EPIC, a standard, lightweight LU algorithm was developed in the lab, following the sorts of algorithms one might find in the standard text, Numerical Recipes [88]. This lightweight algorithm allowed a straightforward parallelization of the routine using OpenMP. However, it was discovered that for some cases, the standard, lightweight LU algorithm experienced a numerical instability when attempting to solve certain algebraic systems (e.g., hypersonic, traveling crossflow of a given wavenumber on a yawed cone). This numerical instability quickly caused divergence of the solution within a few streamwise steps in PSE. The author pivoted and implemented the more robust LU solver known

as MUMPS [107]. Upon retesting these problematic cases, the numerical instability was no longer apparent—the PSE solution behaved well.

3. Implemented the z-symmetry conditions for NPSE as detailed in Eqs. (4.31). These have been qualitatively verified by computing the saturation and nonlinear development of a Görtler vortex at near-incompressible speeds: see Chapter 4 in Patel [82]. The resulting flowfield is indeed symmetric in the z coordinate.

4. Extended capability to account for subharmonics in NPSE. All application of EPIC previously presumed the fundamental had the smallest wavenumber in the simulation. This is not correct when simulating subharmonics, so a brief modification to the logic was made, drastically increasing the physical capability of the EPIC NPSE solver.

5. Modeled Tollmien-Schlichting/stationary-crossflow (TS/SCF) interaction and TS subharmonic resonance in subsonic and transonic flow. These secondary instabilities had not been simulated before with EPIC.

6. Added many miscellaneous functionalities to ease linear and nonlinear analysis from incompressible to hypersonic speeds, such as:

   (a) Streamwise mapping that is non-equispaced.

   (b) Cosine clustering in the wall-normal domain that may occur before Malik mapping. This is useful for stability problems whose freestream boundary ought to not appreciably deresolve in terms of grid resolution.

   (c) Extension of wall-normal mapping such that the clustering height y_i can be defined as some scalar multiple of a selected boundary-layer height. The assignment $y_i = 7\delta_{50}$ is particularly useful for subsonic/transonic analysis, which is now made possible through this capability.

   (d) Porous surface boundary conditions. Briefly, Fedorov et al. modeled the wall-normal perturbation v' as related to the pressure perturbation p' at the surface through an acous-

tic impedance K_{por}, assuming the surface consists of a regularly spaced array of cylindrical pores [114]. The author has implemented these surface conditions into both LST and LPSE on conjunction with researchers from the von Karman Institute (VKI). LST verification was performed privately—results are omitted from this document. The curious reader is referred to the author's results presented in Miró Miró for quantification of non-parallel effects using LPSE [46, §9.1.5].

(e) Compatibility conditions were extended to y-momentum at the surface for $\hat{\rho}$ to improve the conditioning of the coefficient matrices for some problems.

(f) Modeled isothermal disturbances in an adiabatic base-flow, as specified by Eqs. (4.43). This is useful for subsonic/transonic problems with TS and the mean-flow distortion or other steady disturbances simultaneously appearing in an NPSE simulation.

(g) Created a routine to easily initialize PSE upstream of LST branch-I neutral point. This is helpful to accurately capture the branch-I location after the 'LST-transient' has decayed out.

(h) Control phase of NPSE disturbances upon initialization.

(i) Improve memory usage during LPSE to use only one differentiation matrix for all of the (ω, β)-disturbances considered.

(j) Option to purify the LST eigensolution after selecting it from the local spectrum determined by Arnoldi/Krylov subspace methods. This follows the methodology of Malik et al. [100].

(k) Enforced the mean-flow distortion to be purely real in NPSE.

(l) Implemented the energy equation as formulated in terms of internal energy e into EPIC.

7. Made physical modifications to treatment of the mean-flow distortion relevant for subsonic and transonic flows. These include the options to

   (a) zero its complex wavenumber, i.e., $\alpha_{(0,0)} = 0$, as suggested by Hein [101].

(b) eliminate its s-derivatives of the $\hat{v}_{(0,0)}$ shape-function component. This is mathematically consistent with order-of-magnitude analysis from incompressible continuity when $\alpha_{(0,0)} = 0$. For clarity, incompressible continuity in a Cartesian coordinate system for the mean-flow distortion reduces to

$$\begin{aligned} \frac{\partial \hat{u}_{(0,0)}}{\partial s} + \frac{\partial \hat{v}_{(0,0)}}{\partial y} &= 0, \\ \varepsilon_s \frac{\partial \hat{u}_{(0,0)}}{\partial \breve{s}} + \frac{\partial \hat{v}_{(0,0)}}{\partial y} &= 0, \\ \implies \hat{v}_{(0,0)} &= \varepsilon_s \left(- \int_0^{y_{\max}} \frac{\partial \hat{u}_{(0,0)}}{\partial \breve{s}} \, \mathrm{d}y \right) \end{aligned} \tag{4.60}$$

following a procedure identical to that in Eq. (4.10). Then $\hat{v}_{(0,0)}$ is $O(\varepsilon_s)$, implying that $\partial \hat{v}_{(0,0)}/\partial s$ and $\partial^2 \hat{v}_{(0,0)}/(\partial s \, \partial y)$ are negligible.

8. Expanded EPIC's accessibility to many different users and operating systems. EPIC is available to the aerospace community upon request with a user's manual to learn from.

9. Created various features surrounding the code, such as:

   (a) `git` version control.

   (b) `ssh` authentication to the CST lab, increasing security.

   (c) Regression tests as well as unit tests over most of the code, increasing the longevity and reliability of EPIC.

This concludes the discussion of the author's contributions to EPIC. The following chapter will pivot and discuss some numerical difficulties with modeling the mean-flow distortion in PSE in incompressible and subsonic flow.

5. ON THE MEAN-FLOW DISTORTION IN THE PARABOLIZED STABILITY EQUATIONS

The mean-flow distortion Fourier mode can be numerically problematic when solving NPSE. Airiau from 1994 mentions that when solving the NPSE, significant and divergent growth was observed in the $\hat{u}_{(0,0)}$ component of the mean-flow distortion, causing the simulation to halt prematurely [24]. Only by truncating the wall-normal domain to nearly *two boundary-layer thicknesses* could the code produce meaningful results that matched other PSE and DNS calculations in subsonic flows. Schrauf et al. in 1996, when performing NPSE calculations to match measured transition locations over a swept wing in subsonic flight, omitted the mean-flow distortion entirely from their computations with no mention as to why [115]. Hein in his 2005 dissertation asserts that a nonzero wavenumber $\alpha_{(0,0)}$ is inconsistent with the mean-flow distortion's homogeneous Neumann condition, and therefore, asserts $\alpha_{(0,0)} = 0$ identically for all cases considered over the subsonic/transonic speed regimes [101]. Even with this assertion, Hein achieved excellent verification and validation with the NOLOT code against various computations and experimental data for a wide array of instability mechanisms—stationary crossflow, Tollmien-Schlichting, to name a few.

Other PSE analyses in subsonic contexts, however, mention no special treatment needed for the mean-flow distortion. In Haynes' 1996 dissertation demonstrating the classic validation of stationary crossflow with experiments by Reibert et al., there is no mention of any particular difficulty [116, 26]. For instance, the selected stability wall-normal domain is not truncated to $O(2\delta)$, as figures of shape-function profiles extend to at least 10δ. Malik et al. in 1999 performed NPSE analysis for the same validation case with Reibert et al., generating stationary crossflow rollovers with their own distinct NPSE code [100]. No special treatment of the mean-flow distortion was mentioned.

This chapter intends to analyze the linear, freestream dynamics of a disturbance similar to the incompressible mean-flow distortion using the Orr-Sommerfeld equation. The present anal-

ysis will consider both homogeneous and inhomogeneous Neumann boundary conditions in the freestream. The resulting Orr-Sommerfeld $\hat{v}$ profiles will be compared directly against a mean-flow distortion Fourier mode from a sample NPSE simulation. Using the analytical solution, the domain height will be varied to assess the proposal by Airiau in the context of the present analysis. Several proposed limitations on $\alpha_{(0,0)}$ are provided if Airiau's proposal is not sufficient. An outlook for supplementary analysis is given, as well as Maxima code to generate the lengthy analytical expressions used here.

5.1 Linear, freestream dynamics of the Orr-Sommerfeld operator

Continuing the discussion from NPSE on complex conjugates and symmetry relations (§4.3.1.1 and §4.3.1.2, resp.), let us first establish some truths for the mean-flow distortion Fourier mode. Mathematically, it has a few idiosyncrasies compared to the other Fourier modes. In the NPSE ansatz double summation of Eq. (4.22), the $(0,0)$ has no other complex conjugate, i.e., it is not paired with any other harmonic. Since the disturbance q' is real-valued, the mean-flow distortion's shape-function $\hat{q}_{(0,0)}$ then must be purely real and its streamwise wavenumber $\alpha_{(0,0)}$ is purely imaginary. If the laminar base-flow is symmetric in z, i.e., $\overline{w} = 0$, then $\hat{w}_{(0,0)}$ must be identically zero. This follows from the simultaneous requirements that $\hat{q}_{(0,0)}$ is real and $\hat{w}_{(0,0)}$ is imaginary via Eq. (4.32).

Recall from §4.3.1.3 that the quadratic harmonic interactions of $(n,k) + (-n,-k)$ force the $(0,0)$ Fourier mode. From this, one can rightfully state that the MFD is generated nonlinearly through the various other harmonics in the system. With that being said, analyzing the linear dynamics, or the left-hand side operator, of the Fourier mode can be revealing inherently, disregarding these nonlinear forcing terms. With that in mind, let us return to first principles and consider the nondimensional, Orr-Sommerfeld equation with the parallel-flow assumption from [117, §2.3.5]

$$\begin{gathered}\tilde{\mathscr{D}}_{\mathrm{os}} \equiv (-\mathrm{i}\omega + \mathrm{i}\alpha\overline{u} + \mathrm{i}\beta\overline{w})\left(\frac{\mathrm{d}^2}{\mathrm{d}y^2} - \alpha^2 - \beta^2\right) - \mathrm{i}\alpha\frac{\mathrm{d}^2\overline{u}}{\mathrm{d}y^2} - \mathrm{i}\beta\frac{\mathrm{d}^2\overline{w}}{\mathrm{d}y^2} - \frac{1}{\mathrm{Re}}\left(\frac{\mathrm{d}^2}{\mathrm{d}y^2} - \alpha^2 - \beta^2\right)^2, \\ \tilde{\mathscr{D}}_{\mathrm{os}}\hat{v} = 0\end{gathered} \tag{5.1}$$

The disturbance of interest is the mean-flow distortion, so for a similar disturbance character, let us set $\beta = \omega = 0$. Additionally, suppose the velocity profile $\overline{u}$ is constant in y, i.e., $\overline{u} = \overline{u}_\infty$. Since the equations are nondimensional with respect to freestream values, $\overline{u}_\infty \equiv 1$. Then the Orr-Sommerfeld equation simplifies to

$$\left(\mathrm{i}\alpha \left(\frac{\mathrm{d}^2}{\mathrm{d}y^2} - \alpha^2 \right) - \frac{1}{\mathrm{Re}} \left(\frac{\mathrm{d}^2}{\mathrm{d}y^2} - \alpha^2 \right)^2 \right) \hat{v} = 0 \tag{5.2}$$

This is a fourth-order, homogeneous, ordinary differential equation with constant coefficients, expressed as

$$\begin{aligned} &\hat{v}'''' + a\hat{v}'' + b\hat{v} = 0, \\ &a \equiv -2\alpha^2 - \mathrm{i}\alpha\mathrm{Re}, \\ &b \equiv \alpha^4 + \mathrm{i}\alpha^3\mathrm{Re} \end{aligned} \tag{5.3}$$

The general solution is given as

$$\begin{aligned} \hat{v}(y) &= c_1 \mathrm{e}^{yk_2} + c_2 \mathrm{e}^{-yk_2} + c_3 \mathrm{e}^{yk_1} + c_4 \mathrm{e}^{-yk_1}, \\ k_1 \equiv \sqrt{\frac{\sqrt{a^2 - 4b} - a}{2}}, &\qquad k_2 \equiv \sqrt{\frac{-\sqrt{a^2 - 4b} - a}{2}} \end{aligned} \tag{5.4}$$

where c_1, c_2, c_3, and c_4 are complex-valued constants to satisfy the boundary conditions on $\hat{v}$. Since we have assumed $\overline{u} = \overline{u}_\infty$, this solution is only appropriate in the freestream. The y domain then should start not at the wall of $y = 0$, but some nonzero value, say $y = \delta$. The prescribed boundary conditions at $y = \delta$ are inhomogeneous Dirichlet and Neumann conditions, where these nonzero values would be informed from a computation, if necessary. At the top boundary of the wall-normal domain of height $y = L$, we prescribe a homogeneous Neumann condition and an inhomogeneous Dirichlet condition, allowing the streamwise growth of the mean-flow distortion.

Together, they are written as four equations:

$$\hat{v}(\delta) = \hat{v}(\delta), \tag{5.5a}$$

$$\frac{\mathrm{d}\hat{v}(\delta)}{\mathrm{d}y} = \frac{\mathrm{d}\hat{v}(\delta)}{\mathrm{d}y}, \tag{5.5b}$$

$$\frac{\mathrm{d}\hat{v}(L)}{\mathrm{d}y} = 0, \tag{5.5c}$$

$$\hat{v}(L) \neq 0 \text{ (and finite)} \tag{5.5d}$$

Substituting in the general solution for $\hat{v}$ into these four equations leads to

$$c_1\mathrm{e}^{\delta k_2} + c_2\mathrm{e}^{-\delta k_2} + c_3\mathrm{e}^{\delta k_1} + c_4\mathrm{e}^{-\delta k_1} = \hat{v}(\delta), \tag{5.6a}$$

$$c_1k_2\mathrm{e}^{\delta k_2} - c_2k_2\mathrm{e}^{-\delta k_2} + c_3k_1\mathrm{e}^{\delta k_1} - c_4k_1\mathrm{e}^{-\delta k_1} = \frac{\mathrm{d}\hat{v}(\delta)}{\mathrm{d}y}, \tag{5.6b}$$

$$c_1k_2\mathrm{e}^{Lk_2} - c_2k_2\mathrm{e}^{-Lk_2} + c_3k_1\mathrm{e}^{Lk_1} - c_4k_1\mathrm{e}^{-Lk_1} = 0, \tag{5.6c}$$

$$c_1\mathrm{e}^{Lk_2} + c_2\mathrm{e}^{-Lk_2} + c_3\mathrm{e}^{Lk_1} + c_4\mathrm{e}^{-Lk_1} = \hat{v}(L) \tag{5.6d}$$

or, as a matrix equation:

$$\underbrace{\begin{bmatrix} \mathrm{e}^{\delta k_2} & \mathrm{e}^{-\delta k_2} & \mathrm{e}^{\delta k_1} & \mathrm{e}^{-\delta k_1} \\ k_2\mathrm{e}^{\delta k_2} & -k_2\mathrm{e}^{-\delta k_2} & k_1\mathrm{e}^{\delta k_1} & -k_1\mathrm{e}^{-\delta k_1} \\ k_2\mathrm{e}^{Lk_2} & -k_2\mathrm{e}^{-Lk_2} & k_1\mathrm{e}^{Lk_1} & -k_1\mathrm{e}^{-Lk_1} \\ \mathrm{e}^{Lk_2} & \mathrm{e}^{-Lk_2} & \mathrm{e}^{Lk_1} & \mathrm{e}^{-Lk_1} \end{bmatrix}}_{K} \begin{bmatrix} c_1 \\ c_2 \\ c_3 \\ c_4 \end{bmatrix} = \begin{bmatrix} \hat{v}(\delta) \\ \frac{\mathrm{d}\hat{v}(\delta)}{\mathrm{d}y} \\ 0 \\ \hat{v}(L) \end{bmatrix} \tag{5.7}$$

where K is defined as the coefficient matrix. The coefficients c_1, c_2, c_3, and c_4 can be solved for analytically. Their values are omitted for brevity, but can be obtained using a computer algebra system such as Maxima [79]. Example solutions for $\hat{v}$ are shown below for $\delta = 1$, $L = 10\delta$, $\mathrm{Re} = 1000$, $\hat{v}(\delta) = 1$, $\mathrm{d}\hat{v}(\delta)/\mathrm{d}y = 1$, $\hat{v}(L) = 3$, and, selecting $\alpha_i \equiv \mathrm{Imag}(\alpha) = \pm 1/\mathrm{Re} = \pm 0.001$. The figure shows that there a distinct change in character as α_i changes sign. The positive-α_i solution oscillates with a very high amplitude relative to the prescribed, boundary condition values, whereas the

negative-α_i solution smoothly approaches the freestream condition in a polynomial/exponential-like fashion.

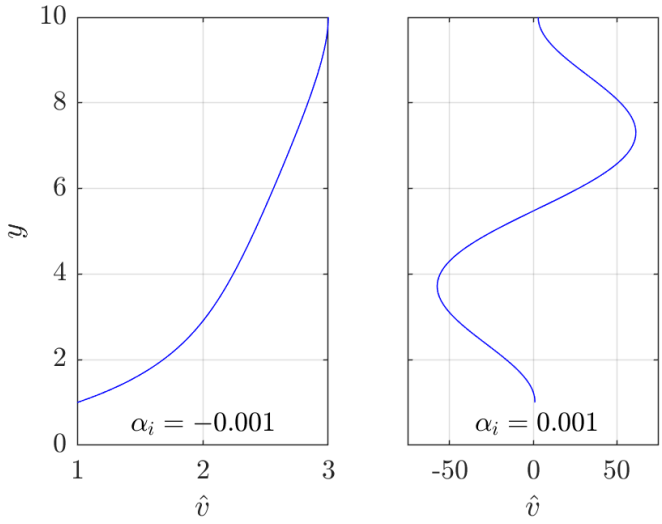

Figure 5.1: Wall-normal profiles of Orr-Sommerfeld $\hat{v}(y)$ with $(\omega, \beta) = (0, 0)$ for two selected values of α_i. Left: $\alpha_i = -0.001$. Right: $\alpha_i = 0.001$.

5.2 Wavenumbers k_1 and k_2

The Reynolds-number dependence and the effect of the sign of α_i on the wall-normal wavenumber are shown below. Let us express the quantities k_1 and k_2 in terms of $\alpha = \mathrm{i}\alpha_i$, where $2k_1^2 = \sqrt{a^2 - 4b} - a$ and $2k_2^2 = -\sqrt{a^2 - 4b} - a$.

$$\begin{aligned} a^2 - 4b &= -\alpha^2 \mathrm{Re}^2 = \alpha_i^2 \mathrm{Re}^2 \in \mathbb{R}, \\ \sqrt{a^2 - 4b} &= |\alpha_i \mathrm{Re}| = |\alpha_i| \mathrm{Re}, \\ 2k_1^2 = \sqrt{a^2 - 4b} - a &= |\alpha_i| \mathrm{Re} - (2\alpha_i^2 + \alpha_i \mathrm{Re}) = \mathrm{Re}(|\alpha_i| - \alpha_i) - 2\alpha_i^2, \\ 2k_2^2 = -\sqrt{a^2 - 4b} - a &= \mathrm{Re}(-|\alpha_i| - \alpha_i) - 2\alpha_i^2 \end{aligned} \tag{5.8}$$

where care has been taken recalling the fact $\sqrt{x^2} = |x|$ for $x \in \mathbb{R}$. With this, k_1^2 and k_2^2 may be

written as piecewise functions dependent upon the sign of α_i:

$$k_1^2 = \begin{cases} -\alpha_i^2, & \alpha_i > 0 \\ -\alpha_i^2 - \alpha_i \mathrm{Re}, & \alpha_i < 0 \end{cases} \tag{5.9a}$$

$$k_2^2 = \begin{cases} -\alpha_i^2 - \alpha_i \mathrm{Re}, & \alpha_i > 0 \\ -\alpha_i^2, & \alpha_i < 0 \end{cases} \tag{5.9b}$$

As α_i increases from negative to positive, k_1 changes from purely real to purely imaginary. On the other hand, k_2 remains purely imaginary for both negative and positive α_i. The above expression also reveals the zero of k_1. If $\alpha_i = -\mathrm{Re}$, then $k_1 = 0$ while $k_2 = \mathrm{i}\mathrm{Re} \neq 0$. Eq. (5.9) is plotted against α_i and expressed directly in terms of Re. Observe that for $\alpha_i > 0$, both wavenumbers are purely imaginary with $\mathrm{Imag}(k_2) > \mathrm{Imag}(k_1)$. In other words, k_2 is directly responsible for the small scale oscillations present in $\hat{v}(y)$, while k_1 corresponds to the large scale oscillations when $\alpha_i > 0$. Conversely, when $-\mathrm{Re} < \alpha_i < 0$, there exists only one imaginary wavenumber k_2, i.e., $\hat{v}(y)$ may only have one oscillatory length scale. The interval of $\alpha_i < -\mathrm{Re}$ is not shown, as instabilities with those growth rates are not of interest. As a side note, observe that the zero of the wavenumber k_1 ($\alpha_i = -\mathrm{Re}$) is equal to analytical results described by Balakumar & Malik in 1992—that is to say, equal to the lower half branch point for the viscous contribution to the incompressible solution with $\omega = 0$ [118].

The governing equation for nonzero α_i in Eq. (5.4) indicates that the roots of the characteristic equation are simply $\pm k_1$ and $\pm k_2$. In the language of systems and controls, these are also called the *poles*, say p_j, as they indicate the response of the homogeneous system. The solution character can be succinctly described based merely on the location of the poles in the complex plane. For the system at hand, there are two distinct cases of interest for nonzero α_i, as shown in Fig. 5.2.

1. $\alpha_i < 0$

   (a) k_1 is real and k_2 is purely imaginary. Then there are two real poles and an imaginary pole pair, i.e., $p_{(1,2)} = \pm k_1$ and $p_{(3,4)} = \pm \mathrm{i}\,\mathrm{Imag}(k_2)$.

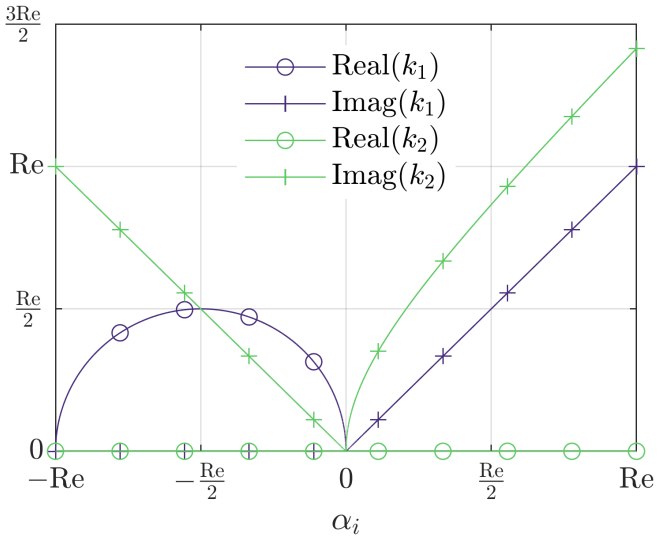

Figure 5.2: Real and imaginary parts of wavenumbers k_1 and k_2 shown against α_i, as defined in Eq. (5.5) and rearranged in Eq. (5.9).

2. $\alpha_i > 0$

   (a) k_1 and k_2 are both purely imaginary. Then there are two imaginary pole pairs, i.e., $p_{(1,2)} = \pm \mathrm{i}\,\mathrm{Imag}(k_1)$ and $p_{(3,4)} = \pm \mathrm{i}\,\mathrm{Imag}(k_2)$.

For $\alpha_i < 0$, the real poles permit the solution $\hat{v}$ to connect between the boundary condition at $y = \delta$ and $y = L$ without significant oscillation, even with the presence of an imaginary pole pair. On the other hand for $\alpha_i > 0$, connecting the prescribed boundary conditions in the y-domain can be *strenuous*, as the only available mechanics are oscillations of two very disparate wavenumbers. This leads to large-amplitude oscillations of the solution $\hat{v}$ in the freestream region. To visualize this phenomenon, consider the same model problem as before: $\delta = 1$, $L = 10\delta$, $\mathrm{Re} = 1000$, $\hat{v}(\delta) = 1$, $\mathrm{d}\hat{v}(\delta)/\mathrm{d}y = 1$, and $\hat{v}(L) = 3$. Vary α_i and compute the corresponding $\hat{v}$. The maximum in $|\hat{v}|$ is extracted for each α_i and is shown in Fig. 5.3. There appear to be specific values of α_i where the y-maximum in $|\hat{v}|$ diverges to very high values with some exceeding $\max_y |\hat{v}| = 1500$—more than 500 times the value of the freestream Dirichlet boundary condition. The extreme and sudden growth in $|\hat{v}|$ is associated to the determinant of the coefficient matrix K

changing sign as it passes through zero, as shown in Fig. 5.4.

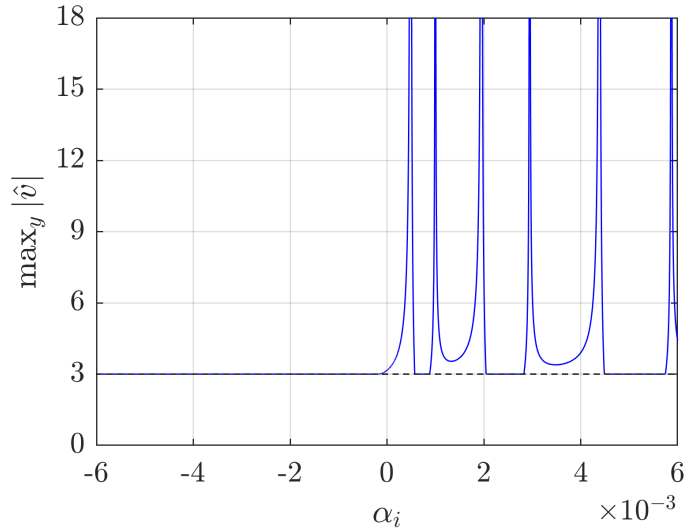

Figure 5.3: The y-maximum of $|\hat{v}|$ as α_i varies for example boundary conditions. The black, dashed line indicates the selected freestream Dirichlet boundary condition, $\hat{v}(L) = 3$.

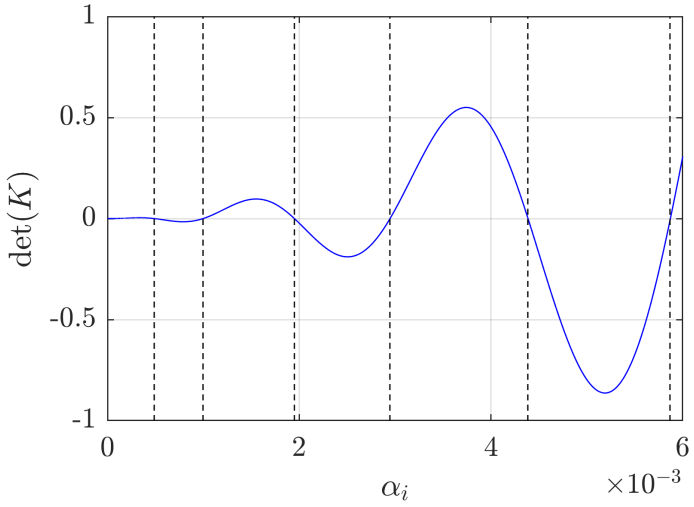

Figure 5.4: Determinant of coefficient matrix K against $\alpha_i > 0$. The dashed lines indicate where $\det(K)$ crosses zero, which is associated with the extreme growth of $|\hat{v}|$ as shown in Fig. 5.3. K is defined in Eq. (5.7).

As the determinant changes sign, the coefficients c_i traverse the complex plane suddenly for small changes in α_i.[1] Since the system has two imaginary pole pairs for $\alpha_i > 0$, the coefficients c_i that correspond to each pole pair are complex conjugates of one another since $\hat{v} \in \mathbb{R}$. That is, $c_1 = c_2^\dagger$ and $c_3 = c_4^\dagger$, where the superscript † implies conjugation. To demonstrate the sudden traversal of the coefficients c_i in the complex plane, consider separately their magnitudes and complex arguments in Fig. 5.5. Only c_1 and c_3 are plotted for brevity using the above conjugate relations. There are several features to note.

1. Near α_i values where $|\hat{v}|$ becomes large, the magnitudes $|c_i|$ grow suddenly and are associated with a sudden argument shift of $\pm\pi$ radians for the coefficients. Here, the argument is defined as $\mathrm{Arg}(c_i) \equiv \mathrm{arctan2}\left(\mathrm{Imag}(c_i), \mathrm{Real}(c_i)\right)$. On the other side of the coefficient traversal, the magnitudes return to a similar value as before and the argument settles.

2. For the pole pair associated with k_2, the coefficients c_1 and c_2 appear to 'roll' in the complex plane. That is, their arguments are nearly linearly varying in α_i, apart from the abrupt shifts as mentioned above. For the other pole pair associated with k_1, the coefficients c_3 and c_4 stay near the imaginary axes with arguments $\approx \pm\pi/2$.

3. The abrupt shifts of the c_3 and c_4 arguments take on a different character that depends on the local slope of the determinant of K. That is, for $\partial \det(K)/\partial\alpha_i < 0$, the growth of $|c_3|$ is extremely short in its α_i-extent. Conversely, for $\partial \det(K)/\partial\alpha_i > 0$, the growth of $|c_3|$ is broader in its α_i-extent. This difference in character is not observed for the other coefficients c_1 and c_2 for this case.

This completes the characterization of the system for nonzero α_i for this sample problem with these prescribed boundary conditions. Let us now consider the case where α_i identically equals zero.

[1] Define c_i as the coefficient c with subscript integer i, not as the imaginary part of some quantity c.

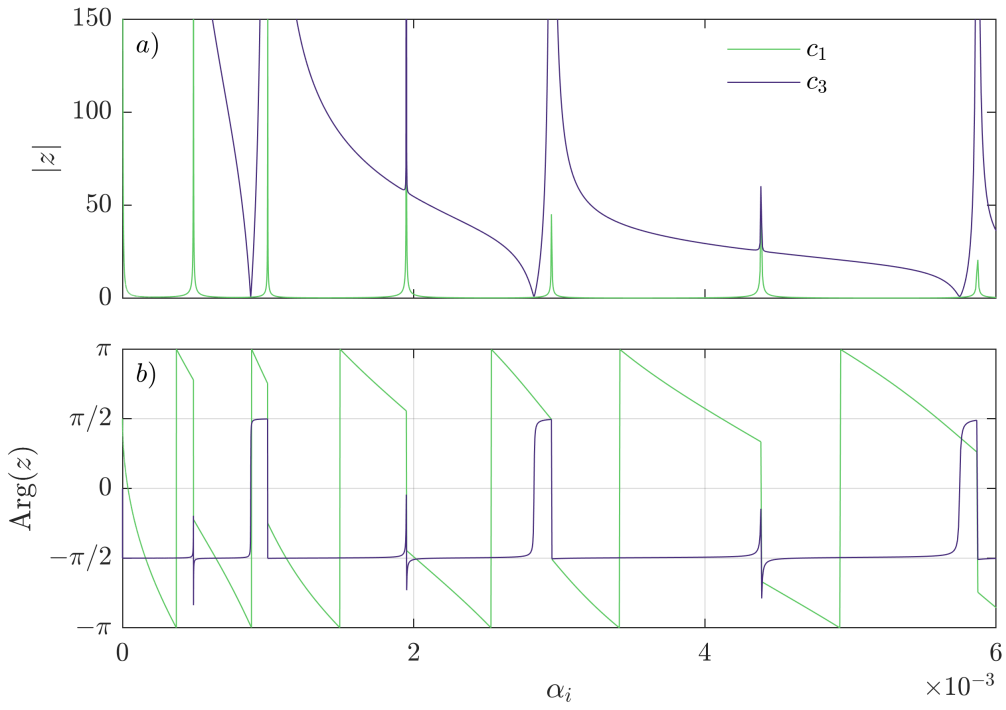

Figure 5.5: $a)$ Magnitudes and $b)$ complex arguments of coefficients c_1 and c_3 shown against $\alpha_i > 0$.

5.3 Solution for a neutrally stable disturbance

If α_i could equal zero in Eq. (5.9), both wavenumbers k_1 and k_2 would equal zero. However, the general solution to this fourth-order differential equation would no longer satisfy the boundary conditions. Zero-valued wavenumbers cause $\hat{v}(y)$ to be constant in the wall-normal direction. That could create an inconsistency between $\hat{v}(\delta)$ and $\hat{v}(L)$, as they are not necessarily equal to one another. It is a peculiar case where those boundary conditions are equal and it is entirely valid. However, to complete the analysis of possible α_i values when $\hat{v}(\delta) \neq \hat{v}(L)$, consider the governing, ordinary differential equation of Eq. (5.2) again as it reduces to

$$\hat{v}'''' = 0 \tag{5.10}$$

which has the general solution of a cubic polynomial and is independent of Re. Applying the same

boundary conditions as above, we can form four equations in the same fashion and solve for the coefficients r_i in $\hat{v}(y) = r_3 y^3 + r_2 y^2 + r_1 y + r_0$.

$$\begin{bmatrix} \delta^3 & \delta^2 & \delta & 1 \\ 3\delta^2 & 2\delta & 1 & 0 \\ 3L^2 & 2L & 1 & 0 \\ L^3 & L^2 & L & 1 \end{bmatrix} \begin{bmatrix} r_3 \\ r_2 \\ r_1 \\ r_0 \end{bmatrix} = \begin{bmatrix} \hat{v}(\delta) \\ \frac{\mathrm{d}\hat{v}(\delta)}{\mathrm{d}y} \\ 0 \\ \hat{v}(L) \end{bmatrix} \tag{5.11}$$

where $\hat{v}(\delta)$, $\mathrm{d}\hat{v}(\delta)/\mathrm{d}y$, and $\hat{v}(L)$ are prescribed. Again, the coefficients r_i are analytically solved for using Maxima. As r_i are more tractable in form than c_i of the nonzero α_i-solution, they are written below:

$$\begin{aligned} r_3 &= \frac{-1}{(\delta - L)^3} \left(2\left(\hat{v}(\delta) - \hat{v}(L)\right) + \frac{\mathrm{d}\hat{v}(\delta)}{\mathrm{d}y}\left(L - \delta\right) \right), \\ r_2 &= \frac{1}{(\delta - L)^3} \left(3\left(\delta\hat{v}(\delta) + L\hat{v}(\delta) - \delta\hat{v}(L) - L\hat{v}(L)\right) + \frac{\mathrm{d}\hat{v}(\delta)}{\mathrm{d}y}\left(2L^2 - L\delta + \delta^2\right) \right), \\ r_1 &= \frac{-L}{(\delta - L)^3} \left(6\delta\left(\hat{v}(\delta) - \hat{v}(L)\right) + \frac{\mathrm{d}\hat{v}(\delta)}{\mathrm{d}y}\left(L^2 + L\delta - 2\delta^2\right) \right), \\ r_0 &= \frac{1}{(\delta - L)^3} \left(3L^2\delta\hat{v}(\delta) - L^3\hat{v}(\delta) + \delta^3\hat{v}(L) - 3L\delta^2\hat{v}(L) + L^2\delta\frac{\mathrm{d}\hat{v}(\delta)}{\mathrm{d}y}\left(L - \delta\right) \right) \end{aligned} \tag{5.12}$$

Shown below is a graphical example of the $\alpha_i = 0$ solution between two nonzero-α_i solutions. Consider then the same boundary conditions as shown in Fig. 5.1, but now with $\alpha_i = \pm 0.1/\mathrm{Re}$, shown in Fig. 5.6. Curiously enough, the cubic polynomial is an asymptote of the general nonzero-α_i solution as $\alpha_i \to 0$ in Eq. 5.4.

Let us note here that as a cubic polynomial, $\hat{v}$ does not inherit any of the issues that are associated with the $\alpha_i > 0$ general solution—i.e., two imaginary pole pairs—as discussed in the previous section.

5.4 Inhomogeneous Neumann boundary condition in the freestream

The above analysis presumes a homogeneous Neumann boundary condition on $\hat{v}$ in the freestream. As some PSE analysis has considered inhomogeneous boundary conditions, i.e., left unprescribed,

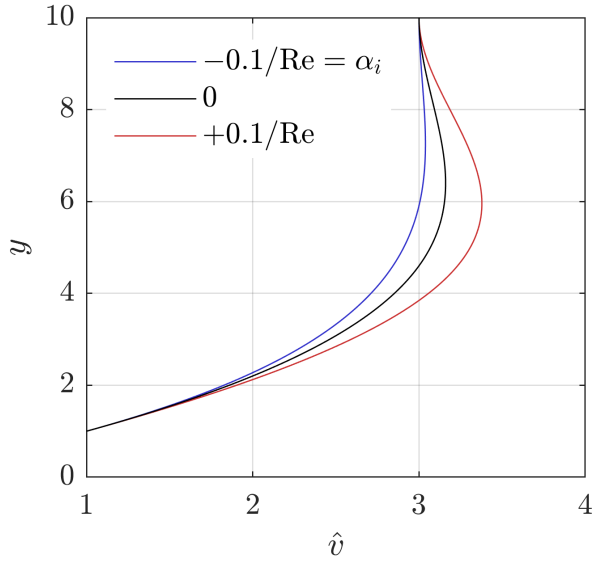

Figure 5.6: Wall-normal profiles of Orr-Sommerfeld $\hat{v}(y)$ with $(\omega, \beta) = (0, 0)$ for three selected values of α_i: $\pm 0.1/\mathrm{Re}$ and 0, where $\mathrm{Re} = 1000$.

it is worth revisiting the same model problem, but with a nonzero slope at the top boundary in order to assess with numerical experiments if the homogeneous boundary condition is responsible for this sporadic divergence of $\max_y |\hat{v}|$. The matrix equation given in Eq. (5.7) is rewritten but with $\mathrm{d}\hat{v}(L)/\mathrm{d}y \neq 0$:

$$\underbrace{\begin{bmatrix} \mathrm{e}^{\delta k_2} & \mathrm{e}^{-\delta k_2} & \mathrm{e}^{\delta k_1} & \mathrm{e}^{-\delta k_1} \\ k_2\mathrm{e}^{\delta k_2} & -k_2\mathrm{e}^{-\delta k_2} & k_1\mathrm{e}^{\delta k_1} & -k_1\mathrm{e}^{-\delta k_1} \\ k_2\mathrm{e}^{Lk_2} & -k_2\mathrm{e}^{-Lk_2} & k_1\mathrm{e}^{Lk_1} & -k_1\mathrm{e}^{-Lk_1} \\ \mathrm{e}^{Lk_2} & \mathrm{e}^{-Lk_2} & \mathrm{e}^{Lk_1} & \mathrm{e}^{-Lk_1} \end{bmatrix}}_{K} \begin{bmatrix} c_1 \\ c_2 \\ c_3 \\ c_4 \end{bmatrix} = \begin{bmatrix} \hat{v}(\delta) \\ \frac{\mathrm{d}\hat{v}(\delta)}{\mathrm{d}y} \\ \frac{\mathrm{d}\hat{v}(L)}{\mathrm{d}y} \\ \hat{v}(L) \end{bmatrix} \tag{5.13}$$

Note that the coefficient matrix K is unchanged from the previous set-up of Eq. (5.7). The matrix equation is solved analytically using Maxima for the problem of both nonzero and zero-valued α_i. Consider then the same presentation as before: $\hat{v}$ profiles for some small, representative α_i values, the $\max_y |\hat{v}|$ distributions against α_i, and the coefficients c_i against α_i. The prescribed model parameters are $\delta = 1$, $L = 10\delta$, $\mathrm{Re} = 1000$, $\hat{v}(\delta) = 1$, $\mathrm{d}\hat{v}(\delta)/\mathrm{d}y = 1$, $\hat{v}(L) = 3$, and now,

$\mathrm{d}\hat{v}(L)/\mathrm{d}y = 1/2$.

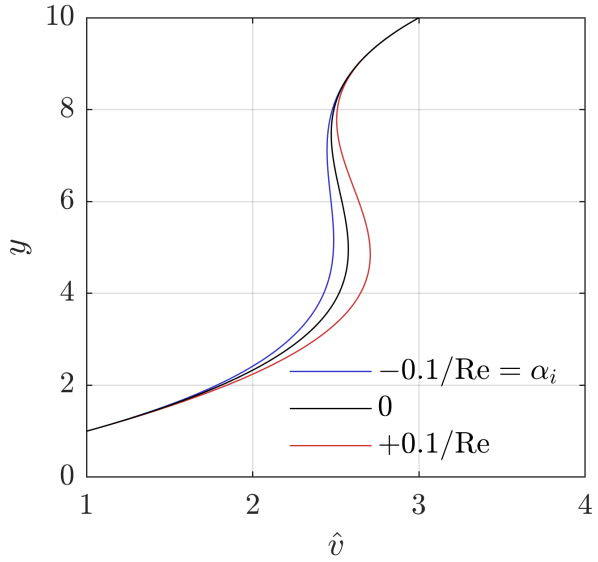

Figure 5.7: Wall-normal profiles of Orr-Sommerfeld $\hat{v}(y)$ with $(\omega, \beta) = (0, 0)$ for three selected values of α_i: $\pm 0.1/\mathrm{Re}$ and 0, where $\mathrm{Re} = 1000$. An inhomogeneous Neumann freestream boundary condition is prescribed as $\mathrm{d}\hat{v}(L)/\mathrm{d}y = 1/2$. Compare with the homogeneous Neumann case in Fig. 5.6.

The distributions of $\max_y |\hat{v}|$ and the complex coefficients c_i in Figs. 5.8 and 5.9 respectively are qualitatively similar to that of the homogeneous Neumann freestream boundary condition case (Figs. 5.3 and 5.5). Quantitatively, there is a very slight difference in some of the brief explosions of $|c_i|$, but the overall trend is indeed the same. Performing this simple experiment for other inhomogeneous values in the freestream (e.g., $\mathrm{d}\hat{v}(L)/\mathrm{d}y \in \{-2, 10\}$, etc.) reveals indeed that the coefficients c_i undergo sudden growth in magnitude at the same particular α_i locations, albeit the magnitudes $|c_i|$ vary slightly in their magnitude. These numerical experiments then suggest that this phenomenon is independent of the freestream Neumann boundary condition and is entirely coded into the coefficient matrix K. Specifically, the locations where the determinant of K crosses zero indicates the points of sudden growth in $|c_i|$ and consequently $|\hat{v}|$.

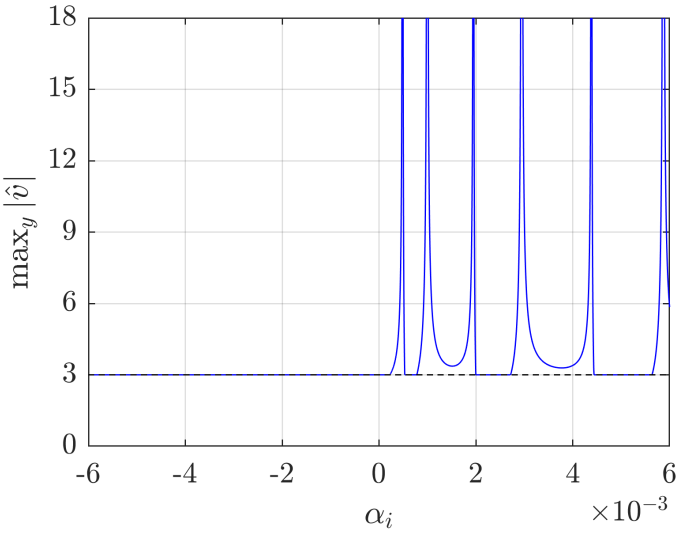

Figure 5.8: The y-maximum of $|\hat{v}|$ as α_i varies for example boundary conditions. The black, dashed line indicates the selected freestream Dirichlet boundary condition, $\hat{v}(L) = 3$. An inhomogeneous Neumann freestream boundary condition is prescribed as $\mathrm{d}\hat{v}(L)/\mathrm{d}y = 1/2$. Compare with the homogeneous Neumann case in Fig. 5.3.

5.5 Comparison of the freestream Orr-Sommerfeld to NPSE simulations

Before extrapolating trends from the behavior of $\tilde{\mathscr{D}}_{\mathrm{os}}$ to NPSE simulations, it is worth demonstrating a comparison between the two methods. Let us use a sample stationary-crossflow NPSE run for near-incompressible flow over a swept wing. The case description was originally printed in [119] and will be rehashed later in this dissertation as well. The relevant details of the NPSE simulation for this comparison are 1) a homogeneous Neumann freestream boundary condition is applied, and 2) $\alpha_{(0,0)} = 0$, as suggested by Hein [101]. The analytical freestream solution to the Orr-Sommerfeld equation with $(\omega, \beta) = (0, 0)$ is assigned the same values of the NPSE solution for the boundary conditions: $\hat{v}(\delta)$, $\mathrm{d}\hat{v}(\delta)/\mathrm{d}y$, and $\hat{v}(L)$. The value of δ is chosen appreciably above the laminar boundary-layer height—about 3 boundary-layer thicknesses. The slope $\mathrm{d}\hat{v}(\delta)/\mathrm{d}y$ is approximated from the NPSE solution by a first-order, nonuniform stencil. Given that the NPSE solution is slightly oscillatory from node to node in the freestream, an average is taken across the neighboring values for an appropriate representation of $\hat{v}(\delta)$ and $\mathrm{d}\hat{v}(\delta)/\mathrm{d}y$. Figure 5.10 shows

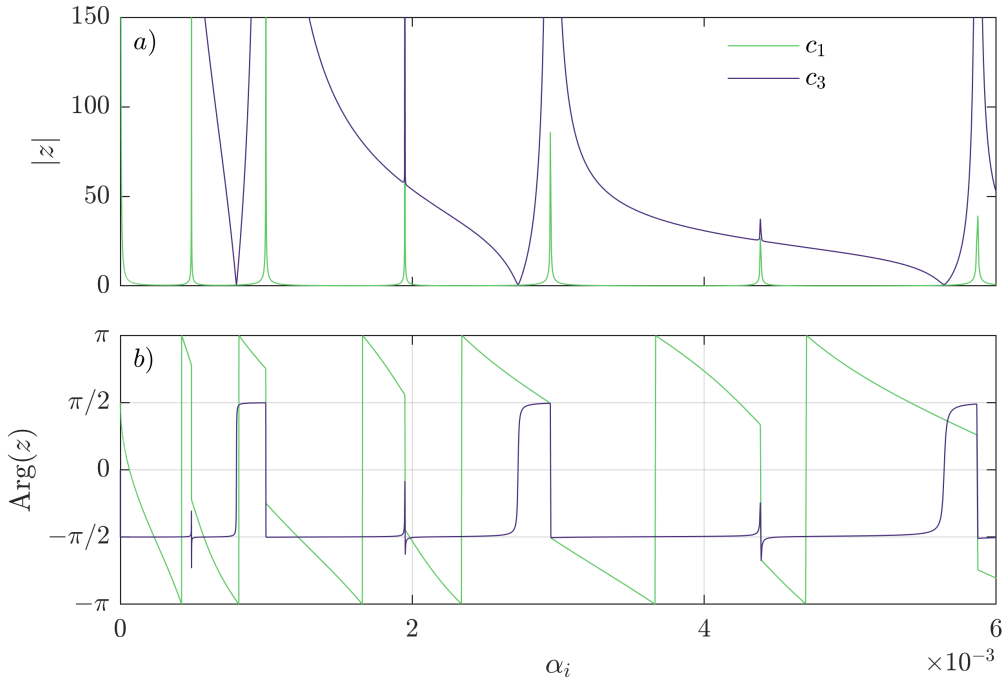

Figure 5.9: $a)$ Magnitudes and $b)$ complex arguments of coefficients c_1 and c_3 shown against $\alpha_i > 0$. An inhomogeneous Neumann freestream boundary condition is prescribed as $\mathrm{d}\hat{v}(L)/\mathrm{d}y = 1/2$. Compare with the homogeneous Neumann case in Fig. 5.5.

the comparison between the NPSE mean-flow distortion and the freestream solution to the Orr-Sommerfeld equation with $(\omega, \beta) = (0, 0)$.

There is a good agreement between the Orr-Sommerfeld (OS) and the NPSE solutions for the $(0, 0)$ disturbance, despite OS neglecting several relevant features. These include a) non-parallel terms, b) surface curvature, c) nonlinearities, and d) compressible effects. Admittedly, the nonlinearities at these x/c stations are quite small, as the amplitude of the MFD is only $10^{-5} < \max_y |u'_{(0,0)}|/Q_\infty < 10^{-3}$. In addition, the compressible effects are weak with a freestream Mach number of $\mathrm{M}_{Q_\infty} = 0.06$. Regardless, the overall trend of the freestream profile is qualitatively captured in the $\tilde{\mathscr{D}}_{\mathrm{os}}$ differential operator's dynamics with $\alpha_{(0,0)} = 0$. This suggests that the mean-flow distortion's behavior in the freestream may be mostly understood by considering the linear dynamics of the differential operator $\tilde{\mathscr{D}}_{\mathrm{os}}$. Let us now use this to assess Airiau's "cut-off" procedure, as originally proposed in 1994.

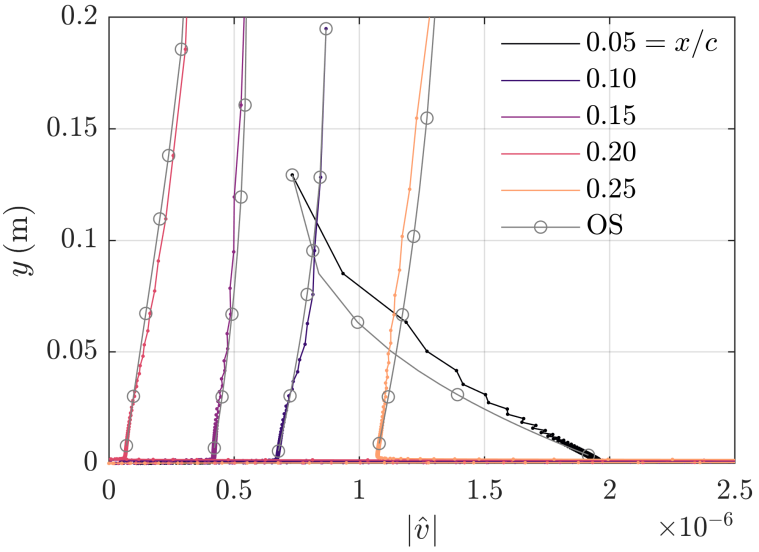

Figure 5.10: Comparison of $|\hat{v}|$ of the mean-flow distortion from NPSE to the freestream Orr-Sommerfeld analytical solution $\hat{v}$ for a sample near-incompressible, stationary-crossflow NPSE run with $\alpha_{(0,0)} = 0$. Colored lines indicate the NPSE MFD at various x/c stations and gray lines with circles indicate the Orr-Sommerfeld (OS) solution evaluated on the same physical y grid.

5.6 Reduction of domain height L

Previously, Airiau identified the source of the supposed numerical error as originating from the freestream behavior of the mean-flow distortion [24, §2.3.3]. As a remedy, Airiau proposed a "cut-off" procedure, truncating the wall-normal domain to about 2 boundary-layer thicknesses. As the dissertation of Airiau is written in French, a rough translation to English of the relevant section in §2.3.3 is given below:

> Initially, we were confronted with problems of explosion of numerical calculations; the results from the DNS (Joslin et al. [120, 27]) show that the longitudinal velocity fluctuation $\hat{u}_{(0,0)}$ is strictly zero outside the boundary layer. Somewhere, the numerical error, inevitable far from the wall, then plays a destabilizing role in the calculation, in particular on the component $\hat{u}_{(0,0)}$. To obtain suitable solutions, we have reduced the y-domain's definition to the neighborhood of the boundary layer ("cut-off"). Thus, the boundary conditions on the modes $(0, k)$, but especially for the mode $(0, 0)$, are

applied to the position $y = 2\ell$, where ℓ is the characteristic length which serves to make the space variables dimensionless and which is of the order of the physical height of the boundary layer. This process is radical and very effective since modes $(0, k)$ are generated which, quickly, behave like those obtained by other PSE calculations (Bertolotti, Chang), or by DNS calculations.

This section intends to address this procedure, investigating the Orr-Sommerfeld solution for $(\omega, \beta) = (0, 0)$ and its dynamics as L is decreased with all else constant, demonstrating similar trends are observed.

Consider the same model problem as before, but with $L = 2\delta$: $\delta = 1$, $\mathrm{Re} = 1000$, $\hat{v}(\delta) = 1$, $\mathrm{d}\hat{v}(\delta)/\mathrm{d}y = 1$, and $\hat{v}(L) = 3$. It is important to note for this problem, the relevant length is not directly L, but instead the freestream extent $L - \delta$. Again, vary α_i and compute the corresponding $\hat{v}$. The maximum in $|\hat{v}|$ is extracted for each α_i and is shown in Fig. 5.11. Notice that there are *no* points over the previously shown domain of $\alpha_i \in (0, 6 \times 10^{-3}]$ where $\max_y |\hat{v}|$ grows beyond the value of the freestream inhomogeneous Dirichlet condition. Only for a much larger value of $\alpha_i \approx 0.039$ does a large and sudden growth of $\max_y |\hat{v}|$ occur.

The extreme and sudden growth in $|\hat{v}|$ still remains associated to the determinant of the coefficient matrix K changing sign as it passes through zero, as shown in Fig. 5.12.

Figure 5.13 shows the magnitude and complex argument of the coefficients c_1 and c_3 for this case with $L = 2\delta$. Notice the same trend holds as before: for $\partial \det(K)/\partial\alpha_i < 0$ at this point of divergence near $\alpha_i \approx 0.039 = 39/\mathrm{Re}$, the growth of $|c_3|$ is extremely short in its α_i-extent.

From the above analysis, we may observe when reducing L with all else constant, the particular α_i values near zero vanish entirely that can cause an explosion of $|\hat{v}|$. Only at much larger, more stable values of $\alpha_i \sim O(10/\mathrm{Re})$ does the phenomenon return.

The trend observed in Airiau's "cut-off" procedure matches precisely the qualitative conclusion of this analysis based solely on the differential operator $\tilde{\mathscr{D}}_{\mathrm{os}}$ in the freestream. Hence, it may be fair to say that what Airiau has observed was not numerical error, but indeed truly a part of the system's freestream dynamics.

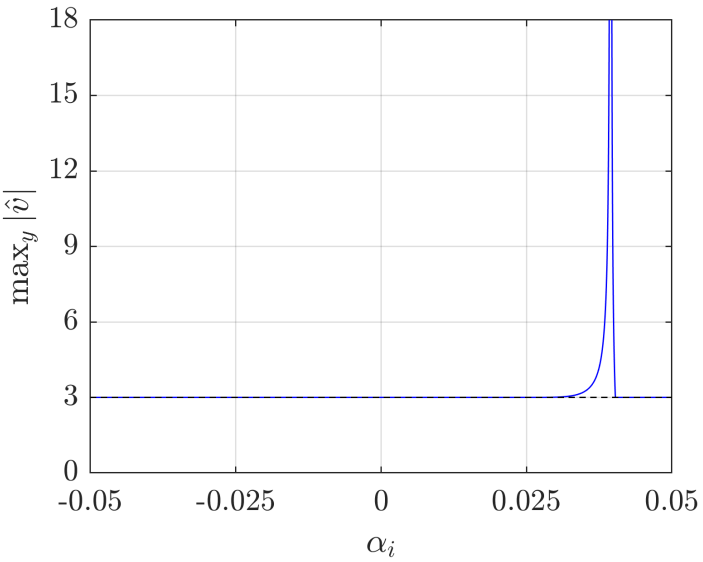

Figure 5.11: The y-maximum of $|\hat{v}|$ as α_i varies for example boundary conditions. The black, dashed line indicates the selected freestream Dirichlet boundary condition, $\hat{v}(L) = 3$. $L = 2\delta$ for this case. Compare to Fig. 5.3 for the $L = 10\delta$ distribution.

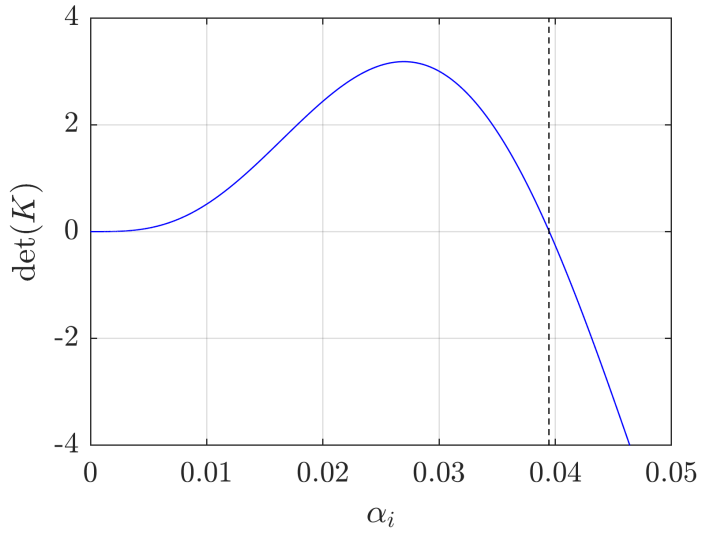

Figure 5.12: Determinant of coefficient matrix K against $\alpha_i > 0$. The dashed line indicates where $\det(K)$ crosses zero, which is associated with the extreme growth of $|\hat{v}|$ as shown in Fig. 5.11. K is defined in Eq. (5.7). $L = 2\delta$ for this case. Compare to Fig. 5.4 for the $L = 10\delta$ distribution.

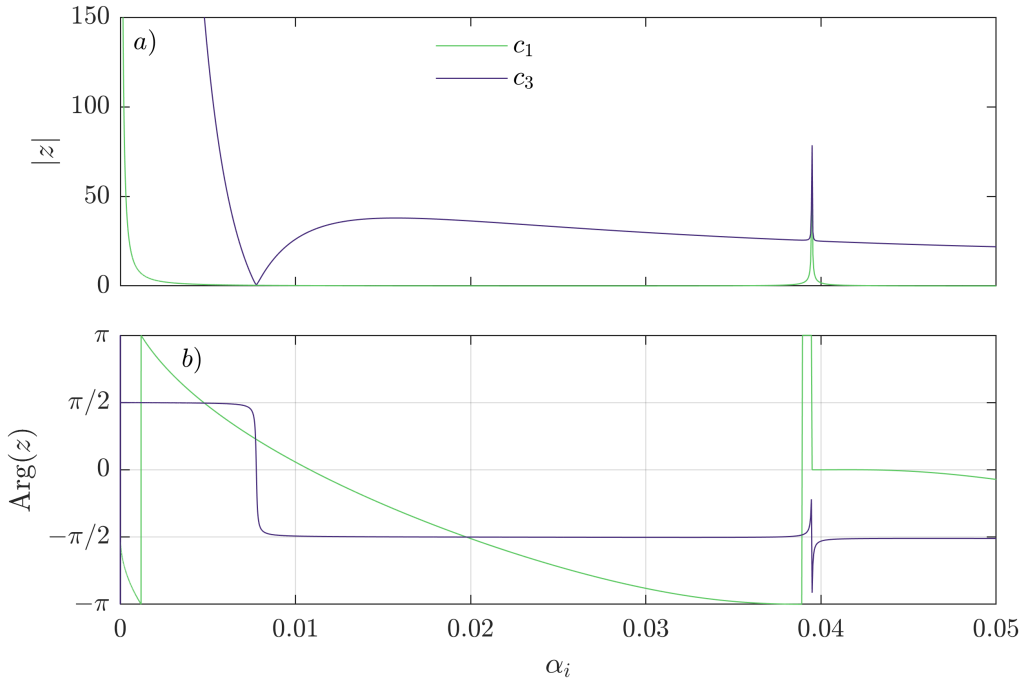

Figure 5.13: $a)$ Magnitudes and $b)$ complex arguments of coefficients c_1 and c_3 shown against $\alpha_i > 0$. $L = 2\delta$ for this case. Compare to Fig. 5.5 for the $L = 10\delta$ distribution.

5.7 Analysis of incompressible continuity

Recall the equation of mass continuity for an incompressible fluid is given as

$$\frac{\partial u}{\partial s} + \frac{\partial v}{\partial y} + \frac{\partial w}{\partial z} = 0 \tag{5.14}$$

Note that there are no nonlinearities in the incompressible context. That is, compressibility gives rise to nonlinearities in continuity via products between density and velocity fluctuations. Since the laminar base-flow is assumed to satisfy the corresponding divergence on $\vec{\overline{V}} = [\overline{u}, \overline{v}, \overline{w}]$, the disturbance equation may be written as

$$\frac{\partial u'}{\partial s} + \frac{\partial v'}{\partial y} + \frac{\partial w'}{\partial z} = 0 \tag{5.15}$$

With the mean-flow distortion as the disturbance of interest, suppose then $\beta = 0$. This causes

$\partial w'/\partial z$ to vanish. Substituting the PSE ansatz, the disturbance quantities are written directly in terms of the shape-function components. Since α is purely imaginary for the mean-flow distortion, $\mathrm{i}\alpha = -\alpha_i$. Then

$$-\alpha_i \hat{u} + \frac{\partial \hat{u}}{\partial s} + \frac{\partial \hat{v}}{\partial y} = 0 \tag{5.16}$$

Consider a point in the domain where $\partial \hat{v}/\partial y = 0$. Then continuity reduces to

$$\frac{\partial \hat{u}}{\partial s} = \alpha_i \hat{u} \tag{5.17}$$

A similar result to this has been mentioned before by Airiau [24, §2.3.3]. This equation can be integrated in space along the path where $\partial \hat{v}/\partial y = 0$. By numerical experiments comparing DNS to PSE, it is anticipated that a path of this nature exists within the boundary layer [27]. Additionally, from NPSE experimental validation of stationary crossflow at near-incompressible speeds, the mean-flow distortion's $\hat{v}$ does reach an extremum within the boundary layer [116]. Note that this integration presumes that $\hat{u}$ is nonzero. However, in the degenerate case where $\hat{u}$ is identically zero, by Eq. (5.17), $\partial \hat{u}/\partial s = 0$ directly. Upon integration, we have

$$\begin{aligned} \int \frac{\mathrm{d}\hat{u}}{\hat{u}} &= \int_{s_1}^{s} \alpha_i(\tilde{s})\,\mathrm{d}\tilde{s}, \\ \hat{u} &= C_1 \mathrm{e}^{\int_{s_1}^{s} \alpha_i(\tilde{s})\,\mathrm{d}\tilde{s}}, \\ \frac{\partial \hat{u}}{\partial s} &= C_1 \alpha_i\, \mathrm{e}^{\int_{s_1}^{s} \alpha_i(\tilde{s})\,\mathrm{d}\tilde{s}}, \end{aligned} \tag{5.18}$$

where C_1 is an arbitrary integration constant. Suppose $s - s_1 \equiv \Delta s$ is small enough such that α_i may be approximated as constant over the interval. Then using the Taylor series for the exponential function, we have

$$\begin{aligned} \mathrm{e}^{\int_{s_1}^{s} \alpha_i(\tilde{s})\,\mathrm{d}\tilde{s}} &\approx \mathrm{e}^{\alpha_i(s-s_1)}, \\ \implies \frac{\partial \hat{u}}{\partial s} &\approx C_1 \alpha_i \left(1 + \alpha_i(s-s_1) + \frac{(\alpha_i(s-s_1))^2}{2!} + \ldots\right), \\ &\approx C_1 \alpha_i, \qquad (\alpha_i(s-s_1) \ll 1) \end{aligned} \tag{5.19}$$

5.7.1 Proposed limiters on the mean-flow distortion's streamwise wavenumber in NPSE

In order for $\partial\hat{u}/\partial s$ to remain small by the PSE approximation, the product $C_1\alpha_i$ then cannot be large in the above Eq. (5.19).[2] Since the value of $C_1 = \hat{u}/\mathrm{e}^{\int_{s_1}^{s}\alpha_i(\tilde{s})\,\mathrm{d}\tilde{s}}$ is not known a priori, one must query the value of C_1 during an incompressible NPSE simulation for the mean-flow distortion. This must occur at a chosen height where where $\partial\hat{v}/\partial y \approx 0$. There are several choices for the local extremum: inside the boundary layer (provided it exists), or at the edge of the boundary layer. Inside the boundary layer appears to be a better choice than at the edge, as $\hat{u}$ still has an appreciable magnitude, which then makes C_1 far from zero. That is, going off of observations from both DNS and NPSE, the mean-flow distortion $\hat{u}$ component decays to zero in the freestream [27, 24, 121].

Recall that the usual length scale associated with ε_s for boundary-layer development is $\varepsilon_s \sim O(1/\mathrm{Re})$ [54]. This may be assumed to be appropriate for PSE analysis as well. Then if $|\alpha_i|$ is limited to stay smaller than $O(1/(|C_1|\mathrm{Re}))$, then $\partial\hat{u}/\partial s \sim O(1/\mathrm{Re})$ at these points where $\partial\hat{v}/\partial y = 0$. Note that this statement asserts that $\hat{u}$ is $O(1)$, so the shape-function must be normalized by its maximum magnitude when calculating C_1. That is,

$$C_1 = \frac{\hat{u}_{\mathrm{extr}\,\hat{v}}}{\max_y|\hat{u}|}\,\mathrm{e}^{\int_{s_1}^{s}-\alpha_i(\tilde{s})\,\mathrm{d}\tilde{s}} \tag{5.20}$$

where $\hat{u}_{\mathrm{extr}\,\hat{v}}$ is the value of the shape-function $\hat{u}$ at the extremum of $\hat{v}$ inside the boundary layer. If there are multiple extrema inside the boundary layer, any one may be selected—the author's choice is the one that maximizes $|C_1|$.

Since α_i is not a function of y, the existence of even one point in the domain that satisfies $\partial\hat{v}/\partial y = 0$ then demands this limitation that $|\alpha_i| < O(1/(|C_1|\mathrm{Re}))$. If one uses a homogeneous Neumann condition in the freestream, then this is clearly guaranteed. If one does not use this boundary condition however, using a compatibility condition such as y-momentum, then there may still exist a local wall-normal extremum in the profile $\hat{v}$ elsewhere. This suggests that regard-

[2] Notice in Airiau's quote at the beginning of this section, it is mentioned that the destabilizing nature of the system is observed in the $\hat{u}_{(0,0)}$ growth. The above analysis may support this observation.

less of the freestream boundary condition used, a limitation ought to be placed on the mean-flow distortion's α_i value in incompressible flows to stay consistent with the PSE approximation.

A limitation on α_i though only needs to be enforced if the "cut-off" procedure of Airiau does not work or is not applicable for the nonlinear simulation of interest. An example where truncating the domain near 2δ is physically dubious is the nonlinear saturation of a Görtler vortex and development downstream. In those problems, the upwelling of low-momentum fluid extends far beyond the laminar boundary-layer height, even exceeding 2δ. Hence an assignment of say, $L = 4\delta$ is worth attempting, but may be insufficient to quell the oscillatory, freestream nature of the differential operator $\tilde{\mathscr{D}}_{\text{os}}$ acting on $\hat{v}$.

If the computationalist does not or cannot reduce the domain height then to $O(2\delta)$ to stabilize the problem, as Airiau has proposed, then there are several different proposals to place a limitation on α_i for the mean-flow distortion:

1. Assign $\alpha_i = 0$ for all s, as suggested by Hein [101]. The assignment of $\alpha_i = 0$ is useful, as the parallel-flow, differential operator $\tilde{\mathscr{D}}_{\text{os}}$ reduces to polynomial general solutions which do not possess freestream oscillations in $\hat{v}$. However, this assignment may be too restrictive and physically inaccurate. All of the disturbance growth of the harmonic is placed now into the shape-function's s-derivative, $\partial\hat{q}_{(0,0)}/\partial s$, which is inherently limited by the PSE approximation.

2. Limit α_i as it varies in s with the following lower and upper bounds:

$$-\frac{a_L}{|C_1|\mathrm{Re}} < \alpha_i \leq 0 \tag{5.21}$$

   where $a_L > 0$ is some positive $O(1)$ constant to designate the lower bound of α_i with respect to the local Reynolds number, Re, based on the Blasius length scale. The integration constant C_1 is computed at runtime via Eq. (5.20) and can be updated during both the nonlinear- and α-iterations. When applying the $\Delta\alpha$ based on the PSE auxiliary condition for the mean-flow distortion, care must be taken since $-a_L/(|C_1|\mathrm{Re})$ now serves as a lower bound for

α. If $\Delta\alpha$ would cause α_i to be less than $-a_L/(|C_1|\mathrm{Re})$, then the update is overwritten to be zero. This happens all the same for the upper bound: if $\Delta\alpha$ would cause α_i to exceed zero, then the update is similarly overwritten to be zero.[3] This has an advantage over the $\alpha_i = 0$ assignment, allowing some exponential growth to be placed in the wave of the PSE ansatz. The drawback is the procedure's sensitivity to the numerical value for a_L as well as no exponential stabilization of the mean-flow distortion.

3. Limit α_i as it varies in s with the following lower and upper bounds:

$$-\frac{a_L}{|C_1|\mathrm{Re}} < \alpha_i < \frac{a_R}{|C_1|\mathrm{Re}} \tag{5.22}$$

where a_L and C_1 are the same as in the previous proposal. The positive $O(1)$ constant a_R is the analogous value of a_L for positive values of α_i. The advantage of this model is that exponential stabilization of the mean-flow distortion is permitted within its streamwise history. The drawback is the procedure's sensitivity to a_R and other potential oscillations present as a result from the Orr-Sommerfeld operator acting on $\hat{v}$ for stable $\alpha_i > 0$.

4. Limit α_i as it varies in s with the following lower and upper bounds:

$$-\frac{a_L}{|C_1|\mathrm{Re}} < \alpha_i < \min\left(\frac{a_R}{|C_1|\mathrm{Re}}, \frac{\alpha^*_{i_1}}{2}\right) \tag{5.23}$$

where a_L, a_R, and C_1 are the same as in the previous proposal. The selection of the positive $\alpha^*_{i_1}$ is more delicate, however. Recall the numerical oscillations from $\tilde{\mathscr{D}}_{\mathrm{os}}$ acting on $\hat{v}$ became worrisome for the sample problem as $\det(K)$ crossed zero: see Fig. 5.4. To avoid α_i becoming that positive to incur large oscillations in $\hat{v}$, the following scheme is proposed. An upper bound for α_i would be the half the value of the first positive root of $\det(K)$. This location is selected as a built-in 'safety factor' such that α_i doesn't get appreciably close to where $\det(K)$ crosses zero. The equation for $\det(K)$ can be written ahead of time through

[3] An alternative strategy is correcting (truncating) the update of $\Delta\alpha$ such that α_i would directly equal $-a_L/(|C_1|\mathrm{Re})$.

performing a symbolic Laplace expansion with a computer algebra code on the matrix K. In other words, numerical computation of the Laplace expansion is not required to compute $\det(K)$. Its first positive root $\alpha^*_{i_1}$ may be found at each α iteration (or even nonlinear iteration) during NPSE. Of course, the first positive root $\alpha^*_{i_1}$ only needs to be computed if α_i is positive or if $\Delta\alpha$ would make α_i positive. This model has the benefit over the previous one, allowing some exponential stabilization while avoiding oscillations spawned from the Orr-Sommerfeld operator in the freestream. The drawbacks are the additional computation of root finding at each desired iteration and the reliance on $\alpha^*_{i_1}/2$ being appreciably far away from $\alpha^*_{i_1}$. For some values of domain height L, $\alpha^*_{i_1}$ may be absurdly small. In these scenarios, it may be best to limit α_i to be strictly non-positive, as suggested in a previous limiter.

Both of the models with a_L, a_R, and $\alpha^*_{i_1}$ rely on these factors to additionally account for a) non-parallel, b) surface curvature, c) nonlinear, and d) compressible effects (if extended to a compressible formulation), as these have been neglected in the present analysis. Non-unity values for a_L and a_R also account for the truncation of the infinite Taylor series for the exponential function going from Eq. (5.17) to Eq. (5.19).

5.8 Extensions of present analysis

Analyzing the mean-flow distortion from its linear, incompressible, freestream operator is a start to making NPSE more robust in this speed regime for appreciable L. This analysis may be extended in several ways.

1. A disturbance with $(\omega, \beta) = (0, 0)$ in *compressible*, parallel, freestream flow could be considered, following the analysis of Li & Malik [108]. This ideally would supply a compressible form of the expression for C_1, which would be useful for high-subsonic/transonic flows.

2. A disturbance with $(\omega, \beta) = (0, 0)$ in incompressible, freestream flow with *nonzero* wall-normal velocity $\overline{v}$ could be considered. The $\overline{v}$ profile could be assumed to be linearly varying in the y direction. From boundary-layer asymptotics, the y-slope of $\overline{v}$ at δ would be

maintained for the freestream. That is to say, the nondimensional $\overline{v}$ may be written as

$$\overline{v}(y) = \overline{v}(\delta) + \frac{\partial \overline{v}(\delta)}{\partial y}(y - \delta), \quad \delta \leq y \leq L \tag{5.24}$$

This causes the governing equation to no longer have constant coefficients, complicating the general solution. Recall the non-parallel form of the Orr-Sommerfeld operator, from [117, §2.3.4]

$$\begin{aligned} \tilde{\mathscr{D}}_{\mathrm{os,\,np}} &\equiv (-\mathrm{i}\omega + \mathrm{i}\alpha\overline{u} + \overline{v}\frac{\mathrm{d}}{\mathrm{d}y} + \frac{\mathrm{d}\overline{v}}{\mathrm{d}y} + \mathrm{i}\beta\overline{w})\left(\frac{\mathrm{d}^2}{\mathrm{d}y^2} - \alpha^2 - \beta^2\right) + ... \\ &\quad - \mathrm{i}\alpha\frac{\mathrm{d}^2\overline{u}}{\mathrm{d}y^2} - \mathrm{i}\beta\frac{\mathrm{d}^2\overline{w}}{\mathrm{d}y^2} - \frac{1}{\mathrm{Re}}\left(\frac{\mathrm{d}^2}{\mathrm{d}y^2} - \alpha^2 - \beta^2\right)^2, \\ \tilde{\mathscr{D}}_{\mathrm{os,\,np}}\hat{v} &= 0 \end{aligned} \tag{5.25}$$

The same assumptions can be made from earlier. Set $\beta = \omega = 0$. Suppose the velocity profile $\overline{u}$ is constant in y, i.e., $\overline{u} = \overline{u}_\infty = 1$. Then the non-parallel Orr-Sommerfeld equation simplifies to

$$\left(\left(\mathrm{i}\alpha + \overline{v}\frac{\mathrm{d}}{\mathrm{d}y} + \frac{\mathrm{d}\overline{v}}{\mathrm{d}y}\right)\left(\frac{\mathrm{d}^2}{\mathrm{d}y^2} - \alpha^2\right) - \frac{1}{\mathrm{Re}}\left(\frac{\mathrm{d}^2}{\mathrm{d}y^2} - \alpha^2\right)^2\right)\hat{v} = 0 \tag{5.26}$$

which may be expressed in terms of parallel vs. non-parallel terms as:

$$\begin{aligned} &\underbrace{\hat{v}'''' + a\hat{v}'' + b\hat{v}}_{\text{parallel}} + \underbrace{\overline{v}\hat{v}''' + \frac{\mathrm{d}\overline{v}}{\mathrm{d}y}\hat{v}'' - \alpha^2\overline{v}\hat{v}' - \alpha^2\frac{\mathrm{d}\overline{v}}{\mathrm{d}y}\hat{v}}_{\text{non-parallel}} = 0, \\ &a \equiv -2\alpha^2 - \mathrm{i}\alpha\mathrm{Re}, \\ &b \equiv \alpha^4 + \mathrm{i}\alpha^3\mathrm{Re} \end{aligned} \tag{5.27}$$

Since $\overline{v}$ is linear in y and acts on odd-orders $\mathrm{d}/\mathrm{d}y$ and $\mathrm{d}^3/\mathrm{d}y^3$, the form of the differential equation in Eq. (5.27) resembles that of the Hermite differential equation, except extended to the fourth derivative. Recall the Hermite differential equation for a function $h = h(x)$ and

Hermite constant λ_{H} is written as

$$\frac{\mathrm{d}^2 h}{\mathrm{d}x^2} - 2x\frac{\mathrm{d}h}{\mathrm{d}x} + \lambda_{\mathrm{H}} h = 0 \tag{5.28}$$

which can be solved using the series method. General solutions take the form of the confluent hypergeometric function of the first kind and Hermite polynomials [122, 123]. This analysis would ideally provide a more physically inclusive value for $\alpha^*_{i_1}$ by examining the first root of the determinant of its coefficient matrix applied to the same boundary-value problem.

5.9 Maxima code used for this chapter

Since Maxima is not a common language within the aerospace community, the author would like to share a snippet of it. It can be quite readable when directly translating simple mathematical manipulations. Presented is a brief script used to generate the analytical expressions for c_i as well as the determinant of K.[4] Numerical calculations of $\det(K)$ matched against the analytical expression within machine error, which verifies the below implementation.

```
/* Orr-Sommerfeld in the freestream with (omega, beta) = (0,0) */
detout : true;

/*dvdyL : 0;*/ /* Uncomment for homogeneous Neumann boundary conditions in the freestream */

/* First consider the case with alpha nonzero */
dirichlet_delta : exp(delta*k2)*c1 + exp(-delta*k2)*c2 + exp(delta*k1)*c3 + exp(-delta*k1)*c4 =
    vdelta;
neumann_delta : k2*exp(delta*k2)*c1 - k2*exp(-delta*k2)*c2 + k1*exp(delta*k1)*c3 -
    k1*exp(-delta*k1)*c4 = dvdydelta;
neumann_fs : k2*exp(L*k2)*c1 - k2*exp(-L*k2)*c2 + k1*exp(L*k1)*c3 - k1*exp(-L*k1)*c4 = dvdyL;
dirichlet_fs : exp(L*k2)*c1 + exp(-L*k2)*c2 + exp(L*k1)*c3 + exp(-L*k1)*c4 = vL;
eqns_alpha_nz : [dirichlet_delta, neumann_delta, neumann_fs, dirichlet_fs];

soln_alpha_nz : linsolve(eqns_alpha_nz, [c1, c2, c3, c4]);

soln_alpha_nz : factor(soln_alpha_nz);
```

[4] The Maxima version used to execute this script is 5.42.

```
disp("For alpha nonzero:");
disp(string(soln_alpha_nz[1]));
disp(string(soln_alpha_nz[2]));
disp(string(soln_alpha_nz[3]));
disp(string(soln_alpha_nz[4]));

disp("And its determinant:");
K : matrix( [exp(delta*k2), exp(-delta*k2), exp(delta*k1), exp(-delta*k1)],
[k2*exp(delta*k2), -k2*exp(-delta*k2), k1*exp(delta*k1), -k1*exp(-delta*k1)],
[k2*exp(L*k2), -k2*exp(-L*k2), k1*exp(L*k1), -k1*exp(-L*k1)],
[exp(L*k2), exp(-L*k2), exp(L*k1), exp(-L*k1)]);
detK : factor(determinant(K));
disp(string(detK));

/* Then consider when alpha = 0 */
dirichlet_delta : c3*delta^3 + c2*delta^2 + c1*delta + c0 = vdelta;
neumann_delta : 3*c3*delta^2 + 2*c2*delta + c1 = dvdydelta;
neumann_fs : 3*c3*L^2 + 2*c2*L + c1 = dvdyL;
dirichlet_fs : c3*L^3 + c2*L^2 + c1*L + c0 = vL;
eqns_a0 : [dirichlet_delta, neumann_delta, neumann_fs, dirichlet_fs];

soln_a0 : linsolve(eqns_a0, [c0, c1, c2, c3]);

soln_a0 : factor(soln_a0);

disp("For zero-valued alpha:");
disp(string(soln_a0[1]));
disp(string(soln_a0[2]));
disp(string(soln_a0[3]));
disp(string(soln_a0[4]));
```

This concludes the present analysis of the mean-flow distortion Fourier mode. The next chapter will now apply these stability theories, both linear and nonlinear, to a slotted, natural-laminar-flow wing.

6. X207.LS SLOTTED, NATURAL-LAMINAR-FLOW AIRFOIL[1]

For creating more energy-efficient aircraft, this work focuses on analyzing the external flow over a wing as part of a NASA University Leadership Initiative (ULI). The aim of the effort is to design an ultra-efficient airframe for next-generation aircraft. Led by The University of Tennessee, Knoxville (UTK), several universities across the U.S. paired with industry seek to accomplish this goal together with A&M.

Air flow over subsonic aircraft has the following usual contributions to drag: skin-friction, lift-induced, interference, and wave [124]. Out of these, the primary drag source is skin friction with nominally 50% for transport aircraft [125]. Note that for a laminar boundary layer, the skin friction can be as much as 90% less than that of a turbulent boundary layer of the same Reynolds number [125]. Additionally, wings consist mostly of skin-friction drag and they contribute about $1/3$ of the total drag of a transport aircraft [126]. From these facts together, it is clear that designing a wing that experiences a laminar boundary layer rather than a turbulent one can have a significant impact on decreasing an aircraft's drag and, consequently, on its energy efficiency.

Laminar flow over swept wings may be obtained through either passive or active methods, referred collectively as Laminar Flow Control (LFC). Work in this chapter and the next will focus on passive methods, namely, through the design of the airfoil shape itself, known as Natural-Laminar-Flow airfoil design, or NLF. This approach creates favorable pressure gradients over the majority of the wing, which tend to stabilize the growth of Tollmien-Schlichting waves. However, since the wing is swept, the three-dimensionality of the boundary layer can trigger the crossflow instability. And with crossflow destabilized by the favorable gradients of NLF, a crossflow-induced transition has the possibility of negating the benefits of the NLF design.

[1]Portions of this chapter are reprinted with permission from two conference articles. The first of which is "Computational Stability Analysis of a Variably Swept, Slotted Natural-Laminar-Flow Airfoil" by Ethan S. Beyak, Koen J. Groot, and Helen L. Reed in AIAA 2021-0946. Copyright 2021 by Ethan S. Beyak, Koen J. Groot, and Helen L. Reed. The second conference article is "Nonlinear Boundary-Layer Stability Analysis of a Swept, Natural-Laminar-Flow Airfoil" by Ethan S. Beyak, Koen J. Groot, Jeppesen G. Feliciano, Jay M. Patel, Andrew K. Riha, James G. Coder, and Helen L. Reed. Copyright 2022 by Ethan S. Beyak, Koen J. Groot, Jeppesen G. Feliciano, Jay M. Patel, Andrew K. Riha, James G. Coder, and Helen L. Reed.

As part of the ULI efforts to design an ultra-efficient wing, the team has proposed not just an NLF airfoil, but a slotted, natural-laminar-flow (SNLF) airfoil known as the S207. The slot allows increasing the extent of the portion of the chord subject to a favorable pressure gradient with respect to a single-element-airfoil configuration, while maintaining a gradual pressure recovery to the freestream value over the surface.

Immediately designing an appropriate SNLF for the transonic configuration space is nearly intractable, and as such, requires preliminary steps in the design. One preliminary step is designing a single-element, NLF airfoil for the transonic regime. After several iterations, Dan Somers created the so-called X207.o, on which the author performed linear stability analysis previously [96, 97]. Another preliminary step involves increasing the confidence in these computational methods through experimental validation. To accomplish this, after the SNLF S207 was designed, an analogous SNLF known as the X207.LS was designed by Dr. James G. Coder to achieve similar pressure gradients at incompressible speeds as experienced in the Klebanoff-Saric Wind Tunnel (KSWT) at Texas A&M. Experimentalists Jeppesen Feliciano and Dr. Edward B. White then measured boundary-layer disturbance characteristics, providing an excellent test bed to validate the computations [127].

This present analysis will focus on one part of the ULI's scope: a wind-tunnel model of the X207.LS. Linear dynamics will first be assessed for a wide range of geometric configurations to inform the experimentalists the relevant ranges of strong linear amplification. Then, a comparison is made between nonlinear simulation and experimental measurements for the development and saturation of stationary crossflow vortices for a highly favorable pressure gradient case on the X207.LS.

6.1 Laminar base flow

To study the stability of the boundary layer over a swept wing, several preliminary steps have to be taken; the most prominent being the highly accurate computation of the laminar base flow. Different approaches can be considered in order to generate representations of the laminar base flow up to increasing levels of fidelity. Going from the highest to lowest fidelity, one can make use

of several options to generate the laminar base flow: a) use a Navier-Stokes solver to model the flow over the model in the KSWT as accurately as possible (i.e., accounting for the wind-tunnel walls' effect on the inviscid flow); b) use the experimentally measured pressure coefficient in a boundary-layer solver; c) use the designed pressure coefficient from the inviscid code, MSES, in a boundary-layer solver [57]. In this dissertation, calculations are performed with the third methodology, i.e., assuming the designed pressure coefficient and importing it into a boundary-layer solver. Following the computation of the basic state, stability analysis can be performed with the in-house stability code, EPIC [47, 48, 49, 50].

To calculate the boundary-layer solutions used over the X207.LS in this work, the spectrally accurate boundary-layer solver DEKAF is used [58, 96, 97]. In what follows, the conditions, the DEKAF boundary-layer base flow, the measured flow in the KSWT, and the nonlinear stability analysis will be discussed.

6.1.1 Conditions

In MSES, the freestream Mach number based on the resultant velocity, $\mathrm{M}_{\overline{Q}_\infty} = \overline{Q}_\infty/\overline{a}_\infty$, is 0.06 to closely match KSWT conditions [127]. The freestream Reynolds number based on resultant velocity and chord reference length c, $\mathrm{Re}_c^{\overline{Q}_\infty} = c\overline{Q}_\infty/\overline{\nu}_\infty$, is 1.0×10^6. The freestream temperature and pressure in the wind tunnel are selected from data of a hot summer day in College Station: $29.60°$C and 761.85 torr (101.57 kPa), respectively. The thermophysical properties of air at these conditions are described by $R_g = 291.171\ \mathrm{J/(kg\,K)}$, and the ratio of specific heats, $\gamma = 1.4$.[2] The reference length in the leading-edge-normal direction x is selected as $c = 30.15$ inches. The Prandtl number is selected to be $\mathrm{Pr} = 0.72$. The constants for Sutherland's law are selected as $\mu_{\mathrm{ref}} = 1.716 \times 10^{-5}\,\mathrm{kg/(m\,s)}$, $T_{\mathrm{ref}} = 273$ K, and $S_\mu = 111$ K.

This section will consider multiple sweep angles: $\Lambda \in \{0°,\ 25°,\ 30°,\ 35°\}$, as well as multiple

[2] This value of R_g is slightly non-standard, but is consistent from otherwise overdefining the thermophysical system. With the Mach number M_{Q_∞}, Reynolds number $\mathrm{Re}_c^{Q_\infty}$, freestream pressure p_∞, temperature T_∞, dynamic viscosity μ_∞, chord c, and ratio of specific heats γ all defined, the specific gas constant R_g is constrained to be

$$R_g = \frac{\left(cp_\infty \mathrm{M}_{Q_\infty}/(\mu_\infty \mathrm{Re}_c^{Q_\infty})\right)^2}{\gamma T_\infty} \tag{6.1}$$

angles of attack: $\alpha \in \{-5.5^\circ, -2.25^\circ, 0^\circ, 2.25^\circ\}$. Following the nomenclature of [96, 97], the prescribed sweep angle and angle of attack are defined by Eq. (6.2).

$$\Lambda = \Lambda^{\overline{w}_\infty}_{\sqrt{\overline{u}^2_\infty + \overline{v}^2_\infty}} \overset{\text{(a)}}{\equiv} \arctan \frac{\overline{w}_\infty}{\sqrt{\overline{u}^2_\infty + \overline{v}^2_\infty}} \qquad \text{and} \qquad \alpha = \alpha^{\overline{v}_\infty}_{\overline{u}_\infty} \overset{\text{(b)}}{\equiv} \arctan \frac{\overline{v}_\infty}{\overline{u}_\infty}. \tag{6.2}$$

Here, $\overline{u}_\infty$ and $\overline{w}_\infty$ denote the leading-edge-orthogonal and -parallel freestream velocity components. The corresponding spatial coordinates are x and z. The freestream velocity component $\overline{v}_\infty$ points in the direction orthogonal to the xz-plane, which is denoted by Y_c. These definitions of sweep and pitch indicate that, colloquially, sweep is applied first, then pitch is applied (about $c/4$). Coordinate systems will be elaborated on extensively in §6.3.1.

MSES computes the pressure coefficient by solving the inviscid Euler equations and converges them to essentially machine zero. The streamwise resolution selected is $N_s = 305$ on the fore element and $N_s = 197$ on the aft element for a total of $N_s = 502$.

The output of MSES is a two-dimensional, inviscid pressure coefficient, defined as:

$$C_p^{\overline{u}_\infty \overline{v}_\infty} \equiv \frac{\overline{p}_w - \overline{p}_\infty}{\frac{1}{2}\overline{\rho}_\infty(\overline{u}^2_\infty + \overline{v}^2_\infty)} \tag{6.3}$$

As the wing is swept in the KSWT, the Reynolds number based on the resultant is constant: $\mathrm{Re}_c^{\overline{Q}_\infty} = 1.0 \times 10^6$. However, the provided MSES pressure coefficients for the various angles of attack suppose a constant *semi-resultant* freestream Mach number of $\mathrm{M}_{\overline{u}_\infty \overline{v}_\infty} = 0.06$. These are then corrected to the appropriate resultant velocity using Prandtl-Glauert relations [128].

Using the definition of sweep, $\overline{Q}_\infty \cos\Lambda = \sqrt{\overline{u}^2_\infty + \overline{v}^2_\infty}$. We may then relate the semi-resultant based nondimensional numbers to that of the resultant, as outlined in Fig. 16 of [96].

$$\mathrm{M}_{\overline{u}_\infty \overline{v}_\infty} = \frac{\sqrt{\overline{u}^2_\infty + \overline{v}^2_\infty}}{a_\infty} = \frac{\overline{Q}_\infty \cos\Lambda}{a_\infty} = \mathrm{M}_{\overline{Q}_\infty} \cos\Lambda \tag{6.4a}$$

$$\mathrm{Re}_c^{\overline{Q}_\infty} = \frac{\overline{Q}_\infty c}{\overline{\nu}_\infty} = \frac{\sqrt{\overline{u}^2_\infty + \overline{v}^2_\infty} c}{\overline{\nu}_\infty \cos\Lambda} = \frac{\mathrm{Re}_c^{\overline{u}_\infty \overline{v}_\infty}}{\cos\Lambda} \tag{6.4b}$$

Since MSES is a two-dimensional inviscid solver, the Reynolds number specified internally is

$\mathrm{Re}_c^{\overline{u}_\infty \overline{v}_\infty} = \mathrm{Re}_c^{\overline{Q}_\infty} \cos\Lambda$, which clearly accounts for sweep Λ.

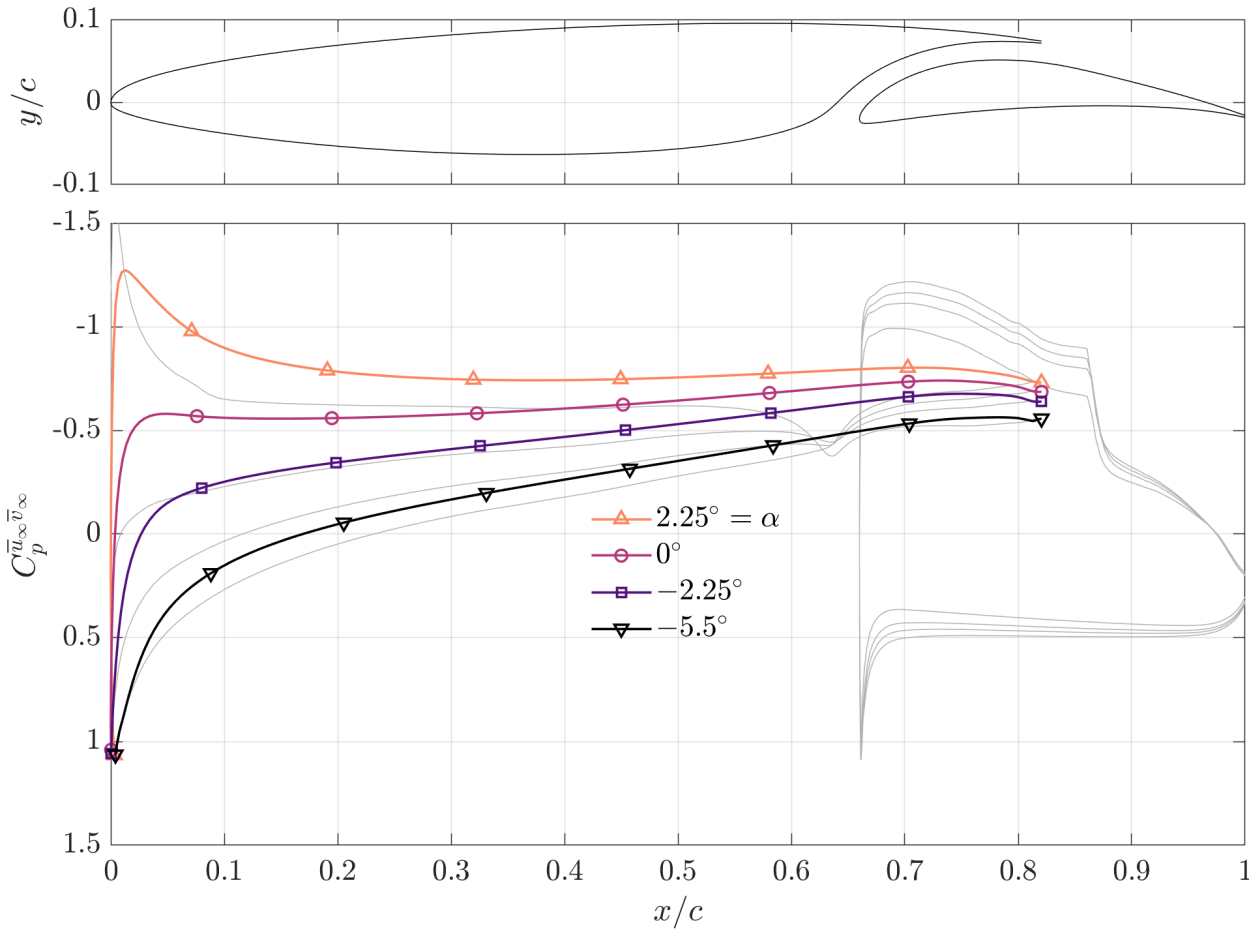

Figure 6.1: Airfoil cross-section and pressure coefficient as defined by (6.3) of the X207.LS for various angles of attack α at $\Lambda = 0°$, calculated with MSES. The thick, colored curves correspond to that of the bottom side of the fore element for the varying α, while the gray curves correspond to that of the top side of the fore element and the aft element. The division between top and bottom is chosen to be the attachment line, indicated with a marker at $C_p^{\overline{u}_\infty \overline{v}_\infty} \approx 1$. Reprinted from [129].

The X207.LS cross-section and resulting pressure coefficients from inviscid code MSES are given for the various angles of attack in Fig. 6.1. The thick, colored curves correspond to that of the bottom side of the fore element for varying α, while the gray curves correspond to that of the top side of the fore element and the aft element. The division between top and bottom is chosen to be the attachment line, indicated with a marker at $C_p^{\overline{u}_\infty \overline{v}_\infty} \approx 1$. The highly favorable pressure gradient

case of $\alpha = -5.5^\circ$ will likely greatly destabilize the crossflow instability mechanism at high sweep and stabilize the growth of Tollmien-Schlichting waves. At the other extremum, the angle of attack $\alpha = 2.25^\circ$ configuration undergoes a significant pressure gradient reversal. Downstream of the stagnation point, an extremely favorable gradient is present—a typical characteristic of NLF or supercritical airfoils. This is subsequently followed by an adverse gradient downstream of $x/c = 0.02$, decaying to a zero-pressure gradient near mid-chord, and ultimately returning to a slight favorable gradient at the aft end.

The inviscid pressure coefficient from MSES at $\alpha = -5.5^\circ$ is given in Fig. 6.2 and is compared against the measured results of experiment. The black line indicates the MSES result, with red/blue lines indicating the inboard/outboard pressure tap measurements, respectively. Uncertainty bounds are given in dash-dotted lines. The inboard and outboard locations are 30 inches apart from each other along the leading-edge-parallel direction, z.[3] For the majority of the chord, there is good agreement, especially with that of the outboard taps. This lends credence to the experimental setup and shows that the angle of attack α is close to commensurate between the inviscid, spanwise-infinite simulation and experiment [127]. The pressure measurements also indicate the very weak spanwise pressure gradient. The fact that the pressure at the outboard ports is slightly lower than that at the inboard ones could be explained through effective blockage. The flow at the outboard station experiences a slightly smaller cross-section, hence it experiences greater acceleration than the inboard section and this induces the slightly lower pressure. There is a mild discrepancy between MSES simulation and experiment from $x/c = [0.05,\ 0.15]$ whose origin is currently unknown.

[3]It is worth quantifying the experimental spanwise pressure gradient for this case and comparing it to the streamwise pressure gradient. Consider then the pressure tap location $x/c = 0.24$, near the first location of hot-wire boundary-layer scans at 25%. The outboard pressure coefficient is $C_p^{\text{out}} = -0.08933$ while the inboard is $C_p^{\text{in}} = -0.05514$. The distance between the pressure ports is 30 inches along the leading-edge-parallel z. A discrete difference then can be computed across this span for $(C_p^{\text{in}} - C_p^{\text{out}})/\Delta(z/c)$ for an approximation to the local spanwise pressure gradient. Since the streamwise resolution of the pressure ports is small, a streamwise derivative approximation is relatively coarse. Then, to compute $\Delta C_p/\Delta(x/c)$, a first-order difference is applied to the MSES solution near $x/c = 0.24$ for the local streamwise pressure gradient. The streamwise pressure gradient is nearly 36 times that of the spanwise gradient magnitude, and from Fig. 6.2, appears to be similar over a large extent of the chord.

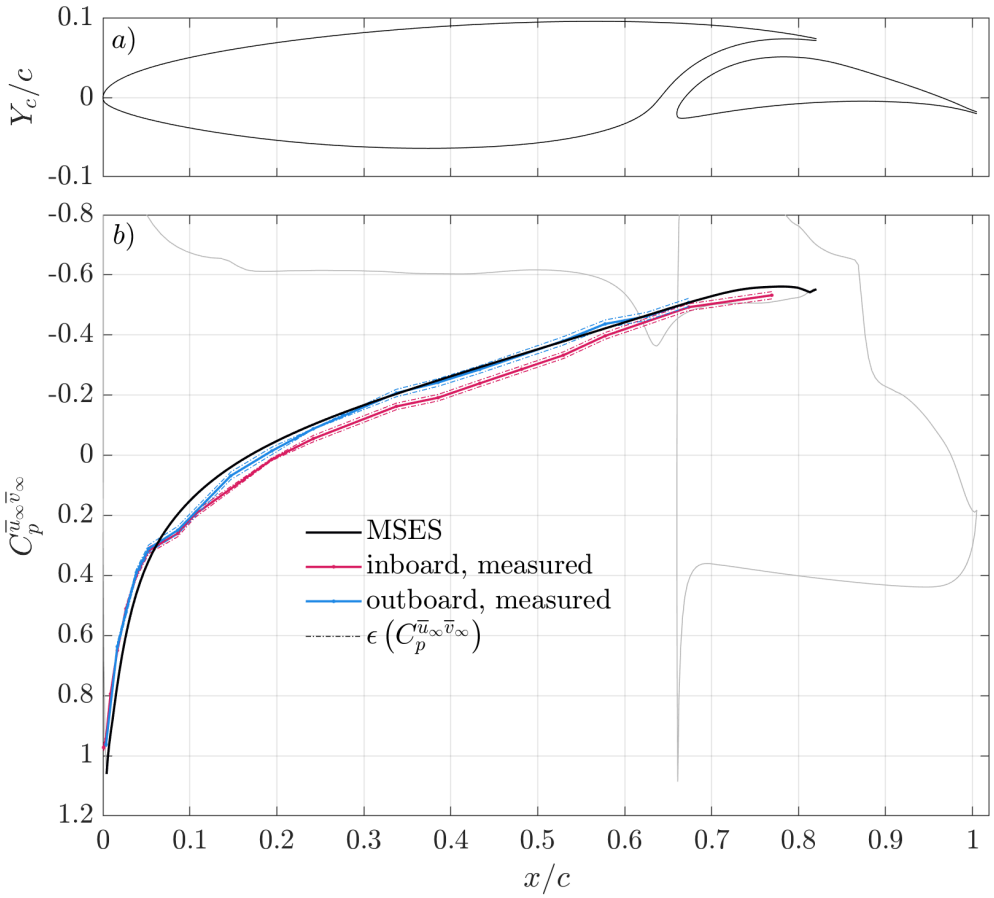

Figure 6.2: $a)$ Airfoil cross-section and $b)$ pressure x/c coefficient $C_p^{\overline{u}_\infty \overline{v}_\infty}$ as defined by Eq. (6.3) of the X207.LS for angle of attack $\alpha = -5.5°$. The black line corresponds to MSES results for $\Lambda = 0°$. The red and blue lines refer to the inboard and outboard experimental measurements by Feliciano, respectively. The dash-dotted lines indicate the uncertainty from the measured pressure distributions, $\epsilon(C_p^{\overline{u}_\infty \overline{v}_\infty})$. The gray curves correspond to MSES results for sections of the wing beyond the scope of present validation—that of the bottom side of the fore element and the aft element. The division between the top and bottom sides is chosen to be the attachment line near $C_p^{\overline{u}_\infty \overline{v}_\infty} \approx 1$. Reprinted from [119].

6.1.2 Solution profiles

Generating the viscous boundary layer first begins with the inviscid pressure coefficient $C_p^{\overline{u}_\infty \overline{v}_\infty}$. Edge conditions are constructed that satisfy isentropic relations, which serve as boundary conditions for DEKAF. See section [96, §III.B] for an in-depth discussion for this procedure. With the boundary conditions established, DEKAF is used to produce a laminar boundary layer. For more details, see Beyak et al. [129].

The boundary-layer solution is computed with $N_\xi = 2000$ nodes for the ξ domain and $N_\eta = 90$ nodes for the η domain. These resolutions have previously been demonstrated to yield fully converged results for the X207.LS [129]. Crossflow velocity profiles are shown for several x/c stations of interest in Fig. 6.3. Crossflow velocity $\overline{w}_s$ is computed as

$$\begin{aligned} \overline{u}_s &= \overline{u}\cos(-\psi_s) - \overline{w}\sin(-\psi_s), \\ \overline{w}_s &= \overline{u}\sin(-\psi_s) + \overline{w}\cos(-\psi_s), \\ \psi_s &= \arctan\frac{\overline{w}_{\delta_{99}}}{\overline{u}_{\delta_{99}}} \end{aligned} \tag{6.5}$$

In other words, $\overline{u}_s$ and $\overline{w}_s$ indicate the velocity components that are parallel/orthogonal to the local inviscid streamline, respectively. The subscript δ_{99} indicates the value was selected at a GICM-interpolated height for δ_{99}. That is, $\overline{u}_{\delta_{99}}/\overline{u}_e = 0.99$. Briefly, GICM interpolation iteratively and carefully inverts the three mappings used in DEKAF to transform from the computational domain to the physical domain. These mappings are a) Illingworth, b) Chebyshev, and c) Malik. For details on machine-accurate GICM interpolation, see Groot et al. [58].

Various boundary-layer properties are shown in Fig. 6.4. These properties include the pressure gradient (Hartree) parameter, β_H; the surface streamwise curvature of the airfoil $1/R$ nondimensionalized by c; and the boundary-layer thickness based on the 99% contour of $\overline{u}$, δ_{99} (in mm).[4] Note that the slight oscillations in β_H from $40\% - 70\%\, x/c$ ultimately stem from the coarse sampling of airfoil coordinates used to generate the MSES solution. A previous study by the author and colleagues analyzed these oscillations' effect on stationary crossflow for a transonic swept wing, the X207.o, and found no macroscopic change in the resulting N-factor distributions: see Fig. 12 in [96]. These oscillations can then be assumed to be innocuous. By convention, $R > 0$ implies convex surface curvature, $R \to \infty$ flat, and $R < 0$ concave surface curvature.

Recall that from a variety of computations in literature, it has been shown that the shape-factor H of the boundary layer corresponds very well to the critical Reynolds number based on

[4]The quantity δ_{99} is computed through GICM-interpolation from the DEKAF solution. To be pedantic, it is not precisely commensurate with the experimental measurements of the boundary-layer thickness, as the hot-wire orientation in the KSWT is not in-line with $\overline{u}$—to be discussed later in this chapter.

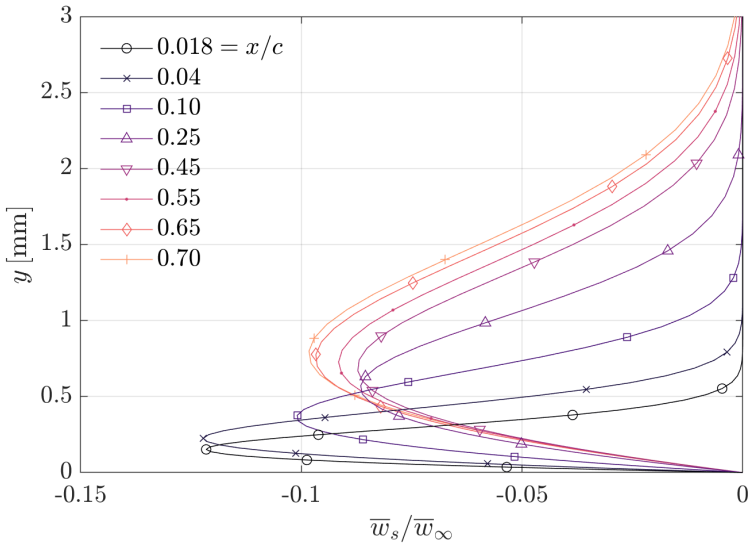

Figure 6.3: Crossflow velocity $\overline{w}_s/\overline{w}_\infty$ profiles of the laminar boundary layer over the top side of the X207.LS's fore element at $\alpha = -5.5°$ and $\Lambda = 35°$. Various profiles are shown for distinct x/c locations disambiguated through line colors and markers. For this case, $\overline{w}_\infty = 12.089\,\mathrm{m/s}$. Reprinted from [119].

displacement thickness, $\mathrm{Re}^{\overline{Q}_\infty}_{\delta^*,\mathrm{crit}}$. This correlation is built upon self-similar profiles by Obremski et al. [130], non-self-similar profiles, Falkner-Skan wedges, flat-plate suction, blowing stability computations of Tsou and Sparrow [131], and wedge flows with hot walls and variable viscosity [132], all assembled by White [54, Fig. 5-12]. This may be used as an initial engineering estimate for which configurations of the X207.LS at $\Lambda = 0°$ will experience unstable Tollmien-Schlichting instability. Additionally, this is useful to consider for the present configuration since it provides a qualitative verification of EPIC. Near-incompressible TS hadn't been computed with the code until the present X207.LS application. Figure 6.5 recreates Fig. 5-12 of White in the context of the X207.LS boundary layers at $\Lambda = 0°$ for the various angles of attack [54]. In Eq. (6.6) below, H is defined through

$$\delta_1^* = \int_0^\infty \left(1 - \frac{\overline{\rho}\,\overline{u}}{\overline{\rho}_e \overline{u}_e}\right) \mathrm{d}y, \quad \Theta = \int_0^\infty \frac{\overline{\rho}\,\overline{u}}{\overline{\rho}_e \overline{u}_e}\left(1 - \frac{\overline{u}}{\overline{u}_e}\right) \mathrm{d}y, \quad \mathrm{H} = \delta_1^*/\Theta \tag{6.6}$$

where the integration is spectrally accurate and is consistent with the Chebyshev discretization of

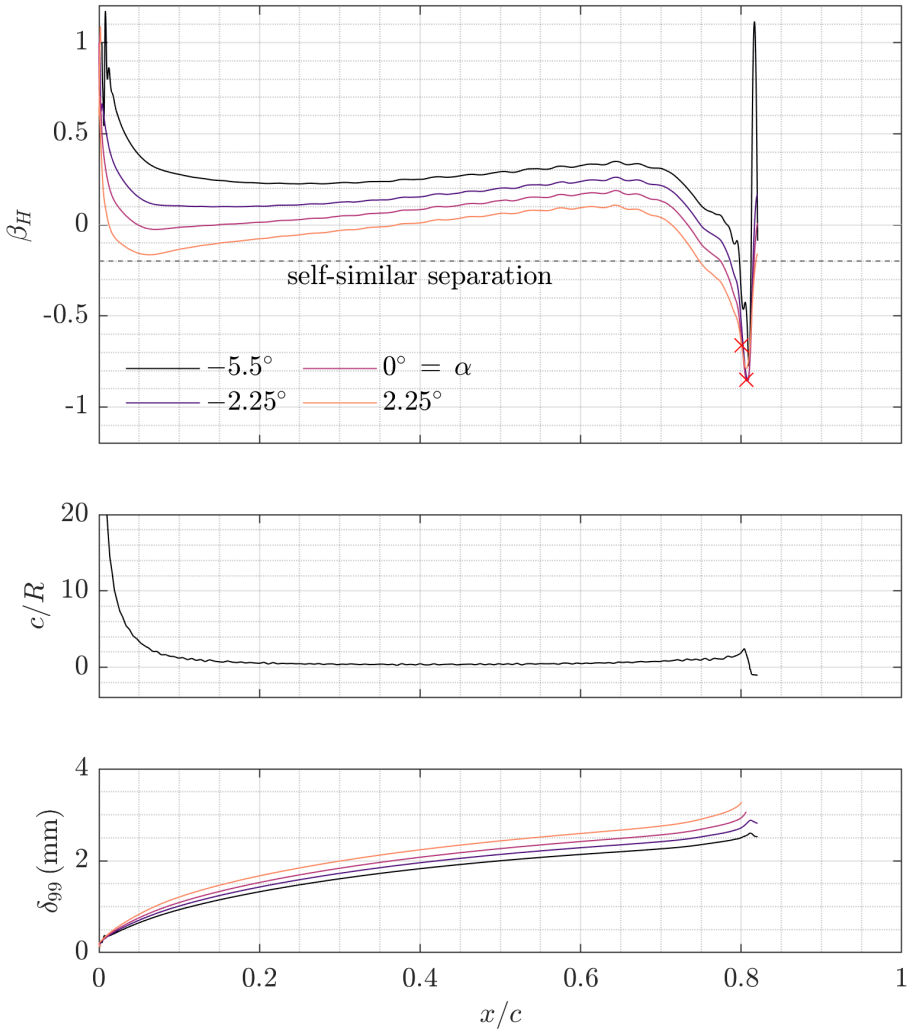

Figure 6.4: Boundary-layer properties versus x/c for the top side of the X207.LS at $\Lambda = 0°$ for various angles of attack. For the top β_H panel, the incompressible self-similar separation value $\beta_H = -0.198838$ is shown for reference. The $\times$ markers indicate the station at which laminar separation is reached. Streamwise radius of curvature is given by R in the middle panel. Reprinted from [129].

the DEKAF solution: see Appendix A of Groot et al. for details [58]. This figure demonstrates through engineering correlation that the $\alpha = 2.25°$ case is expected to experience significant TS growth over the chord due to the adverse gradient, while the $\alpha = 0°$ case is expected to exhibit only mild TS growth over the chord with its near-zero pressure gradient. The boundary layers of

the other angles of attack $\alpha \in \{-5.5°, -2.25°\}$ are within the stable portion of the correlation until $x/c \approx 0.8$, so consequently TS is not expected to be unstable until the vicinity of the trailing edge. This correlation is affirmed through the computed stability results presented later in this chapter: see Fig. 6.6.

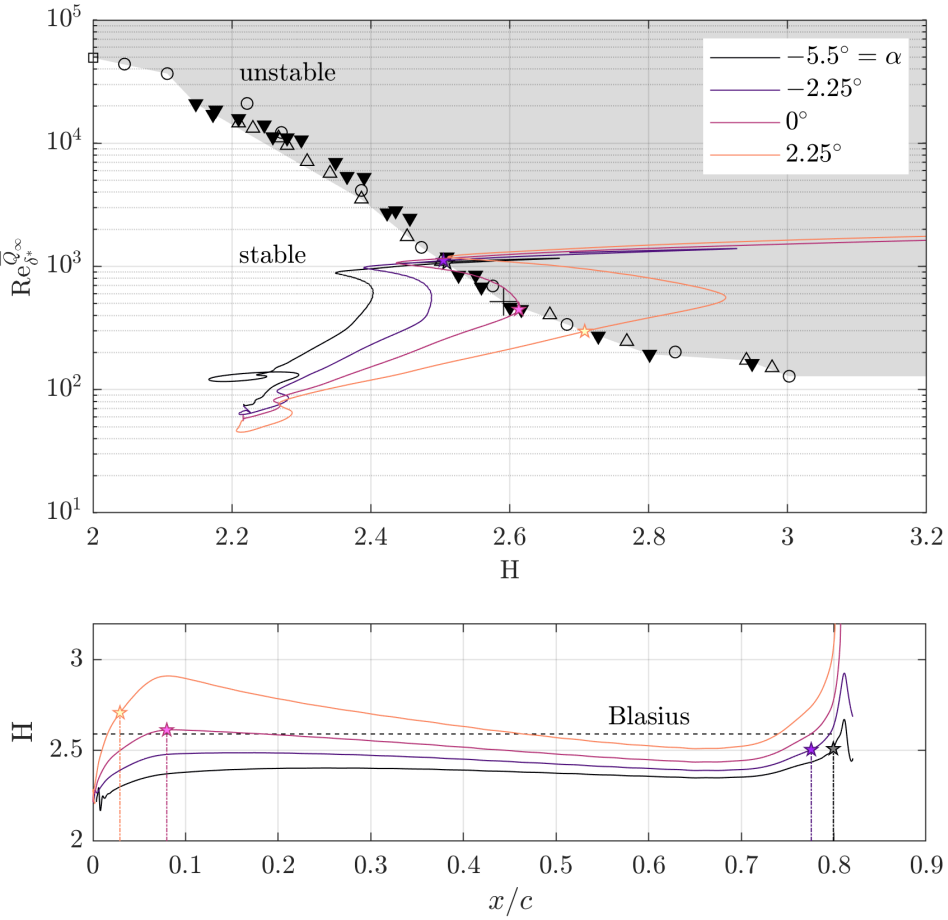

Figure 6.5: Displacement-thickness Reynolds number against the shape factor H and evolution of H versus x/c at $\Lambda = 0°$ for the various angles of attack. Black markers correspond to the critical Reynolds number locations for the incompressible TS instability. The Blasius solution is given as the large '+' symbol in the top panel and as the dashed line in the bottom panel. Colored pentagram symbols indicate the first streamwise station exceeding the critical Reynolds number threshold for the considered angles of attack. The dashed line indicates the shape-factor of the Blasius flat plate solution. Other markers correspond to those shown in Fig. 5-12 of White [54]. Reprinted from [129].

To prepare the DEKAF boundary-layer profiles for EPIC, the profiles' wall-normal resolution must be increased from the sparse $N_\eta = 90$ used in DEKAF. They are GICM-interpolated to a y-resolution of $N_y = 250$ in each streamwise profile. Extrapolation is performed to a physical y height of $0.61\,\mathrm{m}$ to capture the freestream extent of the disturbance shapes—see Eq. (3.11) to review the methodology.

6.2 Linear stability analysis

For stability analysis on swept wings over a broad range of configurations, the present section will highlight simulations of Linear Parabolized Stability Equations (LPSE). The LPSE methodology is selected over LST, as experimental validation in the past has demonstrated the importance of non-parallel effects on swept wings for physical accuracy [25].

Briefly, some simulation inputs are described. The disturbance is presumed to satisfy no-slip and no-penetration at the surface. The freestream boundary conditions set the disturbance to be zero-valued, i.e., a homogeneous Dirichlet condition is prescribed. A Neumann condition, $\partial\hat{T}/\partial y|_w = 0$, can be used for the stationary crossflow instability (SCF), simulating an adiabatic wall, as the laminar base-flow is adiabatic. However, to simplify the calculations, Dirichlet conditions are used for both stationary and unsteady disturbances, as the effect on N-factors is measurably small for the near-incompressible conditions considered. The y-momentum continuity equation is used as a compatibility condition for $\hat{\rho}$ at the wall. The streamwise pressure gradient of the shape function $\partial\hat{p}/\partial s = 0$ is assumed for all disturbances out of simplicity. For additional details on LPSE, see Beyak et al. [129].

The amplification of the perturbations will be presented in terms of N-factors, which are logarithmic ratios of the disturbance amplitude with respect to the first neutrally stable point in the domain. For LST disturbances, the streamwise growth of the instability is contained fully in the negative imaginary part of the eigenvalue: $-\alpha_i$. However for PSE solutions, the streamwise growth is contained in both the shape-function and $-\alpha_i$. To characterize this growth for PSE, often times the leading-edge-normal momentum contribution of the shape-functions $\hat{\rho u}$ is used when calculations accompany hot-wire measurements oriented in the $\overline{u}$ direction from matching experiments.

However, as these calculations are predictive, it is more appropriate to use a measure of the disturbance energy: the Chu norm [133]. This norm represents the total perturbation energy, and appears as the integrand below which is integrated over the wall-normal profile for each streamwise station.

$$\left.\begin{aligned} N(s) &= \int_{s_{\mathrm{I,LPSE}}}^{s} -\mathrm{Imag}(\sigma_{q'})(\bar{s})\,\mathrm{d}\bar{s}, \qquad\qquad \sigma_{q'}(s) = \alpha - \frac{\mathrm{i}}{\Phi}\frac{\partial \Phi}{\partial s}, \\ |\Phi(s)|^2 &= \int_0^{y_{\max}} \underbrace{\left(\overline{\rho}\left(|\hat{u}|^2 + |\hat{v}|^2 + |\hat{w}|^2\right) + \frac{\overline{\rho}}{\gamma(\gamma-1)\mathrm{M}^2\,\overline{T}}|\hat{T}|^2 + \frac{\overline{T}}{\gamma \mathrm{M}^2\,\overline{\rho}}|\hat{\rho}|^2\right)}_{\text{Chu norm}} \mathrm{d}y, \end{aligned}\right\} \tag{6.7}$$

Here, $s_{\mathrm{I,LPSE}}$ represents the most upstream neutral point of the LPSE solution (i.e., the first s location where $\mathrm{Imag}(\sigma_{q'}) = 0$).[5] Integration in both y and s are performed using the trapezoidal rule.

Equation (6.7) returns the N-factor as a function of s, depicting the integration of the instability growth. Calculating this N-factor for a sufficiently large set of frequencies and spanwise wavenumbers gives a maximum amplification factor for all s-locations, creating an N-factor envelope. The N-factor envelope is useful from an engineering perspective to roughly quantify the overall amplification from the assembly of various frequencies and spanwise wavenumbers. With that said, the N-factor envelope should be not be mistaken for the amplification of a specific frequency and/or spanwise wavenumber. The values reached by the N-factor envelope can be compared against a selected 'critical' N-factor value of the corresponding instability mechanism. A critical N-factor value indicates the value above which a primary instability mechanism is anticipated to initiate the onset of turbulence. The Tollmien-Schlichting mechanism is generally selected to have its critical N-factor be 9 units [134, 135]. Additionally, stationary crossflow-induced transition has been observed for LPSE N-factors of 5 units [25].

For detail on frequency and spanwise-wavelength characterization, see Beyak et al. [129].

[5] Note that for LST, $\Phi = 1$, as non-parallel effects are not incorporated. This is not used in this dissertation however, as all results stem from integration of PSE.

6.2.1 N-factor envelopes

Within each panel of Fig. 6.6, different N-factor envelopes are indicated: Tollmien-Schlichting (TS) in green diamonds, traveling crossflow (TCF) in purple squares, stationary crossflow (SCF) in blue, and the maximum of these three categories in red. By definition, all SCF disturbances have a frequency of 0 Hz. Disambiguating between TS and TCF is not as clearly defined, so the physical characteristics of these disturbances must be considered. As a brief aside, below are the definitions of several important wave quantities:

$$c_{\mathrm{ph}} = \frac{\omega}{\sqrt{\alpha_r^2 + \beta^2}} \tag{6.8a}$$

$$\psi_w = \arctan\left(\frac{\beta}{\alpha_r}\right) \tag{6.8b}$$

$$\psi_s = \arctan\left(\frac{\overline{w}_0}{\overline{u}_e}\right) \tag{6.8c}$$

$$f = \frac{\omega}{2\pi} \tag{6.8d}$$

$$\lambda_s = \frac{2\pi}{\alpha_r} \tag{6.8e}$$

$$\lambda_z = \frac{2\pi}{\beta} \tag{6.8f}$$

$$\lambda = \frac{2\pi}{\sqrt{\alpha_r^2 + \beta^2}} = \frac{1}{\sqrt{\frac{1}{\lambda_s^2} + \frac{1}{\lambda_z^2}}} \tag{6.8g}$$

$$\vec{k} = \alpha_r \vec{e}_s + \beta \vec{e}_z \tag{6.8h}$$

Equations (6.8) define the phase speed c_{ph}, wave angle ψ_w, streamline angle ψ_s, frequency f, leading-edge-orthogonal/parallel wavelength components λ_s and λ_z respectively, and wavelength λ in the direction of the wave vector of the disturbance $\vec{k}$. Note $\overline{w}_0 \equiv \overline{w}_\infty$, and that $\vec{e}_s$ and $\vec{e}_z$ are unit vectors in the s- and z-directions, respectively. By definition, ψ_w and ψ_s are zero if the wave vector and streamline are oriented in the leading-edge-orthogonal direction, respectively. When computing the arctangents of (6.8b) and (6.8c), care must be taken with the different quadrant of the arguments: `atan2(y,x)` is used programmatically. It should be noted that by these definitions, the

total wavelength λ is not equal to the square-root-sum-of-squares of the component wavelengths. That is to say, $\lambda \neq \sqrt{\lambda_s^2 + \lambda_z^2}$.

The usual characteristics of the TCF mechanism for the incompressible speed regime are as follows:

1. The most unstable wavelength is near $\lambda \approx 4\delta_{99}$;
2. The phase speed c_{ph} is on the order of $\overline{w}_{s,\max}$;
3. The wave angle ψ_w is oriented near to or opposite of the crossflow direction of the laminar base flow;
4. The frequency f is typically below 200 Hz.

To contrast, the usual characteristics of the TS mechanism are the following:

1. The phase speed c_{ph} is near 0.2 to 0.4 of $\overline{u}_{s,e}$ ($\gg \overline{w}_{s,\max}$);
2. The wave angle ψ_w is oriented roughly near the local inviscid streamline angle ψ_s;
3. The frequency f is around 300 to 900 Hz.

Returning to the original task at hand to disambiguate between TCF and TS content, the orientation of the wave angle with respect to the streamline angle is used. For this analysis, the TCF content has been categorized as any content whose wave angle is near orthogonal to the local streamline angle at some s location downstream of its LPSE branch-I neutral point, with a tolerance subtending $\Delta\psi_{\mathrm{TCF}} = 25^\circ$ in both directions. The TS content is categorized similarly: its wave angle is parallel to the local inviscid streamline angle with an angular tolerance of $\Delta\psi_{\mathrm{TS}} = 35^\circ$.

6.2.1.1 Analysis of N-factor envelopes

A comprehensive quantification of the growth of the various instability mechanisms present on the top side of the fore element of the X207.LS is presented below in Fig. 6.6. The angles of attack considered are $\alpha \in (-5.5^\circ, -2.25^\circ, 0^\circ, 2.25^\circ)$, and for the sweep angles, $\Lambda \in (0^\circ, 25^\circ, 30^\circ, 35^\circ)$.

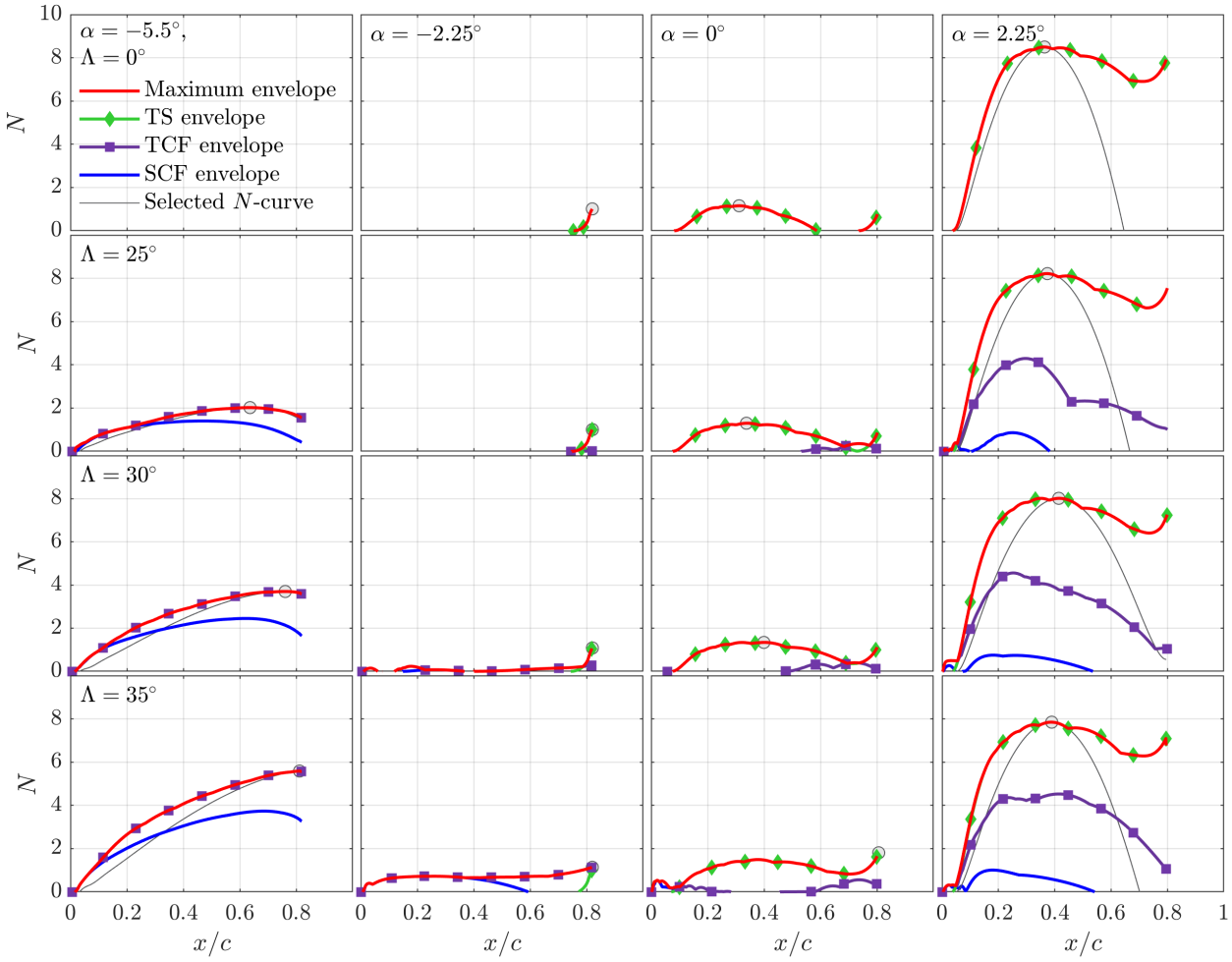

Figure 6.6: Chu-norm LPSE N-factor envelopes vs. x/c for the considered sweep angles and angles of attack. The overall maximum N-factor obtained for each configuration is indicated with a gray circle, and its selected N-curve is shown if the maximum is greater than 2. The corresponding wave characteristics at that location at provided below in table 6.1. Reprinted from [129].

Each column of panels shows data for a given angle of attack, while each row shows data for a given sweep, as indicated by the text box in the top left of the border panels. Note that for the configuration of $(\Lambda, \alpha) = (0°, -5.5°)$, all relevant boundary-layer instability content is stable for the top side of the wing.

For the $\Lambda = 0°$, $\alpha = 2.25°$ configuration, there are some unstable TS waves that are highly oblique—oblique enough to satisfy the TCF criterion of $\Delta\psi_{\text{TCF}} = 25°$. This N-factor envelope is omitted from the top right panel of Fig. 6.6 as the crossflow mechanism also requires $\overline{w} \neq 0$.

Also, one may suppose that the value of $\Delta\psi_{\mathrm{TS}} = 35^\circ$ is rather large for deeming TS a 'streamwise' mechanism. However, using this value ensures that for the entire extent of the $\alpha = 2.25^\circ$ configuration, the maximum envelope is coincident with the TS envelope downstream of $x/c \approx 5\%$—an expected trend for an adverse pressure gradient. A literature review of the work by Rozendaal and Arnal shows that this value of $\Delta\psi_{\mathrm{TS}}$ is reasonable [11, 136, 137, 138]. Similarly, the value of $\Delta\psi_{\mathrm{TCF}} = 25^\circ$ was chosen to ensure that the maximum envelope is coincident with the TCF envelope for the entire extent of the $\alpha = -5.5^\circ$ configuration. Following the work of Mack, the selected value of $\Delta\psi_{\mathrm{TCF}}$ is quite similar [10, §13.3].

With the definitions of the various N-factor envelopes established, the critical N-factors may be applied to the results shown in Fig. 6.6. If the critical stationary crossflow N-factor is naively selected as $N_{\mathrm{SCF,crit}} = 5$, then none of the cases in the configuration matrix are expected to undergo boundary-layer transition from SCF alone. It is worth recalling that the value of 5 assumes a certain receptivity response from the surface roughness near the attachment line and from the freestream disturbance levels. Experimentalists can use discrete roughness elements (DREs) and/or alter the levels of freestream vorticity using turbulence grids to change this receptivity response. This in turn would lead to a potentially drastic change in the $N_{\mathrm{SCF,crit}}$ observed from experiments. As demonstrated by Feliciano, using DREs on the $\alpha = -5.5^\circ$ configuration at $\Lambda = 35^\circ$ forced the stationary crossflow mechanism significantly and stationary streaks were visible near $x/c = 0.20$—approximately an $N = 2$ from Fig. 6.6. The description of the experimental set-up for this configuration will be delayed until the later section considering nonlinear analysis: §6.3.

For traveling crossflow, if the critical N-factor is conservatively selected as $N_{\mathrm{TCF,crit}} = 5$, then that would indicate the boundary layer of the $(\Lambda = 35^\circ, \alpha = -5.5^\circ)$ configuration would undergo transition from TCF alone. Again, this assumes some receptivity response that appreciably tunes into freestream sound and vorticity disturbance levels. At the lowest freestream-disturbance conditions, it has been shown on previous geometries that SCF dominates the boundary-layer transition process due to its larger initial amplitude: see the work by [139, 140]. If this trend holds true for the X207.LS following the upcoming experiments of Feliciano et al. 2022, then a

Table 6.1: Selected wave properties of the most amplified disturbance for each angle of attack and sweep angle as seen in Fig. 6.6. The purple text highlights a property's value indicative of the traveling crossflow mechanism, and green text highlights that of the Tollmien-Schlichting mechanism. The points corresponding to this data are indicated by gray circles in Fig. 6.6. Reprinted from [129].

Λ [°]	α [°]	x/c [%]	$N_{\max}$	$4\delta_{99}$ [mm]	λ_z [mm]	λ [mm]	f [Hz]	$c_{\mathrm{ph}}/\overline{u}_{s,e}$	$c_{\mathrm{ph}}/\lvert\overline{w}_{s,\max}\rvert$	$\psi_w - \psi_s$ [°]
25	−5.50	64	2.0	9.2	9.0	8.6	75	0.026	0.7	+85.9
30	−5.50	76	3.7	10.2	10.0	9.5	100	0.038	1.0	+84.3
35	−5.50	81	5.6	11.5	11.0	10.0	100	0.041	1.1	+85.4
0	−2.25	82	1.0	11.3	∞	18.7	450	0.311	∞	0
25	−2.25	82	1.0	11.9	50.0	22.8	350	0.306	18.4	+7.1
30	−2.25	82	1.1	12.2	50.0	22.7	350	0.311	16.1	+2.8
35	−2.25	82	1.1	12.6	50.0	22.5	350	0.313	14.6	−1.9
0	0	31	1.2	7.5	∞	12.9	750	0.365	∞	0
25	0	34	1.3	8.1	30.0	14.1	650	0.358	57.7	+7.9
30	0	40	1.3	8.9	30.0	16.2	550	0.351	39.3	+8.3
35	0	81	1.8	13.8	30.0	20.4	350	0.280	18.1	+14.6
0	2.25	36	8.5	8.6	∞	13.8	750	0.372	∞	0
25	2.25	37	8.2	9.2	∞	14.4	650	0.351	32.4	−19.5
30	2.25	41	8.0	9.7	∞	16.0	550	0.336	30.8	−23.7
35	2.25	39	7.8	9.8	∞	15.4	550	0.329	24.5	−28.0

more appropriate value $N_{\mathrm{TCF,crit}}$ may be derived.

For the Tollmien-Schlichting instability, if the critical N-factor is selected as $N_{\mathrm{TS,crit}} = 9$, then strictly following the engineering e^N prediction approach, boundary-layer transition is not expected for any of the cases in the configuration matrix. However, for all of the adverse pressure gradient cases of $\alpha = 2.25°$, $N_{\mathrm{TS}} \approx 8$ at $x/c \approx 0.4$, exhibiting significant TS growth nevertheless. Therefore, the TS instability mechanism *may* lead to boundary-layer transition for all sweep angles at $\alpha = 2.25°$, if the freestream disturbances corresponding to the same frequencies happen to have large enough initial amplitudes. This is not expected to be the case when considering the low-turbulence configuration of the KSWT.

The most amplified content indicated with gray circles in Fig. 6.6 can be further characterized in terms of its wave properties, delineated in table 6.1. Note for the angle of attack $\alpha = -5.5°$, the LPSE analysis predicts TCF wavelengths slightly less than $4\delta_{99}$ and phase speeds on the order of the maximum crossflow velocity of the laminar base flow. For the other angles of attack considered, the TS phase speeds nondimensionalized by $\overline{u}_{s,e}$ range from 0.28 to 0.372: within the expected

range of 0.2 to 0.4. Additionally, for the zero sweep cases, the most amplified content is two-dimensional, indicated by $\psi_w = \psi_s = 0°$.

Curiously, for the adverse pressure gradient case of $\alpha = 2.25°$ at nonzero sweep, the most amplified disturbance is two-dimensional (indicated by λ_z as infinite) despite the base flow being three-dimensional. Locally, there exist three-dimensional TS disturbances that are more unstable than the two-dimensional disturbances. However, these three-dimensional disturbances do not remain unstable for long, reaching their branch-II neutral points sooner downstream than that of the two-dimensional disturbances.

6.3 Nonlinear stability analysis for $\alpha = -5.5°$, $\Lambda = 35°$

Let us pivot our attention to now the favorable gradient configuration—the $\alpha = -5.5°$ angle of attack and compare nonlinear simulation results against the measured flowfield.

6.3.1 Coordinate system rotations

To compare the computational results to the experimental ones as carefully as possible, we need to measure the correct velocity component at the right location. The next step is expressing the velocity directly in a coordinate system relevant to the experiments rather than the computations. The velocity vector in the computational-relevant frame $\vec{V}^c$ is coordinatized along the streamwise s, wall-normal y, and spanwise z coordinates. In the wind-tunnel-relevant frame, the velocity vector $\vec{V}^t$ is coordinatized along the global X_t through the test section parallel to the floor, the global Y_t out of the page, and the global Z_t downward with gravity to complete the right-handed system. The velocity $\vec{V}$ may be expressed in either inertial frame given as

$$\begin{aligned} \vec{V}^c &= u\hat{e}_s + v\hat{e}_y + w\hat{e}_z \\ \vec{V}^t &= u_t\hat{e}_{X_t} + v_t\hat{e}_{Y_t} + w_t\hat{e}_{Z_t} \end{aligned} \tag{6.9}$$

where $\hat{e}_{q^i}$ is a unit vector along coordinate q^i. The wing is first swept (shown in Fig. 6.7), then pitch is applied about quarter chord (shown in Fig. 6.8).

The first rotation in this process is a rotation about Y_t of an angle Λ to apply sweep (see Fig.

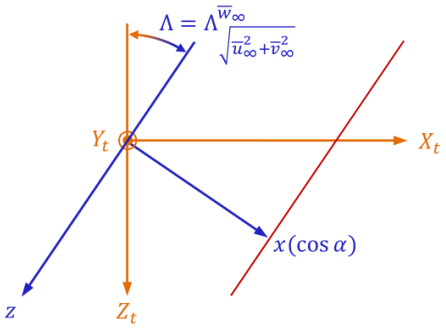

Figure 6.7: Sketch of the wind-tunnel coordinate system $\{X_t, Y_t, Z_t\}$ and the axes $\{x\cos\alpha, Y_t, z\}$ after applying sweep Λ rotating about Y_t. Sweep may also be written as $\Lambda = \Lambda^{\frac{\overline{w}_\infty}{\sqrt{\overline{u}_\infty^2+\overline{v}_\infty^2}}} \equiv \arctan\left(\overline{w}_\infty \Big/ \sqrt{\overline{u}_\infty^2 + \overline{v}_\infty^2}\right)$. Reprinted from [119].

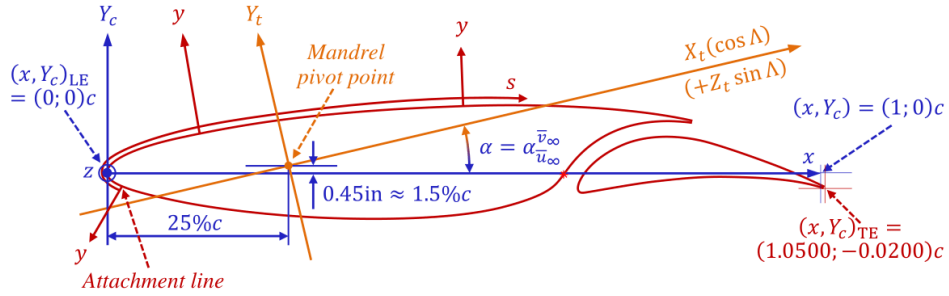

Figure 6.8: Sketch of the X207.LS cross-section and the associated coordinate systems. The wing is pitched about quarter chord along the mandrel about z. Conventional airfoil coordinates are given as $\{x, Y_c, z\}$ with z out of the page. The computational body-fitted orthogonal frame is given as $\{s, y, z\}$. The angle of attack may also be written as $\alpha = \alpha^{\frac{\overline{v}_\infty}{\overline{u}_\infty}} \equiv \arctan\left(\overline{v}_\infty/\overline{u}_\infty\right)$. The attachment line as pictured indicates a positive angle of attack for visualization purposes. Note the airfoil coordinates have been defined such that the trailing edge does not lie on $Y_c = 0$ or $x/c = 1$. Finite thickness at the trailing edges facilitates ease of CAD and machining. Reprinted from [119].

6.7). The third coordinate is now leading-edge-parallel, denoted as z. The second rotation is a rotation about z of an angle $-\alpha$ to apply pitch (see Fig. 6.8).[6] The origin is now shifted from the mandrel pivot point to the leading edge of the airfoil. The first coordinate is now in line with the airfoil's horizontal coordinate, denoted as x. The second coordinate is in line with the airfoil's conventional vertical coordinate, denoted as Y_c. The third and final rotation necessary to marry the

[6]The standard definition of the angle of attack is clockwise, not counter-clockwise, because that yields larger lift as the airfoil is pitched with respect to flow coming from the left. Hence, the negative sign is used because of the standard convention that the airfoil must be pitched in the clockwise direction to yield larger lift.

experimental frame to the computational frame is an adjustment to be locally tangent to the surface of the wing. To be tangent, a final rotation about z of an angle θ is applied, where θ is defined at the selected streamwise station $(x/c)|_{\text{traverse}}$ as

$$\theta = \arctan2(\mathrm{d}Y_c,\, \mathrm{d}x)|_{\text{traverse}} = \arctan2(\mathrm{d}Y_c/\mathrm{d}s,\, \mathrm{d}x/\mathrm{d}s)|_{\text{traverse}} \tag{6.10}$$

where the surface coordinate derivatives $\mathrm{d}Y_c/\mathrm{d}s$ and $\mathrm{d}x/\mathrm{d}s$ are computed with a central, fourth-order accurate, regular finite difference at $(x/c)|_{\text{traverse}}$ on a hyperresolved s-domain. These rotations are given in matrix form as

$$\mathrm{R}_1 = \begin{bmatrix} \cos\Lambda & 0 & -\sin\Lambda \\ 0 & 1 & 0 \\ \sin\Lambda & 0 & \cos\Lambda \end{bmatrix} \tag{6.11a}$$

$$\mathrm{R}_2 = \begin{bmatrix} \cos(-\alpha) & \sin(-\alpha) & 0 \\ -\sin(-\alpha) & \cos(-\alpha) & 0 \\ 0 & 0 & 1 \end{bmatrix} \tag{6.11b}$$

$$\mathrm{R}_3 = \begin{bmatrix} \cos(\theta) & \sin(\theta) & 0 \\ -\sin(\theta) & \cos(\theta) & 0 \\ 0 & 0 & 1 \end{bmatrix} \tag{6.11c}$$

such that the velocity vector coordinatized in the wind-tunnel frame may be rotated into the computational frame by

$$\vec{V}^c = \mathrm{R}_3\mathrm{R}_2\mathrm{R}_1\vec{V}^t \tag{6.12}$$

The inverse relationship is the useful equation for our purposes, transforming the computational frame to that of the wind tunnel. Since rotation matrices are orthonormal, we have that

$$\vec{V}^t = \mathrm{R}_1^{\mathrm{T}}\mathrm{R}_2^{\mathrm{T}}\mathrm{R}_3^{\mathrm{T}}\vec{V}^c \tag{6.13}$$

where the superscript T indicates the transpose operator. The hot wire effectively measures the resultant velocity in the plane orthogonal to the wire's axis. The hot-wire's axis is parallel to the wind tunnel Y_t and the component of velocity parallel to that axis is not measured. In other words,

$$V_{\mathrm{hw}} = ||\vec{V}^t - v_t \hat{e}_{Y_t}|| = \sqrt{u_t^2 + w_t^2} \tag{6.14}$$

Following these equations (6.9) to (6.14) transforms the instantaneous variables u, v, and w from PSE into the measured hot-wire velocity component V_{hw}.

To compare directly with the hot-wire measurements, V_{hw} must be shown against the wind tunnel Y_t axis, as that is the axis in which traverse articulates. The computational field is transformed and ultimately interpolated onto Y_t instead of the locally tangent frame of s and the field of wall-normal y. The surface coordinates of the computational grid are written as x_{surf} and $Y_{c,\mathrm{surf}}$ and are functions of s. Then by vector addition, the computational field off the surface can be written as

$$\begin{aligned} x_{\mathrm{field}} &= x_{\mathrm{surf}} + y\cos(\theta + 90^\circ), \\ Y_{c,\mathrm{field}} &= Y_{c,\mathrm{surf}} + y\sin(\theta + 90^\circ) \end{aligned} \tag{6.15}$$

where θ is defined by (6.10). From inverting (6.11b), $Y_{t,\mathrm{field}}$ is given as

$$Y_{t,\mathrm{field}} = x_{\mathrm{field}}(-\sin\alpha) + Y_{c,\mathrm{field}}\cos\alpha \tag{6.16}$$

Note that the surface of the wing does not have its Y_t value equal to zero, so instead of plotting against Y_t directly, ΔY_t will be the ordinate such that the wall value of Y_t has been subtracted off. In other words, $\Delta Y_t = Y_t - Y_{t,\mathrm{wall}}$. Let us define a query domain onto which the solution field will be interpolated. Select a dense, equispaced ΔY_t as 0 to $4\,\mathrm{mm}$ with $N_{Y_t} = 200$. The coordinates indicated by $(x/c)|_{\mathrm{traverse}}$ are not identically contained within the computational surface coordinates and serve as the query x/c locations. One-dimensional spline interpolation along the surface of the wing occurs then with x_{field} and $Y_{t,\mathrm{field}}$ at these distinct $(x/c)|_{\mathrm{traverse}}$ locations to compute

$Y_{t,\mathrm{wall}}$. The line profile Y_t is then computed as $\Delta Y_t + Y_{t,\mathrm{wall}}$ and is used identically for all spanwise locations in z.

To perform the interpolation from x_{field} and $Y_{t,\mathrm{field}}$ to the grid along the queried $(x/c)|_{\mathrm{traverse}}$ and Y_t profile, MATLAB R2019b's `griddata` function is used with the `'linear'` variable argument. Cubic interpolation caused spurious oscillations near the surface of the wing and, for that reason, is not selected for this application. This interpolation now computes V_{hw} directly on Y_t such that simulation data may be compared against that of the measured hot-wire velocities.

Another crucial detail is that the traverse articulates down the wing at a constant value of Z_t in the wind tunnel coordinate system. The computational methodology is formulated in z, not Z_t, and hence must be corrected by applying an appropriate shift in the NPSE ansatz. This Δz is written as

$$\Delta z = (x - x_{\mathrm{ph,ref}}) \tan \Lambda \tag{6.17}$$

where $x_{\mathrm{ph,ref}}/c = 0.55$.

6.3.2 Measured flow via naphthalene visualization and hot-wire scans

The experiments are conducted in the Klebanoff-Saric Wind Tunnel (KSWT) at Texas A&M University in College Station [141]. The KSWT is a low-speed, low-disturbance, closed-return facility designed for boundary-layer stability and transition analysis. Descriptions of the facility, flow quality, calibration techniques, and data acquisition can all be found in [52, 142, 143]. The KSWT is known for its extremely low freestream turbulence levels representative of flight: $\leq 0.02\%$ (DC – 300 kHz) [52]. The tunnel drives air into a test section with a cross-section of $1.4\,\mathrm{m}$ by $1.4\,\mathrm{m}$ at the inlet [127]. Experiments used a custom mounting system designed and built by Feliciano, such that both sweep and pitch are continuously variable [127]. A picture of the X207.LS in the tunnel with the hot-wire traverse is shown in Fig. 6.9.

The X207.LS contains cylindrical discrete roughness elements (DREs) of diameter $d_{\mathrm{DRE}} = 6.35\,\mathrm{mm}$ that are spaced $\lambda_{z,\mathrm{DRE}} = 12.7\,\mathrm{mm}$ apart along the z leading-edge-parallel axis. Here, $\lambda_{z,\mathrm{DRE}}$ indicates the center-to-center distance of the cylinders. The height of each cylinder is

Figure 6.9: The KSWT test section including the X207.LS and the traverse system. The wing is shown at sweep $\Lambda = 25^\circ$ and pitch $\alpha = -5.5^\circ$. In the top right is the temperature probe used for the Reynolds-number controller and the freestream pitot tube. Reprinted from [119].

$k_{\mathrm{DRE}} = 63.5\,\mu\mathrm{m}$, oriented wall-normal, such that the roughness Reynolds number is $\mathrm{Re}_k^{Q_\infty} \equiv k_{\mathrm{DRE}} Q_\infty / \nu_\infty = 83$. These relatively large DREs are needed to excite the crossflow instability, given the low chord Reynolds number of $\mathrm{Re}_c^{Q_\infty} = 1.0 \times 10^6$. The DREs are installed at $x/c = 0.018$, slightly upstream of the branch-I neutral point for the $\lambda_z = 12.7\,\mathrm{mm}$ SCF content, as computed with LPSE in previous analysis [129]. The SCF wavelength $\lambda_z = 12.7\,\mathrm{mm}$ will be referred to as the fundamental stationary crossflow wavelength $(0, 1)$, whereas $\lambda_z = 6.35\,\mathrm{mm}$ is associated to the (first) superharmonic $(0, 2)$.

Naphthalene flow visualization (NFV) reveals the footprint of the flowfield on the surface of the wing. Regions of higher skin friction/heat flux sublimate away the naphthalene mixture from the wing, unveiling the aluminum beneath, where regions of lower skin friction/heat flux do not sublimate. Experiments follow standard procedures as outlined by Mendes [144]. The most upstream application of the naphthalene is downstream of the DREs: near $x/c \approx 0.05$. NFV experimental results are shown in Fig. 6.10 with a near-surface picture given in Fig. 6.11 oriented in the xz-frame. The experiment indicates staggered and defined periodic structures with a primary

wavelength of approximately $12.7\,\mathrm{mm}$ in the leading-edge-parallel direction z. More faintly, there appear to be streaks of a shorter spanwise wavelength nearly bisecting the primary wavelength. These are presumed to be the wavelength imprint of the superharmonic.

Hot-wire anemometry techniques follow standard methods as outlined by Bruun [145]. The temperature-calibration routine, King's law, and the nonlinear fitting methods relating voltage to velocity have been detailed by White [146]. Two hot wires attached to an automated traverse system simultaneously measure the flowfield. One hot wire is submerged within the boundary layer, while the other probes the inviscid flowfield. The 'inviscid' hot wire is $17\,\mathrm{cm}$ above the 'boundary-layer' hot wire, as measured parallel to the axis Y_t. The traverse affords sub micrometer-resolution toward the model. In the inviscid region, the step size in Y_t starts off as $\Delta Y_t = 0.20\,\mathrm{mm}$ and decreases quadratically once inside the boundary layer [127]. The boundary-layer hot wire does not get closer to the surface once the velocity ratio between the two wires reaches 30%. After crossing this cutoff, the hot wires are retracted to their initial position in the freestream and then shifted by a spanwise step along the wing of $\Delta z = 2.12\,\mathrm{mm} \approx 1/3\,d_{\mathrm{DRE}}$. This process repeats until the end of the measurement window span: for this case, $\Delta z = 50\,\mathrm{mm}$. The sampling frequency of the hot wires is $10\,\mathrm{kHz}$ and measurements are taken for 2 seconds at each location in space [127]. The traverse articulates to a farther downstream x/c location by moving at a constant Z_t value. For this configuration, the traverse halts at five x/c stations, selected as $(x/c)|_{\mathrm{traverse}} \in \{0.25,\, 0.45,\, 0.55,\, 0.65,\, 0.70\}$. The hot wires measure data in a spanwise window near the vertical Y_t centerline of the tunnel. That is, the inboard and outboard pressure taps surrounding the centerline nearly equally enclose the measurement window. For more information, Hunt provides a complete description of the hot-wire data acquisition system [142].

A typical hot-wire scan of the boundary layer with the presently reported resolution can take at least 90 minutes, if not more. Extended run times naturally cause the tunnel to slowly heat up. With hotter air, viscosity increases, so the Reynolds number would decrease. The KSWT however has a Reynolds-number controller which monitors the temperature near the ceiling of the test-section inlet and adjusts the velocity appropriately to maintain a constant Reynolds number

Figure 6.10: Picture of naphthalene flow visualization over the top side of the X207.LS's fore element. Flow is from left to right. The horizontal axis is approximately the wind tunnel X_t and vertical axis is approximately parallel to Z_t. Streamwise-oriented streaks are visible from nearly $x/c \approx 0.20$ onward. Photograph taken by Jeppesen G. Feliciano. Reduction of image quality produces mild discoloration. Reprinted from [119].

Figure 6.11: Near-surface picture of naphthalene flow visualization over the top side of the X207.LS's fore element near $x/c \approx 0.45$. The horizontal axis is approximately leading-edge-orthogonal x and the vertical axis is approximately leading-edge-parallel z. Faint streaks nearly bisecting the darker, primary streaks are visible. Units on the ruler indicate millimeters. Photograph taken by Jeppesen G. Feliciano. Slight barrel distortion is visible given the wide angle lens. Reduction of image quality produces mild discoloration. Reprinted from [119].

$\mathrm{Re}_c^{Q_\infty}$. As such, a dimensional comparison of quantities is not meaningful between simulation and experiment—the KSWT's Q_∞ is a function of time and consequently a function of space. The experimental results are then plotted such that at every point, the velocity is nondimensionalized by the measurement from the hot-wire probe in the inviscid flow. All velocities shown have been time-averaged. Linear interpolation of experimental results is performed onto a grid with constant Y_t heights, leaving z non-equispaced from the natural stepping of the traverse.

Measured disturbance contours at $x/c = 0.45$ are shown in Fig. 6.12, where the vertical axis indicates the distance from the wall along Y_t and the horizontal is leading-edge-parallel z. The velocity, denoted here as u, is measured by the boundary-layer hot wire, whereas the velocity U is measured by the hot wire in the inviscid flowfield. The quantity u_{avg} indicates a spanwise average of u over the measurement window of $50\,\mathrm{mm}$. The hot-wire anemometry reveals the off-wall, stationary-disturbance structures that are responsible for the streaks as seen in the NFV of Fig. 6.11. Pairs of strong high-speed/low-speed regions are neighbored by weaker high-speed/low-speed pairs.

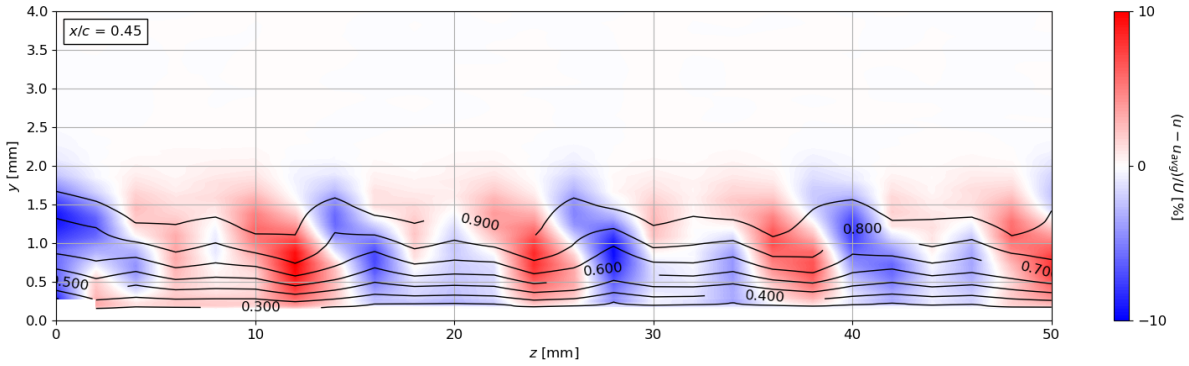

Figure 6.12: Measured disturbance contours at $x/c = 0.45$. The horizontal axis z is the leading-edge-parallel direction and the vertical axis indicates ΔY_t: the change in the wind-tunnel Y_t from the surface of the wing. Colored contours represent the stationary disturbance by subtracting out the spanwise average u_{avg}. Measured results are nondimensionalized by the velocity measured by the hot-wire probe in the inviscid flow U affixed $17\,\mathrm{cm}$ higher in Y_t than the boundary-layer probe. Black contour isolines showcase u/U for $[0.3, 0.9]$, $\Delta = 0.1$. Note that $U = U(z, Y_t)$. Reprinted from [119].

Dr. Edward B. White suggested that this flowfield resembles the summation of two cosines. To demonstrate his intuition, consider a sketch of $\cos(z)$ summed with the superharmonic $\cos(2z)$ in Fig. 6.13. When both are in phase, the summation reaches its global maximum at $z = 0$ with the high positive amplitude $(= 2)$, followed by a mild negative amplitude (≈ -1) and a point of zero. When the superharmonic is out of phase by $+90°$, the pattern is more intricate. For $\cos(z) + \cos(2z - \pi/2) = \cos(z) + \sin(2z)$, the sum reaches its global maximum of ≈ 1.76, followed by an equal and opposite global minimum of ≈ -1.76. Mild local extrema reach $\approx \pm 0.369$ later in the domain, nearly five times smaller than the global extrema in magnitude. The pattern is mirrored in z when the superharmonic is $-90°$ out of phase. This pattern will be used to heuristically assign the initial amplitudes of the $(0, 1)$ and $(0, 2)$ Fourier modes in NPSE. This flowfield exhibits unusually high amplitudes of the superharmonic. Generally, the amplitude of the $(0, 2)$ is $O(A^2_{(0,1)})$ for stationary crossflow simulations, but clearly from these observations, this is not true. The $(0, 2)$ may be forced by the configuration of the DREs themselves: recall that the diameter $d_{\mathrm{DRE}} = 6.35\,\mathrm{mm}$, which is precisely the wavelength of the superharmonic.

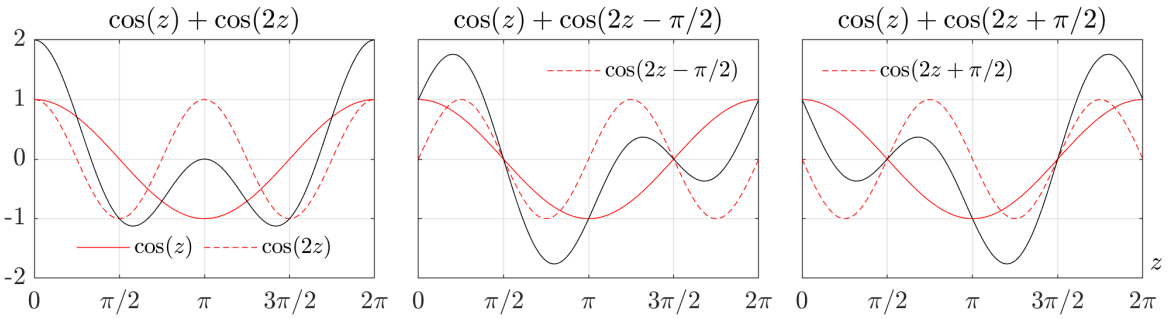

Figure 6.13: Sketches of $\cos(z)$ summed with the superharmonic $\cos(2z)$. The solid red line indicates the fundamental $\cos(z)$, the dashed red indicates the superharmonic $\cos(2z)$, and the sum is given by the black line. The left plot shows no phase difference between the waves, whereas the middle and the right plots show phase differences of $\pm 90°$, respectively. Reprinted from [119].

6.3.3 Stability analysis and comparison to measured flow

Briefly, the simulation inputs are described. The base-flow from DEKAF is first spline-interpolated (not-a-knot) in s onto a selected equispaced resolution $N_s = 250$ from $x/c = 0.02$ to the end of the X207.LS fore element. The resolution in wall-normal y is selected as $N_y = 200$ and is clustered according to Eq. (4.7).

For initial conditions, finite amplitudes were assigned to both the $(0, 1)$ fundamental stationary crossflow $\lambda_z = 12.7\,\mathrm{mm}$ Fourier mode and the $(0, 2)$ $\lambda_z = 6.35\,\mathrm{mm}$ superharmonic. The initial amplitudes were first set such that the $\max_y |u'_{(0,k)}|$ amplitudes near $x/c = 0.55$ became approximately equal from the linear dynamics. This heuristic approach follows Dr. White's observation of the cosine-summation, as discussed previously in §III.6.3.2. A second iteration slightly increased the amplitude for the $(0, 2)$. Precisely, the fundamental initial amplitude at $x/c = 0.02$ is selected as $\max_y |u'_{(0,1)}|/\overline{u}_e = 10^{-2}$ whereas the superharmonic's initial amplitude is selected as $\max_y |u'_{(0,2)}|/\overline{u}_e = 1.25 \times 10^{-2}$.[7]

Figure 6.14 shows the $\max_y |u'_{(0,k)}|$ amplitude distributions for each Fourier mode in the simulation. The fundamental SCF $(0, 1)$ is shown in light blue, the superharmonic $(0, 2)$ in red, the mean-flow distortion $(0, 0)$ in purple, and higher harmonics in gray. For this case, harmonics up to the $(0, 10)$ inclusive were accounted for. Linear behavior of the $(0, 1)$ and $(0, 2)$ is indicated with dashed lines. The nonlinear effects in this simulation are measured to be quite weak, as the fundamental and superharmonic only slightly deviate and stabilize with respect to their linear dynamics.

With respect to the freestream resultant velocity, the initial amplitudes are written as $\max_y |u'_{(0,1)}|/Q_\infty \approx 6.34 \times 10^{-3}$ and $\max_y |u'_{(0,2)}|/Q_\infty \approx 7.92 \times 10^{-3}$. By their respective branch-I locations, $\max_y |u'_{(0,1)}|/Q_\infty \approx 3.02 \times 10^{-3}$ at $x/c \approx 0.04$ and $\max_y |u'_{(0,2)}|/Q_\infty \approx 4.13 \times 10^{-3}$ at $x/c \approx 0.034$. For reference, the validation of Haynes & Reed of stationary crossflow on a swept wing reached an initial amplitude of $\max_y |u'_{(0,1)}|/Q_\infty \approx 2.5/\sqrt{2} \times 10^{-3} \approx 1.77 \times 10^{-3}$ at its

[7] The dimensional value of the streamwise edge velocity $\overline{u}_e \approx 9.44278\,\mathrm{m/s}$ and is selected internally in EPIC as the edge value at the first streamwise station included in the base flow.

branch-I location of $x/c = 0.05$ [25]. It is interesting to note that the initial amplitude found by Haynes & Reed and these initial amplitudes are on a similar order of magnitude, despite different DRE configurations, sweep, Reynolds number, pressure distribution, and wing surface curvature.

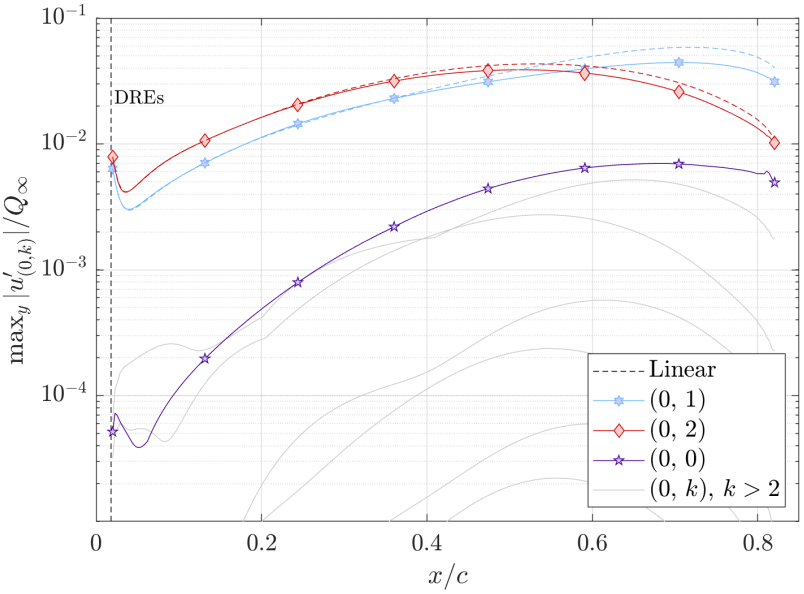

Figure 6.14: Fourier-mode amplitude distributions against x/c. The signature Fourier modes of the fundamental, the superharmonic, and the mean-flow distortion are shown in color with a prescribed marker, while their linear behavior is indicated by dashed lines of the same color. The other nonlinearly generated Fourier modes (greater superharmonics) are shown in gray. The DRE location of $x/c = 0.018$ is marked with a dashed, vertical, black line. Reprinted from [119].

To compare the simulation results to the measured flowfield, details regarding flow reconstruction must be discussed. The resulting spanwise-periodic signal from NPSE is arbitrarily oriented in space, as $z = 0$ has no unique significance. The NPSE signal then can be shifted in z without loss of generality at a single reference x/c station to match between experiment and simulation. For these results, the reference x_{ref}/c was selected as 0.55 where several structures qualitatively aligned 'by eye'.

These first simulations revealed that the computational results were entirely $180°$ out of phase with respect to the measured flowfield. For example, where the measured flowfield indicated low-

speed/high-speed regions, say, moving in $+z$, the simulation indicated high-speed/low-speed regions. Recall that in the context of NPSE, initial amplitudes are complex-valued. The superharmonic's initial phase then was adjusted by applying an 180° phase shift. That is, $A_{0\,(0,2)} = 1.25 \times 10^{-2} \mathrm{e}^{\mathrm{i}\pi} = -1.25 \times 10^{-2}$, which corrected the mismatch between experiment and simulation at $x/c = 0.45$. This change in phase does not visibly affect the amplitude distributions as shown in Fig. 6.14.

Upon applying the Δz shift as described in Eq. (6.17), results qualitatively agreed between simulation and experiment, shown in Figs. 6.15 through 6.19. These charts compare the measured disturbance contours in the top figure to simulation results in the bottom figure at the various x/c stations of the traverse. The horizontal axis z is the leading-edge-parallel direction and ΔY_t is the change in the wind-tunnel Y_t from the surface of the wing. Colored contours represent the stationary disturbance by subtracting out the spanwise average $\mathrm{mean}(V_{\mathrm{hw}}, z)$. Computational hot-wire disturbance quantities are scaled by $V_{\mathrm{hw\,ref}}$ to achieve a value of nearly unity at $\Delta Y_t = 4\,\mathrm{mm}$. Black contour isolines showcase $V_{\mathrm{hw}}/V_{\mathrm{hw\,ref}}$ for $[0.3, 0.9]$, $\Delta = 0.1$. These results indicate good agreement between simulation and experiment for the physical flowfield, especially considering only three, heuristic-driven iterations to match the measured, overall maximum amplitude at $x/c = 0.55$.

It is important to note here for the experimental results that despite the differences in span across the measurement window, all measurements are equally valid representations of reality. There is uncontrollable experimental error present.

There are several reasons for current discrepancies between simulation and experiment:

1. The stability analysis is built on the inviscid pressure coefficient as generated by MSES, which was then input into the boundary-layer code, DEKAF. This creates some discrepancy already with experiment, as the measured pressure coefficient along the wing varies slightly given the weak spanwise pressure gradient. Future studies will use the measured $C_p^{\overline{u}_\infty \overline{v}_\infty}$ as inputs into the boundary-layer code and analyze the nonlinear stability of the resulting boundary layer. This methodology mimics the validation by Haynes & Reed [25].

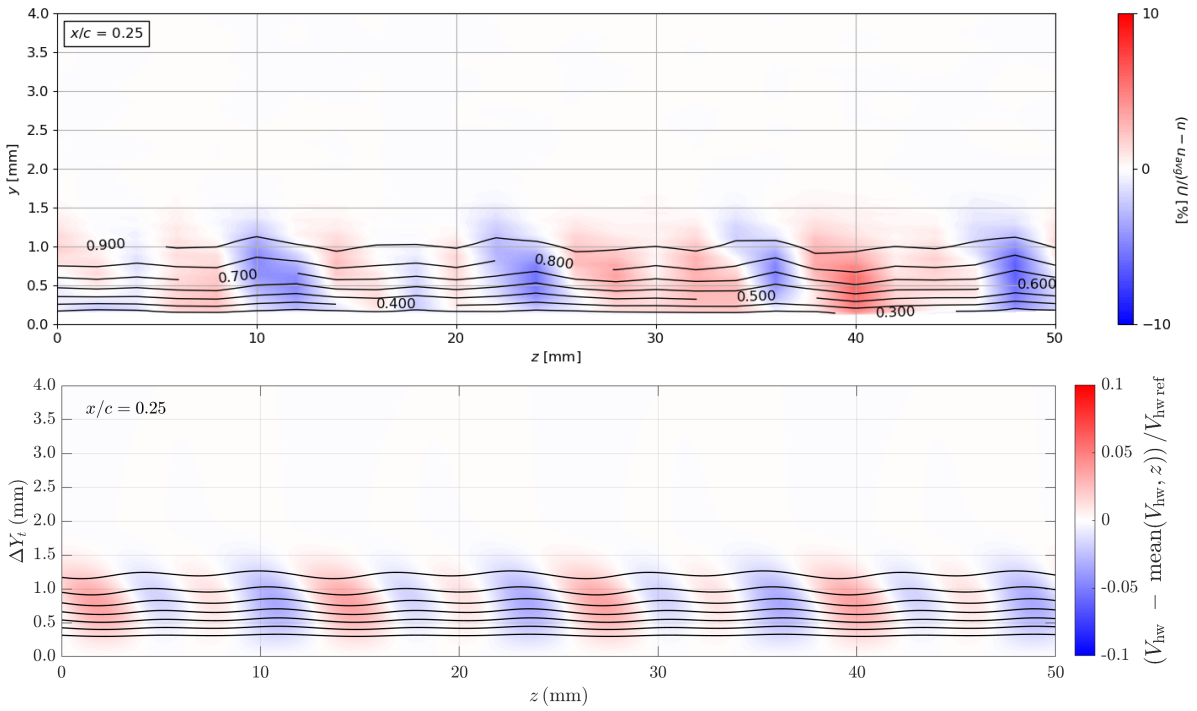

Figure 6.15: Comparison of measured disturbance contours (top figure) to nonlinear computational results (bottom figure) at $x/c = 0.25$. The horizontal axis z is the leading-edge-parallel direction and ΔY_t is the change in the wind-tunnel Y_t from the surface of the wing. Colored contours represent the stationary disturbance by subtracting out the spanwise average $\mathrm{mean}(V_{\mathrm{hw}}, z)$. Computational hot-wire disturbance quantities are scaled by $V_{\mathrm{hw\,ref}}$ to achieve a value of nearly unity at $\Delta Y_t = 4\,\mathrm{mm}$. Black contour isolines showcase $V_{\mathrm{hw}}/V_{\mathrm{hw\,ref}}$ for $[0.3, 0.9]$, $\Delta = 0.1$. Reprinted from [119].

2. The ratio of the $(0, 1)$ and $(0, 2)$ initial amplitudes may be slightly off, predicting inaccurate distributions downstream. For instance, the measured flowfield at $x/c = 0.70$ in Fig. 6.18 appears to be periodic with each period divided into thirds. For the first third, the stationary disturbance is measured to be locally high in speed, whereas for the other two thirds, the disturbance is locally low-speed nearly uniform in magnitude. This is not the case in the results of the simulation, as the flow in the last third differs qualitatively from that of the second third.

3. Not just the ratio of the initial amplitudes, but the overall value of the initial amplitudes may be slightly overestimated in the simulation when compared to the result of the experiments.

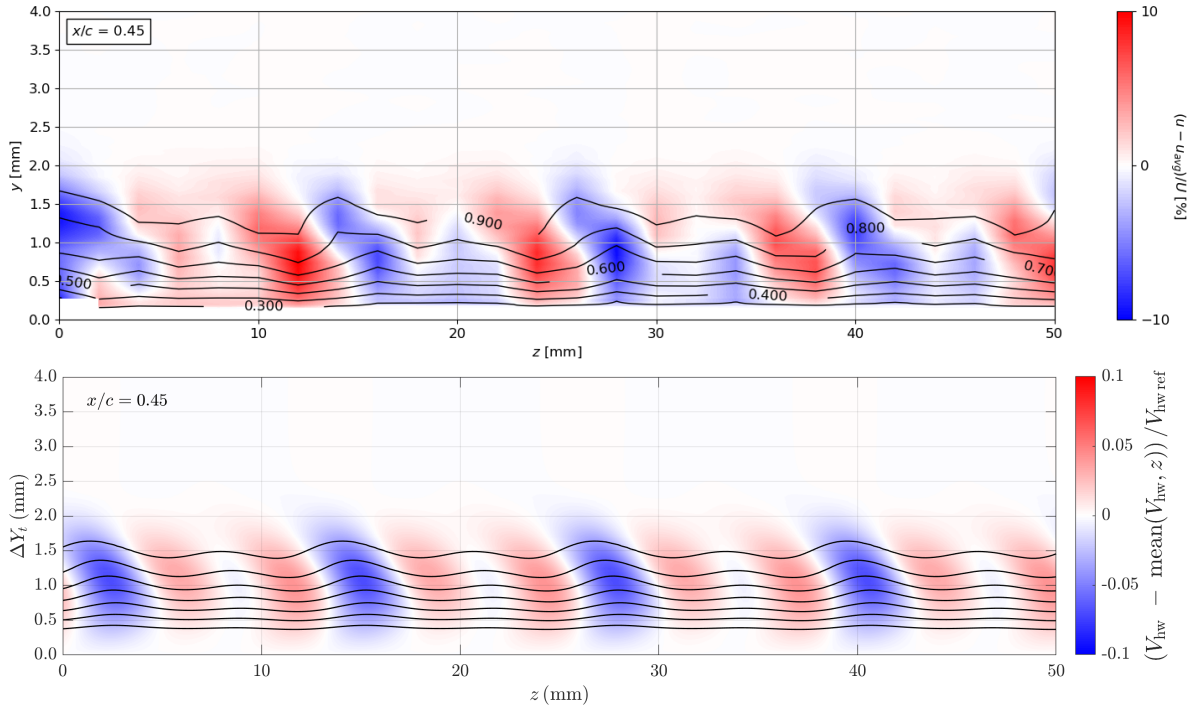

Figure 6.16: Continuation of Fig. 6.15 for $x/c = 0.45$. Reprinted from [119].

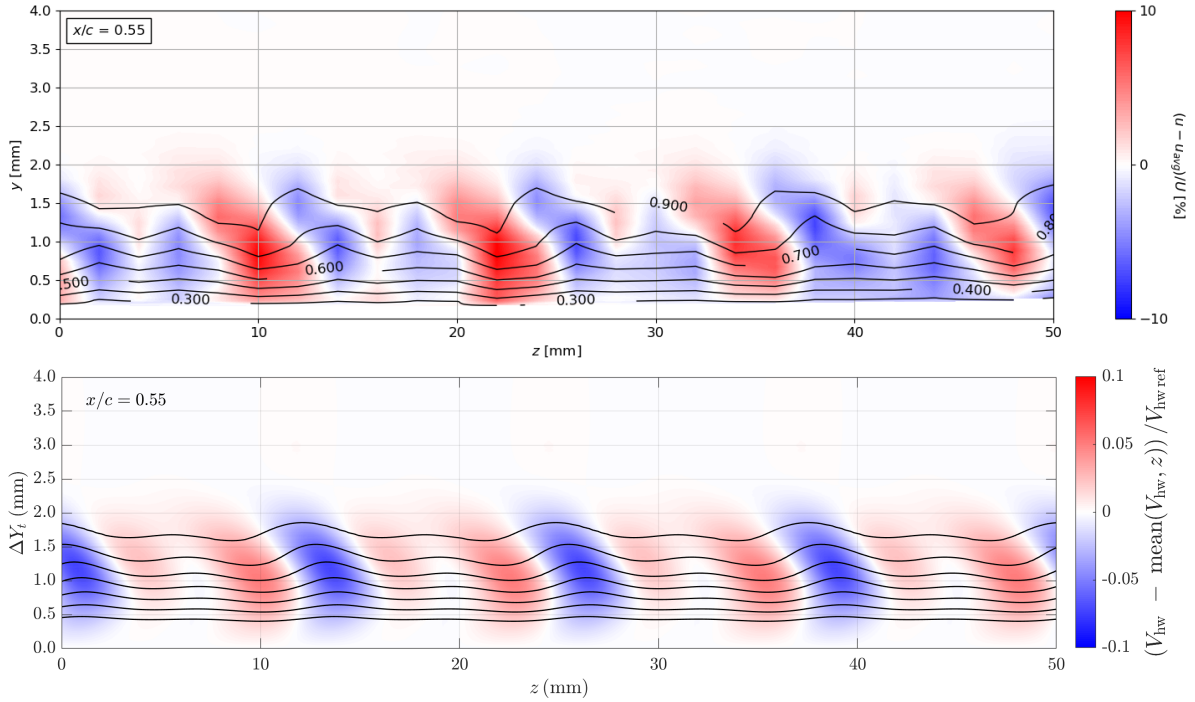

Figure 6.17: Continuation of Fig. 6.15 for $x/c = 0.55$. Reprinted from [119].

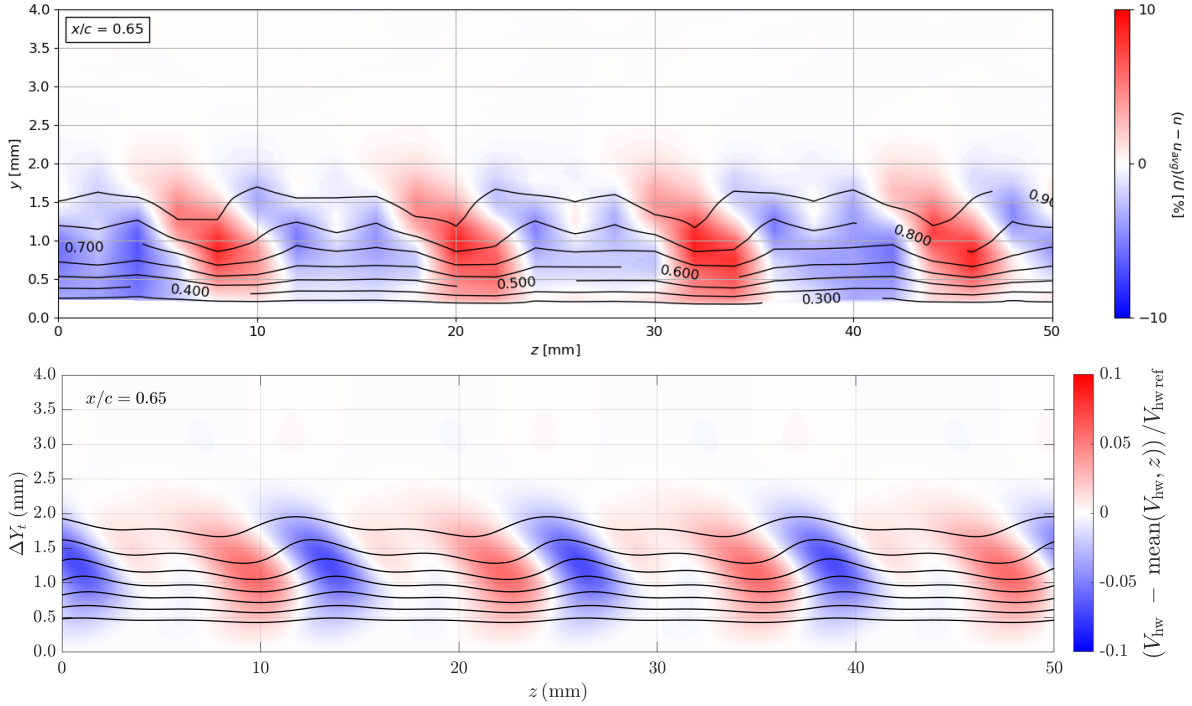

Figure 6.18: Continuation of Fig. 6.15 for $x/c = 0.65$. Reprinted from [119].

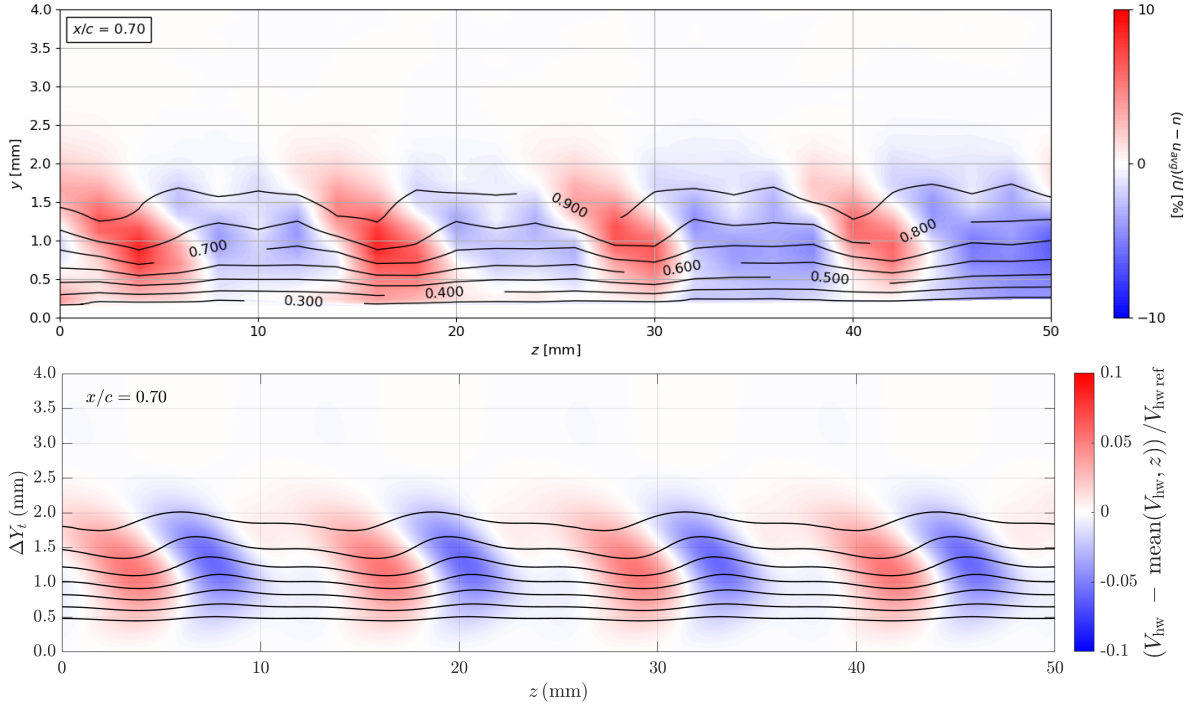

Figure 6.19: Continuation of Fig. 6.15 for $x/c = 0.70$. Reprinted from [119].

This is demonstrated by contour isolines of the simulation slightly farther in ΔY_t than that of the measured flow for many $(x/c)_{\text{traverse}}$.

6.3.4 Linear and nonlinear reconstruction of the flowfield

As mentioned previously, the nonlinearities present in this flowfield appear to be quite weak. That then prompts the question: how does the summation of the *linear* dynamics of the $(0, 1)$ and the $(0, 2)$ compare against the *nonlinear* dynamics of the system, including the mean-flow distortion and higher harmonics? A comparison of the reconstructed flowfields of the linear dynamics versus the nonlinear dynamics is shown in Fig. 6.20.

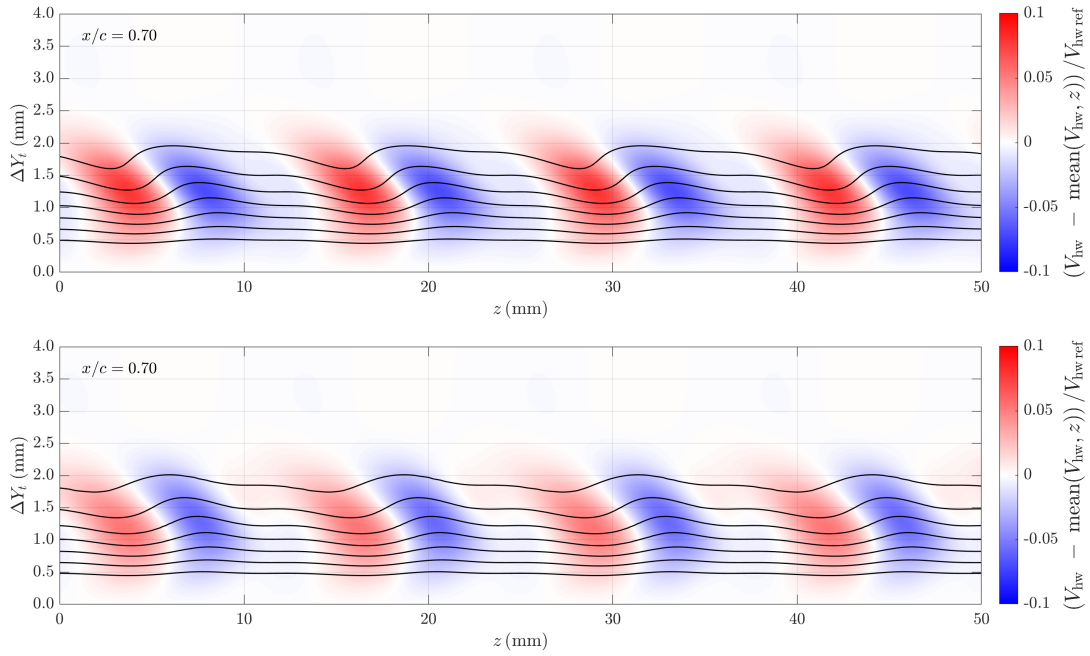

Figure 6.20: Reconstructed flowfield at $x/c = 0.70$ using only the simulation's linear dynamics or incorporating the entire nonlinear system. Top: summation of LPSE results of the $(0, 1)$ and $(0, 2)$ only. Bottom: NPSE results including the $(0, 0)$ and higher superharmonics up to the $(0, 10)$, inclusive. The plot description follows identically from prior figures (e.g., Fig. 6.15). Reprinted from [119].

The sum of the linear dynamics is shown in the top figure, while the entirety of the nonlinear system (NPSE) is given in the bottom figure of Fig. 6.20. Qualitatively, all of the relevant features

of the full nonlinear simulation are captured with the linear simulation. Amplitudes are slightly higher when considering the linear dynamics only, as energy is not transferred into the mean-flow distortion Fourier mode. This figure supports the observation that the measured flowfield is largely a linear superposition of the fundamental and the superharmonic.

6.4 Conclusions

Boundary-layer disturbances on the X207.LS swept wing were quantified across a wide range of geometric configurations as part of a preliminary study to inform the experimentalists the relevant ranges of amplified content. Linear Parabolized Stability Equations (LPSE) indicated appreciable crossflow growth at the angle of attack $\alpha = -5.5^\circ$ and sweep $\Lambda = 35^\circ$, reaching an $N = 4$. Significant Tollmien-Schlichting (TS) amplification was quantified over the wing at angle of attack $\alpha = 2.25^\circ$. Experimental stability measurements of the X207.LS in the Klebanoff-Saric Wind Tunnel (KSWT) have been analyzed. Results are compared against simulations using the Nonlinear Parabolized Stability Equations (NPSE). Coordinate systems have shown the necessary transformations to align the computational frame with the experimental frame to directly compare with the hot-wire anemometry data. Naphthalene flow visualization and hot-wire anemometry data of flow over the wing have been presented. A heuristic approach has been used to assign initial amplitudes of the fundamental stationary crossflow disturbance $(0, 1)$ and its superharmonic $(0, 2)$, which qualitatively recovers the measured flowfield using PSE. There is a good agreement between the simulations and the measured hot-wire velocity contours, matching the streamwise vortices formed in both magnitude and phase at several chordwise stations of the wing. Discrepancies between simulation and experiment exist from several sources: a) the laminar boundary layer was generated with the inviscid pressure coefficient from MSES as opposed to the experimentally measured pressure coefficient along the wing; and b) the values of the initial amplitudes for the $(0, 1)$ and $(0, 2)$ differ slightly from those observed in experiment. Nonlinearities present in this flowfield are quite weak, as the linear superposition of the fundamental and the superharmonic qualitatively resembles that of the full NPSE simulation.

Future work will continue on several fronts:

1. The spanwise interval will be phase-lock averaged in span, presenting the mean over an interval of 12.7 mm. The standard deviation of the mean $\sigma_{\overline{x}}$ can then be reported as well. Here, $\sigma_{\overline{x}} = \sigma_x/\sqrt{n_{\mathrm{sam}}}$, where σ_x is the standard deviation of the data set and n_{sam} is the number of samples, assuming the spanwise data samples are uncorrelated. In truth, the distinct samples along the span are correlated, as neighboring profiles are affected by the same DRE. However, the procedure to quantify the correlation coefficient is currently unknown. The mean profile, as well as the mean bounded by $\pm\sigma_{\overline{x}}$, will serve to generate the initial amplitudes of the $(0,1)$ and the $(0,2)$ for the NPSE simulations.

   (a) Elaborating on this last point, the phase-locked data at the earliest measured $x/c = 0.25$ will be Fourier transformed to compute the $(0,1)$ and the $(0,2)$ components in the wind-tunnel Y_t direction in terms of the hot-wire velocity V_{hw}. With the rotation angles known of Λ, α, and θ, the components of the vector in the wind-tunnel frame $\vec{V}^t = [u_t, v_t, w_t]$ can be found iteratively (see Eq. (6.14)) and subsequently, $[u, v, w]$ in the body-fitted, computational frame. With these known at $x/c = 0.25$, linear behavior may be presumed upstream, such that following LPSE development, an initial amplitude may be found at an arbitrary initialization point upstream. This could be at the DREs directly $(x/c = 0.018)$ or slightly farther downstream at a branch-I neutral point. Alternatively, instead of performing a Fourier transform, the experimental data may be fit nonlinearly to the form $A_{(0,1)}\sin(\beta_{(0,1)}z + \varphi_{(0,1)})$. Here, $\beta_{(0,1)} = 2\pi/(12.7\,\mathrm{mm})$, whereas $A_{(0,1)}$ and $\varphi_{(0,1)}$ are the amplitude and phase respectively, found through the fit at each y height. Similarly, the superharmonic could be fit via $A_{(0,2)}\sin(2\beta_{(0,1)}z + \varphi_{(0,2)})$ instead of performing a Fourier transform.

2. The measured pressure distribution from the experiments can be used instead of that the MSES code. As the experimental measurement window is between the inboard and outboard taps, the pressure coefficients could be averaged and fit smoothly.

3. The mean-flow distortion's streamwise wavenumber will be reassessed, either by considering

Airiau's "cut-off" procedure (see §5.6) or by implementing the proposed limiters (§5.7.1).

This concludes the chapter on the X207.LS analysis. The next chapter will analyze the boundary-layer stability on the S207 wing in cruise at the design conditions of the NASA ULI vision vehicle.

7. S207 SLOTTED, NATURAL-LAMINAR-FLOW AIRFOIL

Under the auspices of the NASA University Leadership Initiative, an effort is underway to design and analyze a swept, slotted, natural-laminar-flow (SNLF) airfoil for transonic flight. Crafted by Dan Somers, the S207 is a wing designed to promote favorable pressure gradients over the majority of the chord. Since favorable gradients are known to stabilize the Tollmien-Schlichting (TS) instability, the likelihood for significant growth based solely on TS is low in cruise. From an aircraft performance perspective, the introduction of sweep to the wing configuration is highly advantageous. Sweeping the wing improves aircraft performance by not only permitting the aircraft to fly faster for the same designed, leading-edge-orthogonal velocity; but it also simultaneously reduces the amount of induced wave drag, which is catastrophic in transonic flight. In the language of aircraft performance, sweep increases the drag-divergence Mach number.

From a laminar-to-turbulent transition perspective, the introduction of sweep, however, spawns the stationary crossflow mechanism within the boundary layer. The misalignment of the inviscid streamline and pressure-gradient direction produces a twisted boundary-layer profile whose inflection point gives rise to the crossflow instability. The natural surface roughness of the wing in conjunction with any freestream vorticity provide a pathway for stationary crossflow disturbances to initialize and develop down the wing. At appreciable sweep, the inflectional profile becomes more unstable, and the disturbance can amplify several orders of magnitude. Once the crossflow disturbance is significant in size, secondary instabilities of high frequency begin to grow in its peaks and troughs. At this stage, laminar breakdown is imminent.

Not only is the primary instability of stationary crossflow a concern, but there exist additional pathways to transition through other nonlinear interactions. Tollmien-Schlichting waves may nonlinearly interact with a weak stationary crossflow vortex to create a highly unstable oblique pair of waves that resonate together and can cause catastrophic breakdown of the laminar flow. A separate but possible nonlinear interaction that may occur is when a Tollmien-Schlichting wave is forced by its subharmonic oblique pair. Both of these are examples of secondary instability mechanisms

present over swept wings that need to be considered.

A natural question then is prompted to the boundary-layer transition analyst: *how much sweep can be applied to this wing while maintaining the benefits of the SNLF design?* To address this question fully, the nonlinear problem must be considered, assessing the various routes to disturbance amplification across different configurations while also quantifying inherent modeling uncertainties. This is the subject of the present work.

7.1 Background

The S207 airfoil was designed for cruise at $\mathrm{M} = 0.70$, $\mathrm{Re} = 13.2 \times 10^6$, and a section lift coefficient $c_l = 0.70$. By iterating on the shape of the airfoil cross-section and dividing the airfoil into two—a fore and aft element separated by a small slot—Dan Somers designed the shape such that the inviscid flow undergoes significant favorable pressure gradients over the wing, minimizing the growth of Tollmien-Schlichting waves. These pressure distributions were first computed at the mid-span angle of attack of $\alpha = -1.520^\circ$ using the code MSES. Dr. James G. Coder then accounted for twist at design conditions by considering a small range of angles of attack. Coder computed OVERFLOW CFD solutions at various sweep angles as well in this range, all assuming a spanwise infinite flowfield. The twist extrema include the most positive angle of attack, $\alpha = -1.022^\circ$, and the most negative $\alpha = -2.252^\circ$. The extrema of twist will be the configurations of interest for this chapter, which exacerbate the growth of various instability mechanisms.

At the heart of boundary-layer stability analysis is the core linear dynamics which cannot be neglected. With that stated though, the present work will focus and magnify the nonlinear simulations. In the words of Arnal and Saric,

> Nonlinearities strongly affect the development of disturbances, and "it seems like 'straining the gnat ...' to discuss the direction of disturbance growth or the most amplified linear disturbance when the real issue is a full nonlinear problem." [11]

Let us preface the stability analysis with a brief discussion on the laminar base flow.

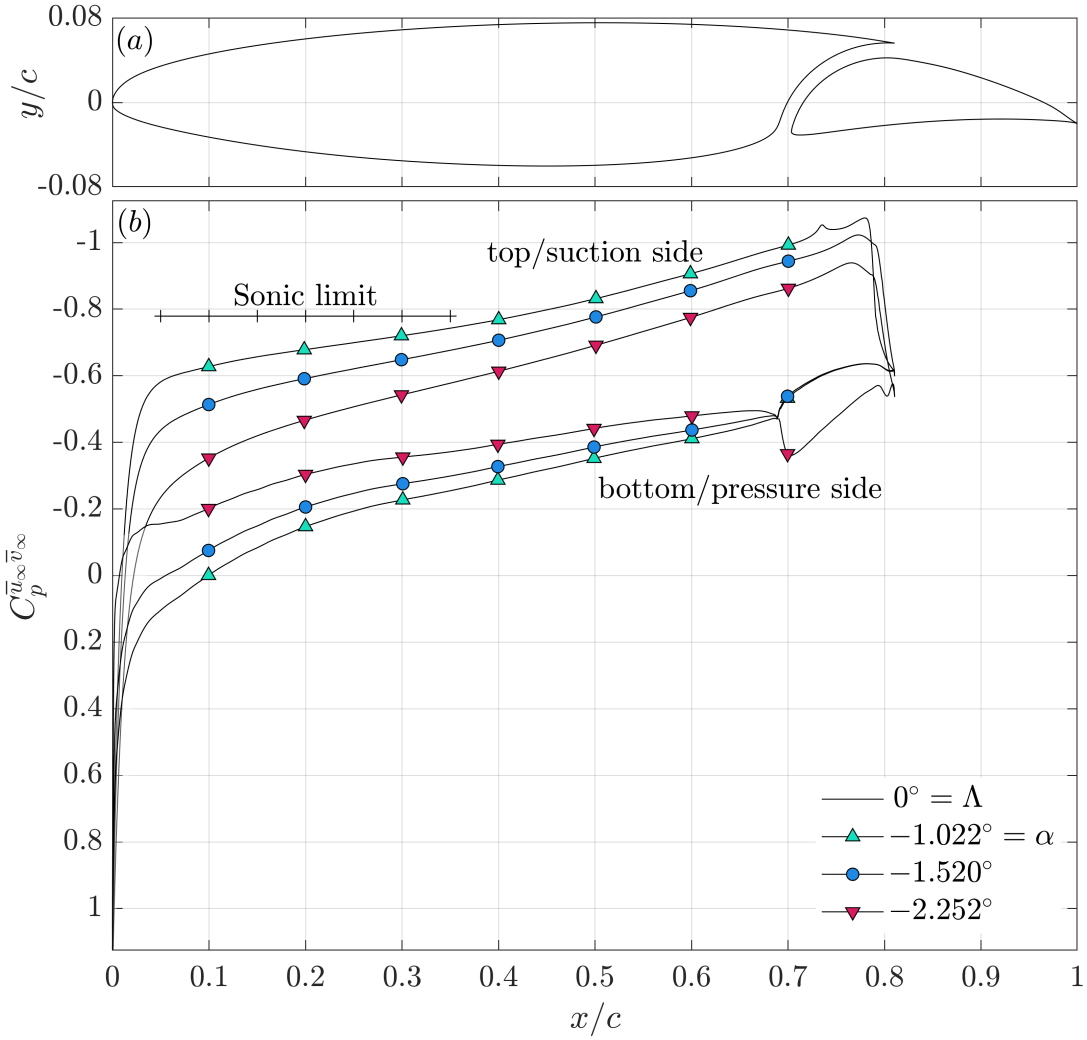

Figure 7.1: a) The S207 airfoil cross-section b) Pressure coefficient $C_p^{\overline{u}_\infty \overline{v}_\infty}$ as a function of x/c at sweep $\Lambda = 0^\circ$ for the fore element as calculated by OVERFLOW. The sonic limit indicates when the boundary-layer-edge velocity is equal to the speed of sound. Angles of attack $\alpha = \{-1.022^\circ, -1.520^\circ, -2.252^\circ\}$ are delineated with markers.

7.2 Laminar base flow

The generation of the viscous boundary layer follows a similar methodology as performed before for the X207.LS, described in Chapter 6. The pressure coefficient is provided by an OVERFLOW CFD solution (as opposed to MSES) at $\Lambda = 0°$. The OVERFLOW solution was computed by Dr. James G. Coder from University of Tennessee at Knoxville. A leading-edge-parallel velocity component $\overline{w}_\infty$ is provided in the freestream within DEKAF to apply sweep to the wing. This methodology was chosen, as some S207 simulations at appreciable sweep could not converge given all the complications: transonic flow, the complex configuration of the slot geometry and internal flow dynamics, the delicate interplay between computing laminar flow versus tripping turbulence—to name a few.

7.2.1 Simulation inputs

Freestream conditions were chosen assuming 44,000 ft altitude cruise. From standard look-up tables, this yields a temperature $T_\infty = 216.65\,\mathrm{K}$ and pressure $p_\infty = 15.4738\,\mathrm{kPa}$. The dimensional chord is restrained from a prescribed Reynolds and Mach number at a given altitude. With the design Reynolds $\mathrm{Re}_c^{\overline{u}_\infty \overline{v}_\infty} = 13.2 \times 10^6$ and Mach $\mathrm{M}_{\overline{u}_\infty \overline{v}_\infty} = 0.70$, the chord reference length is $c \approx 3.65084\,\mathrm{m}$. This calculation presumes specific constants for Sutherland's law: the reference temperature is $T_\mathrm{ref} = 273.15\,\mathrm{K}$, reference dynamic viscosity as $\mu_\mathrm{ref} = 1.716 \times 10^{-5}\,\mathrm{kg/m\text{-}s}$, and Sutherland's temperature $S_\mu = 110.6\,\mathrm{K}$. The specific gas constant used is $R_g = 287.058\,\mathrm{J/kg\text{-}K}$ and the constant Prandtl number is $\mathrm{Pr} = 0.72$, leveraged to compute thermal conductivity $\kappa = \mu\, c_p/\mathrm{Pr}$.

All inputs related to numerics for the viscous boundary-layer solutions of the S207 are identical to that of the X207.LS analysis presented previously in Chapter 6. For brevity, they are omitted.

7.2.2 Convergence in self-similar coordinate ξ

For a high sweep case of $\Lambda = 20°$ and two angles of attack of $\alpha = -1.022°$ and $-2.252°$, let us consider convergence in the self-similar ξ coordinate from the DEKAF solutions. The base streamwise resolution is selected as $N_\xi = 2000$ and the reference solution has $N_{\xi,\mathrm{ref}} = 3999$. The

specific value of 3999 is selected because it is equal to $N_{\xi,\text{ref}} = 2N_\xi - 1$, and since the computational domains are produced with the same streamwise mapping parameters, the two grids will share *every other* streamwise node identically. The same pattern holds for $N_{\xi,\text{ref}} = 3N_\xi - 2$: every *third* streamwise node is identical between the grids, and et cetera for higher integers. This is an incredibly useful technique to demonstrate convergence because the difference between solutions does not demand any interpolation on the common nodes. This convergence methodology has been performed in the past successfully on a swept, NLF airfoil, revealing the prescribed, fourth-order streamwise accuracy of these DEKAF solutions [97].

Figures 7.2 and 7.3 demonstrate the ξ-convergence for various essential parameters of the boundary-layer solution. The vertical axis demonstrates a relative error between the base resolution and the reference resolution, while the horizontal axis shows the x/c of the wing. For clarity, the relative error for a quantity $\overline{\phi}$ is defined as

$$\epsilon(\overline{\phi}) = \frac{\left|\overline{\phi}_{\text{base}} - \overline{\phi}_{\text{ref}}\right|}{\left|\overline{\phi}_{\text{ref}}\right|} \tag{7.1}$$

Here, $\overline{\phi}_{\text{base}}$ refers to $\overline{\phi}$ evaluated on the base $N_\xi = 2000$ grid whereas $\overline{\phi}_{\text{ref}}$ refers to that of the reference solution evaluated on the base grid nodes (via the $2N_\xi - 1$ pattern as described before). The quantity $\overline{\phi}$ is selected as a) the shape-factor H, b) the shear at the wall expressed in self-similar variables $\partial^2 f/\partial\eta^2|_w$, and c) the extremum of the crossflow velocity within the boundary layer $\overline{w}_{s,\max}$.[1] The relative errors are $O(10^{-6})$ or lower for the majority of the chord. The regions with worse error are not relevant for stability analysis. These intervals are a) $x/c > 0.73$ for the top side at $\alpha = -1.022°$, as flow structures develop in front of the shock on the wing here, inducing a sudden acceleration and deceleration; and b) $x/c > 0.65$ for the bottom side, as the flow enters the slot of the SNLF which is beyond the scope of this present analysis. These levels of error are considered appropriate, so the $N_\xi = 2000$ baseline streamwise resolution is used for the following

[1]When finding the extremum of the crossflow velocity, care must be taken according to side of the wing the boundary layer is on. For instance, on the top/suction side, $\overline{w}_s$ is negative for positive sweep. Then the minimum signed value of $\overline{w}_s$ is used for the relative error. The opposite is true for the bottom/pressure side: the maximum signed value of $\overline{w}_s$ is selected.

stability analysis for all sweep and angles of attack.

Once the boundary layer approaches a strong adverse gradient, the boundary-layer code begins to diverge suddenly—This divergence is often referred to as the Goldstein singularity [54]. If this occurs before the end of the domain, the grid is consequently truncated, resulting in points fewer than the base resolution of $N_\xi = 2000$. For instance, for sweep $\Lambda = 20^\circ$ at angle of attack $\alpha = -1.022^\circ$, the presence of the shock in the OVERFLOW solution causes DEKAF to halt prematurely with 1867 points in the streamwise domain.

7.3 Stability analysis at $\Lambda = 15^\circ$ for $\alpha = -1.022^\circ$

For the first set of analysis on the S207, consider the most positive angle of attack along the twist at design conditions: $\alpha = -1.022^\circ$. Following the linear analysis of Heston with the conservative critical N-factors, this configuration at $\Lambda = 15^\circ$ was deemed critical for potential nonlinear interaction. This sweep and angle of attack on top side then is the subject of the first stability section.

7.3.1 Computational grid

The base-flow from DEKAF is first spline-interpolated (not-a-knot) in s onto a selected s-resolution, N_s. For this problem, no streamwise clustering is used, i.e., s is equispaced. Then the solution is spline-interpolated onto the wall-normal y domain, where the clustering height is chosen to be $y_i = 7\delta_{50}$, where $\delta_{50} \equiv \overline{u}/\overline{u}_e \approx 0.50$. Extending this clustering height y_i above the usual δ_{99} is critical for subsonics to capture the shape of the disturbance as it extends into the freestream, especially for the local maximum of $|\hat{v}|$. The distribution of δ_{50} is first fit with a 6^{th}-order polynomial, then y_i is constructed. The edge of the domain is then computed as $y_{\max} = 40y_i$, permitting sufficient space in the freestream for the disturbance to smoothly decay toward zero.

7.3.2 Differentiation schemes

Differentiation of the base-flow uses second-order accurate, central, regular finite differences in the streamwise s direction, while it drops to first-order accurate, one-sided at the boundaries. In the wall-normal logical coordinate η, the base-flow quantities are discretized using fourth-order ac-

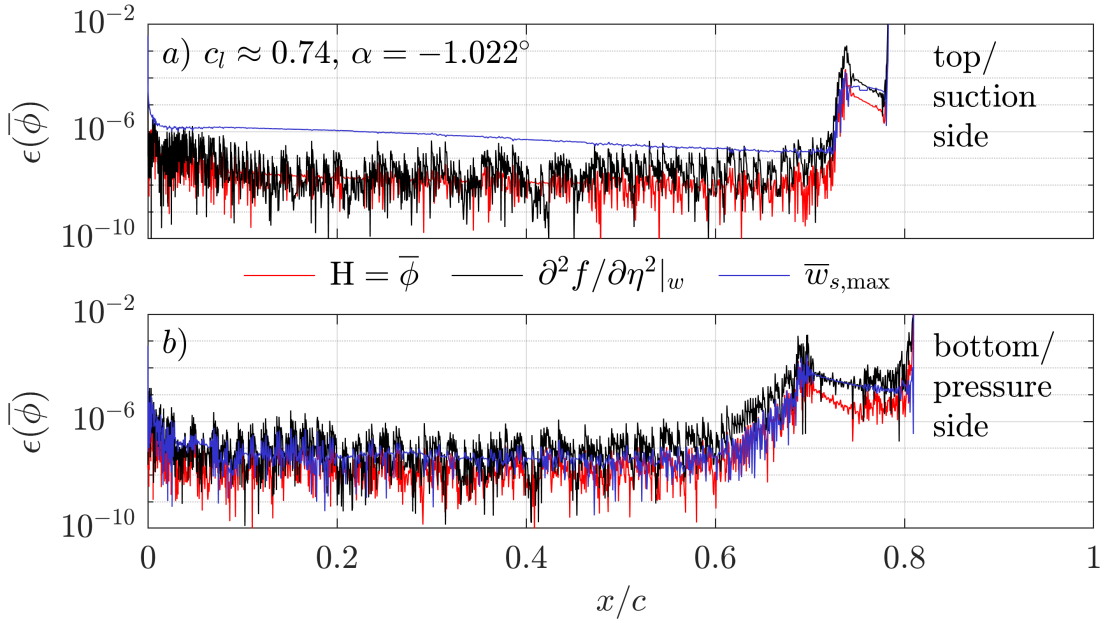

Figure 7.2: Convergence of DEKAF boundary-layer solution in self-similar streamwise coordinate ξ on the S207 at $\alpha = -1.022°$ and $\Lambda = 20°$. Relative errors are shown between the base resolution of $N_\xi = 2000$ and the reference resolution $N_{\xi,\text{ref}} = 3999$ for various boundary-layer properties—the shape-factor H, the shear at the wall $\partial^2 f/\partial\eta^2|_w$, and the extremum of crossflow velocity $\overline{w}_{s,\max}$.

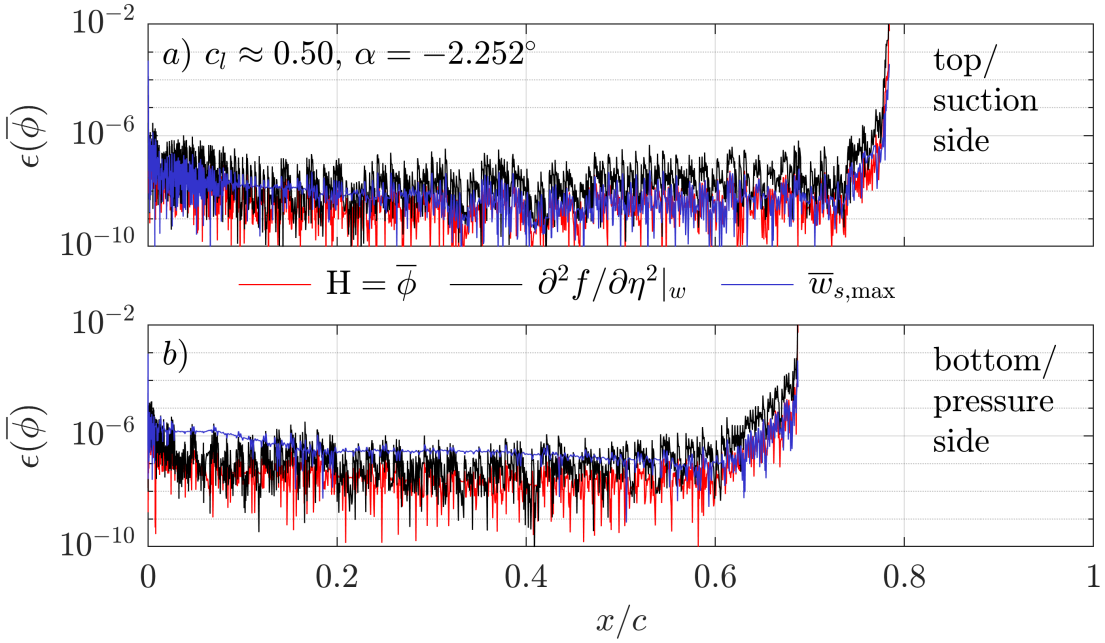

Figure 7.3: Continuation of Fig. 7.2 at $\alpha = -2.252°$

curate polynomial differentiation schemes described by Weideman & Reddy [99, §2]. The derivatives of the shape function $\hat{q}_{(n,k)}$ in the wall-normal direction use the same fourth-order accurate polynomial differentiation, while the streamwise differentiation must be backward. To avoid the ill-posedness of PSE, a first-order, backward regular finite difference scheme is used for this problem.

7.3.3 Boundary conditions

For each Fourier mode, the disturbance is assumed to satisfy no-slip and no-penetration at the surface: $u'_{(n,k)}(s,0) = 0$, $v'_{(n,k)}(s,0) = 0$, and $w'_{(n,k)}(s,0) = 0$. This translates into the shape-function components obtaining a zero value at the wall, also referred to as a homogeneous Dirichlet condition: $\hat{u}_{(n,k)}(s,0) = 0$, $\hat{v}_{(n,k)}(s,0) = 0$, and $\hat{w}_{(n,k)}(s,0) = 0$. The temperature boundary condition of each unsteady Fourier mode $(n \neq 0)$ is asserted to be isothermal, whereas stationary Fourier modes are presumed to be adiabatic. The density boundary condition of each Fourier mode at the surface is given through a compatibility condition satisfying y-momentum.

For the freestream boundary conditions, all disturbances are presumed to decay to zero for velocity and temperature components. The density perturbation is presumed to satisfy continuity in the freestream as a compatibility condition. As an exception to the above boundary conditions, the mean-flow distortion Fourier mode $(0,0)$ is handled specially in the freestream. Its $\hat{v}_{(0,0)}$ component must be allowed to be nonzero, so a homogeneous Neumann condition is applied to accomplish this.

7.3.4 Initial conditions via linear analysis

Since the objective of this analysis is to assess nonlinearities of multiple linear mechanisms simultaneously, we first consider the most linearly amplified content based on Chu-norm LPSE N-factors. This content will serve as the initial condition for marching the NPSE disturbance downstream by providing finite amplitudes to the various mechanisms of interest.

- SCF: $(f, \lambda_z) = (0\,\mathrm{Hz},\ 24\,\mathrm{mm})$
- TCF: $(f, \lambda_z) \approx (900\,\mathrm{Hz},\ 25\,\mathrm{mm})$ [147].

- 3D TS: $(f, \lambda_z) = (2300\,\mathrm{Hz},\ \pm 35\,\mathrm{mm})$
- $\beta = 0$ TS: $(f, \lambda_z) = (2700\,\mathrm{Hz},\ \infty)$

In transition processes on swept wings with significant TS growth, subharmonics too can play an important role. The subharmonics can resonant nonlinearly with the fundamental disturbance, supplying additional growth and ultimately breaking down the laminarity of the flowfield if amplitudes are sufficiently high. See [115] for an analysis on a swept wing in cruise demonstrating a subharmonic breakdown process and [148] for an overview of secondary linear stability theory. For this case, it is appropriate to also consider the presence of subharmonics in the flowfield for the various TS content mentioned above:

- 3D TS subharmonics: $(f, \lambda_z) = (1150\,\mathrm{Hz},\ \pm 70\,\mathrm{mm})$
- $\beta = 0$ TS subharmonic: $(f, \lambda_z) = (1350\,\mathrm{Hz},\ \infty)$

The goal of the present computation is to include all of these mechanisms simultaneously such that if there is an interaction between the disparate mechanisms, the nonlinear simulation will capture it. However, the specific content of the mechanisms considered must be adjusted slightly such that the discrete number of Fourier modes necessary to describe all content is low for reasonable computation time. For example, the greatest common divisor of the frequencies $[900, 2300, 2700]$ Hz is 100, since 23 is prime. That necessitates $\omega_0 \equiv 2\pi \times 100\,\mathrm{rad/s}$, and subsequently, an $n = 27$ would be needed to obtain the fundamental $\beta = 0$ TS disturbance. Assigning $N = 27$ is quite a laborious computation needed to describe the interaction between the linearly most amplified a) TCF, b) 3D TS, and c) $\beta = 0$ TS. Therefore, an approximation on the content's λ_z and f must be made to consider the simultaneous interaction. An outline is given below, homogenizing the content's wavenumbers to be small integer multiples of one another.

1. Consider TCF with the same λ_z as SCF, that is, TCF: $(f, \lambda_z) = (900\,\mathrm{Hz},\ 24\,\mathrm{mm})$.
2. Consider the 3D TS λ_z such that its β is simply related to crossflow wavelength: $(f, \lambda_z) = (2300\,\mathrm{Hz},\ \pm 36\,\mathrm{mm})$ instead of the linearly most amplified $35\,\mathrm{mm}$. With this adjustment,

$\beta_0 \equiv 2\pi/72\,\mathrm{rad/mm}$, such that the SCF Fourier mode of $24\,\mathrm{mm}$ can be described as the $(0, 3)$.

3. Consider the $\beta = 0$ TS frequency equal to that of the 3D TS. This choice is made instead of setting the 3D TS frequency equal to that of the $\beta = 0$ TS because the flowfield is three-dimensional, and the growth out of the 3D TS is greater than that of the $\beta = 0$ TS. Now, $\beta = 0$ TS: $(f, \lambda_z) = (2300\,\mathrm{Hz},\, \infty)$ instead of the linearly most amplified $2700\,\mathrm{Hz}$.

4. To homogenize the TS and TCF frequencies appropriately while also accounting for the subharmonic content, the TCF frequency here may be assumed to be equal to the subharmonic TS frequency. Both can be shifted such that their frequencies are $1100\,\mathrm{Hz}$. This results in five changes to the system's content:

   (a) $\beta = 0$ TS: $(f, \lambda_z) = (2200\,\mathrm{Hz},\, \infty)$ instead of the prior $2300\,\mathrm{Hz}$

   (b) 3D TS: $(f, \lambda_z) = (2200\,\mathrm{Hz},\, \pm 36\,\mathrm{mm})$ instead of the prior $(f, \lambda_z) = (2300\,\mathrm{Hz},\, \pm 36\,\mathrm{mm})$

   (c) TCF: $(f, \lambda_z) = (1100\,\mathrm{Hz},\, \pm 24\,\mathrm{mm})$ instead of the prior $(f, \lambda_z) = (900\,\mathrm{Hz},\, \pm 24\,\mathrm{mm})$

   (d) 3D TS subharmonics: $(f, \lambda_z) = (1100\,\mathrm{Hz},\, \pm 72\,\mathrm{mm})$ instead of the prior $(f, \lambda_z) = (1150\,\mathrm{Hz},\, \pm 72\,\mathrm{mm})$

   (e) $\beta = 0$ TS subharmonic: $(f, \lambda_z) = (1100\,\mathrm{Hz},\, \infty)$ instead of the prior $1150\,\mathrm{Hz}$.

With these adjustments, in summary, $\omega_0 \equiv 2\pi \times 1100\ \mathrm{rad/s}$ and $\beta_0 \equiv 2\pi/72\ \mathrm{rad/mm}$ such that the entire system's extent can be described with small, integer wavenumber multiples of $n = 2$ and $k = 3$. In other words, the baseline resolution of harmonics in the Fourier space then can be described with $N = 2$ and $K = 3$, such that the double-sum of the NPSE ansatz produces $(2N + 1)(2K + 1) = 35$ Fourier modes. Since there is no spanwise symmetry of the disturbance in a three-dimensional boundary layer, the number of Fourier modes needed to be calculated in a simulation is $(N + 1)(2K + 1) - K = 18$, while the other subset of 17 is computed through complex-conjugate relations. A chart of these various subsets of Fourier modes is shown in Fig.

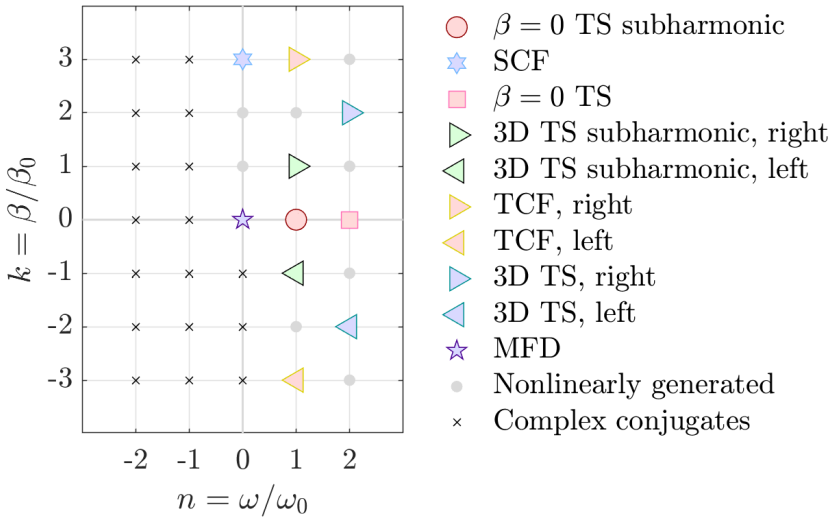

Figure 7.4: Sketch of discretized nk-Fourier space, where $\omega_0 \equiv 2\pi \times 1100$ rad/s and $\beta_0 \equiv 2\pi/72$ rad/mm. The various families of the linearly most amplified content, or signature Fourier modes, are highlighted as Tollmien-Schlichting (TS), crossflow, both stationary and traveling (SCF/TCF), and subharmonics of TS. Nonlinearly generated Fourier modes computed in NPSE are shown with gray circles, while Fourier modes computed through complex-conjugate relations are shown in black $\times$ markers. For this sketch, $N = 2$ and $K = 3$.

7.4, highlighting the signature modes that initialize the simulation and delineating the nonlinearly generated Fourier modes from the complex conjugates.

LST is computed for each of these effective wavenumbers $\beta = k\beta_0$ and $\omega = n\omega_0$ for a resulting $\alpha_{(n,k)}$ and $\hat{q}_{(n,k)}$. A Krylov subspace dimension of 90 is used for the local eigenvalue problem. The solutions are then purified/confirmed up to a tolerance of 10^{-11} satisfying the governing LST equations.

For these initial calculations, the phases (i.e., complex arguments) of these $\hat{q}_{(n,k)}$ are left arbitrary from the resulting eigensolution. The $\alpha_{(n,k)}$ of the nonlinearly generated Fourier modes are initialized through Eq. (4.46), only taking the real part.

The streamwise wavenumbers of these nonlinearly generated Fourier modes are left constant and out of the convergence criteria of the system until the 10^{th} streamwise index while the signature Fourier modes resolve their spatial transient from the LST solution to satisfying the PSE system. The mean-flow distortion is left out of the convergence criteria until the 12^{th} streamwise index.

These indices of 10 and 12 which delay convergence are chosen to be slightly larger than usual values (5 and 7, respectively) due to this case's particularly high initial amplitude (discussed in the section §7.3.6.)

7.3.5 PSE numerics

For these simulations, all slowly varying viscous terms are retained in the system, as neglecting them is an unnecessary simplification and reduction of accuracy. These terms include products such as $1/\mathrm{Re}\,\frac{\partial \alpha_{(n,k)}}{\partial s}$, or mixed derivatives like $1/\mathrm{Re}\,\frac{\partial^2 \hat{v}_{(n,k)}}{\partial s\,\partial y}$ found in viscous dissipation.

These simulations fully incorporate the term $\partial \hat{p}_{(n,k)}/\partial s$ for the unsteady Fourier modes, while the stationary Fourier modes' streamwise shape-function pressure gradients are eliminated. In other words,

$$\Omega_p = \begin{cases} 1, & n \neq 0 \\ 0, & n = 0 \end{cases} \tag{7.2}$$

While including the term fully for the unsteady Fourier modes does limit the available s-resolution, excluding the term, i.e., $\Omega_p \equiv 0$ for all (n, k), does have an appreciable effect on the amplitude distributions. Therefore, to strive for physical accuracy, the term is kept in the following analysis.

The auxiliary condition considered is based on the sum of the components of the nondimensional shape-function $\hat{q}_{(n,k)}$, whose convergence criterion is based on the absolute iterative error of $|\Delta\alpha_{(n,k)}| < 10^{-8}$. The nonlinear iterative loop's convergence criterion is a relative error of 10^{-8} across all of the computed Fourier modes.

The mean-flow distortion $\alpha_{(0,0)}$ is kept purely zero throughout the simulation [101]. Trial runs were performed with purely imaginary $\alpha_{(0,0)}$ for this case, and as the mean-flow distortion stabilized near the aft of the domain, its α-convergence rate would slow drastically compared to that of the other Fourier modes in the system, requiring hundreds, if not more, iterations. For other initial conditions, solution divergence was observed soon after including the mean-flow distortion in the nonlinear convergence criterion. In the spirit of computational efficiency and robustness,

$\alpha_{(0,0)}$ is asserted to be zero. Recall that it is consistent by an order-of-magnitude scaling argument to also zero the s-derivatives of $\hat{v}_{(0,0)}$ if $\alpha_{(0,0)}$ = 0: see Eq. (4.60). That is not performed for these calculations. It is an unneeded reduction of the problem at hand as NPSE converges well still with the inclusion of these s-derivatives of $\hat{v}_{(0,0)}$. In spite of that, trial runs again show that the inclusion of terms with s-derivatives of $\hat{v}_{(0,0)}$ has an appreciably small effect once $\alpha_{(0,0)}$ = 0, as expected.

7.3.6 Baseline NPSE solution at high initial amplitudes

In order to bring about nonlinear effects present in this flowfield, very high amplitudes are first applied as this problem's baseline case. Note that these high amplitudes are likely not representative of those observed in cruise (e.g., ATTAS cruise tests achieving TS amplitudes of 10^{-6} [115]). It is used as a test case of the NPSE mixed-mode capability of EPIC on infinite swept wings at low sweep.

The baseline initial amplitude is $A_{0\,(n,k)} \equiv \max_y |u'_{(n,k)}|/\overline{u}_{\text{ref}} = 3.16 \times 10^{-2}$, where $\overline{u}_{\text{ref}} \approx 255.8\,\text{m/s}$.[2] This initial amplitude is applied to the initialized signature Fourier modes at $x/c = 0.03$. That is to say, it is applied to the crossflow modes $(0,3)$, $(1,\pm3)$; the Tollmien-Schlichting modes $(2,0)$, $(2,\pm2)$; and the TS subharmonics $(1,0)$, $(1,\pm1)$. Figure 7.5 shows the $\max_y |u'_{(n,k)}|$ amplitudes of each Fourier mode nondimensionalized by the freestream resultant velocity $Q_\infty \approx 213.8\,\text{m/s}$. Figure 7.6 shows the components of phase velocity $\vec{c}_{ph\,(n,k)}$ for the unsteady Fourier modes rotated into a frame aligned with the local inviscid streamline. The definition of the three-

[2]This source of this value is the $\overline{u}$ quantity at the last (farthest from the wall) wall-normal node at the first streamwise index of the input basic-state from DEKAF. It is only used in EPIC for nondimensionalization purposes, and is a useful methodology for different geometries across all flow regimes. Note that it is larger than Q_∞ because of the presence of a favorable pressure gradient $\mathrm{d}\overline{p}/\mathrm{d}s < 0$ accelerating the local flowfield.

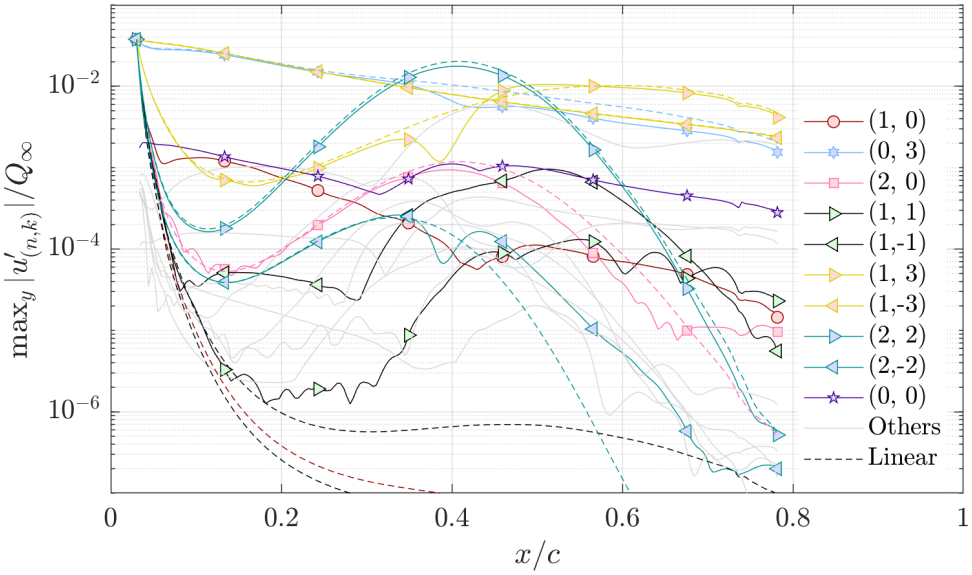

Figure 7.5: Amplitude distributions of various Fourier modes against x/c for the baseline S207 $\alpha = -1.022°$, $\Lambda = 15°$ case on the top side. The signature Fourier modes are shown in color with a prescribed marker, while their linear behavior is indicated by dashed lines of the same color. The nonlinearly generated Fourier modes are shown in gray.

dimensional phase velocity used here is

$$
\begin{aligned}
\vec{c}_{ph\,(n,k)} &= c_{ph,s\,(n,k)}\vec{e}_s + c_{ph,z\,(n,k)}\vec{e}_z = c_{ph,\overline{u}_s\,(n,k)}\vec{e}_{\overline{u}_s} + c_{ph,\overline{w}_s\,(n,k)}\vec{e}_{\overline{w}_s}, \\
c_{ph,s\,(n,k)} &= \text{Real}\left(\frac{\alpha_{(n,k)}\omega_{(n,k)}}{\alpha^2_{(n,k)} + \beta^2_{(n,k)}}\right), \\
c_{ph,z\,(n,k)} &= \text{Real}\left(\frac{\beta_{(n,k)}\omega_{(n,k)}}{\alpha^2_{(n,k)} + \beta^2_{(n,k)}}\right), \\
c_{ph,\overline{u}_s\,(n,k)} &= c_{ph,s\,(n,k)}\cos(-\psi_s) - c_{ph,z\,(n,k)}\sin(-\psi_s), \\
c_{ph,\overline{w}_s\,(n,k)} &= c_{ph,s\,(n,k)}\sin(-\psi_s) + c_{ph,z\,(n,k)}\cos(-\psi_s), \\
\psi_s &= \arctan\frac{\overline{w}_{\delta_{99}}}{\overline{u}_{\delta_{99}}}
\end{aligned}
\tag{7.3}
$$

where $\beta_{(n,k)} = k\beta_0$ and $\omega_{(n,k)} = n\omega_0$, taken from [117, Eq. 2.29]. The quantities $\overline{u}_s$ and $\overline{w}_s$ indicate the velocity components that are parallel/orthogonal to the local inviscid streamline, respectively. The subscript δ_{99} indicates the value was selected at a spline-interpolated height for δ_{99}. That is,

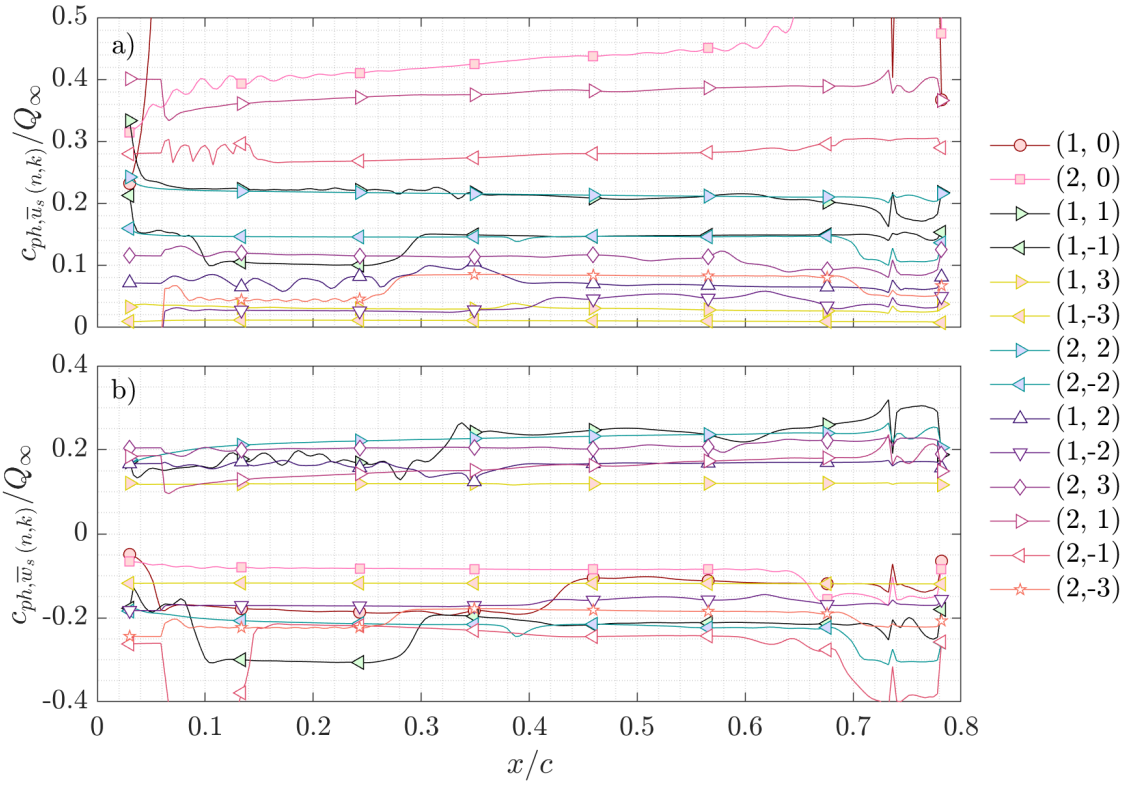

Figure 7.6: Phase-velocity components of the unsteady Fourier modes in the a) inviscid-streamline-parallel and b) inviscid-streamline-orthogonal directions: see Eq. (7.3). Signature modes are prescribed a filled-in marker, while the markers of nonlinearly generated modes are left unfilled.

$\overline{u}_{\delta_{99}}/\overline{u}_e = 0.99$. This rotation is performed such that the streamwise Fourier modes possess phase speed values near $c_{ph,\overline{u}_s\,(n,k)}/Q_\infty = 0.3$. The unsteady crossflow-like Fourier modes have much smaller values for $c_{ph,\overline{u}_s\,(n,k)}/Q_\infty$—near or less than 0.1 for these cases.[3]

There are many rich physics that can be discussed and parsed from the above case. For one, let us start with the 3D subharmonics. The 3D TS subharmonics $(1, \pm 1)$ show considerable deviation from their linear behavior early on. Consider the phase speed components of the left 3D TS subharmonic $(1, -1)$. Between $x/c = 0.25$ and 0.30, the inviscid-streamline-orthogonal component $c_{ph,\overline{w}_s\,(1,-1)}$ increases abruptly from a value of -0.3 to nearly -0.2. In this process, it overshoots the phase speed component of its fundamental $c_{ph,\overline{w}_s\,(2,-2)}$ and by $x/c \approx 0.42$, the phase speeds

[3]Note that the simple methodology initializing $\alpha_{(n,k)}$ for these nonlinearly generated Fourier modes of Eq. (4.46) can produce an initial guess where $c_{ph,\overline{u}_s\,(n,k)} < 0$. For this case, this is true for the $(1, -2)$ Fourier mode, although it is quickly corrected to be positive once it is a part of the convergence criteria of the computation.

between the subharmonic and the fundamental are nearly equal, i.e., $c_{ph,\overline{w}_s\,(1,-1)} \approx c_{ph,\overline{w}_s\,(2,-2)}$. The inviscid-streamline-parallel component $c_{ph,\overline{u}_s\,(1,-1)}$ has the same behavior. The phase speed 'locking' that occurs near $x/c \approx 0.29$ is associated with a sudden large increase in the amplitude of the subharmonic $(1,-1)$. The subharmonic experiences resonance and its amplitude increases at approximately twice the rate of the fundamental's until the subharmonic's amplitude exceeds it near $x/c \approx 0.35$. At this point, the subharmonic approaches the amplitude of the mean-flow distortion $(0,0)$ and begins to weakly interact until both are stabilized downstream at the low amplitude of $\max_y |u'_{(0,0)}|/Q_\infty \approx 10^{-3}$.

A similar trend is observed with the $(2,2)$ right 3D TS and its subharmonic $(1,1)$, resonating near $x/c \approx 0.31$. However, this resonance is not as strong as the left 3D TS pair. This is indicated by the subharmonic's phase speed components oscillating about those of the fundamental. This is known as 'detuning'—when conditions alternate between optimally and suboptimally exchanging energy between the subharmonic and the fundamental; and for optimal energy exchange, phase speeds must be equal [148].

The phase speed is only one component of this interaction however. Another critical part is the phase of the Fourier modes themselves, that is, how the wave is oriented in space. This can be represented by the complex argument of the Fourier mode's shape function. Here, phase $\varphi_{(n,k)}$ is defined through the $\hat{u}$ component as

$$\varphi_{(n,k)} = \arctan2\left(\mathrm{Imag}(\hat{u}_{\max\,(n,k)}), \mathrm{Real}(\hat{u}_{\max\,(n,k)})\right) \tag{7.4}$$

where $\hat{u}_{\max\,(n,k)}$ indicates the complex value of $\hat{u}_{(n,k)}$ evaluated at the y-location of its largest magnitude $|\hat{u}_{(n,k)}|$. As the shape-function varies downstream, this global maximum may abruptly shift in height, as multiple lobes of energy in the y-profile ebb and flow. According to secondary instability theory, not only do phase speeds must be equal, but phases must align as well [148]. A natural question is, at what phase difference does resonance occur? Consider the quadratic nonlinear interaction between the subharmonic and the fundamental: $(n/2,k/2)+(n/2,k/2)=(n,k)$. Since

the disturbance quantities are multiplied in these nonlinear forcing terms, e.g., $u'_{(1,1)}\,\partial u'_{(2,2)}/\partial s$, the phases add. So from the above quadratic interaction, it is observed that if the subharmonic $(n/2, k/2)$ differs in phase by $\pm 180^\circ$ with respect to the fundamental (n, k), then the forcing will constructively align in space, inducing resonance. Similarly, if the phases differ by $\pm 90^\circ$, then the forcing is deconstructive, inducing anti-resonance [149].

Figure 7.7 shows the phase distributions and differences of the fundamental 3D TS Fourier modes and their subharmonics. Note that this figure's oscillatory data against x/c is expected because the shape function varies downstream such that its global maximum for $|\hat{u}|$ abruptly shifts in height. Lobes of energy modulate the disturbance shapes while advecting downstream.

Here, the phase difference is defined as $\Delta\varphi_{(n/2,k/2)} \equiv \varphi_{(n/2,k/2)} - \varphi_{(n,k)}$ and shows for the left subharmonic $(1, -1)$, it is -180° out of phase with respect to the fundamental at $x/c \approx 0.29$: the location where its resonance begins. For the right subharmonic $(1, 1)$, the phase difference does approach $+180^\circ$ at $x/c \approx 0.29$, however resonance is not observed until $x/c \approx 0.31$. To understand this, again reconsider the phase speed component $c_{ph,\overline{w}_s\,(1,1)}$—it does not align with that of the fundamental $c_{ph,\overline{w}_s\,(2,2)}$ until $x/c \approx 0.31$. This observation is in line with Herbert's summary: that both phase and phase speed must be locked for resonance to occur.

On another note separate from subharmonic resonance, note that the amplitude of the $\beta = 0$ TS subharmonic $(1, 0)$ deviates from its linear dynamics very early upstream, as it appears to be forced by the primary resonance between the crossflow waves of high amplitude: $(0, -3)+(1, 3) = (1, 0)$. This results in very high phase speed values of $c_{ph,\overline{u}_s\,(1,0)}/Q_\infty \approx 0.9$ (not pictured) from $x/c = 0.06$ to 0.41: the latter of which correlates to the linear branch-II location of the 3D TS $(2, 2)$.

All of these interactions are examples of secondary instabilities present in boundary layers, and a thorough review of experience, experiment, and computation on the subject is given in the excellent paper by Herbert [148].

Even though these nonlinear resonances observed between the 3D TS and their subharmonics are appreciable, they are not enough even at these high initial amplitudes (and arbitrary initial phases) to cause the more amplified 3D TS $(2, 2)$ to significantly deviate from its linear dynamics.

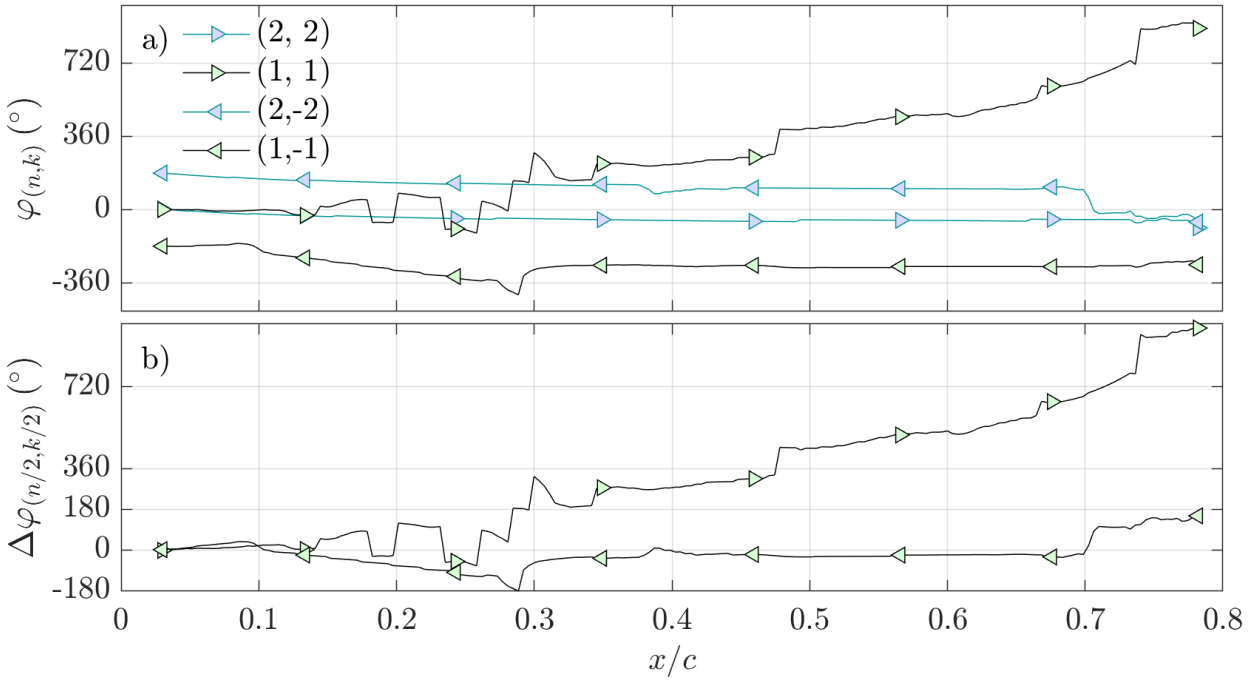

Figure 7.7: a) Phase distributions of 3D TS and their subharmonics. Phase corresponds to the complex argument of $\hat{u}_{(n,k)}$ evaluated at the y-location of its largest magnitude, see Eq. (7.4). b) Phase difference between the subharmonic and the fundamental: $\varphi_{(n/2,k/2)} - \varphi_{(n,k)}$.

With the $(2, 2)$ amplitude distribution mostly linear and the mean-flow distortion small over the wing, the flow does not appreciably deviate from its laminarity for these conditions.

The next sections will demonstrate convergence of this baseline solution in y and in s.

7.3.7 Convergence of baseline NPSE solution in wall-normal y

The convergence in y is demonstrated by considering 5 distinct wall-normal resolutions: $N_y = [150, 350]$, $\Delta = 50$ with the streamwise resolution N_s held constant at 200. The highest resolution of $N_y = 350$ is considered the reference solution since with clustering, that is nearly 175 points within the boundary layer–appropriate resolutions for compressible DNS computations [98]. The Fourier-mode amplitude distributions for the signature modes initialized by LST are shown in Fig. 7.8a. All Fourier modes of lower resolutions show good agreement with the reference solution, barring some oscillations in the $(1, 1)$ TS subharmonic at low amplitudes. At each streamwise station, the amplitude of each Fourier mode can be compared directly to the that of the reference

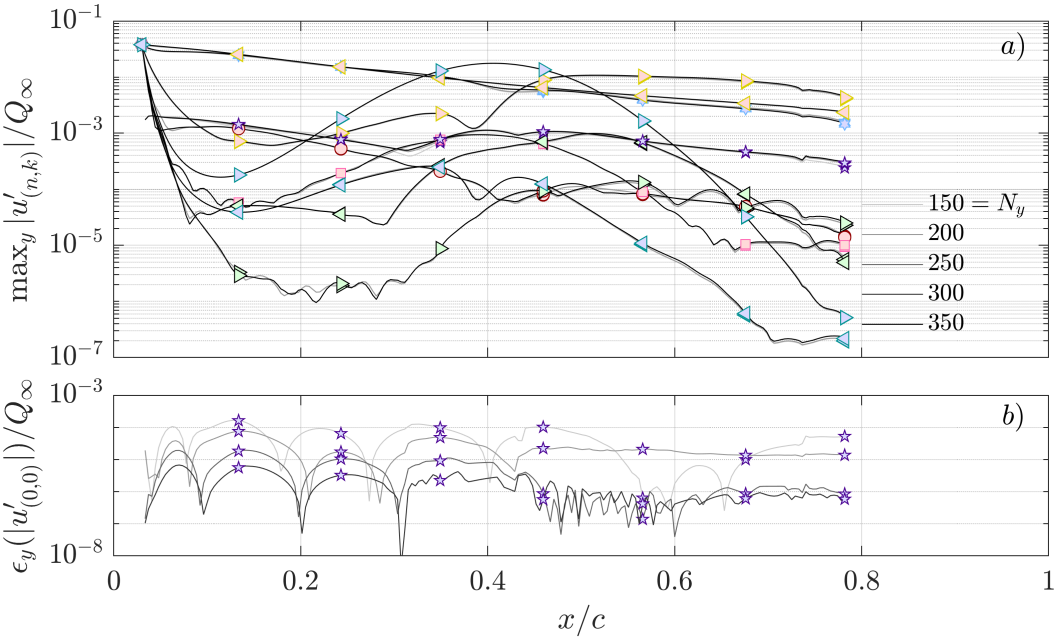

Figure 7.8: a) Amplitude distributions of the signature Fourier modes against x/c for this baseline S207 $\alpha = -1.022°$, $\Lambda = 15°$ case on the top side of the wing. Higher wall-normal resolutions are shown in darker shades of gray. Colored markers indicate which Fourier mode is which, following the same legend in Fig. 7.5. b) Error of $\max_y |u'_{(0,0)}|$ for each streamwise station compared to the reference $N_y = 350$ solution for the mean-flow distortion.

solution. For example, the error of the mean-flow distortion $(0, 0)$ in y, or ϵ_y can be defined as

$$\epsilon_y(|u'_{(0,0)}|) \equiv \max_y |u'_{(0,0)}|_{N_y} - \max_y |u'_{(0,0)}|_{\text{ref}} \tag{7.5}$$

For this equation, note that ϵ_y is a dimensional quantity. The nondimensional error with respect to the freestream resultant velocity Q_∞ is shown in Fig. 7.8b, which is mostly monotonically decreasing as N_y increases. Specifically, for resolutions higher than $N_y \geq 200$, all errors $\epsilon_y(|u'_{(0,0)}|)/Q_\infty$ are less than 10^{-4}, which is sufficient reasoning for choosing $N_y = 200$ as a baseline y-resolution for the amplitude-uncertainty study. There is a balance of accuracy and computational efficiency.

7.3.8 Convergence of baseline NPSE solution in streamwise s

Convergence of PSE solutions in the streamwise coordinate s are ill-posed, as too fine of a prescribed Δs reaches the step-size criterion. Despite this, an effort is made to show that the distur-

bance amplitudes do converge in s before the critical step size is reached. For this baseline case, the number of wall-normal points is held constant at $N_y = 200$ while $N_s = [175, 250]$ with $\Delta = 25$. The reference streamwise resolution of $N_s = 250$ is selected.

The Fourier-mode amplitude distributions for the signature modes initialized by LST are shown in Fig. 7.9a. All Fourier modes show reasonable agreement. There are higher discrepancies among the subharmonics $(1, \pm 1)$, $(1, 0)$, and the mean-flow distortion $(0, 0)$. Since the computational domains do not have the same streamwise nodes, the y-convergence methodology cannot be repeated identically. Instead, an integral quantity $\mathcal{I}(\alpha_{(n,k)})$ over the maximum shape-function magnitude is computed over the entire streamwise domain, and compared to the reference solution in a relative sense. The wavenumber $\alpha_{(n,k)}$ is selected instead of the disturbance $u'_{(n,k)}$ because the differentiation schemes are directly applied to the wavenumber and is more representative of the convergence of the solution in s. This error is shown in Fig. 7.9b for each signature Fourier mode, as well as a reference line of first-order convergence (since a first-order backward scheme is applied to the shape-function $\alpha_{(n,k)}$). The error computed matches observation of the amplitudes in Fig. 7.9a—the subharmonics have higher errors than the fundamentals. Given these errors and the observed convergence rate, $N_s = 200$ is selected as the baseline resolution.

$$\begin{aligned} \mathcal{I}(\alpha_{(n,k)}) &= \int_{s_{\text{init}}}^{s_{\text{final}}} \alpha_{(n,k)} \, \mathrm{d}s, \\ \epsilon_s(\alpha_{(n,k)}) &\equiv \frac{\left| \mathcal{I}(\alpha_{(n,k)})_{N_s} - \mathcal{I}(\alpha_{(n,k)})_{\text{ref}} \right|}{\left| \mathcal{I}(\alpha_{(n,k)})_{\text{ref}} \right|} \end{aligned} \tag{7.6}$$

Not pictured is the convergence of the nonlinearly generated Fourier modes. The errors for these Fourier modes is admittedly worse, but that is a result of the methodology of excluding them from the convergence criteria until the 10^{th} streamwise node, which varies in its physical coordinate between the cases. It is argued that changing the starting index of convergence of those nonlinearly generated Fourier modes needlessly complicates the methodology and interpreting the convergence results. Along this same line of reasoning, since the mean-flow distortion is left out of the convergence criterion until the 12^{th} streamwise node, its s-convergence results are diluted in the same

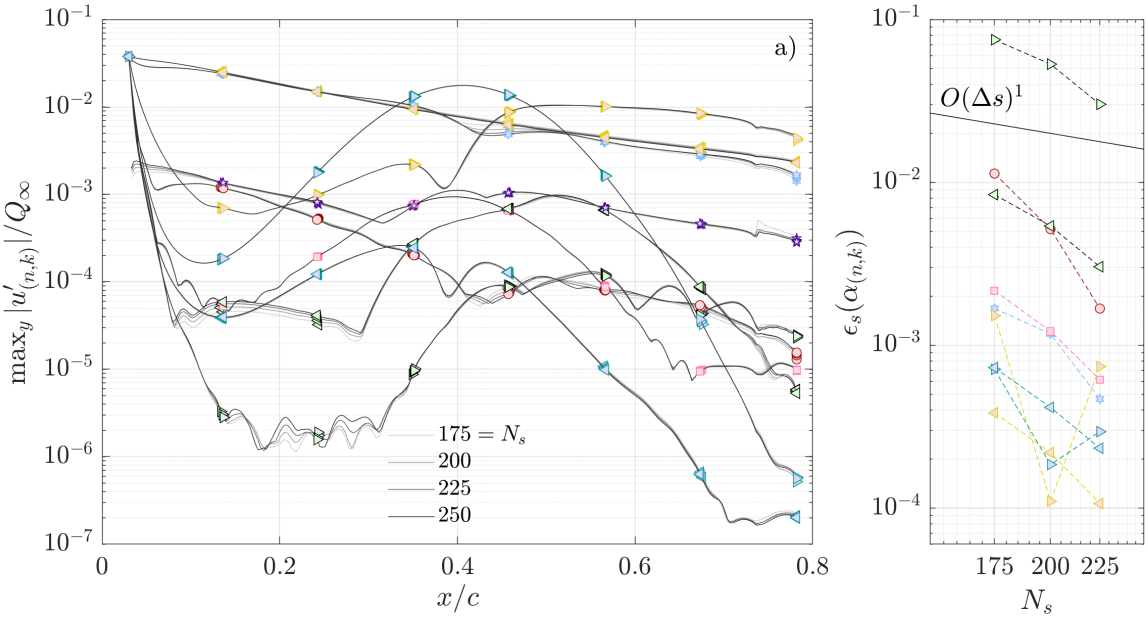

Figure 7.9: a) Amplitude distributions of the signature Fourier modes against x/c for this baseline S207 $\alpha = -1.022°$, $\Lambda = 15°$ case. Higher streamwise resolutions are shown in darker shades of gray. Colored markers indicate which Fourier mode is which, following the same legend in Fig. 7.5. b) Relative error of $\mathcal{I}(\alpha_{(n,k)})$ over s compared to the reference $N_s = 250$ solution for each signature Fourier mode. First-order backward differentiation is used, so a reference first-order convergence is shown in black.

manner. Note that this definition of error does not allow application to the mean-flow distortion. Equation (7.6) will produce zero-division for the $(0,0)$, as its $\alpha_{(0,0)}$ is purely zero. That is to say, $\epsilon_s(\alpha_{(0,0)})$ is indeterminate.

Given the strict limitation in the available streamwise resolution via $\Omega_p = 1$, the NPSE simulation with $N_s = 275$ is susceptible to the step-size limitation, and diverges soon near $x/c = 20\%$. See Fig. 7.10 below. The divergence location matches very well with the critical step size from compressible, linear theory of three-dimensional disturbances by Li & Malik [108], which can be expressed in terms of the NPSE variables.

$$\Delta s_{\text{crit}\,(n,k)} = \frac{1}{\left|\text{Real}(\alpha_{(n,k)}) + \frac{n\omega_0 \text{M}_{\text{ref}}^2 - k\beta_0 \text{M}_{\text{ref}} \text{M}_{z,\,\text{ref}}}{1-\text{M}_{\text{ref}}^2}\right|} \tag{7.7}$$

where M_{ref} and $\text{M}_{z,\,\text{ref}}$ are the local freestream Mach numbers in the streamwise and spanwise directions, respectively. The signature Fourier mode $(1,1)$ reaches this critical step size, and is the first Fourier mode to diverge in Fig. 7.10a. Two other nonlinearly generated Fourier modes do exceed their critical step size—the $(1,2)$ and the $(2,3)$; however, they do not diverge until downstream of the $(1,1)$ divergence. It is not immediately clear why these two Fourier modes do not cause divergence upstream. Note the quadratic nonlinear interactions $(1,1) + (0,1) = (1,2)$ and $(1,1) + (1,2) = (2,3)$. Perhaps the $(0,1)$ with its pressure gradient $\partial \hat{p}_{(0,1)}/\partial s = 0$ distorts the spectrum of the $(1,2)$, causing the $(1,2)$ and subsequently the $(2,3)$ to avoid the dangerous continuous branch causing divergence [108]—however, this is conjecture.

Even with high amplitudes across all Fourier modes—amplitudes likely unrealistic of usual environmental disturbances in cruise at 44,000 ft—breakdown of the laminar boundary is not observed. For this angle of attack $\alpha = -1.022^\circ$ under the modeling assumptions, the top side of the S207 will likely remain laminar and will retain the NLF benefits at $\Lambda = 15^\circ$.

7.4 Stability analysis at $\Lambda = 20^\circ$ for $\alpha = -1.022^\circ$, top side

Continuing the analysis of the S207, since the $\Lambda = 15^\circ$ case didn't indicate significant deviation from laminarity, let us increase the sweep of the wing to $\Lambda = 20^\circ$ while maintaining a constant

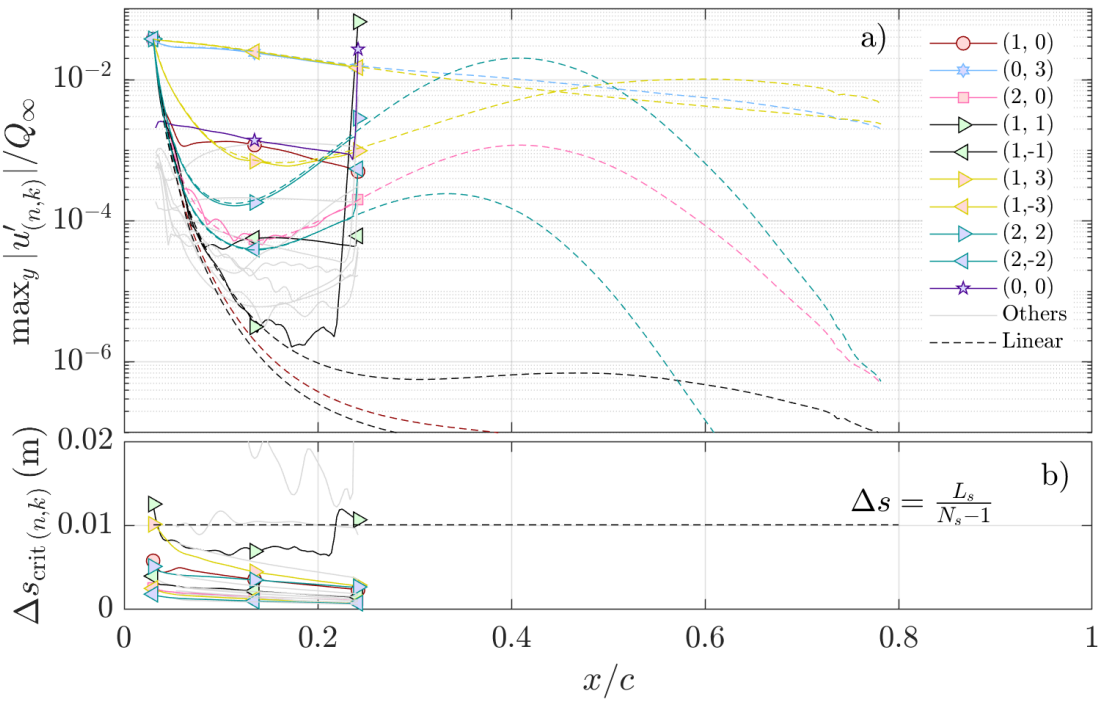

Figure 7.10: a) Amplitude distributions of the Fourier modes against x/c for $N_s = 275$. The signature Fourier modes are shown in color with a prescribed marker, while their linear behavior of $N_s = 200$ is indicated by dashed lines of the same color. The nonlinearly generated Fourier modes are shown in gray. b) The step-size criterion of (7.7) evaluated for all unsteady Fourier modes in the $N_s = 275$ simulation. The constant streamwise step Δs is shown as a solid dashed line near $0.01\,\mathrm{m}$, where L_s is the length of the streamwise domain along the surface of the wing.

velocity component in the leading-edge-orthogonal direction. In other words, the Mach number based on the leading-edge-orthogonal velocity component $\mathrm{M}_{\overline{u}_\infty \overline{v}_\infty} = 0.70$ and with sweep $\Lambda = 20°$, the Mach based on the resultant velocity is $\mathrm{M}_{Q_\infty} = \mathrm{M}_{\overline{u}_\infty \overline{v}_\infty} / \cos\Lambda \approx 0.745$.

The present case of $\Lambda = 20°$ prompts only one minute change to the input settings for the simulation when comparing with those described in previous Sec. 7.3.1, 7.3.2, 7.3.3, and 7.3.5. Instead of fitting δ_{50} with a 6^{th}-order polynomial, a 7^{th}-order polynomial is used instead.[4]

[4]For more information, polynomial orders from 1 through 20 are checked for their fit of δ_{50}. The one that minimizes the sum of the squares of the error across all streamwise nodes is selected.

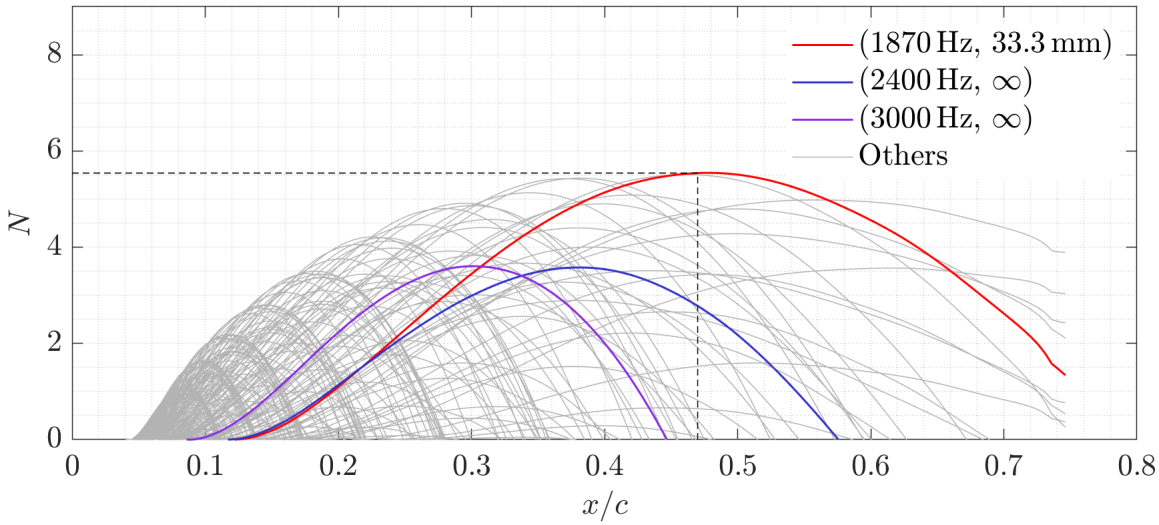

Figure 7.11: TS N-factors on the S207 $\alpha = -1.022°$, $\Lambda = 20°$ on the top side.

7.4.1 TS subharmonic resonance

7.4.1.1 Initial conditions via linear analysis

For initial conditions of the nonlinear analysis, the most linearly amplified content first must be tabulated for various instability mechanisms. Figure 7.11 shows the linear amplification of TS waves in terms of the LPSE Chu-norm N-factors while Without a transition location experimentally prescribed, $x/c = 0.47$ can be selected as the queried location due to the global maximum of 3D TS N-factor for this configuration. The maximally amplified content is $(1870\,\mathrm{Hz},\ 33.3\,\mathrm{mm})$ for 3D TS whereas $2400\,\mathrm{Hz}$ is the maximally amplified $\beta = 0$ TS. However, the disturbance of $3000\,\mathrm{Hz}$ achieves essentially the same N-factor with higher growth rates, which may induce more sudden resonance and nonlinear interaction. For that reason, $2400\,\mathrm{Hz}$ is discarded and $3000\,\mathrm{Hz}$ is the considered $\beta = 0$ TS.

The crossflow content's linear amplification is similarly shown in Fig. 7.12. The SCF disturbance of highest N-factor is $\lambda_z = 12\,\mathrm{mm}$ whereas the traveling crossflow with a maximal N-factor at the aft of the top side is $(625\,\mathrm{Hz},\ 16\,\mathrm{mm})$.

The summary of the linear amplification is itemized below:

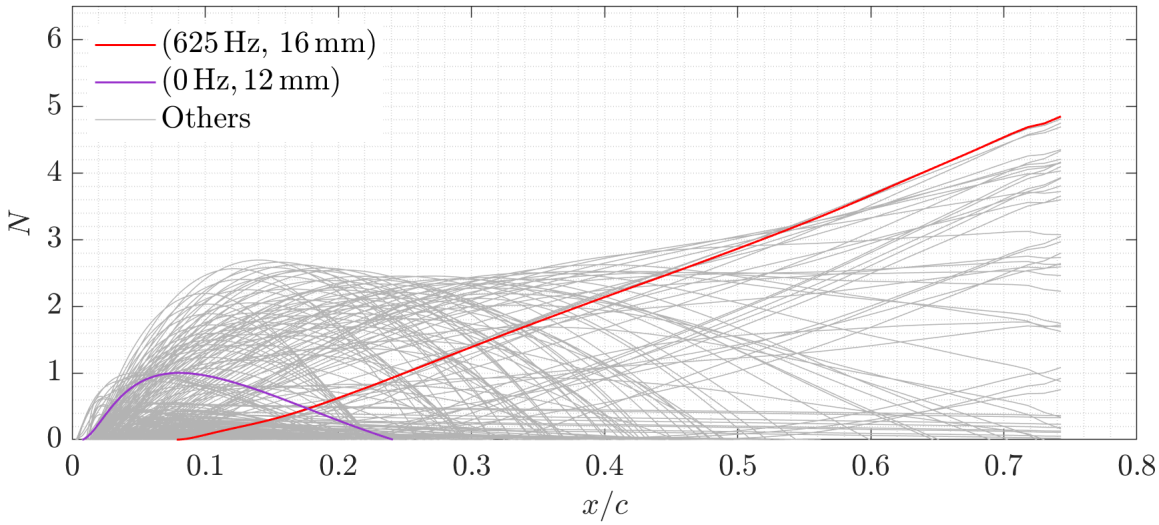

Figure 7.12: Crossflow N-factors on the S207 $\alpha = -1.022°$, $\Lambda = 20°$ on the top side.

- 3D TS: $(f, \lambda_z) = (1870\,\text{Hz},\ +33\,\text{mm})$ with an $N_{\max} = 5.5$ near $x/c = 0.47$.
- $\beta = 0$ TS: $(f, \lambda_z) = (3000\,\text{Hz},\ \infty)$ with an $N_{\max} = 3.6$ near $x/c = 0.30$.
- TCF: $(f, \lambda_z) \approx (625\,\text{Hz},\ 16\,\text{mm})$ with an $N_{\max} = 4.8$ near $x/c = 0.75$.
- SCF: $(f, \lambda_z) = (0\,\text{Hz},\ 12\,\text{mm})$ with an $N_{\max} = 1$ near $x/c = 0.10$.

Given the importance of TS subharmonics, the content is listed below while omitting their linear N-factors:

- 3D TS subharmonics: $(f, \lambda_z) = (935\,\text{Hz},\ \pm 66\,\text{mm})$
- $\beta = 0$ TS subharmonic: $(f, \lambda_z) = (1500\,\text{Hz},\ \infty)$

Performing a similar methodology from Sec. 7.3.4 to reduce the size of the discretized Fourier space,

1. Consider TCF with the same λ_z as SCF, that is, TCF: $(f, \lambda_z) = (625\,\text{Hz},\ 12\,\text{mm})$.
2. Consider the 3D TS λ_z such that its β is simply related to crossflow wavelength: $(f, \lambda_z) = (1870\,\text{Hz},\ \pm 36\,\text{mm})$ instead of the linearly most amplified $33\,\text{mm}$. With this adjustment, $\beta_0 \equiv 2\pi/72\,\text{rad/mm}$, such that the SCF Fourier mode can be described as the $(0, 3)$.

3. Consider the $\beta = 0$ TS frequency equal to that of the 3D TS. Then $\beta = 0$ TS: $(f, \lambda_z) = (1870\,\mathrm{Hz},\, \infty)$ instead of the linearly most amplified $3000\,\mathrm{Hz}$.

4. To homogenize the TS and TCF frequencies appropriately while also accounting for the subharmonic content, the TCF frequency here may be assumed to be equal to the subharmonic TS frequency. Both can be shifted such that their frequencies are $900\,\mathrm{Hz}$. This results in five changes to the system's content:

   (a) $\beta = 0$ TS: $(f, \lambda_z) = (1800\,\mathrm{Hz},\, \infty)$ instead of the prior $1870\,\mathrm{Hz}$

   (b) 3D TS: $(f, \lambda_z) = (1800, \mathrm{Hz},\, \pm 36\,\mathrm{mm})$ instead of the prior $(f, \lambda_z) = (1870\,\mathrm{Hz},\, \pm 36\,\mathrm{mm})$

   (c) TCF: $(f, \lambda_z) = (900\,\mathrm{Hz},\, \pm 12\,\mathrm{mm})$ instead of the prior $(f, \lambda_z) = (625\,\mathrm{Hz},\, \pm 12\,\mathrm{mm})$. This is now an appreciable shift in content and amplification, as the linear maximum N-factor is only 2.5 achieved near $x/c = 0.36$ for this disturbance for this oblique pair.

   (d) 3D TS subharmonics: $(f, \lambda_z) = (900\,\mathrm{Hz},\, \pm 72\,\mathrm{mm})$ instead of the prior $(f, \lambda_z) = (935\,\mathrm{Hz},\, \pm 72\,\mathrm{mm})$

   (e) $\beta = 0$ TS subharmonic: $(f, \lambda_z) = (900\,\mathrm{Hz},\, \infty)$ instead of the prior $1500\,\mathrm{Hz}$.

With this reduction prioritizing the growth of the 3D TS, the considered TCF now is much less amplified—only an $N_{\max} = 2.5$. Additionally, the location of the TCF's max N-factor is at the rear of the domain—$x/c \approx 0.75$, while the present analysis is more meaningful considering possible transition pathways that occur significantly upstream or mid-chord. For the time being, it is worth considering omitting SCF and TCF and focusing on the Tollmien-Schlichting content for subharmonic resonance and oblique pairs resonating with 2D waves. A later section in this chapter will consider the interaction of Tollmien-Schlichting and the stationary crossflow Fourier mode. Traveling crossflow will be omitted entirely, as it is asserted that the boundary-layer receptivity in cruise is not conducive to producing traveling crossflow waves.

With the absence of crossflow, the Fourier-space reduction has fewer steps. Since there is large $\beta = 0$ TS growth at $3000\,\mathrm{Hz}$, the frequency of $3600\,\mathrm{Hz}$ with an $N_{\max} = 3.3$ near $x/c =$

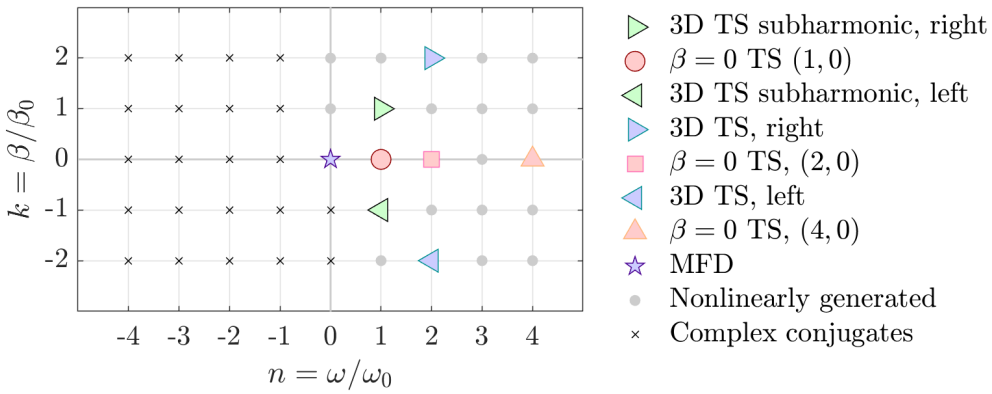

Figure 7.13: Sketch of discretized nk-Fourier space, where $\omega_0 \equiv 2\pi \times 900$ rad/s and $\beta_0 \equiv 2\pi/66$ rad/mm. Tollmien-Schlichting (TS) and its subharmonics are identified as the signature Fourier modes. Nonlinearly generated Fourier modes computed in NPSE are shown with gray circles, while Fourier modes computed through complex-conjugate relations are shown in black $\times$ markers. For this sketch, $N = 4$ and $K = 2$.

0.24 is feasible and commensurate with 3D TS as $(1800\,\mathrm{Hz},\ \pm 33\,\mathrm{mm})$ and subharmonics then as $(900\,\mathrm{Hz},\ \pm 66\,\mathrm{mm})$. With this set, $\omega_0 = 2\pi \times 900\,\mathrm{Hz}$ and $\beta_0 = 2\pi/66\,\mathrm{mm}$. The inclusion of these Fourier modes allows both subharmonic resonance to occur between the $(1, \pm 1)$ and the $(2, \pm 2)$ waves while also allowing the oblique pair of the $(2, \pm 2)$ to resonate and force the $\beta = 0$ TS wave $(4, 0)$. There is additional subharmonic resonance between the $(2, 0)$ and the $(4, 0)$, as well as the $(1, 0)$ with the $(2, 0)$. Geometrically, these oblique interactions form a diamond in Fourier space, as shown in Fig. 7.13.

All Fourier modes are aligned in phase with respect to their $\hat{u}_{(n,k)}$ shape-function component at the initialization location of $x/c = 0.04$, i.e., $\varphi_{(n,k)} = 0$ for all (n, k) at $x/c = 0.04$. For this case, the auxiliary condition was adjusted to be more stringent than the prior analysis: $|\Delta\alpha_{(n,k)}| < 10^{-11}$ now indicates α-convergence. Additionally, the nonlinearly generated Fourier modes $(n, k) \neq (0, 0)$ are set to be included in the convergence criteria at the 5^{th} streamwise node while the mean-flow distortion $(0, 0)$ is included in the criteria at the 7^{th} streamwise node.

7.4.1.2 Initial amplitude variation

Given that the freestream disturbance levels are unknown, there is inherent uncertainty in predictive calculations of boundary-layer transition. And even further, there is uncertainty in the dynamics of how such disturbances (e.g., sound or vorticity) in the freestream then propagate into the boundary layer—if there is a certain range of wavenumbers and frequencies that are more significantly amplified than others, for example. This latter problem is referred to as boundary-layer receptivity and as of writing, no present models exist to predict the transition Reynolds number on a flat plate [7]. With that said, under the assumption that external flows have weak freestream disturbances, computations then focus on the linear development and subsequent nonlinear breakdown to turbulence maintaining the inherent uncertainty in the initial condition. That is the subject of the present computations.

To be predictive relies on some correlation with flight data then as to what the initial disturbance amplitudes could possibly be. Fortunately for transonic swept-wing boundary-layer transition, there does exist some excellent work pairing both experiment and computation. The German laminar flow research program in the 1990s designed a laminar flow glove for the ATTAS/VFW 614 aircraft [150]. The airfoil used for the glove was the NACA 64_2 A015, which maintains favorable pressure gradients over the surface for nearly the first 50% of the chord [151]. The leading-edge sweep, or geometric sweep, on the aircraft was $\Lambda = 18^\circ$, while the maximum Mach number for the tests was $\mathrm{M}_{Q_\infty} \approx 0.7$. For clarity, M_{Q_∞} is the Mach based on the resultant velocity in the freestream: Q_∞ / a_∞. Their Reynolds numbers based on the wing chord and the resultant velocity hit a max value of 30 million, however, several cases at lower Reynolds numbers were run. This Reynolds number here includes the effect of wing sweep doubly, as expressed below:

$$\begin{aligned} \mathrm{Re}^{Q_\infty}_{c\,\sec\Lambda} &\equiv \frac{Q_\infty c \sec\Lambda}{\nu_\infty}, \\ Q_\infty \cos\Lambda &= \sqrt{\overline{u}^2_\infty + \overline{v}^2_\infty}, \\ \implies \mathrm{Re}^{Q_\infty}_{c\,\sec\Lambda} &= \frac{c\sqrt{\overline{u}^2_\infty + \overline{v}^2_\infty}}{\nu_\infty} \sec^2\Lambda \equiv \mathrm{Re}^{\overline{u}_\infty \overline{v}_\infty}_{c} \sec^2\Lambda \end{aligned} \tag{7.8}$$

where the chord perpendicular to the leading edge is denoted with c and the component of velocity perpendicular to leading edge as well is denoted with $\sqrt{\overline{u}_\infty^2 + \overline{v}_\infty^2}$. Additionally, the pilot of the ATTAS/VFW 614 aircraft flew at sideslip, providing an effective sweep to the flowfield that could vary from the geometric sweep by $\pm 5^\circ$. In the boundary-layer transition analysis of the flight data, Schrauf et al. report data for a case where a) $\mathrm{M}_{Q_\infty} = 0.60$, b) $\mathrm{Re}_{c\,\sec\Lambda}^{Q_\infty} = 15.7 \times 10^6$ and c) an effective sweep of $\Lambda = 21.9^\circ$ [115]. This Reynolds number corresponds to $\mathrm{Re}_c^{\overline{u}_\infty \overline{v}_\infty} \approx 13.5 \times 10^6$ using Eq. (7.8). All three of these parameters are reasonably close to the conditions currently considered for this S207 airfoil: $\mathrm{M}_{Q_\infty} \approx 0.745$ at $\Lambda = 20^\circ$ (i.e., $\mathrm{M}_{\overline{u}_\infty \overline{v}_\infty} = 0.70$) with $\mathrm{Re}_c^{\overline{u}_\infty \overline{v}_\infty} = 13.2 \times 10^6$. Then by assumption, the initial amplitudes that Schrauf et al. found to correlate with transition location data may be near those experienced in flight for the current S207 case.

The pressure coefficient as analyzed by Schrauf et al. was not reported; so to compare the present S207 data against that of the VFW 614 flight, a representative pressure coefficient from the pre-flight CFD predictions was extracted and digitized from Redeker et al. [150]. The pressure coefficient was extracted from Fig. 17 in Redeker et al., assuming a mid-span location of $\eta = 0.52$ (using their nomenclature) and a Mach number of $\mathrm{M}_{Q_\infty} = 0.7$. On the figure, the indicated chord reference direction is not leading-edge-perpendicular, rather it is inline with the aircraft's fuselage. Then it is presumed that the reference velocity of the pressure coefficient is the resultant. That is, $C_p^{Q_\infty}$ is provided. A sweep of 18° is supposed, as that is the leading-edge sweep of the wing. As mentioned before, the airfoil used for the glove was the NACA 64_2 A015, and its coordinates were found from an online database. Converting the pressure coefficient to $C_p^{\overline{u}_\infty \overline{v}_\infty}$, Fig. 7.14 compares the present S207 to the representative case for the VFW 614/ATTAS laminar flow glove.

With that in mind, it is not enough to analyze a single initial amplitude, but instead a range, as the assumption is not truth. The subject of this section then will analyze the transition processes while varying the initial amplitudes of the distinct Fourier modes in the NPSE formulation.

As shown in Fig. 7.13, there are several Fourier modes in this first problem formulation which require initialization with LST and a finite amplitude assigned. These include the $\beta = 0$ TS $(4, 0)$, the subharmonic oblique pair $(2, \pm 2)$, their respective subharmonics $(1, \pm 1)$, and the sub-

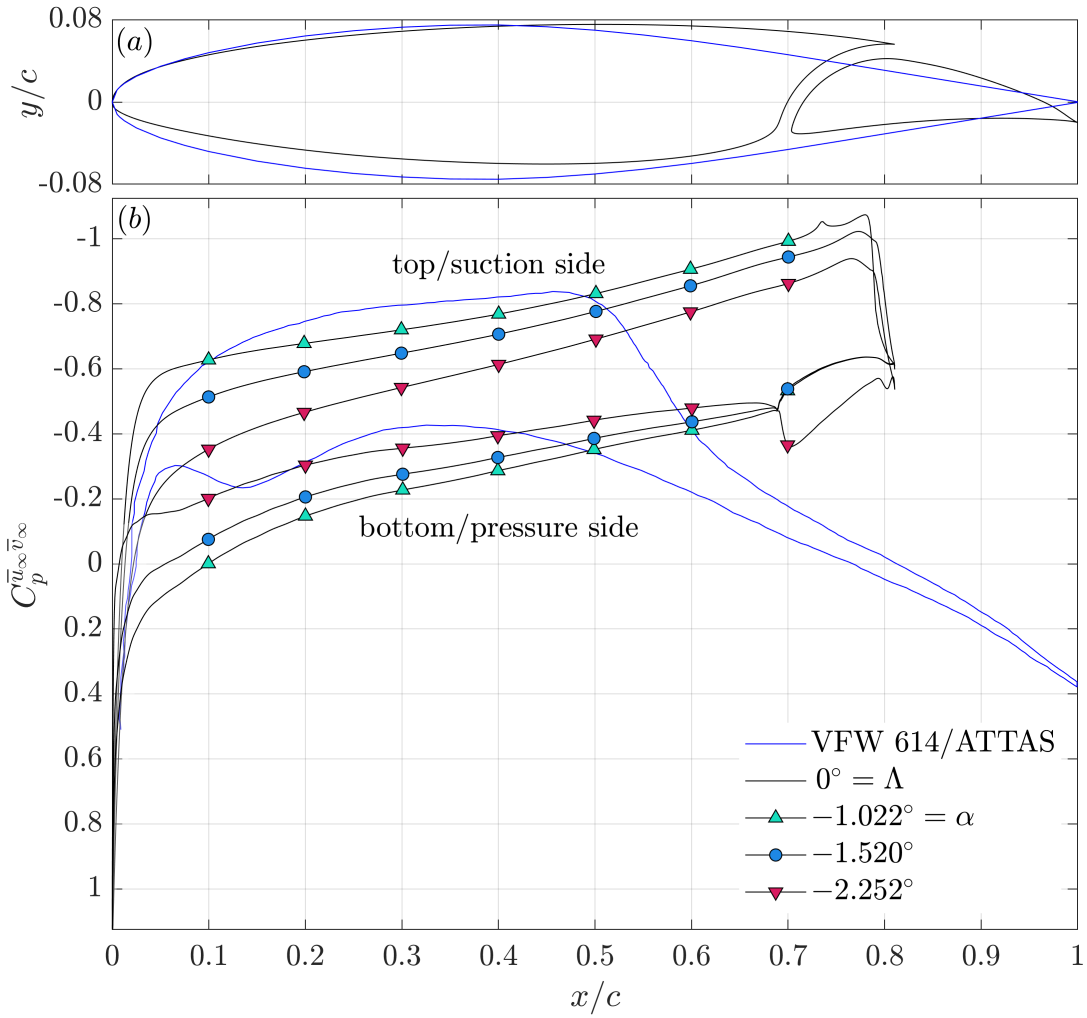

Figure 7.14: a) The S207 airfoil cross-section in black with the NACA 64_2 A015 in blue. b) Pressure coefficients $C_p^{\overline{u}_\infty \overline{v}_\infty}$ for the S207 and the VFW 614/ATTAS laminar flow glove as a function of x/c. This figure is a continuation of Fig. 7.1. The VFW 614/ATTAS laminar flow glove pressure coefficient is indicated in blue. Small oscillations result from digitization of the laminar-flow-glove's data.

harmonics of the $\beta = 0$ TS—the $(2, 0)$ and $(1, 0)$. This amounts to a total number of 7 distinct amplitudes. Note too that this is not the only parameter. Each Fourier mode can have its own initial phase, as it is complex-valued. In other words, $A_{0\,(n,k)} = |A_{0\,(n,k)}| \exp\left(\mathrm{i}\varphi_{(n,k)}\right)$ where $\varphi_{(n,k)}$ is possibly distinct among (n, k). This amounts to then 14 total initial parameters left to be varied, which is a large test matrix to consider. To approach this, let us first assume that at a given x/c location, all Fourier modes have the *same* magnitude and phase. This cuts down the diagonal of this 14-dimensional test matrix and provides some insight on what to expect out of this nonlinear system. Since the first neutral point of the $(4, 0)$ disturbance, or its branch-I location, is near $x/c = 0.06$, the initialization location of $x/c = 0.04$ is selected. Initializing upstream of branch-I allows its location to be accurately identified once the spatial numerical transient from LST to PSE has vanished. The initial amplitude magnitudes are specified such that all disturbances in their u' components achieve a maximum value with respect to the local $\overline{u}_e$ value. Mathematically, this is $\max_y |u'_{(n,k)}|/\overline{u}_e = \mathrm{cst}$, where for the initial amplitude variation, this constant is set to vary as $\log_{10}(\mathrm{cst}) = -6$ to -2.5, $\Delta = 0.25$. The phases of all 7 initialized Fourier modes are all set to zero at $x/c = 0.04$ using the definition provided earlier in Eq. (7.4). Inputting these into the nonlinear parabolized stability equations and marching downstream, a sample distribution of the Fourier mode amplitudes is shown in Fig. 7.15. This distribution shown corresponds with the initial amplitude of $\max_y |u'_{(n,k)}|/\overline{u}_e = 10^{-4.5}$. The fundamental $\beta = 0$ TS wave reaches an amplitude of $\max_y |u'_{(n,k)}|/Q_\infty \approx 5 \times 10^{-6}$ near its branch-I location, which is approximately commensurate with the initial amplitudes reported by Schrauf et al. [115]. In their analysis, transition was correlated with a branch-I TS initial amplitude of 1 to 5×10^{-6}. This range of values will serve as the cornerstone of the present nonlinear analysis.

In Fig. 7.15, the signature Fourier modes are indicated with colors and markers, while the gray lines in the background indicate the other Fourier modes that are nonlinearly generated (aside from the mean-flow distortion). Their linear amplitude distributions are indicated with dashed lines, revealing that at these low amplitude realistic of cruise conditions, the only Fourier mode to appreciably deviate from its linear behavior is the left 3D TS $(2, -2)$. There is some deviation

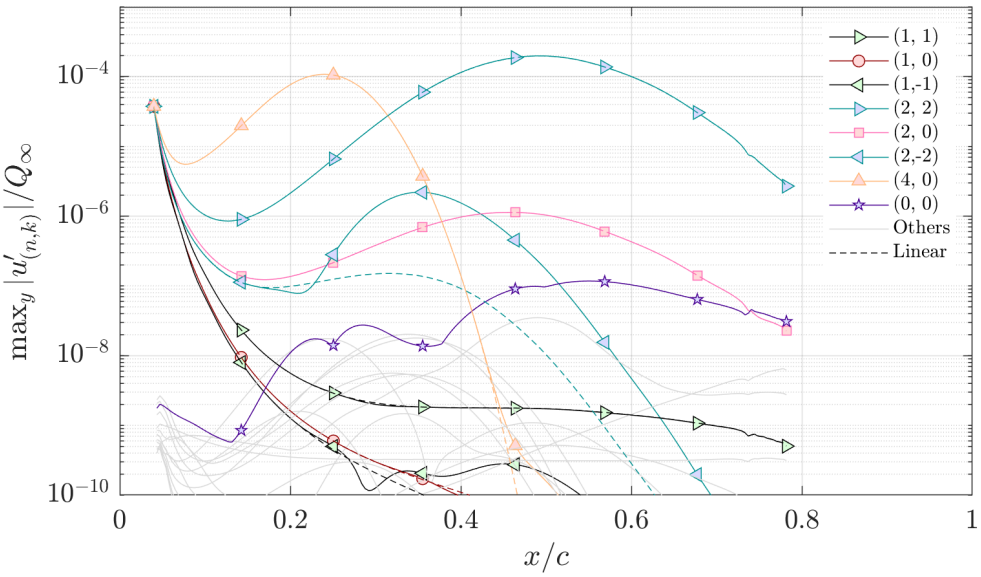

Figure 7.15: Amplitude distributions of various Fourier modes against x/c for the baseline S207 $\alpha = -1.022°$, $\Lambda = 20°$ case on the top side of the wing. The signature Fourier modes are shown in color with a prescribed marker, while their linear behavior is indicated by dashed lines of the same color. The nonlinearly generated Fourier modes are shown in gray.

shown by the $(1, -1)$, however its amplitude is negligibly small. At low amplitudes, the mean-flow distortion tends to primarily be forced by the largest amplitude Fourier mode in the system. This is a consequence of all quadratic interactions for the MFD as $(n, k) + (-n, -k) = (0, 0)$. Note as the $(4, 0)$ TS wave grows from its branch-I location to its branch-II location (the second neutral point), the $(0, 0)$ mean-flow distortion nearly follows its shape, lagging slightly in space. As it grows and approaches the left 3D TS $(2, -2)$, it appears there is an exchange in energy between the two Fourier modes, despite being an order of magnitude apart in amplitude. This excites sudden growth out of the $(2, -2)$; however, amplitudes are not high enough to appreciably force the $(2, -2)$ up to its counterpart $(2, 2)$, the right 3D TS wave. Downstream near $x/c \approx 0.30$, the 3D TS wave $(2, 2)$ becomes the dominant Fourier mode in the system. Observe below that the MFD approximately follows its growth and decay for the rest of the domain.

Consider now the variation of all initial amplitudes from $\max_y |u'_{(n,k)}|/\overline{u}_e = 10^{-6}$ to $10^{-2.5}$. Figure 7.16 shows three of the Fourier mode amplitude distributions for select cases. The line color

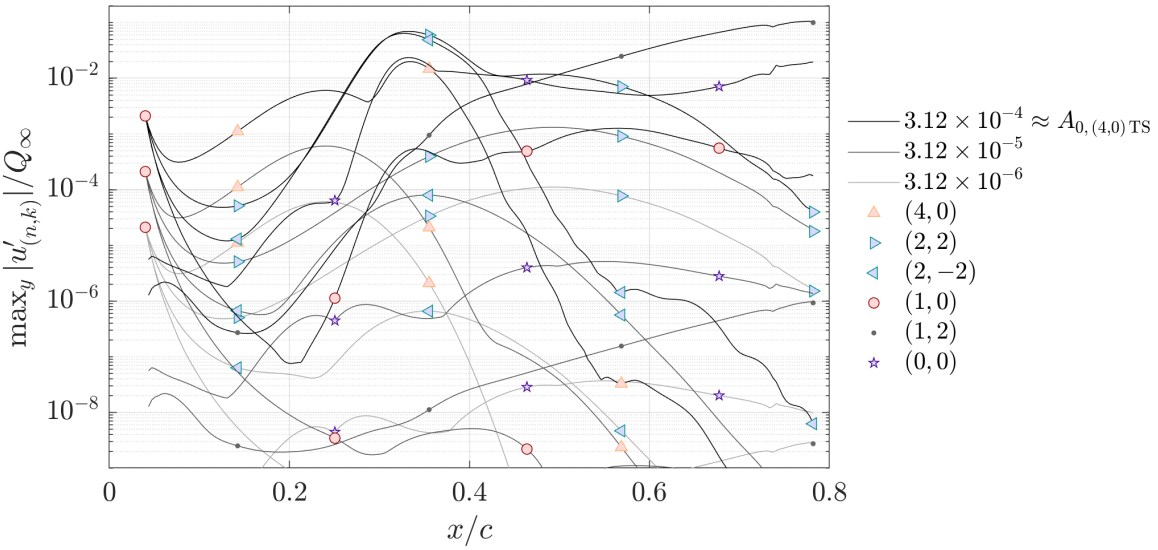

Figure 7.16: Amplitude distributions of various Fourier modes against x/c for the S207 $\alpha = -1.022°$, $\Lambda = 20°$ case on the top side. Three solutions with different initial amplitudes are indicated by varying the line color from black to gray, while some selected Fourier modes are shown with a prescribed marker.

indicates a different initial amplitude considered, expressed as $A_{0,\,(4,0)\,\mathrm{TS}}$. This indicates the amplitude $\max_y |u'_{(4,0)}|/Q_\infty$ of the $(4,0)$ $\beta = 0$ TS wave at its branch-I location, such that the values are commensurate with what Schrauf et al. reported in their 1996 journal article [115]. Different markers indicate distinct Fourier modes of note. In particular, consider the high amplitude case of $A_{0,\,(4,0)\,\mathrm{TS}} \approx 3.12 \times 10^{-4}$. The interaction between the mean-flow distortion and the left 3D TS $(2,-2)$ generates enough growth such that the $(2,-2)$ reaches the same amplitude as the right 3D TS $(2,2)$ near $x/c = 0.20$. They grow together resonating, ultimately peaking at a maximum value of $\max_y |u'_{(2,\pm2)}|/Q_\infty = 7\%$. The abrupt decay soon after is enough though to stabilize the growth of the $(0,0)$ such that its amplitude stays lower than 2%. Downstream highlights the rise of the $(1,2)$ Fourier mode from the background in conjunction with the subharmonic $(1,0)$ as the $(2,2)$ decays. The $(1,2)$ appears to be strongly forced through the quadratic interaction $(2,2) + (-1,0) = (1,2)$.

To showcase the information of all cases, only the maximum amplitude in s is selected beyond each Fourier mode's respective branch-I location. This permits the horizontal axis of the figure

to be the initial amplitude $A_{0,\,(4,0)\,\mathrm{TS}}$, while the vertical axis represents the maximum amplitude of a Fourier mode over the entire (s, y) two-dimensional domain. See Fig. 7.17 for the results of particular Fourier modes. Linear extrapolations are indicated for the LST-initialized content, i.e., the $(2, 2)$ and the $(4, 0)$, whereas the $(1, 0)$ is linearly stable for the entire chord, so its linear extrapolation is not shown. Additional Fourier modes are indicated: the $(1, 2)$ and the $(0, 2)$, the latter of which is a nonlinearly generated streamwise vortical mode which is forced largely by the interaction $(2, 2) + (-2, 0) = (0, 2)$. Its presence becomes appreciable at higher amplitude in late nonlinear regimes and it may be similar to the rope-like structures observed via oblique breakdown in Direct Numerical Simulations by Joslin et al. and Mayer et al. [27, 152]. The range of initial amplitudes of the TS at branch-I associated with the VFW 614/ATTAS laminar flow glove analyzed by Schrauf et al. is indicated by the cyan-colored, transparent patch from 1 to 5×10^{-6}. The onset of the $(1, 0)$ resonance is indicated ($\sim 10^{-5}$), as well as the oblique pair $(2, \pm 2)$ onset of resonance together at a higher initial amplitude: $\sim 5.5 \times 10^{-5}$. At the highest amplitude considered, the system of equations halts during α-convergence of each Fourier mode and couldn't achieve $|\Delta\alpha_{(n,k)}| < 10^{-11}$ uniformly in 200 iterations.[5] This occurred at $x/c = 0.39$ with the dominant mean-flow distortion reaching an amplitude of $\max_y |u'_{(0,0)}|/Q_\infty = 24\%$. At these amplitudes, breakdown to turbulence is soon expected and a small discretized Fourier space of only $N = 4$ and $K = 2$ is likely insufficient to capture all of the relevant scales to accurately simulate the breakdown physics. The purpose of these calculations is not to compute deeply into the breakdown region, but instead to quantify when breakdown occurs as a function of the initial amplitudes.

There are several important conclusions from this chart. First, appreciable deviation from linear dynamics doesn't occur until the branch-I amplitude $A_{0,\,(4,0)\,\mathrm{TS}} \approx 5 \times 10^{-5}$ induces resonance between the subharmonic oblique pair $(2, \pm 2)$—an order of magnitude higher than the

[5]This convergence issue of NPSE in the highly nonlinear stages of breakdown is common to all NPSE codes—not just EPIC. All of the exact reasons are not presently known. But intuitively, at a certain point in a newly generated turbulent boundary layer, the unsteady fluctuations lose their slowly varying, wave-like character as modeled by the PSE ansatz, making PSE inappropriate and physically dubious. This point is nominally soon downstream of where laminar breakdown is predicted by NPSE.

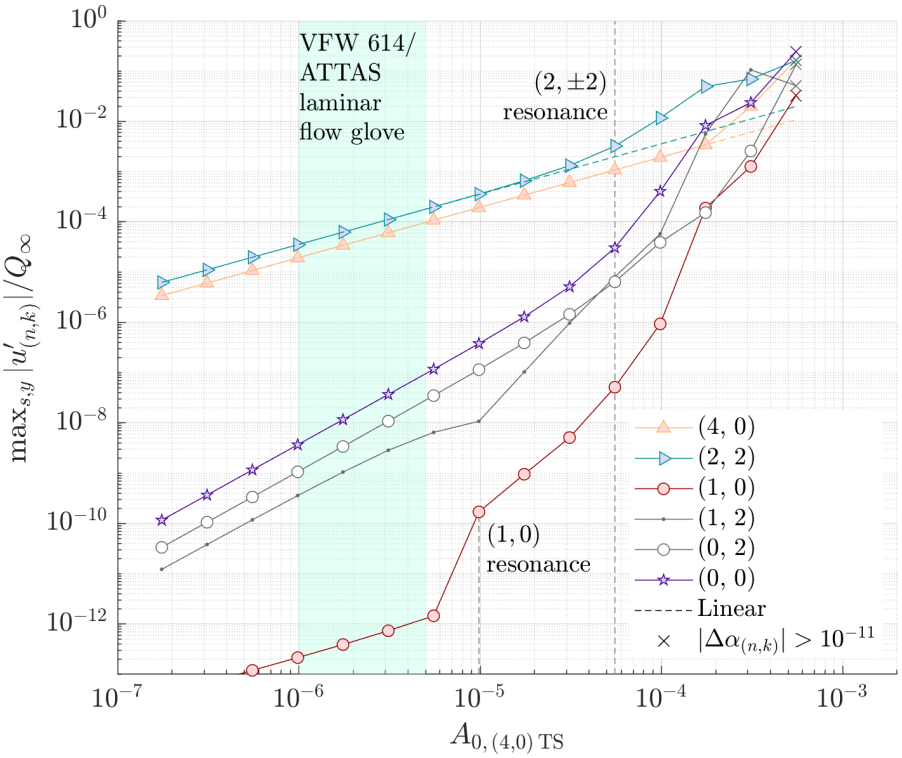

Figure 7.17: Maximum amplitudes in both s and y for selected Fourier modes against the branch-I amplitude of the $(4, 0)$ $\beta = 0$ TS wave, $A_{0,\,(4,0)\,\mathrm{TS}}$. Linear extrapolation for the $(2, 2)$ and the $(4, 0)$ are indicated with dashed lines. The $\times$ marker indicates when the NPSE fails to converge its α-convergence criterion less than 10^{-11} for all Fourier modes. The initial amplitudes that correlate well with transition for the VFW 614/ATTAS laminar flow glove flight experiments are indicated with a transparent cyan patch. Resonance of the $(1, 0)$ as well as the $(2, \pm 2)$ are indicated with dashed lines to the corresponding branch-I TS amplitude.

worst case of the Schrauf correlation [115]. Second, the mean-flow distortion doesn't achieve $\max_y |u'_{(0,0)}|/Q_\infty = 1\%$ until $A_{0,\,(4,0)\,\mathrm{TS}} \approx 2 \times 10^{-4}$—forty times higher than the worst case of Schrauf. Under the *dubious* assumption that the flight in cruise will experience initial amplitudes on the order of what Schrauf et al. computed for the VFW 614/ATTAS laminar flow glove, these conclusions indicate that TS subharmonic resonance will not disrupt the laminarity of the flow over the S207 at cruise for this configuration.

To demonstrate the amplitude distribution for the most catastrophic case, Fig. 7.18 shows the amplitude distributions over x/c for the highest initial amplitude considered. Amplitudes of the oblique pair $(2, \pm 2)$ achieve values of 20% of the freestream velocity near $x/c = 0.34$, which

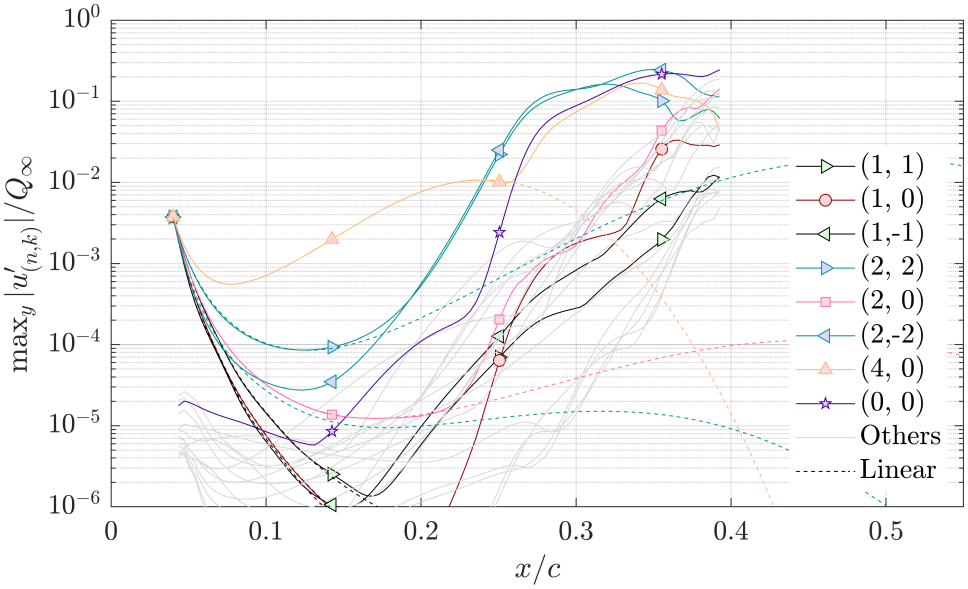

Figure 7.18: Amplitude distributions of various Fourier modes against x/c for the S207 $\alpha = -1.022°$, $\Lambda = 20°$ case on the top side of the wing assuming a high initial amplitude. The signature Fourier modes are shown in color with a prescribed marker, while their linear behavior is indicated by dashed lines of the same color. The nonlinearly generated Fourier modes are shown in gray. NPSE halts convergence near $x/c = 0.39$.

likely indicates laminar breakdown is imminent. The NPSE simulation ceases to converge near $x/c = 0.39$ as all of the harmonics present become appreciable in magnitude.

For the next section, let us consider a simpler model of the TS subharmonic transition process in the pursuit of computational efficiency while maintaining accuracy.

7.4.1.3 Reduced set of Fourier modes for TS subharmonic resonance

When using the Nonlinear Parabolized Stability Equations, it is a natural question to ask: *how many Fourier modes are needed to accurately yet efficiently capture the dynamics of the transition process?* Let us address this for the present TS subharmonic resonance. Recall that for their baseline analysis, Schrauf et al. considered only the subharmonic 3D TS and the $\beta = 0$ TS, even neglecting the mean-flow distortion $(0, 0)$ [115]. Their subsequent analysis then demonstrated the inclusion of additional Fourier modes did not change the result of transition location prediction. The relevant discretized Fourier space may be reduced, neglecting many nonlinearly

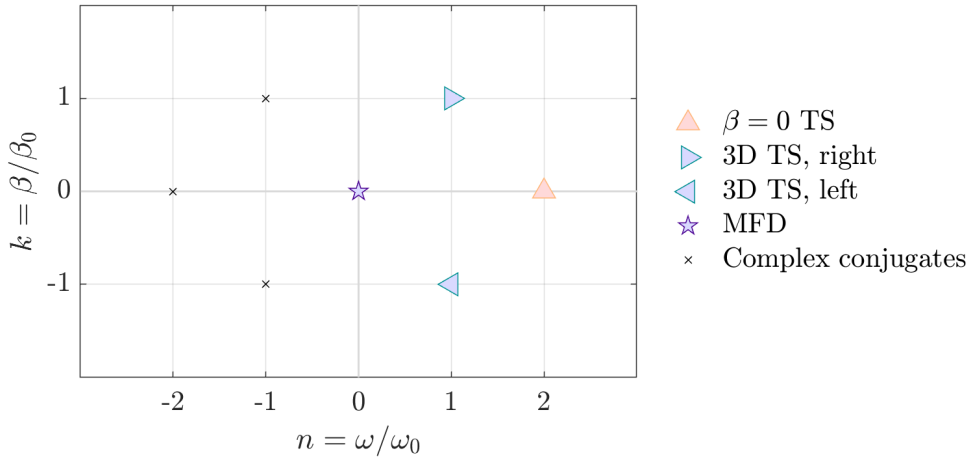

Figure 7.19: Sketch of discretized nk-Fourier space, where $\omega_0 \equiv 2\pi \times 1800$ rad/s and $\beta_0 \equiv 2\pi/33$ rad/mm. Tollmien-Schlichting (TS) and its oblique subharmonics are identified as the signature Fourier modes. Fourier modes computed through complex-conjugate relations are shown in black $\times$ markers. For this sketch, $N = 2$ and $K = 1$ with additional Fourier modes truncated from the NPSE double sum.

generated Fourier modes that aren't essential to the secondary boundary-layer instability that is the TS subharmonic resonance, as shown in Fig. 7.19. For the present analysis, consider now the fundamental angular frequency as $\omega_0 \equiv 2\pi \times 1800$ rad/s and fundamental spanwise wavenumber as $\beta_0 \equiv 2\pi/33$ rad/mm. Then the Fourier modes computed in NPSE are reduced to just four: the $(2, 0)$ TS, the subharmonic oblique pair $(1, \pm 1)$, and the mean-flow distortion $(0, 0)$. This analysis will include the MFD in contrast to Schrauf's. This being said, the MFD still must have its $\alpha_{(0,0)} = 0$, inserting all of its growth into the shape function $\hat{q}_{(0,0)}$. Assuming a purely imaginary $\alpha_{(0,0)}$ for some runs caused its α-convergence to be much slower than the other Fourier modes in the system, often requiring hundreds to reach appreciable levels of $|\Delta\alpha_{(0,0)}| < 10^{-8}$. For some amplitudes, the system would diverge soon downstream, as the real-valued forcing term on the MFD $f_{(0,0)}$ would diverge to ∞. For robustness across the whole suite of runs, $\alpha_{(0,0)} \equiv 0$.

Recall the required number of Fourier modes for NPSE necessary to be solved via distinct governing disturbance equations is $N_m = (N+1)(2K+1) - K$. For the prior case, this evaluates to $N_m = 23$, while the entire discretized rectangle in Fourier space including complex conjugates

is $N_{m,\text{full}} = (2N+1)(2K+1) = 45$. For the reduced set in this nomenclature, $N_m = 4$ and $N_{m,\text{full}} = 7$. Let us compare the solution of $N = 4$ and $K = 2$ to this reduced set of Fourier modes in terms of amplitude distributions, as shown in Fig. 7.20 corresponding to $A_{0,\,\text{TS}} \approx 5 \times 10^{-6}$ at branch-I. The $N_m = 23$ solution is shown in black, while the $N_m = 4$ solution is overlaid in a dashed red line. Distinct Fourier modes are indicated with different markers. The error between the two solutions is shown in the bottom subplot, where the absolute error ϵ_m is defined similarly to the y-convergence error from Eq. (7.5):

$$\epsilon_m(|u'_{(n,k)}|) \equiv \left| \max_y |u'_{(n,k)}|_{N_m=4} - \max_y |u'_{(0,0)}|_{N_m=23} \right| \tag{7.9}$$

where $\max_y |u'_{(n,k)}|_{N_m=4}$ corresponds to the $\max_y |u'_{(n,k)}|$ amplitude for a Fourier mode belonging to the $N_m = 4$ solution and $\max_y |u'_{(0,0)}|_{N_m=23}$ similarly corresponds to an amplitude from the more resolved set of $N_m = 23$. These errors are appreciably low for all streamwise stations: $O(10^{-9})$ and lower. This suggests that for these cases of TS subharmonic resonance on the S207, a reduced set of Fourier modes can be used without worry, maintaining accuracy and greatly improving efficiency. Runtime of these cases drop from $30+$ minutes to less than 4 on the workstations in the CST lab.[6] The defining characteristic between the $N_{m,\text{full}} = 7$ and $N_{m,\text{full}} = 45$ simulations from a computing point of view is the number of possible tuples for the quadratic and cubic interactions. For the $N_{m,\text{full}} = 7$ case, there are a total of only 19 total quadratic tuples forcing the right hand side, while there are 109 total cubic interactions. On the other hand, for the $N_{m,\text{full}} = 45$ case, there are a total of 602 quadratic and $21,362$ cubic interactions.

Now consider the initial amplitude variation study again with this reduced set of Fourier modes. The results are shown in Fig. 7.21. The conclusion is essentially identical to that of Fig. 7.17 from the previous section. Resonance is not observed from the subharmonic oblique pair $(1, \pm 1)$ until a TS branch-I amplitude $\max_y |u'_{(2,0)}|/Q_\infty \equiv A_{0,\,(2,0)\,\text{TS}} \approx 5.5 \times 10^{-5}$. The mean-flow distortion does not reach $\max_y |u'_{(0,0)}|/Q_\infty = 2\%$ until high branch-I TS amplitudes of 3×10^{-4}.

[6]These tests were run on dual-processor workstations with Intel Xeon E5-2640 V4 10-core processors and 64 GB of DDR4-2133 memory with relevant gfortran 7.5.0 flags -O3 -march=native -funroll-all-loops. Neither MPI nor OpenMP was used for these tests.

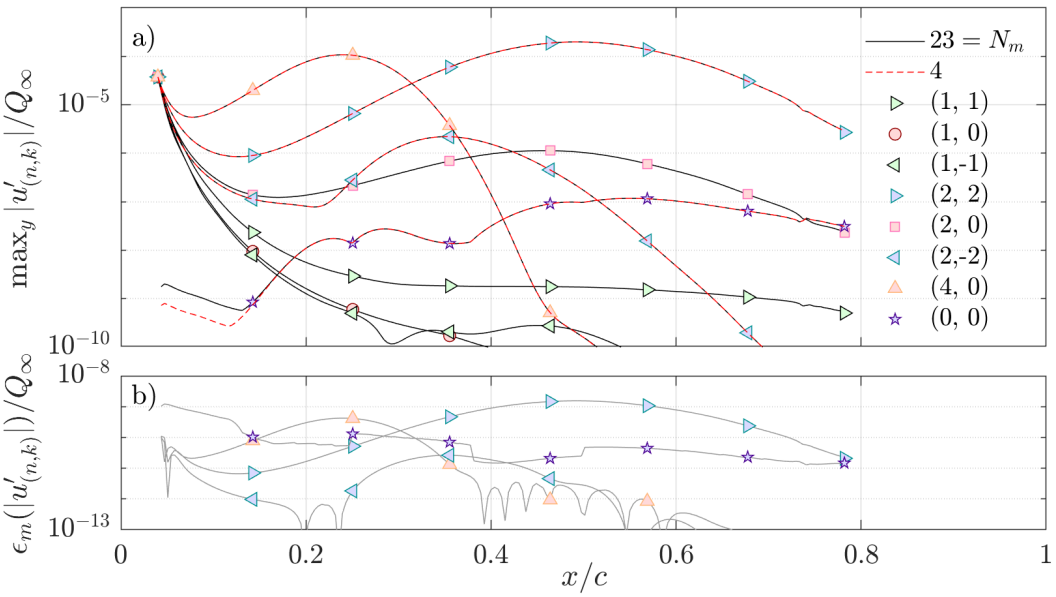

Figure 7.20: a) Amplitude distributions of the signature Fourier modes against x/c for this baseline S207 $\alpha = -1.022°$, $\Lambda = 20°$ case. Solid black lines indicate the solution with $N = 4$, $K = 2$, or $N_m = 23$ computed, while dashed red lines indicate the diamond arrangement of $N_m = 4$ Fourier modes. Colored markers indicate which Fourier mode is which, following the same legend in Fig. 7.15. b) Error of $\max_y |u'_{(n,k)}|$ for each streamwise station compared to the reference $N_m = 23$ solution for each Fourier mode.

Breakdown of the laminar flow via TS subharmonic resonance is not expected for realistic cruise initial amplitudes, even from the reduced set of $N_m = 4$ Fourier modes. Or expressed another way: when the TS subharmonic resonance is the dominant secondary mechanism, only the set of $N_m = 4$ Fourier modes is needed to predict onset of subharmonic resonance and subsequent breakdown of laminarity.

7.4.1.4 Varying initial amplitudes of the subharmonics

Another parameter worth investigating is the assumption all Fourier modes possess the same amplitude at $x/c = 0.04$. Instead, the initial values could be varied such that their amplitudes at respective branch-I locations are the same. This is a reasonable assumption, and Schrauf et al. performed this in their 1996 analysis for the VFW 614/ATTAS laminar flow glove: see their Fig. 19 [115].

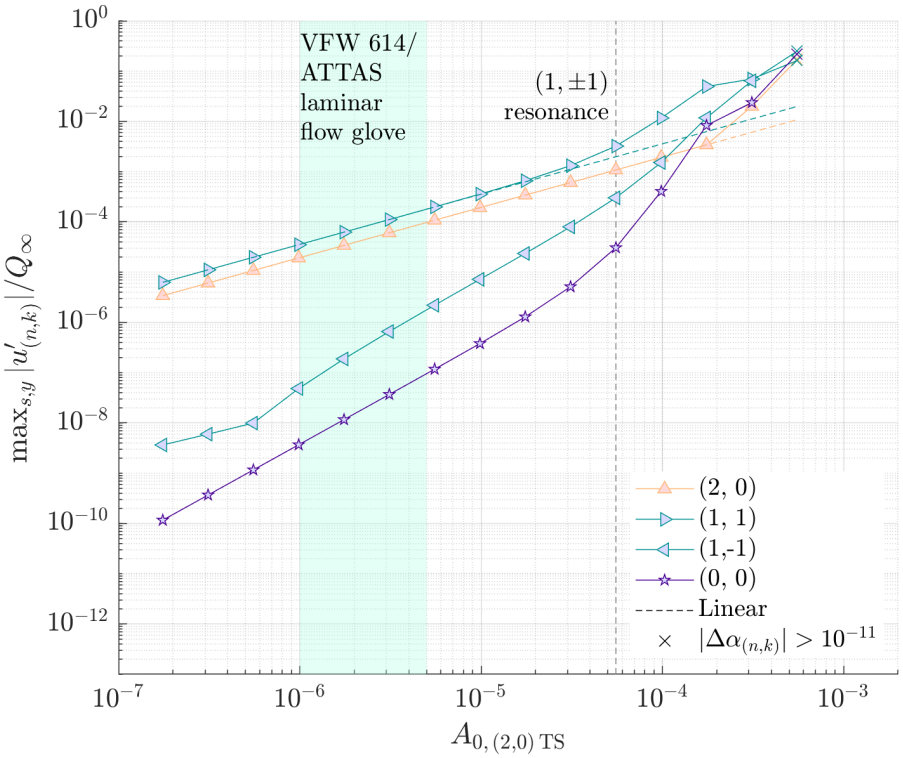

Figure 7.21: Maximum amplitudes in both s and y for selected Fourier modes against the branch-I amplitude of the $(2,0)$ $\beta = 0$ TS wave, $A_{0,\,(2,0)\,\mathrm{TS}}$. Linear extrapolation for the $(1,1)$ and the $(2,0)$ are indicated with dashed lines. The $\times$ marker indicates when the NPSE fails to converge its α-convergence criterion less than 10^{-11} for all Fourier modes. The initial amplitudes that correlate well with transition for the VFW 614/ATTAS laminar flow glove flight experiments are indicated with a transparent cyan patch. Resonance of the $(1,\pm1)$ is indicated with a dashed line to the corresponding branch-I TS amplitude. Compare with Fig. 7.17 for the $N_m = 23$ solutions.

From Fig. 7.22, it is observed that with these branch-I initial amplitudes now equal, the overall dynamics of the system remain linear, barring a brief modulation in the $(1,-1)$. The gradual decrease in amplitude of the $(1,-1)$ is associated with a slight decrease in the inviscid-streamline-parallel component the phase speed $c_{ph,\overline{u}_s\,(1,-1)}$ and increase in the inviscid-streamline-orthogonal component the phase speed $|c_{ph,\overline{w}_s\,(1,-1)}|$ (not pictured). Shortly downstream of this locally minimum amplitude of the $(1,-1)$, the mean-flow distortion $(0,0)$ amplitude grows strongly as the most dominant Fourier mode is now three-dimensional, i.e., the $(1,1)$. In light of this minor nonlinearity, the flowfield does not indicate a significant deviation from linearity and the flow is expected to remain laminar provided these initial conditions. This completes the study and variation

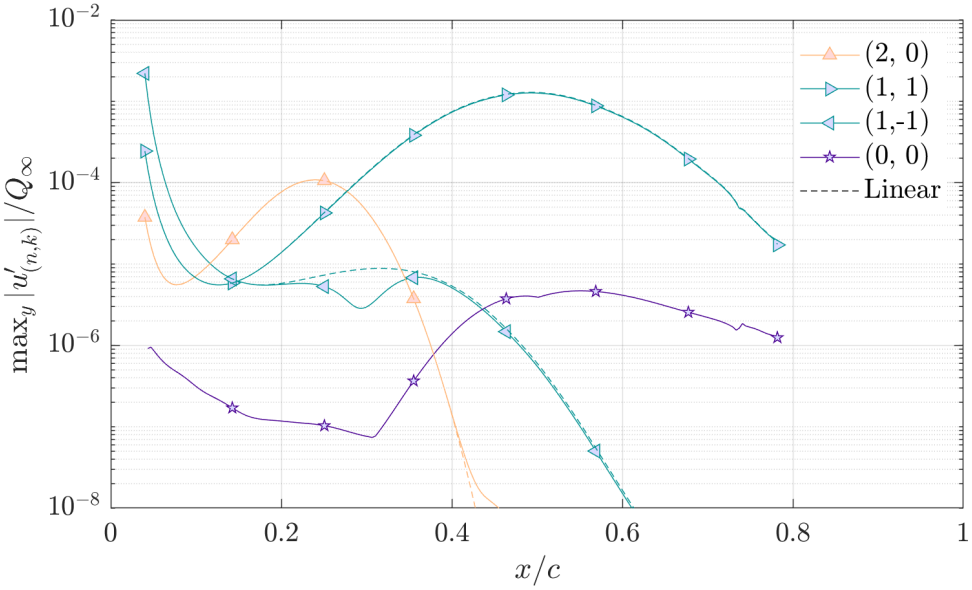

Figure 7.22: Amplitude distributions against x/c for the S207 $\alpha = -1.022°$, $\Lambda = 20°$, top side for NPSE TS subharmonic resonance, assigning the branch-I amplitudes to be equal for the unsteady Fourier modes.

in initial amplitudes for TS subharmonic resonance for this angle of attack and sweep.

7.4.2 TS/SCF interaction

In addition to the secondary mechanism of TS subharmonic resonance, another possible mechanism is the interaction of a Tollmien-Schlichting wave with a crossflow vortex. This secondary mechanism is an example as *primary resonance*, in the language of Herbert, where a spanwise infinite wave and an oblique pair interact with a streamwise stationary vortex [148]. This is in contrast to the subharmonic resonance, or *principal parametric resonance*, of the previous section. On a swept wing, the large growth associated with the $\beta = 0$ TS wave in conjunction with a finite amplitude SCF vortex—even if the SCF is stable—nonlinearly generates a highly unstable set of unsteady, oblique waves. Since the flow is three-dimensional, one of the oblique waves will be more unstable than the other. In the words of Thorwald Herbert,

> Modes of secondary instability and oblique TS waves are qualitatively different; they are "two different kinds of animals." [148]

At a sufficient amplitude, the less unstable oblique wave adjusts its phase and phase speed to match that of the other oblique wave. If the amplitude is high enough, they both begin to resonate together downstream at similar amplitudes. If the resonance has enough inertia (i.e., amplitudes are high enough), then the oblique pair's amplitude will intersect that of the stationary crossflow wave, after which all three will resonate together. Depending again on the amplitude, the resonance may propel all three waves into that of the TS, potentially leading to a catastrophic breakdown of the laminar boundary layer if the TS linear dynamics are not sufficiently stabilizing. See Fig. 10 in Schrauf et al. for a demonstration of this multi-stage process in the literature [115].

The interaction of crossflow and Tollmien-Schlichting has been studied in other contexts besides the work by Schrauf et al. Earlier, Reed applied Floquet theory neglecting the nonlinear distortion of the crossflow vortices [153, 154]. The crossflow in the first analysis was unsteady, while in the second, crossflow was steady; and in both, they were assumed to grow exponentially. For the steady crossflow cases of low-speed experimental conditions and Mach 0.75 LFC configurations, there was no observed crossflow/TS interaction in the leading-edge region. Bassom & Hall [155] considered the interaction of stationary crossflow/TS over a rotating disk using an asymptotic analysis. They found that the effect of the vortex on both linear and weakly nonlinear TS waves could have either a stabilizing or destabilizing effect on the TS wave, depending on the TS wave's obliqueness. However, as those authors note, the trends are only applicable at asymptotically large Reynolds number and lower Reynolds numbers must be addressed through numerical calculations.

The present analysis will assess the interaction of Tollmien-Schlichting and stationary crossflow by means of the Nonlinear Parabolized Stability Equations.

7.4.2.1 Initial conditions

Recall from Fig. 7.20 that when a given secondary boundary-layer instability dominates the transition process, the inclusion of higher harmonics and cross-modes has a small effect. From this and following the methodology of Schrauf et al., we may consider the same simplification for computational efficiency in the context of the TS/SCF interaction. For this case, a discretized Fourier space of $N = 1$ and $K = 1$ is used [115]. Here, the unstable content is slightly different than that

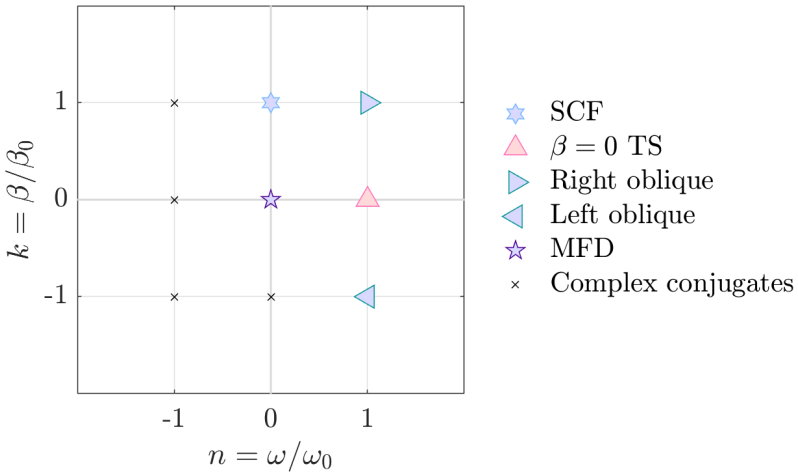

Figure 7.23: Sketch of discretized nk-Fourier space, where $\omega_0 \equiv 2\pi \times 3000$ rad/s and $\beta_0 \equiv 2\pi/12$ rad/mm. Tollmien-Schlichting (TS), stationary crossflow (SCF), the oblique pair, and the mean-flow distortion (MFD) are identified as the signature Fourier modes. The oblique pair is nonlinearly generated. Fourier modes computed through complex-conjugate relations are shown in black $\times$ markers. For this sketch, $N = 1$ and $K = 1$.

of the TS subharmonic resonance of the prior case. The linearly most amplified $\beta = 0$ TS on this geometry is 3000 Hz, reaching an $N \approx 3.5$, while the most linearly amplified SCF is $\lambda_z = 12$ mm, reaching an $N \approx 1$ near $x/c = 0.09$. Even though this SCF disturbance is not significantly amplified, TS may interact with it to nonlinearly generate a highly unstable oblique pair of waves with the same frequency as the $\beta = 0$ TS and the same spanwise wavelength as SCF. That is, the oblique pair is described by $(3000\,\text{Hz}, \pm 12\,\text{mm})$. The sketch of the discretized Fourier space is shown in Fig. 7.23.

7.4.2.2 Initial amplitude variation

Let us address the initial amplitude uncertainty problem again for this TS/SCF secondary mechanism. Initial amplitudes are varied in the same way as done for the TS subharmonic resonance breakdown analysis previously. That is, the two LST-initialized Fourier modes $(0, 1)$ and the $(1, 0)$ are assigned the same magnitude for $\max_y |u'_{(n,k)}|/\overline{u}_e$ at $x/c = 0.05$ upstream of the TS branch-I location. Both phases $\varphi_{(1,0)}$ and $\varphi_{(0,1)}$ are assigned to zero. A sample amplitude distribution is shown in Fig. 7.24 at high initial amplitude to demonstrate the various stages of the TS/SCF break-

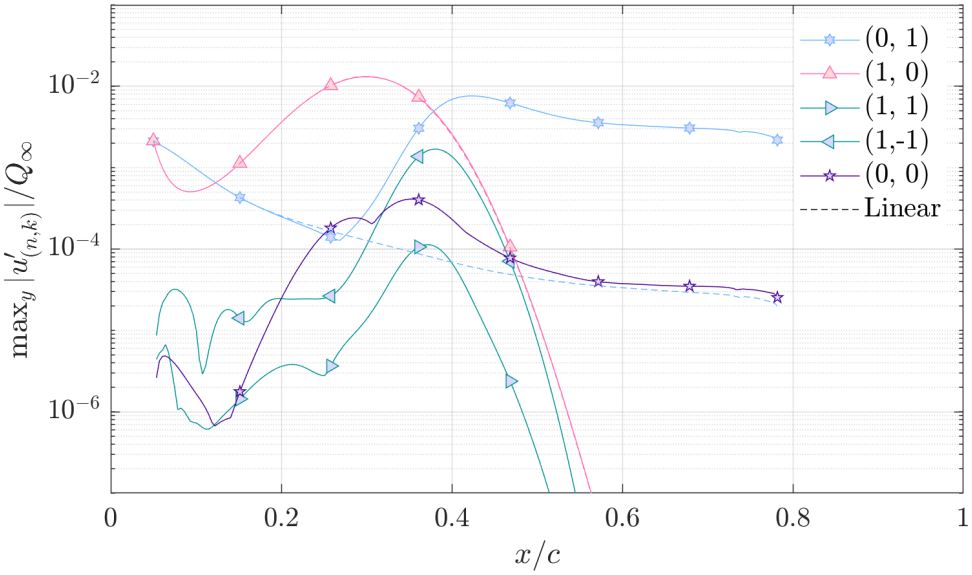

Figure 7.24: Amplitude distributions against x/c for the S207 $\alpha = -1.022°$, $\Lambda = 20°$ top side case for a TS/SCF interaction of high initial amplitude. The amplitudes of the $(1,0)$ and the $(0,1)$ at $x/c = 0.05$ are assigned to $\max_y |u'_{(n,k)}|/\overline{u}_e = 10^{-2.75}$.

down process with the mean-flow distortion. The first stage is indicated by a stable SCF vortex as the dominant Fourier mode and the mean-flow distortion $(0,0)$ is subsequently stabilized. For the second stage, the $(1,0)$ TS becomes unstable and drives the growth of the $(0,0)$ after its amplitude overtakes the SCF. Third: the MFD amplitude intersects that of the SCF, exchanging energy and exciting growth with the three-dimensional Fourier modes: the $(0,1)$ and the $(1,\pm1)$ oblique pair. The fourth stage is marked by the SCF again becoming the dominant Fourier mode, overtaking the TS wave and soon returning to its linear dynamics. The TS $(1,0)$ is highly stable in this region beyond its branch-II location, suppressing further growth of the oblique pair and avoiding a catastrophic breakdown of the laminar flow.

It is worth investigating why the growth of the left oblique wave $(1,-1)$ is larger than that of the $(1,1)$, when comparatively for the TS subharmonic resonance, the right oblique wave was dominant. In this configuration, there is a correlation of the phase speed components in the inviscid-streamline-orthogonal direction $c_{ph,\overline{w}_s\,(n,k)}$ between the $(1,0)$ and the $(1,-1)$ *matching sign*, perhaps easing the transfer of energy from the dominant $(1,0)$ TS to the $(1,-1)$. See Fig. 7.25. This

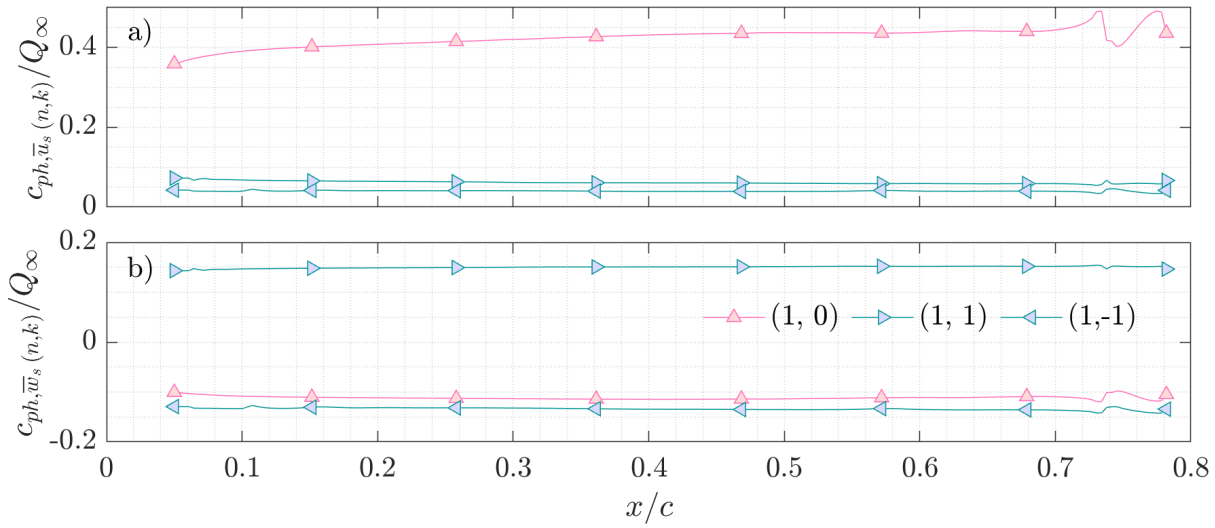

Figure 7.25: Phase-speed distributions of the 3000 Hz TS $(1,0)$ and the oblique pair $(1,\pm1)$. Subplot a) corresponds to the inviscid-streamline-parallel component of phase velocity, whereas b) corresponds to the inviscid-streamline-orthogonal component, as defined in Eq. (7.3).

is a quantitative demonstrative of Herbert's quote: that modes of secondary instability and oblique TS waves are *different kinds of animals*.

Before varying the initial amplitudes similar to the TS subharmonic resonance analysis in the previous section of §7.4.1.2, it is worth discussing another swept-wing transition experiment in flight. In the 1990s, the Fokker 100 (F100) aircraft was equipped with a laminar flow glove on its swept wings and a hybrid laminar-flow-control (HLFC) system that could apply suction to the near-surface flowfield near the leading edge [156]. Test cases considered a range of Reynolds numbers from 17 to 30 million, Mach numbers $\mathrm{M}_{Q_\infty} = 0.50-0.80$, and sweep angles $\Lambda = 17^\circ - 24^\circ$ [157, 158]. The reference velocity and chord direction are not specified, so one may presume it is commensurate with the previous analysis performed by Schrauf on the VFW 614/ATTAS flight experiments. That is, the Reynolds number is expressed as $\mathrm{Re}_{c\,\sec\Lambda}^{Q_\infty}$, defined in Eq. (7.8). Converting to $\mathrm{Re}_c^{\overline{u}_\infty\overline{v}_\infty}$, the Reynolds numbers vary from $\mathrm{Re}_c^{\overline{u}_\infty\overline{v}_\infty} \approx 16.3-27.4\times10^6$—slightly higher than the present analysis of the S207 at $\mathrm{Re}_c^{\overline{u}_\infty\overline{v}_\infty} = 13.2\times10^6$. Schrauf found that in order to match NPSE calculations of a TS/SCF interaction with one of the flight tests on the Fokker 100 flight experiment, a TS initial amplitude of 4×10^{-4} was required [159]. This is quite a stunning

result, as the NPSE TS/SCF analysis over the VFW 614/ATTAS flight correlated the transition location to TS initial amplitudes of nearly *400 times smaller*: $1-5\times10^{-6}$ at the branch-I location. To qualify this, Schrauf notes in the 2004 journal article that the suction system as part of the F100's HLFC system cannot be neglected, and the internal noise may be affecting TS differently than that over the VFW 614/ATTAS wing without suction [158]. That being said, Schrauf's NPSE TS/SCF interaction over the F100 ought to be included in the present discussion to provide an additional reference data point for TS initial amplitudes in flight.

Now having discussed the Fokker 100 analysis by Schrauf, let us vary the initial amplitudes for the TS/SCF interaction over the present S207 configuration. Amplitudes of $\max_y |u'_{(n,k)}|/\overline{u}_e$ at $x/c = 0.05$ for the $(0,1)$ and the $(1,0)$ are varied from 10^{-6} to $10^{-2.5}$. The maximum amplitude across s is then selected and plotted for each Fourier mode against the branch-I TS amplitude $A_{0,\,(1,0)\,\mathrm{TS}}$ as the abscissa of Fig. 7.26.

Note that the resonance of the $(1,\pm1)$ and the SCF $(0,1)$ doesn't occur until high branch-I amplitudes $A_{0,\,(1,0)\,\mathrm{TS}}$. Even further, the nonlinear equations do not halt on convergence until the highest amplitude considered at $A_{0,\,(1,0)\,\mathrm{TS}} \approx 9\times10^{-4}$. For that case, the NPSE simulation diverges at an $x/c = 0.34$. These initial amplitudes are orders of magnitude higher than that observed in Schrauf's correlation with transition on the VFW 614/ATTAS laminar flow glove flight experiments. However, they are on the same order of magnitude of the HLFC flight experiments of the Fokker 100 aircraft where transition was observed. Since there is no plan to implement a suction system near the leading edge of the S207, it is unlikely TS initial amplitudes of 4×10^{-4} will be reached, but may be closer to that of the VFW 614/ATTAS flight experiment. With that in mind, the similar conclusion is reached as before: the interaction of TS and SCF is not expected to incur breakdown to turbulence for the top side of the S207 at cruise for $\alpha = -1.022°$ and $\Lambda = 20°$.

7.5 Stability analysis at $\Lambda = 20°$ for $\alpha = -2.252°$, bottom side

Continuing onward with the predictive analysis of the S207, it is judicious to consider another extreme of the pressure distribution that can potentially destabilize Tollmien-Schlichting waves. For the reader's convenience, the pressure coefficient of Fig. 7.1 is shown again below. The bottom

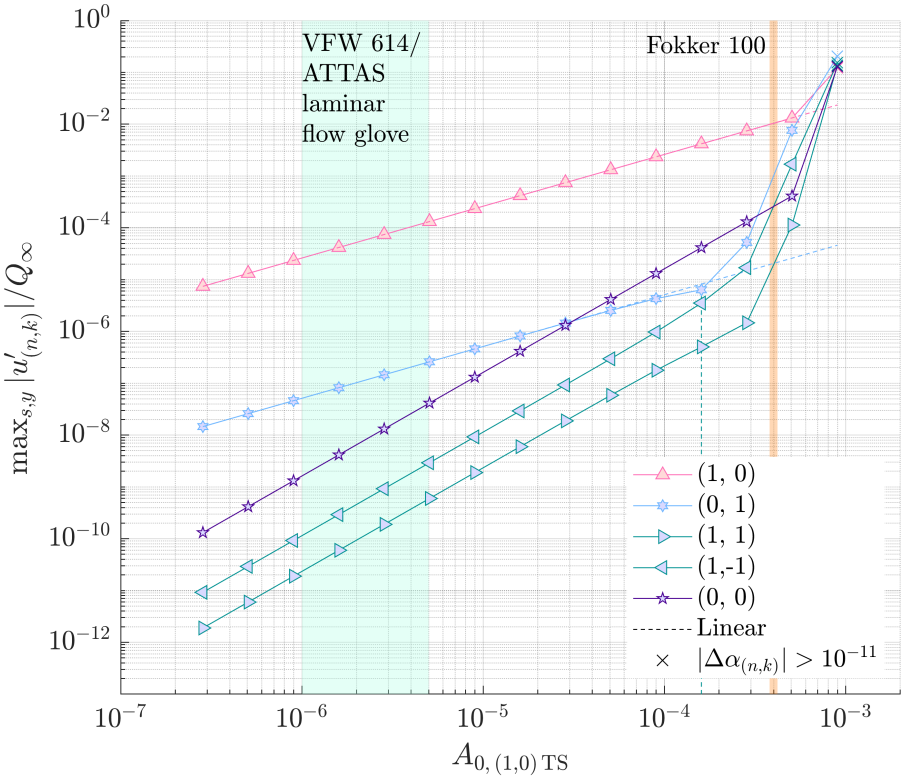

Figure 7.26: Maximum amplitudes in both s and y for selected Fourier modes against the branch-I amplitude of the $(1,0)$ $\beta = 0$ 3000 Hz TS wave, $A_{0,\,(1,0)\,\mathrm{TS}}$. Linear extrapolation for the $(1,0)$ and the $\lambda_z = 12\,\mathrm{mm}$ $(0,1)$ SCF are indicated with dashed lines. The vertical, teal, dashed line indicates when SCF begins to deviate from its linear behavior. The $\times$ marker indicates when the NPSE fails to converge its α-convergence criterion less than 10^{-11} for all Fourier modes. The initial amplitudes that correlate well with transition for the VFW 614/ATTAS laminar flow glove flight experiments are indicated with a transparent cyan patch [115]. The initial TS amplitude of a Fokker 100 flight experiment is indicated with the orange patch [159].

side of the S207 at the lowest angle of attack $-2.252°$ experiences a pressure gradient that is not significantly favorable. This may imply that Tollmien-Schlichting amplification is large. On the other hand, this suggests less crossflow amplification, as the inflectional crossflow velocity profile vanishes at zero pressure gradient. With these in mind, it is worth considering again two possible pathways to transition: a) TS subharmonic resonance and b) TS/SCF interaction.

To preface the stability analysis in this section, the computational domain on the bottom side of a wing at negative angle is nuanced. Since the attachment line for this angle of attack $\alpha = -2.252°$ has a positive airfoil vertical coordinate Y_c, "away" from the attachment line in terms of the bottom

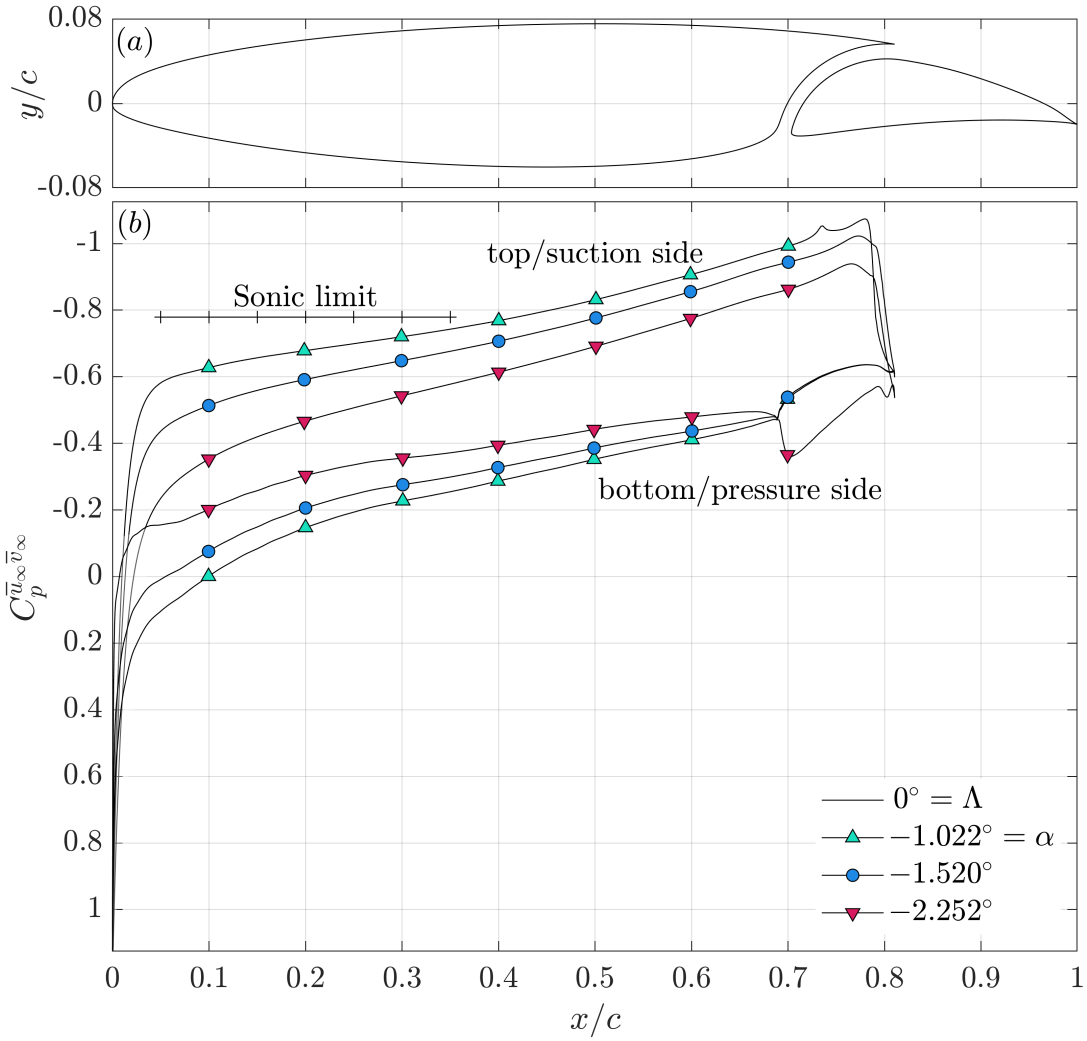

Figure 7.27: a) The S207 airfoil cross-section b) Pressure coefficient $C_p^{\overline{u}_\infty \overline{v}_\infty}$ as a function of x/c at sweep $\Lambda = 0^\circ$ for the fore element. The sonic limit indicates when the boundary-layer-edge velocity is equal to the speed of sound. Angles of attack $\alpha = \{-1.022^\circ, -1.520^\circ, -2.252^\circ\}$ are delineated with markers. This figure is identical to Fig. 7.1, depicted again for the reader's convenience.

side of the airfoil is *non-monotonic* in x. That is to say, for the first several points rounding the airfoil leading edge from the attachment line, the x coordinate decreases, achieves a global minimum, then increases for the rest of the wing. Because of this non-monotonicity in x, the stability computational domain is no longer expressed directly in x, but instead solely in s. In order for results to be shown in x/c though, a spline-interpolation is performed onto the original x grid from the dense, $N_\xi = 2000$ DEKAF base-flow grid.

7.5.1 Linear analysis

In the absence of a transition location, as these calculations are predictive, one can select content based on the maximum N-factors at a given x/c location. Since the value of the 3D-TS N-factor envelope is monotonically increasing in x, a streamwise location x/c must be chosen upstream of the back in order to analyze premature transition. Let us consider $x/c = 0.40$ for the bottom side, as this is proportional to the x/c considered for the top side of $\alpha = -1.022^\circ$ over their respective domains. That is, $0.47/0.80 \approx 0.40/0.70$. The maximally amplified 3D TS at $x/c = 0.40$ corresponds to $(1870\,\mathrm{Hz},\, -30\,\mathrm{mm})$[7] reaching an $N \approx 4.3$. For all of the instabilities with $\beta = 0$, the one reaching the maximum N-factor is $1870\,\mathrm{Hz}$ and is also the highest N-factor of the $\beta = 0$ TS family at $x/c = 0.40$. Note that these TS N-factors are lower than the previous configuration considered by $\Delta N \approx 1$ (for the top side at $\alpha = -1.022^\circ, \Lambda = 20^\circ$.)

We expect this configuration to be more TS-oriented, as the pressure is by and large less favorable than the $\alpha = -1.022^\circ$ top side's distribution. To demonstrate this, consider the stationary crossflow N-factors across the chord in Fig. 7.29. Traveling crossflow is omitted for brevity. As observed, N-factors are quite small: 0.6 at the most for short wavelength content of $\lambda_z = 5\,\mathrm{mm}$ SCF and 0.25 for the long wavelength content of $\lambda_z = 25\,\mathrm{mm}$ SCF. Again note that these SCF N-factors are lower than the previous configuration considered by $\Delta N \approx 0.4$ (for the top side at

[7]The sign on the maximally amplified 3D TS's spanwise wavenumber changes between stability analysis on the top side and bottom side because of the chosen coordinate-system convention in DEKAF. For top sides of airfoils, wall-normal y points mostly upward, so a right-handed z is out of the page. The converse is true for the bottom side: wall-normal y is mostly downward, so z points into the page. This causes the sign of $\overline{w}$ additionally to alternate between the base flows of each side, which is pleasant for computing derivatives directly at the attachment line, as cusps are avoided.

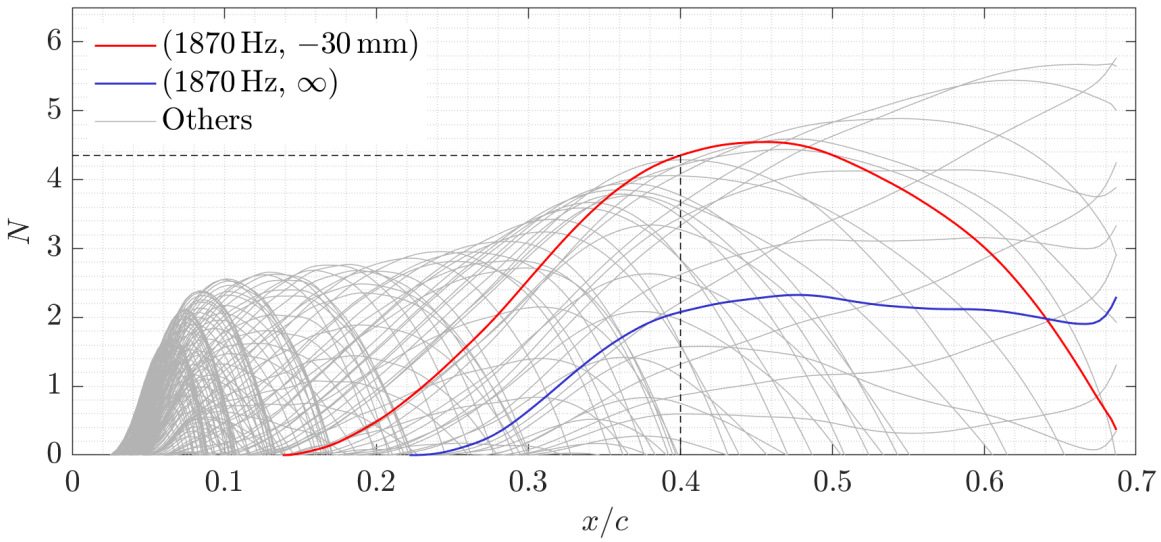

Figure 7.28: TS N-factors on the S207 $\alpha = -2.252°$, $\Lambda = 20°$ for the bottom side. The most amplified 3D TS at a selected $x/c = 0.40$ is $(1870\,\text{Hz}, -30\,\text{mm})$ achieving an N-factor of 4.3. The most amplified $\beta = 0$ TS is 1870 Hz, with a max N-factor of 2.2. Other linear content queried is shown in gray.

$\alpha = -1.022°, \Lambda = 20°$.) Given the primary instability content of this flowfield to be associated with Tollmien-Schlichting, let us first consider the TS subharmonic resonance secondary mechanism as opposed to the TS/SCF interaction.

7.5.2 TS subharmonic resonance

There is an important takeaway from the analysis in the previous section on the S207 at $\Lambda = 20°$ for $\alpha = -1.022°$ on the top side. Using a small discretized Fourier space can be used when using NPSE to accurately and efficiently calculate the deviation from laminar flow for the TS subharmonic resonance mechanism on the S207. This lesson learned will be applied for this configuration immediately, as the larger Fourier space of $N_m = 23$ will be discarded for the reduced Fourier space of $N_m = 4$ instead. The reduced Fourier space models only the MFD $(0, 0)$, the $\beta = 0$ TS wave $(2, 0)$, and the subharmonic oblique pair $(1, \pm 1)$, as shown previously in Fig. 7.19. For this configuration, the smallest angular frequency is chosen such that $\omega_0 = 2\pi \times 1870\,\text{Hz}$ and the smallest spanwise wavenumber multiple is $\beta_0 = 2\pi/30\,\text{mm}$ such that the most amplified 3D TS at $x/c = 0.40$ is the $(1, -1)$ Fourier mode. This indicates then the $(2, 0)$ is a high frequency TS

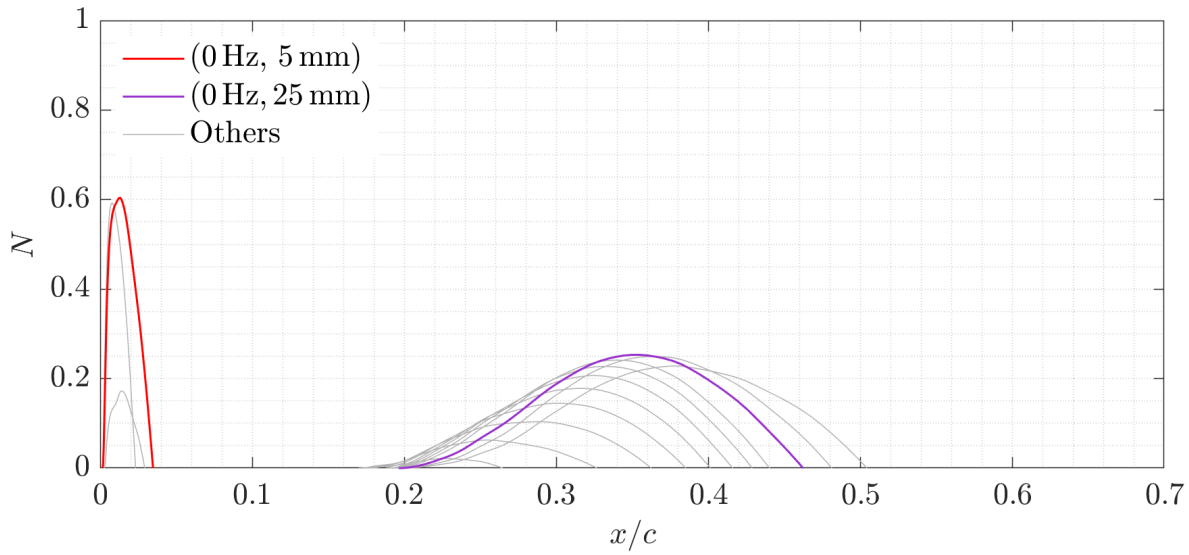

Figure 7.29: SCF N-factors on the S207 $\alpha = -2.252°$, $\Lambda = 20°$ for the bottom side. The most amplified short wavelength SCF is $\lambda_z = 5\,\mathrm{mm}$, achieving an N-factor of 0.6. The most amplified large wavelength SCF is $\lambda_z = 25\,\mathrm{mm}$, achieving an N-factor of 0.25. Other linear content queried is shown in gray.

wave of $3740\,\mathrm{Hz}$.

With smaller TS N-factors than the $\Lambda = 20°$ for $\alpha = -1.022°$, one might expect that this configuration experiences less nonlinear interaction for the TS subharmonic resonance. A calculation of the $(2,0)$, $(1,\pm1)$, and the $(0,0)$ provides the amplitudes shown in Fig. 7.30. Here, the initial amplitude methodology is used by assigning the branch-I values of the $(1,-1)$ and the $(2,0)$ to be approximately the same. Since the $(1,1)$ Fourier mode is highly stabilized in this configuration, its initial amplitude is supposed to equal that of the $(1,-1)$. This specific case demonstrates the dynamics at a realistic cruise level of amplitude, as informed by the flight-informed correlation from Schrauf et al. [115]. The Fourier modes $(1,-1)$ and $(2,0)$ stay linear while there is a slight exchange of energy between the $(1,1)$ and the $(0,0)$ as they approach one another in amplitude at $x/c \approx 0.20$. This weak interaction is not enough to trigger resonance between the oblique pair at these low amplitudes and the flow remains laminar.

The initial amplitudes of this system are varied again to quantify the uncertainty in the transition location prediction. The results are shown in Fig. 7.31, varying the initial amplitudes of the $(2,0)$

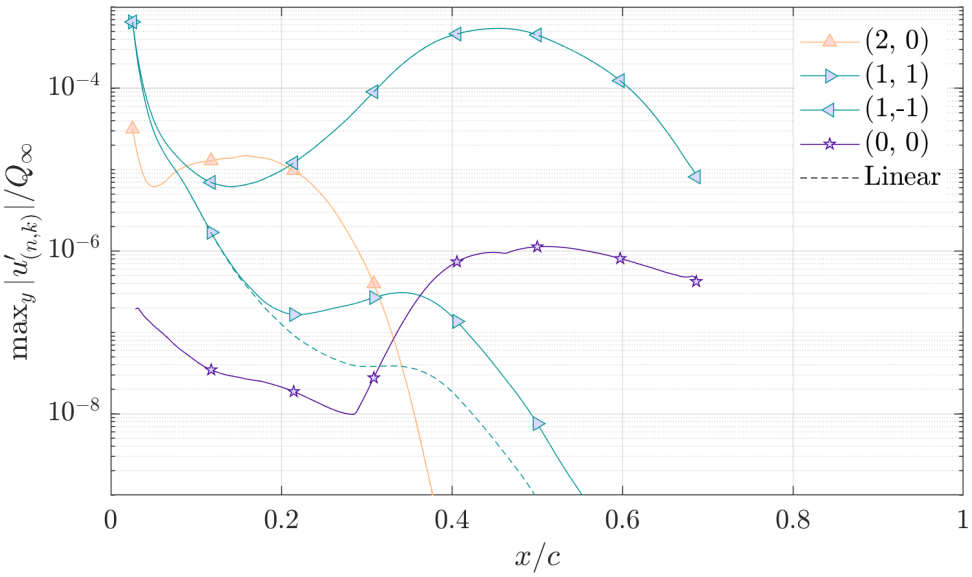

Figure 7.30: Amplitude distributions against x/c for the S207 $\alpha = -2.252°$, $\Lambda = 20°$ case, assigning the branch-I amplitudes to be equal for $(2, 0)$ and the $(1, -1)$ at a realistic cruise level.

TS wave and the oblique subharmonic pair $(1, \pm 1)$ such that the $(2, 0)$ and the $(1, -1)$ achieve approximately the same value at their linear branch-I locations. Initial amplitudes are increased until the branch-I location is modulated due to nonlinear effects. Nonlinearities that far upstream on the chord could instead imply different pathways to transition, such as transient growth [7]. With good judgment, this indicates the upper limit on the initial amplitude applicable for the NPSE disturbance assumption.

Even at high initial amplitudes, there is not enough linear amplification to excite even the $(1, \pm 1)$ resonance. Comparing this chart with Fig. 7.21, this suggests that if the linear amplification is less between distinct configurations, the same physical nonlinear processes (e.g., TS subharmonic resonance) will experience less amplification as well. Intuition is now quantitatively confirmed for these nonlinear calculations. This reasoning will be applied for additional configurations when comparing linear amplification levels.

Directly applying this reasoning, with less TS and SCF amplification, the nonlinear interaction of TS/SCF is expected to be less for this configuration than that of the $\Lambda = 20°$, $\alpha = -1.022°$

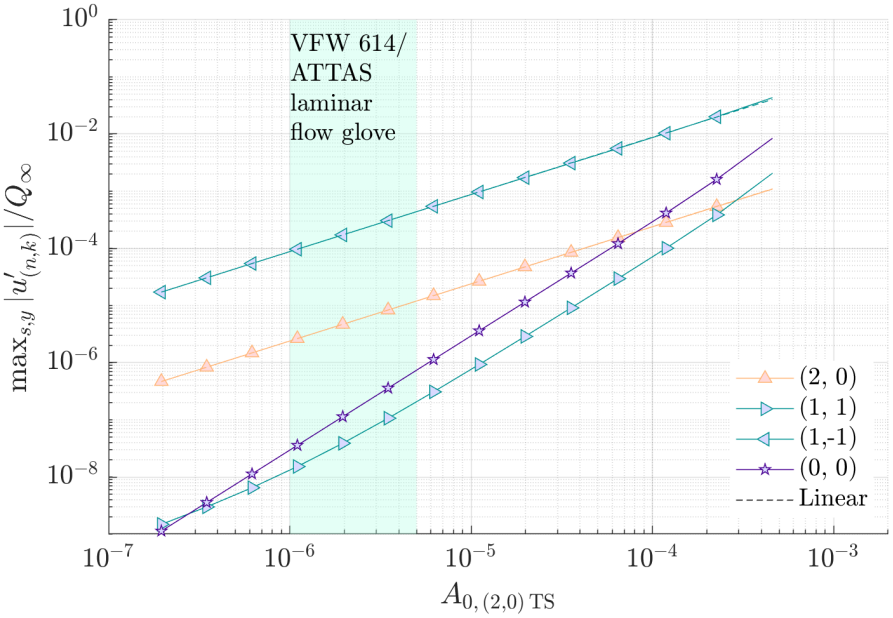

Figure 7.31: Maximum amplitudes in both s and y for selected Fourier modes against the branch-I amplitude of the $(2,0)$ $\beta = 0$ TS wave, $A_{0,\,(2,0)\,\mathrm{TS}}$. Linear extrapolation for the $(1,1)$ and the $(2,0)$ are indicated with dashed lines. The initial amplitudes that correlate well with transition for the VFW 614/ATTAS laminar flow glove flight experiments are indicated with a transparent cyan patch. Resonance of the $(1,\pm1)$ is indicated with a dashed line to the corresponding branch-I TS amplitude. Compare with Fig. 7.21 for the top side at $\alpha = -1.022°$.

case. And recall from Fig. 7.26, resonance from the oblique pair $(1,\pm1)$ didn't initiate breakdown of laminar flow until initial amplitudes unrealistic for cruise levels. With these two observations in mind, it is assumed that the TS/SCF interaction on this configuration will also exhibit a similar trend and is omitted from further study.

To conclude the results of the previous sections to this point, the fore element of the S207 is not expected to experience boundary-layer transition at cruise with sweep $\Lambda = 20°$ on the top side at $\alpha = -1.022°$ and on the bottom side at $\alpha = -2.252°$ due to either TS subharmonic resonance or TS/SCF interaction.

7.6 Stability analysis at $\Lambda = 20°$ for $\alpha = -2.252°$, top side

Let us now pivot the analysis from TS-oriented transition to SCF-oriented transition processes. The pressure coefficient is shown again for the reader's convenience in Fig. 7.32. Note that there

is a strongly favorable pressure gradient over the wing for the angle of attack $\alpha = -2.252^\circ$ on the top side. Since favorable gradients are known to highly destabilize the crossflow (CF) mechanism while stabilizing TS, it is expected the transition process will be dominated by the crossflow primary mechanism for this configuration. Analysis by Heston showed that the S207 at the mid-span angle of attack $\alpha = -1.520^\circ$ experienced appreciable SCF growth to reach an N-factor of 5 [160] for $\Lambda = 20^\circ$. Increasing the favorable gradient is expected to further increase this amplification level.

7.6.1 Linear analysis

For computational efficiency and accuracy with these stationary crossflow calculations, streamwise clustering is employed, as described earlier in §4.2.2. A total number of streamwise nodes $N_s = 350$ is used. The mapping parameters of $\gamma_{\text{map}} = 0.50$ and $\beta_{\text{map}} = 15$ are input to achieve very high resolution at the neutral point while subsequently deresolving as the solution is marched down the chord. The branch-I neutral point of the $8\,\text{mm}$ SCF is at $x/c \approx 0.005$. Again, $x/c = 0.47$ is selected again as the x/c query location on the top side of the S207.

7.6.2 Nonlinear analysis of SCF saturation

Before discussing the nonlinear results of the present S207 analysis, let us first outline relevant observations from stationary crossflow experimental validation in the past.

Reibert et al. analyzed the development of stationary crossflow vortices over a wing known as the NLF(2)-0415 [26]. Discrete roughness elements were adhered to the wing along the span at $x/c = 0.023$ with a height of $k = 6\,\mu\text{m}$, a diameter of $3.7\,\text{mm}$, and a center-to-center spacing of $12\,\text{mm}$ to match the linearly most amplified SCF content. For the case of $\text{Re}_c = 2.4 \times 10^6$, Haynes & Reed performed computations to match the measurements of Reibert et al. on the stationary crossflow development, saturation, and further distortion of the flowfield approaching the transition location. Examining Figure 5.29 from Haynes' dissertation, the branch-I point of the SCF Fourier mode $(0, 1)$ appears to be near the initialization location of $x/c = 0.05$, where a root-mean-square amplitude is given as 2.5×10^{-3} [116]. This amplitude is presumed to be nondimensional with

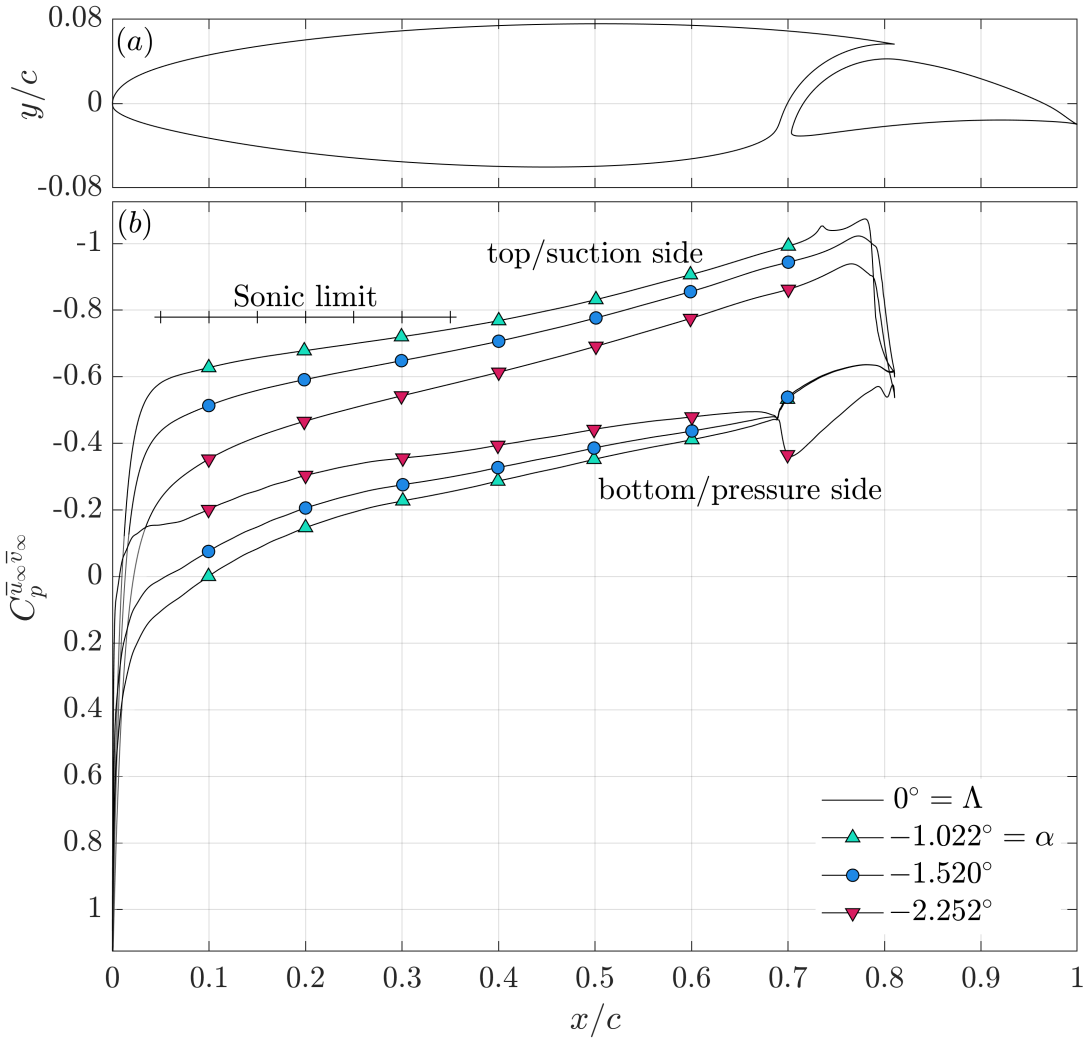

Figure 7.32: a) The S207 airfoil cross-section b) Pressure coefficient $C_p^{\overline{u}_\infty \overline{v}_\infty}$ as a function of x/c at sweep $\Lambda = 0^\circ$ for the fore element. The sonic limit indicates when the boundary-layer-edge velocity is equal to the speed of sound. Angles of attack $\alpha = \{-1.022^\circ, -1.520^\circ, -2.252^\circ\}$ are delineated with markers. This figure is identical to Fig. 7.1, depicted again for the reader's convenience.

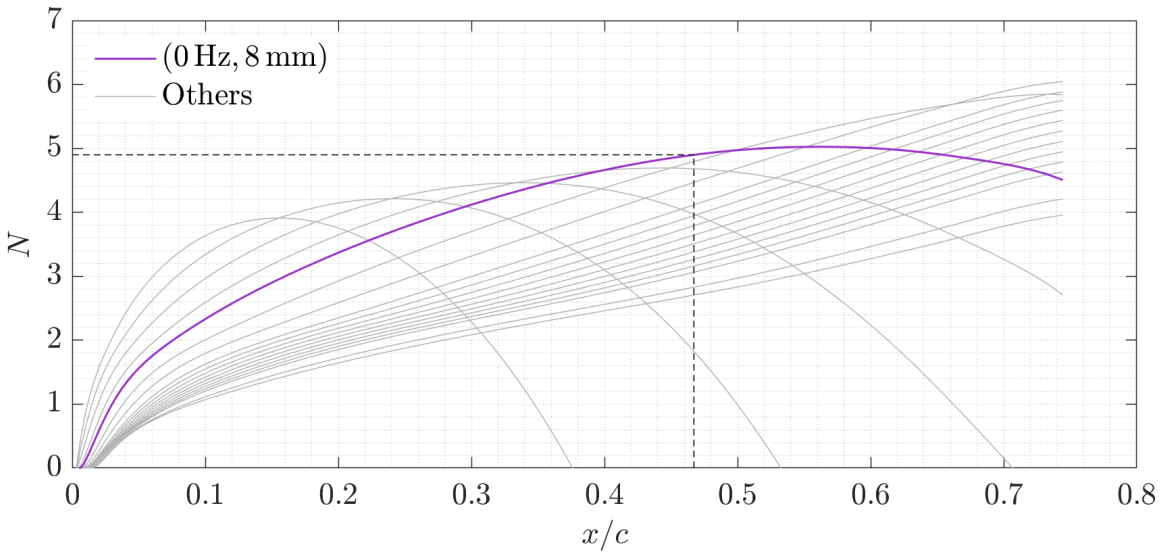

Figure 7.33: Stationary crossflow N-factors on the S207 $\alpha = -2.252°$, $\Lambda = 20°$ on the top side.

respect to the resultant freestream velocity Q_∞. To convert to the convention primarily used in this dissertation, a division by $\sqrt{2}$ must be done, undoing the root-mean-square to specify the magnitude of the perturbation directly. Then for the validation of Haynes & Reed on the $\mathrm{Re}_c = 2.4 \times 10^6$ case, the SCF initial amplitude is written as $\max_y |u'_{(0,1)}|/Q_\infty = 2.5/\sqrt{2} \times 10^{-3} \approx 1.767 \times 10^{-3}$.

Note however that the S207 in cruise will surely not have discrete roughness elements placed along the span. Additionally, freestream disturbances in flight may presumably have lower vorticity than that of a quiet wind tunnel. If one assumes that the boundary-layer receptivity is commensurate between the S207 and the NLF(2)-0415 despite the variation in Mach number, angle of attack, Reynolds number, sweep, and pressure distribution, then the $2.5/\sqrt{2} \times 10^{-3}$ initial amplitude value of Haynes & Reed serves as an upper bound for the initial amplitude on the S207. Discrete roughness elements provide higher initial amplitudes to SCF than natural roughness, provided that the natural roughness is extremely small and the wing has been polished ad nauseum. For instance, Reibert et al. note that submicron irregularities ultimately produce crossflow vortices on the NLF(2)-0415 wing at $\mathrm{Re}_c = 3.0 \times 10^6$, $\alpha = -4°$, and $\Lambda = 45°$ [26]. During operational maintenance of the S207 on an aircraft, roughness near the leading edge should be kept to

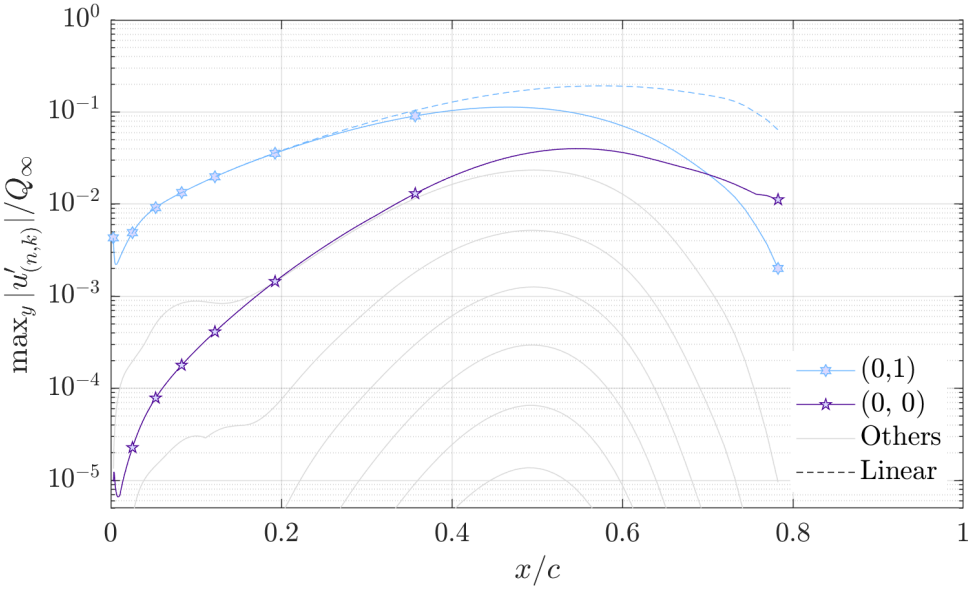

Figure 7.34: SCF amplitude distributions against x/c for the top side of the S207 $\alpha = -2.252°$, $\Lambda = 20°$ case. The initial amplitude assigned for the $(0,1)$ is $\max_y |u'_{(0,1)}|/Q_\infty \approx 2.2 \times 10^{-3}$ at its branch-I location.

an absolute minimum. If the surface roughness conditions have any appreciable peaks and valleys, crossflow will be excited, and with significant amplification as seen in this case for $N > 5$, transition is likely expected.

Let us now consider an example of stationary crossflow saturation over the S207 at cruise conditions. Suppose an initial amplitude of $\max_y |u'_{(0,1)}|/Q_\infty \approx 2.2 \times 10^{-3}$ for the fundamental stationary crossflow harmonic at its branch-I location of $x/c \approx 0.006$. Figure 7.34 demonstrates the amplitude distribution for the fundamental, the mean-flow distortion, and the higher superharmonics over the S207 in this configuration. The highest superharmonic included is the $(0,8)$ for this present simulation to mimic the methodology of Haynes & Reed. The fundamental $(0,1)$ appears to saturate near 8% in amplitude, reaching a global maximum of 10% soon after.

Varying the initial amplitude now, Fig. 7.35 shows the maximum amplitude obtained by each disturbance over the streamwise domain charted against the branch-I amplitude of the $(0,1)$, denoted as $A_{0,\,(0,1)\,\mathrm{SCF}}$. For reference, the initial amplitude found by Haynes & Reed for their experimental validation case with Reibert et al. is shown as a vertical dashed line. The linear dynamics

of the fundamental $(0, 1)$ are indicated in the dashed blue line, which indicates that saturation begins to occur near amplitudes of $\max_{s,y} |u'_{(0,1)}|/Q_\infty = 5\%$, corresponding to a branch-I, initial amplitude of $\max_y |u'_{(0,1)}|/Q_\infty = 7 \times 10^{-4}$.

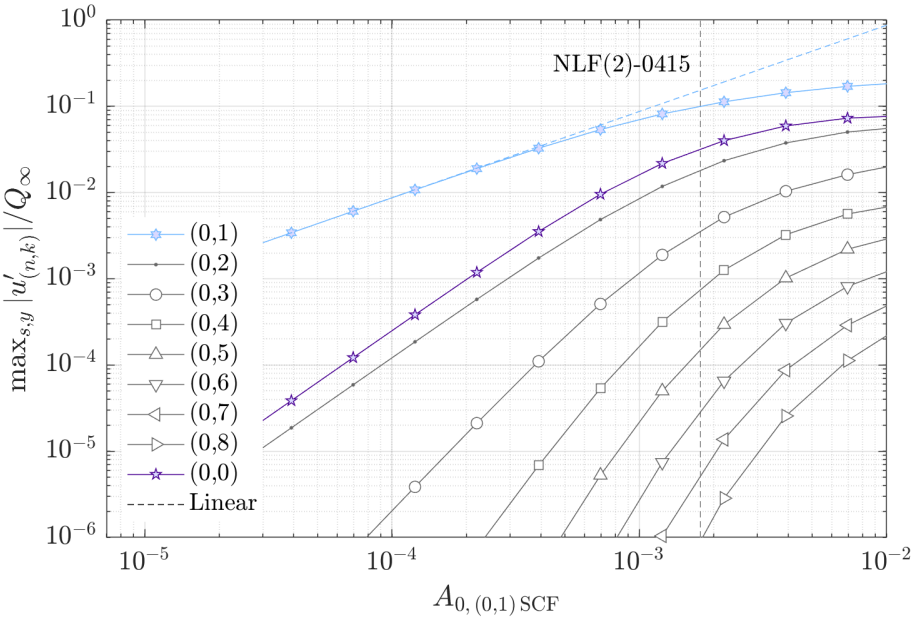

Figure 7.35: Maximum amplitudes in both s and y for a stationary crossflow simulation against the branch-I amplitude of the $(0, 1)$ fundamental SCF, $A_{0,\,(0,1)\,\mathrm{SCF}}$. Linear extrapolation for the $(0, 1)$ is indicated with the blue dashed line. The SCF initial amplitude of Haynes & Reed is indicated by a vertical, dashed line. Superharmonics are included up to $(0, 8)$ inclusive.

If the initial amplitude of Haynes & Reed, i.e., $\max_y |u'_{(0,1)}|/Q_\infty = 2.5/\sqrt{2} \times 10^{-3}$, is presumed for the current S207 case, then from interpolating on Fig. 7.35, SCF achieves a maximum amplitude of $\max_{s,y} |u'_{(0,1)}|/Q_\infty = 0.10$, whereas the mean-flow distortion reaches a maximum of $\max_{s,y} |u'_{(0,0)}|/Q_\infty = 0.02$. This may be enough to induce the growth of secondary instabilities, as Reibert et al. observed appreciably sized vortices at an amplitude of $|u'_{(0,1)}|/Q_\infty = 0.12/\sqrt{2} \approx 0.085$ at $x/c \approx 0.40$ with transition soon thereafter at $x/c \approx 0.47$ [14, 26].

The assumptions relating initial amplitudes is dubious, as they are entirely dependent on the unknown surface roughness conditions on the S207 in cruise. Flying with a SCF N-factor of higher than 5 is dangerous for this reason, considering additionally that this is only the on-design angle

of attack along the twisted span. Off-design angles of attack with pilot tolerance may exacerbate and push these growth rates even higher than reported here.[8] Engineering judgment then suggests decrementing the selected sweep angle. For simplicity, the case $\Lambda = 15^\circ$ can be considered in brevity. This will be considered after a brief section concerning a reduced set of Fourier modes.

7.6.2.1 Reduced set of Fourier modes for SCF saturation

In the spirit of computational efficiency, that is, to assess what fidelity is required to achieve the same quantitative conclusions, the number of Fourier modes for these simulations is reduced. Instead of a simulation with superharmonics up to the $(0, 8)$ inclusive, now suppose only the fundamental and mean-flow distortion are present. Following the nomenclature as before, $N_m = 2$ for this case, while $N_{m,\text{full}} = 3$ when accounting for the complex conjugate $(0, -1)$.

The initial amplitude of the fundamental is varied identically as before and the resulting maximum streamwise amplitudes are charted against the branch-I $(0, 1)$ amplitude in Fig. 7.36. The distribution is qualitatively identical as before for the more finely resolved case of Fig. 7.35. Saturation is predicted at essentially the same initial amplitude. Only at very high initial amplitudes where the superharmonics have appreciable size do the two figures show slight discrepancy. For instance, the fundamental's maximum amplitude $\max_{s,y} |u'_{(0,1)}|/Q_\infty$ at the right axis of $A_{0,(0,1)\,\text{SCF}} = 10^{-2}$ reaches slightly above 20%. For the more finely resolved case shown previously, the $(0, 1)$ reaches a maximum amplitude just slightly under 20%, stabilized by the presence of additional superharmonics.

By comparing these two figures, it is clear that with the goal of the nonlinear analysis to identify when saturation occurs and quantify the corresponding amplitudes of the fundamental and mean-flow distortion, then only a reduced set of Fourier modes is required.

For the same angle of attack and side, the sweep of $\Lambda = 15^\circ$ is now considered.

[8] An example of pilot tolerance on the angle of attack for a boundary-layer transition flight experiment is $\pm 0.1^\circ$ while near $\alpha = -7^\circ$ [161].

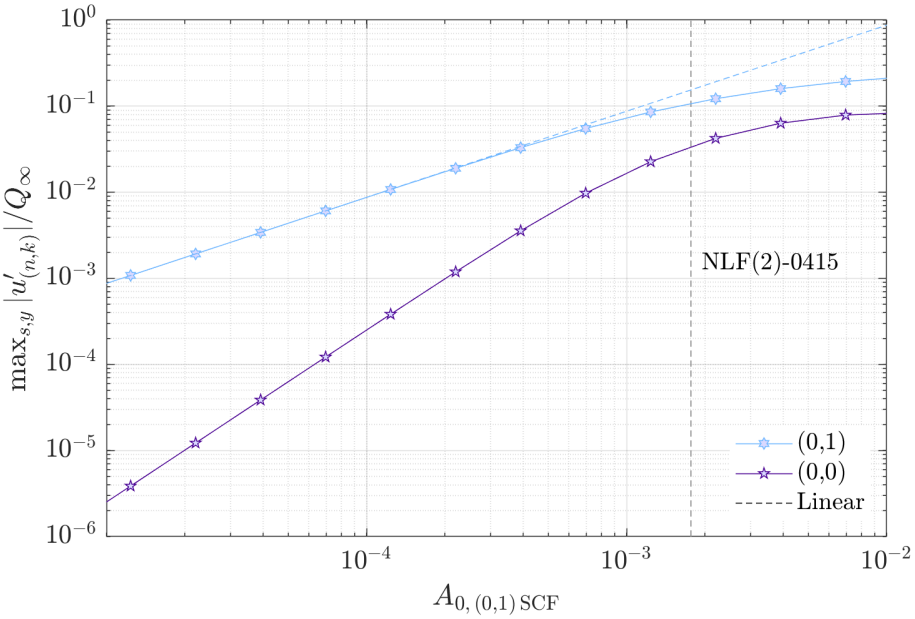

Figure 7.36: Maximum amplitudes in both s and y for a stationary crossflow simulation against the branch-I amplitude of the $(0,1)$ fundamental SCF, $A_{0,\,(0,1)\,\mathrm{SCF}}$. A reduced set of Fourier modes is used, only simulating the fundamental and the mean-flow distortion. Linear extrapolation for the $(0,1)$ is indicated with the blue dashed line. The SCF initial amplitude of Haynes & Reed is indicated by a vertical, dashed line. Compare to the more finely resolved case of $N_m = 9$ shown in Fig. 7.35.

7.7 Stability analysis at $\Lambda = 15°$ for $\alpha = -2.252°$, top side

Following the same methodology as the previous sections, the linear N-factors (based on the Chu norm) are presented for the stationary crossflow disturbances in Fig. 7.37. The amplification levels only reach a maximum of $N = 0.6$ for the $\lambda_z = 7\,\mathrm{mm}$ wavelength. Comparing these results with the higher sweep of $\Lambda = 20°$ in Fig. 7.33, there is a drastic stabilization of the mechanism. With no appreciable linear amplification, a further SCF nonlinear study is omitted for this angle of attack and side of the wing.

The last configuration needed to assess SCF-dominated transition is $\alpha = -1.022°$ on the bottom side of the wing.

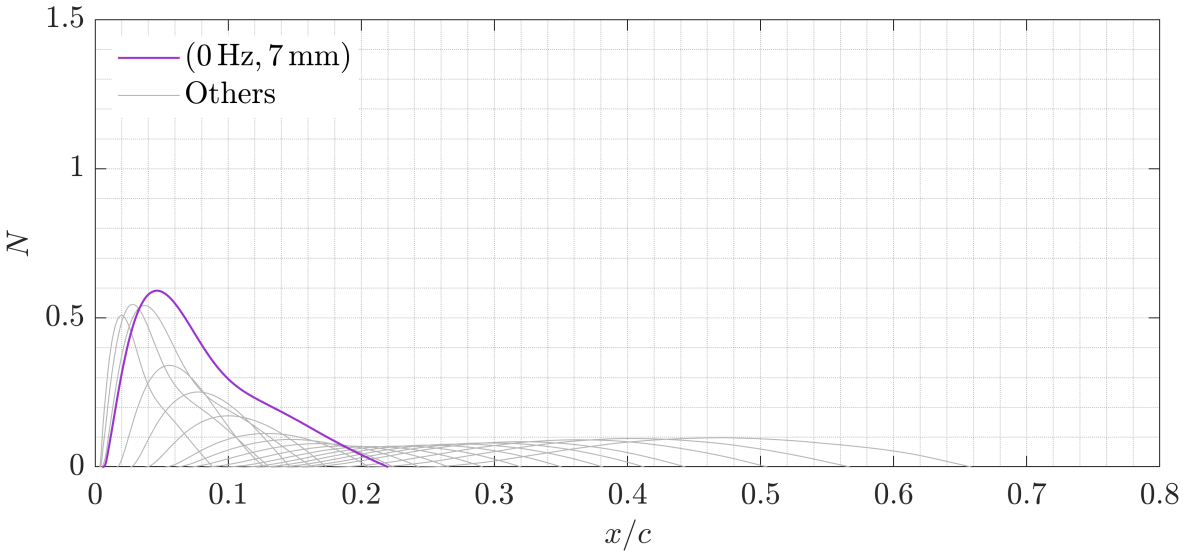

Figure 7.37: Stationary crossflow N-factors on the S207 $\alpha = -2.252°$, $\Lambda = 15°$ on the top side.

7.8 Stability analysis at $\Lambda = 15°$ for $\alpha = -1.022°$, bottom side

For the final considered configuration of $\alpha = -1.022°$ on the bottom side at $\Lambda = 15°$, the linear N-factors (based on the Chu norm) are presented in Fig. 7.38. The maximum N-factor here remains low: 1.2 for a wavelength of $\lambda_z = 10\,\mathrm{mm}$. Again, with no appreciable linear amplification, further nonlinear analyses are omitted.

7.9 Conclusions

A thorough assessment of boundary-layer stability has been presented for the S207 wing. The objective of the analysis was to answer the overarching question: *how much sweep can be applied to this wing while maintaining the benefits of the SNLF design?* Various transition pathways were considered over the vulnerable configurations of angle of attack along the span and sweep—considered in a Pareto-frontier fashion. Specifically, weakly favorable pressure gradients exist on a) the top side of the wing at $\alpha = -1.022°$ and b) the bottom side at $\alpha = -2.252°$. These two configurations prompted an analysis of TS-dominated transition pathways at sweep angles $\Lambda = 15°$ and $20°$. On the other hand, stronger favorable pressure gradients exist for the S207 on a) the top side at $\alpha = -2.252°$ and b) the bottom side at $\alpha = -1.022°$. At an appreciable sweep,

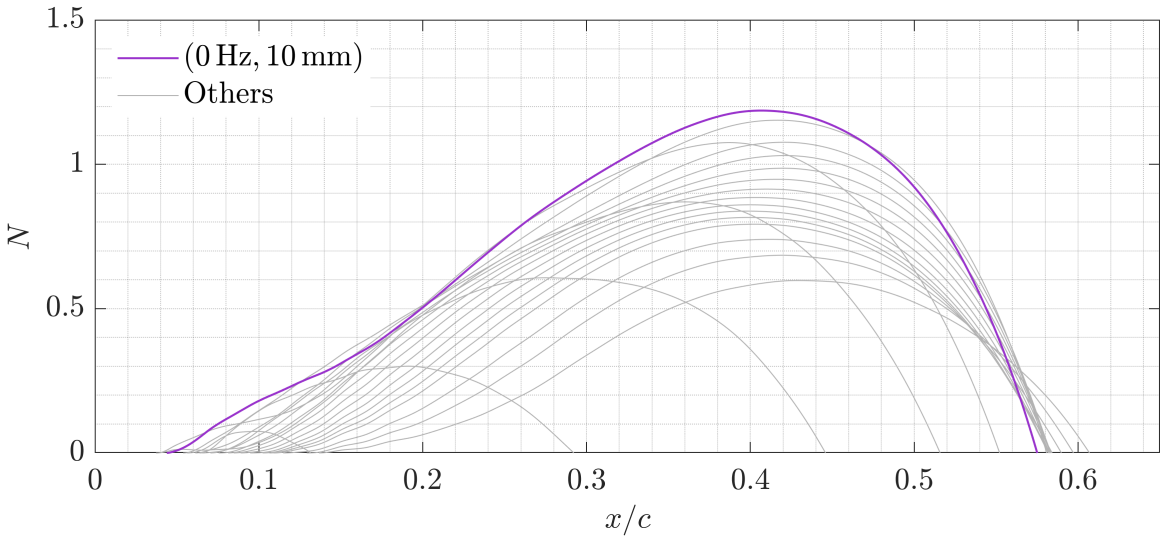

Figure 7.38: Stationary crossflow N-factors on the S207 $\alpha = -1.022°$, $\Lambda = 15°$ on the bottom side.

these configurations prompted analyses of SCF-dominated transition pathways. The individual conclusion of each analysis is enumerated below.

1. For $15°$ sweep at the angle of attack of $-1.022°$ on the top side, a nonlinear simulation including the interaction possibilities of many different primary and secondary instability mechanisms did not demonstrate any breakdown of laminarity—even at very high initial amplitudes for the system.

2. The sweep was then increased to $20°$ for the same angle of attack and side of the wing. The secondary instability mechanism of TS subharmonic resonance only indicated a breakdown of laminarity at very high initial amplitudes for the system: TS branch-I initial amplitudes of 9×10^{-4}. For reference, the initial amplitudes of TS found by Schrauf et al. when computing TS subharmonic resonance over a similar laminar-flow glove were 1×10^{-6} to 5×10^{-6} [115]. These values are nearly 200 times smaller than the aforementioned initial amplitude that would trigger breakdown over the S207 via TS subharmonic resonance. The Fokker 100 flight experiments as analyzed by Schrauf indicated a TS initial amplitude of 4×10^{-4} at branch-I, which is on the same order of magnitude of the present S207 values

that would predict laminar breakdown [159]. However, since the flight experiment featured a hybrid laminar-flow-control (HLFC) system applying suction, it must not be neglected that the HLFC's internal sound production affects TS receptivity and growth. Since the S207 is not planned to be equipped with suction near the leading edge, one could assume these high initial amplitudes will not be experienced in cruise.

3. An alternate transition pathway of TS/SCF interaction was considered for the same configuration. The conclusion was identical: only at high TS branch-I initial amplitudes of 9×10^{-4} did the nonlinear interaction lead to laminar breakdown.

4. Holding sweep constant at 20°, the second configuration sensitive to TS growth was considered next: the bottom side of the wing at $\alpha = -2.252^\circ$. Linear amplification levels of both TS and SCF were found to be lower than those of the top side of the wing at $\alpha = -1.022^\circ$. Subsequent nonlinear analysis of the TS subharmonic resonance demonstrated that there was no significant interaction leading to laminar breakdown for all physically appropriate initial amplitudes. TS/SCF was presumed to follow the same trend, and as such, its nonlinear analysis was omitted. This concluded the analysis of TS-dominated transition pathways for the S207.

5. Pivoting to the SCF-dominated transition pathway, the configuration of $\alpha = -2.252^\circ$ on the top side of the wing was considered next at $\Lambda = 20^\circ$. Saturation of stationary crossflow was computed to occur when the fundamental's branch-I initial amplitude was 7×10^{-4}. This value is more than two times smaller than a reference initial amplitude corresponding to the SCF validation study by Haynes & Reed [25].

6. With appreciable SCF growth present at 20° sweep, the next lower sweep angle was subsequently analyzed: $\Lambda = 15^\circ$. For the configuration of $\alpha = -2.252^\circ$ on the top side of the wing, linear amplification levels of stationary crossflow did not exceed $N = 1$. As such, nonlinear analysis was omitted as laminar flow was presumed.

7. Considering then the second configuration with favorable pressure gradients, the angle of attack $\alpha = -1.022^\circ$ on the bottom side of the wing at $\Lambda = 15^\circ$ was analyzed. Linear amplification levels were similarly low: barely exceeding an $N = 1$ over the extent of the chord. Further nonlinear analysis was not performed as laminar flow was presumed.

With these in mind, let us return to the question of how much sweep can be applied while retaining SNLF benefits. It is critical to first frame these analyses that they concern only the *on-design* cruise conditions for the wing across its span. Then, even with very mild linear and nonlinear amplification observed at a sweep of $\Lambda = 15^\circ$ along both sides of the wing, it would be unwise to recommend that angle directly. Further off-design nonlinear analysis of the S207 should be performed which considers appreciable variation in angle of attack, as well as variation in the Reynolds number and Mach number. Before then, a definitive answer cannot be provided.

There are several other important take-aways concerning the nonlinear simulations over the S207.

1. When using NPSE to estimate the location of breakdown through TS subharmonic resonance or TS/SCF interaction through an initial-amplitude uncertainty study, only a reduced set of Fourier modes is required.

2. The nonlinear amplification of a TS subharmonic resonance was lesser when the corresponding linear N-factors of the oblique pair was lesser.

3. In the same manner that Schrauf et al. could not conclude whether or not an TS/SCF interaction or TS subharmonic resonance led to transition over the VFW 614/ATTAS laminar flow glove, the present analysis provides the same conclusion for the flow over the S207 in one of its configurations [115]. That is, on the top side of the wing at $\alpha = -1.022^\circ$ and $\Lambda = 20^\circ$, breakdown of laminarity for both pathways occurred when the TS initial amplitude at branch-I was 9×10^{-4}. The x/c location of high amplitude and subsequent laminar breakdown was nearly the same between them: 34%.

8. CONCLUSIONS AND FUTURE WORK

8.1 Conclusions

Analysis of laminar-to-turbulent transition in aerodynamics was presented, specifically focusing on various methodologies used to computationally simulate the physical phenomena relevant to transition. A procedure was outlined for the conversion of a wing's pressure coefficient into boundary-layer parameters suitable for the open-source code DEKAF (co-developed by the author.) Contributions by the author to DEKAF were outlined, not only related to swept-wing analysis, but also to modeling a wide array of high-enthalpy effects. The stability theory and computational methodology as implemented in the in-house stability code, EPIC, was delineated for Linear Stability Theory (LST), and both the Linear and Nonlinear Parabolized Stability Equations (LPSE/NPSE). Contributions of the author were detailed, ranging from the development of DERIVE, to improving various aspects of PSE, to increasing EPIC's longevity and reliability.

8.1.1 S207

Boundary-layer stability analysis was performed over the swept, slotted, natural-laminar-flow (SNLF) S207 at transonic speeds in cruise, on-design conditions. The overarching question was *how much sweep can be applied to this wing while maintaining the benefits of the SNLF design?* Various transition pathways were considered over the vulnerable configurations of angle of attack along the span and sweep. Tollmien-Schlichting (TS) subharmonic resonance and TS/stationary-crossflow (SCF) interaction were assessed for configurations susceptible to TS-dominated transition. At a sweep $\Lambda = 20^\circ$ on the top side of the wing at the angle of attack $\alpha = -1.022^\circ$, very high initial amplitudes of TS were necessary in order for the Nonlinear Parabolized Stability Equations (NPSE) to predict breakdown of laminarity—9×10^{-4}. This initial amplitude is nearly 200 times that observed in the successful flight validation analysis by Schrauf et al. at a similar Reynolds number on the VFW 614/ATTAS laminar flow glove [115]. The Fokker 100 flight experiments as analyzed by Schrauf indicated a TS initial amplitude of 4×10^{-4} at branch-I, which is on the same

order of magnitude of the present S207 values that would predict laminar breakdown [159]. However, since the flight experiment featured a hybrid laminar-flow-control (HLFC) system applying suction, it must not be neglected that the HLFC's internal sound production affects TS receptivity and growth. Since the S207 is not planned to be equipped with suction near the leading edge, one could assume these high initial amplitudes will not be experienced in cruise. The other configuration sensitive to TS growth—$\alpha = -2.252^\circ$ on the bottom side of the wing—did not experience laminar breakdown for the same range of initial TS amplitudes. Stationary-crossflow saturation was computed over a configuration sensitive to the crossflow instability mechanism—$\Lambda = 20^\circ$ for $\alpha = -2.252^\circ$ on the top side of the wing. Saturation occurred for an SCF initial amplitude twice as small as that observed by Haynes & Reed for a swept wing over which strong experimental validation was achieved [25]. The sweep was reduced to $\Lambda = 15^\circ$, and linear amplification factors were negligibly small—$N < 1.5$. The other configuration sensitive to SCF growth was then considered: $\alpha = -1.022^\circ$ on the bottom side of the wing. Similarly, linear amplifications levels were low for stationary crossflow: $N < 1.5$.

Overall, very mild linear and nonlinear amplification was observed at $\Lambda = 15^\circ$. At $\Lambda = 20^\circ$, significant crossflow amplification and saturation was quantified while TS-dominant transition pathways did not indicate laminar breakdown unless high initial amplitudes were applied.

Additionally, when using NPSE to estimate the location of laminar breakdown through TS subharmonic resonance or TS/SCF interaction through an initial-amplitude uncertainty study, only a reduced set of Fourier modes is required. A curious trend relating TS/SCF and TS subharmonic resonance was observed for flow over the S207. In the same manner that Schrauf et al. could not conclude whether or not an TS/SCF interaction or TS subharmonic resonance led to transition over the VFW 614/ATTAS laminar flow glove, the present analysis provides the same conclusion for the flow over the S207 in one of its configurations [115]. That is, on the top side of the wing at $\alpha = -1.022^\circ$ and $\Lambda = 20^\circ$, breakdown of laminarity for both pathways occurred when the TS initial amplitude at branch-I was 9×10^{-4}. The x/c location of high amplitude and subsequent laminar breakdown was nearly the same between them: 34%.

8.1.2 X207.LS

As part of a risk-reduction experiment for a NASA University Leadership Initiative, boundary-layer disturbances on the X207.LS swept wing were quantified across a wide range of geometric configurations. This formed a preliminary study, communicating to the experimentalists the relevant ranges of amplified content. Linear Parabolized Stability Equations (LPSE) indicated appreciable stationary crossflow growth at the angle of attack $\alpha = -5.5^\circ$ and sweep $\Lambda = 35^\circ$, reaching an $N = 4$. Significant Tollmien-Schlichting (TS) amplification was quantified over the wing at angle of attack $\alpha = 2.25^\circ$. Experimental stability measurements of the X207.LS in the Klebanoff-Saric Wind Tunnel (KSWT) have been analyzed. Results are compared against simulations using the Nonlinear Parabolized Stability Equations (NPSE). Coordinate systems have been depicted, showing the necessary transformations to align the computational frame with the experimental frame to directly compare with the hot-wire anemometry data. Naphthalene flow visualization and hot-wire anemometry data of flow over the wing have been presented. A heuristic approach has been used to assign initial amplitudes of the fundamental stationary crossflow disturbance $(0, 1)$ and its superharmonic $(0, 2)$, which qualitatively recovers the measured flowfield using PSE. There is a good agreement between the simulations and the measured hot-wire velocity contours, matching the streamwise vortices formed in both magnitude and phase at several chordwise stations of the wing. Discrepancies between simulation and experiment exist from several sources: a) the laminar boundary layer was generated with the inviscid pressure coefficient from MSES as opposed to the experimentally measured pressure coefficient along the wing; b) the values of the initial amplitudes for the $(0, 1)$ and $(0, 2)$ differ slightly from those observed in experiment; and c) the error incurred by asserting the mean-flow-distortion's $\alpha_{(0,0)} = 0$ is currently unknown for this simulation. Nonlinearities present in this flowfield are quite weak, as the linear superposition of the fundamental and the superharmonic qualitatively resembles that of the full NPSE simulation.

8.1.3 Mean-flow distortion

Various researchers over the past few decades have observed some numerical difficulty in NPSE when incorporating the mean-flow distortion (MFD) Fourier mode originating from its freestream behavior. A mathematical analysis on the parallel, freestream Orr-Sommerfeld equation for a disturbance with $(\omega, \beta) = (0, 0)$ was provided, demonstrating the curious phenomenon of strong divergence of the $\hat{v}$ solution profile. The determinant of the governing matrix K crossed zero whenever $\hat{v}$ became large in the freestream. A comparison between the homogeneous and inhomogeneous boundary condition showed no change to the qualitative behavior, as expected: boundary conditions do not change the determinant of the matrix. The numerical behavior of a near-incompressible, mean-flow distortion Fourier mode from a full NPSE simulation was compared against the solution of the freestream Orr-Sommerfeld equation. Good agreement was observed, justifying then that the dynamics observed in the Orr-Sommerfeld formulation will be present in the NPSE simulations at low MFD amplitudes. Airiau's suggestion to reduce the domain height to about two boundary-layer thicknesses, i.e., $L = 2\delta$ [24], was assessed analytically using the the freestream Orr-Sommerfeld solution. The conclusion was qualitatively the same as Airiau's: the numerical divergence of $\hat{v}$ ceased for small values of the disturbance's wavenumber α. A brief analysis of the incompressible continuity equation identified strong growth out of the MFD's $\partial\hat{u}/\partial s$ if the product $C_1\alpha_i$ is large. Two proposals were suggested to limit the value of α_i in an NPSE simulation. By directly computing the integration constant C_1 and finding the first positive zero of $\det(K)$, reasonable upper and lower bounds can be placed on the mean-flow distortion's α_i such that streamwise change of $\hat{u}$ is limited and remains small by the PSE approximation.

8.2 Future Considerations

8.2.1 S207

There are additional considerations for the nonlinear boundary-layer stability analyses over the S207 wing.

1. Assess off-design conditions at sweep $\Lambda = 15^\circ$. Variation in the angle of attack beyond

the limits of wing's twist, as well as variations in freestream Mach and Reynolds can be considered. A Pareto-frontier approach is suggested, considering only the most vulnerable configurations to transition.

2. Reassess some point nonlinear simulations with nonzero $\alpha_{(0,0)}$.

8.2.2 X207.LS

Work comparing simulations to experimental measurements by Feliciano may continue with flows over the X207.LS wing [127].

1. Compute boundary-layer stability analysis directly using the measured pressure coefficient as boundary conditions to the boundary-layer solver. This mimics the methodology as performed by Haynes & Reed [25].

2. Compare spectral mode shapes directly between computation and experiment by performing Fourier transforms on the hot-wire measured velocities.

3. Use the spectral data to directly inform the initial amplitudes of NPSE as an alternative to the heuristic approach.

4. Reassess nonlinear computations with nonzero $\alpha_{(0,0)}$ made possible by proposed limiters on the mean-flow distortion in §8.2.3.

8.2.3 Mean-flow distortion

There are multiple next steps to consider concerning the mathematics of the mean-flow distortion as presented in Chapter 5.

1. Implement the suggested proposals of limiting the values for $\alpha_{(0,0)}$ of the mean-flow distortion in EPIC. Assess the effect on various nonlinear simulations of different instability mechanisms in various speed regimes. Compare results against solutions that successfully applied Airiau's "cut-off" procedure, as well as solutions where $\alpha_{(0,0)} = 0$ per Hein's suggestion [101].

2. Develop a compressible form for the integration constant C_1 from Eq. (5.20) such that the bounds on α_i may be more physically relevant at higher speeds. This work may follow the analytical assumptions of Li & Malik [108].

3. Find a series solution to the freestream Orr-Sommerfeld $(\omega, \beta) = (0, 0)$ problem when wall-normal velocity $\overline{v}$ is linear in y.

8.2.4 General

There are several potential developments to improve the nonlinear PSE methodology.

1. For high-speed compressible flows, develop and implement a better way to compute the perturbations of thermal/transport properties (e.g., μ' and κ'). An N^{th}-order Taylor series is can become computationally inefficient, as the governing disturbance equations grow in size inordinately. Securing this functionality will increase both efficiency and accuracy of the method, which will be needed as more physically demanding simulations are performed at higher speeds.

2. Many PSE computationalists report that by 'adding the mean-flow distortion to the left-hand side', NPSE may now march farther into nonlinear regimes without premature diverge [162, 163]. As far as the author is aware, this has only been implemented in codes where the right-hand side $f_{(n,k)}$ is evaluated in physical space, as opposed to EPIC where its $f_{(n,k)}$ is evaluated in Fourier space. It is then suggested to implement in EPIC a modification of the harmonic balancing routines to accomplish this feature.

3. For large-scale nonlinear problems, NPSE may need to be run on a supercomputer with OpenMP and MPI implemented. An example of such a problem is computing the transitional heating of a crossflow vortex in a quiet wind tunnel, where stationary crossflow and traveling crossflow are present simultaneously: see the work of Moyes [50]. For computational performance, the right-hand-side evaluation of $f_{(n,k)}$ may need to be performed in physical space as opposed to Fourier space, as performed by Hein seamlessly [101].

Lastly, the CFD 2030 vision roadmap is an excellent overview demonstrating directions of progress for aerosciences over the next decade [164]. In particular, uncertainty analysis as discussed by Roache could be applied to all present stability methodologies in EPIC to bolster its usefulness to the designer [165].

REFERENCES

[1] M. Morkovin, "Transition in Open Flow Systems: A Reassessment," *Bull. Am. Phys. Soc.*, vol. 39, p. 1882, 1994.

[2] IPCC, "Global Warming of 1.5°C. An IPCC Special Report on the impacts of global warming of 1.5°C above pre-industrial levels and related global greenhouse gas emission pathways, in the context of strengthening the global response to the threat of climate change, sustainable development, and efforts to eradicate poverty," October 2018.

[3] "Climate clock." `https://climateclock.world/science#deadline`. Accessed: 2021-06-30.

[4] IPCC, "Climate Change 2021: The Physical Science Basis. Contribution of Working Group I to the Sixth Assessment Report of the Intergovernmental Panel on Climate Change," August 2021.

[5] "International Air Transport Association on Climate Change." `https://www.iata.org/en/programs/environment/climate-change/`. Accessed: 2021-07-12.

[6] International Air Transport Association, "IATA Resolution on the 'Implementation of the Aviation Carbon-Neutral Growth (CNG2020) Strategy.'," 2013.

[7] W. S. Saric, H. L. Reed, and E. J. Kerschen, "Boundary-Layer Receptivity to Freestream Disturbances," *Annual review of fluid mechanics*, vol. 34, no. 1, pp. 291–319, 2002.

[8] H. L. Reed, E. Reshotko, and W. S. Saric, "Receptivity: The Inspiration of Mark Morkovin," in *45th AIAA Fluid Dynamics Conference*, p. 2471, 2015.

[9] A. Fedorov, "Transition and Stability of High-Speed Boundary Layers," *Annual review of fluid mechanics*, vol. 43, pp. 79–95, 2011.

[10] L. M. Mack, "Boundary-Layer Linear Stability Theory," in *Special Course on Stability and Transition of Laminar Flow, AGARD 709*, AGARD, 1984.

[11] D. Arnal, "Boundary Layer Transition: Predictions Based on Linear Theory," in *Special Course on Progress in Transition Modeling, AGARD 793*, AGARD, 1994.

[12] T. Herbert, "Parabolized Stability Equations," *Annual Review of Fluid Mechanics*, vol. 29, no. 1, pp. 245–283, 1997.

[13] H. L. Reed, W. S. Saric, and D. Arnal, "Linear Stability Theory Applied to Boundary Layers," *Annual Review of Fluid Mechanics*, vol. 28, no. 1, pp. 389–428, 1996.

[14] W. S. Saric, H. L. Reed, and E. B. White, "Stability and Transition of Three-Dimensional Boundary Layers," *Annual Review of Fluid Mechanics*, vol. 35, no. 1, pp. 413–440, 2003.

[15] N. Gregory, J. T. Stuart, and W. S. Walker, "On the Stability of Three-Dimensional Boundary Layers with Application to the Flow due to a Rotating Disk," *Philosophical Transactions of the Royal Society of London. Series A, Mathematical and Physical Sciences*, vol. 248, no. 943, pp. 155–199, 1955.

[16] E. Reshotko, "Is $\mathrm{Re}_\theta/\mathrm{M}_e$ a meaningful transition criterion?," *AIAA journal*, vol. 45, no. 7, pp. 1441–1443, 2007.

[17] E. Reshotko, "Transition Issues for Atmospheric Entry," *Journal of Spacecraft and Rockets*, vol. 45, no. 2, pp. 161–164, 2008.

[18] W. Tollmien, "Über die entstehung der turbulenz," in *Vorträge aus dem Gebiete der Aerodynamik und verwandter Gebiete*, pp. 18–21, Springer, 1930.

[19] H. Schlichting, "Zur enstehung der turbulenz bei der plattenströmung," *Nachrichten von der Gesellschaft der Wissenschaften zu Göttingen, Mathematisch-Physikalische Klasse*, vol. 1933, pp. 181–208, 1933.

[20] L. M. Mack, "Boundary-Layer Stability Theory. Part B," *Jet Propulsion Lab, Pasadena, California*, vol. Doc. 900-277, 1969.

[21] T. Herbert, "Boundary-Layer Transition-Analysis and Prediction Revisited," in *29th Aerospace Sciences Meeting*, p. 737, 1991.

[22] F. P. Bertolotti, *Linear and nonlinear stability of boundary layers with streamwise varying properties*. Ph.D. Dissertation, The Ohio State University, 1991.

[23] C.-L. Chang, M. R. Malik, G. Erlebacher, and M. Hussaini, "Compressible Stability of Growing Boundary Layers Using Parabolized Stability Equations," in *22nd Fluid Dynamics, Plasma Dynamics and Lasers Conference*, p. 1636, 1991.

[24] C. Airiau, *Stabilité linéaire et faiblement non linéaire d'une couche limite laminaire incompressible par un système d'équations parabolisé (PSE)*. Ph.D. Dissertation, Toulouse, ENSAE, 1994.

[25] T. S. Haynes and H. L. Reed, "Simulation of Swept-Wing Vortices using Nonlinear Parabolized Stability Equations," *Journal of Fluid Mechanics*, vol. 405, pp. 325–349, 2000.

[26] M. Reibert, W. Saric, R. Carrillo, Jr, and K. Chapman, "Experiments in nonlinear saturation of stationary crossflow vortices in a swept-wing boundary layer," in *34th Aerospace Sciences Meeting and Exhibit*, p. 184, 1996.

[27] R. D. Joslin, C. L. Streett, and C.-L. Chang, "Spatial Direct Numerical Simulation of Boundary-Layer Transition Mechanisms: Validation of PSE Theory," *Theoretical and Computational Fluid Dynamics*, vol. 4, no. 6, pp. 271–288, 1993.

[28] P. Paredes, M. M. Choudhari, and F. Li, "Mechanism for frustum transition over blunt cones at hypersonic speeds," *Journal of Fluid Mechanics*, vol. 894, 2020.

[29] R.-S. Lin and M. R. Malik, "On the Stability of Attachment-Line Boundary Layers. Part 1. The Incompressible Swept Hiemenz Flow," *Journal of Fluid Mechanics*, vol. 311, pp. 239–255, 1996.

[30] V. Theofilis, "Advances in global linear instability analysis of nonparallel and three-dimensional flows," *Progress in Aerospace Sciences*, vol. 39, no. 4, pp. 249–315, 2003.

[31] K. J. Groot and S. E. M. Niessen, "Localised eigenmodes in a moving frame of reference representing convective instability," *arXiv preprint arXiv:2001.04124*, 2020.

[32] P. Paredes, V. Theofilis, D. Rodriguez, and J. A. Tendero, "The PSE-3D instability analysis methodology for flows depending strongly on two and weakly on the third spatial dimension," in *6th AIAA Theoretical Fluid Mechanics Conference*, p. 3752, 2011.

[33] A. P. Haas, O. M. Browne, H. F. Fasel, and C. Brehm, "A time-spectral approximate Jacobian based linearized compressible Navier-Stokes solver for high-speed boundary-layer receptivity and stability," *Journal of Computational Physics*, vol. 405, p. 108978, 2020.

[34] A. Towne, G. Rigas, and T. Colonius, "A critical assessment of the parabolized stability equations," *Theoretical and Computational Fluid Dynamics*, vol. 33, no. 3, pp. 359–382, 2019.

[35] O. Kamal, G. Rigas, M. T. Lakebrink, and T. Colonius, "Application of the One-Way Navier-Stokes (OWNS) equations to hypersonic boundary layers," in *AIAA Aviation 2020 Forum*, p. 2986, 2020.

[36] J. A. Franco Sumariva, S. Hein, and E. Valero, "On the Influence of Two-Dimensional Hump Roughness on Laminar-Turbulent Transition," *Physics of Fluids*, vol. 32, no. 3, p. 034102, 2020.

[37] M. M. Peck, K. J. Groot, and H. L. Reed, "Boundary-Layer Instability on a Highly Swept Fin on a Hypersonic Cone," *AIAA Paper, 2022-3555*, 2022.

[38] A. Knutson, S. G. S., and G. V. Candler, "Instabilities in Mach 6 Flow over a Cone with a Swept Fin," in *2018 Fluid Dynamics Conference*, p. 3071, 2018.

[39] O. M. F. Browne, A. P. Haas, H. F. Fasel, and C. Brehm, "An efficient linear wavepacket tracking method for hypersonic boundary-layer stability prediction," *Journal of Computational Physics*, vol. 380, pp. 243–268, 2019.

[40] J. W. Nichols and G. V. Candler, "Input-output analysis of complex hypersonic boundary layers," in *AIAA Scitech 2019 Forum*, p. 1383, 2019.

[41] H. B. Johnson and G. V. Candler, "Hypersonic boundary layer stability analysis using PSE-Chem," *AIAA paper*, vol. 2005-5023, 2005.

[42] H. Johnson, G. Candler, and C. Alba, "Three-Dimensional Hypersonic Boundary Layer Stability Analysis with STABL-3D," in *40th Fluid Dynamics Conference and Exhibit*, p. 5005, 2010.

[43] C.-L. Chang, "Langley Stability and Transition Analysis Code (LASTRAC) Version 1.2 User Manual," 2004.

[44] H. L. Kline, C.-L. Chang, and F. Li, "Hypersonic Chemically Reacting Boundary-Layer Stability using LASTRAC," *AIAA paper*, vol. 2018-3699, 2018.

[45] F. Pinna and K. J. Groot, "Automatic Derivation of Stability Equations in Arbitrary Coordinates and Different Flow Regimes," in *44th AIAA Fluid Dynamics Conference, Atlanta, GA*, 2014.

[46] F. Miró Miró, *Numerical Investigation of Hypersonic Boundary-Layer Stability and Transition in the Presence of Ablation Phenomena*. Ph.D. Dissertation, Université Libre de Bruxelles and von Karman Institute for Fluid Dynamics, 2020.

[47] N. B. Oliviero, T. S. Kocian, A. J. Moyes, and H. L. Reed, "EPIC: NPSE Analysis of Hypersonic Crossflow Instability on Yawed Straight Circular Cone," *AIAA paper, 2015-2772*, 2015.

[48] N. B. Oliviero, "EPIC: A New and Advanced Nonlinear Parabolized Stability Equation Solver," Master's thesis, Texas A&M University, 2015.

[49] T. S. Kocian, *Computational Hypersonic Boundary-Layer Stability and the Validation and Verification of EPIC*. Ph.D. Dissertation, Texas A&M University, 2018.

[50] A. Moyes, *Computational Laminar-to-Turbulent Transition Physics of Complex Three-Dimensional Hypersonic Flow Fields*. Ph.D. Dissertation, Texas A&M University, 2019.

[51] J. Hofferth, R. Bowersox, and W. Saric, "The Mach 6 Quiet Tunnel at Texas A&M: Quiet Flow Performance," in *27th AIAA Aerodynamic Measurement Technology and Ground Testing Conference*, p. 4794, 2010.

[52] L. Hunt, R. Downs, M. Kuester, E. White, and W. Saric, "Flow Quality Measurements in the Klebanoff-Saric Wind Tunnel," in *27th AIAA Aerodynamic Measurement Technology and Ground Testing Conference*, p. 4538, 2010.

[53] J. D. Anderson Jr., *Fundamentals of Aerodynamics*. Tata McGraw-Hill Education, 2010.

[54] F. M. White, *Viscous Fluid Flow*. McGraw-Hill, third ed., 2006.

[55] R. Aris, *Vectors, Tensors and the Basic Equations of Fluid Mechanics*. Courier Corporation, 2012.

[56] F. B. Hildebrand, *Advanced Calculus for Applications*. Englewood Cliffs, N.J: Prentice-Hall, 2nd ed., 1976.

[57] M. Drela, "A User's Guide to MSES 3.05," 2007.

[58] K. J. Groot, F. Miró Miró, E. S. Beyak, A. Moyes, F. Pinna, and H. L. Reed, "DEKAF: spectral multi-regime basic-state solver for boundary layer stability," *AIAA Paper, 2018-3380*, 2018.

[59] F. Miró Miró, E. S. Beyak, D. Mullen, F. Pinna, and H. L. Reed, "Ionization and Dissociation Effects on Hypersonic Boundary-Layer Stability," in *31st ICAS Congress*, (Belo Horizonte, Brazil), International Council of the Aeronautical Sciences, 2018.

[60] F. Miró Miró, E. S. Beyak, F. Pinna, and H. L. Reed, "Ionization and dissociation effects on boundary-layer stability," *Journal of Fluid Mechanics*, vol. 907, 2021.

[61] G. K. Stuckert, *Linear Stability Theory of Hypersonic, Chemically Reacting Viscous Flows*. Ph.D. Dissertation, Arizona State University, 1991.

[62] C. Park, J. T. Howe, R. L. Jaffe, and G. V. Candler, "Chemical-Kinetic Problems of Future NASA Missions," in *29th AIAA Aerospace Sciences Meeting*, 1991.

[63] C. H. Mortensen, *Effects of Thermochemical Nonequilibrium on Hypersonic Boundary-Layer Instability in the Presence of Surface Ablation or Isolated Two-Dimensional Roughness*. University of California, Los Angeles, 2015.

[64] F. G. Blottner, M. Johnson, and M. Ellis, "Chemically Reacting Viscous Flow Program For Multi-Component Gas Mixtures," Tech. Rep. SC-RR-70-754, Sandia Laboratories, 1971.

[65] A. Eucken, "Über das Wärmeleitvermögen, die spezifische Wärme und die innere Reibung der Gase (in german)," *Physikalische Zeitschrift*, vol. XIV, pp. 324–332, 1913.

[66] C. R. Wilke, "A Viscosity Equation for Gas Mixtures," *The Journal of Chemical Physics*, vol. 18, no. 4, pp. 517–519, 1950.

[67] R. N. Gupta, J. M. Yos, R. A. Thompson, and K.-P. Lee, "A Review of Reaction Rates and Thermodynamic and Transport Properties for an 11-Species Air Model for Chemical and Thermal Nonequilibrium Calculations to 30000K," Tech. Rep. RP-1232, NASA, 1990.

[68] J. O. Hirschfelder, C. F. Curtiss, and R. B. Bird, *Molecular Theory of Gases and Liquids*. New York: Wiley, 2 ed., 1954.

[69] J. M. Yos, "Approximate Equations for the Viscosity and Translational Thermal Conductivity of Gas Mixtures," *Contract Report No. AVSSD-0112-67-RM, Avco Corporation, Wilmington, Massachusetts*, 1967.

[70] R. S. Brokaw, "Approximate Formulas for the Viscosity and Thermal Conductivity of Gas Mixtures," *The Journal of Chemical Physics*, vol. 29, no. 2, pp. 391–397, 1958.

[71] J. D. Ramshaw and C. H. Chang, "Ambipolar Diffusion in Multicomponent Plasmas," *Plasma Chemistry and Plasma Processing*, vol. 13, no. 3, pp. 489–498, 1993.

[72] J. D. Ramshaw, "Hydrodynamic Theory of Multicomponent Diffusion and Thermal Diffusion in Multitemperature Gas Mixtures," *Journal of Non-Equilibrium Thermodynamics*, vol. 18, pp. 121–134, 1993.

[73] J. B. Scoggins, *Development of Numerical Methods and Study of Coupled Flow, Radiation, and Ablation Phenomena for Atmospheric Entry*. Ph.D. Dissertation, Université Paris-Saclay and VKI, 2017.

[74] J. B. Scoggins and T. E. Magin, "Development of Mutation++: MUlticomponent Thermodynamics And Transport properties for IONized gases library in C++," *AIAA paper*, vol. 2014-2966, 2014.

[75] J. D. Anderson, "Hypersonic and High-Temperature Gas Dynamics Second Edition," *American Institute of Aeronautics and Astronautics*, 2006.

[76] F. Miró Miró, E. S. Beyak, F. Pinna, and H. L. Reed, "High-Enthalpy Models for Boundary-Layer Stability and Transition," *Physics of Fluids*, vol. 31, no. 044101, 2019.

[77] F. Miró Miró, F. Pinna, E. S. Beyak, P. Barbante, and H. L. Reed, "Diffusion and Chemical Non-Equilibrium Effects on Hypersonic Boundary-Layer Stability," *AIAA paper*, vol. 2018-1824, 2018.

[78] S. Padgen, M. Peck, K. J. Groot, T. Kocian, E. S. Beyak, and H. L. Reed, "Interaction of Second Mode and 3D Instabilities on a Hypersonic Cooled Cone," *AIAA Paper, 2023-XXXX (to be published)*, 2023.

[79] Maxima, "Maxima, a computer algebra system," *Version 5.42*, 2018.

[80] C. D. Mullen, *Advanced Basic State and Stability Analysis of Complex Hypersonic Geometries*. Ph.D. Dissertation, Texas A&M University, 2021.

[81] K. J. Groot, J. Patel, E. S. Beyak, J. G. Coder, and H. L. Reed, "Görtler Instability on a Variably Swept, Slotted, Natural-Laminar-Flow Airfoil," *AIAA Paper, 2021-2590*, 2021.

[82] J. M. Patel, "Boundary-Layer Stability Analysis for a Yawed Cone and a Swept, Slotted Airfoil," Master's thesis, Texas A&M University, 2022.

[83] T. Bridges and P. J. Morris, "Differential eigenvalue problems in which the parameter appears nonlinearly," *Journal of Computational Physics*, vol. 55, no. 3, pp. 437–460, 1984.

[84] A. Tumin, "Wave Packets and Supersonic Second Modes in a High-Speed Boundary Layer," in *AIAA Scitech 2020 Forum*, p. 0106, 2020.

[85] C. P. Knisely, *Supersonic Unstable Modes in Hypersonic Boundary Layers with Thermochemical Nonequilibrium Effects*. University of California, Los Angeles, 2018.

[86] L. Zanus, *Numerical study of chemically reacting hypersonic boundary layers by means of non-linear parabolized stability equations*. Ph.D. Dissertation, von Karman Institute for Fluid Dynamics, 2021.

[87] R.-S. Lin, W.-P. Wang, and M. R. Malik, "Linear stability of incompressible viscous flow along a corner," in *1996 Fluids Engng Div. Conf.*, vol. 2, pp. 633–638, ASME, 1996.

[88] W. H. Press, S. A. Teukolsky, W. T. Vetterling, and B. P. Flannery, *Numerical Recipes 3rd Edition: The Art of Scientific Computing*. Cambridge University Press, 2007.

[89] J. H. Wilkinson, "The Algebraic Eigenvalue Problem," *Clarendon*, 1965.

[90] C. E. Grosch and H. Salwen, "The continuous spectrum of the Orr-Sommerfeld equation. part 1. the spectrum and the eigenfunctions," *Journal of Fluid Mechanics*, vol. 87, pp. 33–54, 1978.

[91] A. Tumin, "LST and the Eigenfunction Expansion Method for Linearized Navier-Stokes Equations–a Summary," in *AIAA Scitech 2020 Forum*, p. 0105, 2020.

[92] M. Malik and S. Orszag, "Efficient Computation of the Stability of Three-Dimensional Compressible Boundary Layers," in *14th Fluid and Plasma Dynamics Conference*, p. 1277, 1981.

[93] A. H. Nayfeh, *Problems in Perturbation*. USA: John Wiley & Sons, Inc., 1986.

[94] T. Herbert and F. Bertolotti, "Stability Analysis of Nonparallel Boundary Layers," *Bull. Am. Phys. Soc*, vol. 32, no. 2079, p. 590, 1987.

[95] C. M. Bender, S. Orszag, and S. A. Orszag, *Advanced Mathematical Methods for Scientists and Engineers I: Asymptotic Methods and Perturbation Theory*, vol. 1. Springer Science & Business Media, 1999.

[96] K. J. Groot, E. S. Beyak, D. T. Heston, and H. L. Reed, "Boundary-Layer Stability of a Natural-Laminar-Flow Airfoil," *AIAA Paper, 2020-1024*, 2020.

[97] K. J. Groot, E. S. Beyak, D. T. Heston, and H. L. Reed, "Boundary-Layer Stability of a Natural-Laminar-Flow Airfoil at Flight Conditions," *AIAA Paper, 2020-3052*, 2020.

[98] C. Hader and H. F. Fasel, "Direct Numerical Simulations of Hypersonic Boundary-Layer Transition for a Flared Cone: Fundamental Breakdown," *Journal of Fluid Mechanics*, vol. 869, pp. 341–384, 2019.

[99] J. A. Weideman and S. C. Reddy, "A MATLAB differentiation matrix suite," *ACM Transactions on Mathematical Software (TOMS)*, vol. 26, no. 4, pp. 465–519, 2000.

[100] M. R. Malik, F. Li, M. M. Choudhari, and C.-L. Chang, "Secondary instability of crossflow vortices and swept-wing boundary-layer transition," *Journal of Fluid Mechanics*, vol. 399, pp. 85–115, 1999.

[101] S. Hein, *Nonlinear Nonlocal Transition Analysis*. Ph.D. Dissertation, DLR Göttingen, 2005.

[102] A. J. Moyes, E. S. Beyak, T. S. Kocian, and H. L. Reed, "Accurate and Efficient Modeling of Boundary-Layer Instabilities," in *AIAA Scitech 2019 Forum*, p. 1907, 2019.

[103] M. R. Malik, "Numerical Methods for Hypersonic Boundary Layer Stability," *Journal of computational physics*, vol. 86, no. 2, pp. 376–413, 1990.

[104] F. Miró Miró and F. Pinna, "Linear Stability Analysis of a Hypersonic Boundary Layer in Equilibrium and Non-Equilibrium," *AIAA paper*, vol. 2017-4518, 2017.

[105] D. Park, J. Park, M. Kim, J. Lim, S. Kim, and S. Jee, "Influence of initial phase on subharmonic resonance in an incompressible boundary layer," *Physics of Fluids*, vol. 33, no. 4, p. 044101, 2021.

[106] F. Li and M. R. Malik, "On the Nature of PSE Approximation," *Theoretical and Computational Fluid Dynamics*, vol. 8, no. 4, pp. 253–273, 1996.

[107] P. R. Amestoy, I. S. Duff, J.-Y. L'Excellent, and J. Koster, "A fully asynchronous multifrontal solver using distributed dynamic scheduling," *SIAM Journal on Matrix Analysis and Applications*, vol. 23, no. 1, pp. 15–41, 2001.

[108] F. Li and M. R. Malik, "Spectral Analysis of Parabolized Stability Equations," *Computers & Fluids*, vol. 26, no. 3, pp. 279–297, 1997.

[109] H. Haj-Hariri, "Characteristics Analysis of the Parabolized Stability Equations," *Studies in Applied Mathematics*, vol. 92, no. 1, pp. 41–53, 1994.

[110] S. Bagheri and A. Hanifi, "The stabilizing effect of streaks on Tollmien-Schlichting and oblique waves: A parametric study," *Physics of fluids*, vol. 19, no. 7, p. 078103, 2007.

[111] D. Tempelmann, A. Hanifi, and D. S. Henningson, "Spatial optimal growth in three-dimensional boundary layers," *Journal of Fluid Mechanics*, vol. 646, pp. 5–37, 2010.

[112] P. Andersson, D. Henningson, and A. Hanifi, "On a Stabilization Procedure for the Parabolic Stability Equations," *Journal of Engineering Mathematics*, vol. 33, no. 3, pp. 311–332, 1998.

[113] P. Paredes, *Advances in Global Instability Computations: from Incompressible to Hypersonic Flow*. Ph.D. Dissertation, Universidad Politécnica de Madrid, 2014.

[114] A. V. Fedorov and A. P. Khokhlov, "Prehistory of Instability in a Hypersonic Boundary Layer," *Theoretical and Computational Fluid Dynamics*, vol. 14, no. 6, pp. 359–375, 2001.

[115] G. Schrauf, T. Herbert, and G. Stuckert, "Evaluation of Transition in Flight Tests using Nonlinear Parabolized Stability Equation Analysis," *Journal of aircraft*, vol. 33, no. 3, pp. 554–560, 1996.

[116] T. S. Haynes, *Nonlinear Stability and Saturation of Crossflow Vortices in Swept-Wing Boundary Layers*. Ph.D. Dissertation, Arizona State University, 1996.

[117] K. J. Groot, *BiGlobal Stability of Shear Flows Spanwise & Streamwise Analyses*. Ph.D. Dissertation, TU Delft and von Karman Institute for Fluid Dynamics, 2018.

[118] P. Balakumar and M. R. Malik, "Discrete modes and continuous spectra in supersonic boundary layers," *Journal of Fluid Mechanics*, vol. 239, pp. 631–656, 6 1992.

[119] E. S. Beyak, K. J. Groot, J. G. Feliciano, J. M. Patel, A. R. Riha, J. G. Coder, and H. L. Reed, "Nonlinear Boundary-Layer Stability Analysis of a Swept, Natural-Laminar-Flow Airfoil," *AIAA Paper, 2022-3674*, 2022.

[120] R. D. Joslin, *Validation of Three-Dimensional Incompressible Spatial Direct Numerical Simulation Code: A Comparison with Linear Stability and Parabolic Stability Equation Theories for Boundary-Layer Transition on a Flat Plate*, vol. 3205. National Aeronautics and Space Administration, Office of Management, 1992.

[121] T. Herbert and G. Schrauf, "Crossflow-dominated transition in flight tests," *AIAA Paper, 1996-0185*, 1996.

[122] E. W. Weisstein, "Hermite Differential Equation." `https://mathworld.wolfram.com/HermiteDifferentialEquation.html`. Accessed: 2022-06-04.

[123] M. Abramowitz and I. A. Stegun, *Handbook of Mathematical Functions with Formulas, Graphs, and Mathematical Tables*, vol. 55. US Government printing office, 1964.

[124] T. Washburn, "Airframe Drag/Weight Reduction Technologies," *Green Aviation Summit-Fuel Burn Reduction, NASA Ames Research Centre*, 2010.

[125] R. D. Joslin, "Aircraft Laminar Flow Control," *Annual review of fluid mechanics*, vol. 30, no. 1, pp. 1–29, 1998.

[126] D. M. Somers, "An Exploratory Investigation of a Slotted, Natural-Laminar-Flow Airfoil," 2012.

[127] J. G. Feliciano, C. P. Finke, and E. B. White, "Boundary-Layer Stability Measurements of a Variably Swept and Pitched, Slotted, Natural-Laminar-Flow Airfoil," *AIAA Paper, 2022-2411*, 2022.

[128] J. Anderson, *Fundamentals of Aerodynamics*. McGraw-Hill, 2006.

[129] E. S. Beyak, K. J. Groot, and H. L. Reed, "Computational Stability Analysis of a Variably Swept, Slotted Natural-Laminar-Flow Airfoil," *AIAA Paper, 2021-0946*, 2021.

[130] H. J. Obremski, M. V. Morkovin, M. Landahl, A. R. Wazzan, T. T. Okamura, and A. M. O. Smith, "A Portfolio of Stability Characteristics of Incompressible Boundary Layers," tech. rep., NATO Advisory Group for Aerospace Research and Development, 1969.

[131] F. K. Tsou and E. M. Sparrow, "Hydrodynamic Stability of Boundary Layers with Surface Mass Transfer," *Applied Scientific Research*, vol. 22, no. 1, pp. 273–286, 1970.

[132] A. R. Wazzan, C. Gazley Jr, and A. M. O. Smith, "Tollmien-Schlichting Waves and Transition: Heated and Adiabatic Wedge Flows with Application to Bodies of Revolution," *Progress in Aerospace Sciences*, vol. 18, pp. 351–392, 1979.

[133] B.-T. Chu, "On the Energy Transfer to Small Disturbances in Fluid Flow (Part I)," *Acta Mechanica*, vol. 1, no. 3, pp. 215–234, 1965.

[134] J. L. Van Ingen, "A Suggested Semi-Empirical Method for the Calculation of the Boundary Layer Transition Region," vth-74, Delft University of Technology, The Netherlands, 1956.

[135] J. L. Van Ingen, "The e^N Method for Transition Prediction. Historical Review of Work at TU Delft," *AIAA Paper, 2008-3830*, 2008.

[136] R. A. Rozendaal, "Natural Laminar Flow Flight Experiments on a Swept Wing Business Jet—Boundary Layer Stability Analyses," tech. rep., NASA Langley, CR 3975, 1986.

[137] R. A. Rozendaal, "Variable Sweep Transition Flight Experiment (VSTFE)-Parametric Pressure Distribution Boundary Layer Stability Study and Wing Glove Design Task," tech. rep., NASA Langley, CR 3992, 1986.

[138] R. A. Rozendaal, "Variable-Sweep Transition Flight Experiment (VSTFE): Stability Code Development and Clean-Up Glove Data Analysis," in *NLF and LFC research, NASA Langley, CP 2487*, 1987.

[139] H. Deyhle and H. Bippes, "Disturbance Growth in an Unstable Three-Dimensional Boundary Layer and its Dependence on Environmental Conditions," *Journal of Fluid Mechanics*, vol. 316, pp. 73–113, 1996.

[140] R. S. Downs and E. B. White, "Free-stream Turbulence and the Development of Cross-flow Disturbances," *Journal of Fluid Mechanics*, vol. 735, pp. 347–380, 2013.

[141] "Klebanoff-Saric Wind Tunnel." `https://kswt.tamu.edu/`, 2022. Accessed: 2022-05-29.

[142] L. E. Hunt, *Boundary-Layer Receptivity to Three-Dimensional Roughness Arrays on a Swept-Wing*. Ph.D. Dissertation, Texas A&M University, 2012.

[143] M. Kuester and E. White, "Acoustic Forcing and Control of Reflected Waves in the Klebanoff-Saric Wind Tunnel," in *28th Aerodynamic Measurement Technology, Ground Testing, and Flight Testing Conference including the Aerospace T&E Days Forum*, p. 2862, 2012.

[144] P. S. Mendes, "The Naphthalene Sublimation Technique," *Experimental Thermal and Fluid Science*, vol. 4, no. 5, pp. 510–523, 1991.

[145] H. H. Bruun, "Hot-Wire Anemometry: Principles and Signal Analysis," *IOP Publishing*, 1996.

[146] E. B. White, *Breakdown of Crossflow Vortices*. Ph.D. Dissertation, Arizona State University, 2000.

[147] D. T. Heston, E. S. Beyak, K. J. Groot, and H. L. Reed, "Boundary-Layer Stability of a Slotted, Natural-Laminar-Flow Airfoil at Flight Conditions," *AIAA Paper, 2021-0845*, 2021.

[148] T. Herbert, "Secondary Instability of Boundary Layers," *Annual review of fluid mechanics*, vol. 20, no. 1, pp. 487–526, 1988.

[149] A. Craik, "A model for subharmonic resonance within wavepackets in unstable boundary layers," *Journal of Fluid Mechanics*, vol. 432, pp. 409–418, 2001.

[150] G. Redeker, K. Horstmann, H. Koester, P. Thiede, and J. Szodruch, "Design for a Natural Laminar Flow glove for a transport aircraft," in *Flight Simulation Technologies Conference and Exhibit*, p. 3043, 1990.

[151] I. H. Abbott and A. E. Von Doenhoff, *Theory of wing sections: including a summary of airfoil data*. Courier Corporation, 2012.

[152] C. S. J. Mayer, D. A. Von Terzi, and H. F. Fasel, "Direct numerical simulation of complete transition to turbulence via oblique breakdown at mach 3," *Journal of Fluid Mechanics*, vol. 674, pp. 5–42, 2011.

[153] H. L. Reed, "Disturbance-Wave Interactions in Flows with Crossflow," in *23rd Aerospace Sciences Meeting*, p. 494, 1985.

[154] H. L. Reed, "Wave Interactions in Swept-Wing Flows," *Physics of fluids*, vol. 30, no. 11, pp. 3419–3426, 1987.

[155] A. P. Bassom and P. Hall, "On the Interaction of Stationary Crossflow Vortices and Tollmien-Schlichting Waves in the Boundary Layer on a Rotating Disc," *Proceedings of the Royal Society of London. Series A: Mathematical and Physical Sciences*, vol. 430, no. 1878, pp. 25–55, 1990.

[156] N. Voogt, "Flight Testing of a Fokker 100 Test Aircraft with Laminar Flow Glove," in *Second European Forum on Laminar Flow Technology*, vol. 2, pp. 2–3, 1996.

[157] G. Schrauf, "Large-Scale Laminar Flow Tests Evaluated with Linear Stability Theory," in *AIAA 2001 Forum*, p. 2444, 2001.

[158] G. Schrauf, "Large-Scale Laminar Flow Tests Evaluated with Linear Stability Theory," *Journal of Aircraft*, vol. 41, no. 2, pp. 224–230, 2004.

[159] G. Schrauf, "Industrial View on Transition Prediction," in *Recent Results in Laminar-Turbulent Transition*, pp. 111–122, Springer, 2003.

[160] D. T. Heston, "The Effects of Off-Design Conditions on the Laminar-To-Turbulent Transition Location on a Slotted, Natural-Laminar-Flow Airfoil," Master's thesis, Texas A&M University, 2020.

[161] W. S. Saric, D. E. West, M. W. Tufts, and H. L. Reed, "Flight Test Experiments on Discrete Roughness Element Technology for Laminar Flow Control," in *53rd AIAA Aerospace Sciences Meeting*, p. 0539, 2015.

[162] L. Zhao, C.-B. Zhang, J.-X. Liu, and J.-S. Luo, "Improved Algorithm for Solving Nonlinear Parabolized Stability Equations," *Chinese Physics B*, vol. 25, no. 8, p. 084701, 2016.

[163] L. Zanus, C. P. Knisely, F. Miró Miró, and F. Pinna, "Multiple-Tool Stability Analysis of Supersonic Modes in Thermo-Chemical Nonequilibrium Boundary Layers," *AIAA paper*, vol. 2020-3067, 2020.

[164] J. P. Slotnick, A. Khodadoust, J. Alonso, D. Darmofal, W. Gropp, E. Lurie, and D. J. Mavriplis, "CFD Vision 2030 Study: A Path to Revolutionary Computational Aerosciences," tech. rep., 2014.

[165] P. J. Roache, "Quantification of Uncertainty in Computational Fluid Dynamics," *Annual Review of Fluid Mechanics*, vol. 29, no. 1, pp. 123–160, 1997.

APPENDIX A

LPSE EQUATIONS

The Linear Parabolized Stability Equations are presented for a calorically perfect gas in an orthogonal, curvilinear coordinate system. These are derived from the governing, instantaneous equations of Eqs. (2.14). There are several important facets to note:

1. The metric h_2 is assumed to be unity and therefore is dropped from the equations.

2. For readability, Stokes' hypothesis is *not* substituted in these equations, i.e., the second coefficient of viscosity of the base flow $\overline{\lambda}_v$ appears in the momentum and energy equations.

3. Since all quantities are nondimensional, $c_p = 1$, so its appearance is subsequently dropped from the energy equation.

4. The imaginary unit whose square is -1 is denoted as i.

5. The presence of slowly varying viscous terms are multiplied by the coefficient Ω_{Re}. These terms are identified in DERIVE as those possessing the coefficient $\varepsilon_s/\mathrm{Re}$. Many researchers neglect these terms, i.e., $\Omega_{\mathrm{Re}} = 0$; however, some retain them by assigning $\Omega_{\mathrm{Re}} = 1$. The switch is left general in the equations to easily transform between the two assertions.

6. The stability equations are presented such that the right-hand side has been subtracted over onto the left-hand side following the original orientation as written in Eqs. (2.14).

7. To save printing space, spatial derivatives are expressed through subscripts. That is, $\overline{q}_s \equiv \partial\overline{q}/\partial s$, $\hat{q}_s \equiv \partial\hat{q}/\partial s$, and $\alpha_s \equiv \mathrm{d}\alpha/\mathrm{d}s$. This holds analogously for subscripts y, sy, and yy. There are also derivatives with respect to the base-flow temperature $\overline{T}$ on the transport variables. For example, $\overline{\mu}_{\overline{T}} \equiv \mathrm{d}\overline{\mu}/\mathrm{d}\overline{T}$ or $\overline{\mu}_{\overline{T}\overline{T}} \equiv \mathrm{d}^2\overline{\mu}/\mathrm{d}\overline{T}^2$. If a variable already has a subscript, the spatial differentiation is separated by a comma with respect to the original variable. For example, $h_{1,y} = \partial h_1/\partial y$.

8. These equations can be extended to NPSE use as well. To merge the two nomenclatures:

   (a) Subscripts would be applied to the shape-function components $\hat{q}_{(n,k)}$ and the streamwise wavenumbers $\alpha_{(n,k)}$.

   (b) Wavenumbers ω and β are *effective* wavenumbers. That is, $\omega = n\omega_0$ and $\beta = k\beta_0$ for a given (n, k)-disturbance.

   (c) The coefficient on the pressure shape-function streamwise gradient Ω_p depends on n of the disturbance: see Eq. (7.2). Recall stationary Fourier modes must have its gradient $\partial\hat{p}_{(n,k)}/\partial s$ vanish entirely.

The order of the equations are s-, y-, and z-momentum, energy (the enthalpy formulation), and mass continuity. These equations have been generated with DERIVE which have then been assembled by both Jay Patel and the author into this document and Patel's thesis [82].

Note the LST equations with the parallel-flow assumption have been omitted from these appendices for brevity. They can be recovered from these equations, however. Assign all s-derivatives to zero, and set $\overline{v} = 0$. To recover the LST equations without the parallel-flow assumption as some PSE codes have modeled, only eliminate the s-derivatives of the shape-function components—or following the nomenclature from before, the eigenfunction components.

A.1 Momentum conservation in the s-direction

$$
-\frac{\mathrm{i}\,\Omega_{\mathrm{Re}}\,\beta\,\overline{\mu}\,\hat{w}_s}{\mathrm{Re}\,h_1\,h_3}-\frac{\mathrm{i}\,\Omega_{\mathrm{Re}}\,\beta\,\overline{\lambda}_v\,\hat{w}_s}{\mathrm{Re}\,h_1\,h_3}-\frac{2\,h_{3,s}\,\overline{\rho}\,\overline{w}\,\hat{w}}{h_1\,h_3}+\frac{3\,\mathrm{i}\,\Omega_{\mathrm{Re}}\,\beta\,h_{3,s}\,\overline{\mu}\,\hat{w}}{\mathrm{Re}\,h_1\,h_3^2}+\frac{\alpha\,\beta\,\overline{\mu}\,\hat{w}}{\mathrm{Re}\,h_1\,h_3}
$$

$$
-\frac{\mathrm{i}\,\Omega_{\mathrm{Re}}\,\overline{T}_s\,\beta\,\overline{\lambda}_{v\overline{T}}\,\hat{w}}{\mathrm{Re}\,h_1\,h_3}+\frac{\mathrm{i}\,\Omega_{\mathrm{Re}}\,\beta\,h_{3,s}\,\overline{\lambda}_v\,\hat{w}}{\mathrm{Re}\,h_1\,h_3^2}+\frac{\alpha\,\beta\,\overline{\lambda}_v\,\hat{w}}{\mathrm{Re}\,h_1\,h_3}-\frac{\mathrm{i}\,\Omega_{\mathrm{Re}}\,\hat{T}\,\beta\,\overline{\mu}_{\overline{T}}\,\overline{w}_s}{\mathrm{Re}\,h_1\,h_3}-\frac{h_{3,s}\,\hat{\rho}\,\overline{w}^2}{h_1\,h_3}
$$

$$
+\frac{\mathrm{i}\,\beta\,\overline{\rho}\,\hat{u}\,\overline{w}}{h_3}+\frac{\mathrm{i}\,\Omega_{\mathrm{Re}}\,\hat{T}\,\beta\,h_{3,s}\,\overline{\mu}_{\overline{T}}\,\overline{w}}{\mathrm{Re}\,h_1\,h_3^2}-\frac{\mathrm{i}\,\alpha\,\overline{\mu}\,\hat{v}_y}{\mathrm{Re}\,h_1}-\frac{\Omega_{\mathrm{Re}}\,\overline{T}_s\,\overline{\lambda}_{v\overline{T}}\,\hat{v}_y}{\mathrm{Re}\,h_1}-\frac{\mathrm{i}\,\alpha\,\overline{\lambda}_v\,\hat{v}_y}{\mathrm{Re}\,h_1}-\frac{\Omega_{\mathrm{Re}}\,\overline{\mu}\,\hat{v}_{s\,y}}{\mathrm{Re}\,h_1}
$$

$$
-\frac{\Omega_{\mathrm{Re}}\,\overline{\lambda}_v\,\hat{v}_{s\,y}}{\mathrm{Re}\,h_1}-\frac{\Omega_{\mathrm{Re}}\,\overline{T}_y\,\overline{\mu}_{\overline{T}}\,\hat{v}_s}{\mathrm{Re}\,h_1}-\frac{\Omega_{\mathrm{Re}}\,h_{3,y}\,\overline{\mu}\,\hat{v}_s}{\mathrm{Re}\,h_1\,h_3}-\frac{3\,\Omega_{\mathrm{Re}}\,h_{1,y}\,\overline{\mu}\,\hat{v}_s}{\mathrm{Re}\,h_1^2}-\frac{\Omega_{\mathrm{Re}}\,h_{3,y}\,\overline{\lambda}_v\,\hat{v}_s}{\mathrm{Re}\,h_1\,h_3}-\frac{\Omega_{\mathrm{Re}}\,h_{1,y}\,\overline{\lambda}_v\,\hat{v}_s}{\mathrm{Re}\,h_1^2}
$$

$$
+\overline{\rho}\,\overline{u}_y\,\hat{v}+\frac{h_{1,y}\,\overline{\rho}\,\overline{u}\,\hat{v}}{h_1}-\frac{2\,\Omega_{\mathrm{Re}}\,\overline{T}_s\,h_{1,y}\,\overline{\mu}_{\overline{T}}\,\hat{v}}{\mathrm{Re}\,h_1^2}-\frac{\mathrm{i}\,\overline{T}_y\,\alpha\,\overline{\mu}_{\overline{T}}\,\hat{v}}{\mathrm{Re}\,h_1}+\frac{2\,\Omega_{\mathrm{Re}}\,h_{3,s}\,h_{3,y}\,\overline{\mu}\,\hat{v}}{\mathrm{Re}\,h_1\,h_3^2}
$$

$$
-\frac{\mathrm{i}\,\alpha\,h_{3,y}\,\overline{\mu}\,\hat{v}}{\mathrm{Re}\,h_1\,h_3}-\frac{2\,\Omega_{\mathrm{Re}}\,h_{1,y}\,h_{3,s}\,\overline{\mu}\,\hat{v}}{\mathrm{Re}\,h_1^2\,h_3}+\frac{2\,\Omega_{\mathrm{Re}}\,h_{1,s}\,h_{1,y}\,\overline{\mu}\,\hat{v}}{\mathrm{Re}\,h_1^3}-\frac{3\,\mathrm{i}\,\alpha\,h_{1,y}\,\overline{\mu}\,\hat{v}}{\mathrm{Re}\,h_1^2}-\frac{2\,\Omega_{\mathrm{Re}}\,h_{1,s\,y}\,\overline{\mu}\,\hat{v}}{\mathrm{Re}\,h_1^2}
$$

$$
-\frac{\Omega_{\mathrm{Re}}\,\overline{T}_s\,h_{3,y}\,\overline{\lambda}_{v\overline{T}}\,\hat{v}}{\mathrm{Re}\,h_1\,h_3}-\frac{\Omega_{\mathrm{Re}}\,\overline{T}_s\,h_{1,y}\,\overline{\lambda}_{v\overline{T}}\,\hat{v}}{\mathrm{Re}\,h_1^2}+\frac{\Omega_{\mathrm{Re}}\,h_{3,s}\,h_{3,y}\,\overline{\lambda}_v\,\hat{v}}{\mathrm{Re}\,h_1\,h_3^2}-\frac{\mathrm{i}\,\alpha\,h_{3,y}\,\overline{\lambda}_v\,\hat{v}}{\mathrm{Re}\,h_1\,h_3}-\frac{\Omega_{\mathrm{Re}}\,h_{3,s\,y}\,\overline{\lambda}_v\,\hat{v}}{\mathrm{Re}\,h_1\,h_3}
$$

$$
+\frac{\Omega_{\mathrm{Re}}\,h_{1,s}\,h_{1,y}\,\overline{\lambda}_v\,\hat{v}}{\mathrm{Re}\,h_1^3}-\frac{\mathrm{i}\,\alpha\,h_{1,y}\,\overline{\lambda}_v\,\hat{v}}{\mathrm{Re}\,h_1^2}-\frac{\Omega_{\mathrm{Re}}\,h_{1,s\,y}\,\overline{\lambda}_v\,\hat{v}}{\mathrm{Re}\,h_1^2}-\frac{\mathrm{i}\,\Omega_{\mathrm{Re}}\,\hat{T}\,\alpha\,\overline{\lambda}_{v\overline{T}}\,\overline{v}_y}{\mathrm{Re}\,h_1}
$$

$$
+\overline{\rho}\,\hat{u}_y\,\overline{v}+\frac{h_{1,y}\,\overline{\rho}\,\hat{u}\,\overline{v}}{h_1}+\hat{\rho}\,\overline{u}_y\,\overline{v}+\frac{h_{1,y}\,\hat{\rho}\,\overline{u}\,\overline{v}}{h_1}-\frac{2\,\mathrm{i}\,\Omega_{\mathrm{Re}}\,\hat{T}\,\alpha\,h_{1,y}\,\overline{\mu}_{\overline{T}}\,\overline{v}}{\mathrm{Re}\,h_1^2}-\frac{\mathrm{i}\,\Omega_{\mathrm{Re}}\,\hat{T}\,\alpha\,h_{3,y}\,\overline{\lambda}_{v\overline{T}}\,\overline{v}}{\mathrm{Re}\,h_1\,h_3}
$$

$$
-\frac{\mathrm{i}\,\Omega_{\mathrm{Re}}\,\hat{T}\,\alpha\,h_{1,y}\,\overline{\lambda}_{v\overline{T}}\,\overline{v}}{\mathrm{Re}\,h_1^2}-\frac{\overline{\mu}\,\hat{u}_{y\,y}}{\mathrm{Re}}-\frac{\overline{T}_y\,\overline{\mu}_{\overline{T}}\,\hat{u}_y}{\mathrm{Re}}-\frac{h_{3,y}\,\overline{\mu}\,\hat{u}_y}{\mathrm{Re}\,h_3}-\frac{h_{1,y}\,\overline{\mu}\,\hat{u}_y}{\mathrm{Re}\,h_1}+\frac{\overline{\rho}\,\overline{u}\,\hat{u}_s}{h_1}
$$

$$
-\frac{4\,\mathrm{i}\,\Omega_{\mathrm{Re}}\,\alpha\,\overline{\mu}\,\hat{u}_s}{\mathrm{Re}\,h_1^2}-\frac{2\,\mathrm{i}\,\Omega_{\mathrm{Re}}\,\alpha\,\overline{\lambda}_v\,\hat{u}_s}{\mathrm{Re}\,h_1^2}+\frac{\overline{\rho}\,\overline{u}_s\,\hat{u}}{h_1}+\frac{\mathrm{i}\,\alpha\,\overline{\rho}\,\overline{u}\,\hat{u}}{h_1}-\mathrm{i}\,\omega\,\overline{\rho}\,\hat{u}+\frac{\overline{T}_y\,h_{1,y}\,\overline{\mu}_{\overline{T}}\,\hat{u}}{\mathrm{Re}\,h_1}
$$

$$
-\frac{2\,\mathrm{i}\,\Omega_{\mathrm{Re}}\,\overline{T}_s\,\alpha\,\overline{\mu}_{\overline{T}}\,\hat{u}}{\mathrm{Re}\,h_1^2}+\frac{h_{1,y}\,h_{3,y}\,\overline{\mu}\,\hat{u}}{\mathrm{Re}\,h_1\,h_3}-\frac{2\,\mathrm{i}\,\Omega_{\mathrm{Re}}\,\alpha\,h_{3,s}\,\overline{\mu}\,\hat{u}}{\mathrm{Re}\,h_1^2\,h_3}+\frac{\beta^2\,\overline{\mu}\,\hat{u}}{\mathrm{Re}\,h_3^2}+\frac{h_{1,y\,y}\,\overline{\mu}\,\hat{u}}{\mathrm{Re}\,h_1}+\frac{(h_{1,y})^2\,\overline{\mu}\,\hat{u}}{\mathrm{Re}\,h_1^2}
$$

$$
+\frac{2\,\mathrm{i}\,\Omega_{\mathrm{Re}}\,\alpha\,h_{1,s}\,\overline{\mu}\,\hat{u}}{\mathrm{Re}\,h_1^3}-\frac{2\,\mathrm{i}\,\Omega_{\mathrm{Re}}\,\alpha_s\,\overline{\mu}\,\hat{u}}{\mathrm{Re}\,h_1^2}+\frac{2\,\alpha^2\,\overline{\mu}\,\hat{u}}{\mathrm{Re}\,h_1^2}-\frac{\mathrm{i}\,\Omega_{\mathrm{Re}}\,\overline{T}_s\,\alpha\,\overline{\lambda}_{v\overline{T}}\,\hat{u}}{\mathrm{Re}\,h_1^2}-\frac{\mathrm{i}\,\Omega_{\mathrm{Re}}\,\alpha\,h_{3,s}\,\overline{\lambda}_v\,\hat{u}}{\mathrm{Re}\,h_1^2\,h_3}
$$

$$
+\frac{\mathrm{i}\,\Omega_{\mathrm{Re}}\,\alpha\,h_{1,s}\,\overline{\lambda}_v\,\hat{u}}{\mathrm{Re}\,h_1^3}-\frac{\mathrm{i}\,\Omega_{\mathrm{Re}}\,\alpha_s\,\overline{\lambda}_v\,\hat{u}}{\mathrm{Re}\,h_1^2}+\frac{\alpha^2\,\overline{\lambda}_v\,\hat{u}}{\mathrm{Re}\,h_1^2}-\frac{\hat{T}\,\overline{\mu}_{\overline{T}}\,\overline{u}_{y\,y}}{\mathrm{Re}}-\frac{\overline{T}_y\,\hat{T}\,\overline{\mu}_{\overline{T}\,\overline{T}}\,\overline{u}_y}{\mathrm{Re}}-\frac{\hat{T}\,h_{3,y}\,\overline{\mu}_{\overline{T}}\,\overline{u}_y}{\mathrm{Re}\,h_3}
$$

$$
\begin{aligned}
&-\frac{\hat{T}\,h_{1,y}\,\overline{\mu}_{\overline{T}}\,\overline{u}_y}{\mathrm{Re}\,h_1}-\frac{\hat{T}_y\,\overline{\mu}_{\overline{T}}\,\overline{u}_y}{\mathrm{Re}}+\frac{\hat{\rho}\,\overline{u}\,\overline{u}_s}{h_1}-\frac{2\,\mathrm{i}\,\Omega_{\mathrm{Re}}\,\hat{T}\,\alpha\,\overline{\mu}_{\overline{T}}\,\overline{u}_s}{\mathrm{Re}\,h_1^2}-\frac{\mathrm{i}\,\Omega_{\mathrm{Re}}\,\hat{T}\,\alpha\,\overline{\lambda}_{v\overline{T}}\,\overline{u}_s}{\mathrm{Re}\,h_1^2}\\
&+\frac{\overline{T}_y\,\hat{T}\,h_{1,y}\,\overline{\mu}_{\overline{T}\,\overline{T}}\,\overline{u}}{\mathrm{Re}\,h_1}+\frac{\hat{T}\,h_{1,y}\,h_{3,y}\,\overline{\mu}_{\overline{T}}\,\overline{u}}{\mathrm{Re}\,h_1\,h_3}+\frac{\hat{T}\,h_{1,y\,y}\,\overline{\mu}_{\overline{T}}\,\overline{u}}{\mathrm{Re}\,h_1}+\frac{\hat{T}\,\left(h_{1,y}\right)^2\,\overline{\mu}_{\overline{T}}\,\overline{u}}{\mathrm{Re}\,h_1^2}+\frac{\hat{T}_y\,h_{1,y}\,\overline{\mu}_{\overline{T}}\,\overline{u}}{\mathrm{Re}\,h_1}\\
&-\frac{\mathrm{i}\,\Omega_{\mathrm{Re}}\,\hat{T}\,\alpha\,h_{3,s}\,\overline{\lambda}_{v\overline{T}}\,\overline{u}}{\mathrm{Re}\,h_1^2\,h_3}+\frac{\Omega_p\,\overline{T}\,\hat{\rho}_s}{\mathrm{M}^2\,\gamma\,h_1}+\frac{\mathrm{i}\,\overline{T}\,\alpha\,\hat{\rho}}{\mathrm{M}^2\,\gamma\,h_1}+\frac{\Omega_p\,\overline{T}_s\,\hat{\rho}}{\mathrm{M}^2\,\gamma\,h_1}+\frac{\Omega_p\,\hat{T}\,\overline{\rho}_s}{\mathrm{M}^2\,\gamma\,h_1}\\
&+\frac{\mathrm{i}\,\hat{T}\,\alpha\,\overline{\rho}}{\mathrm{M}^2\,\gamma\,h_1}+\frac{\Omega_p\,\hat{T}_s\,\overline{\rho}}{\mathrm{M}^2\,\gamma\,h_1}=0
\end{aligned}
$$

A.2 Momentum conservation in the y-direction

$$
-\frac{\mathrm{i}\,\beta\,\overline{\mu}\,\hat{w}_y}{\mathrm{Re}\,h_3}-\frac{\mathrm{i}\,\beta\,\overline{\lambda}_v\,\hat{w}_y}{\mathrm{Re}\,h_3}-\frac{2\,h_{3,y}\,\overline{\rho}\,\overline{w}\,\hat{w}}{h_3}+\frac{3\,\mathrm{i}\,\beta\,h_{3,y}\,\overline{\mu}\,\hat{w}}{\mathrm{Re}\,h_3^2}-\frac{\mathrm{i}\,\overline{T}_y\,\beta\,\overline{\lambda}_{v\overline{T}}\,\hat{w}}{\mathrm{Re}\,h_3}+\frac{\mathrm{i}\,\beta\,h_{3,y}\,\overline{\lambda}_v\,\hat{w}}{\mathrm{Re}\,h_3^2}
$$

$$
-\frac{\mathrm{i}\,\hat{T}\,\beta\,\overline{\mu}_{\overline{T}}\,\overline{w}_y}{\mathrm{Re}\,h_3}-\frac{h_{3,y}\,\hat{\rho}\,\overline{w}^2}{h_3}+\frac{\mathrm{i}\,\beta\,\overline{\rho}\,\hat{v}\,\overline{w}}{h_3}+\frac{\mathrm{i}\,\hat{T}\,\beta\,h_{3,y}\,\overline{\mu}_{\overline{T}}\,\overline{w}}{\mathrm{Re}\,h_3^2}-\frac{2\,\overline{\mu}\,\hat{v}_{y\,y}}{\mathrm{Re}}-\frac{\overline{\lambda}_v\,\hat{v}_{y\,y}}{\mathrm{Re}}
$$

$$
+\overline{\rho}\,\overline{v}\,\hat{v}_y-\frac{2\,\overline{T}_y\,\overline{\mu}_{\overline{T}}\,\hat{v}_y}{\mathrm{Re}}-\frac{2\,h_{3,y}\,\overline{\mu}\,\hat{v}_y}{\mathrm{Re}\,h_3}-\frac{2\,h_{1,y}\,\overline{\mu}\,\hat{v}_y}{\mathrm{Re}\,h_1}-\frac{\overline{T}_y\,\overline{\lambda}_{v\overline{T}}\,\hat{v}_y}{\mathrm{Re}}-\frac{h_{3,y}\,\overline{\lambda}_v\,\hat{v}_y}{\mathrm{Re}\,h_3}
$$

$$
-\frac{h_{1,y}\,\overline{\lambda}_v\,\hat{v}_y}{\mathrm{Re}\,h_1}+\frac{\overline{\rho}\,\overline{u}\,\hat{v}_s}{h_1}-\frac{2\,\mathrm{i}\,\Omega_{\mathrm{Re}}\,\alpha\,\overline{\mu}\,\hat{v}_s}{\mathrm{Re}\,h_1^2}+\overline{\rho}\,\overline{v}_y\,\hat{v}+\frac{\mathrm{i}\,\alpha\,\overline{\rho}\,\overline{u}\,\hat{v}}{h_1}-\mathrm{i}\,\omega\,\overline{\rho}\,\hat{v}-\frac{\mathrm{i}\,\Omega_{\mathrm{Re}}\,\overline{T}_s\,\alpha\,\overline{\mu}_{\overline{T}}\,\hat{v}}{\mathrm{Re}\,h_1^2}
$$

$$
+\frac{2\,\left(h_{3,y}\right)^2\,\overline{\mu}\,\hat{v}}{\mathrm{Re}\,h_3^2}-\frac{\mathrm{i}\,\Omega_{\mathrm{Re}}\,\alpha\,h_{3,s}\,\overline{\mu}\,\hat{v}}{\mathrm{Re}\,h_1^2\,h_3}+\frac{\beta^2\,\overline{\mu}\,\hat{v}}{\mathrm{Re}\,h_3^2}+\frac{2\,\left(h_{1,y}\right)^2\,\overline{\mu}\,\hat{v}}{\mathrm{Re}\,h_1^2}+\frac{\mathrm{i}\,\Omega_{\mathrm{Re}}\,\alpha\,h_{1,s}\,\overline{\mu}\,\hat{v}}{\mathrm{Re}\,h_1^3}-\frac{\mathrm{i}\,\Omega_{\mathrm{Re}}\,\alpha_s\,\overline{\mu}\,\hat{v}}{\mathrm{Re}\,h_1^2}
$$

$$
+\frac{\alpha^2\,\overline{\mu}\,\hat{v}}{\mathrm{Re}\,h_1^2}-\frac{\overline{T}_y\,h_{3,y}\,\overline{\lambda}_{v\overline{T}}\,\hat{v}}{\mathrm{Re}\,h_3}-\frac{\overline{T}_y\,h_{1,y}\,\overline{\lambda}_{v\overline{T}}\,\hat{v}}{\mathrm{Re}\,h_1}-\frac{h_{3,y\,y}\,\overline{\lambda}_v\,\hat{v}}{\mathrm{Re}\,h_3}+\frac{\left(h_{3,y}\right)^2\,\overline{\lambda}_v\,\hat{v}}{\mathrm{Re}\,h_3^2}-\frac{h_{1,y\,y}\,\overline{\lambda}_v\,\hat{v}}{\mathrm{Re}\,h_1}
$$

$$
+\frac{\left(h_{1,y}\right)^2\,\overline{\lambda}_v\,\hat{v}}{\mathrm{Re}\,h_1^2}-\frac{2\,\Omega_{\mathrm{Re}}\,\hat{T}\,\overline{\mu}_{\overline{T}}\,\overline{v}_{y\,y}}{\mathrm{Re}}-\frac{\Omega_{\mathrm{Re}}\,\hat{T}\,\overline{\lambda}_{v\overline{T}}\,\overline{v}_{y\,y}}{\mathrm{Re}}-\frac{2\,\Omega_{\mathrm{Re}}\,\overline{T}_y\,\hat{T}\,\overline{\mu}_{\overline{T}\,\overline{T}}\,\overline{v}_y}{\mathrm{Re}}-\frac{2\,\Omega_{\mathrm{Re}}\,\hat{T}\,h_{3,y}\,\overline{\mu}_{\overline{T}}\,\overline{v}_y}{\mathrm{Re}\,h_3}
$$

$$
-\frac{2\,\Omega_{\mathrm{Re}}\,\hat{T}\,h_{1,y}\,\overline{\mu}_{\overline{T}}\,\overline{v}_y}{\mathrm{Re}\,h_1}-\frac{2\,\Omega_{\mathrm{Re}}\,\hat{T}_y\,\overline{\mu}_{\overline{T}}\,\overline{v}_y}{\mathrm{Re}}-\frac{\Omega_{\mathrm{Re}}\,\overline{T}_y\,\hat{T}\,\overline{\lambda}_{v\overline{T}\,\overline{T}}\,\overline{v}_y}{\mathrm{Re}}-\frac{\Omega_{\mathrm{Re}}\,\hat{T}\,h_{3,y}\,\overline{\lambda}_{v\overline{T}}\,\overline{v}_y}{\mathrm{Re}\,h_3}
$$

$$
-\frac{\Omega_{\mathrm{Re}}\,\hat{T}\,h_{1,y}\,\overline{\lambda}_{v\overline{T}}\,\overline{v}_y}{\mathrm{Re}\,h_1}-\frac{\Omega_{\mathrm{Re}}\,\hat{T}_y\,\overline{\lambda}_{v\overline{T}}\,\overline{v}_y}{\mathrm{Re}}+\frac{2\,\Omega_{\mathrm{Re}}\,\hat{T}\,\left(h_{3,y}\right)^2\,\overline{\mu}_{\overline{T}}\,\overline{v}}{\mathrm{Re}\,h_3^2}+\frac{2\,\Omega_{\mathrm{Re}}\,\hat{T}\,\left(h_{1,y}\right)^2\,\overline{\mu}_{\overline{T}}\,\overline{v}}{\mathrm{Re}\,h_1^2}
$$

$$
-\frac{\Omega_{\mathrm{Re}}\,\overline{T}_y\,\hat{T}\,h_{3,y}\,\overline{\lambda}_{v\overline{T}\,\overline{T}}\,\overline{v}}{\mathrm{Re}\,h_3}-\frac{\Omega_{\mathrm{Re}}\,\overline{T}_y\,\hat{T}\,h_{1,y}\,\overline{\lambda}_{v\overline{T}\,\overline{T}}\,\overline{v}}{\mathrm{Re}\,h_1}-\frac{\Omega_{\mathrm{Re}}\,\hat{T}\,h_{3,y\,y}\,\overline{\lambda}_{v\overline{T}}\,\overline{v}}{\mathrm{Re}\,h_3}+\frac{\Omega_{\mathrm{Re}}\,\hat{T}\,\left(h_{3,y}\right)^2\,\overline{\lambda}_{v\overline{T}}\,\overline{v}}{\mathrm{Re}\,h_3^2}
$$

$$
-\frac{\Omega_{\mathrm{Re}}\,\hat{T}_y\,h_{3,y}\,\overline{\lambda}_{v\overline{T}}\,\overline{v}}{\mathrm{Re}\,h_3}-\frac{\Omega_{\mathrm{Re}}\,\hat{T}\,h_{1,y\,y}\,\overline{\lambda}_{v\overline{T}}\,\overline{v}}{\mathrm{Re}\,h_1}+\frac{\Omega_{\mathrm{Re}}\,\hat{T}\,\left(h_{1,y}\right)^2\,\overline{\lambda}_{v\overline{T}}\,\overline{v}}{\mathrm{Re}\,h_1^2}-\frac{\Omega_{\mathrm{Re}}\,\hat{T}_y\,h_{1,y}\,\overline{\lambda}_{v\overline{T}}\,\overline{v}}{\mathrm{Re}\,h_1}
$$

$$
-\frac{\Omega_{\mathrm{Re}}\,\overline{T}_s\,\overline{\mu}_{\overline{T}}\,\hat{u}_y}{\mathrm{Re}\,h_1}-\frac{\Omega_{\mathrm{Re}}\,h_{3,s}\,\overline{\mu}\,\hat{u}_y}{\mathrm{Re}\,h_1\,h_3}-\frac{\mathrm{i}\,\alpha\,\overline{\mu}\,\hat{u}_y}{\mathrm{Re}\,h_1}-\frac{\Omega_{\mathrm{Re}}\,h_{3,s}\,\overline{\lambda}_v\,\hat{u}_y}{\mathrm{Re}\,h_1\,h_3}-\frac{\mathrm{i}\,\alpha\,\overline{\lambda}_v\,\hat{u}_y}{\mathrm{Re}\,h_1}-\frac{\Omega_{\mathrm{Re}}\,\overline{\mu}\,\hat{u}_{s\,y}}{\mathrm{Re}\,h_1}
$$

$$
-\frac{\Omega_{\mathrm{Re}}\,\overline{\lambda}_v\,\hat{u}_{s\,y}}{\mathrm{Re}\,h_1}+\frac{3\,\Omega_{\mathrm{Re}}\,h_{1,y}\,\overline{\mu}\,\hat{u}_s}{\mathrm{Re}\,h_1^2}-\frac{\Omega_{\mathrm{Re}}\,\overline{T}_y\,\overline{\lambda}_{v\overline{T}}\,\hat{u}_s}{\mathrm{Re}\,h_1}+\frac{\Omega_{\mathrm{Re}}\,h_{1,y}\,\overline{\lambda}_v\,\hat{u}_s}{\mathrm{Re}\,h_1^2}-\frac{2\,h_{1,y}\,\overline{\rho}\,\overline{u}\,\hat{u}}{h_1}
$$

$$
+\frac{\Omega_{\mathrm{Re}}\,\overline{T}_s\,h_{1,y}\,\overline{\mu}_{\overline{T}}\,\hat{u}}{\mathrm{Re}\,h_1^2}+\frac{2\,\Omega_{\mathrm{Re}}\,h_{3,s}\,h_{3,y}\,\overline{\mu}\,\hat{u}}{\mathrm{Re}\,h_1\,h_3^2}+\frac{\Omega_{\mathrm{Re}}\,h_{1,y}\,h_{3,s}\,\overline{\mu}\,\hat{u}}{\mathrm{Re}\,h_1^2\,h_3}-\frac{\Omega_{\mathrm{Re}}\,h_{1,s}\,h_{1,y}\,\overline{\mu}\,\hat{u}}{\mathrm{Re}\,h_1^3}+\frac{3\,\mathrm{i}\,\alpha\,h_{1,y}\,\overline{\mu}\,\hat{u}}{\mathrm{Re}\,h_1^2}
$$

$$
+\frac{\Omega_{\mathrm{Re}}\,h_{1,s\,y}\,\overline{\mu}\,\hat{u}}{\mathrm{Re}\,h_1^2}-\frac{\Omega_{\mathrm{Re}}\,\overline{T}_y\,h_{3,s}\,\overline{\lambda}_{v\overline{T}}\,\hat{u}}{\mathrm{Re}\,h_1\,h_3}-\frac{\mathrm{i}\,\overline{T}_y\,\alpha\,\overline{\lambda}_{v\overline{T}}\,\hat{u}}{\mathrm{Re}\,h_1}+\frac{\Omega_{\mathrm{Re}}\,h_{3,s}\,h_{3,y}\,\overline{\lambda}_v\,\hat{u}}{\mathrm{Re}\,h_1\,h_3^2}-\frac{\Omega_{\mathrm{Re}}\,h_{3,s\,y}\,\overline{\lambda}_v\,\hat{u}}{\mathrm{Re}\,h_1\,h_3}
$$

$$
+\frac{\Omega_{\mathrm{Re}}\,h_{1,y}\,h_{3,s}\,\overline{\lambda}_v\,\hat{u}}{\mathrm{Re}\,h_1^2\,h_3}+\frac{\mathrm{i}\,\alpha\,h_{1,y}\,\overline{\lambda}_v\,\hat{u}}{\mathrm{Re}\,h_1^2}-\frac{\Omega_{\mathrm{Re}}\,\overline{T}_s\,\hat{T}\,\overline{\mu}_{\overline{T}\,\overline{T}}\,\overline{u}_y}{\mathrm{Re}\,h_1}-\frac{\Omega_{\mathrm{Re}}\,\hat{T}\,h_{3,s}\,\overline{\mu}_{\overline{T}}\,\overline{u}_y}{\mathrm{Re}\,h_1\,h_3}
$$

$$
\begin{aligned}
&-\frac{\mathrm{i}\,\hat{T}\,\alpha\,\overline{\mu}_{\overline{T}}\,\overline{u}_y}{\mathrm{Re}\,h_1}-\frac{\Omega_{\mathrm{Re}}\,\hat{T}_s\,\overline{\mu}_{\overline{T}}\,\overline{u}_y}{\mathrm{Re}\,h_1}-\frac{\Omega_{\mathrm{Re}}\,\hat{T}\,h_{3,s}\,\overline{\lambda}_{v\overline{T}}\,\overline{u}_y}{\mathrm{Re}\,h_1\,h_3}-\frac{\Omega_{\mathrm{Re}}\,\hat{T}\,\overline{\mu}_{\overline{T}}\,\overline{u}_{s\,y}}{\mathrm{Re}\,h_1}-\frac{\Omega_{\mathrm{Re}}\,\hat{T}\,\overline{\lambda}_{v\overline{T}}\,\overline{u}_{s\,y}}{\mathrm{Re}\,h_1}\\
&+\frac{3\,\Omega_{\mathrm{Re}}\,\hat{T}\,h_{1,y}\,\overline{\mu}_{\overline{T}}\,\overline{u}_s}{\mathrm{Re}\,h_1^2}-\frac{\Omega_{\mathrm{Re}}\,\overline{T}_y\,\hat{T}\,\overline{\lambda}_{v\overline{T}\,\overline{T}}\,\overline{u}_s}{\mathrm{Re}\,h_1}+\frac{\Omega_{\mathrm{Re}}\,\hat{T}\,h_{1,y}\,\overline{\lambda}_{v\overline{T}}\,\overline{u}_s}{\mathrm{Re}\,h_1^2}-\frac{\Omega_{\mathrm{Re}}\,\hat{T}_y\,\overline{\lambda}_{v\overline{T}}\,\overline{u}_s}{\mathrm{Re}\,h_1}-\frac{h_{1,y}\,\hat{\rho}\,\overline{u}^2}{h_1}\\
&+\frac{\Omega_{\mathrm{Re}}\,\overline{T}_s\,\hat{T}\,h_{1,y}\,\overline{\mu}_{\overline{T}\,\overline{T}}\,\overline{u}}{\mathrm{Re}\,h_1^2}+\frac{2\,\Omega_{\mathrm{Re}}\,\hat{T}\,h_{3,s}\,h_{3,y}\,\overline{\mu}_{\overline{T}}\,\overline{u}}{\mathrm{Re}\,h_1\,h_3^2}+\frac{\Omega_{\mathrm{Re}}\,\hat{T}\,h_{1,y}\,h_{3,s}\,\overline{\mu}_{\overline{T}}\,\overline{u}}{\mathrm{Re}\,h_1^2\,h_3}-\frac{\Omega_{\mathrm{Re}}\,\hat{T}\,h_{1,s}\,h_{1,y}\,\overline{\mu}_{\overline{T}}\,\overline{u}}{\mathrm{Re}\,h_1^3}\\
&+\frac{\mathrm{i}\,\hat{T}\,\alpha\,h_{1,y}\,\overline{\mu}_{\overline{T}}\,\overline{u}}{\mathrm{Re}\,h_1^2}+\frac{\Omega_{\mathrm{Re}}\,\hat{T}_s\,h_{1,y}\,\overline{\mu}_{\overline{T}}\,\overline{u}}{\mathrm{Re}\,h_1^2}+\frac{\Omega_{\mathrm{Re}}\,\hat{T}\,h_{1,s\,y}\,\overline{\mu}_{\overline{T}}\,\overline{u}}{\mathrm{Re}\,h_1^2}-\frac{\Omega_{\mathrm{Re}}\,\overline{T}_y\,\hat{T}\,h_{3,s}\,\overline{\lambda}_{v\overline{T}\,\overline{T}}\,\overline{u}}{\mathrm{Re}\,h_1\,h_3}\\
&+\frac{\Omega_{\mathrm{Re}}\,\hat{T}\,h_{3,s}\,h_{3,y}\,\overline{\lambda}_{v\overline{T}}\,\overline{u}}{\mathrm{Re}\,h_1\,h_3^2}-\frac{\Omega_{\mathrm{Re}}\,\hat{T}\,h_{3,s\,y}\,\overline{\lambda}_{v\overline{T}}\,\overline{u}}{\mathrm{Re}\,h_1\,h_3}+\frac{\Omega_{\mathrm{Re}}\,\hat{T}\,h_{1,y}\,h_{3,s}\,\overline{\lambda}_{v\overline{T}}\,\overline{u}}{\mathrm{Re}\,h_1^2\,h_3}-\frac{\Omega_{\mathrm{Re}}\,\hat{T}_y\,h_{3,s}\,\overline{\lambda}_{v\overline{T}}\,\overline{u}}{\mathrm{Re}\,h_1\,h_3}\\
&+\frac{\overline{T}\,\hat{\rho}_y}{\mathrm{M}^2\,\gamma}+\frac{\overline{T}_y\,\hat{\rho}}{\mathrm{M}^2\,\gamma}+\frac{\hat{T}\,\overline{\rho}_y}{\mathrm{M}^2\,\gamma}+\frac{\hat{T}_y\,\overline{\rho}}{\mathrm{M}^2\,\gamma}=0
\end{aligned}
$$

A.3 Momentum conservation in the z-direction

$$
\begin{aligned}
&-\frac{\overline{\mu}\,\hat{w}_{y\,y}}{\mathrm{Re}}+\overline{\rho}\,\overline{v}\,\hat{w}_y-\frac{\overline{T}_y\,\overline{\mu}_{\overline{T}}\,\hat{w}_y}{\mathrm{Re}}-\frac{h_{3,y}\,\overline{\mu}\,\hat{w}_y}{\mathrm{Re}\,h_3}-\frac{h_{1,y}\,\overline{\mu}\,\hat{w}_y}{\mathrm{Re}\,h_1}+\frac{\overline{\rho}\,\overline{u}\,\hat{w}_s}{h_1}-\frac{2\,\mathrm{i}\,\Omega_{\mathrm{Re}}\,\alpha\,\overline{\mu}\,\hat{w}_s}{\mathrm{Re}\,h_1^2}\\
&+\frac{\mathrm{i}\,\beta\,\overline{\rho}\,\overline{w}\,\hat{w}}{h_3}+\frac{h_{3,y}\,\overline{\rho}\,\overline{v}\,\hat{w}}{h_3}+\frac{h_{3,s}\,\overline{\rho}\,\overline{u}\,\hat{w}}{h_1\,h_3}+\frac{\mathrm{i}\,\alpha\,\overline{\rho}\,\overline{u}\,\hat{w}}{h_1}-\mathrm{i}\,\omega\,\overline{\rho}\,\hat{w}+\frac{\overline{T}_y\,h_{3,y}\,\overline{\mu}_{\overline{T}}\,\hat{w}}{\mathrm{Re}\,h_3}\\
&-\frac{\mathrm{i}\,\Omega_{\mathrm{Re}}\,\overline{T}_s\,\alpha\,\overline{\mu}_{\overline{T}}\,\hat{w}}{\mathrm{Re}\,h_1^2}+\frac{h_{3,y\,y}\,\overline{\mu}\,\hat{w}}{\mathrm{Re}\,h_3}+\frac{(h_{3,y})^2\,\overline{\mu}\,\hat{w}}{\mathrm{Re}\,h_3^2}+\frac{h_{1,y}\,h_{3,y}\,\overline{\mu}\,\hat{w}}{\mathrm{Re}\,h_1\,h_3}-\frac{\mathrm{i}\,\Omega_{\mathrm{Re}}\,\alpha\,h_{3,s}\,\overline{\mu}\,\hat{w}}{\mathrm{Re}\,h_1^2\,h_3}+\frac{2\,\beta^2\,\overline{\mu}\,\hat{w}}{\mathrm{Re}\,h_3^2}\\
&+\frac{\mathrm{i}\,\Omega_{\mathrm{Re}}\,\alpha\,h_{1,s}\,\overline{\mu}\,\hat{w}}{\mathrm{Re}\,h_1^3}-\frac{\mathrm{i}\,\Omega_{\mathrm{Re}}\,\alpha_s\,\overline{\mu}\,\hat{w}}{\mathrm{Re}\,h_1^2}+\frac{\alpha^2\,\overline{\mu}\,\hat{w}}{\mathrm{Re}\,h_1^2}+\frac{\beta^2\,\overline{\lambda}_v\,\hat{w}}{\mathrm{Re}\,h_3^2}-\frac{\hat{T}\,\overline{\mu}_{\overline{T}}\,\overline{w}_{y\,y}}{\mathrm{Re}}+\overline{\rho}\,\hat{v}\,\overline{w}_y\\
&+\hat{\rho}\,\overline{v}\,\overline{w}_y-\frac{\overline{T}_y\,\hat{T}\,\overline{\mu}_{\overline{T}\,\overline{T}}\,\overline{w}_y}{\mathrm{Re}}-\frac{\hat{T}\,h_{3,y}\,\overline{\mu}_{\overline{T}}\,\overline{w}_y}{\mathrm{Re}\,h_3}-\frac{\hat{T}\,h_{1,y}\,\overline{\mu}_{\overline{T}}\,\overline{w}_y}{\mathrm{Re}\,h_1}-\frac{\hat{T}_y\,\overline{\mu}_{\overline{T}}\,\overline{w}_y}{\mathrm{Re}}+\frac{\overline{\rho}\,\hat{u}\,\overline{w}_s}{h_1}+\frac{\hat{\rho}\,\overline{u}\,\overline{w}_s}{h_1}\\
&-\frac{\mathrm{i}\,\Omega_{\mathrm{Re}}\,\hat{T}\,\alpha\,\overline{\mu}_{\overline{T}}\,\overline{w}_s}{\mathrm{Re}\,h_1^2}+\frac{h_{3,y}\,\overline{\rho}\,\hat{v}\,\overline{w}}{h_3}+\frac{h_{3,y}\,\hat{\rho}\,\overline{v}\,\overline{w}}{h_3}+\frac{h_{3,s}\,\overline{\rho}\,\hat{u}\,\overline{w}}{h_1\,h_3}+\frac{h_{3,s}\,\hat{\rho}\,\overline{u}\,\overline{w}}{h_1\,h_3}+\frac{\overline{T}_y\,\hat{T}\,h_{3,y}\,\overline{\mu}_{\overline{T}\,\overline{T}}\,\overline{w}}{\mathrm{Re}\,h_3}\\
&+\frac{\hat{T}\,h_{3,y\,y}\,\overline{\mu}_{\overline{T}}\,\overline{w}}{\mathrm{Re}\,h_3}+\frac{\hat{T}\,(h_{3,y})^2\,\overline{\mu}_{\overline{T}}\,\overline{w}}{\mathrm{Re}\,h_3^2}+\frac{\hat{T}\,h_{1,y}\,h_{3,y}\,\overline{\mu}_{\overline{T}}\,\overline{w}}{\mathrm{Re}\,h_1\,h_3}+\frac{\hat{T}_y\,h_{3,y}\,\overline{\mu}_{\overline{T}}\,\overline{w}}{\mathrm{Re}\,h_3}+\frac{\mathrm{i}\,\Omega_{\mathrm{Re}}\,\hat{T}\,\alpha\,h_{3,s}\,\overline{\mu}_{\overline{T}}\,\overline{w}}{\mathrm{Re}\,h_1^2\,h_3}\\
&-\frac{\mathrm{i}\,\beta\,\overline{\mu}\,\hat{v}_y}{\mathrm{Re}\,h_3}-\frac{\mathrm{i}\,\beta\,\overline{\lambda}_v\,\hat{v}_y}{\mathrm{Re}\,h_3}-\frac{\mathrm{i}\,\overline{T}_y\,\beta\,\overline{\mu}_{\overline{T}}\,\hat{v}}{\mathrm{Re}\,h_3}-\frac{3\,\mathrm{i}\,\beta\,h_{3,y}\,\overline{\mu}\,\hat{v}}{\mathrm{Re}\,h_3^2}-\frac{\mathrm{i}\,\beta\,h_{1,y}\,\overline{\mu}\,\hat{v}}{\mathrm{Re}\,h_1\,h_3}-\frac{\mathrm{i}\,\beta\,h_{3,y}\,\overline{\lambda}_v\,\hat{v}}{\mathrm{Re}\,h_3^2}\\
&-\frac{\mathrm{i}\,\beta\,h_{1,y}\,\overline{\lambda}_v\,\hat{v}}{\mathrm{Re}\,h_1\,h_3}-\frac{\mathrm{i}\,\Omega_{\mathrm{Re}}\,\hat{T}\,\beta\,\overline{\lambda}_{v\overline{T}}\,\overline{v}_y}{\mathrm{Re}\,h_3}-\frac{2\,\mathrm{i}\,\Omega_{\mathrm{Re}}\,\hat{T}\,\beta\,h_{3,y}\,\overline{\mu}_{\overline{T}}\,\overline{v}}{\mathrm{Re}\,h_3^2}-\frac{\mathrm{i}\,\Omega_{\mathrm{Re}}\,\hat{T}\,\beta\,h_{3,y}\,\overline{\lambda}_{v\overline{T}}\,\overline{v}}{\mathrm{Re}\,h_3^2}\\
&-\frac{\mathrm{i}\,\Omega_{\mathrm{Re}}\,\hat{T}\,\beta\,h_{1,y}\,\overline{\lambda}_{v\overline{T}}\,\overline{v}}{\mathrm{Re}\,h_1\,h_3}-\frac{\mathrm{i}\,\Omega_{\mathrm{Re}}\,\beta\,\overline{\mu}\,\hat{u}_s}{\mathrm{Re}\,h_1\,h_3}-\frac{\mathrm{i}\,\Omega_{\mathrm{Re}}\,\beta\,\overline{\lambda}_v\,\hat{u}_s}{\mathrm{Re}\,h_1\,h_3}-\frac{\mathrm{i}\,\Omega_{\mathrm{Re}}\,\overline{T}_s\,\beta\,\overline{\mu}_{\overline{T}}\,\hat{u}}{\mathrm{Re}\,h_1\,h_3}-\frac{3\,\mathrm{i}\,\Omega_{\mathrm{Re}}\,\beta\,h_{3,s}\,\overline{\mu}\,\hat{u}}{\mathrm{Re}\,h_1\,h_3^2}\\
&+\frac{\alpha\,\beta\,\overline{\mu}\,\hat{u}}{\mathrm{Re}\,h_1\,h_3}-\frac{\mathrm{i}\,\Omega_{\mathrm{Re}}\,\beta\,h_{3,s}\,\overline{\lambda}_v\,\hat{u}}{\mathrm{Re}\,h_1\,h_3^2}+\frac{\alpha\,\beta\,\overline{\lambda}_v\,\hat{u}}{\mathrm{Re}\,h_1\,h_3}-\frac{\mathrm{i}\,\Omega_{\mathrm{Re}}\,\hat{T}\,\beta\,\overline{\lambda}_{v\overline{T}}\,\overline{u}_s}{\mathrm{Re}\,h_1\,h_3}-\frac{2\,\mathrm{i}\,\Omega_{\mathrm{Re}}\,\hat{T}\,\beta\,h_{3,s}\,\overline{\mu}_{\overline{T}}\,\overline{u}}{\mathrm{Re}\,h_1\,h_3^2}\\
&-\frac{\mathrm{i}\,\Omega_{\mathrm{Re}}\,\hat{T}\,\beta\,h_{3,s}\,\overline{\lambda}_{v\overline{T}}\,\overline{u}}{\mathrm{Re}\,h_1\,h_3^2}+\frac{\mathrm{i}\,\overline{T}\,\beta\,\hat{\rho}}{\mathrm{M}^2\,\gamma\,h_3}+\frac{\mathrm{i}\,\hat{T}\,\beta\,\overline{\rho}}{\mathrm{M}^2\,\gamma\,h_3}=0
\end{aligned}
$$

A.4 Conservation of energy (enthalpy formulation)

$$
-\frac{2\,\mathrm{Ec}\,\overline{\mu}\,\overline{w}_y\,\hat{w}_y}{\mathrm{Re}}+\frac{2\,\mathrm{Ec}\,h_{3,y}\,\overline{\mu}\,\overline{w}\,\hat{w}_y}{\mathrm{Re}\,h_3}+\frac{2\,\mathrm{Ec}\,h_{3,y}\,\overline{\mu}\,\overline{w}_y\,\hat{w}}{\mathrm{Re}\,h_3}-\frac{2\,\mathrm{i}\,\mathrm{Ec}\,\Omega_{\mathrm{Re}}\,\alpha\,\overline{\mu}\,\overline{w}_s\,\hat{w}}{\mathrm{Re}\,h_1^2}
$$

$$
-\frac{2\,\mathrm{Ec}\,\left(h_{3,y}\right)^2\,\overline{\mu}\,\overline{w}\,\hat{w}}{\mathrm{Re}\,h_3^2}+\frac{2\,\mathrm{i}\,\mathrm{Ec}\,\Omega_{\mathrm{Re}}\,\alpha\,h_{3,s}\,\overline{\mu}\,\overline{w}\,\hat{w}}{\mathrm{Re}\,h_1^2\,h_3}-\frac{2\,\mathrm{i}\,\mathrm{Ec}\,\Omega_{\mathrm{Re}}\,\beta\,\overline{\lambda}_v\,\overline{v}_y\,\hat{w}}{\mathrm{Re}\,h_3}
$$

$$
-\frac{4\,\mathrm{i}\,\mathrm{Ec}\,\Omega_{\mathrm{Re}}\,\beta\,h_{3,y}\,\overline{\mu}\,\overline{v}\,\hat{w}}{\mathrm{Re}\,h_3^2}-\frac{2\,\mathrm{i}\,\mathrm{Ec}\,\Omega_{\mathrm{Re}}\,\beta\,h_{3,y}\,\overline{\lambda}_v\,\overline{v}\,\hat{w}}{\mathrm{Re}\,h_3^2}-\frac{2\,\mathrm{i}\,\mathrm{Ec}\,\Omega_{\mathrm{Re}}\,\beta\,h_{1,y}\,\overline{\lambda}_v\,\overline{v}\,\hat{w}}{\mathrm{Re}\,h_1\,h_3}
$$

$$
-\frac{2\,\mathrm{i}\,\mathrm{Ec}\,\Omega_{\mathrm{Re}}\,\beta\,\overline{\lambda}_v\,\overline{u}_s\,\hat{w}}{\mathrm{Re}\,h_1\,h_3}-\frac{4\,\mathrm{i}\,\mathrm{Ec}\,\Omega_{\mathrm{Re}}\,\beta\,h_{3,s}\,\overline{\mu}\,\overline{u}\,\hat{w}}{\mathrm{Re}\,h_1\,h_3^2}-\frac{2\,\mathrm{i}\,\mathrm{Ec}\,\Omega_{\mathrm{Re}}\,\beta\,h_{3,s}\,\overline{\lambda}_v\,\overline{u}\,\hat{w}}{\mathrm{Re}\,h_1\,h_3^2}
$$

$$
-\frac{\mathrm{Ec}\,\hat{T}\,\overline{\mu}_{\overline{T}}\,\left(\overline{w}_y\right)^2}{\mathrm{Re}}+\frac{2\,\mathrm{Ec}\,\hat{T}\,h_{3,y}\,\overline{\mu}_{\overline{T}}\,\overline{w}\,\overline{w}_y}{\mathrm{Re}\,h_3}-\frac{2\,\mathrm{i}\,\mathrm{Ec}\,\beta\,\overline{\mu}\,\hat{v}\,\overline{w}_y}{\mathrm{Re}\,h_3}-\frac{2\,\mathrm{i}\,\mathrm{Ec}\,\Omega_{\mathrm{Re}}\,\beta\,\overline{\mu}\,\hat{u}\,\overline{w}_s}{\mathrm{Re}\,h_1\,h_3}
$$

$$
-\frac{\mathrm{Ec}\,\hat{T}\,\left(h_{3,y}\right)^2\,\overline{\mu}_{\overline{T}}\,\overline{w}^2}{\mathrm{Re}\,h_3^2}+\frac{2\,\mathrm{i}\,\mathrm{Ec}\,\beta\,h_{3,y}\,\overline{\mu}\,\hat{v}\,\overline{w}}{\mathrm{Re}\,h_3^2}+\frac{2\,\mathrm{i}\,\mathrm{Ec}\,\Omega_{\mathrm{Re}}\,\beta\,h_{3,s}\,\overline{\mu}\,\hat{u}\,\overline{w}}{\mathrm{Re}\,h_1\,h_3^2}-\frac{\mathrm{i}\,\mathrm{Ec}\,\overline{T}\,\beta\,\hat{\rho}\,\overline{w}}{\mathrm{M}^2\,\gamma\,h_3}
$$

$$
-\frac{\mathrm{i}\,\mathrm{Ec}\,\hat{T}\,\beta\,\overline{\rho}\,\overline{w}}{\mathrm{M}^2\,\gamma\,h_3}+\frac{\mathrm{i}\,\hat{T}\,\beta\,\overline{\rho}\,\overline{w}}{h_3}-\frac{4\,\mathrm{Ec}\,\Omega_{\mathrm{Re}}\,\overline{\mu}\,\overline{v}_y\,\hat{v}_y}{\mathrm{Re}}-\frac{2\,\mathrm{Ec}\,\Omega_{\mathrm{Re}}\,\overline{\lambda}_v\,\overline{v}_y\,\hat{v}_y}{\mathrm{Re}}
$$

$$
-\frac{2\,\mathrm{Ec}\,\Omega_{\mathrm{Re}}\,h_{3,y}\,\overline{\lambda}_v\,\overline{v}\,\hat{v}_y}{\mathrm{Re}\,h_3}-\frac{2\,\mathrm{Ec}\,\Omega_{\mathrm{Re}}\,h_{1,y}\,\overline{\lambda}_v\,\overline{v}\,\hat{v}_y}{\mathrm{Re}\,h_1}-\frac{2\,\mathrm{Ec}\,\Omega_{\mathrm{Re}}\,\overline{\lambda}_v\,\overline{u}_s\,\hat{v}_y}{\mathrm{Re}\,h_1}-\frac{2\,\mathrm{Ec}\,\Omega_{\mathrm{Re}}\,h_{3,s}\,\overline{\lambda}_v\,\overline{u}\,\hat{v}_y}{\mathrm{Re}\,h_1\,h_3}
$$

$$
-\frac{2\,\mathrm{Ec}\,\Omega_{\mathrm{Re}}\,\overline{\mu}\,\overline{u}_y\,\hat{v}_s}{\mathrm{Re}\,h_1}+\frac{2\,\mathrm{Ec}\,\Omega_{\mathrm{Re}}\,h_{1,y}\,\overline{\mu}\,\overline{u}\,\hat{v}_s}{\mathrm{Re}\,h_1^2}-\frac{2\,\mathrm{Ec}\,\Omega_{\mathrm{Re}}\,h_{3,y}\,\overline{\lambda}_v\,\overline{v}_y\,\hat{v}}{\mathrm{Re}\,h_3}-\frac{2\,\mathrm{Ec}\,\Omega_{\mathrm{Re}}\,h_{1,y}\,\overline{\lambda}_v\,\overline{v}_y\,\hat{v}}{\mathrm{Re}\,h_1}
$$

$$
-\frac{4\,\mathrm{Ec}\,\Omega_{\mathrm{Re}}\,\left(h_{3,y}\right)^2\,\overline{\mu}\,\overline{v}\,\hat{v}}{\mathrm{Re}\,h_3^2}-\frac{4\,\mathrm{Ec}\,\Omega_{\mathrm{Re}}\,\left(h_{1,y}\right)^2\,\overline{\mu}\,\overline{v}\,\hat{v}}{\mathrm{Re}\,h_1^2}-\frac{2\,\mathrm{Ec}\,\Omega_{\mathrm{Re}}\,\left(h_{3,y}\right)^2\,\overline{\lambda}_v\,\overline{v}\,\hat{v}}{\mathrm{Re}\,h_3^2}
$$

$$
-\frac{4\,\mathrm{Ec}\,\Omega_{\mathrm{Re}}\,h_{1,y}\,h_{3,y}\,\overline{\lambda}_v\,\overline{v}\,\hat{v}}{\mathrm{Re}\,h_1\,h_3}-\frac{2\,\mathrm{Ec}\,\Omega_{\mathrm{Re}}\,\left(h_{1,y}\right)^2\,\overline{\lambda}_v\,\overline{v}\,\hat{v}}{\mathrm{Re}\,h_1^2}-\frac{2\,\mathrm{i}\,\mathrm{Ec}\,\alpha\,\overline{\mu}\,\overline{u}_y\,\hat{v}}{\mathrm{Re}\,h_1}
$$

$$
-\frac{4\,\mathrm{Ec}\,\Omega_{\mathrm{Re}}\,h_{1,y}\,\overline{\mu}\,\overline{u}_s\,\hat{v}}{\mathrm{Re}\,h_1^2}-\frac{2\,\mathrm{Ec}\,\Omega_{\mathrm{Re}}\,h_{3,y}\,\overline{\lambda}_v\,\overline{u}_s\,\hat{v}}{\mathrm{Re}\,h_1\,h_3}-\frac{2\,\mathrm{Ec}\,\Omega_{\mathrm{Re}}\,h_{1,y}\,\overline{\lambda}_v\,\overline{u}_s\,\hat{v}}{\mathrm{Re}\,h_1^2}
$$

$$
-\frac{4\,\mathrm{Ec}\,\Omega_{\mathrm{Re}}\,h_{3,s}\,h_{3,y}\,\overline{\mu}\,\overline{u}\,\hat{v}}{\mathrm{Re}\,h_1\,h_3^2}+\frac{2\,\mathrm{i}\,\mathrm{Ec}\,\alpha\,h_{1,y}\,\overline{\mu}\,\overline{u}\,\hat{v}}{\mathrm{Re}\,h_1^2}-\frac{2\,\mathrm{Ec}\,\Omega_{\mathrm{Re}}\,h_{3,s}\,h_{3,y}\,\overline{\lambda}_v\,\overline{u}\,\hat{v}}{\mathrm{Re}\,h_1\,h_3^2}
$$

$$
-\frac{2\,\mathrm{Ec}\,\Omega_{\mathrm{Re}}\,h_{1,y}\,h_{3,s}\,\overline{\lambda}_v\,\overline{u}\,\hat{v}}{\mathrm{Re}\,h_1^2\,h_3}-\frac{\mathrm{Ec}\,\overline{T}\,\overline{\rho}_y\,\hat{v}}{\mathrm{M}^2\,\gamma}-\frac{\mathrm{Ec}\,\overline{T}_y\,\overline{\rho}\,\hat{v}}{\mathrm{M}^2\,\gamma}+\overline{T}_y\,\overline{\rho}\,\hat{v}
$$

$$
-\frac{2\,\mathrm{i}\,\mathrm{Ec}\,\Omega_{\mathrm{Re}}\,\alpha\,\overline{\lambda}_v\,\hat{u}\,\overline{v}_y}{\mathrm{Re}\,h_1}-\frac{4\,\mathrm{i}\,\mathrm{Ec}\,\Omega_{\mathrm{Re}}\,\alpha\,h_{1,y}\,\overline{\mu}\,\hat{u}\,\overline{v}}{\mathrm{Re}\,h_1^2}-\frac{2\,\mathrm{i}\,\mathrm{Ec}\,\Omega_{\mathrm{Re}}\,\alpha\,h_{3,y}\,\overline{\lambda}_v\,\hat{u}\,\overline{v}}{\mathrm{Re}\,h_1\,h_3}
$$

$$
-\frac{2\,\mathrm{i}\,\mathrm{Ec}\,\Omega_{\mathrm{Re}}\,\alpha\,h_{1,y}\,\overline{\lambda}_v\,\hat{u}\,\overline{v}}{\mathrm{Re}\,h_1^2}-\frac{\mathrm{Ec}\,\overline{T}\,\hat{\rho}_y\,\overline{v}}{\mathrm{M}^2\,\gamma}-\frac{\mathrm{Ec}\,\overline{T}_y\,\hat{\rho}\,\overline{v}}{\mathrm{M}^2\,\gamma}+\overline{T}_y\,\hat{\rho}\,\overline{v}-\frac{\mathrm{Ec}\,\hat{T}\,\overline{\rho}_y\,\overline{v}}{\mathrm{M}^2\,\gamma}
$$

$$
-\frac{\mathrm{Ec}\,\hat{T}_y\,\overline{\rho}\,\overline{v}}{\mathrm{M}^2\,\gamma}+\hat{T}_y\,\overline{\rho}\,\overline{v}-\frac{2\,\mathrm{Ec}\,\overline{\mu}\,\overline{u}_y\,\hat{u}_y}{\mathrm{Re}}+\frac{2\,\mathrm{Ec}\,h_{1,y}\,\overline{\mu}\,\overline{u}\,\hat{u}_y}{\mathrm{Re}\,h_1}+\frac{2\,\mathrm{Ec}\,h_{1,y}\,\overline{\mu}\,\overline{u}_y\,\hat{u}}{\mathrm{Re}\,h_1}
$$

$$-\frac{4\,\mathrm{i}\,\mathrm{Ec}\,\Omega_{\mathrm{Re}}\,\alpha\,\overline{\mu}\,\overline{u}_s\,\hat{u}}{\mathrm{Re}\,h_1^2}-\frac{2\,\mathrm{i}\,\mathrm{Ec}\,\Omega_{\mathrm{Re}}\,\alpha\,\overline{\lambda}_v\,\overline{u}_s\,\hat{u}}{\mathrm{Re}\,h_1^2}-\frac{2\,\mathrm{Ec}\,\left(h_{1,y}\right)^2\,\overline{\mu}\,\overline{u}\,\hat{u}}{\mathrm{Re}\,h_1^2}-\frac{2\,\mathrm{i}\,\mathrm{Ec}\,\Omega_{\mathrm{Re}}\,\alpha\,h_{3,s}\,\overline{\lambda}_v\,\overline{u}\,\hat{u}}{\mathrm{Re}\,h_1^2\,h_3}$$
$$-\frac{\mathrm{Ec}\,\overline{T}\,\overline{\rho}_s\,\hat{u}}{\mathrm{M}^2\,\gamma\,h_1}-\frac{\mathrm{Ec}\,\overline{T}_s\,\overline{\rho}\,\hat{u}}{\mathrm{M}^2\,\gamma\,h_1}+\frac{\overline{T}_s\,\overline{\rho}\,\hat{u}}{h_1}-\frac{\mathrm{Ec}\,\hat{T}\,\overline{\mu}_{\overline{T}}\,\left(\overline{u}_y\right)^2}{\mathrm{Re}}+\frac{2\,\mathrm{Ec}\,\hat{T}\,h_{1,y}\,\overline{\mu}_{\overline{T}}\,\overline{u}\,\overline{u}_y}{\mathrm{Re}\,h_1}$$
$$-\frac{\mathrm{Ec}\,\hat{T}\,\left(h_{1,y}\right)^2\,\overline{\mu}_{\overline{T}}\,\overline{u}^2}{\mathrm{Re}\,h_1^2}-\frac{\mathrm{Ec}\,\Omega_p\,\overline{T}\,\hat{\rho}_s\,\overline{u}}{\mathrm{M}^2\,\gamma\,h_1}-\frac{\mathrm{i}\,\mathrm{Ec}\,\overline{T}\,\alpha\,\hat{\rho}\,\overline{u}}{\mathrm{M}^2\,\gamma\,h_1}-\frac{\mathrm{Ec}\,\Omega_p\,\overline{T}_s\,\hat{\rho}\,\overline{u}}{\mathrm{M}^2\,\gamma\,h_1}+\frac{\overline{T}_s\,\hat{\rho}\,\overline{u}}{h_1}$$
$$-\frac{\mathrm{Ec}\,\Omega_p\,\hat{T}\,\overline{\rho}_s\,\overline{u}}{\mathrm{M}^2\,\gamma\,h_1}-\frac{\mathrm{i}\,\mathrm{Ec}\,\hat{T}\,\alpha\,\overline{\rho}\,\overline{u}}{\mathrm{M}^2\,\gamma\,h_1}-\frac{\mathrm{Ec}\,\Omega_p\,\hat{T}_s\,\overline{\rho}\,\overline{u}}{\mathrm{M}^2\,\gamma\,h_1}+\frac{\mathrm{i}\,\hat{T}\,\alpha\,\overline{\rho}\,\overline{u}}{h_1}+\frac{\hat{T}_s\,\overline{\rho}\,\overline{u}}{h_1}+\frac{\mathrm{i}\,\mathrm{Ec}\,\overline{T}\,\omega\,\hat{\rho}}{\mathrm{M}^2\,\gamma}$$
$$+\frac{\mathrm{i}\,\mathrm{Ec}\,\hat{T}\,\omega\,\overline{\rho}}{\mathrm{M}^2\,\gamma}-\mathrm{i}\,\hat{T}\,\omega\,\overline{\rho}-\frac{\left(\overline{T}_y\right)^2\,\hat{T}\,\overline{\kappa}_{\overline{T}\,\overline{T}}}{\mathrm{Pr}\,\mathrm{Re}}-\frac{\overline{T}_y\,\hat{T}\,h_{3,y}\,\overline{\kappa}_{\overline{T}}}{\mathrm{Pr}\,\mathrm{Re}\,h_3}-\frac{\overline{T}_y\,\hat{T}\,h_{1,y}\,\overline{\kappa}_{\overline{T}}}{\mathrm{Pr}\,\mathrm{Re}\,h_1}$$
$$-\frac{2\,\mathrm{i}\,\Omega_{\mathrm{Re}}\,\overline{T}_s\,\hat{T}\,\alpha\,\overline{\kappa}_{\overline{T}}}{\mathrm{Pr}\,\mathrm{Re}\,h_1^2}-\frac{2\,\overline{T}_y\,\hat{T}_y\,\overline{\kappa}_{\overline{T}}}{\mathrm{Pr}\,\mathrm{Re}}-\frac{\overline{T}_{y\,y}\,\hat{T}\,\overline{\kappa}_{\overline{T}}}{\mathrm{Pr}\,\mathrm{Re}}-\frac{\hat{T}_y\,h_{3,y}\,\overline{\kappa}}{\mathrm{Pr}\,\mathrm{Re}\,h_3}-\frac{\mathrm{i}\,\Omega_{\mathrm{Re}}\,\hat{T}\,\alpha\,h_{3,s}\,\overline{\kappa}}{\mathrm{Pr}\,\mathrm{Re}\,h_1^2\,h_3}$$
$$+\frac{\hat{T}\,\beta^2\,\overline{\kappa}}{\mathrm{Pr}\,\mathrm{Re}\,h_3^2}-\frac{\hat{T}_y\,h_{1,y}\,\overline{\kappa}}{\mathrm{Pr}\,\mathrm{Re}\,h_1}+\frac{\mathrm{i}\,\Omega_{\mathrm{Re}}\,\hat{T}\,\alpha\,h_{1,s}\,\overline{\kappa}}{\mathrm{Pr}\,\mathrm{Re}\,h_1^3}-\frac{\mathrm{i}\,\Omega_{\mathrm{Re}}\,\hat{T}\,\alpha_s\,\overline{\kappa}}{\mathrm{Pr}\,\mathrm{Re}\,h_1^2}+\frac{\hat{T}\,\alpha^2\,\overline{\kappa}}{\mathrm{Pr}\,\mathrm{Re}\,h_1^2}$$
$$-\frac{2\,\mathrm{i}\,\Omega_{\mathrm{Re}}\,\hat{T}_s\,\alpha\,\overline{\kappa}}{\mathrm{Pr}\,\mathrm{Re}\,h_1^2}-\frac{\hat{T}_{y\,y}\,\overline{\kappa}}{\mathrm{Pr}\,\mathrm{Re}}=0$$

A.5 Mass continuity

$$\frac{\mathrm{i}\,\beta\,\overline{\rho}\,\hat{w}}{h_3}+\frac{\mathrm{i}\,\beta\,\hat{\rho}\,\overline{w}}{h_3}+\overline{\rho}\,\hat{v}_y+\overline{\rho}_y\,\hat{v}+\frac{h_{3,y}\,\overline{\rho}\,\hat{v}}{h_3}+\frac{h_{1,y}\,\overline{\rho}\,\hat{v}}{h_1}+\hat{\rho}\,\overline{v}_y$$
$$+\hat{\rho}_y\,\overline{v}+\frac{h_{3,y}\,\hat{\rho}\,\overline{v}}{h_3}+\frac{h_{1,y}\,\hat{\rho}\,\overline{v}}{h_1}+\frac{\overline{\rho}\,\hat{u}_s}{h_1}+\frac{\overline{\rho}_s\,\hat{u}}{h_1}+\frac{h_{3,s}\,\overline{\rho}\,\hat{u}}{h_1\,h_3}+\frac{\mathrm{i}\,\alpha\,\overline{\rho}\,\hat{u}}{h_1}$$
$$+\frac{\hat{\rho}\,\overline{u}_s}{h_1}+\frac{\hat{\rho}_s\,\overline{u}}{h_1}+\frac{h_{3,s}\,\hat{\rho}\,\overline{u}}{h_1\,h_3}+\frac{\mathrm{i}\,\alpha\,\hat{\rho}\,\overline{u}}{h_1}-\mathrm{i}\,\omega\,\hat{\rho}=0$$

APPENDIX B

NPSE FORCING VECTOR

The forcing vector for the Nonlinear Parabolized Stability Equations (NPSE) are presented for a calorically perfect gas in an orthogonal, curvilinear coordinate system. These are derived from the governing, instantaneous equations of Eqs. (2.14), building off of the same notation and detail in the previous appendix A. There are additional notes to be made for NPSE for this forcing vector. Presently in EPIC, the forcing vector $f_{(n,k)}$ is expressed directly in the spectral domain. For a compressible, calorically perfect gas with the state vector $q = [u, v, w, T, \rho]$, there are both quadratic $f^{\text{quad}}_{(n,k)}$ and cubic $f^{\text{cubic}}_{(n,k)}$ nonlinear terms present. $f_{(n,k)}$ may be written then as

$$\begin{aligned} f_{(n,k)} &= f^{\text{quad}}_{(n,k)} + f^{\text{cubic}}_{(n,k)}, \\ &= \underbrace{\sum_{m_1} \sum_{m_2}}_{\substack{n=n_1+n_2 \\ k=k_1+k_2}} F^{\text{quad}}_{(m_1,m_2)} + \underbrace{\sum_{m_1} \sum_{m_2} \sum_{m_3}}_{\substack{n=n_1+n_2+n_3 \\ k=k_1+k_2+k_3}} F^{\text{cubic}}_{(m_1,m_2,m_3)} \end{aligned} \tag{B.1}$$

where the integers m_1, m_2, and m_3 are indices over the disturbances in the NPSE simulation. The m_1-indexed disturbance corresponds to the integer tuple (n_1, k_1), and likewise for higher m_i, $i \in [2, 3]$. The expressions for the summands $F^{\text{quad}}_{(m_1,m_2)}$ and $F^{\text{cubic}}_{(m_1,m_2,m_3)}$ are to follow. To clarify this above equation, recall from §4.3.1.3 that only tuples of disturbances force another disturbance provided the wavenumbers and frequencies add up through these second- and third-order rules. Let us expand on the example demonstrated previously in that section. If $N = 1$ and $K = 1$ in the

NPSE ansatz, then the second-order tuples that force the $(1,1)$ are enumerated as

$$\begin{aligned}(1,1) &= (0,1) + (1,0),\\ &= (1,0) + (0,1),\\ &= (0,0) + (1,1),\\ &= \underbrace{(1,1)}_{m_1} + \underbrace{(0,0)}_{m_2}\end{aligned} \tag{B.2}$$

There is an important property here, that the tuples always appear a second time with their order permuted. A similar relationship holds for the cubic terms: all permutations of the list of third-order tuples satisfy harmonic balancing, because addition over integers is commutative.

Lastly, the summand $F^{\text{quad}}_{(m_1,m_2)}$ contains the product of integrated amplitudes $\mathcal{W}_{(n_1,k_1)}\mathcal{W}_{(n_2,k_2)}$ on each constitutive term. This may be factored out for readability as well as a reduction of FLOPS computationally. The same pattern holds for the cubic summand $F^{\text{cubic}}_{(m_1,m_2,m_3)}$. These products can be abbreviated as $\mathcal{W}^{(m_1)}\mathcal{W}^{(m_2)}$ and $\mathcal{W}^{(m_1)}\mathcal{W}^{(m_2)}\mathcal{W}^{(m_3)}$, respectively.

Below, components in the terms will be further abbreviated such that indices of (m_i) will be reduced to (i), $i \in [1,3]$ to save horizontal space. All shape-function components and streamwise wavenumbers will be denoted to a specific disturbance index via a superscript of (i). Examples are $\hat{u}^{(1)}$ (corresponding to m_1) and $\alpha^{(2)}$ (corresponding to m_2). Integer multiples such as $k^{(1)}$ or $n^{(2)}$ are synonymous with k_1 and n_2, respectively.

B.1 Momentum conservation in the s-direction: quadratic

$$
\begin{aligned}
\frac{-F^{\mathrm{quad}}_{(m_1,m_2)}}{\mathcal{W}^{(1)}\mathcal{W}^{(2)}} = \\
&-\frac{\mathrm{i}\,\Omega_{\mathrm{Re}}\,\hat{T}^{(1)}\,\beta_0\,k^{(2)}\,\overline{\mu}_{\overline{T}}\,\hat{w}_s^{(2)}}{\mathrm{Re}\,h_1\,h_3} - \frac{\mathrm{i}\,\Omega_{\mathrm{Re}}\,\hat{T}^{(1)}\,\beta_0\,k^{(1)}\,\overline{\mu}_{\overline{T}}\,\hat{w}_s^{(2)}}{\mathrm{Re}\,h_1\,h_3} - \frac{\mathrm{i}\,\Omega_{\mathrm{Re}}\,\hat{T}^{(1)}\,\beta_0\,k^{(2)}\,\overline{\lambda}_{v\overline{T}}\,\hat{w}_s^{(2)}}{\mathrm{Re}\,h_1\,h_3} \\
&-\frac{h_{3,s}\,\overline{\rho}\,\hat{w}^{(1)}\,\hat{w}^{(2)}}{h_1\,h_3} - \frac{2\,h_{3,s}\,\hat{\rho}^{(1)}\,\overline{w}\,\hat{w}^{(2)}}{h_1\,h_3} + \frac{\mathrm{i}\,\beta_0\,k^{(1)}\,\overline{\rho}\,\hat{u}^{(1)}\,\hat{w}^{(2)}}{h_3} + \frac{3\,\mathrm{i}\,\Omega_{\mathrm{Re}}\,\hat{T}^{(1)}\,\beta_0\,h_{3,s}\,k^{(2)}\,\overline{\mu}_{\overline{T}}\,\hat{w}^{(2)}}{\mathrm{Re}\,h_1\,h_3^2} \\
&+\frac{\hat{T}^{(1)}\,\alpha^{(2)}\,\beta_0\,k^{(2)}\,\overline{\mu}_{\overline{T}}\,\hat{w}^{(2)}}{\mathrm{Re}\,h_1\,h_3} + \frac{\mathrm{i}\,\Omega_{\mathrm{Re}}\,\hat{T}^{(1)}\,\beta_0\,h_{3,s}\,k^{(1)}\,\overline{\mu}_{\overline{T}}\,\hat{w}^{(2)}}{\mathrm{Re}\,h_1\,h_3^2} + \frac{\hat{T}^{(1)}\,\alpha^{(2)}\,\beta_0\,k^{(1)}\,\overline{\mu}_{\overline{T}}\,\hat{w}^{(2)}}{\mathrm{Re}\,h_1\,h_3} \\
&-\frac{\mathrm{i}\,\Omega_{\mathrm{Re}}\,\overline{T}_s\,\hat{T}^{(1)}\,\beta_0\,k^{(2)}\,\overline{\lambda}_{v\overline{T}\,\overline{T}}\,\hat{w}^{(2)}}{\mathrm{Re}\,h_1\,h_3} + \frac{\mathrm{i}\,\Omega_{\mathrm{Re}}\,\hat{T}^{(1)}\,\beta_0\,h_{3,s}\,k^{(2)}\,\overline{\lambda}_{v\overline{T}}\,\hat{w}^{(2)}}{\mathrm{Re}\,h_1\,h_3^2} + \frac{\hat{T}^{(1)}\,\alpha^{(2)}\,\beta_0\,k^{(2)}\,\overline{\lambda}_{v\overline{T}}\,\hat{w}^{(2)}}{\mathrm{Re}\,h_1\,h_3} \\
&+\frac{\hat{T}^{(1)}\,\alpha^{(1)}\,\beta_0\,k^{(2)}\,\overline{\lambda}_{v\overline{T}}\,\hat{w}^{(2)}}{\mathrm{Re}\,h_1\,h_3} - \frac{\mathrm{i}\,\Omega_{\mathrm{Re}}\,\hat{T}_s^{(1)}\,\beta_0\,k^{(2)}\,\overline{\lambda}_{v\overline{T}}\,\hat{w}^{(2)}}{\mathrm{Re}\,h_1\,h_3} + \frac{\mathrm{i}\,\beta_0\,k^{(2)}\,\hat{\rho}^{(1)}\,\hat{u}^{(2)}\,\overline{w}}{h_3} \\
&-\frac{\mathrm{i}\,\hat{T}^{(1)}\,\alpha^{(2)}\,\overline{\mu}_{\overline{T}}\,\hat{v}_y^{(2)}}{\mathrm{Re}\,h_1} - \frac{\Omega_{\mathrm{Re}}\,\overline{T}_s\,\hat{T}^{(1)}\,\overline{\lambda}_{v\overline{T}\,\overline{T}}\,\hat{v}_y^{(2)}}{\mathrm{Re}\,h_1} - \frac{\mathrm{i}\,\hat{T}^{(1)}\,\alpha^{(2)}\,\overline{\lambda}_{v\overline{T}}\,\hat{v}_y^{(2)}}{\mathrm{Re}\,h_1} - \frac{\mathrm{i}\,\hat{T}^{(1)}\,\alpha^{(1)}\,\overline{\lambda}_{v\overline{T}}\,\hat{v}_y^{(2)}}{\mathrm{Re}\,h_1} \\
&-\frac{\Omega_{\mathrm{Re}}\,\hat{T}_s^{(1)}\,\overline{\lambda}_{v\overline{T}}\,\hat{v}_y^{(2)}}{\mathrm{Re}\,h_1} - \frac{\Omega_{\mathrm{Re}}\,\hat{T}^{(1)}\,\overline{\mu}_{\overline{T}}\,\hat{v}_{sy}^{(2)}}{\mathrm{Re}\,h_1} - \frac{\Omega_{\mathrm{Re}}\,\hat{T}^{(1)}\,\overline{\lambda}_{v\overline{T}}\,\hat{v}_{sy}^{(2)}}{\mathrm{Re}\,h_1} - \frac{\Omega_{\mathrm{Re}}\,\overline{T}_y\,\hat{T}^{(1)}\,\overline{\mu}_{\overline{T}\,\overline{T}}\,\hat{v}_s^{(2)}}{\mathrm{Re}\,h_1} \\
&-\frac{\Omega_{\mathrm{Re}}\,\hat{T}^{(1)}\,h_{3,y}\,\overline{\mu}_{\overline{T}}\,\hat{v}_s^{(2)}}{\mathrm{Re}\,h_1\,h_3} - \frac{3\,\Omega_{\mathrm{Re}}\,\hat{T}^{(1)}\,h_{1,y}\,\overline{\mu}_{\overline{T}}\,\hat{v}_s^{(2)}}{\mathrm{Re}\,h_1^2} - \frac{\Omega_{\mathrm{Re}}\,\hat{T}_y^{(1)}\,\overline{\mu}_{\overline{T}}\,\hat{v}_s^{(2)}}{\mathrm{Re}\,h_1} - \frac{\Omega_{\mathrm{Re}}\,\hat{T}^{(1)}\,h_{3,y}\,\overline{\lambda}_{v\overline{T}}\,\hat{v}_s^{(2)}}{\mathrm{Re}\,h_1\,h_3} \\
&-\frac{\Omega_{\mathrm{Re}}\,\hat{T}^{(1)}\,h_{1,y}\,\overline{\lambda}_{v\overline{T}}\,\hat{v}_s^{(2)}}{\mathrm{Re}\,h_1^2} + \overline{\rho}\,\hat{u}_y^{(1)}\,\hat{v}^{(2)} + \frac{h_{1,y}\,\overline{\rho}\,\hat{u}^{(1)}\,\hat{v}^{(2)}}{h_1} + \hat{\rho}^{(1)}\,\overline{u}_y\,\hat{v}^{(2)} + \frac{h_{1,y}\,\hat{\rho}^{(1)}\,\overline{u}\,\hat{v}^{(2)}}{h_1} \\
&-\frac{2\,\Omega_{\mathrm{Re}}\,\overline{T}_s\,\hat{T}^{(1)}\,h_{1,y}\,\overline{\mu}_{\overline{T}\,\overline{T}}\,\hat{v}^{(2)}}{\mathrm{Re}\,h_1^2} - \frac{\mathrm{i}\,\overline{T}_y\,\hat{T}^{(1)}\,\alpha^{(2)}\,\overline{\mu}_{\overline{T}\,\overline{T}}\,\hat{v}^{(2)}}{\mathrm{Re}\,h_1} + \frac{2\,\Omega_{\mathrm{Re}}\,\hat{T}^{(1)}\,h_{3,s}\,h_{3,y}\,\overline{\mu}_{\overline{T}}\,\hat{v}^{(2)}}{\mathrm{Re}\,h_1\,h_3^2} \\
&-\frac{\mathrm{i}\,\hat{T}^{(1)}\,\alpha^{(2)}\,h_{3,y}\,\overline{\mu}_{\overline{T}}\,\hat{v}^{(2)}}{\mathrm{Re}\,h_1\,h_3} - \frac{2\,\Omega_{\mathrm{Re}}\,\hat{T}^{(1)}\,h_{1,y}\,h_{3,s}\,\overline{\mu}_{\overline{T}}\,\hat{v}^{(2)}}{\mathrm{Re}\,h_1^2\,h_3} + \frac{2\,\Omega_{\mathrm{Re}}\,\hat{T}^{(1)}\,h_{1,s}\,h_{1,y}\,\overline{\mu}_{\overline{T}}\,\hat{v}^{(2)}}{\mathrm{Re}\,h_1^3} \\
&-\frac{3\,\mathrm{i}\,\hat{T}^{(1)}\,\alpha^{(2)}\,h_{1,y}\,\overline{\mu}_{\overline{T}}\,\hat{v}^{(2)}}{\mathrm{Re}\,h_1^2} - \frac{2\,\mathrm{i}\,\hat{T}^{(1)}\,\alpha^{(1)}\,h_{1,y}\,\overline{\mu}_{\overline{T}}\,\hat{v}^{(2)}}{\mathrm{Re}\,h_1^2} - \frac{2\,\Omega_{\mathrm{Re}}\,\hat{T}_s^{(1)}\,h_{1,y}\,\overline{\mu}_{\overline{T}}\,\hat{v}^{(2)}}{\mathrm{Re}\,h_1^2} \\
&-\frac{2\,\Omega_{\mathrm{Re}}\,\hat{T}^{(1)}\,h_{1,s\,y}\,\overline{\mu}_{\overline{T}}\,\hat{v}^{(2)}}{\mathrm{Re}\,h_1^2} - \frac{\mathrm{i}\,\hat{T}_y^{(1)}\,\alpha^{(2)}\,\overline{\mu}_{\overline{T}}\,\hat{v}^{(2)}}{\mathrm{Re}\,h_1} - \frac{\Omega_{\mathrm{Re}}\,\overline{T}_s\,\hat{T}^{(1)}\,h_{3,y}\,\overline{\lambda}_{v\overline{T}\,\overline{T}}\,\hat{v}^{(2)}}{\mathrm{Re}\,h_1\,h_3} \\
&-\frac{\Omega_{\mathrm{Re}}\,\overline{T}_s\,\hat{T}^{(1)}\,h_{1,y}\,\overline{\lambda}_{v\overline{T}\,\overline{T}}\,\hat{v}^{(2)}}{\mathrm{Re}\,h_1^2} + \frac{\Omega_{\mathrm{Re}}\,\hat{T}^{(1)}\,h_{3,s}\,h_{3,y}\,\overline{\lambda}_{v\overline{T}}\,\hat{v}^{(2)}}{\mathrm{Re}\,h_1\,h_3^2} - \frac{\mathrm{i}\,\hat{T}^{(1)}\,\alpha^{(2)}\,h_{3,y}\,\overline{\lambda}_{v\overline{T}}\,\hat{v}^{(2)}}{\mathrm{Re}\,h_1\,h_3} \\
&-\frac{\mathrm{i}\,\hat{T}^{(1)}\,\alpha^{(1)}\,h_{3,y}\,\overline{\lambda}_{v\overline{T}}\,\hat{v}^{(2)}}{\mathrm{Re}\,h_1\,h_3} - \frac{\Omega_{\mathrm{Re}}\,\hat{T}_s^{(1)}\,h_{3,y}\,\overline{\lambda}_{v\overline{T}}\,\hat{v}^{(2)}}{\mathrm{Re}\,h_1\,h_3} - \frac{\Omega_{\mathrm{Re}}\,\hat{T}^{(1)}\,h_{3,s\,y}\,\overline{\lambda}_{v\overline{T}}\,\hat{v}^{(2)}}{\mathrm{Re}\,h_1\,h_3} \\
&+\frac{\Omega_{\mathrm{Re}}\,\hat{T}^{(1)}\,h_{1,s}\,h_{1,y}\,\overline{\lambda}_{v\overline{T}}\,\hat{v}^{(2)}}{\mathrm{Re}\,h_1^3} - \frac{\mathrm{i}\,\hat{T}^{(1)}\,\alpha^{(2)}\,h_{1,y}\,\overline{\lambda}_{v\overline{T}}\,\hat{v}^{(2)}}{\mathrm{Re}\,h_1^2} - \frac{\mathrm{i}\,\hat{T}^{(1)}\,\alpha^{(1)}\,h_{1,y}\,\overline{\lambda}_{v\overline{T}}\,\hat{v}^{(2)}}{\mathrm{Re}\,h_1^2}
\end{aligned}
$$

$$-\frac{\Omega_{\mathrm{Re}}\,\hat{T}_s^{(1)}\,h_{1,y}\,\overline{\lambda}_{v\overline{T}}\,\hat{v}^{(2)}}{\mathrm{Re}\,h_1^2}-\frac{\Omega_{\mathrm{Re}}\,\hat{T}^{(1)}\,h_{1,s\,y}\,\overline{\lambda}_{v\overline{T}}\,\hat{v}^{(2)}}{\mathrm{Re}\,h_1^2}+\hat{\rho}^{(1)}\,\hat{u}_y^{(2)}\,\overline{v}+\frac{h_{1,y}\,\hat{\rho}^{(1)}\,\hat{u}^{(2)}\,\overline{v}}{h_1}$$
$$-\frac{\hat{T}^{(1)}\,\overline{\mu}_{\overline{T}}\,\hat{u}_{y\,y}^{(2)}}{\mathrm{Re}}-\frac{\overline{T}_y\,\hat{T}^{(1)}\,\overline{\mu}_{\overline{T}\,\overline{T}}\,\hat{u}_y^{(2)}}{\mathrm{Re}}-\frac{\hat{T}^{(1)}\,h_{3,y}\,\overline{\mu}_{\overline{T}}\,\hat{u}_y^{(2)}}{\mathrm{Re}\,h_3}-\frac{\hat{T}^{(1)}\,h_{1,y}\,\overline{\mu}_{\overline{T}}\,\hat{u}_y^{(2)}}{\mathrm{Re}\,h_1}$$
$$-\frac{\hat{T}_y^{(1)}\,\overline{\mu}_{\overline{T}}\,\hat{u}_y^{(2)}}{\mathrm{Re}}+\frac{\overline{\rho}\,\hat{u}^{(1)}\,\hat{u}_s^{(2)}}{h_1}+\frac{\hat{\rho}^{(1)}\,\overline{u}\,\hat{u}_s^{(2)}}{h_1}-\frac{4\,\mathrm{i}\,\Omega_{\mathrm{Re}}\,\hat{T}^{(1)}\,\alpha^{(2)}\,\overline{\mu}_{\overline{T}}\,\hat{u}_s^{(2)}}{\mathrm{Re}\,h_1^2}$$
$$-\frac{2\,\mathrm{i}\,\Omega_{\mathrm{Re}}\,\hat{T}^{(1)}\,\alpha^{(1)}\,\overline{\mu}_{\overline{T}}\,\hat{u}_s^{(2)}}{\mathrm{Re}\,h_1^2}-\frac{2\,\mathrm{i}\,\Omega_{\mathrm{Re}}\,\hat{T}^{(1)}\,\alpha^{(2)}\,\overline{\lambda}_{v\overline{T}}\,\hat{u}_s^{(2)}}{\mathrm{Re}\,h_1^2}-\frac{\mathrm{i}\,\Omega_{\mathrm{Re}}\,\hat{T}^{(1)}\,\alpha^{(1)}\,\overline{\lambda}_{v\overline{T}}\,\hat{u}_s^{(2)}}{\mathrm{Re}\,h_1^2}$$
$$+\frac{\mathrm{i}\,\alpha^{(2)}\,\overline{\rho}\,\hat{u}^{(1)}\,\hat{u}^{(2)}}{h_1}+\frac{\hat{\rho}^{(1)}\,\overline{u}_s\,\hat{u}^{(2)}}{h_1}+\frac{\mathrm{i}\,\alpha^{(2)}\,\hat{\rho}^{(1)}\,\overline{u}\,\hat{u}^{(2)}}{h_1}$$
$$-\mathrm{i}\,n^{(2)}\,\omega_0\,\hat{\rho}^{(1)}\,\hat{u}^{(2)}+\frac{\overline{T}_y\,\hat{T}^{(1)}\,h_{1,y}\,\overline{\mu}_{\overline{T}\,\overline{T}}\,\hat{u}^{(2)}}{\mathrm{Re}\,h_1}-\frac{2\,\mathrm{i}\,\Omega_{\mathrm{Re}}\,\overline{T}_s\,\hat{T}^{(1)}\,\alpha^{(2)}\,\overline{\mu}_{\overline{T}\,\overline{T}}\,\hat{u}^{(2)}}{\mathrm{Re}\,h_1^2}$$
$$+\frac{\hat{T}^{(1)}\,\left(\beta_0\,k^{(2)}\right)^2\,\overline{\mu}_{\overline{T}}\,\hat{u}^{(2)}}{\mathrm{Re}\,h_3^2}+\frac{\hat{T}^{(1)}\,{\beta_0}^2\,k^{(1)}\,k^{(2)}\,\overline{\mu}_{\overline{T}}\,\hat{u}^{(2)}}{\mathrm{Re}\,h_3^2}+\frac{\hat{T}^{(1)}\,h_{1,y}\,h_{3,y}\,\overline{\mu}_{\overline{T}}\,\hat{u}^{(2)}}{\mathrm{Re}\,h_1\,h_3}$$
$$-\frac{2\,\mathrm{i}\,\Omega_{\mathrm{Re}}\,\hat{T}^{(1)}\,\alpha^{(2)}\,h_{3,s}\,\overline{\mu}_{\overline{T}}\,\hat{u}^{(2)}}{\mathrm{Re}\,h_1^2\,h_3}+\frac{\hat{T}^{(1)}\,h_{1,y\,y}\,\overline{\mu}_{\overline{T}}\,\hat{u}^{(2)}}{\mathrm{Re}\,h_1}+\frac{\hat{T}^{(1)}\,\left(h_{1,y}\right)^2\,\overline{\mu}_{\overline{T}}\,\hat{u}^{(2)}}{\mathrm{Re}\,h_1^2}$$
$$+\frac{\hat{T}_y^{(1)}\,h_{1,y}\,\overline{\mu}_{\overline{T}}\,\hat{u}^{(2)}}{\mathrm{Re}\,h_1}+\frac{2\,\mathrm{i}\,\Omega_{\mathrm{Re}}\,\hat{T}^{(1)}\,\alpha^{(2)}\,h_{1,s}\,\overline{\mu}_{\overline{T}}\,\hat{u}^{(2)}}{\mathrm{Re}\,h_1^3}-\frac{2\,\mathrm{i}\,\Omega_{\mathrm{Re}}\,\hat{T}^{(1)}\,\alpha_s^{(2)}\,\overline{\mu}_{\overline{T}}\,\hat{u}^{(2)}}{\mathrm{Re}\,h_1^2}$$
$$+\frac{2\,\hat{T}^{(1)}\,\left(\alpha^{(2)}\right)^2\,\overline{\mu}_{\overline{T}}\,\hat{u}^{(2)}}{\mathrm{Re}\,h_1^2}+\frac{2\,\hat{T}^{(1)}\,\alpha^{(1)}\,\alpha^{(2)}\,\overline{\mu}_{\overline{T}}\,\hat{u}^{(2)}}{\mathrm{Re}\,h_1^2}-\frac{2\,\mathrm{i}\,\Omega_{\mathrm{Re}}\,\hat{T}_s^{(1)}\,\alpha^{(2)}\,\overline{\mu}_{\overline{T}}\,\hat{u}^{(2)}}{\mathrm{Re}\,h_1^2}$$
$$-\frac{\mathrm{i}\,\Omega_{\mathrm{Re}}\,\overline{T}_s\,\hat{T}^{(1)}\,\alpha^{(2)}\,\overline{\lambda}_{v\overline{T}\,\overline{T}}\,\hat{u}^{(2)}}{\mathrm{Re}\,h_1^2}-\frac{\mathrm{i}\,\Omega_{\mathrm{Re}}\,\hat{T}^{(1)}\,\alpha^{(2)}\,h_{3,s}\,\overline{\lambda}_{v\overline{T}}\,\hat{u}^{(2)}}{\mathrm{Re}\,h_1^2\,h_3}-\frac{\mathrm{i}\,\Omega_{\mathrm{Re}}\,\hat{T}^{(1)}\,\alpha^{(1)}\,h_{3,s}\,\overline{\lambda}_{v\overline{T}}\,\hat{u}^{(2)}}{\mathrm{Re}\,h_1^2\,h_3}$$
$$+\frac{\mathrm{i}\,\Omega_{\mathrm{Re}}\,\hat{T}^{(1)}\,\alpha^{(2)}\,h_{1,s}\,\overline{\lambda}_{v\overline{T}}\,\hat{u}^{(2)}}{\mathrm{Re}\,h_1^3}-\frac{\mathrm{i}\,\Omega_{\mathrm{Re}}\,\hat{T}^{(1)}\,\alpha_s^{(2)}\,\overline{\lambda}_{v\overline{T}}\,\hat{u}^{(2)}}{\mathrm{Re}\,h_1^2}+\frac{\hat{T}^{(1)}\,\left(\alpha^{(2)}\right)^2\,\overline{\lambda}_{v\overline{T}}\,\hat{u}^{(2)}}{\mathrm{Re}\,h_1^2}$$
$$+\frac{\hat{T}^{(1)}\,\alpha^{(1)}\,\alpha^{(2)}\,\overline{\lambda}_{v\overline{T}}\,\hat{u}^{(2)}}{\mathrm{Re}\,h_1^2}-\frac{\mathrm{i}\,\Omega_{\mathrm{Re}}\,\hat{T}_s^{(1)}\,\alpha^{(2)}\,\overline{\lambda}_{v\overline{T}}\,\hat{u}^{(2)}}{\mathrm{Re}\,h_1^2}+\frac{\hat{T}^{(1)}\,\hat{\rho}_s^{(2)}}{\mathrm{M}^2\,\gamma\,h_1}$$
$$+\frac{\mathrm{i}\,\hat{T}^{(1)}\,\alpha^{(2)}\,\hat{\rho}^{(2)}}{\mathrm{M}^2\,\gamma\,h_1}+\frac{\mathrm{i}\,\hat{T}^{(1)}\,\alpha^{(1)}\,\hat{\rho}^{(2)}}{\mathrm{M}^2\,\gamma\,h_1}+\frac{\hat{T}_s^{(1)}\,\hat{\rho}^{(2)}}{\mathrm{M}^2\,\gamma\,h_1}$$

B.2 Momentum conservation in the y-direction: quadratic

$$
\begin{aligned}
&\frac{-F^{\text{quad}}_{(m_1,m_2)}}{\mathcal{W}^{(1)}\mathcal{W}^{(2)}} = \\
&-\frac{\mathrm{i}\,\hat{T}^{(1)}\,\beta_0\,k^{(2)}\,\overline{\mu}_{\overline{T}}\,\hat{w}_y^{(2)}}{\mathrm{Re}\,h_3} - \frac{\mathrm{i}\,\hat{T}^{(1)}\,\beta_0\,k^{(1)}\,\overline{\mu}_{\overline{T}}\,\hat{w}_y^{(2)}}{\mathrm{Re}\,h_3} - \frac{\mathrm{i}\,\hat{T}^{(1)}\,\beta_0\,k^{(2)}\,\overline{\lambda}_{v\overline{T}}\,\hat{w}_y^{(2)}}{\mathrm{Re}\,h_3} \\
&-\frac{h_{3,y}\,\overline{\rho}\,\hat{w}^{(1)}\,\hat{w}^{(2)}}{h_3} - \frac{2\,h_{3,y}\,\hat{\rho}^{(1)}\,\overline{w}\,\hat{w}^{(2)}}{h_3} + \frac{\mathrm{i}\,\beta_0\,k^{(1)}\,\overline{\rho}\,\hat{v}^{(1)}\,\hat{w}^{(2)}}{h_3} + \frac{3\,\mathrm{i}\,\hat{T}^{(1)}\,\beta_0\,h_{3,y}\,k^{(2)}\,\overline{\mu}_{\overline{T}}\,\hat{w}^{(2)}}{\mathrm{Re}\,h_3^2} \\
&+\frac{\mathrm{i}\,\hat{T}^{(1)}\,\beta_0\,h_{3,y}\,k^{(1)}\,\overline{\mu}_{\overline{T}}\,\hat{w}^{(2)}}{\mathrm{Re}\,h_3^2} - \frac{\mathrm{i}\,\overline{T}_y\,\hat{T}^{(1)}\,\beta_0\,k^{(2)}\,\overline{\lambda}_{v\overline{T}\,\overline{T}}\,\hat{w}^{(2)}}{\mathrm{Re}\,h_3} + \frac{\mathrm{i}\,\hat{T}^{(1)}\,\beta_0\,h_{3,y}\,k^{(2)}\,\overline{\lambda}_{v\overline{T}}\,\hat{w}^{(2)}}{\mathrm{Re}\,h_3^2} \\
&-\frac{\mathrm{i}\,\hat{T}_y^{(1)}\,\beta_0\,k^{(2)}\,\overline{\lambda}_{v\overline{T}}\,\hat{w}^{(2)}}{\mathrm{Re}\,h_3} + \frac{\mathrm{i}\,\beta_0\,k^{(2)}\,\hat{\rho}^{(1)}\,\hat{v}^{(2)}\,\overline{w}}{h_3} - \frac{2\,\hat{T}^{(1)}\,\overline{\mu}_{\overline{T}}\,\hat{v}_{yy}^{(2)}}{\mathrm{Re}} - \frac{\hat{T}^{(1)}\,\overline{\lambda}_{v\overline{T}}\,\hat{v}_{yy}^{(2)}}{\mathrm{Re}} + \overline{\rho}\,\hat{v}^{(1)}\,\hat{v}_y^{(2)} \\
&+\hat{\rho}^{(1)}\,\overline{v}\,\hat{v}_y^{(2)} - \frac{2\,\overline{T}_y\,\hat{T}^{(1)}\,\overline{\mu}_{\overline{T}\,\overline{T}}\,\hat{v}_y^{(2)}}{\mathrm{Re}} - \frac{2\,\hat{T}^{(1)}\,h_{3,y}\,\overline{\mu}_{\overline{T}}\,\hat{v}_y^{(2)}}{\mathrm{Re}\,h_3} - \frac{2\,\hat{T}^{(1)}\,h_{1,y}\,\overline{\mu}_{\overline{T}}\,\hat{v}_y^{(2)}}{\mathrm{Re}\,h_1} - \frac{2\,\hat{T}_y^{(1)}\,\overline{\mu}_{\overline{T}}\,\hat{v}_y^{(2)}}{\mathrm{Re}} \\
&-\frac{\overline{T}_y\,\hat{T}^{(1)}\,\overline{\lambda}_{v\overline{T}\,\overline{T}}\,\hat{v}_y^{(2)}}{\mathrm{Re}} - \frac{\hat{T}^{(1)}\,h_{3,y}\,\overline{\lambda}_{v\overline{T}}\,\hat{v}_y^{(2)}}{\mathrm{Re}\,h_3} - \frac{\hat{T}^{(1)}\,h_{1,y}\,\overline{\lambda}_{v\overline{T}}\,\hat{v}_y^{(2)}}{\mathrm{Re}\,h_1} - \frac{\hat{T}_y^{(1)}\,\overline{\lambda}_{v\overline{T}}\,\hat{v}_y^{(2)}}{\mathrm{Re}} \\
&+\frac{\overline{\rho}\,\hat{u}^{(1)}\,\hat{v}_s^{(2)}}{h_1} + \frac{\hat{\rho}^{(1)}\,\overline{u}\,\hat{v}_s^{(2)}}{h_1} - \frac{2\,\mathrm{i}\,\Omega_{\mathrm{Re}}\,\hat{T}^{(1)}\,\alpha^{(2)}\,\overline{\mu}_{\overline{T}}\,\hat{v}_s^{(2)}}{\mathrm{Re}\,h_1^2} - \frac{\mathrm{i}\,\Omega_{\mathrm{Re}}\,\hat{T}^{(1)}\,\alpha^{(1)}\,\overline{\mu}_{\overline{T}}\,\hat{v}_s^{(2)}}{\mathrm{Re}\,h_1^2} + \hat{\rho}^{(1)}\,\overline{v}_y\,\hat{v}^{(2)} \\
&+\frac{\mathrm{i}\,\alpha^{(2)}\,\overline{\rho}\,\hat{u}^{(1)}\,\hat{v}^{(2)}}{h_1} + \frac{\mathrm{i}\,\alpha^{(2)}\,\hat{\rho}^{(1)}\,\overline{u}\,\hat{v}^{(2)}}{h_1} - \mathrm{i}\,n^{(2)}\,\omega_0\,\hat{\rho}^{(1)}\,\hat{v}^{(2)} - \frac{\mathrm{i}\,\Omega_{\mathrm{Re}}\,\overline{T}_s\,\hat{T}^{(1)}\,\alpha^{(2)}\,\overline{\mu}_{\overline{T}\,\overline{T}}\,\hat{v}^{(2)}}{\mathrm{Re}\,h_1^2} \\
&+\frac{\hat{T}^{(1)}\,\left(\beta_0\,k^{(2)}\right)^2\,\overline{\mu}_{\overline{T}}\,\hat{v}^{(2)}}{\mathrm{Re}\,h_3^2} + \frac{\hat{T}^{(1)}\,{\beta_0}^2\,k^{(1)}\,k^{(2)}\,\overline{\mu}_{\overline{T}}\,\hat{v}^{(2)}}{\mathrm{Re}\,h_3^2} + \frac{2\,\hat{T}^{(1)}\,\left(h_{3,y}\right)^2\,\overline{\mu}_{\overline{T}}\,\hat{v}^{(2)}}{\mathrm{Re}\,h_3^2} \\
&-\frac{\mathrm{i}\,\Omega_{\mathrm{Re}}\,\hat{T}^{(1)}\,\alpha^{(2)}\,h_{3,s}\,\overline{\mu}_{\overline{T}}\,\hat{v}^{(2)}}{\mathrm{Re}\,h_1^2\,h_3} + \frac{2\,\hat{T}^{(1)}\,\left(h_{1,y}\right)^2\,\overline{\mu}_{\overline{T}}\,\hat{v}^{(2)}}{\mathrm{Re}\,h_1^2} + \frac{\mathrm{i}\,\Omega_{\mathrm{Re}}\,\hat{T}^{(1)}\,\alpha^{(2)}\,h_{1,s}\,\overline{\mu}_{\overline{T}}\,\hat{v}^{(2)}}{\mathrm{Re}\,h_1^3} \\
&-\frac{\mathrm{i}\,\Omega_{\mathrm{Re}}\,\hat{T}^{(1)}\,\alpha_s^{(2)}\,\overline{\mu}_{\overline{T}}\,\hat{v}^{(2)}}{\mathrm{Re}\,h_1^2} + \frac{\hat{T}^{(1)}\,\left(\alpha^{(2)}\right)^2\,\overline{\mu}_{\overline{T}}\,\hat{v}^{(2)}}{\mathrm{Re}\,h_1^2} + \frac{\hat{T}^{(1)}\,\alpha^{(1)}\,\alpha^{(2)}\,\overline{\mu}_{\overline{T}}\,\hat{v}^{(2)}}{\mathrm{Re}\,h_1^2} \\
&-\frac{\mathrm{i}\,\Omega_{\mathrm{Re}}\,\hat{T}_s^{(1)}\,\alpha^{(2)}\,\overline{\mu}_{\overline{T}}\,\hat{v}^{(2)}}{\mathrm{Re}\,h_1^2} - \frac{\overline{T}_y\,\hat{T}^{(1)}\,h_{3,y}\,\overline{\lambda}_{v\overline{T}\,\overline{T}}\,\hat{v}^{(2)}}{\mathrm{Re}\,h_3} - \frac{\overline{T}_y\,\hat{T}^{(1)}\,h_{1,y}\,\overline{\lambda}_{v\overline{T}\,\overline{T}}\,\hat{v}^{(2)}}{\mathrm{Re}\,h_1} \\
&-\frac{\hat{T}^{(1)}\,h_{3,y\,y}\,\overline{\lambda}_{v\overline{T}}\,\hat{v}^{(2)}}{\mathrm{Re}\,h_3} + \frac{\hat{T}^{(1)}\,\left(h_{3,y}\right)^2\,\overline{\lambda}_{v\overline{T}}\,\hat{v}^{(2)}}{\mathrm{Re}\,h_3^2} - \frac{\hat{T}_y^{(1)}\,h_{3,y}\,\overline{\lambda}_{v\overline{T}}\,\hat{v}^{(2)}}{\mathrm{Re}\,h_3} \\
&-\frac{\hat{T}^{(1)}\,h_{1,y\,y}\,\overline{\lambda}_{v\overline{T}}\,\hat{v}^{(2)}}{\mathrm{Re}\,h_1} + \frac{\hat{T}^{(1)}\,\left(h_{1,y}\right)^2\,\overline{\lambda}_{v\overline{T}}\,\hat{v}^{(2)}}{\mathrm{Re}\,h_1^2} - \frac{\hat{T}_y^{(1)}\,h_{1,y}\,\overline{\lambda}_{v\overline{T}}\,\hat{v}^{(2)}}{\mathrm{Re}\,h_1} \\
&-\frac{\Omega_{\mathrm{Re}}\,\overline{T}_s\,\hat{T}^{(1)}\,\overline{\mu}_{\overline{T}\,\overline{T}}\,\hat{u}_y^{(2)}}{\mathrm{Re}\,h_1} - \frac{\Omega_{\mathrm{Re}}\,\hat{T}^{(1)}\,h_{3,s}\,\overline{\mu}_{\overline{T}}\,\hat{u}_y^{(2)}}{\mathrm{Re}\,h_1\,h_3} - \frac{\mathrm{i}\,\hat{T}^{(1)}\,\alpha^{(2)}\,\overline{\mu}_{\overline{T}}\,\hat{u}_y^{(2)}}{\mathrm{Re}\,h_1} - \frac{\mathrm{i}\,\hat{T}^{(1)}\,\alpha^{(1)}\,\overline{\mu}_{\overline{T}}\,\hat{u}_y^{(2)}}{\mathrm{Re}\,h_1}
\end{aligned}
$$

$$
\begin{aligned}
&-\frac{\Omega_{\mathrm{Re}}\,\hat{T}_s^{(1)}\,\overline{\mu}_{\overline{T}}\,\hat{u}_y^{(2)}}{\mathrm{Re}\,h_1}-\frac{\Omega_{\mathrm{Re}}\,\hat{T}^{(1)}\,h_{3,s}\,\overline{\lambda}_{v\overline{T}}\,\hat{u}_y^{(2)}}{\mathrm{Re}\,h_1\,h_3}-\frac{\mathrm{i}\,\hat{T}^{(1)}\,\alpha^{(2)}\,\overline{\lambda}_{v\overline{T}}\,\hat{u}_y^{(2)}}{\mathrm{Re}\,h_1}-\frac{\Omega_{\mathrm{Re}}\,\hat{T}^{(1)}\,\overline{\mu}_{\overline{T}}\,\hat{u}_{s\,y}^{(2)}}{\mathrm{Re}\,h_1}\\
&-\frac{\Omega_{\mathrm{Re}}\,\hat{T}^{(1)}\,\overline{\lambda}_{v\overline{T}}\,\hat{u}_{s\,y}^{(2)}}{\mathrm{Re}\,h_1}+\frac{3\,\Omega_{\mathrm{Re}}\,\hat{T}^{(1)}\,h_{1,y}\,\overline{\mu}_{\overline{T}}\,\hat{u}_s^{(2)}}{\mathrm{Re}\,h_1^2}-\frac{\Omega_{\mathrm{Re}}\,\overline{T}_y\,\hat{T}^{(1)}\,\overline{\lambda}_{v\overline{T}\,\overline{T}}\,\hat{u}_s^{(2)}}{\mathrm{Re}\,h_1}+\frac{\Omega_{\mathrm{Re}}\,\hat{T}^{(1)}\,h_{1,y}\,\overline{\lambda}_{v\overline{T}}\,\hat{u}_s^{(2)}}{\mathrm{Re}\,h_1^2}\\
&-\frac{\Omega_{\mathrm{Re}}\,\hat{T}_y^{(1)}\,\overline{\lambda}_{v\overline{T}}\,\hat{u}_s^{(2)}}{\mathrm{Re}\,h_1}-\frac{h_{1,y}\,\overline{\rho}\,\hat{u}^{(1)}\,\hat{u}^{(2)}}{h_1}-\frac{2\,h_{1,y}\,\hat{\rho}^{(1)}\,\overline{u}\,\hat{u}^{(2)}}{h_1}+\frac{\Omega_{\mathrm{Re}}\,\overline{T}_s\,\hat{T}^{(1)}\,h_{1,y}\,\overline{\mu}_{\overline{T}\,\overline{T}}\,\hat{u}^{(2)}}{\mathrm{Re}\,h_1^2}\\
&+\frac{2\,\Omega_{\mathrm{Re}}\,\hat{T}^{(1)}\,h_{3,s}\,h_{3,y}\,\overline{\mu}_{\overline{T}}\,\hat{u}^{(2)}}{\mathrm{Re}\,h_1\,h_3^2}+\frac{\Omega_{\mathrm{Re}}\,\hat{T}^{(1)}\,h_{1,y}\,h_{3,s}\,\overline{\mu}_{\overline{T}}\,\hat{u}^{(2)}}{\mathrm{Re}\,h_1^2\,h_3}-\frac{\Omega_{\mathrm{Re}}\,\hat{T}^{(1)}\,h_{1,s}\,h_{1,y}\,\overline{\mu}_{\overline{T}}\,\hat{u}^{(2)}}{\mathrm{Re}\,h_1^3}\\
&+\frac{3\,\mathrm{i}\,\hat{T}^{(1)}\,\alpha^{(2)}\,h_{1,y}\,\overline{\mu}_{\overline{T}}\,\hat{u}^{(2)}}{\mathrm{Re}\,h_1^2}+\frac{\mathrm{i}\,\hat{T}^{(1)}\,\alpha^{(1)}\,h_{1,y}\,\overline{\mu}_{\overline{T}}\,\hat{u}^{(2)}}{\mathrm{Re}\,h_1^2}+\frac{\Omega_{\mathrm{Re}}\,\hat{T}_s^{(1)}\,h_{1,y}\,\overline{\mu}_{\overline{T}}\,\hat{u}^{(2)}}{\mathrm{Re}\,h_1^2}\\
&+\frac{\Omega_{\mathrm{Re}}\,\hat{T}^{(1)}\,h_{1,s\,y}\,\overline{\mu}_{\overline{T}}\,\hat{u}^{(2)}}{\mathrm{Re}\,h_1^2}-\frac{\Omega_{\mathrm{Re}}\,\overline{T}_y\,\hat{T}^{(1)}\,h_{3,s}\,\overline{\lambda}_{v\overline{T}\,\overline{T}}\,\hat{u}^{(2)}}{\mathrm{Re}\,h_1\,h_3}-\frac{\mathrm{i}\,\overline{T}_y\,\hat{T}^{(1)}\,\alpha^{(2)}\,\overline{\lambda}_{v\overline{T}\,\overline{T}}\,\hat{u}^{(2)}}{\mathrm{Re}\,h_1}\\
&+\frac{\Omega_{\mathrm{Re}}\,\hat{T}^{(1)}\,h_{3,s}\,h_{3,y}\,\overline{\lambda}_{v\overline{T}}\,\hat{u}^{(2)}}{\mathrm{Re}\,h_1\,h_3^2}-\frac{\Omega_{\mathrm{Re}}\,\hat{T}^{(1)}\,h_{3,s\,y}\,\overline{\lambda}_{v\overline{T}}\,\hat{u}^{(2)}}{\mathrm{Re}\,h_1\,h_3}+\frac{\Omega_{\mathrm{Re}}\,\hat{T}^{(1)}\,h_{1,y}\,h_{3,s}\,\overline{\lambda}_{v\overline{T}}\,\hat{u}^{(2)}}{\mathrm{Re}\,h_1^2\,h_3}\\
&-\frac{\Omega_{\mathrm{Re}}\,\hat{T}_y^{(1)}\,h_{3,s}\,\overline{\lambda}_{v\overline{T}}\,\hat{u}^{(2)}}{\mathrm{Re}\,h_1\,h_3}+\frac{\mathrm{i}\,\hat{T}^{(1)}\,\alpha^{(2)}\,h_{1,y}\,\overline{\lambda}_{v\overline{T}}\,\hat{u}^{(2)}}{\mathrm{Re}\,h_1^2}-\frac{\mathrm{i}\,\hat{T}_y^{(1)}\,\alpha^{(2)}\,\overline{\lambda}_{v\overline{T}}\,\hat{u}^{(2)}}{\mathrm{Re}\,h_1}\\
&+\frac{\hat{T}^{(1)}\,\hat{\rho}_y^{(2)}}{\mathrm{M}^2\,\gamma}+\frac{\hat{T}_y^{(1)}\,\hat{\rho}^{(2)}}{\mathrm{M}^2\,\gamma}
\end{aligned}
$$

B.3 Momentum conservation in the z-direction: quadratic

$$
\begin{aligned}
&\frac{-F^{\text{quad}}_{(m_1,m_2)}}{\mathcal{W}^{(1)}\mathcal{W}^{(2)}} = \\
&-\frac{\hat{T}^{(1)}\,\overline{\mu}_{\overline{T}}\,\hat{w}^{(2)}_{y\,y}}{\mathrm{Re}} + \overline{\rho}\,\hat{v}^{(1)}\,\hat{w}^{(2)}_{y} + \hat{\rho}^{(1)}\,\overline{v}\,\hat{w}^{(2)}_{y} - \frac{\overline{T}_{y}\,\hat{T}^{(1)}\,\overline{\mu}_{\overline{T}\,\overline{T}}\,\hat{w}^{(2)}_{y}}{\mathrm{Re}} - \frac{\hat{T}^{(1)}\,h_{3,y}\,\overline{\mu}_{\overline{T}}\,\hat{w}^{(2)}_{y}}{\mathrm{Re}\,h_3} \\
&-\frac{\hat{T}^{(1)}\,h_{1,y}\,\overline{\mu}_{\overline{T}}\,\hat{w}^{(2)}_{y}}{\mathrm{Re}\,h_1} - \frac{\hat{T}^{(1)}_{y}\,\overline{\mu}_{\overline{T}}\,\hat{w}^{(2)}_{y}}{\mathrm{Re}} + \frac{\overline{\rho}\,\hat{u}^{(1)}\,\hat{w}^{(2)}_{s}}{h_1} + \frac{\hat{\rho}^{(1)}\,\overline{u}\,\hat{w}^{(2)}_{s}}{h_1} - \frac{2\,\mathrm{i}\,\Omega_{\mathrm{Re}}\,\hat{T}^{(1)}\,\alpha^{(2)}\,\overline{\mu}_{\overline{T}}\,\hat{w}^{(2)}_{s}}{\mathrm{Re}\,h_1^2} \\
&-\frac{\mathrm{i}\,\Omega_{\mathrm{Re}}\,\hat{T}^{(1)}\,\alpha^{(1)}\,\overline{\mu}_{\overline{T}}\,\hat{w}^{(2)}_{s}}{\mathrm{Re}\,h_1^2} + \frac{\mathrm{i}\,\beta_0\,k^{(2)}\,\overline{\rho}\,\hat{w}^{(1)}\,\hat{w}^{(2)}}{h_3} + \frac{\mathrm{i}\,\beta_0\,k^{(2)}\,\hat{\rho}^{(1)}\,\overline{w}\,\hat{w}^{(2)}}{h_3} + \frac{h_{3,y}\,\overline{\rho}\,\hat{v}^{(1)}\,\hat{w}^{(2)}}{h_3} \\
&+\frac{h_{3,y}\,\hat{\rho}^{(1)}\,\overline{v}\,\hat{w}^{(2)}}{h_3} + \frac{h_{3,s}\,\overline{\rho}\,\hat{u}^{(1)}\,\hat{w}^{(2)}}{h_1\,h_3} + \frac{\mathrm{i}\,\alpha^{(2)}\,\overline{\rho}\,\hat{u}^{(1)}\,\hat{w}^{(2)}}{h_1} + \frac{h_{3,s}\,\hat{\rho}^{(1)}\,\overline{u}\,\hat{w}^{(2)}}{h_1\,h_3} \\
&+\frac{\mathrm{i}\,\alpha^{(2)}\,\hat{\rho}^{(1)}\,\overline{u}\,\hat{w}^{(2)}}{h_1} - \mathrm{i}\,n^{(2)}\,\omega_0\,\hat{\rho}^{(1)}\,\hat{w}^{(2)} + \frac{\overline{T}_{y}\,\hat{T}^{(1)}\,h_{3,y}\,\overline{\mu}_{\overline{T}\,\overline{T}}\,\hat{w}^{(2)}}{\mathrm{Re}\,h_3} - \frac{\mathrm{i}\,\Omega_{\mathrm{Re}}\,\overline{T}_{s}\,\hat{T}^{(1)}\,\alpha^{(2)}\,\overline{\mu}_{\overline{T}\,\overline{T}}\,\hat{w}^{(2)}}{\mathrm{Re}\,h_1^2} \\
&+\frac{2\,\hat{T}^{(1)}\,\left(\beta_0\,k^{(2)}\right)^2\,\overline{\mu}_{\overline{T}}\,\hat{w}^{(2)}}{\mathrm{Re}\,h_3^2} + \frac{2\,\hat{T}^{(1)}\,{\beta_0}^2\,k^{(1)}\,k^{(2)}\,\overline{\mu}_{\overline{T}}\,\hat{w}^{(2)}}{\mathrm{Re}\,h_3^2} + \frac{\hat{T}^{(1)}\,h_{3,y\,y}\,\overline{\mu}_{\overline{T}}\,\hat{w}^{(2)}}{\mathrm{Re}\,h_3} \\
&+\frac{\hat{T}^{(1)}\,\left(h_{3,y}\right)^2\,\overline{\mu}_{\overline{T}}\,\hat{w}^{(2)}}{\mathrm{Re}\,h_3^2} + \frac{\hat{T}^{(1)}\,h_{1,y}\,h_{3,y}\,\overline{\mu}_{\overline{T}}\,\hat{w}^{(2)}}{\mathrm{Re}\,h_1\,h_3} + \frac{\hat{T}^{(1)}_{y}\,h_{3,y}\,\overline{\mu}_{\overline{T}}\,\hat{w}^{(2)}}{\mathrm{Re}\,h_3} - \frac{\mathrm{i}\,\Omega_{\mathrm{Re}}\,\hat{T}^{(1)}\,\alpha^{(2)}\,h_{3,s}\,\overline{\mu}_{\overline{T}}\,\hat{w}^{(2)}}{\mathrm{Re}\,h_1^2\,h_3} \\
&+\frac{\mathrm{i}\,\Omega_{\mathrm{Re}}\,\hat{T}^{(1)}\,\alpha^{(1)}\,h_{3,s}\,\overline{\mu}_{\overline{T}}\,\hat{w}^{(2)}}{\mathrm{Re}\,h_1^2\,h_3} + \frac{\mathrm{i}\,\Omega_{\mathrm{Re}}\,\hat{T}^{(1)}\,\alpha^{(2)}\,h_{1,s}\,\overline{\mu}_{\overline{T}}\,\hat{w}^{(2)}}{\mathrm{Re}\,h_1^3} - \frac{\mathrm{i}\,\Omega_{\mathrm{Re}}\,\hat{T}^{(1)}\,\alpha^{(2)}_{s}\,\overline{\mu}_{\overline{T}}\,\hat{w}^{(2)}}{\mathrm{Re}\,h_1^2} \\
&+\frac{\hat{T}^{(1)}\,\left(\alpha^{(2)}\right)^2\,\overline{\mu}_{\overline{T}}\,\hat{w}^{(2)}}{\mathrm{Re}\,h_1^2} + \frac{\hat{T}^{(1)}\,\alpha^{(1)}\,\alpha^{(2)}\,\overline{\mu}_{\overline{T}}\,\hat{w}^{(2)}}{\mathrm{Re}\,h_1^2} - \frac{\mathrm{i}\,\Omega_{\mathrm{Re}}\,\hat{T}^{(1)}_{s}\,\alpha^{(2)}\,\overline{\mu}_{\overline{T}}\,\hat{w}^{(2)}}{\mathrm{Re}\,h_1^2} \\
&+\frac{\hat{T}^{(1)}\,\left(\beta_0\,k^{(2)}\right)^2\,\overline{\lambda}_{v\overline{T}}\,\hat{w}^{(2)}}{\mathrm{Re}\,h_3^2} + \frac{\hat{T}^{(1)}\,{\beta_0}^2\,k^{(1)}\,k^{(2)}\,\overline{\lambda}_{v\overline{T}}\,\hat{w}^{(2)}}{\mathrm{Re}\,h_3^2} + \hat{\rho}^{(1)}\,\hat{v}^{(2)}\,\overline{w}_{y} + \frac{\hat{\rho}^{(1)}\,\hat{u}^{(2)}\,\overline{w}_{s}}{h_1} \\
&+\frac{h_{3,y}\,\hat{\rho}^{(1)}\,\hat{v}^{(2)}\,\overline{w}}{h_3} + \frac{h_{3,s}\,\hat{\rho}^{(1)}\,\hat{u}^{(2)}\,\overline{w}}{h_1\,h_3} - \frac{\mathrm{i}\,\hat{T}^{(1)}\,\beta_0\,k^{(2)}\,\overline{\mu}_{\overline{T}}\,\hat{v}^{(2)}_{y}}{\mathrm{Re}\,h_3} - \frac{\mathrm{i}\,\hat{T}^{(1)}\,\beta_0\,k^{(2)}\,\overline{\lambda}_{v\overline{T}}\,\hat{v}^{(2)}_{y}}{\mathrm{Re}\,h_3} \\
&-\frac{\mathrm{i}\,\hat{T}^{(1)}\,\beta_0\,k^{(1)}\,\overline{\lambda}_{v\overline{T}}\,\hat{v}^{(2)}_{y}}{\mathrm{Re}\,h_3} - \frac{\mathrm{i}\,\overline{T}_{y}\,\hat{T}^{(1)}\,\beta_0\,k^{(2)}\,\overline{\mu}_{\overline{T}\,\overline{T}}\,\hat{v}^{(2)}}{\mathrm{Re}\,h_3} - \frac{3\,\mathrm{i}\,\hat{T}^{(1)}\,\beta_0\,h_{3,y}\,k^{(2)}\,\overline{\mu}_{\overline{T}}\,\hat{v}^{(2)}}{\mathrm{Re}\,h_3^2} \\
&-\frac{\mathrm{i}\,\hat{T}^{(1)}\,\beta_0\,h_{1,y}\,k^{(2)}\,\overline{\mu}_{\overline{T}}\,\hat{v}^{(2)}}{\mathrm{Re}\,h_1\,h_3} - \frac{\mathrm{i}\,\hat{T}^{(1)}_{y}\,\beta_0\,k^{(2)}\,\overline{\mu}_{\overline{T}}\,\hat{v}^{(2)}}{\mathrm{Re}\,h_3} - \frac{2\,\mathrm{i}\,\hat{T}^{(1)}\,\beta_0\,h_{3,y}\,k^{(1)}\,\overline{\mu}_{\overline{T}}\,\hat{v}^{(2)}}{\mathrm{Re}\,h_3^2} \\
&-\frac{\mathrm{i}\,\hat{T}^{(1)}\,\beta_0\,h_{3,y}\,k^{(2)}\,\overline{\lambda}_{v\overline{T}}\,\hat{v}^{(2)}}{\mathrm{Re}\,h_3^2} - \frac{\mathrm{i}\,\hat{T}^{(1)}\,\beta_0\,h_{1,y}\,k^{(2)}\,\overline{\lambda}_{v\overline{T}}\,\hat{v}^{(2)}}{\mathrm{Re}\,h_1\,h_3} - \frac{\mathrm{i}\,\hat{T}^{(1)}\,\beta_0\,h_{3,y}\,k^{(1)}\,\overline{\lambda}_{v\overline{T}}\,\hat{v}^{(2)}}{\mathrm{Re}\,h_3^2} \\
&-\frac{\mathrm{i}\,\hat{T}^{(1)}\,\beta_0\,h_{1,y}\,k^{(1)}\,\overline{\lambda}_{v\overline{T}}\,\hat{v}^{(2)}}{\mathrm{Re}\,h_1\,h_3} - \frac{\mathrm{i}\,\Omega_{\mathrm{Re}}\,\hat{T}^{(1)}\,\beta_0\,k^{(2)}\,\overline{\mu}_{\overline{T}}\,\hat{u}^{(2)}_{s}}{\mathrm{Re}\,h_1\,h_3} - \frac{\mathrm{i}\,\Omega_{\mathrm{Re}}\,\hat{T}^{(1)}\,\beta_0\,k^{(2)}\,\overline{\lambda}_{v\overline{T}}\,\hat{u}^{(2)}_{s}}{\mathrm{Re}\,h_1\,h_3}
\end{aligned}
$$

$$-\frac{\mathrm{i}\,\Omega_{\mathrm{Re}}\,\hat{T}^{(1)}\,\beta_0\,k^{(1)}\,\overline{\lambda}_{v\overline{T}}\,\hat{u}_s^{(2)}}{\mathrm{Re}\,h_1\,h_3}-\frac{\mathrm{i}\,\Omega_{\mathrm{Re}}\,\overline{T}_s\,\hat{T}^{(1)}\,\beta_0\,k^{(2)}\,\overline{\mu}_{\overline{T}\,\overline{T}}\,\hat{u}^{(2)}}{\mathrm{Re}\,h_1\,h_3}-\frac{3\,\mathrm{i}\,\Omega_{\mathrm{Re}}\,\hat{T}^{(1)}\,\beta_0\,h_{3,s}\,k^{(2)}\,\overline{\mu}_{\overline{T}}\,\hat{u}^{(2)}}{\mathrm{Re}\,h_1\,h_3^2}$$
$$+\frac{\hat{T}^{(1)}\,\alpha^{(2)}\,\beta_0\,k^{(2)}\,\overline{\mu}_{\overline{T}}\,\hat{u}^{(2)}}{\mathrm{Re}\,h_1\,h_3}+\frac{\hat{T}^{(1)}\,\alpha^{(1)}\,\beta_0\,k^{(2)}\,\overline{\mu}_{\overline{T}}\,\hat{u}^{(2)}}{\mathrm{Re}\,h_1\,h_3}-\frac{\mathrm{i}\,\Omega_{\mathrm{Re}}\,\hat{T}_s^{(1)}\,\beta_0\,k^{(2)}\,\overline{\mu}_{\overline{T}}\,\hat{u}^{(2)}}{\mathrm{Re}\,h_1\,h_3}$$
$$-\frac{2\,\mathrm{i}\,\Omega_{\mathrm{Re}}\,\hat{T}^{(1)}\,\beta_0\,h_{3,s}\,k^{(1)}\,\overline{\mu}_{\overline{T}}\,\hat{u}^{(2)}}{\mathrm{Re}\,h_1\,h_3^2}-\frac{\mathrm{i}\,\Omega_{\mathrm{Re}}\,\hat{T}^{(1)}\,\beta_0\,h_{3,s}\,k^{(2)}\,\overline{\lambda}_{v\overline{T}}\,\hat{u}^{(2)}}{\mathrm{Re}\,h_1\,h_3^2}$$
$$+\frac{\hat{T}^{(1)}\,\alpha^{(2)}\,\beta_0\,k^{(2)}\,\overline{\lambda}_{v\overline{T}}\,\hat{u}^{(2)}}{\mathrm{Re}\,h_1\,h_3}-\frac{\mathrm{i}\,\Omega_{\mathrm{Re}}\,\hat{T}^{(1)}\,\beta_0\,h_{3,s}\,k^{(1)}\,\overline{\lambda}_{v\overline{T}}\,\hat{u}^{(2)}}{\mathrm{Re}\,h_1\,h_3^2}+\frac{\hat{T}^{(1)}\,\alpha^{(2)}\,\beta_0\,k^{(1)}\,\overline{\lambda}_{v\overline{T}}\,\hat{u}^{(2)}}{\mathrm{Re}\,h_1\,h_3}$$
$$+\frac{\mathrm{i}\,\hat{T}^{(1)}\,\beta_0\,k^{(2)}\,\hat{\rho}^{(2)}}{\mathrm{M}^2\,\gamma\,h_3}+\frac{\mathrm{i}\,\hat{T}^{(1)}\,\beta_0\,k^{(1)}\,\hat{\rho}^{(2)}}{\mathrm{M}^2\,\gamma\,h_3}$$

B.4 Conservation of energy (enthalpy formulation): quadratic

$$
\begin{aligned}
&\frac{-F^{\mathrm{quad}}_{(m_1,m_2)}}{\mathcal{W}^{(1)}\mathcal{W}^{(2)}} = \\
&-\frac{\mathrm{Ec}\,\overline{\mu}\,\hat{w}_y^{(1)}\,\hat{w}_y^{(2)}}{\mathrm{Re}} + \frac{2\,\mathrm{Ec}\,h_{3,y}\,\overline{\mu}\,\hat{w}^{(1)}\,\hat{w}_y^{(2)}}{\mathrm{Re}\,h_3} - \frac{2\,\mathrm{Ec}\,\hat{T}^{(1)}\,\overline{\mu}_{\overline{T}}\,\overline{w}_y\,\hat{w}_y^{(2)}}{\mathrm{Re}} \\
&+\frac{2\,\mathrm{Ec}\,\hat{T}^{(1)}\,h_{3,y}\,\overline{\mu}_{\overline{T}}\,\overline{w}\,\hat{w}_y^{(2)}}{\mathrm{Re}\,h_3} - \frac{2\,\mathrm{i}\,\mathrm{Ec}\,\beta_0\,k^{(1)}\,\overline{\mu}\,\hat{v}^{(1)}\,\hat{w}_y^{(2)}}{\mathrm{Re}\,h_3} - \frac{\mathrm{i}\,\mathrm{Ec}\,\Omega_{\mathrm{Re}}\,\alpha^{(1)}\,\overline{\mu}\,\hat{w}^{(1)}\,\hat{w}_s^{(2)}}{\mathrm{Re}\,h_1^2} \\
&-\frac{2\,\mathrm{i}\,\mathrm{Ec}\,\Omega_{\mathrm{Re}}\,\beta_0\,k^{(1)}\,\overline{\mu}\,\hat{u}^{(1)}\,\hat{w}_s^{(2)}}{\mathrm{Re}\,h_1\,h_3} - \frac{\mathrm{i}\,\mathrm{Ec}\,\Omega_{\mathrm{Re}}\,\alpha^{(2)}\,\overline{\mu}\,\hat{w}_s^{(1)}\,\hat{w}^{(2)}}{\mathrm{Re}\,h_1^2} + \frac{2\,\mathrm{Ec}\,{\beta_0}^2\,k^{(1)}\,k^{(2)}\,\overline{\mu}\,\hat{w}^{(1)}\,\hat{w}^{(2)}}{\mathrm{Re}\,h_3^2} \\
&-\frac{\mathrm{Ec}\,\left(h_{3,y}\right)^2\,\overline{\mu}\,\hat{w}^{(1)}\,\hat{w}^{(2)}}{\mathrm{Re}\,h_3^2} + \frac{2\,\mathrm{i}\,\mathrm{Ec}\,\Omega_{\mathrm{Re}}\,\alpha^{(2)}\,h_{3,s}\,\overline{\mu}\,\hat{w}^{(1)}\,\hat{w}^{(2)}}{\mathrm{Re}\,h_1^2\,h_3} + \frac{\mathrm{Ec}\,\alpha^{(1)}\,\alpha^{(2)}\,\overline{\mu}\,\hat{w}^{(1)}\,\hat{w}^{(2)}}{\mathrm{Re}\,h_1^2} \\
&+\frac{\mathrm{Ec}\,{\beta_0}^2\,k^{(1)}\,k^{(2)}\,\overline{\lambda}_v\,\hat{w}^{(1)}\,\hat{w}^{(2)}}{\mathrm{Re}\,h_3^2} + \frac{2\,\mathrm{Ec}\,\hat{T}^{(1)}\,h_{3,y}\,\overline{\mu}_{\overline{T}}\,\overline{w}_y\,\hat{w}^{(2)}}{\mathrm{Re}\,h_3} - \frac{2\,\mathrm{i}\,\mathrm{Ec}\,\Omega_{\mathrm{Re}}\,\hat{T}^{(1)}\,\alpha^{(2)}\,\overline{\mu}_{\overline{T}}\,\overline{w}_s\,\hat{w}^{(2)}}{\mathrm{Re}\,h_1^2} \\
&-\frac{2\,\mathrm{Ec}\,\hat{T}^{(1)}\,\left(h_{3,y}\right)^2\,\overline{\mu}_{\overline{T}}\,\overline{w}\,\hat{w}^{(2)}}{\mathrm{Re}\,h_3^2} + \frac{2\,\mathrm{i}\,\mathrm{Ec}\,\Omega_{\mathrm{Re}}\,\hat{T}^{(1)}\,\alpha^{(2)}\,h_{3,s}\,\overline{\mu}_{\overline{T}}\,\overline{w}\,\hat{w}^{(2)}}{\mathrm{Re}\,h_1^2\,h_3} - \frac{2\,\mathrm{i}\,\mathrm{Ec}\,\beta_0\,k^{(2)}\,\overline{\lambda}_v\,\hat{v}_y^{(1)}\,\hat{w}^{(2)}}{\mathrm{Re}\,h_3} \\
&-\frac{4\,\mathrm{i}\,\mathrm{Ec}\,\beta_0\,h_{3,y}\,k^{(2)}\,\overline{\mu}\,\hat{v}^{(1)}\,\hat{w}^{(2)}}{\mathrm{Re}\,h_3^2} + \frac{2\,\mathrm{i}\,\mathrm{Ec}\,\beta_0\,h_{3,y}\,k^{(1)}\,\overline{\mu}\,\hat{v}^{(1)}\,\hat{w}^{(2)}}{\mathrm{Re}\,h_3^2} - \frac{2\,\mathrm{i}\,\mathrm{Ec}\,\beta_0\,h_{3,y}\,k^{(2)}\,\overline{\lambda}_v\,\hat{v}^{(1)}\,\hat{w}^{(2)}}{\mathrm{Re}\,h_3^2} \\
&-\frac{2\,\mathrm{i}\,\mathrm{Ec}\,\beta_0\,h_{1,y}\,k^{(2)}\,\overline{\lambda}_v\,\hat{v}^{(1)}\,\hat{w}^{(2)}}{\mathrm{Re}\,h_1\,h_3} - \frac{2\,\mathrm{i}\,\mathrm{Ec}\,\Omega_{\mathrm{Re}}\,\hat{T}^{(1)}\,\beta_0\,k^{(2)}\,\overline{\lambda}_{v\overline{T}}\,\overline{v}_y\,\hat{w}^{(2)}}{\mathrm{Re}\,h_3} \\
&-\frac{4\,\mathrm{i}\,\mathrm{Ec}\,\Omega_{\mathrm{Re}}\,\hat{T}^{(1)}\,\beta_0\,h_{3,y}\,k^{(2)}\,\overline{\mu}_{\overline{T}}\,\overline{v}\,\hat{w}^{(2)}}{\mathrm{Re}\,h_3^2} - \frac{2\,\mathrm{i}\,\mathrm{Ec}\,\Omega_{\mathrm{Re}}\,\hat{T}^{(1)}\,\beta_0\,h_{3,y}\,k^{(2)}\,\overline{\lambda}_{v\overline{T}}\,\overline{v}\,\hat{w}^{(2)}}{\mathrm{Re}\,h_3^2} \\
&-\frac{2\,\mathrm{i}\,\mathrm{Ec}\,\Omega_{\mathrm{Re}}\,\hat{T}^{(1)}\,\beta_0\,h_{1,y}\,k^{(2)}\,\overline{\lambda}_{v\overline{T}}\,\overline{v}\,\hat{w}^{(2)}}{\mathrm{Re}\,h_1\,h_3} - \frac{2\,\mathrm{i}\,\mathrm{Ec}\,\Omega_{\mathrm{Re}}\,\beta_0\,k^{(2)}\,\overline{\lambda}_v\,\hat{u}_s^{(1)}\,\hat{w}^{(2)}}{\mathrm{Re}\,h_1\,h_3} \\
&-\frac{4\,\mathrm{i}\,\mathrm{Ec}\,\Omega_{\mathrm{Re}}\,\beta_0\,h_{3,s}\,k^{(2)}\,\overline{\mu}\,\hat{u}^{(1)}\,\hat{w}^{(2)}}{\mathrm{Re}\,h_1\,h_3^2} + \frac{2\,\mathrm{i}\,\mathrm{Ec}\,\Omega_{\mathrm{Re}}\,\beta_0\,h_{3,s}\,k^{(1)}\,\overline{\mu}\,\hat{u}^{(1)}\,\hat{w}^{(2)}}{\mathrm{Re}\,h_1\,h_3^2} \\
&+\frac{2\,\mathrm{Ec}\,\alpha^{(2)}\,\beta_0\,k^{(1)}\,\overline{\mu}\,\hat{u}^{(1)}\,\hat{w}^{(2)}}{\mathrm{Re}\,h_1\,h_3} - \frac{2\,\mathrm{i}\,\mathrm{Ec}\,\Omega_{\mathrm{Re}}\,\beta_0\,h_{3,s}\,k^{(2)}\,\overline{\lambda}_v\,\hat{u}^{(1)}\,\hat{w}^{(2)}}{\mathrm{Re}\,h_1\,h_3^2} \\
&+\frac{2\,\mathrm{Ec}\,\alpha^{(1)}\,\beta_0\,k^{(2)}\,\overline{\lambda}_v\,\hat{u}^{(1)}\,\hat{w}^{(2)}}{\mathrm{Re}\,h_1\,h_3} - \frac{2\,\mathrm{i}\,\mathrm{Ec}\,\Omega_{\mathrm{Re}}\,\hat{T}^{(1)}\,\beta_0\,k^{(2)}\,\overline{\lambda}_{v\overline{T}}\,\overline{u}_s\,\hat{w}^{(2)}}{\mathrm{Re}\,h_1\,h_3} \\
&-\frac{4\,\mathrm{i}\,\mathrm{Ec}\,\Omega_{\mathrm{Re}}\,\hat{T}^{(1)}\,\beta_0\,h_{3,s}\,k^{(2)}\,\overline{\mu}_{\overline{T}}\,\overline{u}\,\hat{w}^{(2)}}{\mathrm{Re}\,h_1\,h_3^2} - \frac{2\,\mathrm{i}\,\mathrm{Ec}\,\Omega_{\mathrm{Re}}\,\hat{T}^{(1)}\,\beta_0\,h_{3,s}\,k^{(2)}\,\overline{\lambda}_{v\overline{T}}\,\overline{u}\,\hat{w}^{(2)}}{\mathrm{Re}\,h_1\,h_3^2} \\
&-\frac{\mathrm{i}\,\mathrm{Ec}\,\overline{T}\,\beta_0\,k^{(1)}\,\hat{\rho}^{(1)}\,\hat{w}^{(2)}}{\mathrm{M}^2\,\gamma\,h_3} - \frac{\mathrm{i}\,\mathrm{Ec}\,\hat{T}^{(1)}\,\beta_0\,k^{(1)}\,\overline{\rho}\,\hat{w}^{(2)}}{\mathrm{M}^2\,\gamma\,h_3} + \frac{\mathrm{i}\,\hat{T}^{(1)}\,\beta_0\,k^{(1)}\,\overline{\rho}\,\hat{w}^{(2)}}{h_3}
\end{aligned}
$$

$$-\frac{2\,\mathrm{i}\,\mathrm{Ec}\,\hat{T}^{(1)}\,\beta_0\,k^{(2)}\,\overline{\mu}_{\overline{T}}\,\hat{v}^{(2)}\,\overline{w}_y}{\mathrm{Re}\,h_3}-\frac{2\,\mathrm{i}\,\mathrm{Ec}\,\Omega_{\mathrm{Re}}\,\hat{T}^{(1)}\,\beta_0\,k^{(2)}\,\overline{\mu}_{\overline{T}}\,\hat{u}^{(2)}\,\overline{w}_s}{\mathrm{Re}\,h_1\,h_3}$$
$$+\frac{2\,\mathrm{i}\,\mathrm{Ec}\,\hat{T}^{(1)}\,\beta_0\,h_{3,y}\,k^{(2)}\,\overline{\mu}_{\overline{T}}\,\hat{v}^{(2)}\,\overline{w}}{\mathrm{Re}\,h_3^2}+\frac{2\,\mathrm{i}\,\mathrm{Ec}\,\Omega_{\mathrm{Re}}\,\hat{T}^{(1)}\,\beta_0\,h_{3,s}\,k^{(2)}\,\overline{\mu}_{\overline{T}}\,\hat{u}^{(2)}\,\overline{w}}{\mathrm{Re}\,h_1\,h_3^2}$$
$$-\frac{\mathrm{i}\,\mathrm{Ec}\,\hat{T}^{(1)}\,\beta_0\,k^{(2)}\,\hat{\rho}^{(2)}\,\overline{w}}{\mathrm{M}^2\,\gamma\,h_3}-\frac{\mathrm{i}\,\mathrm{Ec}\,\hat{T}^{(1)}\,\beta_0\,k^{(1)}\,\hat{\rho}^{(2)}\,\overline{w}}{\mathrm{M}^2\,\gamma\,h_3}+\frac{\mathrm{i}\,\hat{T}^{(1)}\,\beta_0\,k^{(1)}\,\hat{\rho}^{(2)}\,\overline{w}}{h_3}$$
$$-\frac{2\,\mathrm{Ec}\,\overline{\mu}\,\hat{v}_y^{(1)}\,\hat{v}_y^{(2)}}{\mathrm{Re}}-\frac{\mathrm{Ec}\,\overline{\lambda}_v\,\hat{v}_y^{(1)}\,\hat{v}_y^{(2)}}{\mathrm{Re}}-\frac{2\,\mathrm{Ec}\,h_{3,y}\,\overline{\lambda}_v\,\hat{v}^{(1)}\,\hat{v}_y^{(2)}}{\mathrm{Re}\,h_3}-\frac{2\,\mathrm{Ec}\,h_{1,y}\,\overline{\lambda}_v\,\hat{v}^{(1)}\,\hat{v}_y^{(2)}}{\mathrm{Re}\,h_1}$$
$$-\frac{4\,\mathrm{Ec}\,\Omega_{\mathrm{Re}}\,\hat{T}^{(1)}\,\overline{\mu}_{\overline{T}}\,\overline{v}_y\,\hat{v}_y^{(2)}}{\mathrm{Re}}-\frac{2\,\mathrm{Ec}\,\Omega_{\mathrm{Re}}\,\hat{T}^{(1)}\,\overline{\lambda}_{v\overline{T}}\,\overline{v}_y\,\hat{v}_y^{(2)}}{\mathrm{Re}}-\frac{2\,\mathrm{Ec}\,\Omega_{\mathrm{Re}}\,\hat{T}^{(1)}\,h_{3,y}\,\overline{\lambda}_{v\overline{T}}\,\overline{v}\,\hat{v}_y^{(2)}}{\mathrm{Re}\,h_3}$$
$$-\frac{2\,\mathrm{Ec}\,\Omega_{\mathrm{Re}}\,\hat{T}^{(1)}\,h_{1,y}\,\overline{\lambda}_{v\overline{T}}\,\overline{v}\,\hat{v}_y^{(2)}}{\mathrm{Re}\,h_1}-\frac{2\,\mathrm{Ec}\,\Omega_{\mathrm{Re}}\,\overline{\lambda}_v\,\hat{u}_s^{(1)}\,\hat{v}_y^{(2)}}{\mathrm{Re}\,h_1}-\frac{2\,\mathrm{Ec}\,\Omega_{\mathrm{Re}}\,h_{3,s}\,\overline{\lambda}_v\,\hat{u}^{(1)}\,\hat{v}_y^{(2)}}{\mathrm{Re}\,h_1\,h_3}$$
$$-\frac{2\,\mathrm{i}\,\mathrm{Ec}\,\alpha^{(1)}\,\overline{\lambda}_v\,\hat{u}^{(1)}\,\hat{v}_y^{(2)}}{\mathrm{Re}\,h_1}-\frac{2\,\mathrm{Ec}\,\Omega_{\mathrm{Re}}\,\hat{T}^{(1)}\,\overline{\lambda}_{v\overline{T}}\,\overline{u}_s\,\hat{v}_y^{(2)}}{\mathrm{Re}\,h_1}-\frac{2\,\mathrm{Ec}\,\Omega_{\mathrm{Re}}\,\hat{T}^{(1)}\,h_{3,s}\,\overline{\lambda}_{v\overline{T}}\,\overline{u}\,\hat{v}_y^{(2)}}{\mathrm{Re}\,h_1\,h_3}$$
$$-\frac{\mathrm{i}\,\mathrm{Ec}\,\Omega_{\mathrm{Re}}\,\alpha^{(1)}\,\overline{\mu}\,\hat{v}^{(1)}\,\hat{v}_s^{(2)}}{\mathrm{Re}\,h_1^2}-\frac{2\,\mathrm{Ec}\,\Omega_{\mathrm{Re}}\,\overline{\mu}\,\hat{u}_y^{(1)}\,\hat{v}_s^{(2)}}{\mathrm{Re}\,h_1}+\frac{2\,\mathrm{Ec}\,\Omega_{\mathrm{Re}}\,h_{1,y}\,\overline{\mu}\,\hat{u}^{(1)}\,\hat{v}_s^{(2)}}{\mathrm{Re}\,h_1^2}$$
$$-\frac{2\,\mathrm{Ec}\,\Omega_{\mathrm{Re}}\,\hat{T}^{(1)}\,\overline{\mu}_{\overline{T}}\,\overline{u}_y\,\hat{v}_s^{(2)}}{\mathrm{Re}\,h_1}+\frac{2\,\mathrm{Ec}\,\Omega_{\mathrm{Re}}\,\hat{T}^{(1)}\,h_{1,y}\,\overline{\mu}_{\overline{T}}\,\overline{u}\,\hat{v}_s^{(2)}}{\mathrm{Re}\,h_1^2}-\frac{\mathrm{i}\,\mathrm{Ec}\,\Omega_{\mathrm{Re}}\,\alpha^{(2)}\,\overline{\mu}\,\hat{v}_s^{(1)}\,\hat{v}^{(2)}}{\mathrm{Re}\,h_1^2}$$
$$+\frac{\mathrm{Ec}\,{\beta_0}^2\,k^{(1)}\,k^{(2)}\,\overline{\mu}\,\hat{v}^{(1)}\,\hat{v}^{(2)}}{\mathrm{Re}\,h_3^2}-\frac{2\,\mathrm{Ec}\,\left(h_{3,y}\right)^2\,\overline{\mu}\,\hat{v}^{(1)}\,\hat{v}^{(2)}}{\mathrm{Re}\,h_3^2}-\frac{2\,\mathrm{Ec}\,\left(h_{1,y}\right)^2\,\overline{\mu}\,\hat{v}^{(1)}\,\hat{v}^{(2)}}{\mathrm{Re}\,h_1^2}$$
$$+\frac{\mathrm{Ec}\,\alpha^{(1)}\,\alpha^{(2)}\,\overline{\mu}\,\hat{v}^{(1)}\,\hat{v}^{(2)}}{\mathrm{Re}\,h_1^2}-\frac{\mathrm{Ec}\,\left(h_{3,y}\right)^2\,\overline{\lambda}_v\,\hat{v}^{(1)}\,\hat{v}^{(2)}}{\mathrm{Re}\,h_3^2}-\frac{2\,\mathrm{Ec}\,h_{1,y}\,h_{3,y}\,\overline{\lambda}_v\,\hat{v}^{(1)}\,\hat{v}^{(2)}}{\mathrm{Re}\,h_1\,h_3}$$
$$-\frac{\mathrm{Ec}\,\left(h_{1,y}\right)^2\,\overline{\lambda}_v\,\hat{v}^{(1)}\,\hat{v}^{(2)}}{\mathrm{Re}\,h_1^2}-\frac{2\,\mathrm{Ec}\,\Omega_{\mathrm{Re}}\,\hat{T}^{(1)}\,h_{3,y}\,\overline{\lambda}_{v\overline{T}}\,\overline{v}_y\,\hat{v}^{(2)}}{\mathrm{Re}\,h_3}-\frac{2\,\mathrm{Ec}\,\Omega_{\mathrm{Re}}\,\hat{T}^{(1)}\,h_{1,y}\,\overline{\lambda}_{v\overline{T}}\,\overline{v}_y\,\hat{v}^{(2)}}{\mathrm{Re}\,h_1}$$
$$-\frac{4\,\mathrm{Ec}\,\Omega_{\mathrm{Re}}\,\hat{T}^{(1)}\,\left(h_{3,y}\right)^2\,\overline{\mu}_{\overline{T}}\,\overline{v}\,\hat{v}^{(2)}}{\mathrm{Re}\,h_3^2}-\frac{4\,\mathrm{Ec}\,\Omega_{\mathrm{Re}}\,\hat{T}^{(1)}\,\left(h_{1,y}\right)^2\,\overline{\mu}_{\overline{T}}\,\overline{v}\,\hat{v}^{(2)}}{\mathrm{Re}\,h_1^2}$$
$$-\frac{2\,\mathrm{Ec}\,\Omega_{\mathrm{Re}}\,\hat{T}^{(1)}\,\left(h_{3,y}\right)^2\,\overline{\lambda}_{v\overline{T}}\,\overline{v}\,\hat{v}^{(2)}}{\mathrm{Re}\,h_3^2}-\frac{4\,\mathrm{Ec}\,\Omega_{\mathrm{Re}}\,\hat{T}^{(1)}\,h_{1,y}\,h_{3,y}\,\overline{\lambda}_{v\overline{T}}\,\overline{v}\,\hat{v}^{(2)}}{\mathrm{Re}\,h_1\,h_3}$$
$$-\frac{2\,\mathrm{Ec}\,\Omega_{\mathrm{Re}}\,\hat{T}^{(1)}\,\left(h_{1,y}\right)^2\,\overline{\lambda}_{v\overline{T}}\,\overline{v}\,\hat{v}^{(2)}}{\mathrm{Re}\,h_1^2}-\frac{2\,\mathrm{i}\,\mathrm{Ec}\,\alpha^{(2)}\,\overline{\mu}\,\hat{u}_y^{(1)}\,\hat{v}^{(2)}}{\mathrm{Re}\,h_1}$$
$$-\frac{4\,\mathrm{Ec}\,\Omega_{\mathrm{Re}}\,h_{1,y}\,\overline{\mu}\,\hat{u}_s^{(1)}\,\hat{v}^{(2)}}{\mathrm{Re}\,h_1^2}-\frac{2\,\mathrm{Ec}\,\Omega_{\mathrm{Re}}\,h_{3,y}\,\overline{\lambda}_v\,\hat{u}_s^{(1)}\,\hat{v}^{(2)}}{\mathrm{Re}\,h_1\,h_3}-\frac{2\,\mathrm{Ec}\,\Omega_{\mathrm{Re}}\,h_{1,y}\,\overline{\lambda}_v\,\hat{u}_s^{(1)}\,\hat{v}^{(2)}}{\mathrm{Re}\,h_1^2}$$
$$-\frac{4\,\mathrm{Ec}\,\Omega_{\mathrm{Re}}\,h_{3,s}\,h_{3,y}\,\overline{\mu}\,\hat{u}^{(1)}\,\hat{v}^{(2)}}{\mathrm{Re}\,h_1\,h_3^2}+\frac{2\,\mathrm{i}\,\mathrm{Ec}\,\alpha^{(2)}\,h_{1,y}\,\overline{\mu}\,\hat{u}^{(1)}\,\hat{v}^{(2)}}{\mathrm{Re}\,h_1^2}-\frac{4\,\mathrm{i}\,\mathrm{Ec}\,\alpha^{(1)}\,h_{1,y}\,\overline{\mu}\,\hat{u}^{(1)}\,\hat{v}^{(2)}}{\mathrm{Re}\,h_1^2}$$
$$-\frac{2\,\mathrm{Ec}\,\Omega_{\mathrm{Re}}\,h_{3,s}\,h_{3,y}\,\overline{\lambda}_v\,\hat{u}^{(1)}\,\hat{v}^{(2)}}{\mathrm{Re}\,h_1\,h_3^2}-\frac{2\,\mathrm{i}\,\mathrm{Ec}\,\alpha^{(1)}\,h_{3,y}\,\overline{\lambda}_v\,\hat{u}^{(1)}\,\hat{v}^{(2)}}{\mathrm{Re}\,h_1\,h_3}-\frac{2\,\mathrm{Ec}\,\Omega_{\mathrm{Re}}\,h_{1,y}\,h_{3,s}\,\overline{\lambda}_v\,\hat{u}^{(1)}\,\hat{v}^{(2)}}{\mathrm{Re}\,h_1^2\,h_3}$$

$$-\frac{2\,\mathrm{i}\,\mathrm{Ec}\,\alpha^{(1)}\,h_{1,y}\,\overline{\lambda}_v\,\hat{u}^{(1)}\,\hat{v}^{(2)}}{\mathrm{Re}\,h_1^2}-\frac{2\,\mathrm{i}\,\mathrm{Ec}\,\hat{T}^{(1)}\,\alpha^{(2)}\,\overline{\mu}_{\overline{T}}\,\overline{u}_y\,\hat{v}^{(2)}}{\mathrm{Re}\,h_1}-\frac{4\,\mathrm{Ec}\,\Omega_{\mathrm{Re}}\,\hat{T}^{(1)}\,h_{1,y}\,\overline{\mu}_{\overline{T}}\,\overline{u}_s\,\hat{v}^{(2)}}{\mathrm{Re}\,h_1^2}$$
$$-\frac{2\,\mathrm{Ec}\,\Omega_{\mathrm{Re}}\,\hat{T}^{(1)}\,h_{3,y}\,\overline{\lambda}_{v\overline{T}}\,\overline{u}_s\,\hat{v}^{(2)}}{\mathrm{Re}\,h_1\,h_3}-\frac{2\,\mathrm{Ec}\,\Omega_{\mathrm{Re}}\,\hat{T}^{(1)}\,h_{1,y}\,\overline{\lambda}_{v\overline{T}}\,\overline{u}_s\,\hat{v}^{(2)}}{\mathrm{Re}\,h_1^2}$$
$$-\frac{4\,\mathrm{Ec}\,\Omega_{\mathrm{Re}}\,\hat{T}^{(1)}\,h_{3,s}\,h_{3,y}\,\overline{\mu}_{\overline{T}}\,\overline{u}\,\hat{v}^{(2)}}{\mathrm{Re}\,h_1\,h_3^2}+\frac{2\,\mathrm{i}\,\mathrm{Ec}\,\hat{T}^{(1)}\,\alpha^{(2)}\,h_{1,y}\,\overline{\mu}_{\overline{T}}\,\overline{u}\,\hat{v}^{(2)}}{\mathrm{Re}\,h_1^2}$$
$$-\frac{2\,\mathrm{Ec}\,\Omega_{\mathrm{Re}}\,\hat{T}^{(1)}\,h_{3,s}\,h_{3,y}\,\overline{\lambda}_{v\overline{T}}\,\overline{u}\,\hat{v}^{(2)}}{\mathrm{Re}\,h_1\,h_3^2}-\frac{2\,\mathrm{Ec}\,\Omega_{\mathrm{Re}}\,\hat{T}^{(1)}\,h_{1,y}\,h_{3,s}\,\overline{\lambda}_{v\overline{T}}\,\overline{u}\,\hat{v}^{(2)}}{\mathrm{Re}\,h_1^2\,h_3}$$
$$-\frac{\mathrm{Ec}\,\overline{T}\,\hat{\rho}_y^{(1)}\,\hat{v}^{(2)}}{\mathrm{M}^2\,\gamma}-\frac{\mathrm{Ec}\,\overline{T}_y\,\hat{\rho}^{(1)}\,\hat{v}^{(2)}}{\mathrm{M}^2\,\gamma}+\overline{T}_y\,\hat{\rho}^{(1)}\,\hat{v}^{(2)}-\frac{\mathrm{Ec}\,\hat{T}^{(1)}\,\overline{\rho}_y\,\hat{v}^{(2)}}{\mathrm{M}^2\,\gamma}$$
$$-\frac{\mathrm{Ec}\,\hat{T}_y^{(1)}\,\overline{\rho}\,\hat{v}^{(2)}}{\mathrm{M}^2\,\gamma}+\hat{T}_y^{(1)}\,\overline{\rho}\,\hat{v}^{(2)}-\frac{2\,\mathrm{i}\,\mathrm{Ec}\,\Omega_{\mathrm{Re}}\,\hat{T}^{(1)}\,\alpha^{(2)}\,\overline{\lambda}_{v\overline{T}}\,\hat{u}^{(2)}\,\overline{v}_y}{\mathrm{Re}\,h_1}$$
$$-\frac{4\,\mathrm{i}\,\mathrm{Ec}\,\Omega_{\mathrm{Re}}\,\hat{T}^{(1)}\,\alpha^{(2)}\,h_{1,y}\,\overline{\mu}_{\overline{T}}\,\hat{u}^{(2)}\,\overline{v}}{\mathrm{Re}\,h_1^2}-\frac{2\,\mathrm{i}\,\mathrm{Ec}\,\Omega_{\mathrm{Re}}\,\hat{T}^{(1)}\,\alpha^{(2)}\,h_{3,y}\,\overline{\lambda}_{v\overline{T}}\,\hat{u}^{(2)}\,\overline{v}}{\mathrm{Re}\,h_1\,h_3}$$
$$-\frac{2\,\mathrm{i}\,\mathrm{Ec}\,\Omega_{\mathrm{Re}}\,\hat{T}^{(1)}\,\alpha^{(2)}\,h_{1,y}\,\overline{\lambda}_{v\overline{T}}\,\hat{u}^{(2)}\,\overline{v}}{\mathrm{Re}\,h_1^2}-\frac{\mathrm{Ec}\,\hat{T}^{(1)}\,\hat{\rho}_y^{(2)}\,\overline{v}}{\mathrm{M}^2\,\gamma}-\frac{\mathrm{Ec}\,\hat{T}_y^{(1)}\,\hat{\rho}^{(2)}\,\overline{v}}{\mathrm{M}^2\,\gamma}$$
$$+\hat{T}_y^{(1)}\,\hat{\rho}^{(2)}\,\overline{v}-\frac{\mathrm{Ec}\,\overline{\mu}\,\hat{u}_y^{(1)}\,\hat{u}_y^{(2)}}{\mathrm{Re}}+\frac{2\,\mathrm{Ec}\,h_{1,y}\,\overline{\mu}\,\hat{u}^{(1)}\,\hat{u}_y^{(2)}}{\mathrm{Re}\,h_1}-\frac{2\,\mathrm{Ec}\,\hat{T}^{(1)}\,\overline{\mu}_{\overline{T}}\,\overline{u}_y\,\hat{u}_y^{(2)}}{\mathrm{Re}}$$
$$+\frac{2\,\mathrm{Ec}\,\hat{T}^{(1)}\,h_{1,y}\,\overline{\mu}_{\overline{T}}\,\overline{u}\,\hat{u}_y^{(2)}}{\mathrm{Re}\,h_1}-\frac{2\,\mathrm{i}\,\mathrm{Ec}\,\Omega_{\mathrm{Re}}\,\alpha^{(1)}\,\overline{\mu}\,\hat{u}^{(1)}\,\hat{u}_s^{(2)}}{\mathrm{Re}\,h_1^2}-\frac{\mathrm{i}\,\mathrm{Ec}\,\Omega_{\mathrm{Re}}\,\alpha^{(1)}\,\overline{\lambda}_v\,\hat{u}^{(1)}\,\hat{u}_s^{(2)}}{\mathrm{Re}\,h_1^2}$$
$$-\frac{2\,\mathrm{i}\,\mathrm{Ec}\,\Omega_{\mathrm{Re}}\,\alpha^{(2)}\,\overline{\mu}\,\hat{u}_s^{(1)}\,\hat{u}^{(2)}}{\mathrm{Re}\,h_1^2}-\frac{\mathrm{i}\,\mathrm{Ec}\,\Omega_{\mathrm{Re}}\,\alpha^{(2)}\,\overline{\lambda}_v\,\hat{u}_s^{(1)}\,\hat{u}^{(2)}}{\mathrm{Re}\,h_1^2}+\frac{\mathrm{Ec}\,{\beta_0}^2\,k^{(1)}\,k^{(2)}\,\overline{\mu}\,\hat{u}^{(1)}\,\hat{u}^{(2)}}{\mathrm{Re}\,h_3^2}$$
$$-\frac{\mathrm{Ec}\,\left(h_{1,y}\right)^2\,\overline{\mu}\,\hat{u}^{(1)}\,\hat{u}^{(2)}}{\mathrm{Re}\,h_1^2}+\frac{2\,\mathrm{Ec}\,\alpha^{(1)}\,\alpha^{(2)}\,\overline{\mu}\,\hat{u}^{(1)}\,\hat{u}^{(2)}}{\mathrm{Re}\,h_1^2}-\frac{2\,\mathrm{i}\,\mathrm{Ec}\,\Omega_{\mathrm{Re}}\,\alpha^{(2)}\,h_{3,s}\,\overline{\lambda}_v\,\hat{u}^{(1)}\,\hat{u}^{(2)}}{\mathrm{Re}\,h_1^2\,h_3}$$
$$+\frac{\mathrm{Ec}\,\alpha^{(1)}\,\alpha^{(2)}\,\overline{\lambda}_v\,\hat{u}^{(1)}\,\hat{u}^{(2)}}{\mathrm{Re}\,h_1^2}+\frac{2\,\mathrm{Ec}\,\hat{T}^{(1)}\,h_{1,y}\,\overline{\mu}_{\overline{T}}\,\overline{u}_y\,\hat{u}^{(2)}}{\mathrm{Re}\,h_1}-\frac{4\,\mathrm{i}\,\mathrm{Ec}\,\Omega_{\mathrm{Re}}\,\hat{T}^{(1)}\,\alpha^{(2)}\,\overline{\mu}_{\overline{T}}\,\overline{u}_s\,\hat{u}^{(2)}}{\mathrm{Re}\,h_1^2}$$
$$-\frac{2\,\mathrm{i}\,\mathrm{Ec}\,\Omega_{\mathrm{Re}}\,\hat{T}^{(1)}\,\alpha^{(2)}\,\overline{\lambda}_{v\overline{T}}\,\overline{u}_s\,\hat{u}^{(2)}}{\mathrm{Re}\,h_1^2}-\frac{2\,\mathrm{Ec}\,\hat{T}^{(1)}\,\left(h_{1,y}\right)^2\,\overline{\mu}_{\overline{T}}\,\overline{u}\,\hat{u}^{(2)}}{\mathrm{Re}\,h_1^2}$$
$$-\frac{2\,\mathrm{i}\,\mathrm{Ec}\,\Omega_{\mathrm{Re}}\,\hat{T}^{(1)}\,\alpha^{(2)}\,h_{3,s}\,\overline{\lambda}_{v\overline{T}}\,\overline{u}\,\hat{u}^{(2)}}{\mathrm{Re}\,h_1^2\,h_3}-\frac{\mathrm{Ec}\,\overline{T}\,\hat{\rho}_s^{(1)}\,\hat{u}^{(2)}}{\mathrm{M}^2\,\gamma\,h_1}-\frac{\mathrm{i}\,\mathrm{Ec}\,\overline{T}\,\alpha^{(1)}\,\hat{\rho}^{(1)}\,\hat{u}^{(2)}}{\mathrm{M}^2\,\gamma\,h_1}$$
$$-\frac{\mathrm{Ec}\,\overline{T}_s\,\hat{\rho}^{(1)}\,\hat{u}^{(2)}}{\mathrm{M}^2\,\gamma\,h_1}+\frac{\overline{T}_s\,\hat{\rho}^{(1)}\,\hat{u}^{(2)}}{h_1}-\frac{\mathrm{Ec}\,\hat{T}^{(1)}\,\overline{\rho}_s\,\hat{u}^{(2)}}{\mathrm{M}^2\,\gamma\,h_1}-\frac{\mathrm{i}\,\mathrm{Ec}\,\hat{T}^{(1)}\,\alpha^{(1)}\,\overline{\rho}\,\hat{u}^{(2)}}{\mathrm{M}^2\,\gamma\,h_1}$$
$$-\frac{\mathrm{Ec}\,\hat{T}_s^{(1)}\,\overline{\rho}\,\hat{u}^{(2)}}{\mathrm{M}^2\,\gamma\,h_1}+\frac{\mathrm{i}\,\hat{T}^{(1)}\,\alpha^{(1)}\,\overline{\rho}\,\hat{u}^{(2)}}{h_1}+\frac{\hat{T}_s^{(1)}\,\overline{\rho}\,\hat{u}^{(2)}}{h_1}-\frac{\mathrm{Ec}\,\hat{T}^{(1)}\,\hat{\rho}_s^{(2)}\,\overline{u}}{\mathrm{M}^2\,\gamma\,h_1}$$
$$-\frac{\mathrm{i}\,\mathrm{Ec}\,\hat{T}^{(1)}\,\alpha^{(2)}\,\hat{\rho}^{(2)}\,\overline{u}}{\mathrm{M}^2\,\gamma\,h_1}-\frac{\mathrm{i}\,\mathrm{Ec}\,\hat{T}^{(1)}\,\alpha^{(1)}\,\hat{\rho}^{(2)}\,\overline{u}}{\mathrm{M}^2\,\gamma\,h_1}-\frac{\mathrm{Ec}\,\hat{T}_s^{(1)}\,\hat{\rho}^{(2)}\,\overline{u}}{\mathrm{M}^2\,\gamma\,h_1}+\frac{\mathrm{i}\,\hat{T}^{(1)}\,\alpha^{(1)}\,\hat{\rho}^{(2)}\,\overline{u}}{h_1}$$

$$+\frac{\hat{T}_s^{(1)}\,\hat{\rho}^{(2)}\,\overline{u}}{h_1}+\frac{\mathrm{i}\,\mathrm{Ec}\,\hat{T}^{(1)}\,n^{(2)}\,\omega_0\,\hat{\rho}^{(2)}}{\mathrm{M}^2\,\gamma}+\frac{\mathrm{i}\,\mathrm{Ec}\,\hat{T}^{(1)}\,n^{(1)}\,\omega_0\,\hat{\rho}^{(2)}}{\mathrm{M}^2\,\gamma}-\mathrm{i}\,\hat{T}^{(1)}\,n^{(1)}\,\omega_0\,\hat{\rho}^{(2)}$$
$$+\frac{\hat{T}^{(1)}\,\hat{T}^{(2)}\,{\beta_0}^2\,\overline{\kappa}_{\overline{T}}\,\left(k^{(2)}\right)^2}{\mathrm{Pr}\,\mathrm{Re}\,h_3^2}+\frac{\hat{T}^{(1)}\,\hat{T}^{(2)}\,{\beta_0}^2\,\overline{\kappa}_{\overline{T}}\,k^{(1)}\,k^{(2)}}{\mathrm{Pr}\,\mathrm{Re}\,h_3^2}-\frac{\mathrm{i}\,\Omega_{\mathrm{Re}}\,\overline{T}_s\,\hat{T}^{(1)}\,\hat{T}^{(2)}\,\alpha^{(2)}\,\overline{\kappa}_{\overline{T}\,\overline{T}}}{\mathrm{Pr}\,\mathrm{Re}\,h_1^2}$$
$$-\frac{\overline{T}_y\,\hat{T}^{(1)}\,\hat{T}_y^{(2)}\,\overline{\kappa}_{\overline{T}\,\overline{T}}}{\mathrm{Pr}\,\mathrm{Re}}-\frac{\hat{T}^{(1)}\,\hat{T}_y^{(2)}\,h_{3,y}\,\overline{\kappa}_{\overline{T}}}{\mathrm{Pr}\,\mathrm{Re}\,h_3}-\frac{\mathrm{i}\,\Omega_{\mathrm{Re}}\,\hat{T}^{(1)}\,\hat{T}^{(2)}\,\alpha^{(2)}\,h_{3,s}\,\overline{\kappa}_{\overline{T}}}{\mathrm{Pr}\,\mathrm{Re}\,h_1^2\,h_3}$$
$$-\frac{\hat{T}^{(1)}\,\hat{T}_y^{(2)}\,h_{1,y}\,\overline{\kappa}_{\overline{T}}}{\mathrm{Pr}\,\mathrm{Re}\,h_1}+\frac{\mathrm{i}\,\Omega_{\mathrm{Re}}\,\hat{T}^{(1)}\,\hat{T}^{(2)}\,\alpha^{(2)}\,h_{1,s}\,\overline{\kappa}_{\overline{T}}}{\mathrm{Pr}\,\mathrm{Re}\,h_1^3}-\frac{\mathrm{i}\,\Omega_{\mathrm{Re}}\,\hat{T}^{(1)}\,\hat{T}^{(2)}\,\alpha_s^{(2)}\,\overline{\kappa}_{\overline{T}}}{\mathrm{Pr}\,\mathrm{Re}\,h_1^2}$$
$$+\frac{\hat{T}^{(1)}\,\hat{T}^{(2)}\,\left(\alpha^{(2)}\right)^2\,\overline{\kappa}_{\overline{T}}}{\mathrm{Pr}\,\mathrm{Re}\,h_1^2}+\frac{\hat{T}^{(1)}\,\hat{T}^{(2)}\,\alpha^{(1)}\,\alpha^{(2)}\,\overline{\kappa}_{\overline{T}}}{\mathrm{Pr}\,\mathrm{Re}\,h_1^2}-\frac{2\,\mathrm{i}\,\Omega_{\mathrm{Re}}\,\hat{T}^{(1)}\,\hat{T}_s^{(2)}\,\alpha^{(2)}\,\overline{\kappa}_{\overline{T}}}{\mathrm{Pr}\,\mathrm{Re}\,h_1^2}$$
$$-\frac{\mathrm{i}\,\Omega_{\mathrm{Re}}\,\hat{T}_s^{(1)}\,\hat{T}^{(2)}\,\alpha^{(2)}\,\overline{\kappa}_{\overline{T}}}{\mathrm{Pr}\,\mathrm{Re}\,h_1^2}-\frac{\mathrm{i}\,\Omega_{\mathrm{Re}}\,\hat{T}^{(1)}\,\hat{T}_s^{(2)}\,\alpha^{(1)}\,\overline{\kappa}_{\overline{T}}}{\mathrm{Pr}\,\mathrm{Re}\,h_1^2}-\frac{\hat{T}^{(1)}\,\hat{T}_{y\,y}^{(2)}\,\overline{\kappa}_{\overline{T}}}{\mathrm{Pr}\,\mathrm{Re}}-\frac{\hat{T}_y^{(1)}\,\hat{T}_y^{(2)}\,\overline{\kappa}_{\overline{T}}}{\mathrm{Pr}\,\mathrm{Re}}$$

B.5 Mass continuity: quadratic

$$\frac{-F^{\text{quad}}_{(m_1,m_2)}}{\mathcal{W}^{(1)}\mathcal{W}^{(2)}} =$$
$$\frac{\mathrm{i}\,\beta_0\,k^{(2)}\,\hat{\rho}^{(1)}\,\hat{w}^{(2)}}{h_3} + \frac{\mathrm{i}\,\beta_0\,k^{(1)}\,\hat{\rho}^{(1)}\,\hat{w}^{(2)}}{h_3} + \hat{\rho}^{(1)}\,\hat{v}^{(2)}_y + \hat{\rho}^{(1)}_y\,\hat{v}^{(2)} + \frac{h_{3,y}\,\hat{\rho}^{(1)}\,\hat{v}^{(2)}}{h_3}$$
$$+\frac{h_{1,y}\,\hat{\rho}^{(1)}\,\hat{v}^{(2)}}{h_1} + \frac{\hat{\rho}^{(1)}\,\hat{u}^{(2)}_s}{h_1} + \frac{\hat{\rho}^{(1)}_s\,\hat{u}^{(2)}}{h_1} + \frac{h_{3,s}\,\hat{\rho}^{(1)}\,\hat{u}^{(2)}}{h_1\,h_3} + \frac{\mathrm{i}\,\alpha^{(2)}\,\hat{\rho}^{(1)}\,\hat{u}^{(2)}}{h_1} + \frac{\mathrm{i}\,\alpha^{(1)}\,\hat{\rho}^{(1)}\,\hat{u}^{(2)}}{h_1}$$

B.6 Momentum conservation in the s-direction: cubic

Only convective terms on the left-hand side produce cubic terms. The pressure gradient and the viscous stress tensor do not possess third-order products in the conservation of momentum.

$$\frac{-F^{\text{cubic}}_{(m_1,m_2,m_3)}}{\mathcal{W}^{(1)}\mathcal{W}^{(2)}\mathcal{W}^{(3)}} = -\frac{h_{3,s}\,\hat{\rho}^{(1)}\,\hat{w}^{(2)}\,\hat{w}^{(3)}}{h_1\,h_3} + \frac{\mathrm{i}\,\beta_0\,k^{(2)}\,\hat{\rho}^{(1)}\,\hat{u}^{(2)}\,\hat{w}^{(3)}}{h_3} + \hat{\rho}^{(1)}\,\hat{u}^{(2)}_y\,\hat{v}^{(3)} + \frac{h_{1,y}\,\hat{\rho}^{(1)}\,\hat{u}^{(2)}\,\hat{v}^{(3)}}{h_1} + \frac{\hat{\rho}^{(1)}\,\hat{u}^{(2)}\,\hat{u}^{(3)}_s}{h_1} + \frac{\mathrm{i}\,\alpha^{(3)}\,\hat{\rho}^{(1)}\,\hat{u}^{(2)}\,\hat{u}^{(3)}}{h_1}$$

B.7 Momentum conservation in the y-direction: cubic

$$\frac{-F^{\text{cubic}}_{(m_1,m_2,m_3)}}{\mathcal{W}^{(1)}\mathcal{W}^{(2)}\mathcal{W}^{(3)}} = -\frac{h_{3,y}\,\hat{\rho}^{(1)}\,\hat{w}^{(2)}\,\hat{w}^{(3)}}{h_3} + \frac{\mathrm{i}\,\beta_0\,k^{(2)}\,\hat{\rho}^{(1)}\,\hat{v}^{(2)}\,\hat{w}^{(3)}}{h_3} + \hat{\rho}^{(1)}\,\hat{v}^{(2)}\,\hat{v}^{(3)}_y + \frac{\hat{\rho}^{(1)}\,\hat{u}^{(2)}\,\hat{v}^{(3)}_s}{h_1} + \frac{\mathrm{i}\,\alpha^{(3)}\,\hat{\rho}^{(1)}\,\hat{u}^{(2)}\,\hat{v}^{(3)}}{h_1} - \frac{h_{1,y}\,\hat{\rho}^{(1)}\,\hat{u}^{(2)}\,\hat{u}^{(3)}}{h_1}$$

B.8 Momentum conservation in the z-direction: cubic

$$\frac{-F^{\text{cubic}}_{(m_1,m_2,m_3)}}{\mathcal{W}^{(1)}\mathcal{W}^{(2)}\mathcal{W}^{(3)}} = \hat{\rho}^{(1)}\,\hat{v}^{(2)}\,\hat{w}^{(3)}_y + \frac{\hat{\rho}^{(1)}\,\hat{u}^{(2)}\,\hat{w}^{(3)}_s}{h_1} + \frac{\mathrm{i}\,\beta_0\,k^{(3)}\,\hat{\rho}^{(1)}\,\hat{w}^{(2)}\,\hat{w}^{(3)}}{h_3} + \frac{h_{3,y}\,\hat{\rho}^{(1)}\,\hat{v}^{(2)}\,\hat{w}^{(3)}}{h_3} + \frac{h_{3,s}\,\hat{\rho}^{(1)}\,\hat{u}^{(2)}\,\hat{w}^{(3)}}{h_1\,h_3} + \frac{\mathrm{i}\,\alpha^{(3)}\,\hat{\rho}^{(1)}\,\hat{u}^{(2)}\,\hat{w}^{(3)}}{h_1}$$

B.9 Conservation of energy (enthalpy formulation): cubic

$$
\begin{aligned}
\frac{-F^{\text{cubic}}_{(m_1,m_2,m_3)}}{\mathcal{W}^{(1)}\mathcal{W}^{(2)}\mathcal{W}^{(3)}} &= -\frac{\mathrm{Ec}\,\hat{T}^{(1)}\,\overline{\mu}_{\overline{T}}\,\hat{w}_y^{(2)}\,\hat{w}_y^{(3)}}{\mathrm{Re}} \\
&+\frac{2\,\mathrm{Ec}\,\hat{T}^{(1)}\,h_{3,y}\,\overline{\mu}_{\overline{T}}\,\hat{w}^{(2)}\,\hat{w}_y^{(3)}}{\mathrm{Re}\,h_3} - \frac{2\,\mathrm{i}\,\mathrm{Ec}\,\hat{T}^{(1)}\,\beta_0\,k^{(2)}\,\overline{\mu}_{\overline{T}}\,\hat{v}^{(2)}\,\hat{w}_y^{(3)}}{\mathrm{Re}\,h_3} \\
&-\frac{\mathrm{i}\,\mathrm{Ec}\,\Omega_{\mathrm{Re}}\,\hat{T}^{(1)}\,\alpha^{(2)}\,\overline{\mu}_{\overline{T}}\,\hat{w}^{(2)}\,\hat{w}_s^{(3)}}{\mathrm{Re}\,h_1^2} - \frac{2\,\mathrm{i}\,\mathrm{Ec}\,\Omega_{\mathrm{Re}}\,\hat{T}^{(1)}\,\beta_0\,k^{(2)}\,\overline{\mu}_{\overline{T}}\,\hat{u}^{(2)}\,\hat{w}_s^{(3)}}{\mathrm{Re}\,h_1\,h_3} \\
&-\frac{\mathrm{i}\,\mathrm{Ec}\,\Omega_{\mathrm{Re}}\,\hat{T}^{(1)}\,\alpha^{(3)}\,\overline{\mu}_{\overline{T}}\,\hat{w}_s^{(2)}\,\hat{w}^{(3)}}{\mathrm{Re}\,h_1^2} + \frac{2\,\mathrm{Ec}\,\hat{T}^{(1)}\,{\beta_0}^2\,k^{(2)}\,k^{(3)}\,\overline{\mu}_{\overline{T}}\,\hat{w}^{(2)}\,\hat{w}^{(3)}}{\mathrm{Re}\,h_3^2} \\
&-\frac{\mathrm{Ec}\,\hat{T}^{(1)}\,\left(h_{3,y}\right)^2\,\overline{\mu}_{\overline{T}}\,\hat{w}^{(2)}\,\hat{w}^{(3)}}{\mathrm{Re}\,h_3^2} + \frac{2\,\mathrm{i}\,\mathrm{Ec}\,\Omega_{\mathrm{Re}}\,\hat{T}^{(1)}\,\alpha^{(3)}\,h_{3,s}\,\overline{\mu}_{\overline{T}}\,\hat{w}^{(2)}\,\hat{w}^{(3)}}{\mathrm{Re}\,h_1^2\,h_3} \\
&+\frac{\mathrm{Ec}\,\hat{T}^{(1)}\,\alpha^{(2)}\,\alpha^{(3)}\,\overline{\mu}_{\overline{T}}\,\hat{w}^{(2)}\,\hat{w}^{(3)}}{\mathrm{Re}\,h_1^2} + \frac{\mathrm{Ec}\,\hat{T}^{(1)}\,{\beta_0}^2\,k^{(2)}\,k^{(3)}\,\overline{\lambda}_{v\overline{T}}\,\hat{w}^{(2)}\,\hat{w}^{(3)}}{\mathrm{Re}\,h_3^2} \\
&-\frac{2\,\mathrm{i}\,\mathrm{Ec}\,\hat{T}^{(1)}\,\beta_0\,k^{(3)}\,\overline{\lambda}_{v\overline{T}}\,\hat{v}_y^{(2)}\,\hat{w}^{(3)}}{\mathrm{Re}\,h_3} - \frac{4\,\mathrm{i}\,\mathrm{Ec}\,\hat{T}^{(1)}\,\beta_0\,h_{3,y}\,k^{(3)}\,\overline{\mu}_{\overline{T}}\,\hat{v}^{(2)}\,\hat{w}^{(3)}}{\mathrm{Re}\,h_3^2} \\
&+\frac{2\,\mathrm{i}\,\mathrm{Ec}\,\hat{T}^{(1)}\,\beta_0\,h_{3,y}\,k^{(2)}\,\overline{\mu}_{\overline{T}}\,\hat{v}^{(2)}\,\hat{w}^{(3)}}{\mathrm{Re}\,h_3^2} - \frac{2\,\mathrm{i}\,\mathrm{Ec}\,\hat{T}^{(1)}\,\beta_0\,h_{3,y}\,k^{(3)}\,\overline{\lambda}_{v\overline{T}}\,\hat{v}^{(2)}\,\hat{w}^{(3)}}{\mathrm{Re}\,h_3^2} \\
&-\frac{2\,\mathrm{i}\,\mathrm{Ec}\,\hat{T}^{(1)}\,\beta_0\,h_{1,y}\,k^{(3)}\,\overline{\lambda}_{v\overline{T}}\,\hat{v}^{(2)}\,\hat{w}^{(3)}}{\mathrm{Re}\,h_1\,h_3} - \frac{2\,\mathrm{i}\,\mathrm{Ec}\,\Omega_{\mathrm{Re}}\,\hat{T}^{(1)}\,\beta_0\,k^{(3)}\,\overline{\lambda}_{v\overline{T}}\,\hat{u}_s^{(2)}\,\hat{w}^{(3)}}{\mathrm{Re}\,h_1\,h_3} \\
&-\frac{4\,\mathrm{i}\,\mathrm{Ec}\,\Omega_{\mathrm{Re}}\,\hat{T}^{(1)}\,\beta_0\,h_{3,s}\,k^{(3)}\,\overline{\mu}_{\overline{T}}\,\hat{u}^{(2)}\,\hat{w}^{(3)}}{\mathrm{Re}\,h_1\,h_3^2} + \frac{2\,\mathrm{i}\,\mathrm{Ec}\,\Omega_{\mathrm{Re}}\,\hat{T}^{(1)}\,\beta_0\,h_{3,s}\,k^{(2)}\,\overline{\mu}_{\overline{T}}\,\hat{u}^{(2)}\,\hat{w}^{(3)}}{\mathrm{Re}\,h_1\,h_3^2} \\
&+\frac{2\,\mathrm{Ec}\,\hat{T}^{(1)}\,\alpha^{(3)}\,\beta_0\,k^{(2)}\,\overline{\mu}_{\overline{T}}\,\hat{u}^{(2)}\,\hat{w}^{(3)}}{\mathrm{Re}\,h_1\,h_3} - \frac{2\,\mathrm{i}\,\mathrm{Ec}\,\Omega_{\mathrm{Re}}\,\hat{T}^{(1)}\,\beta_0\,h_{3,s}\,k^{(3)}\,\overline{\lambda}_{v\overline{T}}\,\hat{u}^{(2)}\,\hat{w}^{(3)}}{\mathrm{Re}\,h_1\,h_3^2} \\
&+\frac{2\,\mathrm{Ec}\,\hat{T}^{(1)}\,\alpha^{(2)}\,\beta_0\,k^{(3)}\,\overline{\lambda}_{v\overline{T}}\,\hat{u}^{(2)}\,\hat{w}^{(3)}}{\mathrm{Re}\,h_1\,h_3} - \frac{\mathrm{i}\,\mathrm{Ec}\,\hat{T}^{(1)}\,\beta_0\,k^{(2)}\,\hat{\rho}^{(2)}\,\hat{w}^{(3)}}{\mathrm{M}^2\,\gamma\,h_3} \\
&-\frac{\mathrm{i}\,\mathrm{Ec}\,\hat{T}^{(1)}\,\beta_0\,k^{(1)}\,\hat{\rho}^{(2)}\,\hat{w}^{(3)}}{\mathrm{M}^2\,\gamma\,h_3} + \frac{\mathrm{i}\,\hat{T}^{(1)}\,\beta_0\,k^{(1)}\,\hat{\rho}^{(2)}\,\hat{w}^{(3)}}{h_3} - \frac{2\,\mathrm{Ec}\,\hat{T}^{(1)}\,\overline{\mu}_{\overline{T}}\,\hat{v}_y^{(2)}\,\hat{v}_y^{(3)}}{\mathrm{Re}} \\
&-\frac{\mathrm{Ec}\,\hat{T}^{(1)}\,\overline{\lambda}_{v\overline{T}}\,\hat{v}_y^{(2)}\,\hat{v}_y^{(3)}}{\mathrm{Re}} - \frac{2\,\mathrm{Ec}\,\hat{T}^{(1)}\,h_{3,y}\,\overline{\lambda}_{v\overline{T}}\,\hat{v}^{(2)}\,\hat{v}_y^{(3)}}{\mathrm{Re}\,h_3} - \frac{2\,\mathrm{Ec}\,\hat{T}^{(1)}\,h_{1,y}\,\overline{\lambda}_{v\overline{T}}\,\hat{v}^{(2)}\,\hat{v}_y^{(3)}}{\mathrm{Re}\,h_1} \\
&-\frac{2\,\mathrm{Ec}\,\Omega_{\mathrm{Re}}\,\hat{T}^{(1)}\,\overline{\lambda}_{v\overline{T}}\,\hat{u}_s^{(2)}\,\hat{v}_y^{(3)}}{\mathrm{Re}\,h_1} - \frac{2\,\mathrm{Ec}\,\Omega_{\mathrm{Re}}\,\hat{T}^{(1)}\,h_{3,s}\,\overline{\lambda}_{v\overline{T}}\,\hat{u}^{(2)}\,\hat{v}_y^{(3)}}{\mathrm{Re}\,h_1\,h_3} \\
&-\frac{2\,\mathrm{i}\,\mathrm{Ec}\,\hat{T}^{(1)}\,\alpha^{(2)}\,\overline{\lambda}_{v\overline{T}}\,\hat{u}^{(2)}\,\hat{v}_y^{(3)}}{\mathrm{Re}\,h_1} - \frac{\mathrm{i}\,\mathrm{Ec}\,\Omega_{\mathrm{Re}}\,\hat{T}^{(1)}\,\alpha^{(2)}\,\overline{\mu}_{\overline{T}}\,\hat{v}^{(2)}\,\hat{v}_s^{(3)}}{\mathrm{Re}\,h_1^2}
\end{aligned}
$$

$$-\frac{2\,\mathrm{Ec}\,\Omega_{\mathrm{Re}}\,\hat{T}^{(1)}\,\overline{\mu}_{\overline{T}}\,\hat{u}_y^{(2)}\,\hat{v}_s^{(3)}}{\mathrm{Re}\,h_1}+\frac{2\,\mathrm{Ec}\,\Omega_{\mathrm{Re}}\,\hat{T}^{(1)}\,h_{1,y}\,\overline{\mu}_{\overline{T}}\,\hat{u}^{(2)}\,\hat{v}_s^{(3)}}{\mathrm{Re}\,h_1^2}-\frac{\mathrm{i}\,\mathrm{Ec}\,\Omega_{\mathrm{Re}}\,\hat{T}^{(1)}\,\alpha^{(3)}\,\overline{\mu}_{\overline{T}}\,\hat{v}_s^{(2)}\,\hat{v}^{(3)}}{\mathrm{Re}\,h_1^2}$$
$$+\frac{\mathrm{Ec}\,\hat{T}^{(1)}\,{\beta_0}^2\,k^{(2)}\,k^{(3)}\,\overline{\mu}_{\overline{T}}\,\hat{v}^{(2)}\,\hat{v}^{(3)}}{\mathrm{Re}\,h_3^2}-\frac{2\,\mathrm{Ec}\,\hat{T}^{(1)}\,\left(h_{3,y}\right)^2\,\overline{\mu}_{\overline{T}}\,\hat{v}^{(2)}\,\hat{v}^{(3)}}{\mathrm{Re}\,h_3^2}$$
$$-\frac{2\,\mathrm{Ec}\,\hat{T}^{(1)}\,\left(h_{1,y}\right)^2\,\overline{\mu}_{\overline{T}}\,\hat{v}^{(2)}\,\hat{v}^{(3)}}{\mathrm{Re}\,h_1^2}+\frac{\mathrm{Ec}\,\hat{T}^{(1)}\,\alpha^{(2)}\,\alpha^{(3)}\,\overline{\mu}_{\overline{T}}\,\hat{v}^{(2)}\,\hat{v}^{(3)}}{\mathrm{Re}\,h_1^2}$$
$$-\frac{\mathrm{Ec}\,\hat{T}^{(1)}\,\left(h_{3,y}\right)^2\,\overline{\lambda}_{v\overline{T}}\,\hat{v}^{(2)}\,\hat{v}^{(3)}}{\mathrm{Re}\,h_3^2}-\frac{2\,\mathrm{Ec}\,\hat{T}^{(1)}\,h_{1,y}\,h_{3,y}\,\overline{\lambda}_{v\overline{T}}\,\hat{v}^{(2)}\,\hat{v}^{(3)}}{\mathrm{Re}\,h_1\,h_3}$$
$$-\frac{\mathrm{Ec}\,\hat{T}^{(1)}\,\left(h_{1,y}\right)^2\,\overline{\lambda}_{v\overline{T}}\,\hat{v}^{(2)}\,\hat{v}^{(3)}}{\mathrm{Re}\,h_1^2}-\frac{2\,\mathrm{i}\,\mathrm{Ec}\,\hat{T}^{(1)}\,\alpha^{(3)}\,\overline{\mu}_{\overline{T}}\,\hat{u}_y^{(2)}\,\hat{v}^{(3)}}{\mathrm{Re}\,h_1}$$
$$-\frac{4\,\mathrm{Ec}\,\Omega_{\mathrm{Re}}\,\hat{T}^{(1)}\,h_{1,y}\,\overline{\mu}_{\overline{T}}\,\hat{u}_s^{(2)}\,\hat{v}^{(3)}}{\mathrm{Re}\,h_1^2}-\frac{2\,\mathrm{Ec}\,\Omega_{\mathrm{Re}}\,\hat{T}^{(1)}\,h_{3,y}\,\overline{\lambda}_{v\overline{T}}\,\hat{u}_s^{(2)}\,\hat{v}^{(3)}}{\mathrm{Re}\,h_1\,h_3}$$
$$-\frac{2\,\mathrm{Ec}\,\Omega_{\mathrm{Re}}\,\hat{T}^{(1)}\,h_{1,y}\,\overline{\lambda}_{v\overline{T}}\,\hat{u}_s^{(2)}\,\hat{v}^{(3)}}{\mathrm{Re}\,h_1^2}-\frac{4\,\mathrm{Ec}\,\Omega_{\mathrm{Re}}\,\hat{T}^{(1)}\,h_{3,s}\,h_{3,y}\,\overline{\mu}_{\overline{T}}\,\hat{u}^{(2)}\,\hat{v}^{(3)}}{\mathrm{Re}\,h_1\,h_3^2}$$
$$+\frac{2\,\mathrm{i}\,\mathrm{Ec}\,\hat{T}^{(1)}\,\alpha^{(3)}\,h_{1,y}\,\overline{\mu}_{\overline{T}}\,\hat{u}^{(2)}\,\hat{v}^{(3)}}{\mathrm{Re}\,h_1^2}-\frac{4\,\mathrm{i}\,\mathrm{Ec}\,\hat{T}^{(1)}\,\alpha^{(2)}\,h_{1,y}\,\overline{\mu}_{\overline{T}}\,\hat{u}^{(2)}\,\hat{v}^{(3)}}{\mathrm{Re}\,h_1^2}$$
$$-\frac{2\,\mathrm{Ec}\,\Omega_{\mathrm{Re}}\,\hat{T}^{(1)}\,h_{3,s}\,h_{3,y}\,\overline{\lambda}_{v\overline{T}}\,\hat{u}^{(2)}\,\hat{v}^{(3)}}{\mathrm{Re}\,h_1\,h_3^2}-\frac{2\,\mathrm{i}\,\mathrm{Ec}\,\hat{T}^{(1)}\,\alpha^{(2)}\,h_{3,y}\,\overline{\lambda}_{v\overline{T}}\,\hat{u}^{(2)}\,\hat{v}^{(3)}}{\mathrm{Re}\,h_1\,h_3}$$
$$-\frac{2\,\mathrm{Ec}\,\Omega_{\mathrm{Re}}\,\hat{T}^{(1)}\,h_{1,y}\,h_{3,s}\,\overline{\lambda}_{v\overline{T}}\,\hat{u}^{(2)}\,\hat{v}^{(3)}}{\mathrm{Re}\,h_1^2\,h_3}-\frac{2\,\mathrm{i}\,\mathrm{Ec}\,\hat{T}^{(1)}\,\alpha^{(2)}\,h_{1,y}\,\overline{\lambda}_{v\overline{T}}\,\hat{u}^{(2)}\,\hat{v}^{(3)}}{\mathrm{Re}\,h_1^2}$$
$$-\frac{\mathrm{Ec}\,\hat{T}^{(1)}\,\hat{\rho}_y^{(2)}\,\hat{v}^{(3)}}{\mathrm{M}^2\,\gamma}-\frac{\mathrm{Ec}\,\hat{T}_y^{(1)}\,\hat{\rho}^{(2)}\,\hat{v}^{(3)}}{\mathrm{M}^2\,\gamma}+\hat{T}_y^{(1)}\,\hat{\rho}^{(2)}\,\hat{v}^{(3)}-\frac{\mathrm{Ec}\,\hat{T}^{(1)}\,\overline{\mu}_{\overline{T}}\,\hat{u}_y^{(2)}\,\hat{u}_y^{(3)}}{\mathrm{Re}}$$
$$+\frac{2\,\mathrm{Ec}\,\hat{T}^{(1)}\,h_{1,y}\,\overline{\mu}_{\overline{T}}\,\hat{u}^{(2)}\,\hat{u}_y^{(3)}}{\mathrm{Re}\,h_1}-\frac{2\,\mathrm{i}\,\mathrm{Ec}\,\Omega_{\mathrm{Re}}\,\hat{T}^{(1)}\,\alpha^{(2)}\,\overline{\mu}_{\overline{T}}\,\hat{u}^{(2)}\,\hat{u}_s^{(3)}}{\mathrm{Re}\,h_1^2}$$
$$-\frac{\mathrm{i}\,\mathrm{Ec}\,\Omega_{\mathrm{Re}}\,\hat{T}^{(1)}\,\alpha^{(2)}\,\overline{\lambda}_{v\overline{T}}\,\hat{u}^{(2)}\,\hat{u}_s^{(3)}}{\mathrm{Re}\,h_1^2}-\frac{2\,\mathrm{i}\,\mathrm{Ec}\,\Omega_{\mathrm{Re}}\,\hat{T}^{(1)}\,\alpha^{(3)}\,\overline{\mu}_{\overline{T}}\,\hat{u}_s^{(2)}\,\hat{u}^{(3)}}{\mathrm{Re}\,h_1^2}$$
$$-\frac{\mathrm{i}\,\mathrm{Ec}\,\Omega_{\mathrm{Re}}\,\hat{T}^{(1)}\,\alpha^{(3)}\,\overline{\lambda}_{v\overline{T}}\,\hat{u}_s^{(2)}\,\hat{u}^{(3)}}{\mathrm{Re}\,h_1^2}+\frac{\mathrm{Ec}\,\hat{T}^{(1)}\,{\beta_0}^2\,k^{(2)}\,k^{(3)}\,\overline{\mu}_{\overline{T}}\,\hat{u}^{(2)}\,\hat{u}^{(3)}}{\mathrm{Re}\,h_3^2}$$
$$-\frac{\mathrm{Ec}\,\hat{T}^{(1)}\,\left(h_{1,y}\right)^2\,\overline{\mu}_{\overline{T}}\,\hat{u}^{(2)}\,\hat{u}^{(3)}}{\mathrm{Re}\,h_1^2}+\frac{2\,\mathrm{Ec}\,\hat{T}^{(1)}\,\alpha^{(2)}\,\alpha^{(3)}\,\overline{\mu}_{\overline{T}}\,\hat{u}^{(2)}\,\hat{u}^{(3)}}{\mathrm{Re}\,h_1^2}$$
$$-\frac{2\,\mathrm{i}\,\mathrm{Ec}\,\Omega_{\mathrm{Re}}\,\hat{T}^{(1)}\,\alpha^{(3)}\,h_{3,s}\,\overline{\lambda}_{v\overline{T}}\,\hat{u}^{(2)}\,\hat{u}^{(3)}}{\mathrm{Re}\,h_1^2\,h_3}+\frac{\mathrm{Ec}\,\hat{T}^{(1)}\,\alpha^{(2)}\,\alpha^{(3)}\,\overline{\lambda}_{v\overline{T}}\,\hat{u}^{(2)}\,\hat{u}^{(3)}}{\mathrm{Re}\,h_1^2}$$
$$-\frac{\mathrm{Ec}\,\hat{T}^{(1)}\,\hat{\rho}_s^{(2)}\,\hat{u}^{(3)}}{\mathrm{M}^2\,\gamma\,h_1}-\frac{\mathrm{i}\,\mathrm{Ec}\,\hat{T}^{(1)}\,\alpha^{(2)}\,\hat{\rho}^{(2)}\,\hat{u}^{(3)}}{\mathrm{M}^2\,\gamma\,h_1}-\frac{\mathrm{i}\,\mathrm{Ec}\,\hat{T}^{(1)}\,\alpha^{(1)}\,\hat{\rho}^{(2)}\,\hat{u}^{(3)}}{\mathrm{M}^2\,\gamma\,h_1}-\frac{\mathrm{Ec}\,\hat{T}_s^{(1)}\,\hat{\rho}^{(2)}\,\hat{u}^{(3)}}{\mathrm{M}^2\,\gamma\,h_1}$$
$$+\frac{\mathrm{i}\,\hat{T}^{(1)}\,\alpha^{(1)}\,\hat{\rho}^{(2)}\,\hat{u}^{(3)}}{h_1}+\frac{\hat{T}_s^{(1)}\,\hat{\rho}^{(2)}\,\hat{u}^{(3)}}{h_1}$$

B.10 Mass continuity: cubic

There are no terms to generate any third-order products in mass continuity.

$$\frac{F^{\text{cubic}}_{(m_1,m_2,m_3)}}{\mathcal{W}^{(1)}\mathcal{W}^{(2)}\mathcal{W}^{(3)}} = 0$$